



Dedicated to building research infrastructure and the promotion of Science, Technology, Engineering and Math (STEM) education in West Virginia

2015–2016 STUDENT RESEARCH REPORTS

Summer Internships

Undergraduate Research Fellowship Program

Graduate Research Fellowship Program

NASA West Virginia Space Grant Consortium
West Virginia University
PO Box 6070
Morgantown, WV 26506-6070
(304) 293-4099

www.wvspacegrant.org

Published July 2016



PREFACE

The National Space Grant College and Fellowship Program (also known as Space Grant) was first established under Title II of the National Aeronautics and Space Administration (NASA) Authorization Act of 1988 (P.L. 100-147). Space Grant is a unique national state-based network in 50 states, Puerto Rico and the District of Columbia. The program is a component of NASA's Education Directorate portfolio charged with carrying out effective education, research, and public outreach activities in science, technology, engineering and mathematics (STEM), particularly in fields most relevant to NASA's future workforce.

Currently, Space Grant is comprised of 52 consortia that engage over 1,000 affiliates nationally, including more than 600 colleges/universities, and state, industry, non-profit and federal partners, including NASA Centers. They work collectively to meet the nation's needs for developing and training a high-tech workforce to sustain a robust U.S. space science and space exploration program.

As one of the 52 university-based Space Grant consortia, the West Virginia Space Grant Consortium (WVSGC or Consortium) was established in August 1991. The Consortium is housed in the Benjamin M. Statler College of Engineering and Mineral Resources on the Evansdale Campus of West Virginia University in Morgantown, West Virginia. It is comprised of 12 West Virginia academic institutions and 8 corporate and scientific partners (a list of affiliates is listed on page 2). It is dedicated to building research infrastructure and promoting STEM education in West Virginia. The Consortium's programs focus on research, collaborations with high technology industries, student fellowships as well as K-12, and public outreach programs. This is consistent with the strategic vision for the state's participation in the nation's current and future endeavors in science and technology.

This publication is a compilation of student reports from summer internships, the NASA Undergraduate Research Fellowship Program and the NASA Graduate Research Fellowship Program for the 2015- 2016 fiscal year.

On behalf of the Board of Directors of NASA WVSGC, we would like to take this opportunity to express our appreciation to students who applied for these programs, the mentoring offered to West Virginia students by their faculty advisors in their research projects as well as the different internship locations that provided these opportunities. Without them, our internships and fellowship programs would not be where they are today: a crucial step in the workforce development pipeline for NASA and the high technology sector in the United States.

For additional information on our programs, please contact our office or visit wvspacegrant.org.

CONSORTIUM AFFILIATES

West Virginia University (Lead)

Bethany College

Bluefield State College

Fairmont State University

Glenville State College

Marshall University

NASA Independent Verification & Validation Facility

National Radio Astronomy Observatory

Polyhedron Learning Media, Inc.

Shepherd University

TechConnect WV

The Clay Center for the Arts and Sciences of West Virginia

TMC Technologies, Inc.

West Liberty University

WV High Technology Consortium Foundation

West Virginia State University

WVU Institute of Technology

West Virginia Wesleyan College

Wheeling Jesuit University

Table of Contents

LIST OF PROGRAMS	1
I. SUMMER INTERNSHIPS	1
II. NASA WVSGC UNDERGRADUATE RESEARCH FELLOWSHIP PROGRAM ...	2
III. NASA WVSGC GRADUATE RESEARCH FELLOWSHIP PROGRAM	4
I. Summer Internships Reports	6
Cavender, Hannah. West Virginia State University. <i>Synthesizing and Trialing Triesterified Monosaccharides on the Biocontrol Generalist Predator, Green Lacewig, Chrysoperia rufilabris</i>	7
Gosnell, Taylor. West Virginia University. <i>Development of a System for Extended Depth of Field Imaging</i>	19
Itschner, Jonathan. West Virginia University. <i>Temperature and Flow Rate Sensor Fabrication</i>	38
Katrib, Alnairouz. West Virginia State University. <i>Anti-tumor Activity of Organometallic Compounds</i>	46
Kosko, Steven. West Virginia University. <i>Long-Duration, Low-Gravity Propellant Sloshing Experiment</i>	56
Liounis, Andrew. West Virginia University. <i>Simultaneous Localization and Mapping of Small Planetary Bodies</i>	61
Mardmomen, Nadia. West Virginia University. <i>A Meta-analysis of Distinct Audio-visual, Multimodal Interaction Sites in the Human Brain</i>	68
Riley, Amelia. West Virginia Wesleyan College. <i>Materials Research into Nanotubes</i>	76
Zober, Wolfgang. Wheeling Jesuit University. <i>Solar Physics using Laser Spectroscopy of Sodium in the Earth Mesosphere</i>	89
II. NASA WVSGC Undergraduate Research Fellowship Reports	98
Beard, Jared. West Virginia University. <i>Patterning and Characterization of Direct Written Inks and Films for Extraterrestrial Solar Cell Applications</i>	99
Flamenco, Evelin. West Virginia University. <i>Leaf Angle Phenology: Implications for Carbon, Energy, and Water Fluxes from Forests in the Anthropocene</i>	107
Garretson, Samantha. Marshall University. <i>Modification of Nitinol Nanoparticles with Phosphonic Acid Films</i>	113
Hager, Lydia. Marshall University. <i>Fibrin-based Microenvironments for Recruitment of Adult Neural Stem Cells</i>	118
Hensley, Andrea. Marshall University. <i>DNA Origami Platform for Protein Fluorescence Enhancement with Gold Nanoparticles</i>	127

Holland, Aaron. Marshall University. <i>Isotopic Characterization of Lipid Content in Chlorella Vulgaris</i>	138
Kastigar, Alexis. Marshall University. <i>Investigation of Enzymatic Mechanism and Cellular Expression of DPY-19L4</i>	144
Krasny, Magdalena. West Virginia University. <i>Analytical Comparison of Electrode Material for use with Plasma Dielectric Barrier Discharge Actuators with Experimental Validation</i>	150
Melroy, Samantha. West Virginia University. <i>Terra Response – Detection of Underground Amonalies</i>	157
Ohi, Nicholas. West Virginia University. <i>Precise Orbit Determination on STF-1 CubeSat Mission</i>	167
Poultney, Marissa. West Virginia University. <i>Remote Sensing Water Body Extaction and Downscaling</i>	176
Searls, Noah. Marshall University. <i>Polymorphism: Changing Active Pharmaceuticals by Surface Modification</i>	186
Sias, Eric. Marshall University. <i>The Thermal Decomposition of 4-Nitrosooxy-2-Butanone</i> . ..	197
Szeligo, Brett. Wheeling Jesuit University. <i>Preparation and Stability of Cis-Dicarbonylbis(dibenzylthiocarbamato)Iron(II)</i>	207
Wiseman, Robyn. West Virginia University. <i>Discrimination of Inkjet Printer Inks using Raman by Laser Induced Breakdown Spectroscopy</i>	214
III. NASA WVSGC Graduate Research Fellowship Reports.....	222
Amos, Deborah. Marshall University. <i>Exercise Improves Skeletal Muscle Function in the ‘Stress-less’ Mouse</i>	223
Cooper, Robert. Marshall University. <i>Effects of Low-level Silver Nanoparticle Exposure on Adult Neural Stem Cell Differentiation</i>	233
Cordonier, John. West Virginia University. <i>Modeling and Simulation of a Direct-wire Manufacturing Process</i>	250
Cox, Jordan. West Virginia University. <i>Comparative Analysis of Uninhibited and Constrained Avian Wing Aerodynamics</i>	260
Heres, Berlynn. Marshall University. <i>Ambush Site Selection in Eastern Diamondback Rattlesnakes (Crotalus Adamanteus)</i>	270
Hunter, Caroline. Marshall University. <i>Fyn-dependent Phosphorylation of Mitochondrial Elongation Factor Tu May Lead to Metabolic Syndrome by Mitochondrial Dysfunction</i>	280
Murphy, Rachel. Marshall University. <i>Tenofovir Induced Nephrotoxicity: A Mechanistic Study</i>	295
Sivaneri, Victor. West Virginia University. <i>Collaborative Navigation Between a Ground Vehicle and an Unmanned Aerial Vehicle in GNSS-Challenged Environments</i>	305

Spada, Vincent. West Virginia University. *Research and Development of a Multi Component Balance System for Wind Tunnel Applications.* 314

Tomblin, Justin. Marshall University. *Aryl Hydrocarbon Receptor Regulation of L-Type Amino Acid Transporter 1 (LAT1) in Breast Cancer Cells.* 325

LIST OF PROGRAMS

I. SUMMER INTERNSHIPS

For the 2015–2016 fiscal year, we have eight undergraduate and one graduate students who successfully received internship opportunities. Below is a list of their names, the university they attend, the internship facility as well as their research topic. A copy of their research reports is included under Section I.

Cavender, Hannah

University: West Virginia State University

Location: West Virginia State University

Research: *Synthesizing and Trialing Triesterified Monosaccharides on the Biocontrol Generalist Predator, Green Lacewing, Chrysoperia rufilabris*

Gosnell, Taylor

University: West Virginia University

Location: NASA Goddard Space Flight Facility

Research: *Development of a System for Extended Depth of Field Imaging*

Itschner, Jonathan

University: West Virginia University

Location: NASA Goddard Space Flight Facility

Research: *Temperature and Flow Rate Sensor Fabrication*

Katrib, Alnairouz

University: West Virginia State University

Location: West Virginia State University

Research: *Anti-tumor Activity of Organometallic Compounds*

Kosko, Steven

University: West Virginia University

Location: NASA Goddard Space Flight Facility

Research: *Long-Duration, Low-Gravity Propellant Sloshing Experiment*

Liounis, Andrew

University: West Virginia University

Location: NASA Goddard Space Flight Facility

Research: *Simultaneous Localization and Mapping of Small Planetary Bodies*

Mardmomen, Nadia

University: West Virginia University

Location: West Virginia University Health Sciences Center, Erma Byrd Biomedical Building

Research: *A Meta-analysis of Distinct Audio-visual, Multimodal Interaction Sites in the Human Brain*

Riley, Amelia

University: West Virginia Wesleyan College
Location: West Virginia Wesleyan College
Research: *Materials Research into Nanotubes*

Zober, Wolfgang

University: Wheeling Jesuit University
Location: NASA Goddard Space Flight Facility
Research: *Solar Physics Using Laser Spectroscopy of Sodium in the Earth Mesosphere*

II. NASA WVSGC UNDERGRADUATE RESEARCH FELLOWSHIP PROGRAM

The NASA WVSGC Undergraduate Research Fellowship Program provides support for undergraduate students under the supervision of their academic advisor. For the 2015-2016 fiscal year, we have fifteen undergraduate students who were awarded research fellowships. Below is a list of their names, the university they attend, their mentor as well as their research topic. A copy of their research reports is included under Section II.

Beard, Jared

University: West Virginia University
Mentor: Dr. Konstatinos Sierros
Research: *Patterning and Characterization of Direct Written Inks and Films for Extraterrestrial Solar Cell Applications*

Flamenco, Evelin

University: West Virginia University
Mentor: Dr. Brenden McNeil
Research: *Leaf Angle Phenology: Implications for Carbon, Energy, and Water Fluxes from Forests in the Anthropocene*

Garretson, Samantha

University: Marshall University
Mentor: Dr. Rosalynn Quiones
Research: *Modification of Nitinol Nanoparticles with Phosphonic Acid Films*

Hager, Lydia

University: Marshall University
Mentor: Dr. Elmer Price
Research: *Fibrin-based Microenvironments for Recruitment of Adult Neural Stem Cells*

Hensley, Andrea

University: Marshall University
Mentor: Dr. Michael Norton
Research: *DNA Origami Platform for Protein Fluorescence Enhancement with Gold Nanoparticles*

Holland, Aaron

University: Marshall University
Mentor: Dr. Derrick Kolling
Research: *Isotopic Characterization of Lipid Content in Chlorella Vulgaris*

Kastigar, Alexis

University: Marshall University
Mentor: Dr. John Rakus
Research: *Investigation of Enzymatic Mechanism and Cellular Expression of DPY-19L4*

Krasny, Magdalena

University: West Virginia University
Mentor: Dr. Patrick Browning
Research: *Analytical Comparison of Electrode Material for use with Plasma Dielectric Barrier Discharge Actuators with Experimental Validation*

Melroy, Samantha

University: West Virginia University
Mentor: Dr. James Smith
Research: *Terra Response – Detection of Underground Amonalies*

Ohi, Nicholas

University: West Virginia University
Mentor: Dr. Jason Gross
Research: *Precise Orbit Determination on STF-1 CubeSat Mission*

Poultney, Marissa

University: West Virginia University
Mentor: Dr. Autar Jutla
Research: *Remote Sensing Water Body Extaction and Downscaling*

Searls, Noah

University: Marshall University
Mentor: Dr. Rosalynn Quiones
Research: *Polymorphism: Changing Active Pharmaceuticals by Surface Modification*

Sias, Eric

University: Marshall University
Mentor: Dr. Laura McCunn
Research: *The Thermal Decomposition of 4-Nitrosooxy-2-Butanone*

Szeligo, Brett

University: Wheeling Jesuit University
Mentor: Dr. James Coffield
Research: *Preparation and Stability of Cis-Dicarbonylbis (dibenzylthiocarbamate) Iron (II)*

Wiseman, Robyn

University: West Virginia University

Mentor: Dr. Patrick Buzzini

Research: *Discrimination of Inkjet Printer Inks using Raman by Laser Induced Breakdown Spectroscopy*

III. NASA WVSGC GRADUATE RESEARCH FELLOWSHIP PROGRAM

The NASA WVSGC Graduate Research Fellowship Program provides funding for graduate students working on a thesis or dissertation with faculty from member institutions. For the 2015-2016 fiscal year, we have ten graduate students who were awarded research fellowships. Below is a list of their names, the university they attend, their mentor as well as their research topic. A copy of their research reports is included under Section III.

Amos, Deborah

University: Marshall University

Mentor: Dr. Nalini Santanam

Research: *Exercise Improves Skeletal Muscle Function in the 'Stress-less' Mouse*

Cooper, Robert

University: Marshall University

Mentor: Dr. Nadja Spitzer

Research: *Effects of Low-level Silver Nanoparticle Exposure on Adult Neural Stem Cell Differentiation*

Cordonier, John

University: West Virginia University

Mentor: Dr. Debangsu Bhattacharyya

Research: *Modeling and Simulation of a Direct-wire Manufacturing Process*

Cox, Jordan

University: West Virginia University

Mentor: Dr. Patrick Browning

Research: *Comparative Analysis of Uninhibited and Constrained Avian Wing Aerodynamics*

Heres, Berlyna

University: Marshall University

Mentor: Dr. Jayme Waldron

Research: *Ambush Site Selection in Eastern Diamondback Rattlesnakes (*Crotalus Adamanteus*)*

Hunter, Caroline

University: Marshall University

Mentor: Dr. Emine Koc

Research: *Fyn-dependent Phosphorylation of Mitochondrial Elongation Factor Tu May Lead to Metabolic Syndrome by Mitochondrial Dysfunction*

Murphy, Rachel

University: Marshall University

Mentor: Dr. Monica Vazentovic

Research: *Tenofovir Induced Nephrotoxicity: A Mechanistic Study*

Sivaneri, Victor

University: West Virginia University

Mentor: Dr. Jason Gross

Research: *Collaborative Navigation Between a Ground Vehicle and an Unmanned Aerial Vehicle in GNSS-Challenged Environments*

Spada, Vincent

University: West Virginia University

Mentor: Dr. Peter Gall

Research: *Research and Development of a Multi Component Balance System for Wind Tunnel Applications*

Tomblin, Justin

University: Marshall University

Mentor: Dr. Travis Salisbury

Research: *Aryl Hydrocarbon Receptor Regulation of L-Type Amino Acid Transporter 1 (LAT1) in Breast Cancer Cells*

I. Summer Internships Reports

SYNTHESIZING AND TRIALING TRIESTERIFIED MONOSACCHARIDES ON THE BIOCONTROL GENERALIST PREDATOR, GREEN LACEWING, *CHRYSOPERIA RUFILABRIS*

Hannah Cavender
Biology
West Virginia State University
Institute, WV 25112

PROJECT SUMMARY

Protected culture production of most crops including tomatoes use biological controls, such as *Chrysoperia rufilabris*, as a part of their integrated pest management (IPM) program. Thus, it is important to assess any changes in the production system and how they will affect the IPM system being used before implementation. Breeding acylsugar mediated resistance into tomato varieties for the protected culture system offers the potential to control whiteflies and aphids, the two top insect pests. However, no research has assessed these compounds potential effects on biological control agents. Acylsugars could prove to be an environmentally friendlier alternative to harsh pesticides, so optimizing their natural production would be ideal.

Our first step will be synthesize specific acylsugars in order to quantify their effects on biological controls in the greenhouse. The target compound was investigated from a retrosynthetic perspective, which allowed for the development of a synthetic route. The procedure follows a five-step synthesis beginning with an initial selective protection of the primary hydroxyl group with the silyl ether. The anomeric carbon is then protected with a sulfide (Tanaka, Matsumoto et al. 2009) and the remaining positions 2, 3 and 4 are then esterified with excess acid chlorides. The final two steps are deprotections of the primary hydroxyl position and the anomeric position (Holton, Kim et al. 1994, Waschke, Leshch et al. 2012).

After the completion of the synthesis and complete characterization of the acyl glucoses, the product was ready for trialing on the biological control, *Chrysoperia rufilabris*. The method of trialing is based off of a newer modified exposure assay that involves multiple routes of subjection including oral, direct, and residual (Amarasekare and Shearer 2013). Following exposure, the larval stages were monitored for examination of lethal and sub-lethal affects. Any changes in fecundity and fertility in adults emerging from larval trial will also be investigated. The following report focuses on the data collected from the trialing portion of the project.

BACKGROUND

According to the USDA, the United States is in the lead in the worldwide production of tomatoes. California and Florida each produce fresh-market tomatoes on 30,000-40,000 acres, accounting

for two-thirds of the total U.S. fresh market varieties (Thornsbury 2012). Tomatoes can be grown by one of two production systems: in open-field or in protected culture. Protected culture systems vary from being highly sophisticated with large scale greenhouses, to less advanced systems with high and micro tunnels (Welbaum 2015). Protected culture has the benefit of allowing the grower to have more control over elements that affect the crop year-round. In these systems, the ventilation, light intensity, and temperature are adjustable for optimization of plant growth (Welbaum 2015).

Having optimal condition for plant growth is ideal, especially in the case of tomatoes, since they are an integral part of the worldwide diet. There have been several studies conducted that establish a link between the consumption of tomatoes, and the reduced risk of chronic diseases. A diet rich in tomatoes (300g daily for one month) increases HDL-cholesterol by 15.2% (Blum, Merei et al. 2006). Tomatoes are a major source of carotenoid antioxidant lycopene. The lycopene content in various tomato products ranges from 42 ppm to 365 ppm, with the average daily consumption being estimated around 25.2 mg/day. The intake of fresh tomatoes actually accounts for 50% of the total lycopene intake (Rao, Waseem et al. 1998). There is also a suggestion in recent epidemiologic studies that there is potential benefit of this carotenoid against the risk of prostate cancer, with emphasis on the more lethal forms of this cancer (Giovannucci 2002). The consumption of two to four servings of tomato sauce per week was associated with about a 35% risk reduction of total prostate cancer and a 50% reduction of advanced (extraprostatic) prostate cancer (Giovannucci 2002).

Given the fact that tomatoes are essential to a healthy human diet, and that consumer demand is on the rise, the ability to grow tomatoes year round is crucial. Tomatoes are not only a dietary importance; they also have high economic value. The role of round field tomatoes is shrinking; in 2011 protected-culture tomatoes made up 40 percent of the U.S. tomato supply (Thornsbury 2012). Currently, tomatoes produced in protected culture are dominating the retail industry and becoming more common in food service (Thornsbury 2012).

However, as in field production, protected-culture is not without its complications. Humans are not the only ones with an appetite for this betacarotenoid-rich crop, insect pests are a limiting factor for quality production. Insect pests such as thrips, whitefly and aphid species can cause massive losses in tomatoes both directly (feeding on plant components), or indirectly (transmission of plant viruses) (Polston and Anderson 1997, (Morales and Anderson 2005, Pappu, Jones et al. 2009). High densities of silverleaf whitefly (SLW) can induce an irregular ripening disorder in tomatoes as a result of their phloem feeding and toxic saliva (Schuster 2001). This damage results in an economic loss due to unmarketable fruits (Schuster 2001). In addition, SLW is a vector of multiple viruses in the *Geminiviridae* family, which includes the severe tomato yellow leaf curl virus (TYLCV) (Polston and Anderson 1997). Tomato production can come to a complete halt with the transmission of TYLCV, with losses reaching up to 100% (Saikia and Muniyappa 1989).

The primary aphid species of concern are the green peach aphid, *Myzus persicae* and the potato aphid, *Macrosiphum euphorbiae*. However, only the green peach aphid is known to transmit viruses to tomatoes, which include *Alfalfa mosaic virus*, *Potato virus Y*, and *Tobacco etch virus* (Davis, Pernezny et al. 2012). While the potato aphid does not serve as a vector of viruses, the damage induced by these pests when they are present in high volume is substantial (Davis, Pernezny et al. 2012). Potato aphids can distort leaves and stems, stunt plants, and cause necrotic spots on leaves (Davis, Pernezny et al. 2012). The green peach aphid and potato aphid can both result in the production of sooty mold on foliage and fruit due to their secretion of honeydew (Davis, Pernezny et al. 2012).

Solanum pennellii is a wild tomato that exhibits insect resistance and contains high densities of type IV glandular trichomes. (Goffreda et al. 1989, Hawthorne et al. 1992, Juvik et al. 1994, Liedl et al. 1995, Rodriguez et al. 1993). These glandular trichomes excrete a mixture of 2,3,4-tri-O-acylated glucose esters that function as a physical and chemical deterrent to small arthropod pests (Walters and Steffens 1990). The acyl moieties can consist of iso-branched, ante-iso-branched, and straight chain fatty acid side chains ranging from 4 to 12 carbons in length (Burke et al. 1987; Sharpio et al. 1994). Acyl sugars can consist of a variation of different acyl moiety acyl glucoses and acyl sucroses. Southern *S. pennellii* accessions exude acylglucoses consisting primarily of i4:0 and its extension products as the predominant fatty acid constituents (Leckie et al. 2014). Southern accessions tend to have higher acylsugar levels than do northern accessions (Shapiro et al. 1994). Cultivated tomato leaves also produce acylsugars, at very low levels, consisting of tri and tetra-O-acylsucrose esters with the esterified fatty acids ranging from 2 to 12 carbons in length (Schilmiller et al. 2010).

The non-toxicity and broad spectrum of the resistance are major advantages to the use of this in tomato production. Since acylsugars are non-toxic to the pests controlled, most of which feed on multiple hosts, the pressure for insects to become acylsugar resistant should be less than is commonly seen for pesticides and high antibiosis-mediated plant resistance mechanisms (Kennedy et al. 1987). Acylsucroses have been synthetically produced, where the sucrose is reacted with an aliphatic acid chloride in an aprotic polar solvent (Chortyk 1996). In this process, all of the hydroxyl groups are acylated. There is no such method for the synthesis of acyl glucoses due to the more complex nature of the limited esterification of positions 2, 3, and 4. The application of purified *S. pennellii* LA716 acyl glucoses to cultivated tomato leaves has shown that these compounds are effective, rate dependent feeding deterrents of potato aphids, green peach aphids, tomato fruitworm, beet armyworm, American serpentine leafminer, and silverleaf whitefly (Goffreda et al. 1988; Goffreda and Mutschler 1989; Juvik et al. 1994; Hawthorne et al. 1992; Liedl et al. 1995).

The cultivated tomato does not possess type IV glandular trichomes and therefore does not accumulate acyl sugars on its surface (Fobes, Mudd et al. 1985). Breeding of cultivated lines using *S. pennellii* LA716 as the donor parent has led to the development of the acylsugar-producing tomato breeding line CU071026 (Leckie, De Jong et al. 2012). However, the existence of synthetic

acylglucoses will allow application to cultivars at times of vulnerability such as after wetting, and for heirloom varieties that lack the appropriate genes. Also, synthetic acylglucoses can be used for trialing on pest and biological control insects. Additionally, there is potential to use these acylglucoses on other crops if they prove to be non-toxic to biological controls. Before these acylglucoses can be synthesized, a blueprint for their construction must be taken under consideration via retrosynthesis. Examination of the final expected product, will allow for a stepwise determination of the precursor products. Once all of the precursor products are determined, the synthetic route can be delved into further.

Integrated pest management (IPM) systems incorporate the application of selective pesticides and biological controls. The pesticides are evaluated based on action threshold, level of pests and natural enemies, surveillance and monitoring systems, use of pheromones, traps, bio-pesticides, and narrow spectrum pesticides to minimize undesirable side-effects (Haskell and McEwen 1998). Biological control is defined as the use of living natural enemies to suppress pest populations (Heinz, Van Driesche et al. 2004). Natural enemies of insects and mites include parasitic wasps that use pests as hosts for their offspring, predators that consume their prey, and pathogens that cause disease (Heinz, Van Driesche et al. 2004). Since the efficient use of biological control involves maintaining a balance in the population levels of beneficial organisms and of pests, it is necessary before the implementation of a pesticide to examine potential side-effects on beneficial organisms (Haskell and McEwen 1998).

Green lacewings (*Chrysoperla rufilabris* and *Chrysoperla carnea*) can also be utilized in aphid and whitefly control (McEwen, New et al. 2007). Larval lacewings fulfill many of the requirements of an effective biological control agent since they are avid predators with an efficient prey localizing capacity (Sundby 1966, Bond 1980). One *C. carnea* larva can consume an average of 487 aphids or 511 whitefly pupae before pupation (Afzal 1978). Lacewings are polyphagous, feeding on a wide range of pests including aphids, whitefly, mites, mealybugs, Colorado potato beetle, and various lepidopteran pests such as bollworms (Séméria and New 1984). Additional benefits of lacewings are their high resistance to common insecticides, as well as their high reproductive rate (McEwen, New et al. 2007). Larval rearing has become economically viable, and when this stage is released it will stay in targeted area (McEwen, New et al. 2007).

In 1974, the Working Group ‘Pesticides and Beneficial Organisms’ of the International Organization for Biological Control/ West Palaearctic Regional Section (IOBC/WPRS) was established with a major aim to encourage development of standard methods for testing side-effects of pesticides on natural enemies that would be acceptable to all cooperating institutions (Hassan 1994). Parasites and predators of agricultural pests naturally work to reduce the population of their prey or host, therefore decreasing the damage caused by the pest (Haskell and McEwen 1998). Thus, the importance of selective pesticides that work in concert with the biological control is of high relevance. The IOBC developed standard laboratory, semi-field, and field methods to test the side-effects of pesticides on beneficial organisms (Hassan 1994). Guidelines to test the side effects of pesticides on natural enemies has been published in multi-author publications (Suter

1978, Bigler 1988, Hassan 1998, Vogt, Degrande et al. 1998, Amarasekare and Shearer 2013). Harmlessness of pesticides can be shown by laboratory experiments, however harmfulness can only be confirmed under practical conditions in the field (Hassan 1994). Pesticides found to be harmless to a particular beneficial organism in the laboratory test are most likely to be harmless to the same organism in the field and no further testing in semi-field or field experiments is therefore recommended (Haskell and McEwen 1998).

Vogt (1998) described a laboratory method for testing the side-effects of pesticides on *C. carnea*, which is the first tier within the sequential testing scheme. This method was based on the laboratory glass plate test developed by Suter (1978) and Bigler (1988). This test was designed to evaluate the acute residual toxicity of a pesticide as well as sub-lethal effects on reproductive performance of the emerging adults. However, Amarasekare and Shearer (2013) proposed the use of a more robust assay that combines contact, residual, and oral routes of exposure.

Since, bio control agents and selective pesticides are used in concert to control pests in integrated pest management, multiple elements must be reviewed before introducing a new component into an IPM system. Currently, the knowledge of the mode of action of acylsugars is that they can terminate entrapped herbivores by suffocation (Puterka, Farone et al. 2003), starvation, or by ingestion of toxins (Simmons, Gurr et al. 2004). However, there is no current information on the use of acylsugars in an integrated pest management system and their effect on the biological control agent, *C. rufilabris*.

JUSTIFICATION AND RATIONALE

A straightforward synthesis of acyl glucoses has been developed since the use of purified compounds from crude plant extracts is problematic as they are difficult to obtain and separate due to the similar structures. Synthesizing acylglucoses allows for the production of pure products for test and perhaps future use as an insecticide. Use of a single acylglucose has allowed for testing on *Chrysoperia rufilabris* to determine if plants expressing or having acylsugar sprayed will interfere with the existing IPM system in tomato production in protected culture and if breeding acylsugar resistance into tomato varieties for protected culture is feasible.

PROJECT OBJECTIVES

The overall goal of this research is to develop a synthetic route to generate triesterified monosaccharides (acylsugar) and assess the effect on the biocontrol generalist predator, green lacewing, *Chrysoperia rufilabris*.

- 1) Development of synthetic route for acyl glucose, and successful synthesis (completed)
- 2) Construct experimental parameters to carry out trialing on 2nd instar larval stage
- 3) Track fertility and fecundity of adults emerging from larval trailing

MATERIALS AND METHODS

***C. rufilabris* Colony Rearing**

C. rufilabris adult, larval, and egg specimens were obtained from beneficiary insectary (Redding, CA) to generate the colony used for these experiments. All three stages were purchased in order to construct parameters for appropriate rearing.

Adults were kept in open-top glass aquarium (26 by 30 by 50 cm) with a wire mesh lid. The mesh lid was covered with a piece of cheesecloth (~56-92 cm) to facilitate egg laying. Adults were fed a diet of wheat (wheat mix, sugar, deionized H₂O) that was applied to a piece of Benchkote surface protector paper (~12 by 24 cm). Water was supplied to colony via a cotton wick inserted into the lid of clear plastic vial (5-cm diameter, 196 ml). Adults were provided with new food, water, and cheesecloth twice a week. Eggs were collected 12 hours after new laying occurred. These eggs were placed in individual 28-ml translucent portion cups and supplied with *E. kuehniella* eggs as a food source. The emerging larvae were used for trialing as mentioned below.

Larval stages were placed in 28-ml translucent portion cups due to their cannibalistic nature. Amarasekare and Shearer (2013) called for a layer of insect-a-slip to be placed on top rim of portion cups in order to keep larvae from becoming smashed in the lid. However, when larvae attempted to molt on this layer, it was noted that the molt was not successful. Due to this observation, insect-a-slip was not used for the larvae that were to be trialed for the experiments.

Spray Efficacy, Deposition and Coverage

Spray efficacy was evaluated using 10.16 X 10.16 cm sheets of paper towel. Three volumes (1 ml, 2 ml, 3 ml) were assessed, with 20 replicates for each volume. A fixed height of 11.91 cm was used (home sense clear plastic cup). Paasche H Airbrush in combination with a mini air compressor (model TC-20) was used for application of spray (pressure 1 kg cm⁻²). Dry weight before application and wet weight after were measured using an electronic balance.

Spray deposition and coverage were assessed using water sensitive paper (52 x 76 mm). Twenty sheets were sprayed with 50 μ l of DI H₂O were sprayed at the same height and pressure as mentioned above. Cards were scanned using an Epson scanner and analyzed using DepositScan Image J software.

Bio-Assay Lethal Effects 2nd Instar Larval Stages

Arenas to house the larval stages consisted of glass petri dishes (9 cm diameter, r=4.29 cm, h=1.59 cm). Three treatments were to be assessed, consisting of the control DI H₂O, synthesized acyl glucose compound (AGP), and the complex acyl glucose product mixture (AGCM) isolated from *S. pennellii*. The amount of each treatment applied corresponded to the threshold amount of the product necessary for deterring settling and oviposition of pests (50-70 μ g/cm²) (Liedl, Lawson et al. 1995). For this investigation, 60 μ g/cm² was used. AGP and AGCM compounds were heated

in DI H₂O for 30 minutes in order to increase solubility. Once the compounds were in solution, the top and bottom lids of the petri dish were treated, (60 petri dishes per treatment). The dishes were left to air dry two days prior to treatment. *E. kuehniella* eggs were saturated in 10 ml of the various treatments for 30 s, and then air-dried.

Larvae were treated in a 9 cm-dia glass petri dish as a group of three larvae per replicate per treatment (larvae; n=20 [3 replicates]). Treated insects were carefully transferred to glass arenas with a soft brush. Larvae were reared individually, and provided with treated *E. kuehniella* eggs (0.2-0.3 g). Arenas were placed in environmental growth chamber at 23°C, 60% RH, and photoperiod of 16:8 (L:D) h. *C. rufilabris* were assessed for mortality by observing movement or lack thereof daily for 10 d after treatment (Amarasekare and Shearer 2013). Untreated *E. kuehniella* eggs (0.2-0.3 g) and fresh adult food were provided to surviving larvae, 72 hours after treatment. Treated larvae were reared until emergence of adults, and their development time was determined. Gender was also determined with emergence of adults using methods described by Vogt et al. (2000). The adult sex ratio was then calculated as the percentage of females [females/(males+females)] *100 (Amarasekare and Shearer 2013).

The adults that emerged from each replicate per treatment were combined, and provided with food and water. The cheese cloth lids from adult arenas are being collected every third day to evaluate the number of eggs each female laid and subsequent egg hatch for 18 d. The eggs will be counted and separated into petri-dishes (Amarasekare and Shearer 2013) with *E. kuehniella* eggs as the larval food source. The petri dishes have been placed into an environmental growth chamber (23°C, 60% RH, photoperiod of 16:8 (L:D) h) and monitored for emergence of larvae.

Statistical Analyses

One-way analysis of variance (ANOVA) will be performed for mortality, developmental time, survival, sex ratio, fecundity, fertility, and egg viability. Two-way ANOVA will be performed for adult longevity by gender (Amarasekare and Shearer 2013). The means will be compared at P≤0.05 significance level.

RESULTS AND DISCUSSION

Spray Deposition, and Coverage

Spray efficacy, deposition, and coverage averages were calculated using Excel. The spray efficacy was high for all three volumes 70.98% (1 ml), 73.42% (2 ml), and 64.61% (3 ml). The percent coverage was 55%, which may have been lower than expected due to the method of measurement. These values are comparable to the standard potter spray tower method, and shows that this method for application is efficient (Liu and Stansly 1995)

Bio-Assay Lethal Effects 2nd Instar Larval Stages

Lethal effects were recorded as 1 for live, or zero for dead over ten days. Each day after treatment was compared to see if there was any significance between live/dead among treatments. Below is summaries for day 1, day 2, and day 10 after treatment.

1 DAT

Means for Oneway Anova					
Level	Number	Mean	Std Error	Lower 95%	Upper 95%
AGCM	60	0.98333	0.01657	0.95063	1.0160
AGP	60	1.00000	0.01657	0.96730	1.0327
Water	60	0.96667	0.01657	0.93396	0.9994

2 DAT

Means for Oneway Anova					
Level	Number	Mean	Std Error	Lower 95%	Upper 95%
AGCM	60	0.98333	0.01657	0.95063	1.0160
AGP	60	1.00000	0.01657	0.96729	1.0327
Water	60	0.96667	0.01657	0.93396	0.9994

10 DAT

Means for Oneway Anova					
Level	Number	Mean	Std Error	Lower 95%	Upper 95%
AGCM	60	0.933333	0.03490	0.86445	1.0022
AGP	60	0.933333	0.03490	0.86445	1.0022
Water	60	0.900000	0.03490	0.83112	0.9689

There was no significant larval mortality in lethal effects among the three treatments across ten days. As can be noted above, AGP or AGCM can be applied to larvae without any toxic effects.

Bioassay-Sublethal Effects Larva to Adult Survival

Larva to adult survival was consistant across all three treatments.

Analysis of Variance

Source	DF	Sum of Squares	Mean Square	F Ratio	Prob > F
Treatment	2	5.555556	2.77778	1.7857	0.2463
Error	6	9.333333	1.55556		
C. Total	8	14.888889			

Means for Oneway Anova

Level	Number	Mean	Std Error	Lower 95%	Upper 95%
AGCM	3	18.6667	0.72008	16.905	20.429
AGP	3	18.6667	0.72008	16.905	20.429
Water	3	17.0000	0.72008	15.238	18.762

Std Error uses a pooled estimate of error variance

Bioassay-Sublethal Effects Larva to Adult Developmental Time

Although there appears to be a difference in means within adult developmental time, it is not significant. Therefore, there is no interruption in larva to adult developmental time across treatments.

Analysis of Variance

Source	DF	Sum of Squares	Mean Square	F Ratio	Prob > F
treatment	2	115.8778	57.9389	1.7183	0.1824
Error	177	5968.3167	33.7193		
C. Total	179	6084.1944			

Means for Oneway Anova

Level	Number	Mean	Std Error	Lower 95%	Upper 95%
AGCM	60	18.3667	0.74966	16.887	19.846
AGP	60	18.1500	0.74966	16.671	19.629
Water	60	16.5667	0.74966	15.087	18.046

Std Error uses a pooled estimate of error variance

Bioassay-Sublethal Effects Sex Ratio of Adults Emerged from Treated Larvae

There were no differences among the treatments for the sex ratio of adults that emerged from *C. rufilabris* larvae. The sex ratio was approximately 1:1 of females to males (F=0.0709, df=2, P=0.9323).

CONCLUSION

Overall it is apparent that acyl glucoses, either in pure form or complex mixture, will not harm any element of larval development. However, data collection is not yet complete for fecundity and fertility. Also, lethal effects on adults has yet to be evaluated. More data needs to be collected before an absolute answer can be posed for the safe incorporation of acyl glucoses into IPM programs.

In addition to monitoring the effects on the adults, ViewPoint will be used to assess behavioral changes in 3rd instar larvae upon introduction to the compounds. This final piece will wrap up the project to answer whether or not these compound effect any element of lacewing behavior.

REFERENCES

- Afzal, M. K., M.R. (1978). "Life history and feeding behavior of green lacewing *Chrysopa carnea* Steph. (Neuroptera, Chrysopidae)." Pakistan Journal of Zoology(10): 83-90.
- Amarasekare, K. and P. Shearer (2013). "Comparing effects of insecticides on two green lacewings species, *Chrysoperla johnsoni* and *Chrysoperla carnea* (Neuroptera: Chrysopidae)." Journal of economic entomology **106**(3): 1126-1133.
- Amarasekare, K. G. and P. W. Shearer (2013). "Comparing Effects of Insecticides on Two Green Lacewings Species, *Chrysoperla johnsoni* and *Chrysoperla carnea* (Neuroptera: Chrysopidae)." Journal of Economic Entomology **106**(3): 1126-1133.
- Bigler, F. (1988). "A laboratory method for testing side-effects of pesticides on larvae of the green lacewing, *Chrysoperla carnea* Steph.(Neuroptera, Chrysopidae)." Bulletin SROP (France).
- Blum, A., et al. (2006). "Effects of tomatoes on the lipid profile." Clin Invest Med **29**(5): 298-300.
- Bond, A. B. (1980). "Optimal foraging in a uniform habitat: The search mechanism of the green lacewing." Animal Behaviour **28**(1): 10-19.
- Chortyk, O. T. (1996). Chemically synthesized sugar esters for the control of soft-bodied arthropods, Google Patents.
- Davis, R. M., et al. (2012). Tomato Health Management, APS Press.
- Fobes, J. F., et al. (1985). "Epicuticular Lipid Accumulation on the Leaves of *Lycopersicon pennellii* (Corr.) D'Arcy and *Lycopersicon esculentum* Mill." Plant Physiol **77**(3): 567-570.
- Giovannucci, E. (2002). "A Review of Epidemiologic Studies of Tomatoes, Lycopene, and Prostate Cancer." Experimental Biology and Medicine **227**(10): 852-859.
- Haskell, P. T. and P. K. McEwen (1998). Ecotoxicology: pesticides and beneficial organisms, Kluwer Academic Publishers.
- Hassan, S. A. (1994). "Activities of the IOBC/WPRS working group" Pesticides and beneficial organisms"." IOBC WPRS BULLETIN **17**: 1-1.
- Hassan, S. A. (1998). The initiative of the IOBC/WPRS working group on pesticides and beneficial organisms. Ecotoxicology, Springer: 22-27.
- Heinz, K. M., et al. (2004). Biocontrol in protected culture, Ball Publishing.
- Holton, R. A., et al. (1994). "First total synthesis of taxol. 2. Completion of the C and D rings." Journal of the American Chemical Society **116**(4): 1599-1600.

- Leckie, B., et al. (2012). "Quantitative trait loci increasing acylsugars in tomato breeding lines and their impacts on silverleaf whiteflies." Molecular Breeding **30**(4): 1621-1634.
- Liedl, B. E., et al. (1995). "Acylsugars of wild tomato *Lycopersicon pennellii* alters settling and reduces oviposition of *Bemisia argentifolii* (Homoptera: Aleyrodidae)." Journal of Economic Entomology **88**(3): 742-748.
- Liu, T.-X. and P. A. Stansly (1995). "Deposition and bioassay of insecticides applied by leaf dip and spray tower against *Bemisia argentifolii* nymphs (Homoptera: Aleyrodidae)." Pesticide Science **44**(4): 317-322.
- McEwen, P. K., et al. (2007). Lacewings in the Crop Environment, Cambridge University Press.
- Morales, F. J. and P. K. Anderson (2005). Whitefly and whitefly-borne viruses in the tropics: building a knowledge base for global action, CIAT.
- Pappu, H., et al. (2009). "Global status of tospovirus epidemics in diverse cropping systems: successes achieved and challenges ahead." Virus research **141**(2): 219-236.
- Polston, J. E. and P. K. Anderson (1997). "The emergence of whitefly-transmitted geminiviruses in tomato in the western hemisphere." Plant Disease **81**(12): 1358-1369.
- Puterka, G. J., et al. (2003). "Structure-function relationships affecting the insecticidal and miticidal activity of sugar esters." Journal of economic entomology **96**(3): 636-644.
- Rao, A. V., et al. (1998). "Lycopene content of tomatoes and tomato products and their contribution to dietary lycopene." Food Research International **31**(10): 737-741.
- Saikia, A. and V. Muniyappa (1989). "Epidemiology and control of tomato leaf curl virus in Southern India." Tropical Agriculture **66**(4): 350-354.
- Schuster, D. J. (2001). "Relationship of silverleaf whitefly population density to severity of irregular ripening of tomato." HortScience **36**(6): 1089-1090.
- Séméria, Y. and T. R. New (1984). Biology of Chrysopidae, Springer Netherlands.
- Simmons, A. T., et al. (2004). "Entrapment of *Helicoverpa armigera* (Hübner)(Lepidoptera: Noctuidae) on glandular trichomes of *Lycopersicon* species." Australian Journal of Entomology **43**(2): 196-200.
- Sundby, R. A. (1966). "A comparative study of the efficiency of three predatory insects—*Coccinella septempunctata* L. [Coleoptera, coccinellidae], *Chrysopa carnea* St. [Neuroptera, Chrysopidae] and *Syrphus ribesii* L. [Diptera, Syrphidae] at two different temperatures." Entomophaga Entomophaga **11**(4): 395-404.

- Suter, H. (1978). "Prüfung der Einwirkung von Pflanzenschutzmitteln auf die Nutzarthropodenart *Chrysopa carnea* Steph.(Neuroptera; Chrysopidae): Methodik und Ergebnisse." Schweizerische landwirtschaftliche Forschung. La Recherche agronomique en Suisse.
- Tanaka, T., et al. (2009). "Direct Transformation of Unprotected Sugars to Aryl 1-Thio- BETA-glycosides in Aqueous Media Using 2-Chloro-1, 3-dimethylimidazolium Chloride." Chemistry Letters **38**(5): 458-459.
- Thornsbury, S. (2012). "Low Prices Continue for Fresh-Market Vegetables " Vegetables and Pulses Outlook **350**: 1-52.
- Vogt, H., et al. (1998). Side-effects of pesticides on larvae of *Chrysoperla carnea* (Neuroptera, Chrysopidae): actual state of the laboratory method. Ecotoxicology, Springer: 123-136.
- Walters, D. S. and J. C. Steffens (1990). "Branched Chain Amino Acid Metabolism in the Biosynthesis of *Lycopersicon pennellii* Glucose Esters." Plant Physiol **93**(4): 1544-1551.
- Waschke, D., et al. (2012). "Synthesis of fluorinated ketoheptoses as specific diagnostic agents." European Journal of Organic Chemistry **2012**(5): 948-959.
- Welbaum, G. E. (2015). Vegetable Production and Practices, CABI.

DEVELOPMENT OF A SYSTEM FOR EXTENDED DEPTH OF FIELD IMAGING

Taylor Gosnell
Aerospace Engineering
West Virginia University
Morgantown, WV 26506

ABSTRACT

For materials characterization and analysis, it is common for objects to have a varying degree of contour and topology, leading to problems with conventional microscopes when trying to capture an image which shows the full depth of the object's features. This limitation relates to the depth of field of the imaging system, which becomes shallower with increasing magnification. To combat this problem, a stack of images, taken at different elevations, can be processed into one composite image. Advanced digital microscopes exist with this capability, but are very costly. A mechanical system was developed using existing hardware for the Microscale Mechanical Testing Laboratory at GSFC. The system allows the lab to view different components and samples with an extended depth of field. The system is driven using a LabVIEW interface and uses a linear actuator to move the sample on a z-stage through a distance which encompasses the topology of the object. The system is automated so the actuator stops at desired positions to gather an image before moving on to the next position. This process is repeated until the desired depth of field is captured. The stack of images are then saved and analyzed using ImagePro software for EDF processing. The device was successfully able to capture an extended depth of field image on a variety of samples.

INTRODUCTION

The issue of limited depth of field can be examined with an everyday occurrence. A friend wants their picture taken with a scenic background. The camera focuses on the friend's face, but the background is out of focus. The camera has a limited depth of field of which it can capture. This problem becomes even greater in microscopy because the depth of field shrinks as the magnification is increased. This makes it very hard to capture a large depth of field of an object with varying contour. To extend the depth of field, a stack of images is taken at different distances. This stack of images is then processed using advanced algorithms to create an in focus composite image. This phenomenon can be seen in Figure 1 below.



Figure 1: Limited Depth of Field, Face in focus but background out of focus

To examine a shallow depth of field on a much smaller scale, a fly is examined in Figure 2 below. The first two images in the sequence demonstrate a shallow depth of field as the whole body of the fly is not in focus. Using extended depth of field (EDF), the third image is created to show a full in focus composite of the fly.



Figure 2: Small Fly EDF Example: https://en.wikipedia.org/wiki/Focus_stacking

LABVIEW PROGRAM

LabVIEW is utilized to control the system. The main interface of the code allows the user to control all aspects of the experiment. The user has the ability to control imaging settings as well as motor frequency. The main interface is also where the user controls the experimental parameters. The user interface can be seen below in Figure 5.

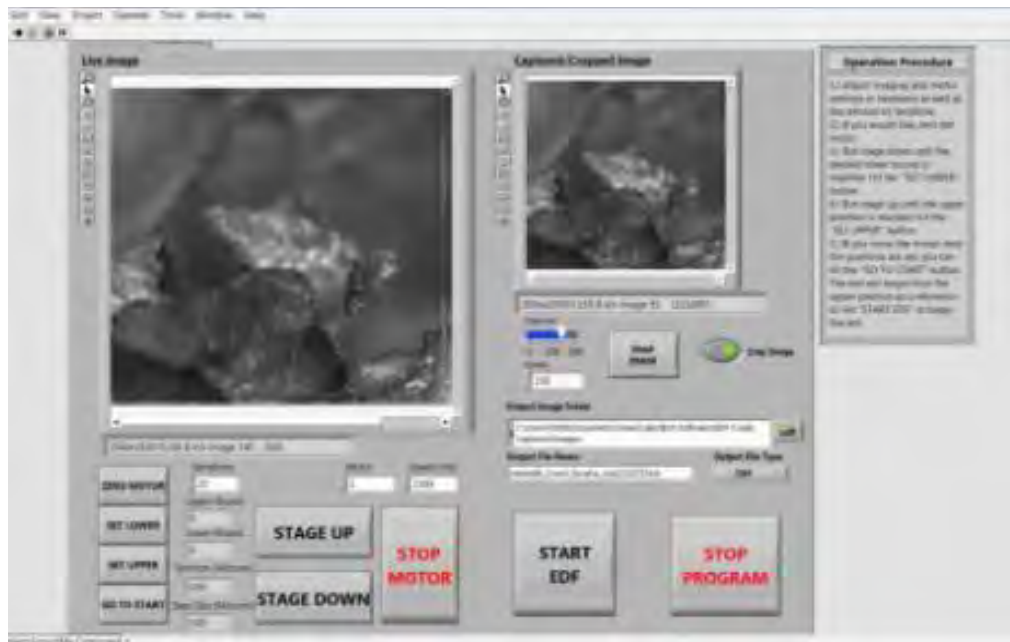


Figure 3: LabVIEW GUI

Since the system has so many dependent operations, a state machine structure was chosen to build the code. A state machine is composed of a while loop and a case structure. On each iteration of

the while loop, a different case is executed based on enum controls wired to a shift register, which feeds information from a prior loop iteration. An enum or enumeration is a collection of elements that correspond to a number. For example, the default case, "Initialize Camera" corresponds to a zero in the enum. The extended depth of field code consists of fourteen different cases or "states". Each state executes a specific function based on the users input. The program starts by running an initialization sequence for the camera based on the camera the user has selected. This can be seen in Figure 6 below.

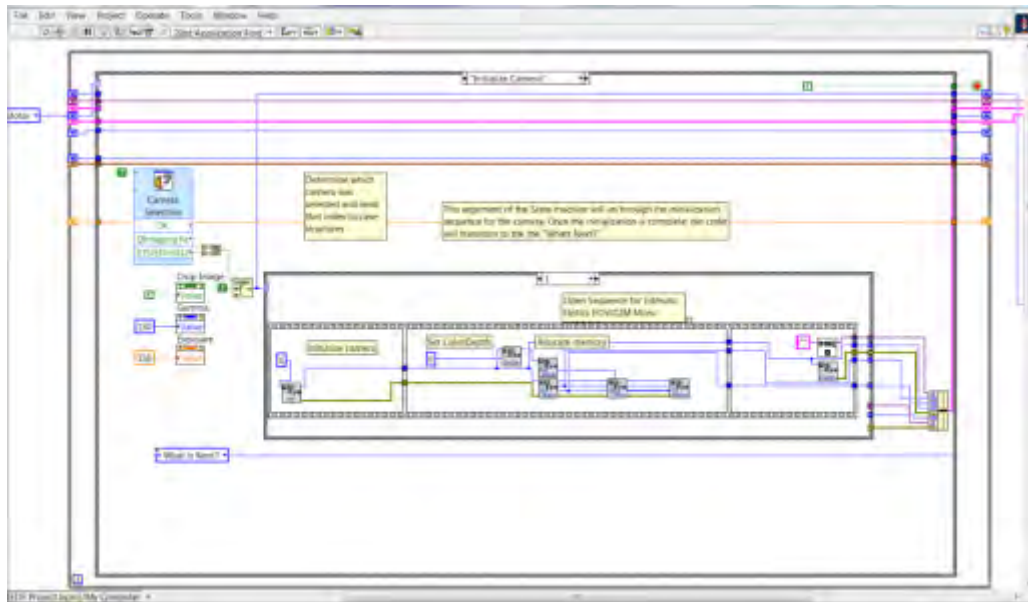


Figure 4: Opening Sequence for Camera

After the camera is initialized and setup, the code will transition to the initialization sequence for the picomotor. A screenshot of the motor initialization case can be seen in the Figure 7.

If the event structure times out, the code transitions to the "Get Image" state. This state runs through the sequence to produce an image. Once in this state, logic is built in to tell the program where to transition next. If the user has not started the EDF process, the code transitions back to the main terminal; however, if the EDF process has started, the code gathers an image and transitions to a state that saves the image. This logic is used to produce a live image feed in the program for the user to see the sample. There is also an optional image cropping feature built into this state for the user to use if they would like. This case can be seen in Figure 9 below.

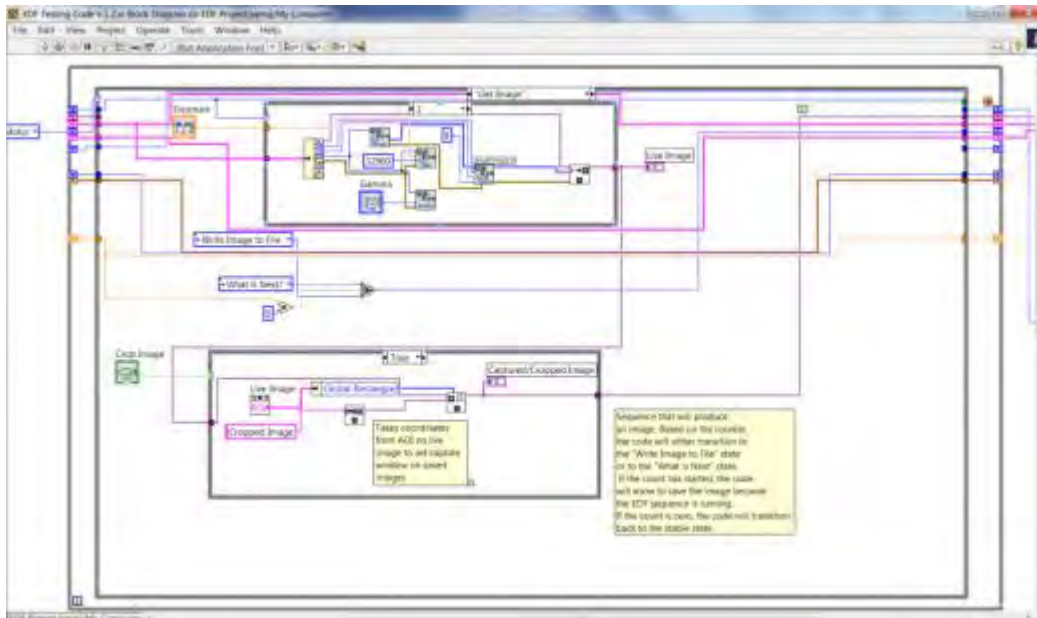


Figure 7: "Get Image" State

All of the manual motor controls are also triggered by the event structure in the main code terminal. The user has the ability to zero the motor, run the motor forward or reverse, and stop the motor by clicking the buttons on the main code terminal. After each one of these cases is executed, the program transitions back to the main terminal to wait for the next event. Figures 10, 11, 12, and 13 show each of these states in the order specified above.

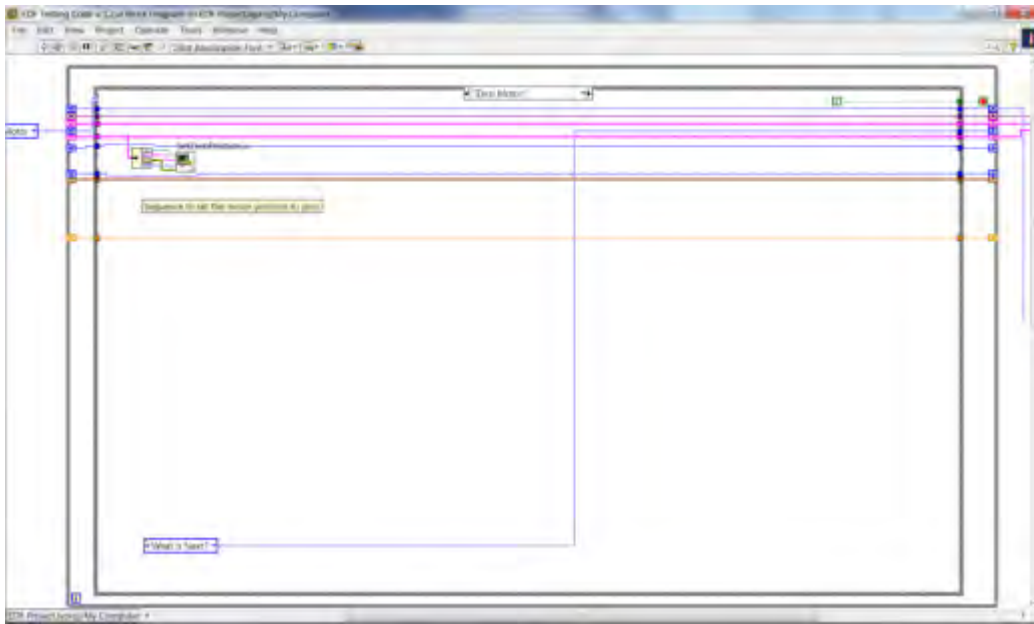


Figure 8: Zero Motor Case

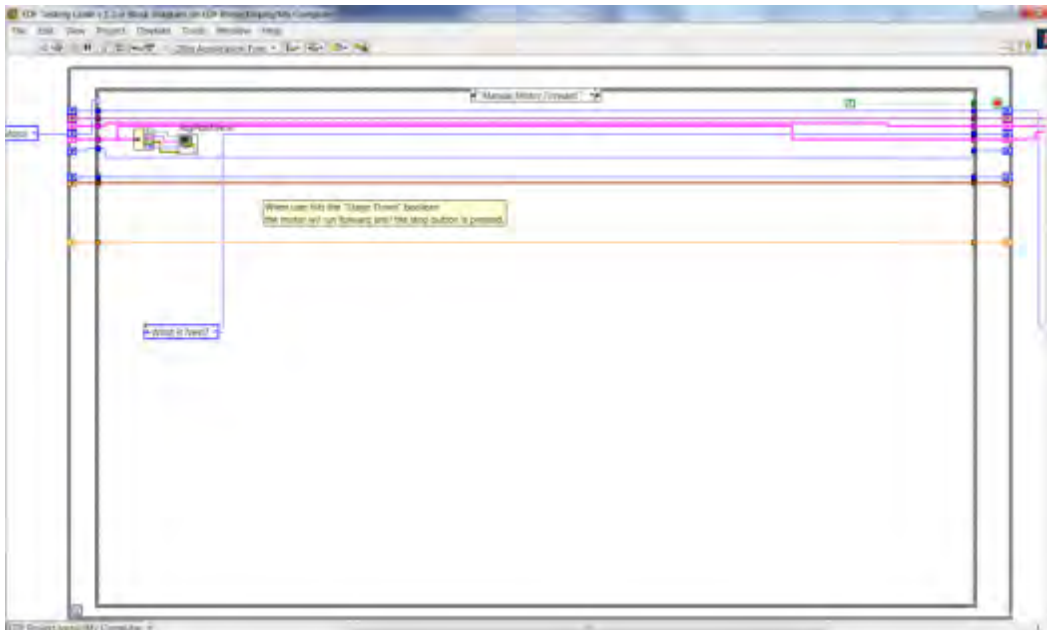


Figure 9: Manual Motor Forward Case

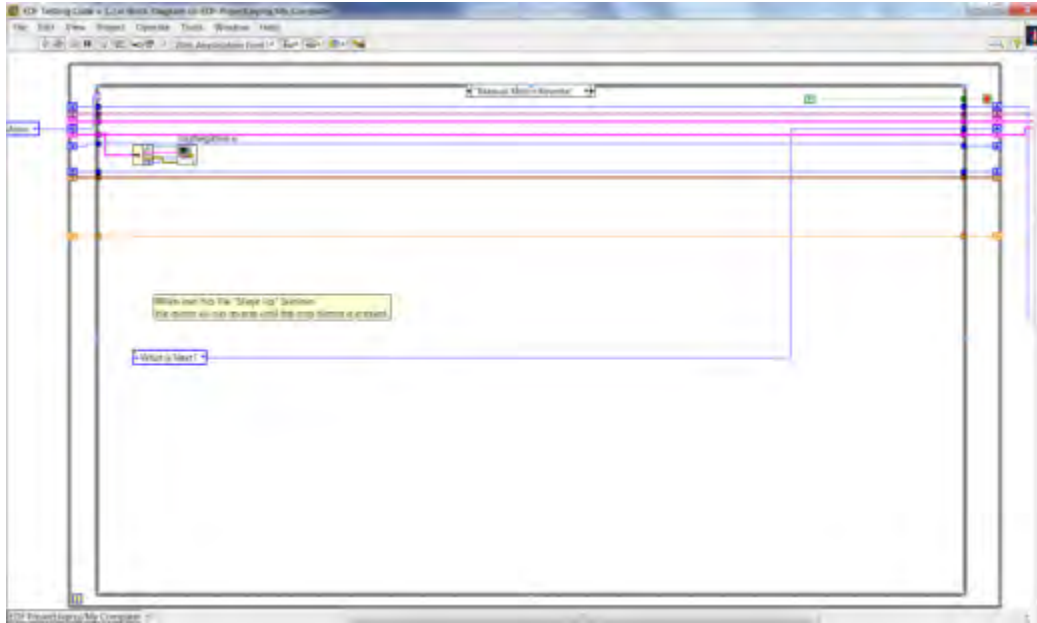


Figure 10: Manual Motor Reverse Case

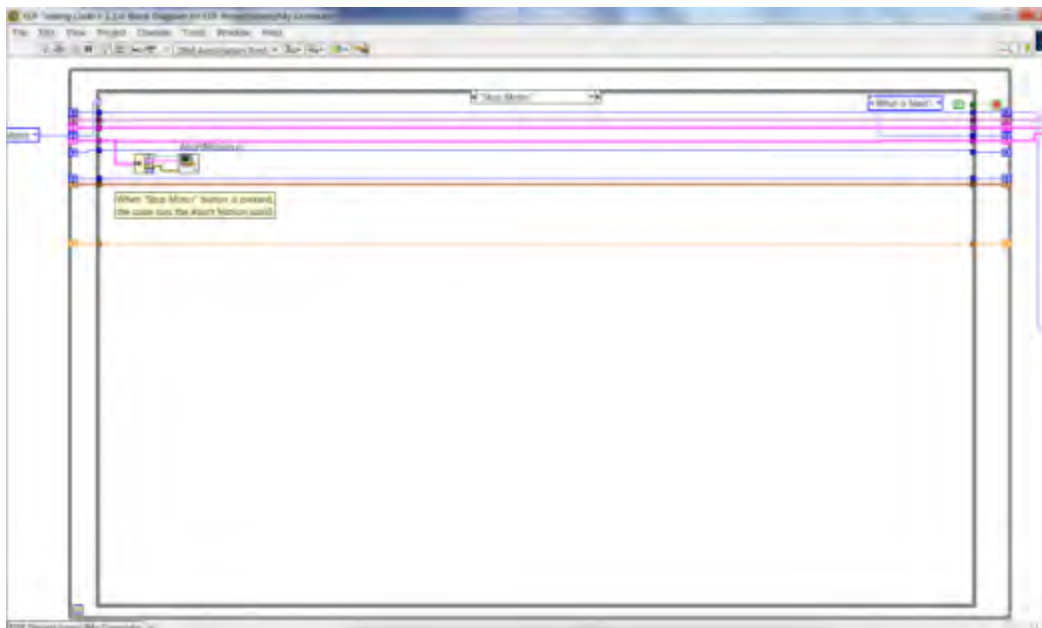


Figure 11: Stop Motor Case

The user is able to set the upper and lower bounds of the depth of field they which to capture. Again, this process is triggered by Boolean operators and the event structure. When the user chooses to set an upper or lower bound, the code will display those values on the main interface. The upper and lower bounds are used for calculating the travel distance of the motor when it steps through the field and gathers images. The states for setting these bounds are shown in Figures 14 and 15.

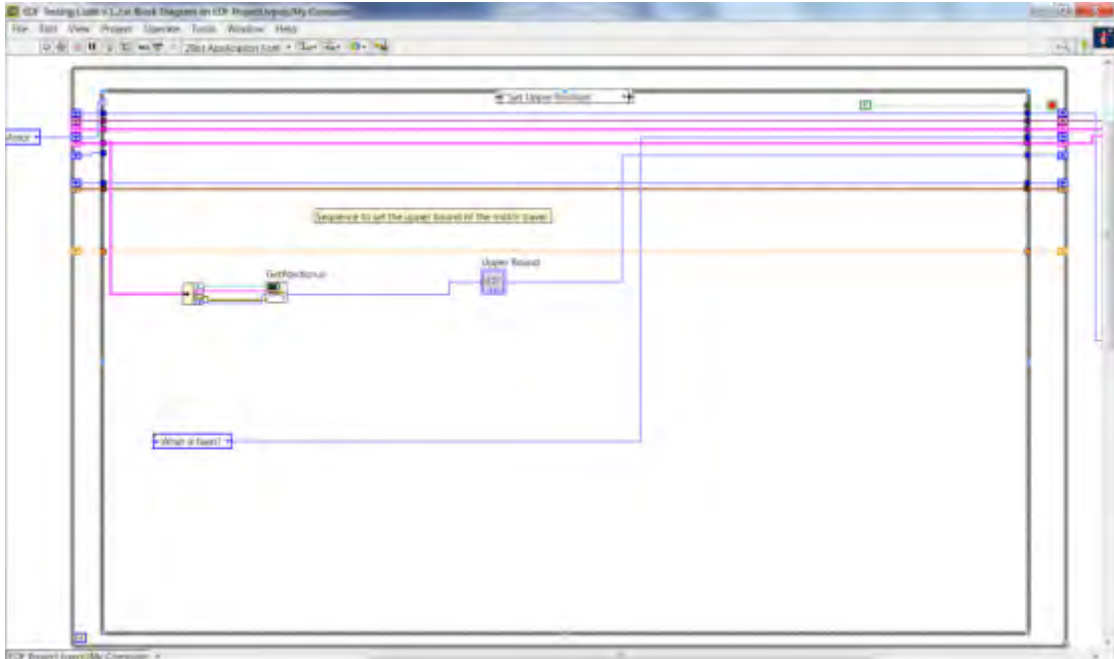


Figure 12: Set Upper Bound Case

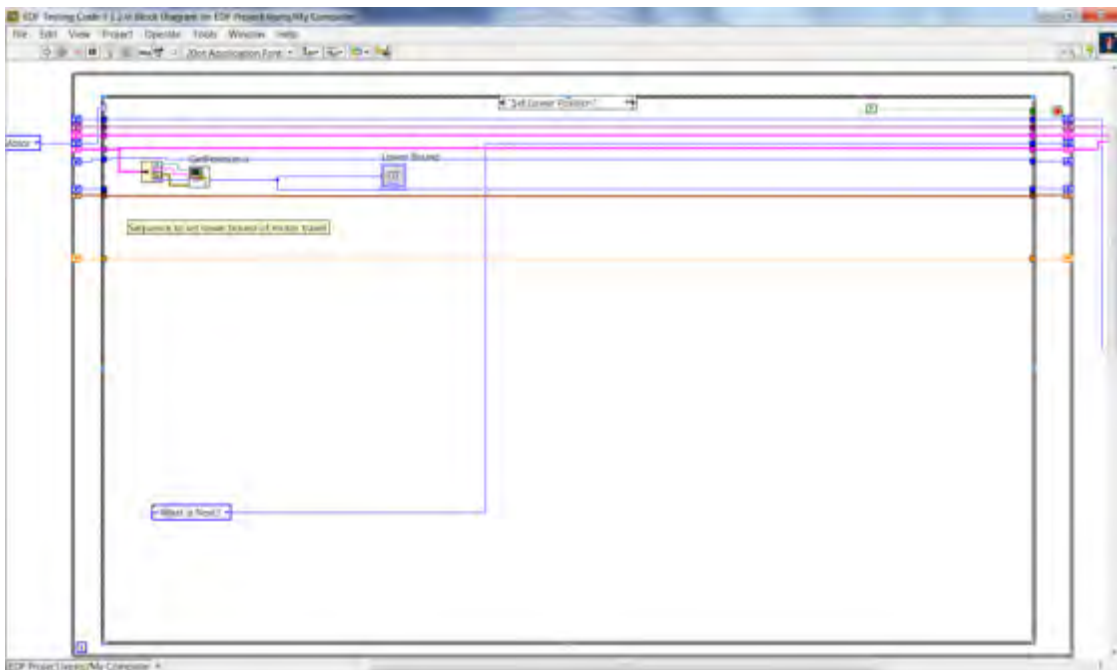


Figure 13: Set Lower Bound Case

When beginning the EDF image stacking, the code is set to start at the upper bound of the focal field. In many cases, the user may be at some arbitrary location within the field before they want to start the image capturing. For this reason, a "GO TO START" button is incorporated so the motor will run to the position necessary to start the imaging. This state is triggered by the user clicking the Boolean described above. There is logic built in that calculates the necessary amount

of steps as well as the direction the motor will have to move to get to the starting position. This can be seen below in Figure 16.

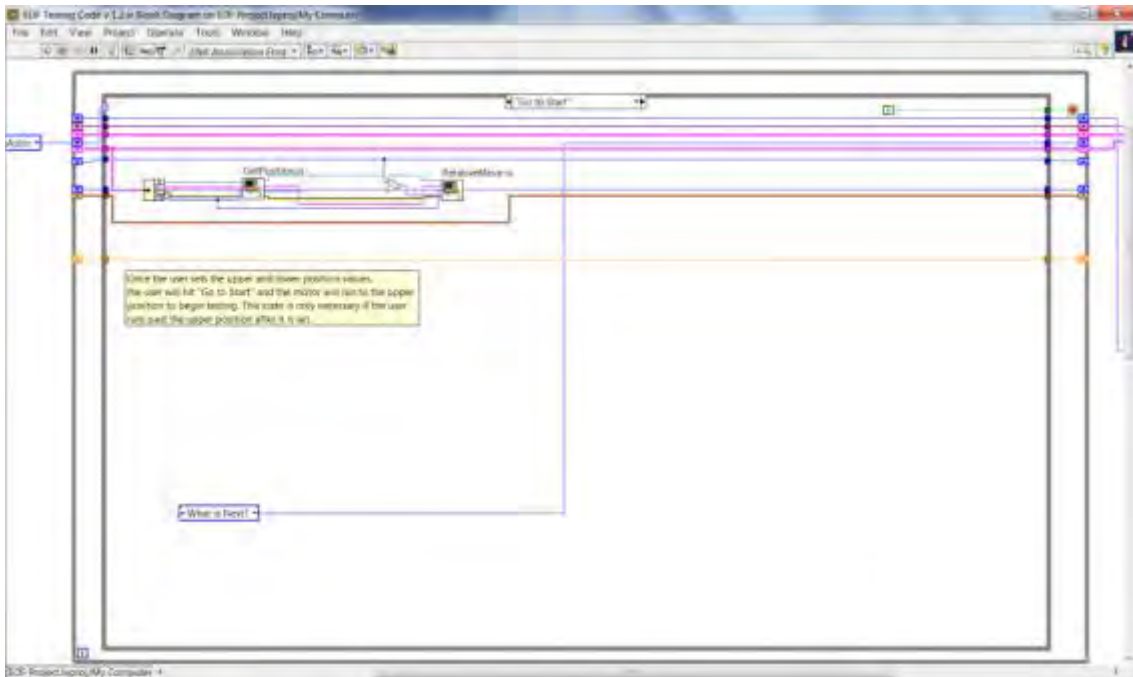


Figure 14: Go to Start Case

When the user is ready to begin imaging the sample, the "START EDF" Boolean is triggered on the user interface. Once this happens, the code enters the "Run Motor for Test" case. Here, the motor will run the distance that is calculated and displayed in the "Step Size" indicator. This is also where the counter in the code starts. Once this case is triggered, a counter begins that counts how many times the code has entered that state. If the count is less than the desired iterations the code will continue to run the motor and gather in image at each stop. The count is also transferred to the "Get Image" and "Write Image to File" cases to control how the code will behave there. The logic control for the "Get Image" state was described earlier, while the "Write Image to File" case will be described later. Once the user starts the EDF image capturing, there is real time position feedback calibrated in microns. The logic and code can be seen in Figure 17.

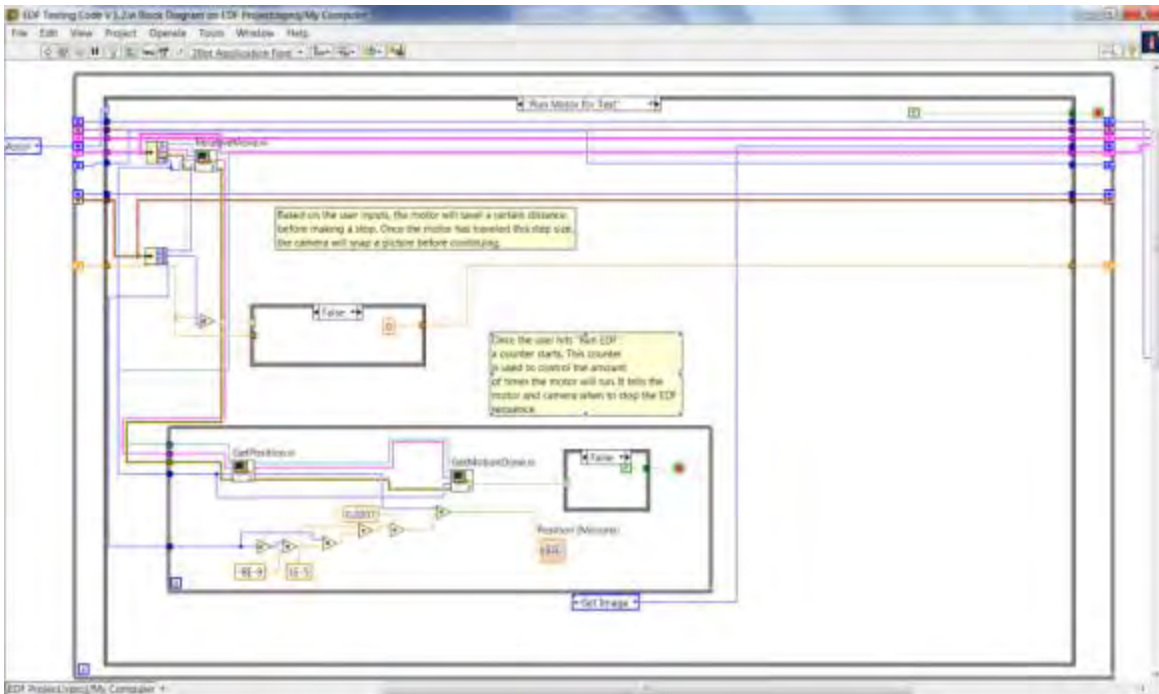


Figure 15: Run Motor for Test State

Since the user has started the EDF process, the "Get Image" state transitions to the "Write Image to File" state. Here, the images are saved and exported to a folder specified by the user. The user also has the ability to name the files and specify the image file type. The counter is also used here to dictate where the code transitions next. If the number of captured images equals the amount of iterations specified, the code knows the process is complete and goes back to the main terminal. If not, the image capturing process continues. This process can be seen below in Figure 18.

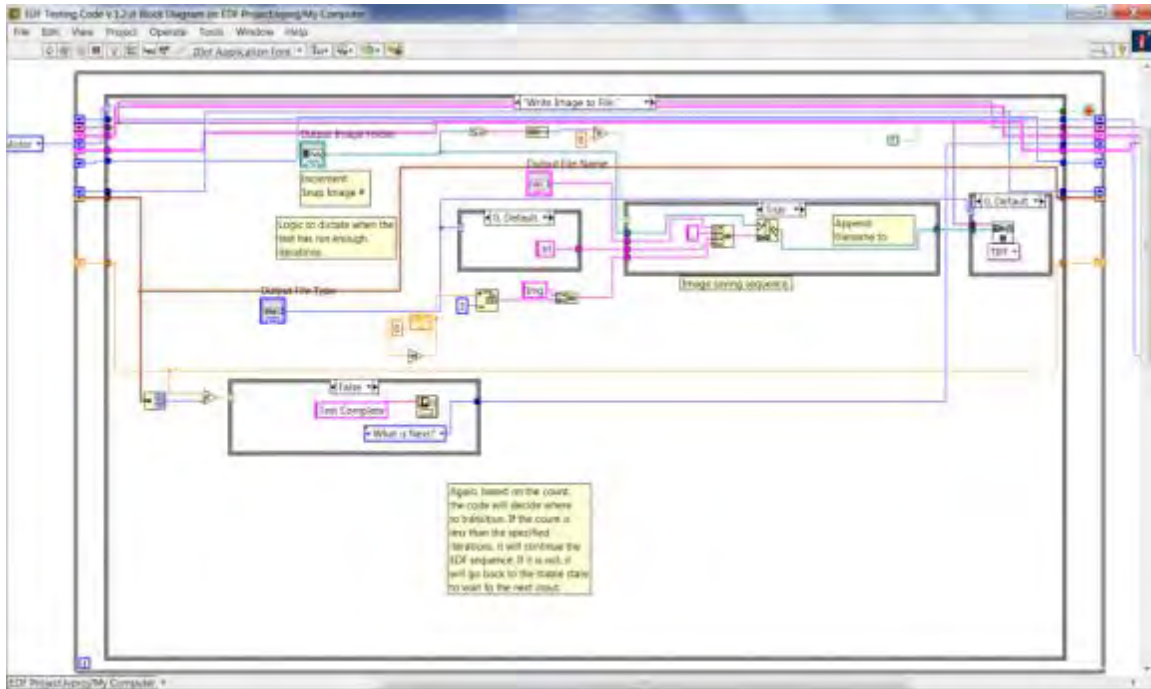


Figure 16: Write Image to File Case

The final case is a simple case that will stop the program. This is triggered when the user hits the "Stop Program" button on the interface. Here a constant true boolean is read by the stop terminal in the while loop. This can be seen in Figure 19.

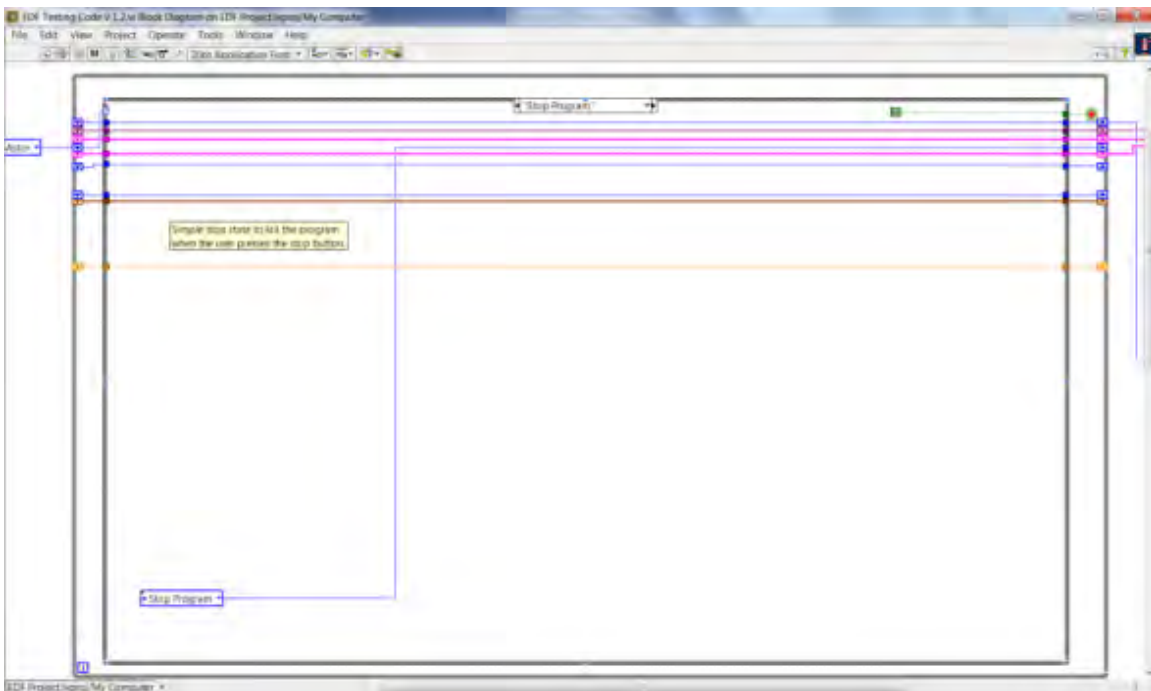


Figure 17: Stop Program Case

PROCEDURE

1. The camera on the z-stage is fine tuned to get some of the sample in focus
2. User adjusts imaging and motor settings as necessary. The user has the ability to control exposure time, gamma, and the actuator speed. These may need changed based on the sample being examined. Samples with higher relief may need a larger EDF; therefore, a higher motor speed is used.
3. User selects output folder and names files for saving
4. User sets the desired amount of images on the "Iterations" controller
5. The actuator is zeroed at its current position
6. The actuator is run until the lower focal region is found. The user then selects the "SET LOWER" Boolean.
7. The actuator is run until the upper focal region is found. The user then selects the "SET UPPER" Boolean.
8. If the user runs the actuator before starting the EDF imaging, the "GO TO START" button can be used to get to the starting upper position
9. Once everything is set, "START EDF" is pressed
10. The actuator runs for a calculated distance then stops to gather and save an image
11. Step 10 is automated and is repeated for the desired amount of intervals
12. The image stack is imported into ImagePro for EDF analysis

RESULTS

Two different samples were examined during the characterization of the system. The first sample was the surface of a piece of metallic foam. This sample has a varying degree of topography and contour. The surface had many small cracks and craters encompassing it. This made it an ideal candidate for EDF analysis because it was nearly impossible to find a spot on the surface that was completely in focus under the lens. The second sample that was examined was a circuit board. In general, circuit boards have many small elements at a variety of elevations. For this reason, EDF imaging is important to be able to examine specific elements to look for defects or problems. The experiment targeted a capacitor on the board.

Metallic Foam

Experiment Specs

Motor Frequency	Step Size	# of Images in Stack
1500 Hz	3485 Motor Steps	40

Capacitor

Experiment Specs

Motor Frequency	Step Size	# of Images in Stack
------------------------	------------------	-----------------------------

1500 Hz	2456 Motor Steps	25
---------	------------------	----

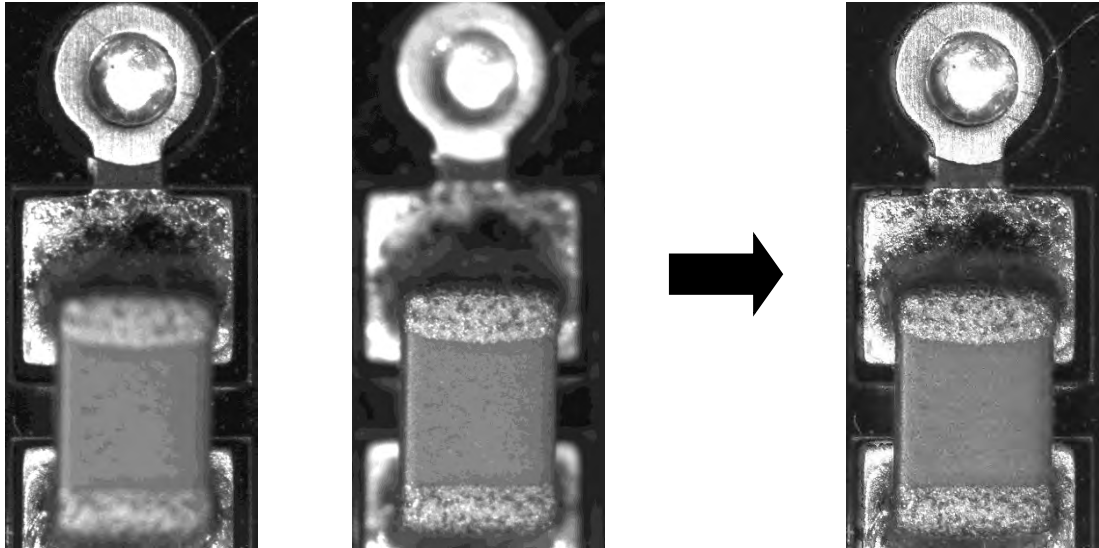


Figure 18: Capacitor EDF

CHALLENGES

Challenges

One of the main challenges with the experiment was producing real time position feedback on the LabVIEW GUI in measurable units instead of just "Motor Steps". Since many image processing software packages rely on the user to specify the image stack distance, having accurate position feedback is extremely important for best results. During actuator calibrations, it was determined that the device produced different values of displacement increment (microns per step) whether the device was running up or down. Because of this, two different calibration curves existed making it challenging to produce accurate position values. At first, the motor was calibrated only moving the linear stage up and down without the added weight of the sample stage and angle bracket attachment. A total of four calibrations, two running the motor forward and two running the motor in reverse, were ran at frequencies of 500, 1000 and 1500Hz. The results for the reverse motion can be seen in Table 2 and the results for the forward motion can be seen in Table 3.

Table 1: Reverse Motion Calibration No Weight

Upward Motion Calibrations					
Frequency	Run	mm/step	Average	microns/step	Average
500	1	2.3366E-05	2.3511E-05	0.0233662	0.023511
	2	2.3655E-05		0.023655	
1000	1	0.000019641	0.000019553	0.019641	0.019553
	2	1.9465E-05		0.019465	
1500	1	2.3168E-05	2.3352E-05	0.023168	0.023352

	2	2.3535E-05		0.023535	
					0.022138

Table 2: Forward Motion Calibration No Weight

Downward Motion Calibrations					
Frequency	Run	mm/step	Average	microns/step	Average
500	1	2.5693E-05	2.5862E-05	0.025693	0.025862
	2	0.00002603		0.02603	
1000	1	0.000025915	0.000026758	0.0259151	0.026758
	2	0.0000276		0.0276	
1500	1	2.2948E-05	2.2436E-05	0.022948	0.022436
	2	2.1924E-05		0.0219244	
					0.025018

When plotting the averages, general trends for both data sets confirmed that the calibration was repeatable. The plots of the above data can be seen in Figures 22 and 23 below.

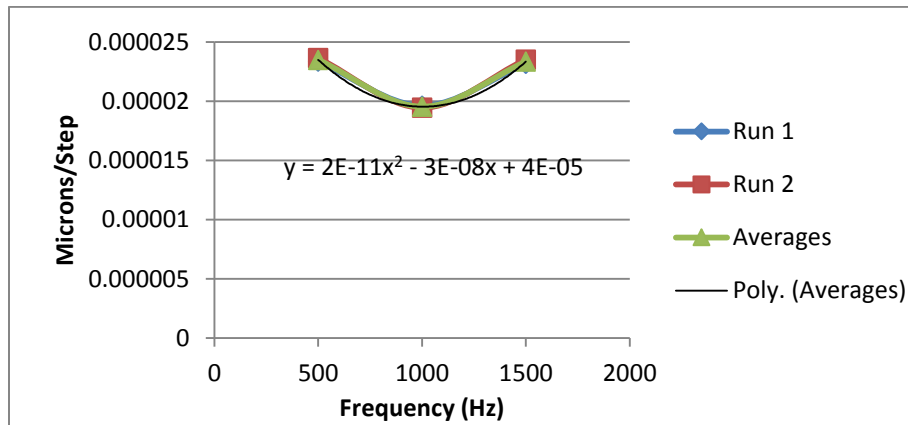


Figure 19: Reverse Motion Calibration Graph

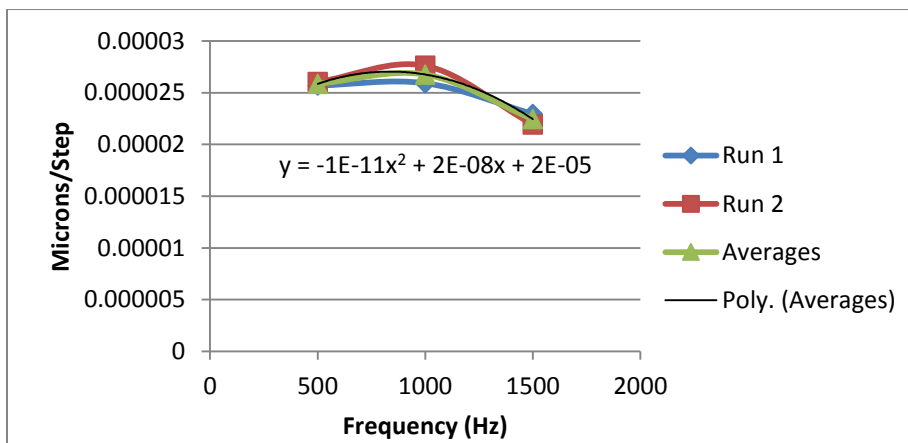


Figure 20: Forward Motion Calibration Graph

Next, calibrations were performed that simulated the weight of the sample stage and mounting bracket to confirm the above results. One run was completed in each direction at each of the desired motor frequencies. This data can be seen in Table 4 below.

Table 3: Weighted Calibrations

Weighted Calibrations					
Frequency	Run	mm/step	Average	microns/step	Average
500	Down	2.6139E-05	2.3684E-05	0.026139	Down
	Up	2.1229E-05		0.021229	0.026353
1000	Down	0.000027415	0.000024481	0.027415	Up
	Up	2.1547E-05		0.021547	0.021729
1500	Down	2.5505E-05	2.3958E-05	0.025505	
	Up	2.2411E-05		0.022411	

When plotting this data, different trends were observed compared to the zero calibrations. The trends were similar, but not exactly the same. This plot can be seen below in Figure 24.

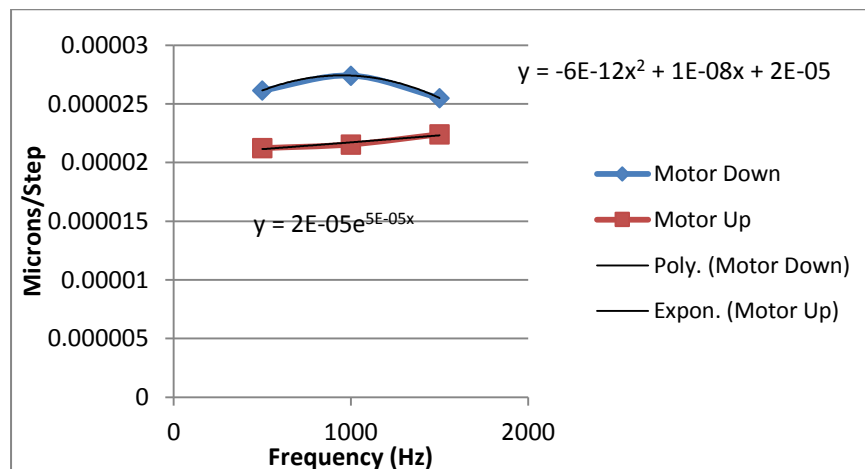


Figure 21: Weighted Calibration Chart

Since different trends were examined, the averages from all the reverse motion were plotted and fit to a curve to produce an upward motion calibration curve. The same thing was done for the forward (downward) motion. The final calibration curves for each of the motor motions are shown in Figures 25 and 26.

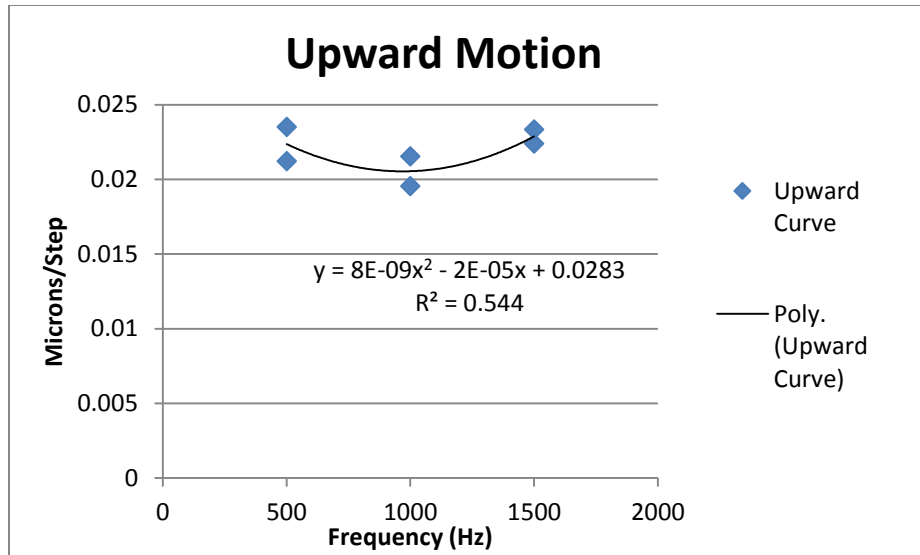


Figure 22: Final Upward Motion Calibration

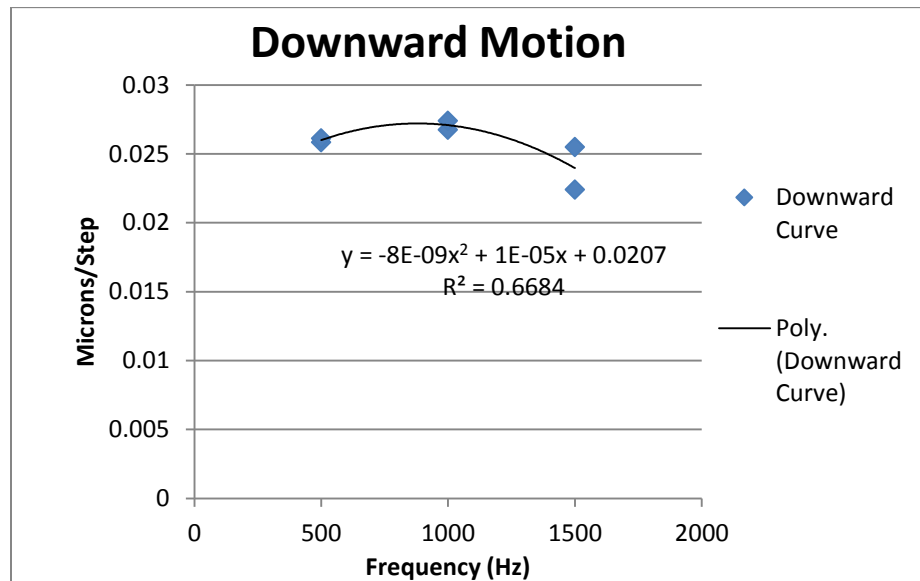


Figure 23: Final Downward Motion Calibration

Three Dimensional Topographic Map

Another problem arose when trying to generate a three dimensional topographic map of the samples being examined. This tool can be very useful when trying to do a surface topography analysis of a material, but ImagePro produced unsatisfactory results. The algorithm in ImagePro seemed to produce a topography based on bright and dark spots. It called the bright spots high elevation and the dark spots low elevation. This is shown in Figure 27.

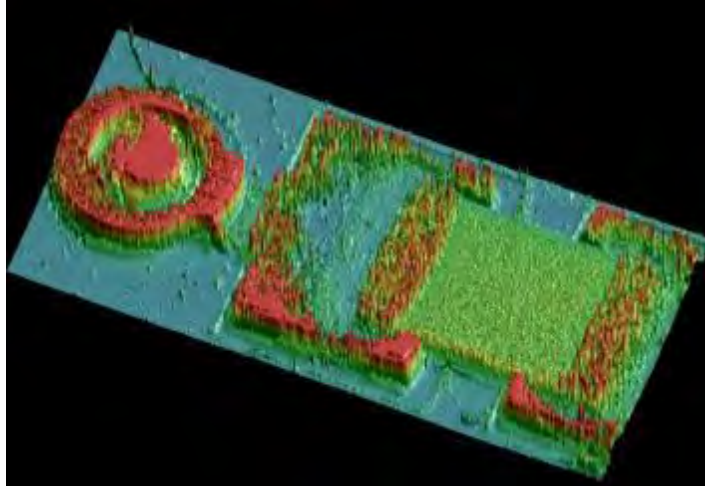


Figure 24: 3-D Topographic Map

The actual image of the capacitor can be seen in Figure 21. The capacitor is clearly higher on the circuit board, but appears darker in the image. Because of this, the algorithm in ImagePro takes it to be a low point even though it is not. It is believed that this is because the software is producing the topographic map based on local brightness in the composite image.

Lighting

Lighting also introduced issues in the experiment. Two different lighting sources were used in the experiment. The first was a single source aimed at the sample from the side. This produced unsatisfactory results because the lighting from one side caused a lot of the sample to be shaded. The first lighting configuration can be seen in Figure 28

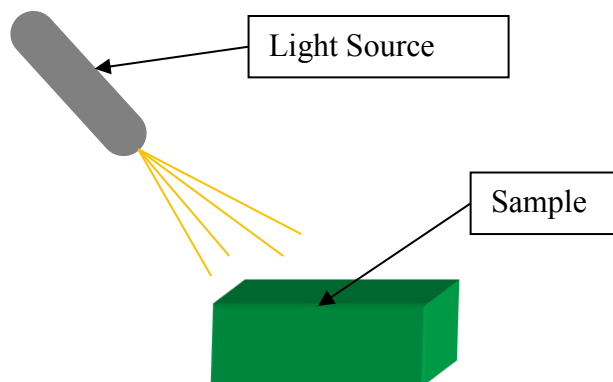


Figure 25: Lighting Configuration 1

To attempt to fix this issue, a different adapter was attached to the light source. In this case, light was angled at the sample from both sides to prevent shadows. This configuration yielded better

results, but there were still some lingering contrast issues that may have affected the extended depth of field analysis in ImagePro. The second lighting configuration can be seen in Figure 29.

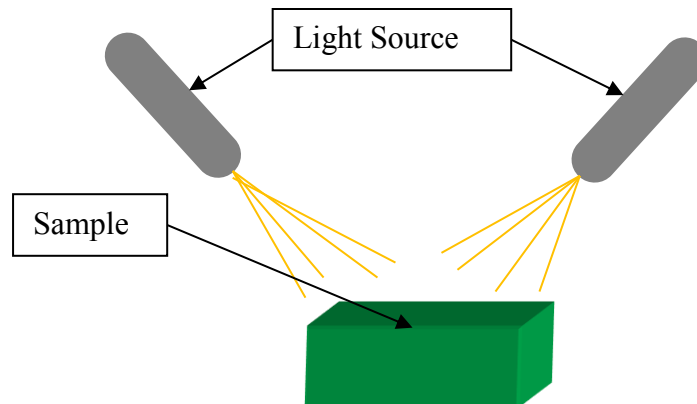


Figure 26: Lighting Configuration 2

CONCLUSIONS

The device was successfully able to capture extended depth of field images of a variety of samples. The system was built entirely of off the shelf components at a relatively low cost and the LabVIEW code is ready to be integrated into the existing micro-scale mechanical test system code as well. Even though there are still some remaining issues in the image processing, the system will enhance the abilities of the Microscale Mechanical Testing Laboratory at GSFC.

FUTURE WORK

The system was successful; however, there is still work that needs to be completed. First, it is recommended that a LabVIEW code is developed that completes the EDF processing in real time. For example, as each image is taken, LabVIEW takes the image and puts it in the stack and the stack is analyzed. This will make the system much more efficient. Next, it is recommended that a better position feedback system is integrated into the system. This could be done a variety of ways, but the use of capacitance gages in the lab is recommended. Finally, it is recommended that other image processing software packages are explored to complete the EDF analysis. ImagePro produced nice composites, but lacked a 3-D topographic map. Since this feature of the software is desirable for the lab, other software packages should be explored to see if they produce better results. A list of some available EDF processing is listed at: https://en.wikipedia.org/wiki/Focus_stacking.

ACKNOWLEDGEMENTS

First, I would like to thank Justin Jones and Devin Burns for mentoring me and providing help and insight with my summer project. I would like to thank the West Virginia Space Grant Consortium for sponsoring me to participate in this invaluable intern experience. I would also like to thank all the staff, engineers, scientists and interns in Code 541 for their support, discussions and help with anything I needed this summer.

REFERENCES

- [1] Foster, B., Van De Ville, D., Berent, J., Sage, D., & Unser, M. (2004). Complex Wavelets for Extended Depth-of-Field: A New Method for the Fusion of Multichannel Microscopy Images. *Microscopy Research and Technique*, 33-42.
- [2] Lee, V. B. (2014). *Evaluation of a Piezoelectric Stack Actuator for Micro-Mechanical Testing*. Goddard Space Flight Center Greenbelt, Maryland.
- [3] Magargee, J. (2012). *Development of a Microscale Mechanical Testing System*. Goddard Space Flight Center Greenbelt, Maryland.
- [4] Ortiz, L. C. (2013). *Development of Small Scale Mechanical Test System*. Goddard Space Flight Center Greenbelt, Maryland.
- [5] Pieper, R., & Korpel, A. (1983). Image processing for extended depth of field. *Applied Optics*, 1449-1453.

TEMPERATURE AND FLOW RATE SENSOR FABRICATION

Jonathan Itschner
Electrical Engineering
West Virginia University
Morgantown, WV 26506

ABSTRACT

Microfabrication processes allow for the development of compact electrical sensors and mechanisms nearly invisible to the naked eye. A fluid flow and temperature sensor is one such device that can be used to measure the temperature and flow rate of a fluid through a specially designed channel. This project is unique in that it incorporates the fluid flow into the sensor chip, creating a "Lab on a Chip" type of system. It eliminates the need to route fluids outside of the sensor area, resulting in a more streamlined and efficient process for sensor measurements. Various microfabrication procedures such as photolithography, reactive ion etching, and metal deposition are used to construct such a sensor. The careful planning and ordering of each step of the manufacturing process ensures the end product will closely match the original design. Once the sensors are assembled, they are packaged in such a way so that data can be read from them and their functionality tested. A properly functioning sensor with expected data outputs indicates a successful fabrication run and verifies the sensor design.

INTRODUCTION

The microfabrication steps required to produce a working sensor involve numerous procedures and the careful ordering of the each process. A sequential worksheet outlining the specifics of each step of the fabrication process was drafted before work began in the laboratory. During the time spent in the Detector Development Laboratory, the photolithography process was completed numerous times from start to finish. Additionally, both wet and dry etching techniques were performed. Due to the potentially hazardous nature of the Detector Development Laboratory, certain safety precautions and training were necessary. Many of the processes involved the use of hazardous chemicals, and the proper personal protective equipment, such as aprons, face shields, and Trionic gloves, were required. A strong emphasis was placed on lab cleanliness, especially when working with acids or bases. Additionally, each machine used for the photolithography and etching processes required specialized training. Among these were a photoresist spinning machine, mask aligner, spray developer, profilometer, microscope, and a reactive ion etcher.

BACKGROUND

Thermal mass flow meters are a relatively common way to measure the rate at which a fluid with known thermal properties moves past a given point. A central heating element with a known temperature heats the fluid, and temperature sensors downstream and upstream of the fluid flow are used to determine the change in temperature, and by extension, the flow rate, due to the heating element. The temperature sensors can be made out of doped silicon. Due to the differing electrical characteristics of the p-type and n-type silicon, a temperature change in the fluid directly affects the current flow, which is a measurable quantity.

Microfabrication of sensors this small require careful planning and a specific ordering of fabrication steps. The process can be viewed in layers, in that most steps are additive or subtractive of each film made of different materials. General microfabrication techniques such as photolithography add a layer of UV light sensitive material called photoresist to the top layer, which can be selectively removed with a UV light source shining through a mask. This patterned photoresist acts as a protective layer in other stages of the fabrication process. Other techniques such as sputtering can be used to deposit materials onto a wafer. A target material, usually a metal, is bombarded with charged particles which transfer some of the metal onto the wafer.

These techniques are certainly not inclusive, as there are numerous other ways to deposit or remove layered materials from a wafer. However, the end result of each type of process is usually the same, in that it is either additive or subtractive. By adding and subtracting different layered materials in the proper order, a sensor design can be realized.

METHODS

The microfabrication processes used in the Detector Development Laboratory during the internship were photolithography, wet etching, and reactive ion etching. Photolithography could be considered an additive process, while both types of etching could be considered subtractive.

Photolithography

The photolithography process is relatively straightforward. The three major steps involved are photoresist spinning, exposure, and development. The end result of the process is a patterned layer of photoresist with a specific thickness as the top layer. Photolithography is performed in a specially lit area of the cleanroom which blocks UV wavelengths that would otherwise chemically affect the photoresist. Once the process has begun, the time spent between each step should be kept to a minimum due to the sensitivity of the photoresist. It should also be noted that there are both positive and negative photoresists that can be used in this process. The important difference between the two is the positive photoresist that is exposed to UV light is removed during development, whereas the negative photoresist exposed to UV light remains during development. A positive photoresist was used in this process.

Photoresist spinning is perhaps the most error prone step in the process. This is one of the reasons why performing this type of work in a clean room environment is critical. Any particles of dust or other types of debris that fall onto the surface of the wafer or into the photoresist render the end result useless if severe enough. As such, cleanliness practices are a crucial component of this step. Mouths of the bottles used to pour the photoresist onto the wafers must be thoroughly cleaned with acetone wipes before and after each pour to ensure no dried residue contaminates the photoresist. Special care must be taken to ensure the wafer surface is clean before pouring the photoresist. It is also important to ensure the spinning machine enclosure is clear of photoresist residue. All of these practices help limit potential sources of particle contamination.

The machine used for this step was a photoresist spinner. This type of machine involves a platform which vacuum seals to the underside of the wafer, and spins the wafer at high speeds around its center. The dynamic dispense spin coating method was used to distribute the photoresist onto the wafer surface. The photoresist is poured out onto the wafer from the center towards the edge while it is spinning at a low speed. This approach allows for greater uniformity of the photoresist coating.

After the photoresist is done being dispensed, the wafer is spun at a higher speed for a set amount of time. The spin speed and time generally determine the thickness of the final layer of a given type of photoresist. After the photoresist is finished being spun, the wafer is heated for a set amount of time in order to remove some of the solvent from the photoresist. This allows the photoresist to properly react to the UV light exposure in the next step.

After the photoresist is deposited onto the wafer surface, it is exposed to a UV light source through a patterned layer, called a mask. A mask in this context is a clear plate with a light-blocking pattern on one side of the plate. By placing the patterned side of the mask in contact with the photoresist layer, the UV light only interacts with the photoresist under the clear portions of the mask as seen in Figure 1.

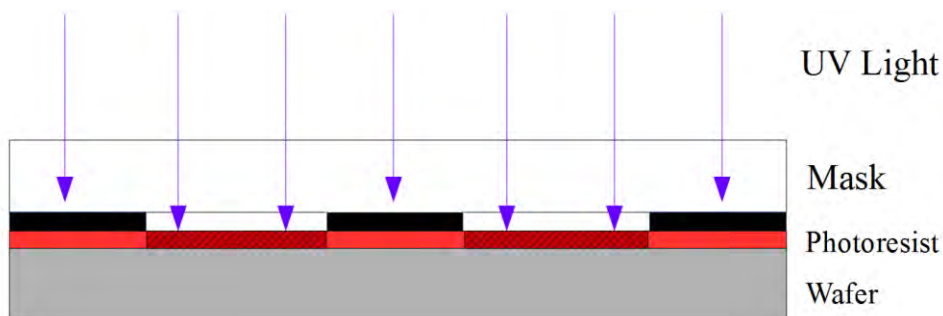


Figure 1: Photolithography Exposure Step

Important factors that affect the exposure results are the intensity of the UV light and the amount of time the photoresist is exposed to the light. The combination of both of these factors can be referred to as the dosage. It is critical to use the correct dosage of the UV light during the exposure step to ensure an accurate transference of the mask pattern onto the photoresist.

The machine used for the exposure step is called a mask aligner. This device houses a UV light source, and allows for the mask to come into contact with the photoresist surface. Both the mask and the wafer are placed into separate trays, and the exposure time is set to ensure the correct dosage. The process is relatively automatic, and once exposure finishes, the mask and wafer can be removed from the machine. It is important that the development step is completed soon after exposure due to the chemically sensitive nature of the photoresist affected by the UV light.

The final stage of the photolithography process is development. This involves the use of an aqueous basic solution applied directly onto the photoresist surface. Since a positive photoresist was used, chemical interactions between the portions of photoresist exposed to UV light and the development solution result in the removal of the exposed pattern, as seen in Figure 2.



Figure 2: Photolithography Development Step (Positive Photoresist)

The machine used for this step was a spray developer. The spray developer dispenses the development solution as a fine mist onto the photoresist, resulting in an evenly dispersed

application. The wafer is loaded into the machine, the proper development recipe is selected, and the cycle completes automatically. Since the development solution was basic, protective equipment such as Trionic gloves were used, and the wafer was thoroughly rinsed with distilled water after the cycle completed.

Wet Etching

Wet etching is used to remove specific layers of material based on chemical interactions. A buffered oxide etch (BOE) was used to remove the top oxide layer from the wafers. The BOE solution only interacts with patterned, or exposed, portions of the photoresist layer as a result of the photolithography step. Wet etching is an isotropic process, in that the chemical solution (etchant) reacts with the underlying material in all directions. Because of this, the wafer should not be immersed in the etchant solution any longer than necessary. If the etchant is allowed to interact for too long, the layer becomes over etched due to the undercutting of the etch, as seen in Figure 3.



Figure 3: Buffered Oxide Etching

The equipment used for this process was a chemical bench containing the BOE solution. The amount of time the wafer was immersed in the etchant solution was calculated using previously recorded etch rates. It is important to note that in this process, the layer underlying the oxide did not chemically interact with the etchant used for the oxide. This ensured that the etch did not go any deeper than the total depth of the oxide layer.

Reactive Ion Etching

Reactive Ion Etching is a dry etching technique used to remove a layer of a given material. It is considered "dry" since the process relies on the use of chemically reactive ions contained in a plasma rather than a liquid etchant. Because of this, it is critical that the process is carried out in a vacuum to ensure only the desired gas composition is used for ion formation. The ions bombard the exposed portions of the layer, and remove parts of the layer through chemical interactions. Reactive Ion Etching is highly anisotropic, in that there is little to no undercutting of the material beneath the protective layer of photoresist. It should also be noted that the layering of the materials that were dry etched were considered to be excellent "stop" layers. That is, it was much more difficult to remove the material under the layer being actively etched due to the lack of chemical interactions between the ions and the underlying material.

The machine used for this process was a reactive ion etcher. The wafer was loaded onto a platform inside a hinged chamber, and a high powered vacuum sealed the chamber after loading. The proper recipe detailing the ratio of reactive gases to be used, radio frequency power for plasma formation, and the run time for the process was selected and the etching was started. After the process finished, the vacuum was released and the wafer was removed from the chamber.

Methods of Observation

Throughout each of the fabrication processes, accurate and consistent observations were an important way to monitor progress and verify that each step was completed. Due to the subtractive nature of each of the etching steps, it was useful to measure the height of the newly formed feature in the etched layer. Based on the step height measurement and a predicted step height based on expected etch rates, the progress of a given etch could be determined. This was a useful way to determine whether or not a given etching step was completed.

A profilometer machine was used to measure the step height before and after a given etch. The operation of the profilometer was computer driven and involved minimal physical interaction. The etched wafer was placed onto a platform with a vacuum system to hold the wafer in place. The platform receded to a position beneath a specialized probe sensor used to measure the height differences. The probe was then lowered onto the surface of the wafer after the proper positioning adjustments were made, and height measurements were recorded on the computer as the probe traveled across the surface features on the wafer.

Visual observations were another key method used to check the progress of the etching process. Since each layer had a unique coloration, a microscope was used to observe the coloration of the features before and after the etch. Based on a predicted coloration of a layer, this visual approach used in tandem with the profilometer helped confirm the completion of an etch.

RESULTS

To reach the predicted outcomes for each process, a good deal of troubleshooting was required. Each of the steps did not seem to work as predicted due to the level of experience with cleanroom practices and variability in the equipment functionality.

Photolithography

The photolithography process was perhaps the most time consuming activity. The subsequent etching steps relied on an accurate pattern transfer from the mask, so the results from the photoresist step needed to be high quality. Significant challenges faced in this step were particle contamination during spinning and the determination of the proper UV light dosage.

Particle contamination was a common occurrence throughout the spinning process. If any particles were in the photoresist or on the surface of the wafer, large streaks of uneven photoresist coating towards the edge of the wafer would appear. In addition, sometimes particles in the photoresist did not reveal themselves as problematic until later steps, sometimes even after development. This had the potential to directly affect the transference of the mask pattern onto the photoresist. In Figure 4, particles in the photoresist interfered with the pattern exposed to the UV light source, which resulted in the spots of underexposed and underdeveloped photoresist in the feature area that would otherwise be free of photoresist.

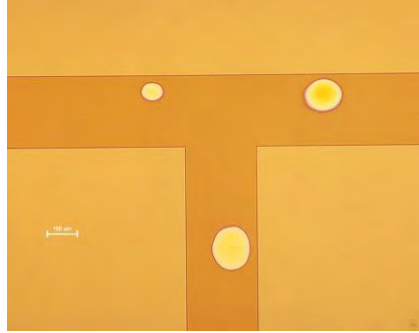


Figure 4: Particle Contamination Affecting Features

Another issue faced during photolithography was determining the proper dosage of UV light. Factors that directly affected the proper dosage included the reflectivity of the material beneath the photoresist and the size of the features on the mask. If the photoresist was exposed to the UV light for too long (the dosage was too high), then the features transferred to the photoresist did not match the mask. This was generally evident through deformed corners, and a general lack of feature sharpness, as seen on the left in Figure 5. With the correct dosage of UV light, the features exactly match the pattern on the mask, and generally have sharply defined corners, as seen on the right in Figure 5.

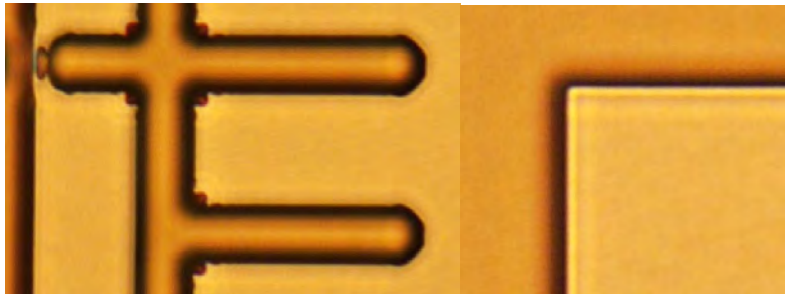


Figure 5: UV Dosage Effects on Feature Definition

Wet Etching

The most important variable considered during the Buffered Oxide Etch was the amount of time the wafer spent in the etchant solution. In two separate instances, severe overetching and minimal overetching were observed, as seen on the left and right in Figure 6, respectively.

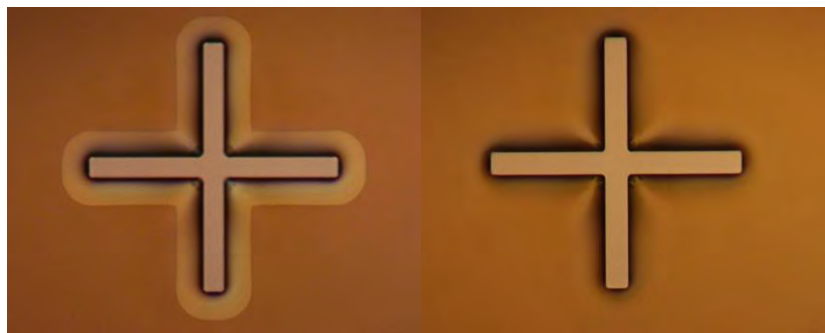


Figure 6: Severe vs. Minimal Wet Etching

Another notable result of the wet etching process was the observable color change under a microscope, as seen in Figure 7. In the image on the right (after wet etching), a distinct coloration difference between the photoresist layer (yellow) and the polysilicon layer (gray) can be seen. Since the layer beneath the etched away oxide is polysilicon, this is a good indicator of a successful etch.



Figure 7: Color Change after Wet Etch

Reactive Ion Etching

The results of the reactive ion etching process were generally similar to the results of the wet etch, except there was no observable undercutting due to the anisotropic nature of the process. The step heights of each etched layer were predicted, and the profilometer was used to monitor the progress of each etching step. Often more etching was required after measuring the step height and visually checking the coloration under the microscope. Some of the colors were predictable, which was useful in determining completion of the etch, as seen by the distinctive coloration in Figure 8.

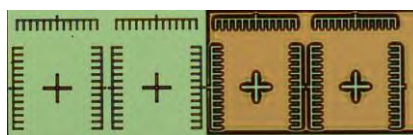


Figure 8: Distinguishable Coloration after Dry Etch

DISCUSSION

Perhaps the most significant lesson learned from this experience is the disparity between theory and practice. A good portion of the summer was spent researching the various microfabrication techniques, and while reading the steps of a process in a book or website may be a good way to become familiar with a process, it is no substitute for a hands on experience. This was clearly the case with the photolithography process, as evidenced by the issues with particle contamination and determining the correct UV dosage. This principle was also evident in both of the etching processes. Direct, hands on involvement with both the wet and dry etching processes helped to develop a better understanding of how each process worked in the real world. For example, the expected etch rates that were researched turned out to be more of a guideline than an authoritative number. It was only once the process was underway and direct observations could be made with the profilometer and microscope that the process was fully understood. Seeing the physical realization of something that was theoretical in a textbook was an extremely satisfying experience.

A noteworthy aspect of the internship was the training required to use the equipment required for the processes. The Detector Development Laboratory contains hazardous chemicals and potentially dangerous equipment. As such, being properly trained to use the machines was a critical aspect of working in the lab. Since there were a limited number of machines, communication among lab workers was a key element of a successful work flow. This was a fantastic experience that drastically helped improve interpersonal skills.

Overall, this experience proved to be an effective introduction to the world of microfabrication, encompassing the design methodologies, processes, and techniques used to create such miniscule devices.

ACKNOWLEDGEMENTS

Special acknowledgement and thanks is extended to the WV Space Grant Consortium for providing the financial means for this experience. Additional thanks goes to George Manos, whose mentorship and guidance were invaluable, and Manuel Balvin, for providing assistance with the fabrication processes.

REFERENCES

Madou, Marc J. Fundamentals of Microfabrication: The Science of Miniaturization. Boca Raton: CRC, 2002. Print.

"Spin Coating Theory." Spin Coating Theory. Web. 11 Aug. 2015.

"Photolithography." Yaşam Bilim Merkezi. N.p., n.d. Web. 11 Aug. 2015.

<http://www.lifesci.boun.edu.tr/en/merkez_altyapilari/item/5_fotolitografi>.

ANTI-TUMOR ACTIVITY OF ORGANOMETALLIC COMPOUNDS

Alnairouz Katrib
Genetics and Biotechnology
West Virginia State University
Charleston, WV 25112

ABSTRACT

Metallic compounds play an important and a large role in cancer treatment. Cisplatin and its derivatives are the most notable case and are used in over half of the treatment plans for cancer. However, there are many tumors that are resistant to these compounds and additional compounds are needed for cancer therapy. We tested the anticancer activity *in vitro* of some new organometallic compounds that were constructed in the lab of Dr. Joseph Merola at Virginia Tech, a collaborator of Drs. Molnar and Hankins. The objectives of this study were to test compounds from Dr. Merola's lab and to construct a new Ruthenium II/Paladium II compound and to evaluate the effects of this new compound and other new organometallic compounds on proliferation of human tumor cells *in vitro*.

INTRODUCTION

The American Cancer Society projects that in the United States alone there will be over 1.6 million new cancer cases and almost six hundred thousand cancer deaths in 2015. While cancer survival rates have improved over time, the survival rates are still low for many cancers. Examples include the deadly brain cancer glioblastoma for which there is less than a 10% five-year survival post-diagnosis and pancreatic cancer with a five- year survival rate or only 6%. Even largely benign tumors, when not completely surgically resectable may cause mortality due to their impact on surrounding tissue. Notable among these are meningiomas, one-half of which arise in the skull base where complete removal is often not possible. There is no effective chemotherapy for meningiomas.

Metals are essential components of living organisms that are highly regulated under normal conditions and abnormalities of metal ion concentrations are associated with cancer as well as other pathologies. Metallic compounds already play a large role in cancer treatment. The most notable case is cisplatin and its derivatives, which are used in over half of the treatment plans for cancer. However many tumors are resistant to these platinum compounds. Further, targeting of platinum compounds has proved problematical and toxicity, particularly nephrotoxicity, can be a serious side effect. There is, a therefore, need for additional metallic compounds for cancer therapy and efforts to develop these have been reviewed by Gasser *et al.* (2011) and Martins *et al.* (2014). Compounds, such as the organometallic compounds developed by Dr. Merola's group, with known antibacterial activity are promising candidates in the search for novel organometallic anti-cancer compounds.

Although the activity of the new compounds cannot be accurately predicted, because of the extensive use of metal ions in biological systems, the reactivity towards organic substrates, their

characteristics such as redox activity and the known anti-bacterial activity of some of the compounds that we will be investigating, it would be extremely surprising if none of the compounds demonstrated anti-cancer cell activity. Compounds containing some metals, such as arsenic and cadmium, have not been useful because of toxic side-effects. Some ruthenium-containing compounds are currently in clinical trials. The compounds that we are interested include some ruthenium compounds as well as novel compounds containing rhodium and iridium. The work initiated here is only the first step in evaluation since the ultimate usefulness will depend on mechanism of action and overall toxicity.

MATERIALS AND METHODS

Cell Culture

Culture of meningioma cells CH157-MN, pancreatic cancer cells PANC-1, and glioblastoma cells U87 was in DMEM (Life Science Technologies) with 5% FBS (CH157-MN). The cell work was performed under Biosafety Level 2 practices and containment.

Organometallic compounds

Four compounds based on the same five carbon ring structure were received from Dr. Merola's lab. Of these, two were not highly soluble in the cell culture media, so testing this summer was confined to the other four compounds each of which had cobalt or iridium with ring attached as well as ethambutol (Ir(EMB)Cl₂), proline (Ir(pro)Cl), alanine (Co(ala)I) or phenylalanine and glycine (Ir(phegly)Cl) attached.

Treatment of cells with organometallic compounds

Cells were plated in 96 wells plates. The solid compounds were initially dissolved in DMSO and the initial solution diluted in DMEM. In all cases (including 0 concentration for each compound) the final concentration of DMSO in the media was 0.1%. After 24 hours of plating, the media was replaced with phenol red free media and cells were treated with the organometallic compounds, Ir (EMB) Cl₂, Ir (Pro) Cl, and Ir (phegly) Cl. Then on the second day, the substrate WST8 was added to the treated cells. After one, two or three days of treatment, the assay substrate (WST-8) was added.

Cell viability/proliferation assays

WST-8 assay was used to evaluate the cell proliferation and viability (Dojindo Molecular Technologies). Cells were plated into 96-well tissue culture plates. The WST-8 assay is a modification of the MTT cell proliferation assay, but the reagent is less toxic than MTT and is reduced to a soluble rather than insoluble product. Before we received the compounds from Dr. Merola's lab, serial dilutions were made of each of the three cell lines and these were used to verify the linearity of the assay for each cell line over the cell concentrations that we were using. Since the WST-8 assay is based on reduction of the substrate, reduction of substrate was evaluated for the compounds without the presence of cells (at the same concentrations used to treat the cells). For assaying the effects of the compounds on the cells, the cells were allowed to attach to the plate overnight before treatment. Three replicates were done for each concentration of each compound. Number of viable cells was assessed at 1, 2, and 3 days post-treatment. WST-8 assays were performed according to the manufacture's protocol and absorbance at 450 nm was measured on a BioTek Synergy HT microplate reader.

RESULTS

Verification of linearity of the WST-8 assay for CH157-MN, PANC-1 and U87 cells

The linearity of the WST-8 assay was evaluated for each of the cell lines we used was verified over a range of cell concentrations. It should be noted that the concentration shown is the concentration plated. The concentration of cells could be as much as 2 times as great as tested 24 hours later and as much as 4 times as great after 48 hours.

- **WST-8 Assay for meningioma cells CH157-MN after 24 hours**

Concentration of cells/ μL	Absorbance at 450 nm
0	0.22
1	0.24
5	0.27
10	0.27
25	0.31
50	0.35
100	0.45

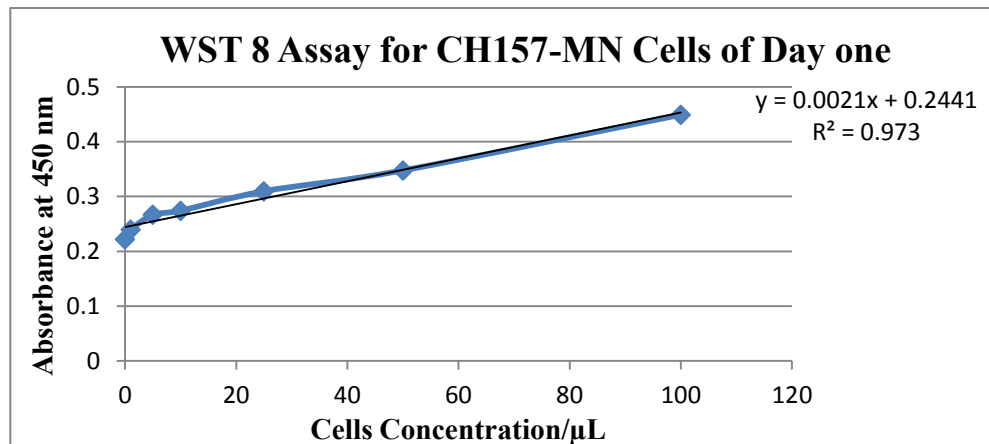


Figure 1: Linearity of the WST-8 assay for CH157-MN cells. Cells were plated into 96-well plate. 24 hours later, the substrate was added, and the plate was incubated for two hours before taking the readings.

- **WST-8 Assay for meningioma cells CH157-MN after 48 hours**

Concentration of cells/ μL	Absorbance at 450 nm
0	0.059
1	0.064
5	0.075
10	0.096
25	0.136
50	0.208
100	0.352

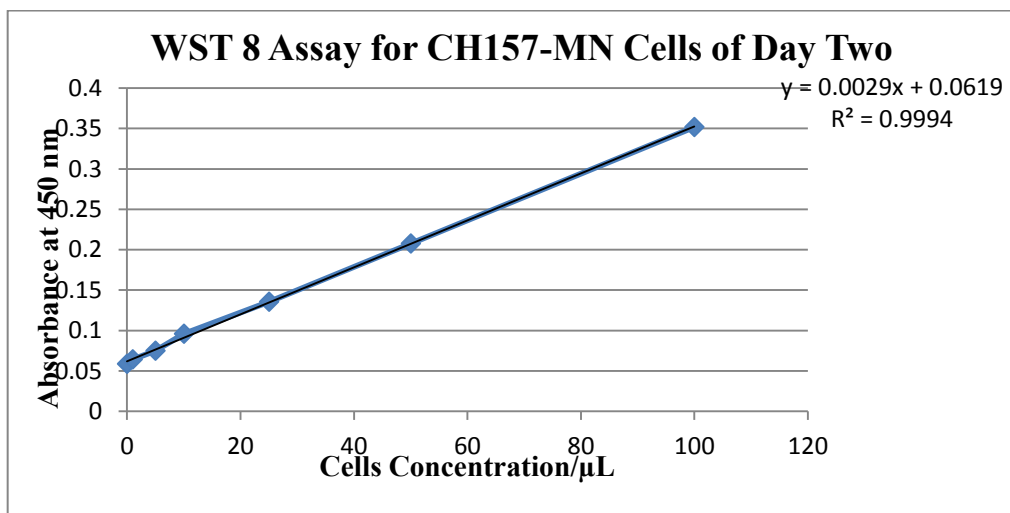


Figure 2: Linearity of the WST-8 assay for CH157-MN cells. Cells were plated into 96-well plate and after 48 hours, the substrate was added, and the plate was incubated for two hours before taking the readings.

- **WST-8 Assay for Pancreatic cancer cells PANC-1 after 24 hours**

Concentration of cells/ μ L	Absorbance at 450 nm
0	0.118
1	0.117
5	0.105
10	0.138
25	0.150
50	0.159
100	0.262

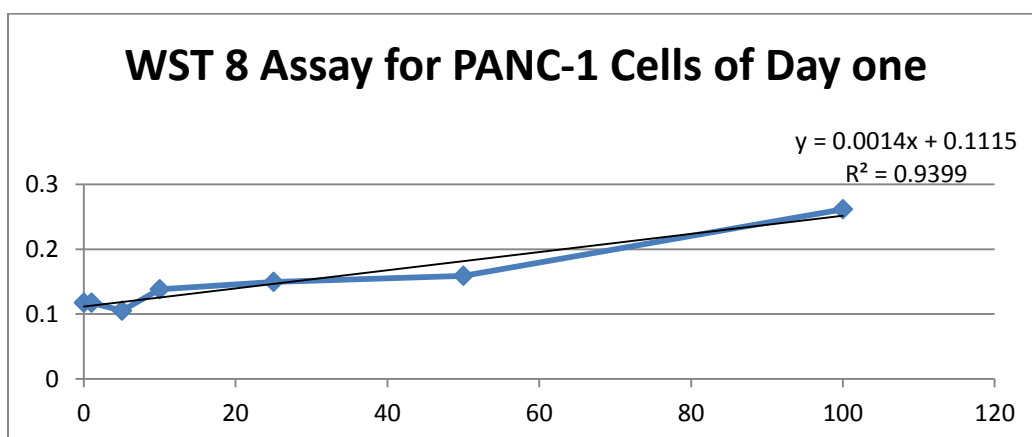


Figure 3: Linearity of the WST-8 assay for PANC-1 cells. Cells were plated in 96-well plate for one day, then the substrate was added, and the plate was incubated for two hours before taking the readings.

- **WST-8 Assay for U87 Glioblastoma cells after 24 hours**

Concentration of cells/ μ L	Absorbance at 450 nm
0	0.116
1	0.117
5	0.133
10	0.142
25	0.153
50	0.167
100	0.180

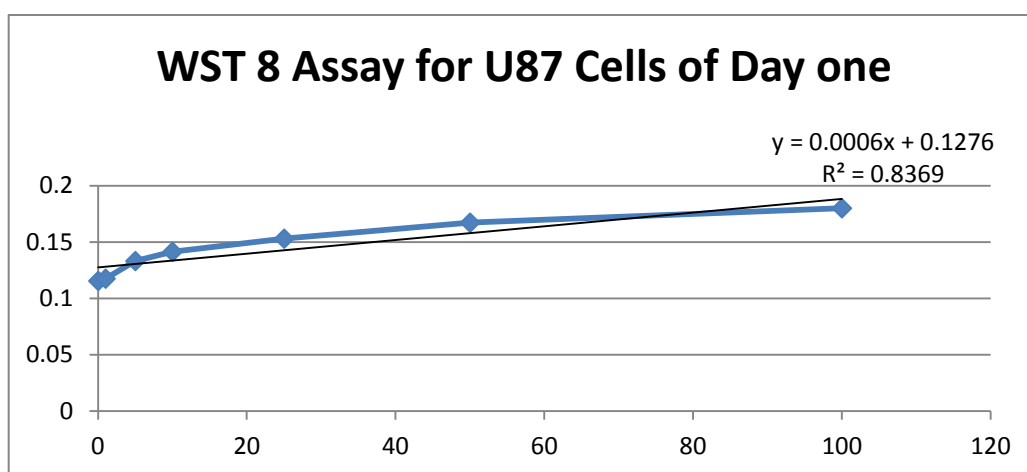


Figure 4: Linearity of the WST-8 assay for U87 cells. Cells were plated into 96-well plate for one day, then the substrate was added, and the plate was incubated for two hours before taking the readings.

Evaluation of reduction of WST-8 substrate by the compounds in the absence of cells

Reduction of the WST-8 substrate by the organometallic compounds in the absence of cells was evaluated over the range of concentrations that we used in the cell viability/proliferation assay. Two of the compounds (Ir(Pro)Cl and Ir(Phegly)Cl) reduced the substrate in a concentration dependent manner (below). The Ir(EMB)Cl₂ and Co(ala)I compounds did not show any reducing activity (data not shown).

- **WST-8 reduction by Ir(Pro)Cl.**

Compound's Concentration	Absorbance at 450 nm
0.0 mg/mL (DMSO vehicle control)	0.074
0.0625 mg/mL	0.090
0.125 mg/mL	0.109
0.250 mg/mL	0.142

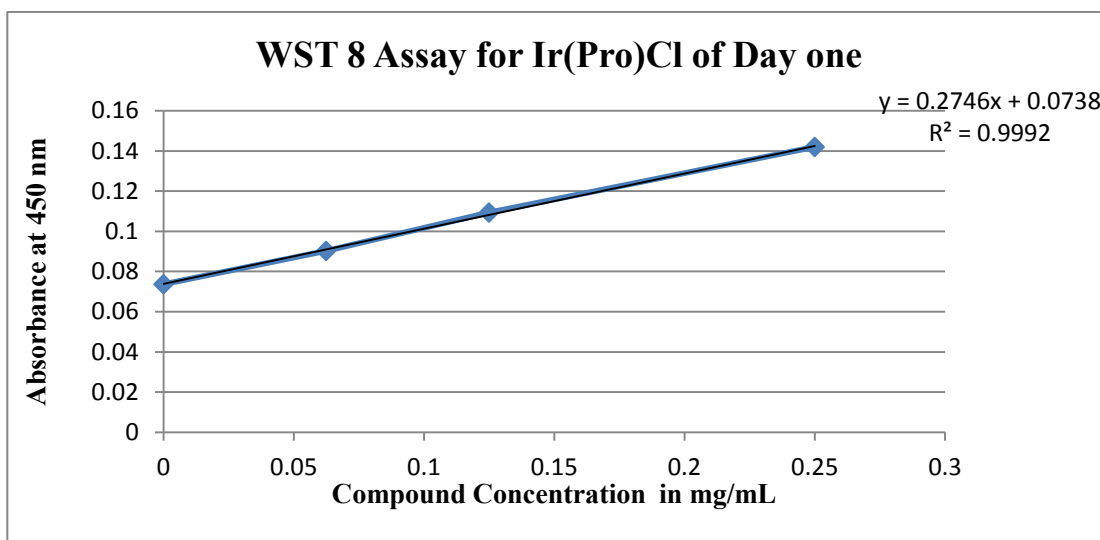


Figure 5: The organometallic compound Ir(Pro)Cl was plated in 96-well plate for one day, then the substrate was added, and the plate was incubated for two hours before taking the readings.

- **WST-8 reduction by Ir(Phegly)Cl.**

Compound's Concentration	Absorbance at 450 nm
0.0 mg/mL (DMSO vehicle control)	0.07
0.0625 mg/mL	0.097
0.125 mg/mL	0.129
0.250 mg/mL	0.176

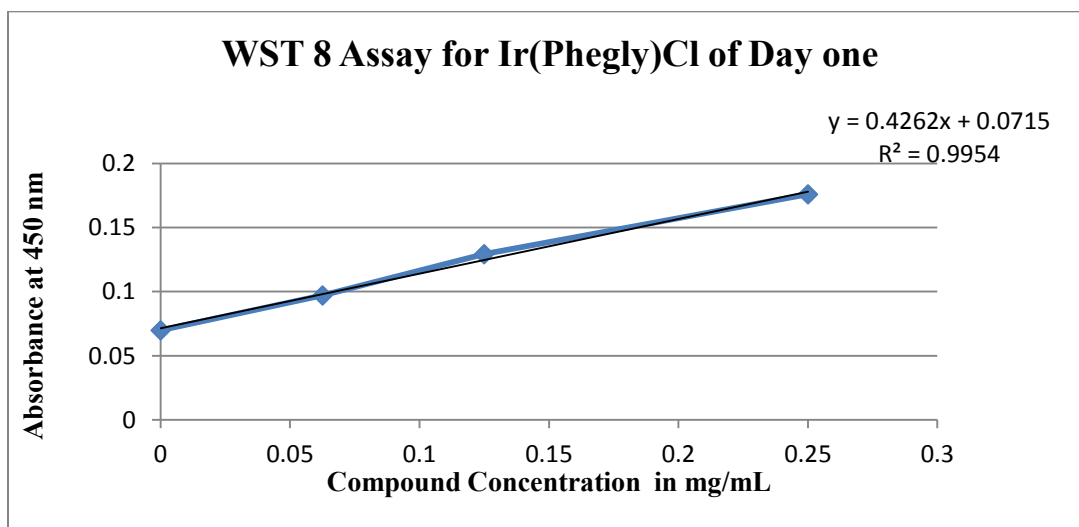


Figure 6: The organometallic compound Ir(Phegly)Cl was plated in 96-well plate for one day, then the substrate was added, and the plate was incubated for two hours before taking the readings.

Cell Proliferation/Viability after Treatment with the Organometallic Compounds

Based on WST-8 assay, reduction in the numbers of viable CH157-MN cells was apparent for the Ir(Pro)Cl compound by day one, for the Co(Ala)I compound by day two and for the Ir(PheGly)Cl compound by day 3 (below). No effect on viable cell numbers was observed for the Ir(EMB)Cl₂ compound. Results were too variable for the U87 and PanC-1 cells due to problems with cell clumping. Towards the end of the period of the work described here we found a way to avoid the clumping, but did not have time remaining to further evaluate the effects of the compounds.

- **WST-8 Assay for CH157-MN cells treated with the Ir(Phegly)Cl compound for 72 hours**

Compound's Concentration	Relative to DMSO
0.0 mg/mL (DMSO vehicle control)	1
0.0625 mg/mL	0.81
0.125 mg/mL	0.77
0.250 mg/mL	0.66

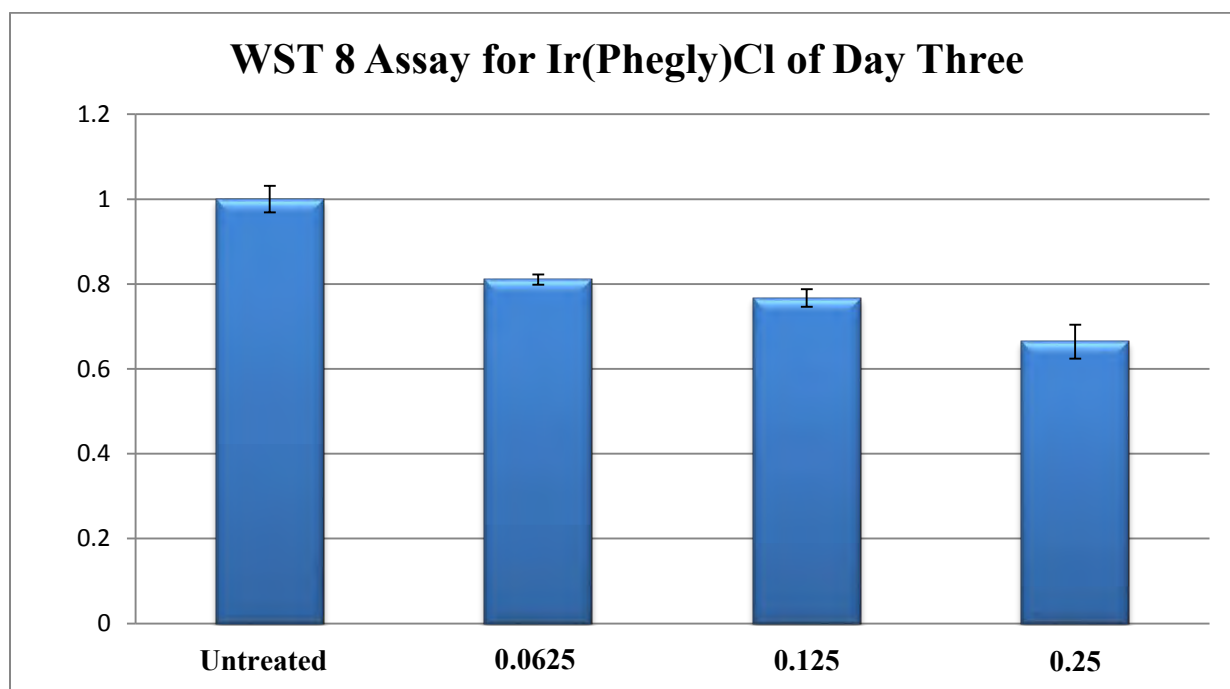


Figure 7: The CH157-MN cells were plated and treated with the organometallic compound Ir(Phegly)Cl in 96-well plate for three days, then the substrate was added, and the plate was incubated for two hours before taking the readings.

- WST-8 Assay for CH157-MN cells treated with the Ir(Pro)Cl compound for 24 hours

Compound's Concentration	Relative to DMSO
DMSO	1
0.0625 mg/mL	1.02
0.125 mg/mL	0.90
0.250 mg/mL	0.68

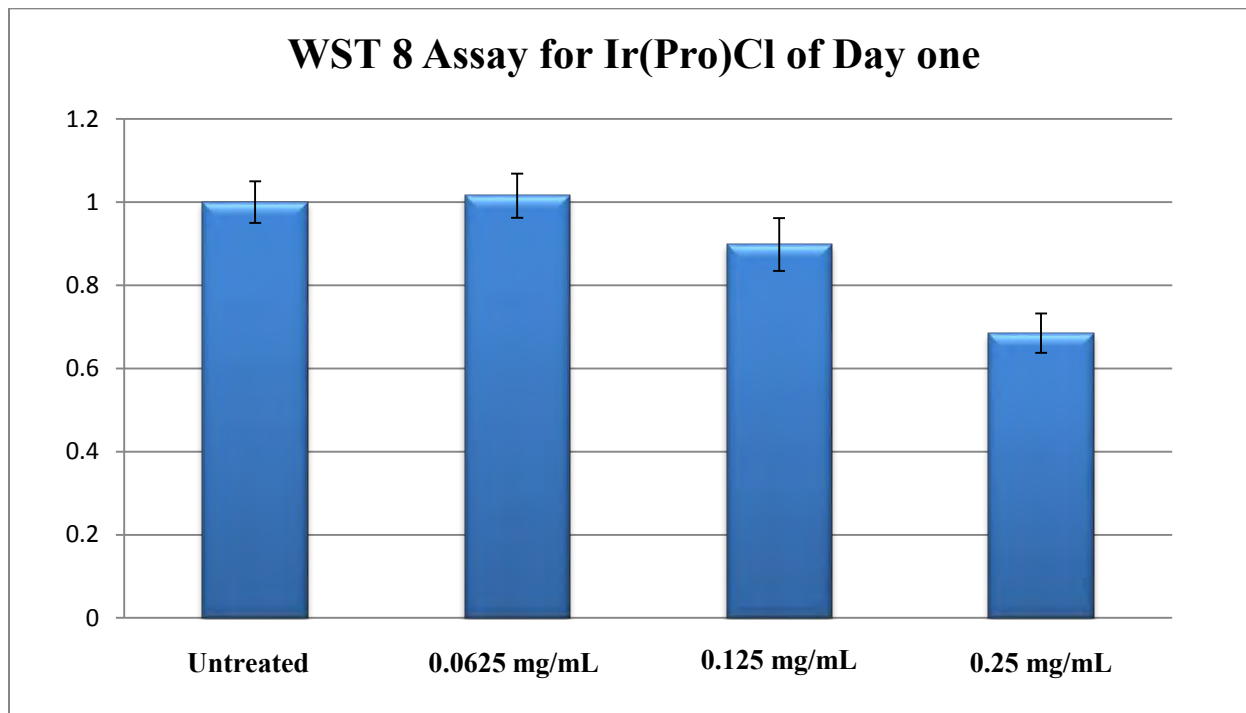


Figure 8: The CH157-MN cells were plated and treated with the organometallic compound Ir(Pro)Cl in 96-well plate for one day, then the substrate was added, and the plate was incubated for two hours before taking the readings.

- WST-8 Assay for CH157-MN cells treated with the Co(ala)I compound for 48 hours

Compound's Concentration	Relative to DMSO
DMSO	1
0.0625 mg/mL	0.91
0.125 mg/mL	0.88
0.250 mg/mL	0.90

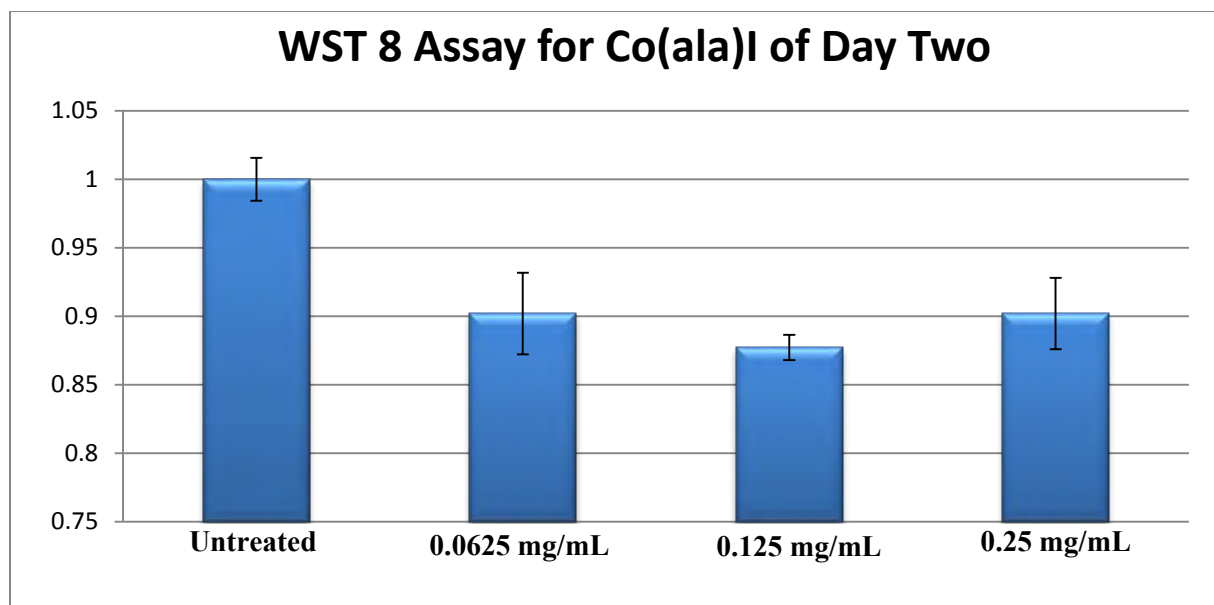


Figure 9: The CH157-MN cells were plated and treated with the organometallic compound Co(ala)I in 96-well plate for two day, then the substrate was added, and the plate was incubated for two hours before taking the readings.

CONCLUSIONS

The WST-8 assay gave a linear response for the different cancer cell lines, CH157-MN meningioma, PANC-1 pancreatic cancer, and U87 glioblastoma as the concentration of the cells increased. When we evaluated whether the organometallic compounds alone were capable of reducing WST-8, we found that Ir(Pro)Cl and Ir(Phegly)Cl reduced WST-8 in a concentration dependent manner while the other two compounds did not show any reducing activity. Because of this, the reduction in viable cells after treatment with these two compounds would be expected to be an under measurement of the true effect of the compounds on the cells. Different kinds of assays could be used in the future like Cell Titer Glo (Promega) or Cell Titer Fluor (Promega) in order to get more sensitive measures of the effects of these compounds on cell viability/proliferation.

After three days of treating CH157-MN cells with Ir(Phegly)Cl, the highest does of the compound showed lower number of cells compared to cells treated with only DMSO.

For the compound Ir(Pro)Cl, the results after 24 hours of treatment showed that the compound lowered the number of cells by increasing the does.

By 48 hours of treatment with Co(ala)I viable numbers of CH157-MN cells were significantly decreased, although there was no clear concentration dependence.

For the fourth compound Ir(EMB)Cl₂ we did not observe any effect at any of the time points.

So, organometallic compounds have different effects at different time intervals based on the type of cancer cell line used. As this research is still at its initiative stage, no specific pattern detected to draw the exact effect of the four compounds that were tested and further testing is needed.

FUTURE PLANS

- The meningioma cells CH157-MN will be treated again with the four different organometallic compounds Ir(EMB)Cl₂, Ir(Pro)Cl, Co(ala)I, and Ir(Phegly)Cl for 24 hours, 48 hours, and 72 hours and we will use an alternative assay to evaluate the results.
- The same experiment will be repeated with the PANC-1 cell line and U87 cells. For these cells, the cells will be pelleted at a lower relative centrifugal force to allow better re-suspension of the cells and less clumping.

ACKNOWLEDGEMENTS

I would like to thank NASA WV Space Grant Consortium for funding my research work for the summer of 2015 which helped me to explore a new section in the field of cancer research. Special thanks for my mentor Dr. Gerald Hankins who helped and guided me and my lab partner Amanda Smith during our work on this project. Also, Thanks to our Chemistry mentor Dr. Sharon Molnar who we collaborated with and with her lab assistants Aaron Smith and Justin Spradling.

REFERENCES

- Gasser G, Ott I, Metzler-Nolte N: Organometallic anticancer compounds. **J Med Chem** **54**: 3-25, 2011.
- Karpin GW, Merola JS, Falkinham III JO: Transition metal- α -amino acid complexes with antibiotic activity against *Mycobacterium* ssp. **Antimicrob Agents Chemother** **57**: 3434-3436, 2013.
- Klajner MJ: Organometallic compounds as anti-cancer agents: interaction with DNA and migration in cells. PhD Dissertation, University of Strasbourg France and Wroclaw University of Technology Poland, 2011.
- Martins P, Marques M, Coito L, Pombeiro AJL, Baptista PV, Fernandes AR: Organometallic compounds in cancer therapy: past lesions and future directions. **Anti-Cancer Agents Med Chem** **14**: 1199-1212, 2014.

LONG-DURATION, LOW-GRAVITY PROPELLANT SLOSHING EXPERIMENT

Steven Kosko

Mechanical Engineering and Aerospace Engineering
West Virginia University
Morgantown, WV 26505

ABSTRACT

The sloshing of propellant inside spacecraft hinders the ability to control its orientation and therefor the spacecraft's overall performance. For this reason an increased understanding of propellant slosh is needed. Current computational fluid dynamic (CFD) models of propellant sloshing have yet to be validated for the long duration effects of propellant sloshing. Validating current CFD models will enable engineers to improve tank design and attitude control systems to better account for the long duration effects. For collecting the data necessary to validate the CFD a free floating experiment has been designed to be tested on the International Space Station (ISS). This experiment will be able to record the forces generated by the propellant slosh, video of the sloshing as well as the effects of the sloshing on the orientation of the experiment. Through collecting this data current CFD models can be validated for simulating long duration propellant slosh.

INTRODUCTION

The sloshing dynamics of liquid propellant tanks in micro-gravity environments present many current problems that affect the performance of spacecraft attitude control. Movement of the propellant in fuel tanks affects the gyroscopic stability of spacecraft, this instability can lead to catastrophic control issues caused by nutation (rocking, swaying, or nodding motion). Currently, there is a deficit of experimental benchmarks to validate CFD sloshing predictions and because of this, predicting slosh motion continues to be of great difficulty to the aerospace industry. The purpose of this project is to begin designing an experiment that will read the forces and moments on the inside walls of a propellant management device (PMD) and propellant tank, while collecting low-gravity, long-duration sloshing image and location data for the purpose of validating CFD slosh motion models [Chato 2005].

BACKGROUND

Sloshing problems have occurred many times throughout the history of space flight. These issues are becoming of increasing concern in spacecraft design and application. The effects of propellant slosh have interfered with multiple processes and operations which are critical to mission success of the spacecraft, such as desired trajectory, docking operations, gyroscopic stability, and pointing accuracy. Propellant slosh has had major effects on several missions. In 2007 one of SpaceX's falcon one rockets experienced a premature engine shutdown due to propellant slosh. During the launch, fuel sloshed away from the intake of the engine intake, which starved the engine of propellant causing it to shut down. This resulted in the rocket failing to achieve its intended orbit [Shallhorn 2014]. Another instance of a propellant slosh related malfunction involved a NEAR satellite. The uncontrolled osculation developed in the propellant which disrupted the attitude control system of the satellite causing it to tumble uncontrollably. The satellite eventually entered

safe mode, which allowed the osculation to be dampened out and for control to be regained by the satellite. During satellite's attempt to regain attitude control, it expended a significant amount of fuel, nearly depleting its fuel margin. [Reyhanoglu]

Currently CFD models are used to predict the motion of the propellant inside the fuel tank for rocket launches and other mission critical maneuvers. However these models have yet to be validated for such low gravity environments and can still show inconsistent results. In one instance two separate groups simulated the propellant slosh in the second stage of a Delta IV rocket for a particular launch. Even though both groups used the same program, the results differed significantly. This caused a delay in the launch until a conclusion on the simulation was reached [Burke, 2010]. To close this gap it is imperative that CFD models be calibrated with long-duration, low-gravity sloshing data to achieve better accuracy of the fluid dynamic modeling. With improved models validated by experimental data, NASA, as well as other aerospace companies will be able to better predict the effects of propellant slosh, and design new tanks to better control propellant slosh.

OBJECTIVE

To collect the experimental data needed to validate the CFD models a testing apparatus needed to be designed. The objective of this project Research and develop the preliminary design of a long-duration, low-gravity sloshing experiment for testing in orbit. Necessary objectives of the preliminary design include.

- Create list of possible off-the-shelf sensors and hardware to capture fluid behavior that meets the requirements for experimental demands in a space environment.
- Create list of support equipment needed to support sensor function
- Determine sensor and hardware mounting positions
- Design structure necessary for experiment

EXPERIMENTAL DESIGN

The design of the experiment consists of a free floating platform on the ISS which will contain a partially filled acrylic tank. This platform will then be subjected to several maneuvers to initiate sloshing of the propellant, while the experiment collects force, acceleration and video recordings of the entire sloshing event. The free floating platform utilizes the selected instrumentation, as well as components flown on previous experiments currently on the ISS, to collect visual and force data on the effects of propellant slosh. The design consists of an acrylic tank mounted on force sensors, inside a containment box designed to be compatible with existing Spheres and Vertigo hardware, shown in Figure 1.

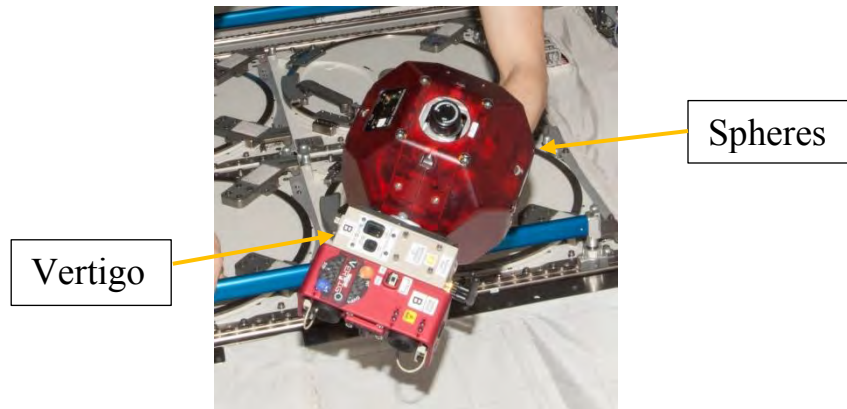


Figure 1, Spheres and Vertigo.

Spheres or Synchronized Position Hold, Engage, Reorient, Experimental Satellites, are experimental platforms on the ISS for conducting research on automated docking and formation flying of spacecraft, as well as other experiments. Each of the modules of the Spheres module is a self-contained satellite which uses compressed CO₂ for maneuvering on the ISS [Burke 2010]. For this experiment 2 Spheres modules will be attached to the experiment, one at each end of the tank. These modules can and have been programmed to work in tandem with each other, and will work in tandem to conduct maneuvers of the free floating experiment. These maneuvers will excite propellant and initiate the sloshing of the fluid in a similar manner as other spacecraft.

The Vertigo system, is an expansion payload used with Spheres and other experiments as a test bed for space based experiments. This hardware can function as an avionics platform for this experiment. Each Vertigo system contains Pico – ITX P830 computers, SSD storage, a stereo vision camera system, power regulators, expansion ports and control panel [Burke 2010]. This modular system contains more than half of the support hardware needed for this experiment. By utilizing this modular hardware which is still currently on the ISS, the size and weight of the experiment which needs to be launched can be greatly reduced.

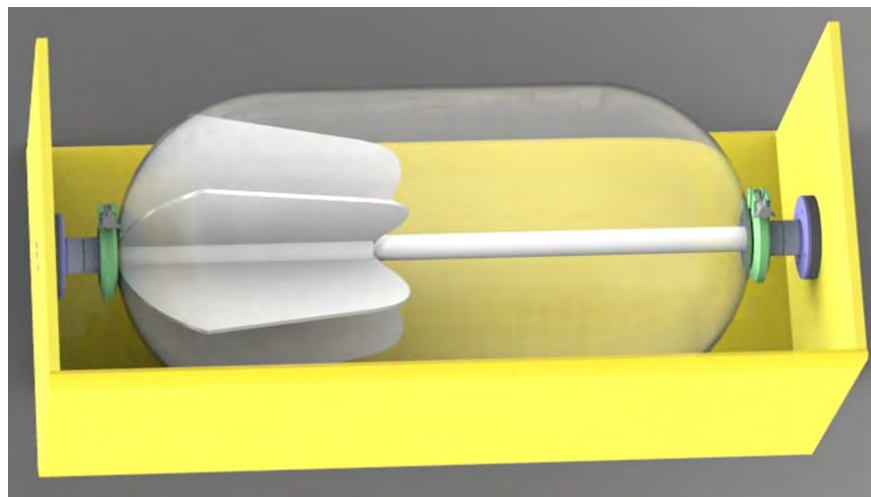


Figure 2

The design also allows for easy tank removal and interchangeable tanks. The acrylic tank is a hemispherical tank 30 cm in length and 15 cm in diameter. Designed by ATK the tank will include a propellant management device (PMD). Figure 2 depicts the acrylic tank with PMD mounted on force sensors inside the containment. The tank will be sealed with the fluid inside before launch. The ends of the tank will consist of flat plates to which the force sensors can be mounted. The mounting for the tank as shown in Figure 2 will consist of round flat plates which will be secured to the flat plates on the ends of the tank by V band clamps. The attachment by the V-band clamp was selected to make the tank easily removable without the use of screws. The flat plates are bolted to the force sensors which serve as the only contact between the acrylic tank and the containment.

INSTRUMENTATION

To validate CFD models the experiment must be able to collect, the reaction forces on the tank from the sloshing, as well as a video recording of the sloshing event. Additionally the position and acceleration of the experimental apparatus will need to be recorded.

For the recording of the reaction forces of the sloshing the Nano 17 force sensor is to be used. This is a high resolution 6 axis force sensor, designed for robotic surgery. This sensor can resolve 0.0381 gram–force. This level of precision is needed to measure the small reaction forces of the sloshing event. The capability to sense forces in all 6 axis, allows the tank to be mounted on only 2 sensors which minimized the interference with the video recording of the sloshing. The silicon strain gauge in this force sensor also experiences near zero noise.

To record video of the propellant sloshing the Aptica UI-5580CP was selected. With a resolution of 2560 x 1920, frame rate of 14.1 Fps, and a 5Mp pixel class, the UI-5580CP will handle high quality video of the tank sloshing behavior and meets all communication, space environment, and power specifications. Additionally this camera has already been flown on the ISS.

To record the position and acceleration of the experiment the CHR-UM7 IMU was selected. This IMU meets and exceeds our objectives for recording both linear and rotational accelerations on 6 axis. The UM7 combines triaxial accelerometer, rate gyro, and magnetometer data using a sophisticated Extended Kalman Filter to produce attitude and heading estimates. This system will be used to record the maneuvers conducted by the experiment as well as the experiments response to the propellant sloshing.

CONCLUSION

The validation of current CFD models is an imperative goal for future space exploration. Such validation is necessary for accurate predictions of spacecraft behavior. For the validation of current CFD models an experiment must be conducted to test the long duration effects of propellant sloshing in a microgravity environment. The experiment developed for producing this data consists of a partially filled acrylic tank with PMD which will be launched on and tested onboard a small satellite of international space station. The acrylic tank will be subjected to different maneuvers in the low gravity environment while data of the sloshing event is collected. The data will be collected by force sensors, inertial measurement units, and digital video cameras. The data collected will consist of the force of the fluid on the wall of the tank as well as the effects of the

propellant slosh on the orientation of the spacecraft. From this data current CFD models can be validated for the simulation of long duration propellant slosh.

REFERENCES

- Bakkum "Investigation of Propellant Sloshing and Zero Gravity Equilibrium for the Orion Service Module Propellant Tanks," Department of Physics, Carthage, WI, (August 15, 2010).
- Burke, Caley. Nutation in the Spinning SPHERES Spacecraft and Fluid Slosh. PhD thesis, Massachusetts Institute of Technology, Cambridge, Massachusetts, June 2010. 13
- Chato, "Approaches to Validation of Models for Low Gravity Fluid Behavior," AIAA-1150 (2005).
- J.P.B. Vreeburg. Spacecraft maneuvers and slosh control. IEEE Control Systems, 25(3):12-16, June 2005. 13, 14
- Moiseyev, N.N. & V.V. Rumyantsev. "Dynamic Stability of Bodies Containing Fluid." Springer-Verlag, 1968.
- Reyhanoglu, M. "Maneuvering control problems for a spacecraft with unactuated fuel slosh dynamics". s
- Shallhorn Marshal, B, Miller, D. "Liquid Sloshing Behavior in Microgravity with Application to Spacecraft Propulsion Systems," http://www.astronautical.org/sites/attachment/AAS_SLOSH_ISS2014, (2014)
- Spyros A Karamanos, Lazaros A Patkas, and Manolis A Platyrrachos, "Sloshing Effects on the Seismic Design of Horizontal-Cylindrical and Spherical Industrial Vessels," Journal of Pressure Vessel Technology, vol. 128, 2006.

SIMULTANEOUS LOCALIZATION AND MAPPING OF SMALL PLANETARY BODIES

Andrew Liounis
Aerospace Engineering
West Virginia University
Morgantown, West Virginia 26506

ABSTRACT

Simultaneous Localization and Mapping (SLAM) processes attempt to both model the scene being observed (mapping) and estimate the location of the observer in the scene (localization). For space-based applications, the current state of the art SLAM technique is the process of Stereophotoclinometry (SPC) developed by Dr. Robert Gaskell of the Planetary Science Institute. SPC works by using motion induced stereovision to generate a topographical map of the surface, and then uses the developed map to refine the state vector (position and attitude) of the spacecraft. The SPC processes were originally developed using the FORTRAN programming language, which has a shrinking user-base, and rely solely on a command line interface with limited visualization capabilities. The goal of this work was to recreate the current SPC processes in the MATLAB programming language to make them more accessible to a wider audience as well as to simplify the user-experience with a graphical user interface (GUI). The translation from MATLAB to FORTRAN was straightforward and the developed MATLAB program was tested and compared against the original routines for different cases to ensure no errors were introduced. In addition, during the translation the code was refactored and better documented to assist with future development efforts. The GUI was used to make the routines more robust to user input and introduced better visualization tools for analyzing the steps in the SPC processes. The developed MATLAB utilities will serve as a confirmation step for the Origins Spectral Interpretation Resource identification Security – Regolith Explorer (OSIRIS – REx) mission (in checking the output from the original Fortran routines) and will also allow future development of the SPC methods for use on upcoming missions.

INTRODUCTION

In September of 2016 the Origins Spectral Interpretation Resource Identification Security – Regolith Explorer (OSIRIS-REx) will launch towards its target destination of Asteroid 1999 RQ36 (Bennu). The primary goal for this mission is to touch down on Bennu’s surface and collect a sample of dust to return to Earth for closer study. While at Bennu, the OSIRIS-REx spacecraft will use the process known as Stereophotoclinometry to form a full 3-Dimensional model of Bennu’s surface and will then use optical navigation (OPNAV) in conjunction with the built model in order to track the relative position between it and Bennu.

The first step for OSIRIS-REx upon arrival at Bennu is to begin forming the 3D model of the surface using the SPC routines and algorithms. This is done by stitching together images that cover the entire surface into a fully realized scale model. After forming the model of Bennu, future images can be registered to this model and used to navigate the spacecraft about the asteroid using various techniques.

For the OSIRIS-REx mission, the Goddard navigation team will provide Independent Verification and Validation of the KinetX primary navigation solution through the use of SPC. This will involve using the SPC routines to process downlinked images from the spacecraft and generate a navigation solution. In addition, the Goddard navigation team will occasionally be in charge of primary navigation, and will also use the SPC software during these times.

The goal of this work was to modernize the SPC software and interface. This goal was met by translating the SPC routines from the FORTRAN programming language into the MATLAB programming language. In addition, the SPC routines were commented and refactored to increase documentation of the software and readability of the code. Finally, a graphical user interface (GUI) was created to replace the command line interface of the SPC routines.

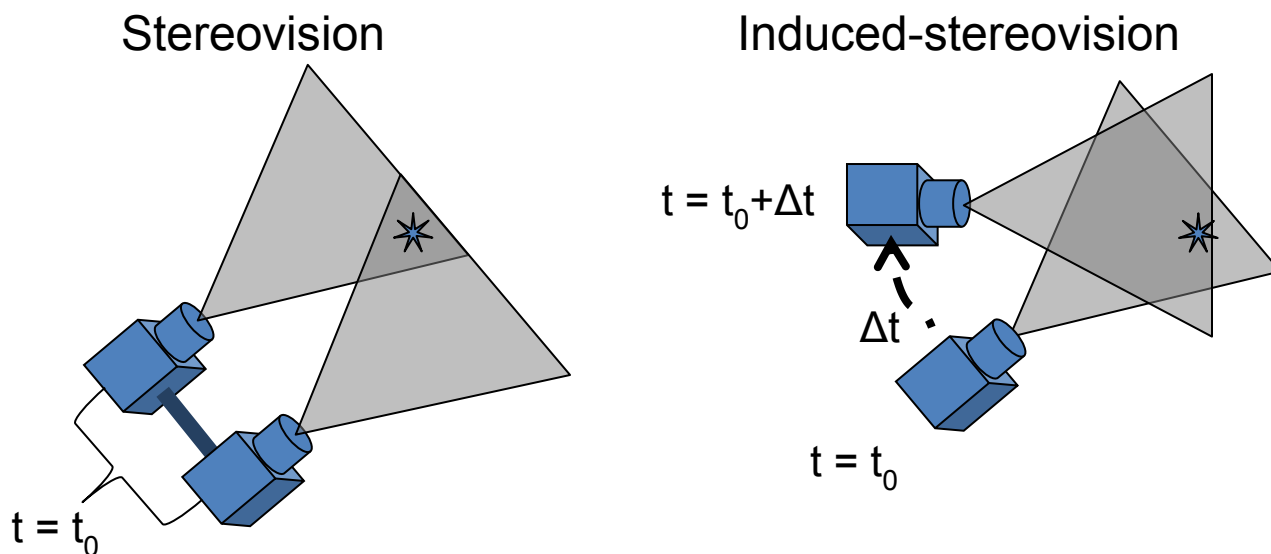


Figure 27. Stereovision uses 2 different cameras at a fixed and known separation to image the same scene at the same time. Induced-stereovision involves a single camera imaging a scene and then being moved over time to image the scene from a different angle.

The rest of this paper first provides an overview of the SPC process and the use of SPC for navigation. It then proceeds to express the reasoning behind the SPC software modernization. Finally, the modernization steps and results are discussed. The paper concludes with recommendations for future improvements to the SPC routines.

BACKGROUND

SPC is a process by which a full 3 Dimensional model of a planetary body is formed through a series of 2 Dimensional visible light images developed by Dr. Robert Gaskell of the Planetary Science Institute [1-6]. The model is formed through the use of induced-stereovision and changes in shadow. Tying these two processes together, height data can be computed for overlapping regions in images. When the entire surface has been imaged, the shape data is stitched together to form the model.

Stereovision occurs when you have two cameras with a known separation imaging the same scene at the same time. In each image, the same location is identified. This gives two line-of-sight

direction vectors originating at the camera centers and passing through the similar point. Taking these line-of-sight direction vectors and the known separation of the camera centers, it is easy to form a geometric constraint of the location of the object in 3 Dimensional space of the camera

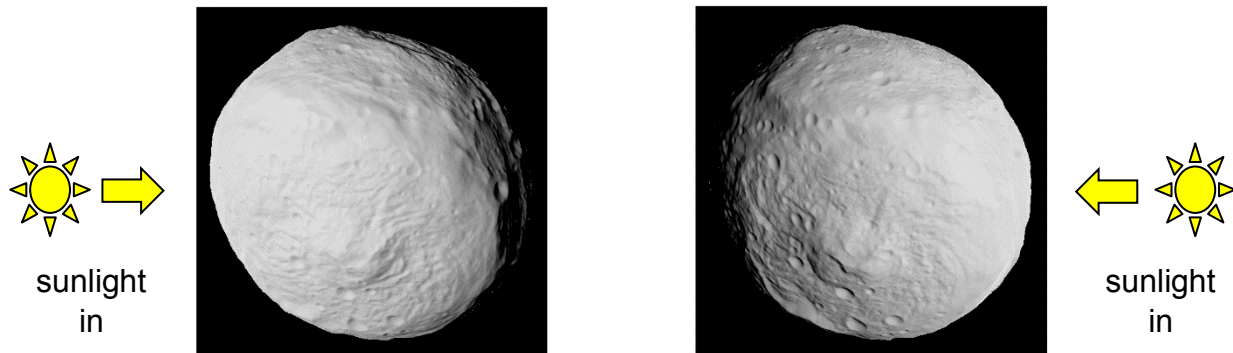


Figure 28. Changes in the direction of the illumination source cause shadows in a scene to move. This can be used to infer the structure of the scene.

frame in the form of a triangle. Induced-stereovision works in much the same way as stereovision. In this case, however, instead of having a known separation between the two cameras, a single camera images a scene, then goes through some known translation and rotation and images the same scene from a different vantage point [8]. All of the principles are the same. Each image provides a line-of-sight direction vector expressed in the local camera frame to the same point. Using these line-of-sight vectors in addition to the known translation and rotation that the camera underwent between the two images enables the geometric constraint to be placed on the point through the use of another triangle.

Changes in shadow occur when the same scene is imaged multiple times with the light source coming from different directions each time. By moving the light source, the shadows created by

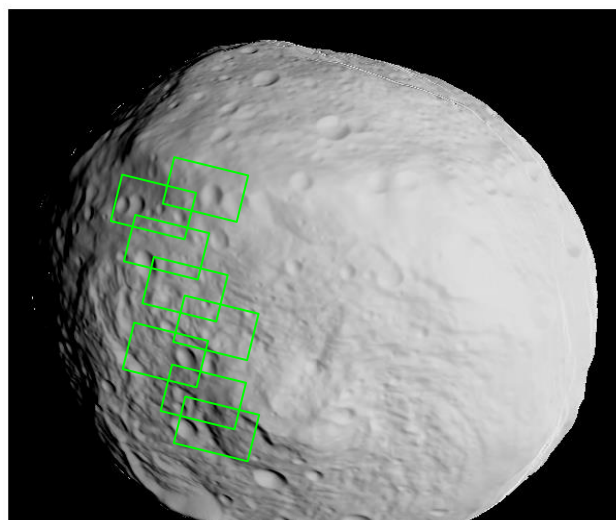


Figure 3. Landmarks are point on an image. Maplets are small sections of the model surrounding each landmark.

the texture of the scene change. By comparing how the shadows move with the known change in the direction of the light source it is possible to estimate a model of the observed scene [9].

Combining induced-stereovision with changes in shadow yields the process used by SPC to model planetary bodies. These techniques work well together because they can operate on the same images. As the camera moves to a new imaging location to help with the induced-stereovision, the body is rotating about its axis and orbiting the sun, causing the direction of the light source to change, providing the information required for shape from shadow.

Once the model of the spacecraft has been built it can start being used to help navigate the spacecraft around the body. This is done by matching future images with parts of the model in order to determine where the photo was taken. The entire image is not matched to the model; instead, sections of the image and model are matched. These sections are referred to as landmarks and surface features. A landmark is a location on the body being observed that is identifiable in multiple images. A maplet is a small section of the model surrounding the landmark. To match images with the model once it is formed, first the locations of the landmarks are identified based off of the *a priori* knowledge of the location the image was taken from. Next, the area that the maplets should cover in the image is extracted from the image. Then the actual maplet is illuminated using the *a priori* knowledge of where the picture was taken from and the direction of the light source (the sun) when the photo was taken. Now the extracted and illuminated maplets can be matched using 2 dimensional cross correlation. This gives the actual location of each maplet in the image.

Once the location of each maplet in the image is identified, the location and attitude of the camera can be estimated by using the reverse process of stereovision. The landmark locations in the image form line-of-sight direction vectors to these points on the surface. Since the location of the points on the surface is known from the model this provides the required geometric constraint for triangulating the camera's location at the time of the image. It also provides information about the orientation of the camera at the time of the image.

In practice SPC is an iterative process. It begins with forming a rough model of the body using the induced-stereovision and the changes in shadow using the estimated position of the camera through radiometric tracking and other navigation techniques. Once the rough model is formed, the position and attitude of the camera are refined by navigating using the formed model. Once the position and attitude are refined, the model can be further refined. This repeats until a satisfactory model has been built, at which point navigation becomes the sole process.

PURPOSE

The original SPC routines were created in the FORTRAN programming language and the only interface is through a command line interface (CLI). The CLI is an ideal interface for scripting and batch runs of the SPC processes; however, it is not user friendly. The CLI requires inputs to be given exactly as specified or the entire program crashes and all progress is lost. It also does not provide any visual aids to assist with the SPC processes. The only way to view the current image and maplets is through the use of additional third party software that needs to be run separately from the SPC programs.

The FORTRAN programming language is a very old (and very fast) programming language. It is a compiled language (it requires a compiler before anything can be run) and the syntax can be difficult to understand. Because of these reasons, the popularity of FORTRAN has been decreasing for many years, especially when it comes to engineers (very few new engineers are taught how to use FORTRAN in school). In fact, according to tiobe.com, the popularity of FORTRAN has been decreasing for over 20 years [10].

The above issues have made the SPC programs difficult to use and the source code inaccessible to many engineers. Because of this, an effort was made to modernize the SPC routines by creating a Graphical User Interface (GUI) to replace the CLI and translating some of the original routines from FORTRAN into MATLAB. The goal of these steps was to make SPC more accessible on the whole by improving the user experience, and by increasing the accessibility, readability, and simplicity of the code. A GUI was developed to increase the robustness of the SPC routines to user input. In addition, the GUI allows real time visualization of the current SPC processes without additional program, and adds new features that the CLI did not offer. The routines were translated into the MATLAB programming language because it is a very popular language, especially among engineers, and it has been gaining in popularity for the last few years [10].

METHODS

The work described in this paper managed to achieve both sets of goals. The steps for these goals are as follows

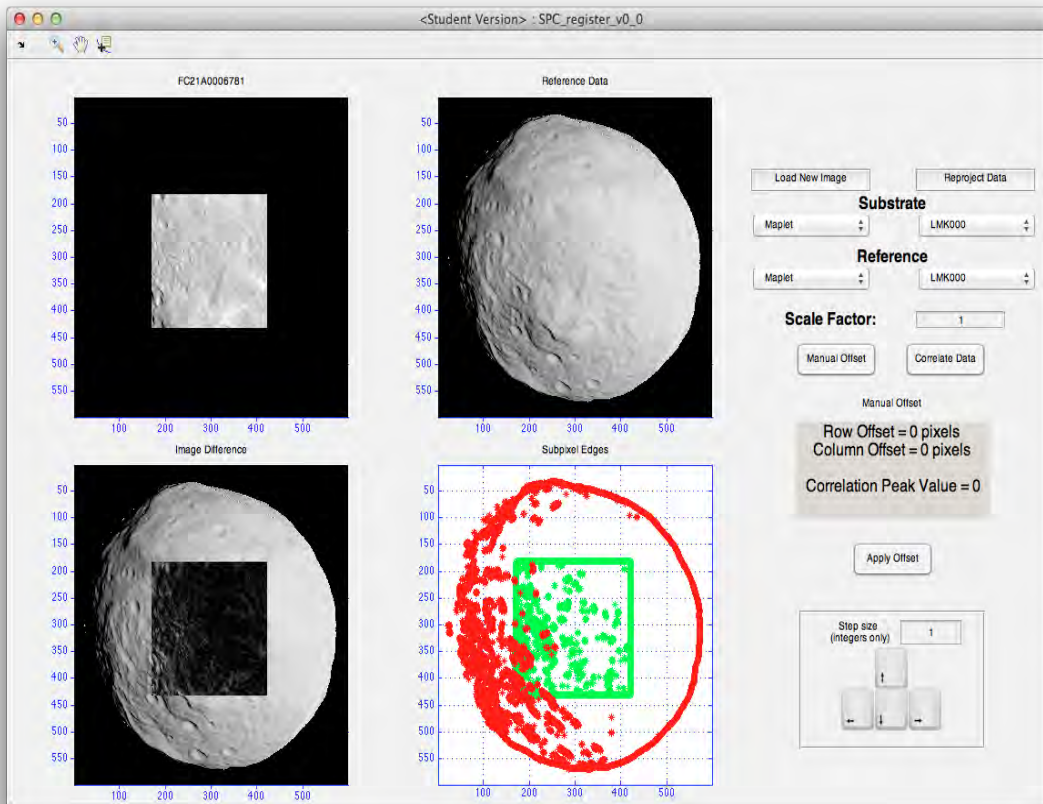
Increasing Readability, Accessibility, and Simplicity

The translation to the MATLAB programming language was undertaken in two distinct stages. In the first stage the FORTRAN code was copied as is, simply adjusting to the MATLAB syntax. This allowed an easy way to be sure that the output from the MATLAB code matched the output from the FORTRAN programs. This increased the accessibility of the routines.

After the base transformation, the MATLAB code was refactored and rewritten to use the more readable MATLAB format. These transformations included writing out the matrix multiplication steps the way they are written by hand in linear algebra (instead of using loops as is required in Fortran) and renaming the variables to indicate what they represented (the original Fortran routines were written when the size of the source code was an important fact, thus 1 or 2 letter variables were used frequently). In addition, comments were added describing what was happening in the code (again, due to the source code length issues, the original FORTRAN had very few comments). All three of these steps greatly increased the readability and simplicity of the routines.

Bettering the User Experience

The created GUI successfully bettered the user experience. The GUI provides a simplified interface that provides easy access to most of the SPC options and features. In addition, the GUI provides a live display of the SPC processes, making it much easier to perform the SPC routines. Finally, the GUI introduces new intuitive displays that were not included in the original SPC routines to help with processing, such as an overlay of the sub-pixel edges in the image and the model and an image difference (absolute value of the difference between the illumination values of the image and reference). The GUI also introduces a new way to manually align the image and reference, which is much faster than the techniques used in the CLI version of SPC.



FUTURE WORK

Now that the SPC routines have been modernized, attention can be turned to improving on the methods presented. In addition, more thorough documentation of the SPC routines can now be developed based on the refactored and commented code. Finally, attention can be turned to further improving the GUI in order to make it more powerful.

ACKNOWLEDGEMENTS

The author would like to thank his mentor Kenny Getzandanner for his guidance and assistance during the duration of this project. He would also like to thank the West Virginia Space Grant for providing funding to complete this project.

Figure 29. An example of the GUI developed for the SPC routines. The current progress is displayed without requiring an external program and all of the options are easily accessible.

REFERENCES

- [1] Gaskell, Robert W. "Landmark Navigation and Target Characterization in a Simulated Itokawa Encounter." (2005)Web.
- [2] ---. "Martian Surface Simulations." *Journal of Geophysical Research: Planets (1991–2012)* 98.E6 (1993): 11099-103. Web.
- [3] ---. "Optical Navigation Near Small Bodies." *Spaceflight Mechanics* 140 (2011)Web.
- [4] ---. *Small Body Simulations for Navigation Approach and Landing*. Pasadena, CA: Jet Propulsion Laboratory, National Aeronautics and Space Administration, 2005. Web.
- [5] ---. *Small Body Simulations for Navigation Approach and Landing*. Pasadena, CA: Jet Propulsion Laboratory, National Aeronautics and Space Administration, 2005. Web.
- [6] Gaskell, RW, et al. "Characterizing and Navigating Small Bodies with Imaging Data." *Meteoritics & Planetary Science* 43.6 (2008): 1049-61. Web.
- [7] Koenderink, Jan J., and Andrea J. Van Doorn. "Affine structure from motion." *JOSA A* 8.2 (1991): 377-385.
- [8] Mastrodemos, Nickolaos, et al. "Optical Navigation for the Dawn Mission at Vesta". *23rd International Symposium on Space Flight Dynamics, Pasadena, California, October 29-November 2, 2012*, Web.
- [9] Prados, Emmanuel, and Olivier Faugeras. "Shape from shading." *Handbook of mathematical models in computer vision*. Springer US, 2006. 375-388.
- [10] "TIOBE Index for August 2015." *TIOBE Software: The Coding Standards Company*. TIOBE Software BV, 01 Aug. 2015. Web. 09 Aug. 2015. <<http://www.tiobe.com/index.php/content/paperinfo/tpci/index.html>>.

A META-ANALYSIS OF DISTINCT AUDIO-VISUAL, MULTIMODAL INTERACTION SITES IN THE HUMAN BRAIN

Nadia Mardmomen
Biology
West Virginia University
Morgantown, WV 26506

ABSTRACT

Our ability to perceive and recognize objects, people, and meaningful action events is a cognitive function of prime importance, which is characterized by an interplay of visual, auditory, and sensory-motor processing. One goal of sensory neuroscience is to better understand multisensory perception, including how information from auditory and visual systems may merge in the brain to create stable, unified representations of objects and actions in our environment. My project sought to summarize and compare results from 74 paradigms published over the past decade that have explicitly examined human brain regions associated with audio-visual interactions using functional magnetic resonance imaging (fMRI) or Positron Emission Tomography (P.E.T.). A series of meta-analyses compare and contrast distinct cortical networks preferentially activated under five major types of audio-visual interactions: (1) matching spatial and/or temporal features of non-natural objects, (2-3) matching crossmodal features characteristic of natural objects (moving versus static images), and (4) associating artificial audio-visual pairings (e.g. written/spoken language). These results newly reveal a striking dorsal versus ventral network of brain regions involved in artificial versus natural audio-visual stimuli. This finding is expected to have significant impact on our understanding of fundamental principles of human brain organization as well as disorders that affect people, such as those with autism and sensory processing disorders. These meta-analysis results are discussed in the context of cognitive theories regarding how object knowledge representations may mesh with the multiple parallel pathways that appear to mediate audio-visual perception.

INTRODUCTION

A critical cognitive function for survival is the ability to integrate auditory and visual sensory features to recognize things such as objects, people, and communicative gestures. As a young child, a person typically develops the ability to bind auditory and visual inputs coming from natural actions, such as a mother speaking to her child. This seemingly effortless integration of auditory and visual inputs becomes so habituated that one does not have any trouble when it comes to illusory events such as hearing and seeing actions and characters on television. One aspect of audio-visual (A-V) interaction entails processing of intermodal invariant feature is temporal coherence, where the timing of changes in intensity or energy conveyed via the visual and auditory systems are in synchrony, such as viewing and hearing a basketball bounce to rest. The notion of matching intermodal invariant features will be an important theme for interpreting results regarding audio-visual processing pathways revealed through a series of meta-analyses.

This study's main question is, "How do these two separate sources of sensory inputs integrate in the brain to provide a unified percept of objects and people in the environment?" (Lewis, 2010). Notwithstanding, precise criteria for identifying audio-visual "*integration*" remains somewhat open to interpretation with regard to how rigorously one can apply principles from single unit

studies of superadditivity, subadditivity, and inverse effectiveness to hemodynamic studies that measure changes in blood flow. Consequently, this analysis includes results from a relatively broad range of studies that examined audio-visual “interactions”, which includes findings that were derived using potentially more liberal criteria for revealing multisensory associations.

Although the focus of this analysis is on perception of everyday “natural objects”, results from a wide variety of audio-visual interaction studies from over roughly the past 15 years have been compiled to provide a broader context for interpretation. This includes meta-analysis results from 74 neuroimaging paradigms, illustrating a substantial, though not exhaustive, portion of the functional magnetic resonance imaging literature on this topic to date. A categorical distinction in the literature, and based on hearing perception cortical network processing by our group natural versus artificial audio-visual pairings. More specifically, an earlier meta-analysis revealed a ventral versus dorsal network for processing natural vs artificial audio-visual pairings (Lewis 2010).

The present study sought to revisit that concept with 5 years of new articles for inclusion. Moreover, an ulterior motive and emphasis in the PI’s lab was to use these meta-analysis results for comparison with audio-visual fMRI data being collected with adults and children with autism. In particular, we wanted to compare cortical processing strategies used by neurotypical individuals with those who have sensory dysfunctions, which is especially common in people with autism.

METHODS

In the Lewis lab we primarily use a 3T scanner at the Center of Advanced Imaging to conduct most of our studies. Functional magnetic resonance imaging (fMRI) and positron emission tomography (PET) review human brain regions, networks, and parallel hierarchical processing pathways in which audio-visual interactions are found and is based predominantly on hemodynamic neuroimaging studies. PET is not as commonly used as fMRI, but is not completely outdated. This specific study is to study the audio-visual integration pathways via studies that used fMRI. The current study has been compiled with perceptions of everyday (natural) objects because of the large clinical relevance. This study is not limited to only natural audio-visual integration, it also includes artificial AV to support the claim that natural AV stimuli is processed using different pathways. This hypothesis will help us to support our future study on people with autism and their different cortical processing pathways. Due to the fact that it is an open interpretation on precise criteria for identifying audio-visual integration, this project includes a broad range of studies. These studies include findings derived using criteria for revealing multisensory associations.

Search Procedures

A systematic review of functional neuroimaging studies of audio-visual multisensory integration was performed. For the fMRI studies of audio-visual integration, studies evaluating the brain responses evoked in natural and non-natural stimuli (hearing and seeing a mother compared to hearing and seeing figures on a computer screen) were used. All papers and books published in 2010 and after were considered for the review, subject to two general limitations: the scientific publication had to be a manuscript, chapter, or book; and the title and abstract had to have been available in English. Materials were identified through computer-based search.

Computer Search Procedures

A systematic computer-based search of the literature was performed using the West Virginia University's electronic database. Two specific databases used were PubMed and Web of Science. In the databases the following keywords were searched: "audio-visual processing," "multisensory integration," "audio," "visual," "fMRI," and "neuroimaging" to add to our previously data. Only studies from 2010 to 2015 were included to create a subsequent five-year time span.

Selection Criteria

The set of publications identified were then subjected to the following narrower criteries: (i) the studies had to be reported with a neuroimaging exam; (ii) no participants had any history of schizophrenia, neurological disease, drug abuse, or alcohol abuse; and (iii) all studies had to be conducted in line with ethical standards and under the supervision of the responsible human subject's committees. Only fMRI neuroimaging studies will be included, as the present review focuses on brain networks.

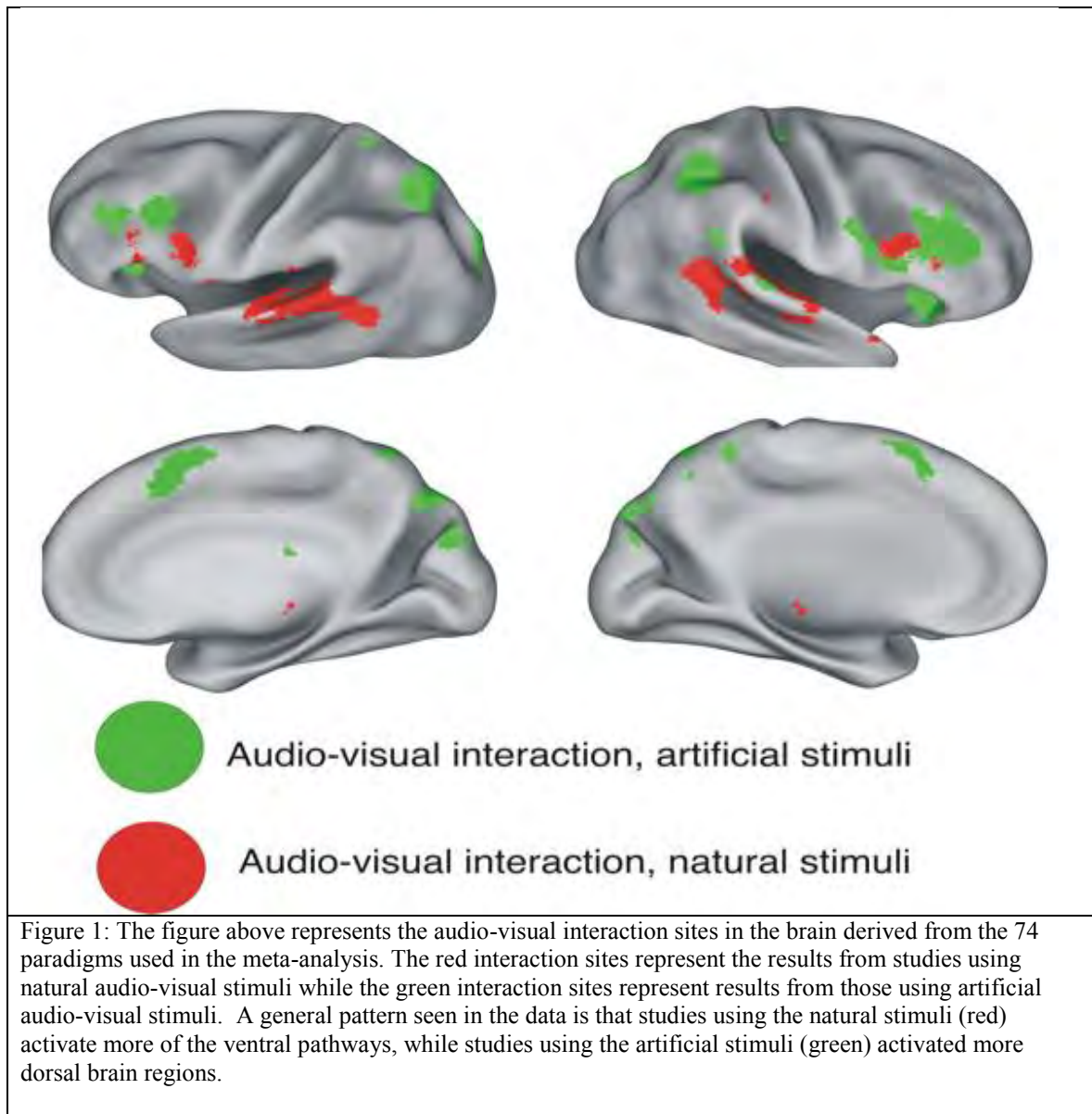
fMRI Meta-analysis

To provide readers with a synthesized and statistical review of the common and different brain networks mediating audio-visual multisensory integration, a meta-analysis was performed. I have converted all reported brain coordinates from excel into an online computer system called GingerALE. All coordinates were recorded using Talairach coordinate system. The coordinate system allows for more direct comparisons of data across individuals and across studies by accounting for variations in the size and shape of different people's brains. Activation volumes were be approximated by spheres to match the size and location of the illustrated results and then this data will be projected into a brain volume space using GingerALE software. The brain volumes were then projected onto AFNI to create a 2D brain with activation sites of natural and artificial audio-visual integration.

RESULTS

Table 1: References used for the collected data

Study Type	
Natural with motion (red)	(Balk et al., 2010), (Callan, Jones, & Callan, 2014) (Blank & von Kriegstein, 2013; De Haas, Schwarzkopf, Urner, & Rees, 2013; Erickson et al., 2014; Ethofer et al., 2013; He et al., 2015; Jessen & Kotz, 2015; Okada, Venezia, Matchin, Saberi, & Hickok, 2013; Watson et al., 2014; Watson, Latinus, Charest, & Crabbe, 2013; Wyk et al., 2010)
Natural with static (red)	(Doehrmann, Weigelt, Altmann, Kaiser, & Naumer, 2010; Kim et al., 2015)
Artificial simple (green)	(Bonath et al., 2014)
Artificial complex (green)	(Bonath et al., 2013; Hove, Fairhurst, Kotz, & Keller, 2013; Ogawa & Macaluso, 2013)



Networks associated with the perception of natural and semantically congruent pairings of audio-visual motion prominently activated more ventral brain regions, including posterior temporal cortex: (Calvert et al., 1999; Calvert et al., 2000; Olson et al., 2002; Beauchamp et al., 2004; Beauchamp et al., 2004; Kreifelts et al., 2007; Robins et al., 2009; Stevenson and James, 2009) and new references in table 1. All of these paradigms depicted complex natural actions that were produced by humans (or implied human agency), together with emphasis on semantic congruence and effectively recognizing *what* the multisensory action was. These paradigms included talking faces and hand tools in use contrasting matched audio-visual presentations with each of the unimodal conditions ($AV > A, V$), while other paradigms contrasted congruent (matched) versus incongruent (mis-matched) audio-visual pairings (e.g. $AV_{\text{cong}} > AV_{\text{incong}}$).

A common type of audio-visual interaction study that contrasted to those in the previous two sections involved matching real-world sounds to semantically corresponding static images or

pictures (Belardinelli et al., 2004; Taylor et al., 2006; Hein et al., 2007; Naghavi et al., 2007; Hocking and Price, 2008; Taylor et al., 2009) and refer to table 1 references. Because the visual images were static, these paradigms greatly minimized the processing and matching of intermodal invariant features, thereby placing greater emphasis on semantic-level matching and memory—again mostly using images depicting people (and other biological agents) and sounds produced by living things (humans or animals). These studies incorporated varying degrees of semantic encoding.

Along with studies that used natural stimuli, other studies used artificial or abstract audio-visual pairings. The paradigms included AV>AV, congruent versus incongruent audio-visual pairings (e.g. AV_{cong}>AV_{incong}). Categorizing the artificial stimuli were harder because it could be biased decision as to what would be considered simple or more complex and naturalistic. Animated human stimuli were a debated topic because humans are natural, but the animated humans are computer generated. Mainly artificial stimuli included beeps, freebles and greebles, video games such as pong and other computer generated objects.

DISCUSSION

My project reviewed evidence derived from meta-analyses across 74 paradigms, revealing several parallel and hierarchical processing pathways for purposes of audio-visual perception of objects. The main finding was a dorsally directed network of brain regions preferential that were for processing features of artificial, non-natural object-actions. In contrast, a set of brain regions were ventrally directed preferential for processing intermodal invariant, and/or semantic features of natural object-actions. All studies were used with typically developed adult humans, which will now help us create a meta-analysis that can be used in comparison to brain images of people with autism that are being collected by our group. This meta-analysis will help us potentially distinct cortical processing mechanisms and adaptations used by children with autism. That knowledge may then be useful for developing more targeted interventions for children diagnosed with ASD.

CONCLUSIONS

My primary lab project entailed spearheading a meta-analysis of previous neuroimaging studies revealing audio-visual interaction sites in the human brain. This project is timely because our group is also conducting a fMRI project involving individuals with versus without autism. My future work will now entail finishing the analysis for publication in Review Neuroscience, and participation in a new study in the Lewis Lab here at West Virginia University. The Lewis lab has asked me to become an undergraduate researcher for the coming academic year where I will work on the new autism study focusing on multisensory integration. I have become MRI safety certified so that I can participate in volunteer scanning at Ruby Memorial Hospital. I will also help with data collection and analysis in the lab's computer lab due to my new expertise in Unix, Excel, GingerALE, AFNI, Caret5, and other software 3D brain projections and data statistical analyses. This lab has given me the opportunity to work in a scientific environment with other professionals and the general public. In our lab we held meetings with other researchers, as well as, meetings with families that have had a autistic family member volunteer for us. Also I was spearheading a meta-analysis, I was involved in many things concerning our lab as a whole including lab meetings and manuscript editions. In the fall I will start my junior year as a biology major and hope to begin an honors thesis in multisensory integration in children and adults with autism. I hope to continue

to work with the NASA West Virginia Space Grant Consortium as I continue my career in undergraduate research here at WVU.

ACKNOWLEDGEMENTS

Thanks to NASA West Virginia Space Grant Consortium for granting me with the financial funds to conduct this project at West Virginia University with Dr. James Lewis. Also, thanks to Dr. James Lewis for all of his support during my summer fellowship and future endeavors.

REFERENCES

- Balk, M. H., Ojanen, V., Pekkola, J., Autti, T., Sams, M., & Jääskeläinen, I. P. (2010). Synchrony of audio-visual speech stimuli modulates left superior temporal sulcus. *Neuroreport*, *21*(12), 822–826. <http://doi.org/10.1097/WNR.0b013e32833d138f>
- Blank, H., & von Kriegstein, K. (2013). Mechanisms of enhancing visual-speech recognition by prior auditory information. *NeuroImage*, *65*, 109–118. <http://doi.org/10.1016/j.neuroimage.2012.09.047>
- Bonath, B., Noesselt, T., Krauel, K., Tyll, S., Tempelmann, C., & Hillyard, S. a. (2014). Audio-visual synchrony modulates the ventriloquist illusion and its neural/spatial representation in the auditory cortex. *NeuroImage*, *98*, 425–434. <http://doi.org/10.1016/j.neuroimage.2014.04.077>
- Bonath, B., Tyll, S., Budinger, E., Krauel, K., Hopf, J. M., & Noesselt, T. (2013). Task-demands and audio-visual stimulus configurations modulate neural activity in the human thalamus. *NeuroImage*, *66*, 110–118. <http://doi.org/10.1016/j.neuroimage.2012.10.018>
- Callan, D. E., Jones, J. a., & Callan, A. (2014). Multisensory and modality specific processing of visual speech in different regions of the premotor cortex. *Frontiers in Psychology*, *5*(MAY), 1–11. <http://doi.org/10.3389/fpsyg.2014.00389>
- De Haas, B., Schwarzkopf, D. S., Urner, M., & Rees, G. (2013). Auditory modulation of visual stimulus encoding in human retinotopic cortex. *NeuroImage*, *70*, 258–267. <http://doi.org/10.1016/j.neuroimage.2012.12.061>
- Doehrmann, O., Weigelt, S., Altmann, C. F., Kaiser, J., & Naumer, M. J. (2010). Audiovisual functional magnetic resonance imaging adaptation reveals multisensory integration effects in object-related sensory cortices. *The Journal of Neuroscience : The Official Journal of the Society for Neuroscience*, *30*(9), 3370–3379. <http://doi.org/10.1523/JNEUROSCI.5074-09.2010>
- Erickson, L. C., Zielinski, B. a, Zielinski, J. E. V, Liu, G., Turkeltaub, P. E., Leaver, A. M., & Rauschecker, J. P. (2014). Distinct cortical locations for integration of audiovisual speech and the McGurk effect. *Frontiers in Psychology*, *5*(June), 534. <http://doi.org/10.3389/fpsyg.2014.00534>
- Ethofer, T., Brettecher, J., Wiethoff, S., Bisch, J., Schlipf, S., Wildgruber, D., & Kreifelts, B. (2013). Functional responses and structural connections of cortical areas for processing

- faces and voices in the superior temporal sulcus. *NeuroImage*, 76, 45–56. <http://doi.org/10.1016/j.neuroimage.2013.02.064>
- He, Y., Gebhardt, H., Steines, M., Sammer, G., Kircher, T., Nagels, A., & Straube, B. (2015). The EEG and fMRI signatures of neural integration: An investigation of meaningful gestures and corresponding speech. *Neuropsychologia*, 72, 27–42. <http://doi.org/10.1016/j.neuropsychologia.2015.04.018>
- Hove, M. J., Fairhurst, M. T., Kotz, S. a., & Keller, P. E. (2013). Synchronizing with auditory and visual rhythms: An fMRI assessment of modality differences and modality appropriateness. *NeuroImage*, 67, 313–321. <http://doi.org/10.1016/j.neuroimage.2012.11.032>
- James, T. W., VanDerKlok, R. M., Stevenson, R. a., & James, K. H. (2011). Multisensory perception of action in posterior temporal and parietal cortices. *Neuropsychologia*, 49(1), 108–114. <http://doi.org/10.1016/j.neuropsychologia.2010.10.030>
- Jessen, S., & Kotz, S. a. (2015). Affect differentially modulates brain activation in uni- and multisensory body-voice perception. *Neuropsychologia*, 66, 134–143. <http://doi.org/10.1016/j.neuropsychologia.2014.10.038>
- Jola, C., Mcaleer, P., & Morison, G. (2013). Uni- and multisensory brain areas are synchronised across spectators when watching unedited dance recordings. *I-Perception*, 4.
- Kim, H., Hahm, J., Lee, H., Kang, E., Kang, H., & Lee, D. S. (2015). Brain Networks Engaged in Audiovisual Integration During Speech Perception Revealed by Persistent Homology-Based Network Filtration. *Brain Connectivity*, 5(4), 150302122147005. <http://doi.org/10.1089/brain.2013.0218>
- Lewis, JW (2010) Audio-Visual Perception of Everyday Natural Objects- Hemodynamic Studies in Humans
- Ogawa, A., & Macaluso, E. (2013). Audio-visual interactions for motion perception in depth modulate activity in visual area V3A. *NeuroImage*, 71, 158–167. <http://doi.org/10.1016/j.neuroimage.2013.01.012>
- Okada, K., Venezia, J. H., Matchin, W., Saberi, K., & Hickok, G. (2013). An fMRI Study of Audiovisual Speech Perception Reveals Multisensory Interactions in Auditory Cortex. *PLoS ONE*, 8(6), 1–9. <http://doi.org/10.1371/journal.pone.0068959>
- Watson, R., Latinus, M., Charest, I., & Crabbe, F. (2013). People-selectivity, audiovisual integration and heteromodality in the superior temporal sulcus. *SciVerse Science Direct*.
- Watson, R., Latinus, M., Noguchi, T., Garrod, O., Crabbe, F., & Belin, P. (2014). Crossmodal adaptation in right posterior superior temporal sulcus during face-voice emotional integration. *The Journal of Neuroscience: The Official Journal of the Society for Neuroscience*, 34(20), 6813–21. <http://doi.org/10.1523/JNEUROSCI.4478-13.2014>

Wyk, B. C. Vander, Ramsay, G. J., Hudac, C. M., Jones, W., Lin, D., Klin, A., ... Pelphrey, K. a. (2010). Cortical integration of audio-visual speech and non-speech stimuli. *Brain and Cognition*, 74(2), 97–106. <http://doi.org/10.1016/j.bandc.2010.07.002>

MATERIALS RESEARCH INTO NANOTUBES

Amelia Riley
Applied Physics
West Virginia Wesleyan College
Buckhannon, WV 26201

ABSTRACT

For the research this summer a TEM electron microscope will be used. The research used carbon nanotubes, (CNT) in three different varieties, one plain and two doped. CNT is the lightest, strongest and most conducting material known today; its versatility makes it the perfect choice for multiple projects. CNT is 200x the strength and 5x the elasticity of steel; 5x the electrical conductivity, 15x the thermal conductivity, and 1000x the current of copper, all of this while being half the density of aluminum. Carbon nanotubes are allotropes of carbon that hold a cylindrical nanostructure. They are extremely special because of their unique properties, which include extraordinary thermal conductivity, mechanical, electrical and optical properties. This makes it an ideal material for multiple uses including structural reinforcement, car parts and space craft gas sensor equipment. This gives it a large importance which makes it great for research and testing.

INTRODUCTION

The world is always looking for the next best thing to come about. It wants the newest phone, the fastest car and recently the best battery to run both. Electric cars are among one of the biggest technologies being developed. However, the big concern that challenges this advancement is how to get batteries strong enough and durable enough to make this idea a plausible reality. The best batteries for cars today only last around three hundred miles before needing recharged. To add insecurity most electric car's charge drops over time. For people to dish out the big money for an electric car they need to at least know they can go farther than they would with a regular tank. This is where just some of the pressure to make better batteries comes from.

One theoretical way to make the best is to combine the super properties of lithium with the superconductive properties of carbon nanotubes. This was the beginning purpose for the research completed this summer.

BACKGROUND

Carbon, one of the most useful elements discovered is the fourth most abundant element in the known universe and one of the oldest known elements to date. Diamonds (a form of carbon) have been used since 2500BCE in China. The graphene form was used in the Roman time period as charcoal. Although it was used centuries ago these branches of carbon were not connected and recognized to be carbon for years to come. One reason for the many steps of discovery is due to the fact that carbon has four main types of allotropes. Carbon as we know it today was recognized in 1722 when Rene Antoine Ferchault deReaumur proved that iron is turned into steel by the absorption of carbon. Later in 1772 Antoine Lavoisier proved that diamonds were carbon by burning a sample of each and comparing the residue and gases released. Both samples released equal amounts of carbon dioxide, and neither released water which led to the conclusion that at the source they must come from the same substance. The next step for carbon came in 1779 when

Carl Wilhelm Scheele showed that graphene was also a form of carbon instead of lead which it had previously been believed. This was also proven when break down of graphene gave off carbon dioxide. Carbon first gained status as an element in 1789 by Antoine Lavoisiers. In 1985 fullerene was shown to be another form of carbon. Discovered by Robert Curl, Harold Kroto and Richard Smalley, this form of carbon includes the buckyballs and nanostructured forms. For this research, nanotubes were the main focus.

Carbon has an atomic number of six and falls in the fourteenth group on the periodic table. This placement gives it nonmetallic and tetravalent characteristics. This placement also includes three naturally occurring isotopes ^{12}C , ^{13}C , and ^{14}C . Due to the number of valence electrons and carbon's unique properties it creates many stable C-C bonds, which form long chains of interlocking carbon atoms. This ability allows carbon to make many combinations easily; in fact carbon has the most combinations of any other element besides hydrogen. Examples of these combinations are antibiotics to alcohol and sugars to DNA. Carbon is also known for having three allotropes of carbon, including graphite diamond and amorphous carbon. Each of these allotropes has many different physical and chemical properties, which all versatility and uniqueness. However, they do carry common traits, such as being solid and unreactive at most temperatures.

The two best known allotropes are graphite and diamonds. Although, they both source from the same element their characteristics are very different. The most obvious difference is that graphite is opaque while diamonds are transparent. Another noticeable difference is that graphene is one of the softest materials known while diamonds are the hardest material known today. Graphene is also a great lubricant while diamond is considered the ultimate abrasive material. In a practical difference graphene is an electrical conductor and a thermal insulator, while diamonds are an excellent electrical insulator and a great thermal conductor. The last main difference is the basic structure; graphene is formed in a hexagonal structure while diamonds are formed in a cubic structure.

The last and most recent allotrope is the fullerene. Fullerenes include the most well-known branches, nanotubes and buckyballs in addition to buckytubes and nanobuds. The structure of fullerene is closest to that of the graphene. Instead of just having a hexagonal structure they also have pentagonal and heptagonal structures. This allows carbon to form more unique structures which include sphere, ellipses and cylinders.

One of the most relevant structures is the carbon nanotube. Although it is entirely unclear where or who deserves the credit for discovering carbon nanotubes, the most widely believed discoverer was a French scientist Morinobu Endo. In 1970, carbon filaments were grown by Endo. These were believed to be the first carbon nanotubes but later were ruled out due to their radius and length ratio. However, there are still many people that get credit in the development of the nanotube. The first known article that showed clear pictures of this new structure appeared in 1952 in a Russian paper by L.V. Radushkevich and V. M. Lukyanovich. This paper was not released worldwide until years later after the cold war. Another paper from 1976, discussed what is now referred to as a single-walled nanotube. Other theories of origin include John Abrahamson's paper released in 1979 at the 14th Biennial Conference of Carbon.

Additional research in 1981 was published by a group of scientists from Soviet Union. Through the use of TEM images and XRD patterns, it was theorized that the carbon multi-layered tubular

crystals were created by rolling graphene layers into the well-known cylinder shape. When the nanotubes are rolled the two ends come together to form a connected line. Although some cylinders have nice patterns that connect uniformly, some graphene sheets have hexagonal patterns that are not uniform which allow them to create more unique shapes and structures. This allowed them to a hypothesis that by rolling the graphene they would be able to make other arrangements of graphene hexagonal nets. The hypothesis was confirmed and the two most popular structures were the armchair nanotube which occurs at (n,n) and a zigzag arrangement which occurs at (n,0).

The next leap for carbon nanotubes came in 1987 when a patent was issued to Howard G. Tennett of Hyperion Catalysis. The patent was for the production of cylindrical discrete carbon fibrils specifically ones with a constant diameter between 3.5 and 70 nanometers. From this point on thousands of people have spent time researching this exciting field and giving light on the many questions the beginning scientist had.

However, a majority of the population gives credit to Sumio Iijima for releasing his work in 1991. He has noticed cage-like fullerenes in images earlier and sent them to Kroto, one of the discoverers of fullerenes in 1989. It took him until 1991 to clearly identify them with the use of an electron microscope. His images showed nanotubes with lengths that ranged from 30nm to 1 μ m, he also found Multi-walled nanotubes that went up to 50 walls. He is given most of the credit because it was his work that brought carbon nanotubes into the eyes of the scientific world on a large scale. Later on he would also come up with a system of controlling the growth of the carbon nanotubes. The process of arc-discharge to grow these nanotubes created lots of material but the nanotubes were uneven in size making the material not as useful. After a few years of research Iijima discovered that by adding iron catalysts to one of the electrodes he was able to produce single-wall tubes. Although the diameters still varied in size two diameters, (.8nm and 1.05nm) took dominance over the others, making it a more uniform material. Due to his research modern research has been able to create better controlled formations and longer formation, the longest length of a nanotube today is at 18mm.

In the simplest terms a carbon nanotube is a rolled graphene sheet. More specifically a graphene sheet is a nanotube when it has a length-to-diameter of roughly 132,000,000 to 1. This is a significant clarification because it is much larger than most nanoparticles. Another great characteristic is that these nanotubes are unique to their larger structures of graphene and diamond. Some characteristic that make nanotubes special include thermal conductivity, electrical conductivity and unique mechanical properties which include the largest tensile strength and elastic modulus. Thermal conductivity is just the start of all of the amazing aspects of SWNT's and MWNT's. Nanotubes have an average thermal conductivity of about 5000 W/mK and a predicted value of 6600 W/mK, they also have a predicted conductivity of over 3000 W/mK. This is very impressive when you compare is to the conductivity of copper which is 400 W/mk. When the two are compared theoretically the same size bar would carry a power of 21W for copper and in impressive 150 W for carbon nanotubes. The electrical conductivity is one of the properties that greatly separate it from the fullerenes field. Most fullerenes are isolated molecules unless they are assembled in a solid fullerene, this gives them pour electrical conductivity. However, the carbon nanotubes have such a large ration between diameter and length that they create the form of small wires. This special property makes them excellent at conductive electricity.

Carbon nanotubes have many mechanical properties that make them different from the other forms of carbon. One of the most important aspects of their unique mechanical properties is their impressive strength. The strength found in carbon nanotubes is a direct result of the sp² bonds that make up the graphene sheets. This is significant because the bonds of diamonds are sp³ which are weaker than the sp² bonds found in the graphene. This base strength only grows when the sheets roll into cylinders to form the carbon nanotubes. This strength is much more impressive when looking at the young's modulus values and the tensile strength. The Young's modulus is predicted to be about 100GPa and then tensile strength is about 300 GPa. On its own this might not seem to impressive unless you know a lot about tensile stress and strain, however when you compare these figures to that of steel which are 200 GPa for Young's modulus and 1 GPa for tensile strength it is much more clear. In one study that tested multiple carbon nanotubes for tensile strength they found that even the weakest nanotube was still twenty times stronger than the maximum strength of steel. Along with the impressive tensile strength and stress, nanotubes also have another mechanical property that makes them useful is their flexibility. When placed under extreme strength the carbon nanotubes buckle and kink, but when the stresses are removed they quickly go back to their original state. This makes them an ideal candidate for ultra-strong cables. Although individually the nanotubes have the highest strength of any material today, when linked with others their strength as a whole drops dramatically. This is due to a weak bond between nanotubes. However, research has gone into finding ways to interlock the tubes to create a much stronger material.

When you start looking into this field one thing that needs clarities are the differences between the single walled tubes and the multi walled tubes. The difference seems easy enough but there is more too it then how many walls a nanotube contains. The single-walled nanotubes (SWNT) typically have a diameter of one nanometer, with a length of up to a million times longer. Their structure is that of a one-atom-thick layer of graphene wrapped into a perfect single layered cylinder. They have a large conductivity which allows them to be great candidates for electronics and energy wires. One recent use for SWNT's was in the creation of the first intermolecular field-effect transistors (FET). This was then used to create the first intermolecular logic gate which used FET's. Although SWNT's could be used in many developments it is not used as often because it is still very pricey for large quantities. The price has dropped drastically in the last fifteen years so the prospect of it being used more is a reality in the future.

The other type of carbon nanotubes is the multi-walled nanotubes (MWNT). In the simplest form these are made by rolling multiple layers of graphene into a cylindrical shape. There are two common models to explain this process, the first one is the Russian Doll theory and the other is the Parchment model. The first and most common is the Russian Doll model which states that SWNT form concentric cylinders, what this means is that a SWNT is formed and then another larger SWNT is wrapped around it and so on until the desired MWNT is formed. The second model, Parchment, describes the formation as a single layer of graphene that wraps around multiple times, similar to the look of a rolled up piece of parchment.

Were the basic form of carbon nanotubes can be assigned to either SWNT's or MWNT's, it doesn't complete describe the formation. Some nanotubes form other more unique aspects. One of the first ones discovered was found by Sumio Iijima in 1991. While doing his research he discovered what is today referred to as a carbon nanohorn. This special formation occurs when a nanotube created a cone shape with a fullerene at one end. This cone shaped nanoparticle is formed when the graphene sheets are connected at an angle. This may not seem that important but it does create a

practical use. These cones have a large surface area and a large cavity which is ideal to store gases such as hydrogen. Being able to store hydrogen is a current problem that faces the electric car today. If using these carbon nanohorns can safely store carbon then there could be a huge breakthrough for the energy industry. Another one of these is referred to as the Torus. A torus is simply a carbon nanotube that is bent to create a donut shaped structure. This benefits the tube by creating a larger magnetic moment, although research is being done it is still unclear all of the benefits that can be gained from this formation. Another unique structure is the nanobud. A nanobud is a hybrid structure between carbon nanotubes and fullerenes. When a fullerene attaches itself to the side of a SWNT it creates a bubble, which is where the name comes from. This hybrid is important because the bud can be used as an anchor to keep the nanotubes from slipping which allows improved mechanical properties. The next hybrid is the carbon peapod. A peapod is a fullerene that is surrounded by a carbon nanotube. This benefits the structure by giving its own unique heating properties.

The wide spread of nanotube's properties make them an exceptional choice for many fields including, healthcare, electronics, technology, environmental and energy. More specifically you can find this technology in many items people use every day. Most carbon fibered baseball bats, gold clubs and car parts are designed and built with this form of technology. Ideas are also being researched to find more uses for this new technology. One in particular that could be great for mankind is use in the healthcare system. One specific idea is to use the extreme strength of nanotubes to cut soft tissues and cells for research by using the MWNT to form a wire that can be used as a "cheese wire". This could mean great leaps and bounds for biologists but also for engineers. In years to come carbon nanotubes will be noticed in all aspects of people lives. One of the theories that scientist have been playing with is the idea of a space elevator. The idea is to have a long cable that reaches from the earth to outer space in order to send materials without the need of rockets. The basics are that a large weight would be placed on the space end creating a centripetal force, while the gravitational force would keep the earth side in place. This type of set up would require a tensile strength of at least 60 GPa. Before the discovery and testing of carbon nanotubes this theory was very unrealistic because no materials were able to withstand that force. However, now they have an opportunity to create this kind of elevator to space.

In this research the focus was applied on the doped nanotubes. One of the great aspects of carbon nanotubes is that they have a very high surface area. This allows many different processes for doping many of which are being tested and perfected. These nanotubes are created through multiple processes, some of the most common processes are chemical vapor deposition, high-temperature and high-pressure reactions, gas-solid reaction at high temperatures, solid reactions, solvothermal syntheses, tube wrapping with electropositive or electronegative polymers, tube coating with metal ions, and even surface coating with nanoscopic layers of inorganic material. For the doping of nitrogen into carbon nanotubes the only method we looked into is the direct insertion of nitrogen through the carbon nanotube walls. For the doping of Boron,

The beginning of the electron microscope starts in 1926 when Hans Busch invented the first electromagnetic lens. Leo Szilard tried to convince him to create the first electron microscope in 1928 after filing for a patent, but ultimately was unsuccessful. In less than three years though, German physicist Ernest Ruska and electrical engineer Max Knoll, constructed the first electron microscope. Although it comes short of modern technology it was capable of four-hundred power magnification, and was the first successful microscope using the principles of electron microscopy.

Two years later Ruska, improved the system enough to surpass the finest optical microscope in attainable resolution. The first commercial microscope was developed in 1938, at the University of Toronto, by Eli Franklin, Cecil Hall, James Hillier, and Albert Prebus. However, today's electron microscopes still used the principles developed in Ruska's prototype. Although the basic design hasn't changed over the years, improvements have been made.

In electron microscope is similar to the more popular light microscope except that it uses electrons instead of light. This allows a larger spectrum of visual options; this is due to the fact that most light microscopes are limited by the wavelength of light. When electrons are used instead their wavelength is much lower so the resolution can be increased drastically. One way to show just how great in electron microscopes capability is by comparing the resolution to that of a rock compared to Mount Everest. Electron microscopes are identified as one of two main types – TEM and SEM. The first one is referred to as a transmission electron microscope, while the second one is a scanning electron microscope. This TEM uses a high voltage electron beam to create an image. An electron gun is used in and usually is fitted with a tungsten cathode, as the electron source. The electron beam is accelerated by an anode at 40- 400 kV, depending on the specific cathode. This beam is focused by electrostatic and electromagnetic lenses and then transmitted through the specimen. After emerging from the specimen the electrons are magnified by the objective lens system. This is then projected onto a fluorescent viewing screen usually coated with a scintillator or phosphor material, allowing the information to be examined. More recently the phosphor material has been coupled with a charge-coupled device camera that allows information to be displaced on a monitor. The main disadvantage of this design is that the samples need to be extremely thin slices, usually with a maximum thickness of about 100 nm. This becomes a problem when dealing with biological specimens. Another drawback to the TEM mode is that it's limited by spherical aberrations, although research is being done to overcome this obstacle. However, the TEM is still used for multiple research projects and experiments. When working with carbon nanotubes the TEM works well because the nanotubes are already thin enough to work with.

Many great inventions and developments have been brought about by the invention of the electron microscope. Some of the reasons the electron microscope had so much force behind its discovery was because it would allow scientists and biologist to examine and learn more about the diseases that before we couldn't really examine. Some very important ones include the discovery of viruses that lead to the vaccines for those viruses. In 1948 the electron microscope was used to see the differences between the smallpox virus and the chicken pox viruses. Another leap was made by this new microscope when it was used to create the first image of the poliovirus in 1952. This was the start of a research to understand the virus-host relationship that was being done in the 1950s. However, the electron microscope did even more for the study of diseases when it was used to examine many different feces in order to be used to classify and discern morphology from many different intestinal viruses. It was also used to discover parvovirus B19 which is what causes the hepatitis B virus. Another discovery was the cause of transient aplastic crisis which occurs in patients with sickle cell disease. Although these discoveries came early on in the development of the electron microscope, their data is still used today to describe and discern different viruses and cells. The electron microscope has been heavily used and depended on in the medical field, however with time the microscope is being used in almost all sources of research.

MATERIALS AND EQUIPMENT

The TEM used for this project is referred to as the JEOL microscope. The nickname comes from the model of the TEM. This particular machine is a JEOL TEM-2100 LaB6 Transmission Electron Microscope and is located in the engineering labs on WVU's Evansdale campus. The TEM has three condenser lenses that work independently to produce the highest probe current at any size. This allows the machine to have a wider and improved range for analytical and diffraction uses. The TEM also has a patented JEOL Alpha Selector which gives its user the option to choose from a variety of illumination conditions ranging from full convergent beam to parallel illumination.

Another aspect of this model is that it has two digital Gatan cameras, the ES500W and the SC1000 Orius CCD. The ES500W camera is able to capture high speed as well as high quality images with a larger field of view than the average TEM field. This advantage allows the operator to take images of intense electron diffraction patterns without the problem of the "blooming effect". The SC100 Orius CCD can provide the latest generation of large format, which is currently 11 Megapixel, retractable and fiber-optical coupled CCD camera. This can produce an outstanding image quality at high speeds for high resolution electron microscopes.

The materials used for this research were all produced and purchased from Nano Tech Labs Inc. which is based in Yadkinville, North Carolina. Three materials were produced including a base carbon nanotube. For the lab all three materials purchased were MWNT and two of them were doped. The first nanotubes purchased were M-Grade Multi-Walled Carbon Nanotubes. The grade has a diameter range of 70-80nm with eight percent residual iron and cost twenty dollars a gram. The second gram that was purchased was a Nitrogen Doped Multi-Walled Carbon Nanotube. These nanotubes had a product grade of N-MWNT and contained a nitrogen lattice doped percentage of 1-2. The average length was 50 μ m and a diameter range of 20-40nm. It had an eight percent residual iron, a melting point range of 3652-3687 °C, and a density at 20°C of 2.1 g/cm³. This purchase was \$75 a gram. The third material purchased was Boron Doped Multi-Walled Carbon Nanotubes. This gram has a product grade of B-MWNT and contains Boron doped of 1-2%. The average length is 50 μ m with a diameter range of 20-40 nm. It has a density at 20 °C of 2.1g/cm³ and a melting point range of 3652-3697 °C. The purchase price was \$75 a gram. To prepare the samples all of these materials were added to a liquid solution of acetone. This allowed them to be easily seen and picked up by the TEM.

METHODS

This project taught me many important techniques required to operate a TEM. One of the first was sample preparation for the TEM was to ensure that the sample is thin enough to be able to produce an image. Large solids and metals can be extremely difficult to make thin enough to allow electrons to be transmitted through them. The nanotubes purchased for this research arrived in a fine powder which allowed set-up to be a quick process.

The first step involved combining the nanotubes with a fast evaporating solution. Once a soluble mixture was created, a dropper was used to place a single drop of solution onto each pre-purchased grid. In this research carbon 300 square grids were used. These grids are then set aside until the solution evaporates leaving behind the carbon nanotubes which have attached to the carbon lens of the grid. After the grid discs are assembled they can be placed into a specimen holder, and are ready for the TEM.

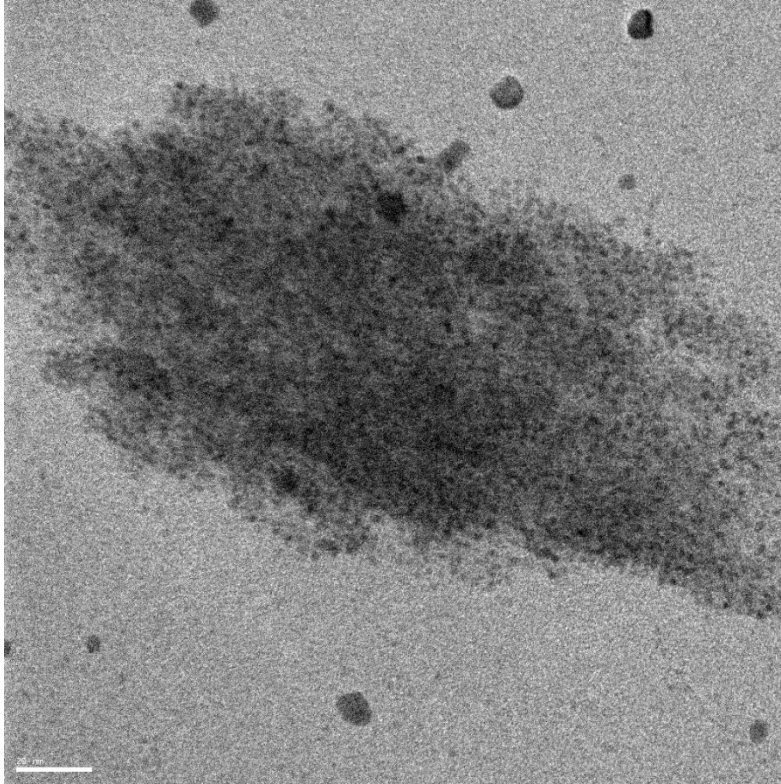
The next step was set-up of the machine. The TEM has many parts and extra pieces of equipment that are used to make sure it runs properly. One of these is a high pressured vacuum used to pump air out of the chambers. Minimal manual setup is done to the vacuum although it is crucial to make sure that it is working properly before starting any research. Another key aspect to obtain valid results is making sure a filament is in place and that it is still functioning properly. Most filaments last approximately 700 hours of use. WVU was able to create the record for longest use of a single filament which was over 1000 hours.

After verification these parts are functioning correctly, the next step involves checking to ensure the water chiller is properly working for all aspects of the TEM. This is completed by measuring the pressure levels of each of the exit pipes. After you have made sure all elements going into the TEM are functioning properly, fill the nitrogen ring with fresh liquid nitrogen. This is the most crucial point since without the liquid nitrogen; the electrons would over heat the sample and create a fast growing carbon sheet over the sample. This would make the sample useless and the data and images substandard. To prevent this error, nitrogen is used to counter the heat given off so that the sample is not contaminated. The nitrogen is good for four hours and then needs refilled. It is important to remember when doing long experiment. When finished using the TEM, the nitrogen is boiled out to prevent the electron beam running. With nothing to counter balance the nitrogen the chamber inside will have a large drop in temperature causing any air inside to condense.

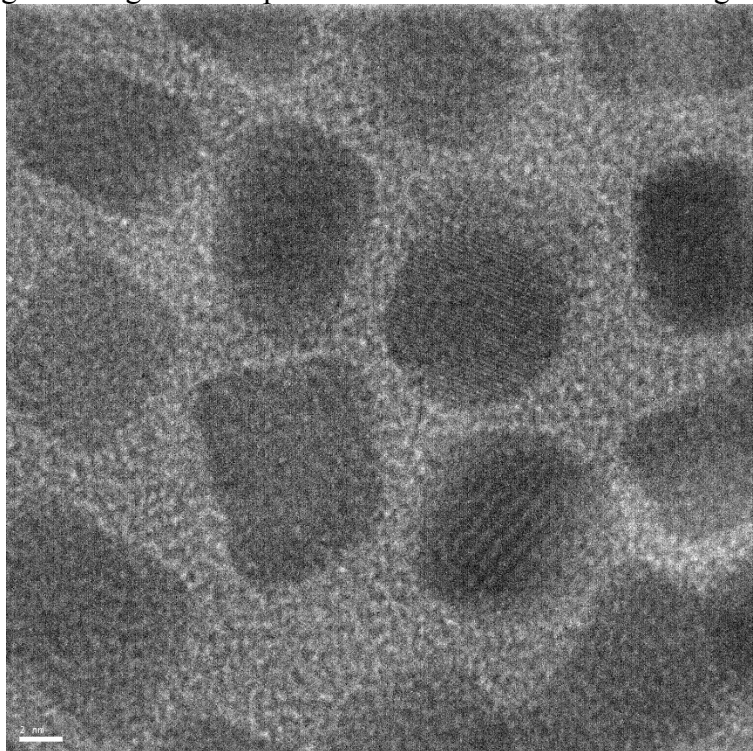
After the machine is prepared it is turned on and the voltage is set to 180kV. The current is slowly increased to about 90-110. It is important that this is done slowly so that it doesn't short circuit the machine, approximately twenty minutes. Once the current is set a prepared sample is inserted slowly and carefully. Insert the sample half way using the vacuum to remove the air from the chamber before continuing. The filament can then be activated. An important safety issue is to ensure the sample is already in the chamber before the filament is turned on or the operator could be severely electrocuted. Once the sample is inserted and the filament is turned on increase the voltage to 200kV and start aligning the magnets and electron beam. Once aligned a point on the grid is selected to examine and the smaller top camera can be used to examine the chosen sample. Following that, the lower level camera can be used to show a better resolution image of a smaller area chosen from the image. This final picture is examined and compared to the other samples.

DATA

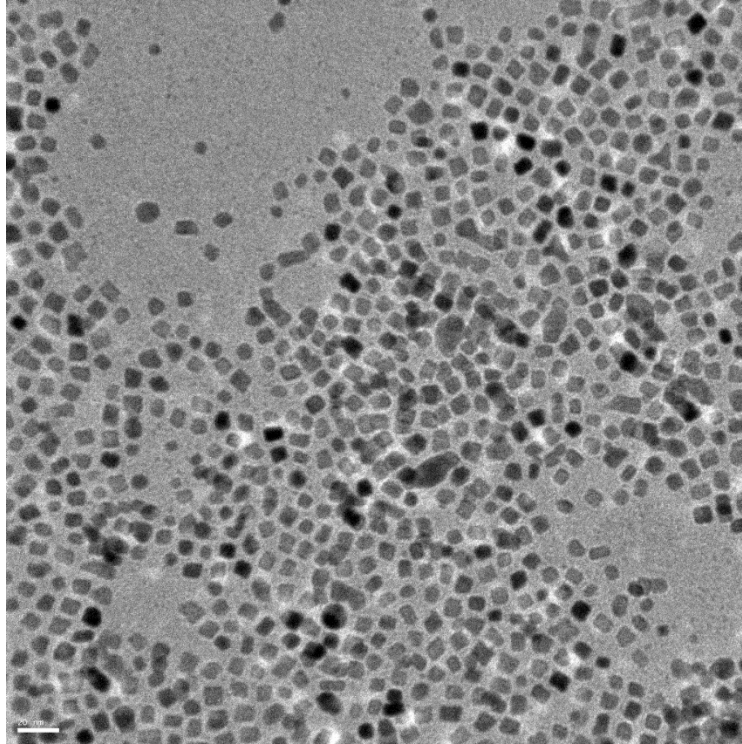
The following pictures were taken using the TEM machine at the shared research facility at West Virginia University.



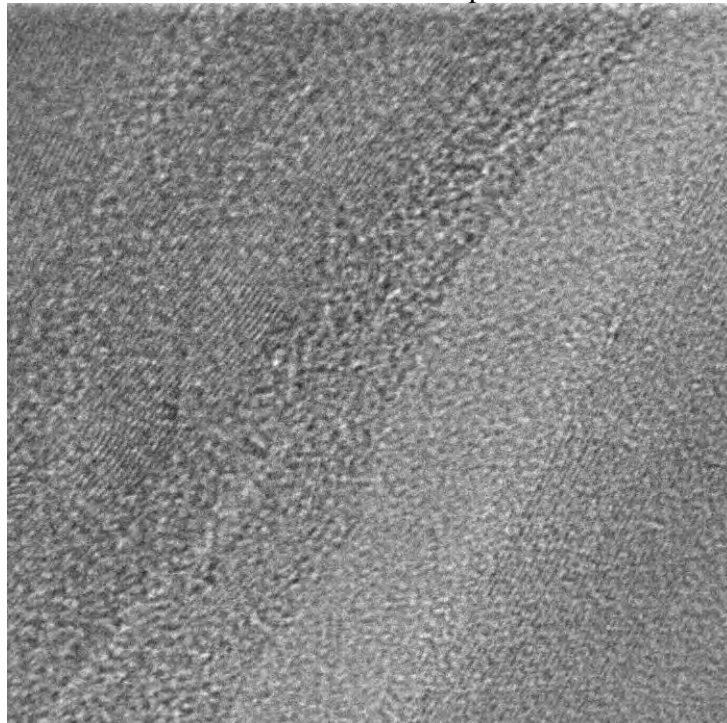
This image is of a gold nano-particle cloud found in an iron and gold sample.



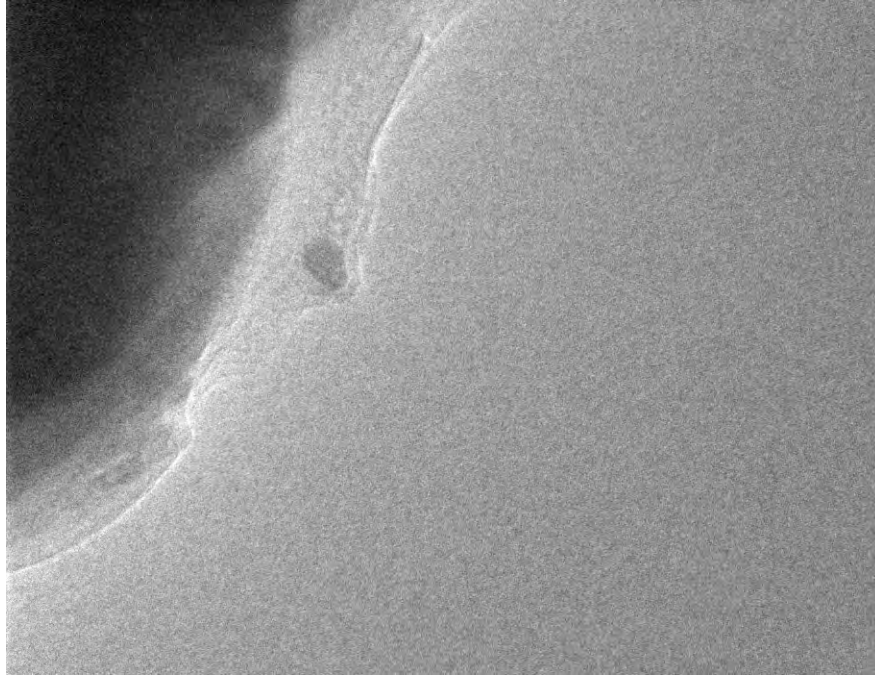
This image is of iron nanoparticles and their crystalline structures. It is clear to see the alignment in multiple particles in this image.



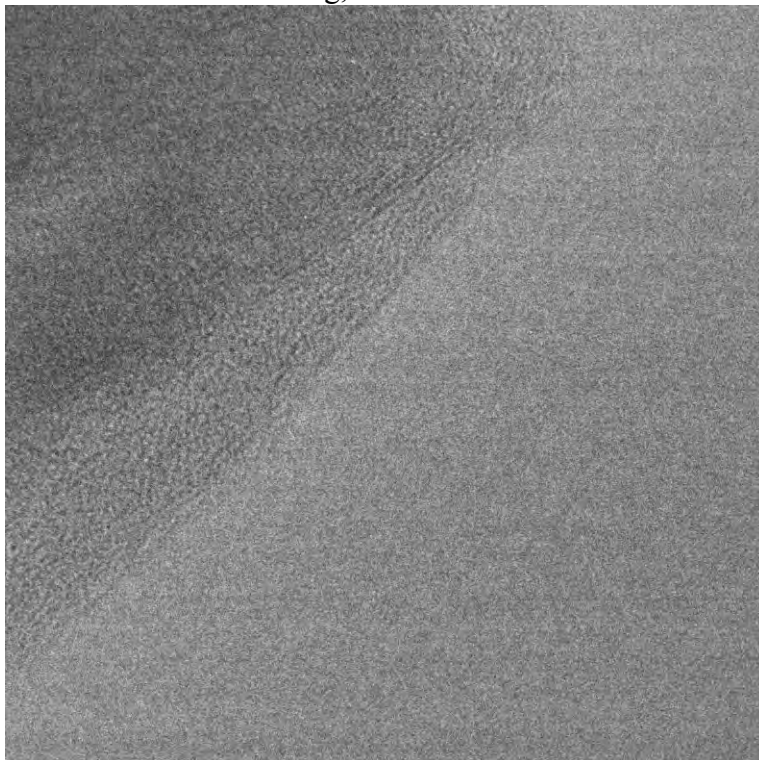
This image is of iron particles, it has a relatively lower magnification which allows the image to show a whole cluster of particles.



This image is of the multi-walled carbon nanotubes. The crystalline alignments are easy to see. In this picture there are multiply nanotubes, each set of lines is one nanotube. The darker lines are nanotubes that are laying on other nanotubes and the lighter ones are typically nanotubes that are alone.



This picture shows organic material that was attached to the Nitrogen doped MWNT. With the material removed images of the MWNT would have been cleaner and clearer to see. This is the materials that would have been removed from the samples before creating new samples for further testing, if time had allowed.



This image is the best picture of the nitrogen doped multi-walled carbon nanotubes that was produced. Had more time and time for cleaning been left more clear pictures would have been created.

RESULTS

During the initiation of the project, some barriers were encountered. The first was that the technology provided at West Virginia Wesleyan College, a Transmitting Electron Microscope, was not operational in time to complete the work. This problem was solved by collaborating with West Virginia University and using their TEM equipment. The second problem that arose was finding a nanolab that could produce the materials selected for the project. Once the option of gaining lithium doped carbon nanotubes was eliminated, the focus then changed to predicting what would happen once the two super materials were combined. This was done by comparing plain carbon nanotubes with one doped versions. The original plan was to compare the changes the two elements made to the original to draw conclusions about how a third element (lithium) would change the structure. Unfortunately, time got the best of this research and the third element was not tested, making a hypothesis on lithium very hard to create.

CONCLUSION

At the end of the project several things were accomplished by this grant. First, I learned new information and details about carbon nanotubes and the amount of work that has already been done with this item. Second, I learned there is a complex multi-step process for scientific research. Conducting the literature search, preparing documents, and collaborating with another organization were steps in this process. I also learned that barriers to equipment access, finances, and resources can limit the ability to perform experiment based research.

The most important aspect of the project was completing the training and certification required to operate the TEM. Completing this learning experience provided me the opportunity to examine the carbon nanotube samples and hypothesize a conclusion when carbon nanotubes are doped with lithium.

ACKNOWLEDGEMENTS

This internship was made possible by several different groups and people. We acknowledge use of the WVU Shared Research Facilities. Primarily, the NASA West Virginia Grant Consortium Grant, which provided the financial resources to conduct the project. Dr. Marcela Redigolo and West Virginia University provided the access and training to the TEM, which was fundamental to conduct an experiment of this type. Dr. Joseph Weist, my advisor at West Virginia Wesleyan was encouraging and supportive.

REFERENCES

- Bellucci, S. (2005). "Carbon nanotubes: Physics and applications". *Physica Status Solidi (c)* 2 (1): 34–47.
- Binns, Chris. *Introduction to Nanoscience and Nanotechnology*. Hoboken, NJ: Wiley, 2010. Print.
- Combined team of physicists and biologists build Lyme disease detector using carbon nanotube sensor. (n.d.). Retrieved April 24, 2015, from <http://phys.org/news/2013-06-combined-team-physicists-biologists-lyme.html>

- Crewe, A. (1966). Scanning Electron Microscopes: Is High Resolution Possible? *Science* , 729-738.
- Dunbar, B. (2005, March 8). Carbon Nanotube Sensors for Gas Detection. Retrieved April 24, 2015, from http://www.nasa.gov/centers/ames/research/technology-onepaggers/gas_detection.html
- Electron microscopes. (n.d.). Retrieved April 24, 2015, from <http://www.explainthatstuff.com/electronmicroscopes.html>
- Fowles, G. (1986). *Analytical mechanics* (4th ed.). Philadelphia: Saunders College Pub.
- "How Long Will An Electric Car's Battery Last? - HybridCars.com." *HybridCars.com How Long Will An Electric Cars Battery Last Comments*. N.p., 30 Apr. 2014. Web. 27 July 2015.
- Johnson, D. (n.d.). Graphene and Carbon Nanotubes Join Forces to Tackle Supercapacitors. Retrieved April 24, 2015, from <http://spectrum.ieee.org/nanoclast/semiconductors/nanotechnology/graphene-and-carbon-nanotubes-join-forces-to-tackle-supercapacitor>
- Kaplan, I. (1963). *Nuclear physics* (2d ed.). Reading, Mass.: Addison -Wesley Pub.
- Kittel, C. (1966). *Introduction to solid state physics* (3d ed.). New York: Wiley.
- Qu, L., Dai, L., Stone, M., Xia, Z., & Wang, Z. (2008). Carbon Nanotube Arrays with Strong Shear Binding-On and Easy Normal Lifting-Off. *Science*, 238-242.
- Prabaharan, S. R. S., and M. S. Michael. *Nanotechnology in Advanced Electrochemical Power Sources*. N.p.: n.p., n.d. Print.
- Smith, Brian W.; Monthioux, Marc; Luzzi, David E. (1998). "Encapsulated C-60 in carbon nanotubes". *Nature* 396 (6709): 323–324
- Stoner, Brian R.; Jeffrey T. Glass (2012). "Carbon nanostructures: a morphological classification for charge density optimization". *Diamond and Related Materials* 23: 130–4
- VanVlack, L. (1964). *Elements of material science: An introductory text for engineering students* (2nd [rev. and enl.] ed.). Reading, MA [etc.: Addison-Wesley.
- Volder, M., Tawfick, S., Baughman, R., & Hart, A. (n.d.). Carbon Nanotubes: Present and Future Commercial Applications. *Science*, 535-539.
- Zhong, Y.; Jaidann, M.; Zhang, Y.; Zhang, G.; Liu, H.; Ioan Ionescu, M.; Li, R.; Sun, X.; Abou-Rachid, H.; Lussier, L. S. (2010). "Synthesis of high nitrogen doping of carbon nanotubes and modeling the stabilization of filled DAATO@CNTs (10,10) for nanoenergetic materials". *Journal of Physics and Chemistry of Solids* 71 (2): 134

SOLAR PHYSICS USING LASER SPECTROSCOPY OF SODIUM IN THE EARTH MESOSPHERE

Wolfgang Zober
Physics and Mathematics
Wheeling Jesuit University
Wheeling, WV 26003

ABSTRACT

Within the upper atmosphere, specifically the mesosphere, there is a layer of non-ionized sodium atoms between 80 km and 105 km above the surface. This layer, created through the ablation of meteors, weakly emits a doublet, two spectral lines D2 and D1 which are respectively 589 nm and 589.6 nm. Through a process known as sodium fluorescence lidar, researchers can specifically target these wavelengths to measure the concentration of sodium in the mesosphere. This provides temperature measurements in this region and allows scientists to explain and separate solar and Earth induced heat changes in the atmosphere. This will also enable scientists to further understand middle and upper atmospheric chemistry, structure, dynamics, and gravity waves, all of which play a fundamental role in atmospheric modeling. As such this project is an in-depth analysis of building a laser for this purpose.

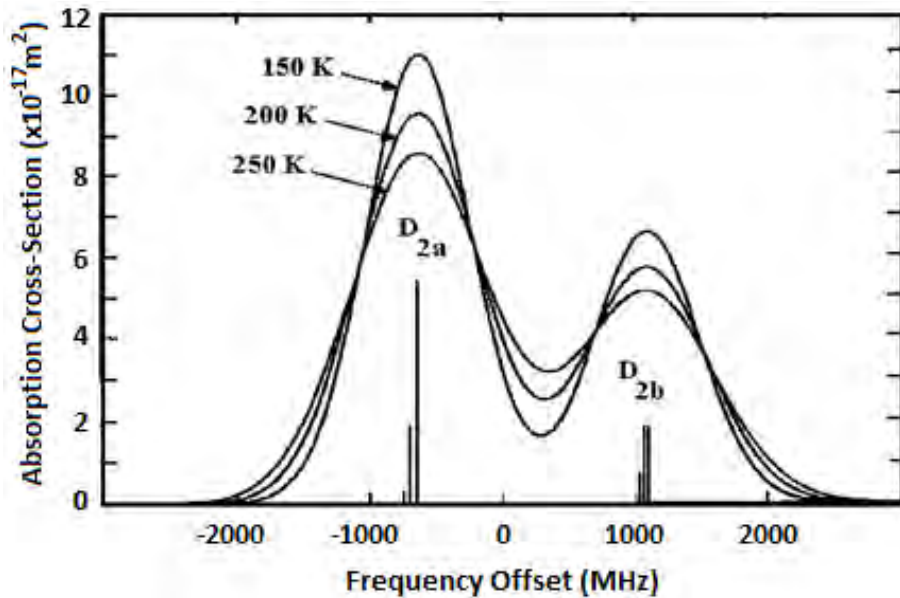
INTRODUCTION

This project was an investigation into creating a tunable Nd:YVO4 self-Raman laser as a tool for sodium lidar. Throughout the time period of this internship multiple steps were taken to create this laser. For the first few weeks a variety of papers were read to gain an understanding of the laser being built and other similar designs. After this a mathematical model of the laser was created using the software Mathcad. At the same time, a variety of equipment was tested with a spectrophotometer to see if they would work in a potential design. Once all of this was completed the design was finalized as the following. A C-cut Nd:YVO4 crystal would be pumped with 808 nm light from a laser diode to produce 1066 nm light within the crystal. The crystal would then undergo Stokes emission at 1178 nm. This newly emitted light is then taken through a process known as frequency doubling which halves the wavelength into the desired 589 nm. From here the laser would be able to be adjusted through differing temperatures to make the laser tunable. This would allow the changing of the final output wavelength of the laser and allow the full mapping of the Sodium doublet spectrum.

BACKGROUND

It is believed that the existence of Sodium alongside other metals such as Mg, K, Fe, and Ca within the upper atmosphere is due to ablation from meteors. These metals exist in a non-ionized state. If photons of the proper wavelength are directed onto these metals in the mesosphere, they can cause them to resonate. This technique is called resonance fluorescence lidar. This process can provide temperature measurements to explain and separate solar versus Earth induced heat causing change within the Earth atmospheric temperature. These lines for sodium's resonance is 589 nm and 589.6 nm.

Additionally, these lines change as a function of temperature. As temperatures decrease, the intensity of the lines increase and become more compact. By measuring the intensity of both lines, the temperature at that point in the mesosphere can be obtained. And if this is done throughout the atmosphere a temperature map can be generated.



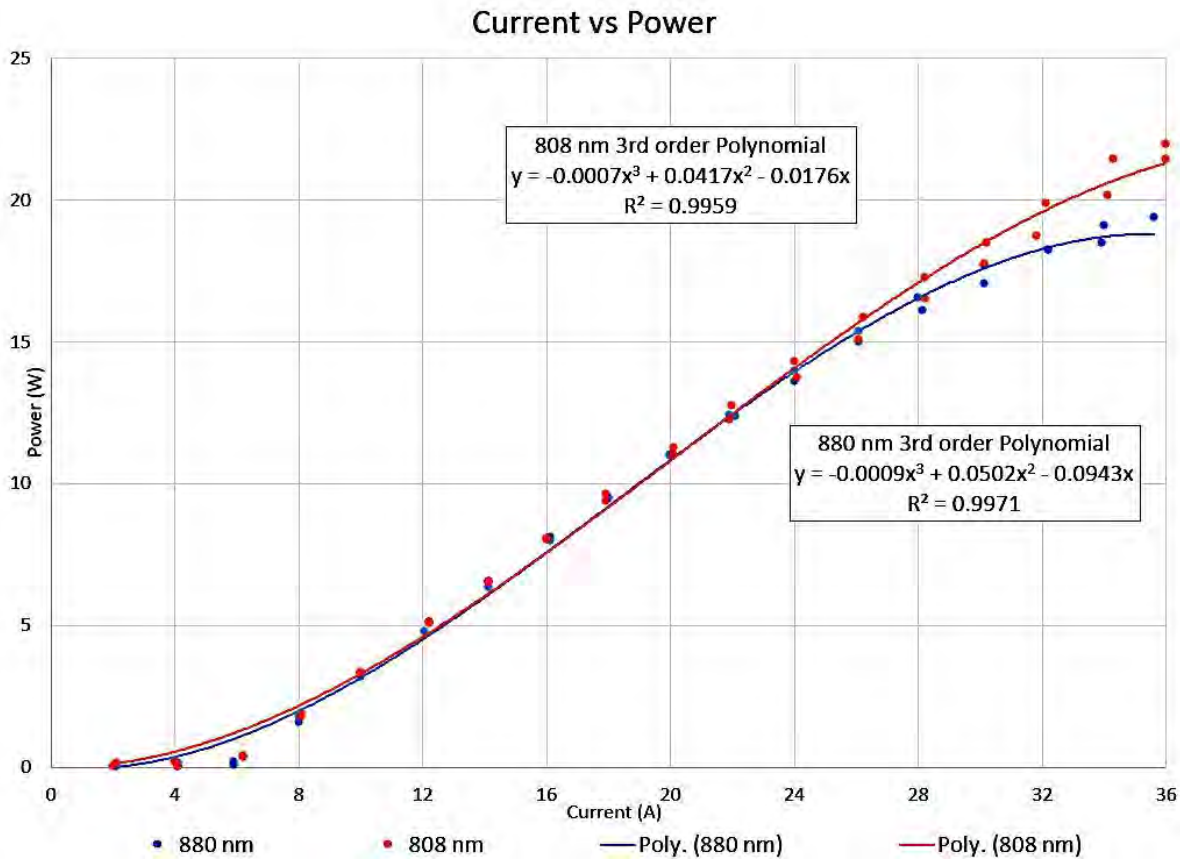
This graph shows how the Sodium absorption lines change with temperature. As temperature increases, the peaks for both lines reduce and the gap between the two dissipates. For purposes of clarity it should be noted that the reason for the measured wavelength to be in frequency offset rather than wavelength is due to this graph being taken from an oscilloscope and the zero point on the line is roughly the center between the two lines at approximately 589.3 nm.

METHODOLOGY

Designing a tunable laser is a multiple step process. There are a number of elements that needs to be decided on. This includes what pump diode is used as an input, the type of crystal used, Nd:YVO₄, and the lenses within the laser cavity. Deciding on some of these pieces can be streamlined by modeling these parameters within Mathcad, Excel, and other programs. While others are often chosen by testing itself.

Choosing the Pump Diode

In this design, the best possible efficiency between the input current and the output power from the diode is desired. There are two different pump diodes that will produce wavelengths capable of inducing Stokes emission within the crystal, an 808 nm and a 880 nm. To properly analyze which is more efficient, both diodes outputs were tested over an input range of 36 A, with measurements taken about every 2 A. The data was then plotted with a third order polynomial fit.

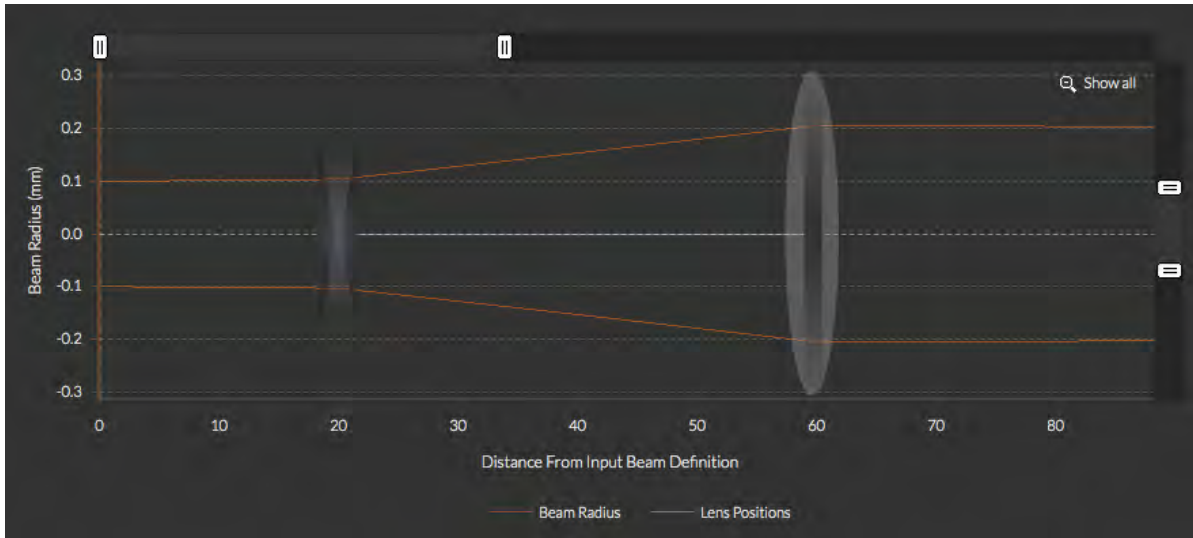


As shown above the 808 nm pump diode has the better capabilities and should be used for this project. It has both a higher output power and a later drop off point where the output/input efficiency decreases compared to the 880 nm pump diode.

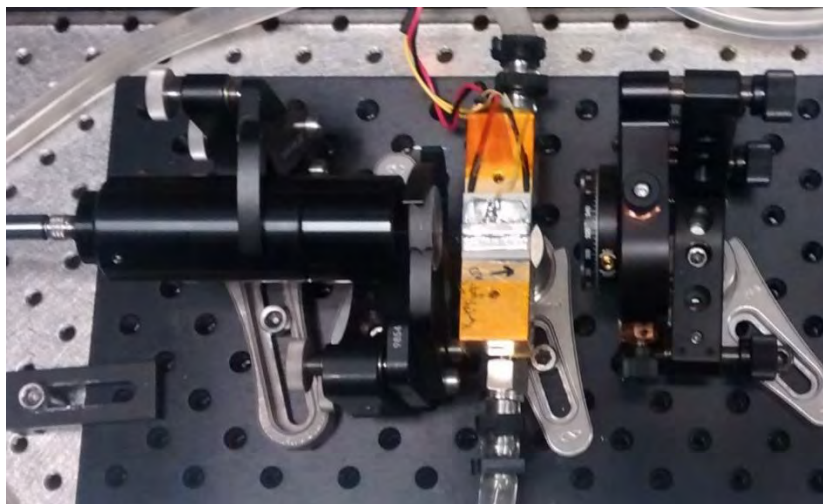
Lens Selection

To properly select the lenses needed for this tunable laser, information must be known about the pump diode being used and the crystal itself. For the pump diode the following is known, the output wavelength of 808 nm, the output beam diameter is 200 μm , and the fiber used has a NA of 0.22. This is all necessary as lasers have Gaussian beam distributions. Meaning that the incident beam divergence needs to be calculated. This is how much the beam grows in diameter over distance, as light will spread out from its source. The other valuable piece of information is that at the center of the crystal the width of the focused beam needs to be around 400 μm . All of this is needed for the proper selection of lenses for this laser.

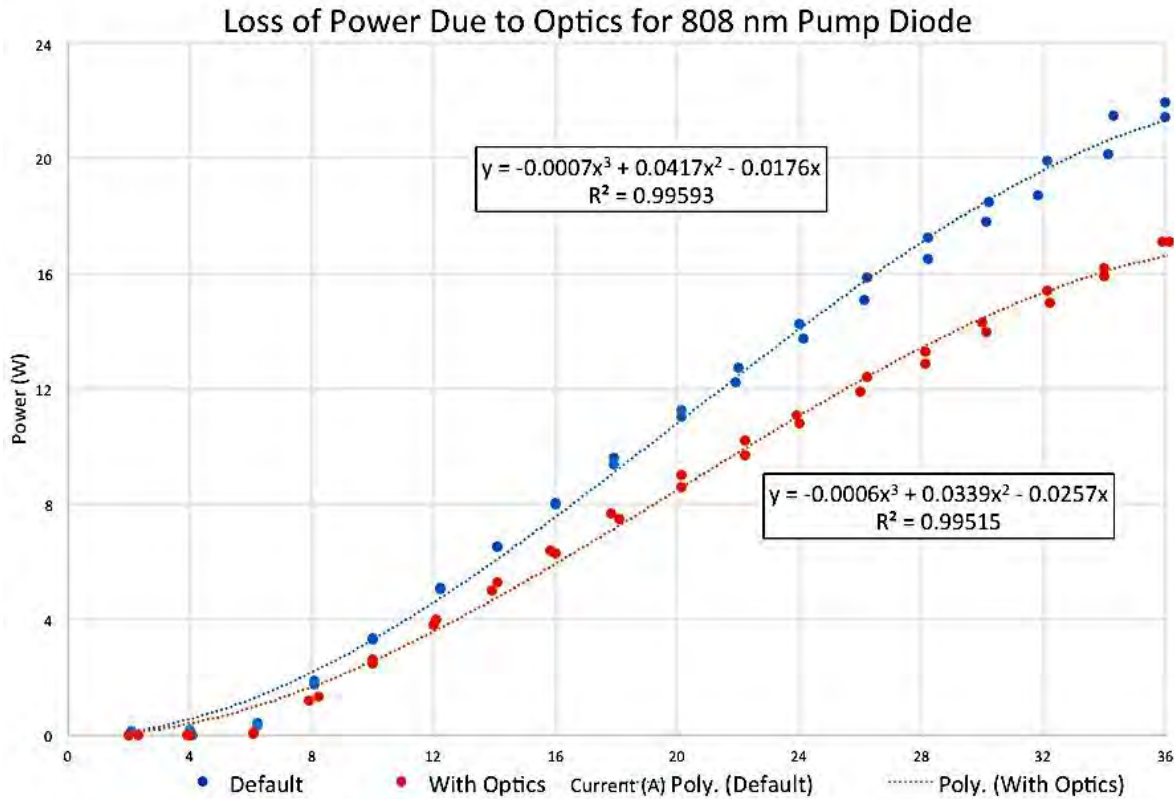
Two different methods were used for selecting lenses for this laser. At first multiple designs were created by using a calculator to create different spot sizes, distances, and focal points. One such design shown on the right used two lenses, a -50 mm and a 75 mm spaced 4 cm apart to create a spot size of 400 μm .



This design however, much like the others, was not accurate in the following testing phase and was discarded. While testing these lenses it was discovered that the calculator used was not accurate, and lens selection was needed to be done by hand. Further experimentation led to the following set up: First, right after the fiber input, there is a collimating lens with a focal length of 18.7 mm which then leads to a 30 mm lens 5 cm away. This set up is shown in the photo below.



This set up was then checked with a filtered IR camera and a power meter to find the focal point and to make sure that there was not a large loss of light from the lens set up. Which is shown by the graph below.

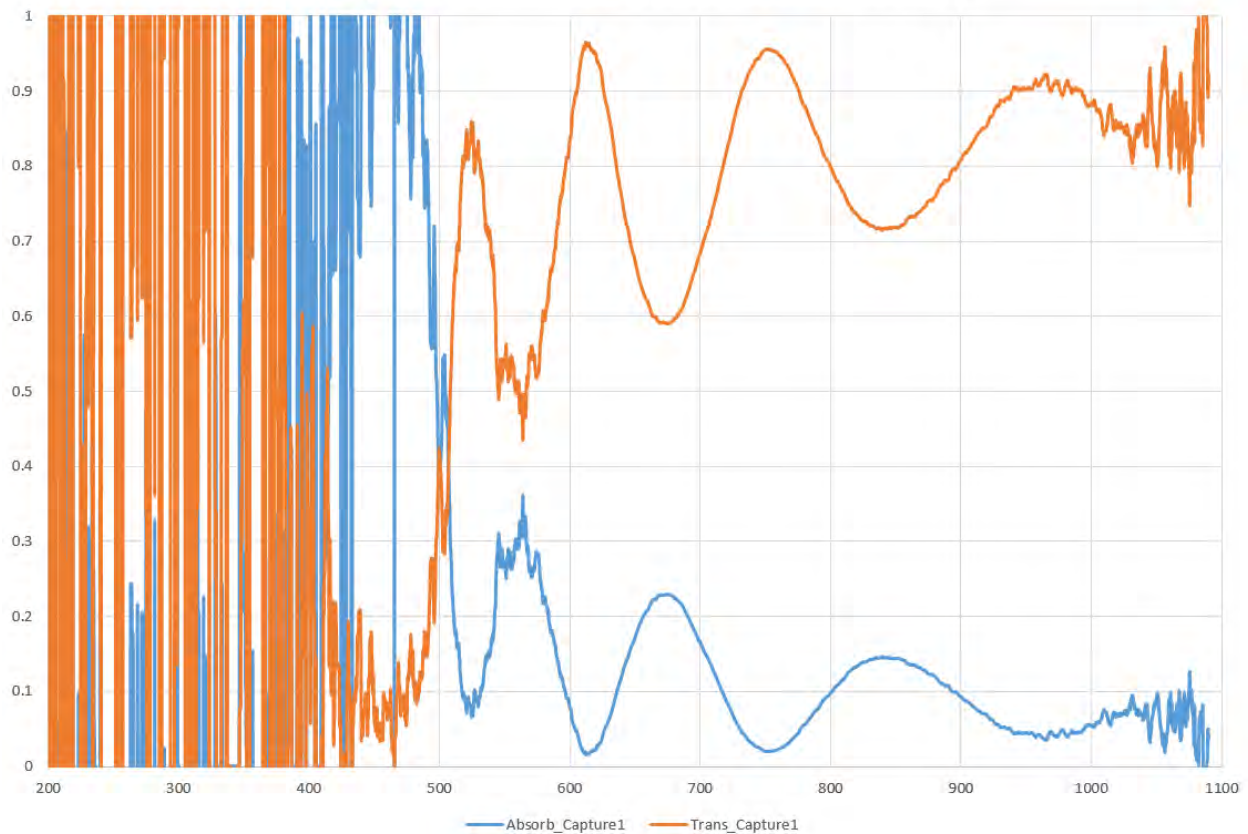


In this graph, it shows how much of a drop-off is caused by the addition of lenses compared to the original. Through integration of the polynomial fits it is determinable that this optical design has an approximate loss of 25 percent. This is by no means ideal but it can be worked with nonetheless.

Crystal Selection

There also must be a selection of which type of High Reflective crystal should be used between the lenses and the crystal itself. This is used to reduce light that may be lost from back reflections off of the Nd:YVO₄ crystal. There were multiple crystals tested with a spectrophotometer, to see which wavelengths of light pass through the crystal.

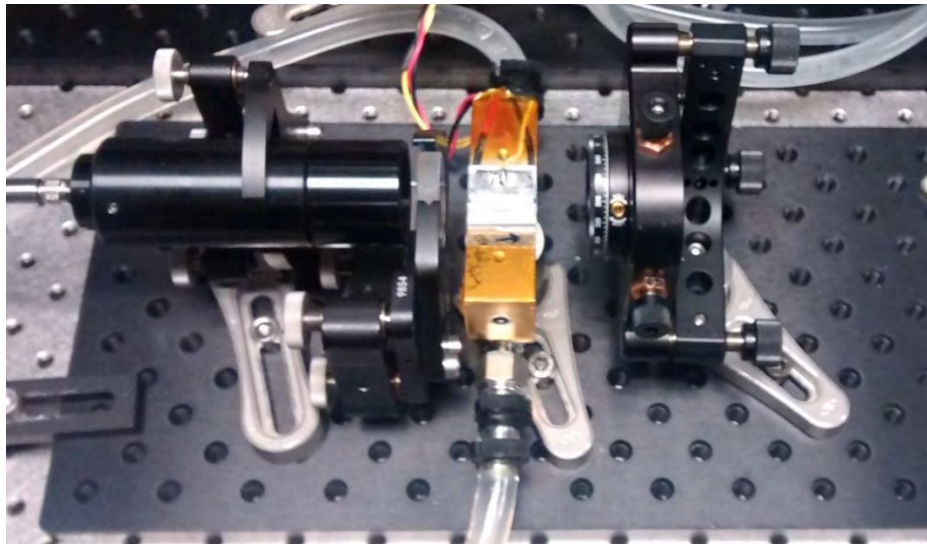
Absorption Transmission BS-400-450-R90-UF-1025



As shown in this graph this element has decent transmission capabilities compared to absorption. There were about 25 other elements tested and graphed in this manner. This testing was also completed for another crystal, the reflective filter, which is to be placed after the Nd:YVO₄ crystal, to block out all wavelengths below 1 μm . This is necessary for both safety reasons and to make sure the laser stays at the desired wavelength.

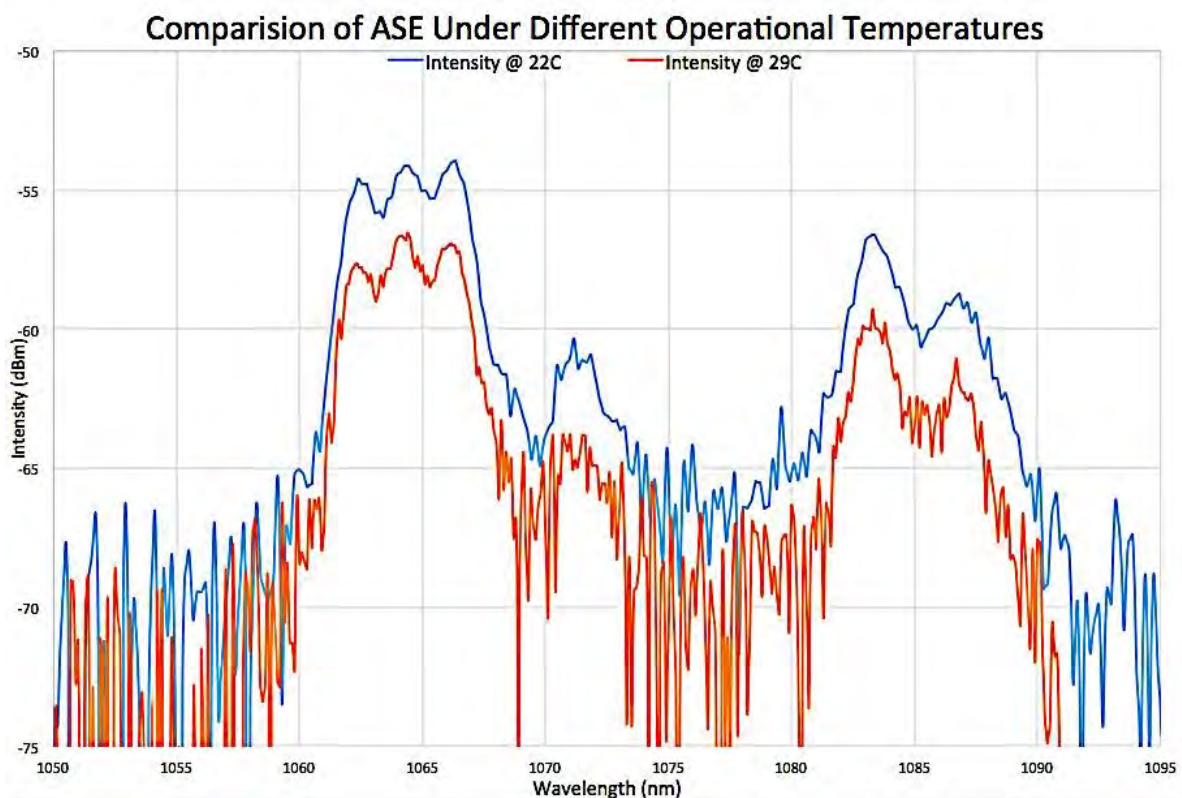
Final Assembly

After checking the lenses and the focal point, all of the pieces can then be placed into their respective locations in the cavity. First, a HeNe laser is set up to be aligned in the opposite direction as the constructed laser. This is to enable the continuous checking of alignment of the various elements of laser cavity. After this the input and the two lenses are aligned with the laser. Next, the Nd:YVO₄ crystal is placed such that the crystal itself is directly centered on the focal point of the lenses. Then the HR-mirror is placed between the lenses and the Nd:YVO₄ to act as a reflector. Then the reflective filter is added after the Nd:YVO₄ crystal to block wavelengths below 1 μm .



CURRENT RESULTS

At this point in the experiment, the equipment is then tested with a spectrum analyzer to see if it properly creates a Stokes emission at the desired wavelength. As shown on the graph to the left the pump diode was tested twice at two different temperatures to see if the output could be forced into creating a cleaner ASE.



Which as shown above, changing the temperature made a slight difference, but did not bring the ASE to the desired output. This means that the assembled laser cavity is still not perfectly aligned and will need further adjustments.

CONCLUSION

At this point the remaining steps would be to continue tinkering with the set up in order to adjust the outputted ASE and then add in the frequency doubler to create the laser. Once those steps are done the laser would be tested with a spectrophotometer to ensure the laser is properly calibrated to the D lines of sodium. After which it would then be combined with a seed laser to increase the output power.

In my opinion the most valuable thing to me here this summer has been the support and guidance I have received from those in my branch and the other researchers, scientists, and engineers at Goddard. They have all been a massive influence on me and as such have been the most important take away during my time here at Goddard Space Flight Center. I fully expect to be contacting those I mainly worked with in the future for grad school references.

ACKNOWLEDGEMENTS

This project was possible due to NASA Goddard Space Flight Center, WV Space Grant, my mentors Michael Krainak and Tony Yu, and their branch, Code 554 – Lasers and Electro-Optics.

REFERENCES

- [1] Pask, H. M. *Review The design and operation of solid-state Raman lasers*. Progress in Quantum Mechanics, Vol. 27 (2003) 3-56
- [2] Piper, James A. and Helen M. Pask. *Crystalline Raman Lasers*. IEEE Journal of Selected Topics in Quantum Electronics, Vol 13, No. 3, May/June 2007 692-704
- [3] Ding, Shuangqing, Xingyu Zhang, Qingpu Wang, Jun Chang, Shumei Wang, and Yuru Liu *Modeling of Actively Q-switched Intracavity Raman Lasers*. IEEE Journal of Quantum Electronics, Vol 43, No. 8, August 2007 722-729
- [4] Ding, Shuangqing, Xingyu Zhang, Qingpu Wang, Fufang Su, Peng Jia, Shutao Li, Shuzen Fan, Jun Chang, Sasa Zhang, and Zhaojun Liu. *Theoretical and Experimental Study on the Self-Raman Laser With Nd:YVO4 Crsytal*. IEEE Journal of Quantum Electronics, Vol 42, No. 9, September 2006, 927-933
- [5] Spence, David J., Xiaoli Li, Andrew J. Lee, Helen M. Pask. *Modeling of wavelength-selectable visible Raman lasers*. Optics Communications 285 (2012) 3849-3854
- [6] Zhu, Feihu, Ke Gong Yujing Huo. *Optimization of an AO Q-switched solid-state Raman laser*. Optics Communications 285 (2012) 2128-2133
- [7] Ding, S., X Zhang, Q. Wang, F. Su, S. Li, S. Fan, S. Zhang, J. Chang, S. Wang, Y. Liu *Theoretical models for the extracavity Raman laser with crystalline Raman medium Appl. Phys. B 85, 89-95, (2006)*

- [8] Su, Fufang, Xingyu Zhang, Qingpu Wang, Shuanghong Ding, peng Jia, Shutao Li, Shuzhen Fan, Chan Zhang and Bo Liu. *Diode pumped actively Q-switched ND: Nd:YVO4 self-Raman laser*. Journal of Physics D: Applied Physics 39 (2006) 2090-2093
- [9] O'Shea Donald C. *Elements of Modern Optical Design*. Wiley. New York, 1985
- [10] Injayan, Hagop and Gregory D. Goodno. *High Powered Laser Handbook*. McGraw Hill, 2011
- [11] Xiao, Guohua and Michael Bass. *A Generalized Model for Passively Q-Switched Lasers Including Excited State Absorption in the Saturable Absorber*. IEEE JOURNAL OF QUANTUM ELECTRONICS, VOL 33, NO 1, JANUARY 1997. 41-44
- [12] Degnan, John J. *Optimization of Passively Q Switched Lasers*. IEEE JOURNAL OF QUANTUM ELECTRONICS, VOL. 31, NO. 11, NOVEMBER 1995. 1890-1901
- [13] Degnan, John J. *Theory of the Optimally Coupled Q-Switch Laser*. IEEE JOURNAL OF QUANTUM ELECTRONICS, VOL. 25, NO. 2, FEBURARY 1989. 214-220
- [14] Raymond, T. D. and A. V. Smith *Two-Frequency Injection-Seeded Nd:YAG Laser* IEEE JOURNAL OF QUANTUM ELECTRONICS, VOL. 31, NO. 10, OCTOBER 1995. 1734-1737
- [15] Schmitt, Randal L. and Larry A. Rahn. *Diode-laser-pumped Nd:YAG laser injection seeding system*. APPLIED OPTICS, Vol. 25, No. 5, 1 March 1986. 629-633
- [16] See, Brian A. *Mathematical modeling of an Nd:YAG laser*. OPTICAL ENGINEERING October 1994, Vol. 33 No. 10. 3364-3367
- [17] Shu, Hong, Ying Chen, and Michael Bass and Madhu A. Acharekar. *Modeling a diode pumped Nd: YAG rod laser* Solid State Lasers XV: Technology and Devices. SPIE Vol. 6100, 61001J, 2006
- [18] Peng, Xiaoyuan, Lei Xu, and Anand Asundi. *Power Scaling of Diode-Pumped Nd:YVO4 Lasers*. IEEE JOURNAL OF QUANTUM ELECTRONICS, VOL. 38, NO. 9, SEPTEMBER 2002 1291-1299

II. NASA Undergraduate Research Fellowship Reports

PATTERNING AND CHARACTERIZATION OF DIRECT WRITTEN INKS AND FILMS FOR EXTRATERRESTRIAL SOLAR CELL APPLICATIONS

Jared Beard
Mechanical and Aerospace Engineering
West Virginia University
Morgantown, WV 26505

ABSTRACT

There is a developing need for production of optoelectronic devices under ambient conditions and to be suitable for use on nonplanar and pliable surfaces. Due to the brittle nature of silicon based solar cells and the highly controlled, expensive environments necessary to produce them, this represents a considerable obstacle for space missions and day-to-day life. This report aims to show the viability of direct writing films for use in the production of dye-sensitized solar cells and perovskite solar cells, as an alternative to traditional silicon based solar cells. The research performed involves joint progress by members of the Flexible Electronics for Sustainable Technologies Lab at WVU. This work involved the formulation of three separate inks, a silver sol-gel, an iodine-based electrolyte, and a titania sol-gel for use in a nozzle based robotic deposition method. Inks were then characterized for rheological properties. Following which, electrolyte and titania films were direct written on glass, while silver was direct written on polyethylene naphthalate (PEN). Direct writing here involved the use of nozzle based robotic deposition techniques. Concluding the work, the patterns and films deposited were characterized for electrical, mechanical, and optical performance.

INTRODUCTION

Three-dimensional (3D) printing shows promise in the production of electrical and mechanical devices. In particular, use of 3D printing techniques offers the capability to produce complex devices from precursor solutions with minimal waste. This is particularly useful in astronautic endeavors, which place heavy restrictions on mass and space allowances. For example, to produce optoelectronic devices will incur a cost on these allowances. Production of silicon-based solar cells requires resource-intensive, difficult lab techniques. In extraterrestrial missions, this does not offer a sustainable option as new solar cells would have to be transported from earth to the new settlements. For a settlement on Mars, the six month journey could be the difference between mission success and failure when harvesting light energy is time-sensitive.

Through the use of 3D printing, the proper materials for repairs, be they tools or replacement parts, could be made on site. This does little to assuage the constraints imposed by silicon solar cells. The proposed alternative is the use of quasi-solid-state dye-sensitized solar cells (DSSCs) and perovskite solar cells, as they show strong potential for roll-to-roll fabrication in ambient conditions [1, 2]. It is suggested that direct write 3D printing of materials could be used in place of roll-to-roll fabrication. Thus, this research focuses on direct writing of various materials used in the production of DSSCs.

BACKGROUND

To understand what makes DSSCs and perovskite solar cells suitable for use in future exploratory missions and why 3D printing offers a potential means of production, it is necessary to explain their structure and function, efficiencies, and economic factors.

DSSCs consist of a transparent glass or polymer substrate, front and back contacts, a mesoporous metal oxide ceramic separating layer with light-sensitizing molecules attached, an electrolyte, and a catalyst (Fig. 1). A superstrate made of glass will typically be coated with a transparent conducting oxide (TCO), such as indium doped tin oxide or fluorine doped tin oxide, for use as electrodes. TCOs allow for conduction of electrons without sacrificing optical transparency. There has also been interest in making these devices flexible. Consequently, research has been done into the creation of flexible metal patterns for use as electrodes to replace brittle transparent conducting electrodes. Beneath this is the mesoporous dye-coated metal oxide layer. As photons are absorbed by the dye, electrons become excited and move in the metal oxide separating layer. These electrons are then conducted to the electrode. The mesoporous metal oxide layer allows for a large surface area for dye attachment, increasing the potential for electrons to be excited from the dye. The electrolyte layer, either quasi-solid state or liquid, replenishes the supply of electrons to the dye through a redox reaction. The catalyst layer will draw electrons from the counter electrode to complete the circuit. Perovskite solar cells have a similar structure, however, they include a dense metal oxide layer and an insulator. They lack an electrolyte layer and the dye is replaced by a perovskite (Fig. 2). For these cells, perovskite refers to the crystal structure of the light-sensitizing material, which is usually an organic-inorganic halide material. A perovskite crystal structure, named after its discoverer, L.A. Perovski, is one with a cubo-octohedral lattice structure consisting of two differently size cations and anion which is typically oxygen or a halogen [3].

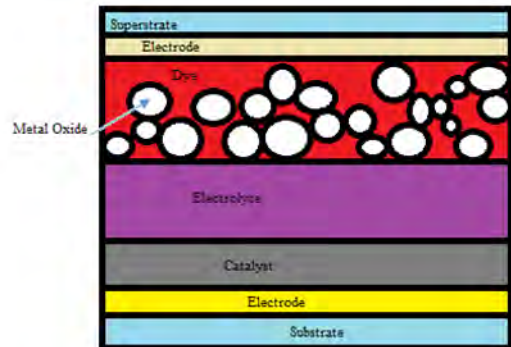


Figure 30 Schematic of DSSC layers: superstrate, electrode, metal oxide and dye, electrolyte, catalyst, electrode, substrate

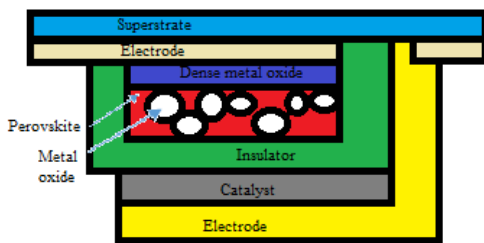


Figure 31 Schematic of perovskite solar cell layers: superstrate, electrode, dense

metal oxide, perovskite, metal oxide, insulator, catalyst, electrode, substrate

The fabrication method for the layered structure of DSSCs can be formulated to work with direct write 3D printing, i.e., direct writing. Direct writing is a nozzle-based robotic deposition method wherein inks are extruded in resolute patterns to produce films and features. Precursor solutions, or inks can be made for each layer of the solar cells for printing. To direct write the layers, inks must be formulated with easily achieved printing requirements, such as low viscosity and minimal nozzle wetting. Direct writing is a low-waste fabrication technique. After printing, each layer, if necessary, will require annealing to form the proper crystal structure. Next, the dye

or perovskite—depending on the type of cell—will need to adhere to the metal oxide scaffold. The solar cells can then be sandwiched together, completing the devices.

Dye-sensitized solar cells were first introduced by Grätzel in 1988 [4]. Perovskite solar cells are an evolution of DSSCs developed in 2009 by Miyasaka [5]. As of 2016, DSSCs and perovskite solar cells have reached efficiencies of 11.9% and 22.1% [6]. In their current state perovskite solar cells tend to be unstable if not properly sealed, due to the sensitivity of the perovskite material to humidity. Similarly, liquid-state DSSCs, will tend to leak and degrade rapidly if not effectively sealed. Quasi-solid state DSSCs are considered more stable as they tend to decay over longer periods and are less susceptible to leaking.

EXPERIMENTAL METHODS

The experiment conducted was in the characterization of layer-wise production of silver electrode films, a titania metal oxide layer, and a quasi-solid state I₂/I₃⁻ electrolyte for use in solar cells. Inks were created using prior research and modified to fulfill the needs of nozzle based deposition [7]. These inks were then characterized with respect to their rheological properties, specifically viscosity. A program was written to develop patterning commands for the 3D printing apparatus. Following, patterns were printed and then thermally annealed. The resulting films were characterized. My involvement in the research of the silver ink was largely analysis of the optical data, though the ink synthesis and other results will be briefly discussed for continuity. For the titania and electrolyte layer production, my work was primarily printing and ink characterization. Further detail on the work with silver patterns, can be found in work by Arango, et al. [8]. Methods conducted and results collected from the titania study are prepared for publication in a scientific journal and cannot be released at this time. As such, specifics are elaborated on in the ensuing sections.

Ink Synthesis and Characterization

The electrolyte inks were produced according to 4 formulations, each of which had varying concentrations of I₂/I₃⁻: 0.03 M, 0.05M, and 0.10 M, and 0.25 M. 0.95 N I₂/I₃⁻ was mixed with deionized water according to the necessary ratio. Following which, 4.45 g of polyvinyl alcohol (avg. MW 95000) was added to increase the viscosity of the iodine solution and create a PVA-iodine quasi-solid state sol-gel. After, 0.5 g of diethylene glycol was added as a plasticizer to allow sol-gel to flow more freely. The solution was stirred for 1 hour (or until complete dissolution) at 60 °C.

For the silver ink, two solutions were prepared. 0.57 g of Polyacrylic acid was mixed with 17.95 g of deionized water. Concurrently, 10.19 g of silver nitrate was mixed with 17.95 g of deionized water. These were then mixed together with 8.9 g of ethanolamine for approximately 14 hours at 60 °C; then for 2 hours as it cooled. The particles were collected after centrifuging for 30 minutes at 4400 RPM the day of mixing and 15 days after. The collected particles were dispersed in a solution by ultrasonication. The particles made of 70% w/w of the solution; 29.4 %w/w was deionized water; and 0.6 %w/w was methyl cellulose. Thus concluded fabrication of the ink [8].

The viscosity of the inks were characterized using a Brookfield DV-II + Pro rotational viscometer. Data was collected over a range of shear rates.

Film Patterning and Characterization

To pattern films, a program was written in MATLAB[®] which could provide coordinate information to a Nordson JR2300N robotic arm and an in-house built 3D printer (both equipped with Performus V pneumatic pressure controller). The program uses iterative processes to assemble patterns in a line, grid, or spiral configuration.

The electrolyte inks were deposited on glass. The solutions were printed at 1.38, 2.07, and 2.76 MPa at speeds of 1, 5, and 10 mm/s. Nozzle sizes included 0.1, 0.15, and 0.2 mm. The printed patterns consisted of three parallel 1 cm long lines. The silver inks were deposited on PEN using 0.1 mm tips.

Print parameters included pressures between 100 kPa and 150 kPa and speeds between 3 mm/s and 10 mm/s. The patterns consisted of grids with line spacing of 0.5 mm and lines with separations of 0.5 mm and 1 mm (Fig. 5). Afterwards, the samples were annealed at temperatures of 150 °C, 120 °C, and 90 °C for 30 minutes. Heating was at a rate of 5 °C/min. Using ImageJ photo-analytic software, images of the silver films were characterized with respect to surface morphology. The images used were taken with a Hitachi S-4700 scanning electron microscope (SEM). From this, particle size and the surface areas of patterns were obtained. The structure of the films was elucidated using x-ray diffraction with a Bruker D8 Discovery XRD machine. Optical transmittance (wavelength 500–900 nm) of patterns was conducted using a JAZ UV-Vis Spectrometer by Ocean Optics. Samples were either loaded monotonically, up to 10% strain, or cyclically loaded to 2% strain at a rate of 2 mm/min using an ADMET MTESTQuattro unit. The resistance of patterns was measured during loading using an Agilent 34970A digital multimeter; concurrently, the surface was monitored for cracking using a Dino Edge-Digital optical microscope [8].

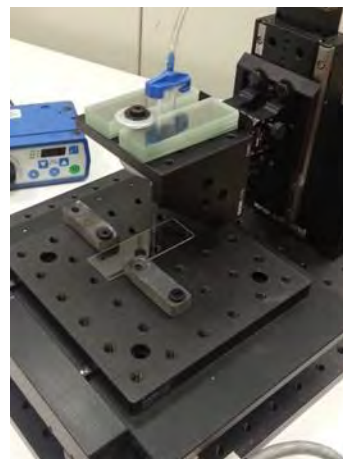


Figure 32 In-house built 3D printing apparatus

RESULTS & DISCUSSION

Most testing of the electrolyte proved inconclusive. More specifically, they exhibited the capability to be printed at high pressures (greater than 138 kPa) or high temperatures (those unsafe for humans to work in and around), but not in near ambient conditions, i.e., room temperature. The ink required heating to ~40 °C readily flow. At room temperatures, the ink acted as a highly elastic solid. This resulted in inaccurate output from the viscometer. Furthermore, patterns could be produced for all molarities, however, these required pressures which far exceed atmospheric. The 0.10 M and 0.25 M could not be extruded with tips of 100 microns or less—for the parameters used—limiting the resolution of printed films' features.

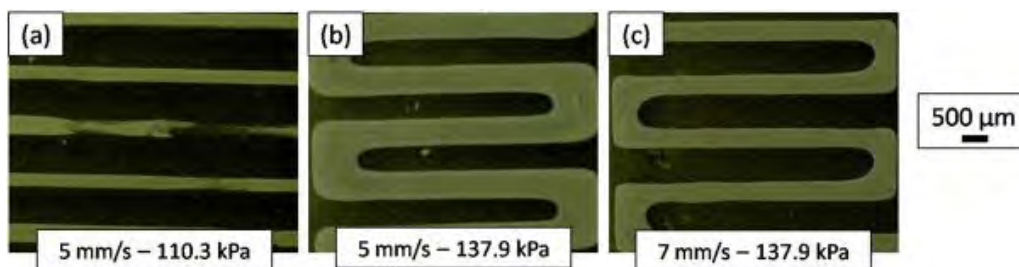


Figure 33 Silver ink print samples varying by speed and pressure. Note line discontinuities in (a) and spreading in (b) [8]

Viscosity measurements showed shear thinning behavior of the ink and is observed to lay in the range of 0.05-0.1 Pa*s for printing. Printing of the films showed that high resolution lines could be produced at pressures around 137.9 kPa and a print speed of 7 mm/s (Fig. 4). In performing image analysis on the silver inks, it was found that average particle size increased by approximately 40 nm in the samples annealed at 150 °C compared to room temperature. This was reflected by a decrease in resistivity from $10^{-2} \Omega \cdot \text{cm}$ to $1.75 \cdot 10^{-4} \Omega \cdot \text{cm}$. This suggests that higher annealing temperatures could further decrease resistivity, though the goal of flexible electronics disallow this as the necessary substrates, such as PEN, will burn or suffer damage at higher temperatures. X-ray diffraction data also reflected this, showing more prominent peaks indicative of increased crystallinity. Optical transmittance showed an inverse relationship to surface area coverage. When the films covered a surface area of ~75%, approximately 50% of visible light was transmitted. At 30% surface area coverage, transmittance reached approximately 82% (Fig. 5). Mechanical testing showed an increase in resistivity of 15% after 1000 cycles of 2% strain, surpassing the arbitrarily set failure point of 20%. After conducting the 1000 cycles, there were no visible signs of cracking (Fig. 6). The cyclical testing data support use of the silver films in strain gauges or similar applications. In the monotonic testing, the film does not exhibit failure, however, it was found that at 10% strain, the adhesive layer between the film and substrate began cracking.

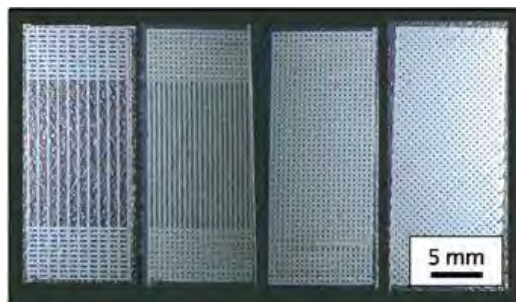


Figure 34 From left to right: 1 mm line spacing, 0.5 mm line spacing, and 0.5 mm line spacing grids (the latter offset by 45°. The corresponding surface area coverages are 30%, ~48%, and ~75% [8]

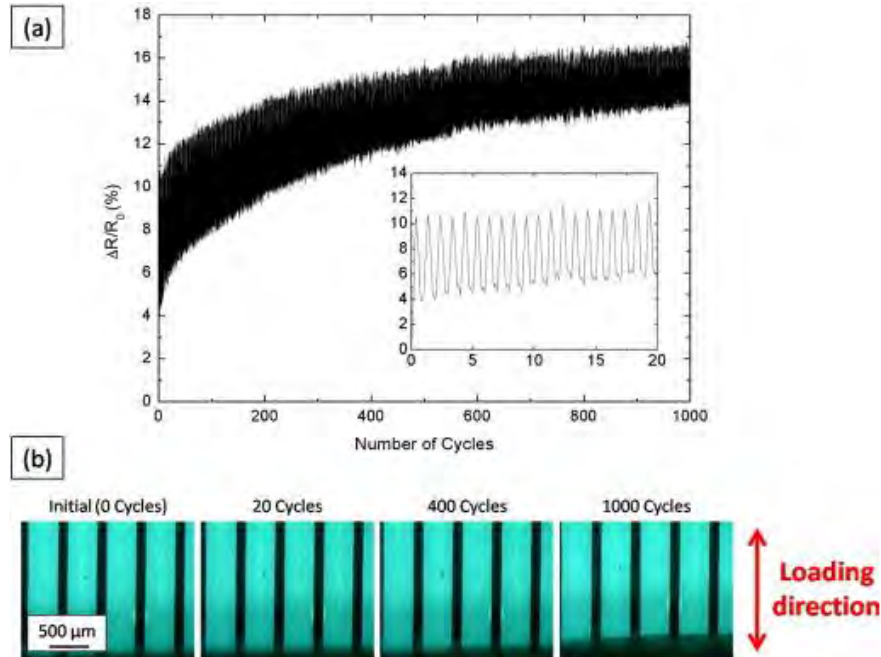


Figure 35 (a) Change in electrical resistance of films with respect to load cycle (b) Images of films at various loading cycles [8]

CONCLUSION

While there is considerable effort to be spent in perfecting ink formulations, the research completed shows significant support for the use of 3D printing in manufacturing layers for use in flexible optoelectronic devices. Furthermore, the production of successful films outside of a clean room and with pressures, under 140kPa lend support for economic, large scale production.

In printing the electrolyte solution, the inconclusive nature of the results lends ink to further investigation. It is believed that increasing the concentration of the plasticizer (the diethylene glycol) and decreasing that of the polyvinyl alcohol and iodine, will reduce the viscosity and elastic behavior of the material. As patterns were produced at high temperatures, these details lend to the possibility of printing at lower pressures.

The silver ink could be printed at low pressures (at and below 138 kPa), signifying potential large scale use of direct writing in manufacturing silver films. The silver films proved to have resistivity competitive with TCOs [8]. The film had resistivity ($1.75 * 10^{-4} \Omega \cdot \text{cm}$) was two orders of magnitude greater than bulk silver ($\sim 10^{-6} \Omega \cdot \text{cm}$), lending itself to future improvements. Mechanical testing data bears evidence for use in flexible devices due to its strength against fatigue.

FUTURE WORK

To achieve fully printed optoelectronic devices, there are several obstacles which must be overcome. One of which, is the formulation of electrolyte inks which print more readily in ambient conditions. This, however, should not come at a considerable cost to the film's ability to perform its job, electron conduction. As such, optimization of the electrolyte characteristics will be investigated concurrently. In researching silver as a potential electrode, there should be effort put towards increasing the particle size and coherent structure of the printed films. Doing so should

further reduce the resistivity of the electrons and the degradation of film as a result of successive mechanical loadings.

Moving forward, these findings will be used towards the end of producing operable dye-sensitized solar cells and perovskite solar cells. Currently, the Flexible Electronics for Sustainable Technologies lab is beginning the direct writing of carbon catalysts. Furthermore, there is work into to most effectively join the separate layers, so as to avoid repeated annealing of layers and other difficulties.

PERSONAL OUTCOMES

Thanks to the undergraduate fellowship I was awarded by the WV NASA Space Grant Consortium, I was afforded the opportunity to actively engage in cutting edge research, allowing me to grow significantly as a researcher. My experience exposed me to the environment and thought processes becoming of a research scientist. I am now familiar with various production and characterization techniques among which include—but are not limited to—3D printing methods and rheological analysis. I intend to use the knowledge and experience gained working in the lab to further contribute to the field of materials science and its applications.

ACKNOWLEDGEMENTS

I would like to thank the WV NASA Space Grant Consortium making possible this opportunity to pursue research. I would, also like to thank Konstantinos Sierros, Guy Cordonier, and Maria Torres-Arango for their guidance and support.

DISSEMINATION

Key findings of the silver ink study were published to *Thin Solid Films* [8]. A poster on this work was presented at the West Virginia Undergraduate Research Day at the Capitol (26 Feb 2016), and the NASA SPACE Day (16 Apr 2016) [9]. Both events offered the ability to network with other researchers and keep up to date on other cutting edge research locally. The Undergraduate Research Day, gave undergraduate researchers like myself to explain topics that are being researched around the state to West Virginia legislators and show them the importance of research as it relates to the state and its people. At the SPACE Day, we were able to interact more directly with the public and inspire younger minds to develop an interest in science.

REFERENCES

1. Kololuoma, T. K., Tuomikoski, M., Makela, T., Heilmann, J., Haring, T., Kallioinen, J., Hagberg, J., Kettunen, I., Kopola, H. K. 25 Jun 2004. "Towards roll-to-roll fabrication of electronics, optics, and optoelectronics for smart and intelligent packaging." *Proc. SPIE*. 77(5363).
2. Hwang, K., Jung, Y. S., Heo, Y. J., Scholes, F. H., Watkins, S. E., Subbiah, J., Jones, D. J., Kim, D. Y., Vak, D. 7 Jan 2015. "Toward Large Scale Roll-to-Roll Production of Fully Printed Perovskite Solar Cells." *Adv. Mater.*, 27: 1241-1247.
3. Park, N. G. 2 Mar 2015. "Perovskite solar cells: an emerging photovoltaic technology." *Mater. Today*, 18(2): 65-72.

4. Vlachopoulos, N., Liska, P., Augustynski, J., Grätzel, M. 1988 “Very efficient visible light energy harvesting and conversion by spectral sensitization of high surface area polycrystalline titanium dioxide films.” *J. Am. Chem. Soc.*, 110 (4), 1216-1220.
5. Kojima, A., Teshima, K., Shirai, Y., Miyasaka, T., 14 Apr 2009. “Organometal halide Perovskites as Visible-Light Sensitizers for Photovoltaic Cells.” *J. Am. Chem. Soc.*, 131(17): 6050-6051.
6. 25 Feb 2016 “Best Research-Cell Efficiencies” National Center for Photovoltaics. <http://www.nrel.gov/ncpv/images/efficiency_chart.jpg> 17 Apr 2016.
7. Ahn, B. Y., Duoss, E. B., Motala, M. J., Guo, X., Park, S. I., Xiong, Y., Yoon, J., Nuzzo, R. G., Rogers, J. A., Lewis, J. A., 2009 “Omnidirectional printing of flexible, stretchable, and spanning silver microelectrodes” *Science* 323: 1590-1593
8. Arango, M. A. T., Cokeley, A. M., Beard, J. J., Sierros, K. A., 1 Dec 2015 "Direct writing and electro-mechanical characterization of Ag micro-patterns on polymer substrates for flexible electronics." *Thin Solid Films* 596: 167-173
9. Beard, J. J., Cokeley, A. M., Arango, M. A. T., Sierros, K. A. Feb 2016. “Silver based direct written electrodes on pliant substrates.” Presented at the West Virginia Undergraduate Research Day at the Capitol, Charleston, WV and the National Air and Space Administration Student Partnership for the Advancement of Cosmic Exploration Day, Fairmont, WV.

LEAF ANGLE PHENOLOGY: IMPLICATIONS FOR CARBON, ENERGY, AND WATER FLUXES FROM FORESTS IN THE ANTHROPOCENE

Evelin Flamenco
Environmental Geoscience and Geography
West Virginia University
Morgantown, West Virginia 26506

ABSTRACT

The large effects of forests on global cycles of carbon, energy, and water depends in part on human actions, but also strongly upon how individual tree species adjust to the novel environmental conditions of the Anthropocene. In this study, we seek to identify how one adaptation, the inclination angle of leaves, differs by species and season. Leaf angle is known to have important effects on forest photosynthesis, albedo, and evapotranspiration, but there is relatively little data on its variation among species, seasons, and environmental gradients. For this study we employed a relatively new technique of using an electronic protractor to measure leaf angles on leveled digital photographs of the upper canopy of trees. From a suite of observation platforms (e.g. fire towers, bridges) in broadleaf deciduous forests of the eastern USA, we measured leaf angles on the same set of marked branches at weekly or monthly intervals throughout the 2015 growing season. Based on over 12,472 measurements taken from 15 tree species, we found significant differences in mean leaf angle between species and observation date. We discuss these empirical results in light of an emerging theoretical framework that positions leaf angle phenology as a functional trait that is not only an essential part of the adaptive resource strategy of each tree species, but also could be used to better constrain model predictions of carbon, energy, and water fluxes from forests in the Anthropocene.

INTRODUCTION

Forests play important roles in the cycles of carbon and energy that regulate global climate change. As they grow, forests slow climate change as they currently absorb over a quarter of all the carbon that humans emit to the atmosphere from burning fossil fuels. Forests also cover over thirty percent of the earth's land surface and thus play a large role in affecting how much solar energy is absorbed to warm the land and planet and how much is reflected back to space. I have been working on a research project that addresses a key uncertainty in these roles played by forests in slowing global climate change. My research aims to understand how leaf inclination angles of individual tree species in the eastern and mid-western United States respond to climatic variability. More horizontal leaves not only cool the climate by increasing forest albedo, but also stimulate more photosynthesis and removal of heat-trapping carbon dioxide from the atmosphere (Bonan, 1997). However, these cooling mechanisms may be tempered as trees cope with droughts in a warmer climate, particularly by adjusting leaves to more vertical positions that minimize water loss. Overall, the new data we collected shows how tree species create geographies of photosynthesis, albedo, and evapotranspiration that should help improve forecasts of how these essential ecosystem functions might change in the Anthropocene.

METHODS

There are eight observational platforms in total. Six observational platforms are located in the Central Appalachian Mountains: West Virginia, Maryland, Pennsylvania. These six observational platforms include Olson Tower, Pleasant Street Bridge, Mt. Davis Tower, Kinton Knob Tower, Town Hill Tower, and Green Ridge Overlook (Figure 2). The other two observational platforms are located in Mid-western states in Michigan and Indiana. These two observational platforms are Morgan-Monroe State Forest (MMSF) Ameriflux and University of Michigan Biological Station (UMBS). For this study, we took canopy images that were visible from the observational platforms. We observed 15 tree species.



Figure 1. Measurement of leaf angle (α) between the zenith (Z) and the normal (N) to the leaf surface (L).

We used a digital camera to take images of the upper canopy. I employed a recently developed technique (Pisek, Jan, et al. 2011), (Ryu, Youngryel, et al. 2010) for measuring leaf angles on level photographs. First we climbed the tower and stationed parallel to the canopy. We then used a tripod to place the digital camera. Next, we used a level to balance the digital camera. We focused on the top part of the tree by zooming in. images were taken in calm conditions. We took the same exact images in June, July and August 2015 of 15 different tree species. However, the Pleasant St. Bridge images were taken every week, starting in June and ending in November. The Pleasant St. Bridge images followed the same procedures as the other locations. After taking the images, we went back to the lab where we analyzed the images in Adobe Photoshop. In Adobe Photoshop we set four grid rows and columns. We measured every other grid box that contained leaves. We recorded the inclination angle of leaves that were parallel to the image plane. Then, we used an electronic protractor to draw the normal, the line perpendicular to the leaf surface (Figure 1).

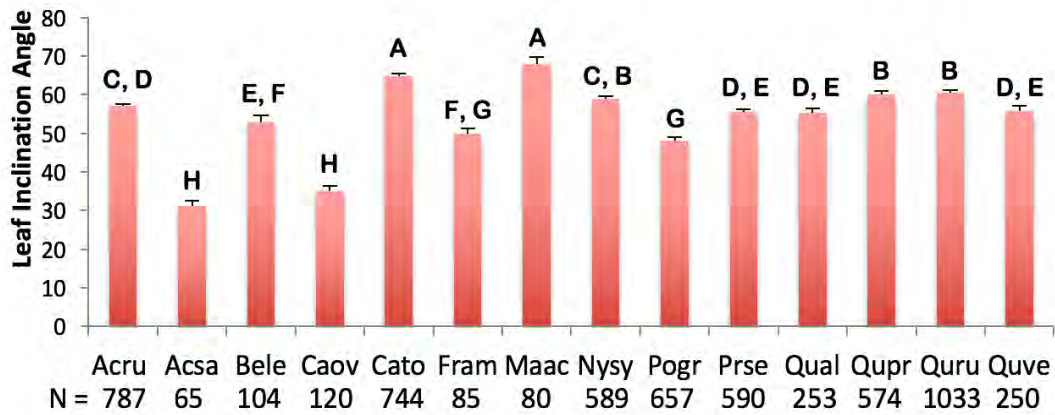
The leaf angle is between the normal and zenith. Zenith is the direction that points towards the sun. Next, we recorded the measurements in excel. The equation for the actual leaf inclination angle is $= \text{IF}(\text{LIA PS} > 90, 180 - \text{LIA PS}, \text{LIA PS})$. LIA PS is the value we receive when we use the electronic protractor. This equation considers the normal. After submitting the data entries in excel, we then used all the images to generate statistical summaries of angles by tree species to identify significant differences.



Figure 2. Olson Tower

RESULTS

Each tree species reacts differently throughout the season. There are highly significant differences in mean leaf angle among the 15 tree species. Species that do not share the same letter have a significantly different mean leaf inclination angle (Figure 3). The mean leaf angle among all tree species ranges between 31.13° - 67.99° . The *Magnolia Acuminata* (Maac) has the most vertical mean leaf inclination angle, resulting in a lower albedo. *Acer Saccharum* (Acsa) has the most horizontal mean leaf inclination angle signifying that it produces more photosynthesis and a high albedo. There are 12,472 leaf measurements in total from 15 tree species.



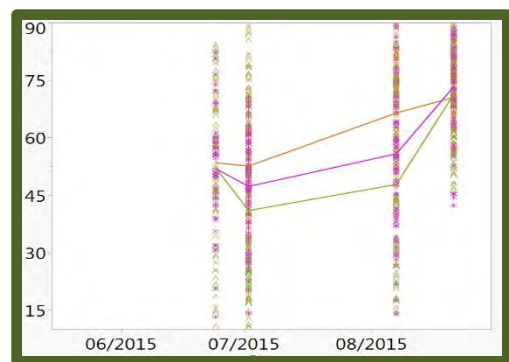
Species observed at different locations had similar leaf angle phenologies. Most tree species had a leaf angle phenology towards a more vertical angle later in the season. The more horizontal the leaf angle the less change has occurred by the tree species observed. For example *Quercus Alba* (Qual) (Figure 4 A, B) became more vertical, but *Quercus Rubra* (Quru) (Figure 4 C, D, H) had little change.

We took images of *Quercus Rubra* (Quru) at Pleasant St. Bridge (Figure 4 H) and the tree species mean leaf angle measurements support that there is no significant change, displaying a more horizontal angle inclination.

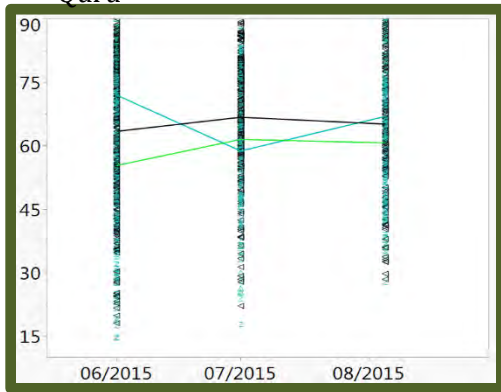
A. Green Ridge Overlook: Qual



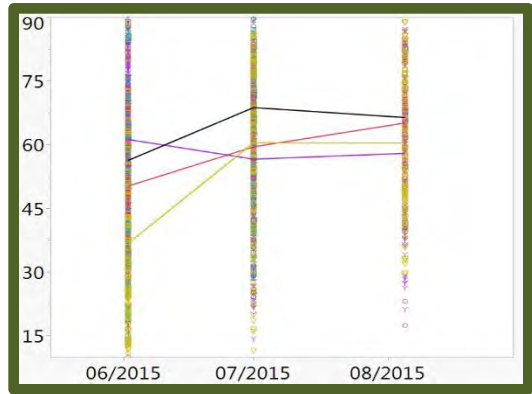
B. MMSF Ameriflux: Qual, Litu, Saal



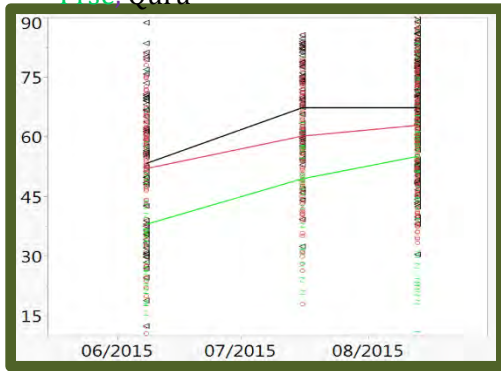
C. Kinton Tower: **Maac**, **Prse**, **Quru**



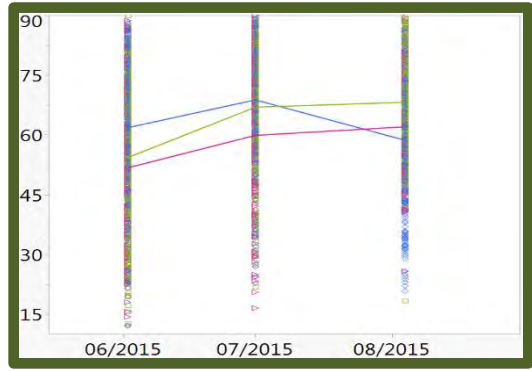
D. Mt. Davis: **Acru**, **Nysy**, **Pogr**, **Quru**



E. Olson Tower: **Acru**, **Prse**, **Quru**



F. Town Hill Tower: **Cato**, **Qupr**, **Quve**



G. UMBS Ameriflux: **Acru**, **Pogr**



H. Pleasant St. Bridge: **Quru**

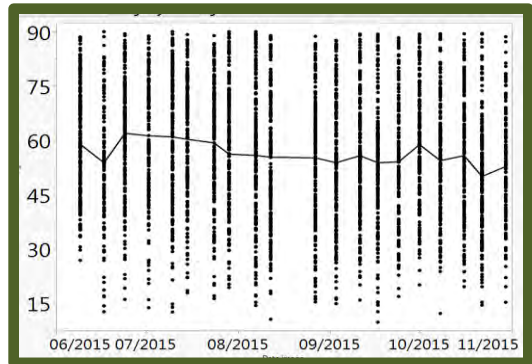


Figure 4. Leaf angle phenologies observed from the 8 platforms. Species codes are as in Figure 3. Lines connect means from each date. Due to large sample sizes, most differences in mean leaf angle are highly significant.

DISCUSSION

Individual tree species react differently to the environment. Leaf angle is an adaptive strategy, which affects how each tree species react to the environmental conditions. Our findings show that the 15 tree species have a significant difference in mean leaf angle. For example, *Quercus Alba* (Qual) had a more vertical leaf angle, which would reduce albedo and evapotranspiration water loss, but likely at the expense of carbon gain.

Throughout the summer months most of the tree species became more vertical. This new finding shows how trees lose productivity as the growing season is reaching its end. This adaptation can help support the satellite phenology observations of “greendown” (Elmore et al. 2012) and may help trees adapt to drier conditions later in the season. As mention, the more horizontal the leaf angle the higher the albedo, additionally it will produce more photosynthesis and carbon dioxide removal, and works vice versa to a more vertical leaf angle. However, *Acer Rubrum* (Acru) shows in interesting pattern. In Olson tower and Mt. Davis Tower, both located in the Central Appalachian display *Acer Rubrum* (Acru) with the same trend that the leaf angles become more vertical throughout the summer season. But, at UMBS Ameriflux the *Acer Rubrum* (Acru) shows an opposite trend (Figure 4 D, E, G). These leaf angle pattern results is due to the location of each observational platforms, there is a difference in elevation and other environmental components that are affecting the way *Acer Rubrum* (Acru) responds back to the environment surrounding it.

These results highlight a new pathway by which species affect climate change through photosynthesis and albedo. Our data provide new information of how tree species reduce levels of atmospheric carbon dioxide, reflect sunlight back to space, and respond to changes in temperature and precipitation throughout the growing season.

FUTURE PLANS

We are looking to incorporate leaf angle data into models of carbon, energy, and water fluxes from forest ecosystems. We plan to expand our observation network by using webcams and UAV platforms to increase the resolution of leaf angle data in time, space, and canopy height.

Through my research, I have come to appreciate the differences in how tree species will respond to, and indeed affect climate change. As this leaf angle research continues to produce interesting results, I am excited to continue this work during my remaining time at West Virginia University and in graduate school. In future work, I want to uncover which tree species adapt their photosynthesis through leaf angles in order to respond to disturbance and global change. As mentioned, photosynthesis not only makes trees grow faster, it also plays an important role alleviating climate change. Forests act as carbon sinks, which is crucial in the Anthropocene epoch. Human activity is contributing to dramatic changes in environmental processes on earth. With these significant alterations in the environment happening, each individual tree species will be required to adjust to the environmental conditions in this era. These findings can be valuable and applied to restore disturbed forests.

CONCLUSION

Leaf angle is an understudied pathway by which tree species affect climate change. The measurements collected in the summer of 2015 show that leaf angle phenology becomes more

vertical throughout the season. Among the 15 tree species observed, they all show a high significant difference in mean leaf angle. These two findings demonstrate that the leaf angle phenology is a key part of the adaptive resource strategy of each individual tree species. Furthermore, leaf angles help each tree species to acclimate to varying environmental conditions.

RESEARCH EXPERIENCE

Being awarded with the NASA West Virginia Space Grant Consortium has given me the opportunity to expand my knowledge of trees. Another valuable part in this research is the hands-on experience, understanding what these leaf angle measurements indicate and learning the overall research process.

Additionally, my advisor and I recently published a paper in a leading journal, *Agricultural and Forest Meteorology*, detailing a new UAV method (McNeil et al. 2016). In order to establish this new method for measuring leaf angle in the majority of forests that do not have observation tower access, we compared leaf angle measurements from one tower against photos taken from an Unmanned Aerial Vehicle (UAV). The UAV has a camera on a self-leveling gimbal to capture the canopy images following the same leveled-camera method described above. After analyzing the photos taken by the UAV and from the tower, we found no significant difference between the tower and UAV leaf angle measurements.

ACKNOWLEDGMENTS

Thank you for the generous support from NASA West Virginia EPSCoR and Space Grant Consortium, WVU Summer Undergraduate Research Experience (SURE), WVU Department of Geology and Geography, the Department of Energy (Ameriflux program). I want to thank my research advisor, Brenden McNeil for helping and guiding me in this research. I also want to thank Sam Rescorl and Chris King for helping to measure hundreds of leaf angles.

REFERENCES

- Bonan, Gordon B. "Effects of land use on the climate of the United States." *Climatic Change* 37.3 (1997): 449-486.
- Elmore, A.J., et al. Landscape controls on the timing of spring, autumn, and growing season length in mid-Atlantic forests. *Global Change Biology* (2012) 18- 656
- McNeil, Brenden E., et al. "Measuring leaf angle distribution in broadleaf canopies using UAVs." *Agricultural and Forest Meteorology* 218 (2016): 204-208
- Pisek, Jan, et al. "Estimating leaf inclination and G-function from leveled digital camera photography in broadleaf canopies." *Trees* 25.5 (2011): 919-924.
- Ryu, Youngryel, et al. "How to quantify tree leaf area index in an open savanna ecosystem: a multi-instrument and multi-model approach." *Agricultural and Forest Meteorology* 150.1 (2010): 63-76.

MODIFICATION OF NITINOL NANOPARTICLES WITH PHOSPHONIC ACID FILMS

Samantha Garretson
Biology
Marshall University
Huntington, West Virginia 25703

ABSTRACT

Nitinol nanoparticles, which are composed of fifty-percent nickel and fifty-percent titanium, are a valuable metal alloy due to shape memory, corrosion resistance, and superelasticity. Depending on the temperature, nitinol can have either an austenite or a martensite structure. These qualities make the nanoparticle ideal for medical use such as in self-expandable stents, braces, and eyeglasses. However, the presence of nickel brings concern that the substance, an allergen and possible carcinogen, could be released in the body and cause more damage. In oxidative environments, such as the human body, the nanoparticles are very reactive. Therefore, the nitinol must be treated in a way to reduce the chance of the release of a free radical. A proposed method has been the formation of a self-assembled monolayer. Here, phosphonic acids of various concentrations such as 16-phosphonohexadecanoic acid, octadecylphosphonic acid, and 12-aminododecylphosphonic acid were used to form a film on the nitinol powder. These modifications were characterized by using X-ray photoelectron spectroscopy (XPS) and a scanning electron microscope with energy-dispersive X-ray spectroscopy (SEM-EDS). Furthermore, powder X-ray diffraction (PXRD) and infrared spectroscopy were used to characterize the “fingerprint” of the chemicals involved with three dimensional patterns and to identify the presence of the acid. Solid state nuclear magnetic resonance (SS-NMR) was used to analyze the attachment of the phosphorous on the surface of the nitinol. Oxidation-reduction reaction was characterized with cyclic voltammetry and electron impedance spectroscopy (EDS). There is evidence that the phosphonic acids are binding to the surface of the nitinol in a manner that decreases the reactivity of the nickel at the surface.

INTRODUCTION

Nanoparticles are particles with a diameter of less than 100 nanometers. The phenomenon is new to the scientific community, but nanoparticles have been in use unwittingly since the 1600s century. In 1679, Johann Kunckel prepared a compound of gold and tin to produce a purple precipitate to stain glass red, but there was no understanding of the science behind this.¹ This particle was identified in the late 1800s by Michael Faraday, but still were not measured or studied until the 1980s. Nanoparticles were discovered to have the same bond length as the bulk companions, but to exhibit a different electronic spectrum.²

Nitinol, discovered by William J. Buehler and Frederick Wang in 1959 for Goodyear Aerospace Corp., is metal alloy of equal atomic percentages of nickel and titanium.¹ Originally, it was designed to produce a missile nose cone resistant to heat and fatigue. Nitinol is best known for superelasticity, shape-memory, and corrosion resistance, the ideal ingredient for aerospace and biomedical tools.² This nanoparticle is capable of undergoing a controlled distortion, and then return to the original morphology at a slightly higher temperature. The transformation temperature

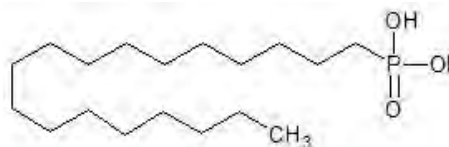
is the line between martensite and austenite, in which the alloy is more flexible. This process is reversible, so that the product can be used again and again with little fatigue.³ Nitinol is also ten to thirty times more elastic than the average metal.⁴ Nitinol is a choice material for a variety of aeronautical engineering devices. The nanomaterial is useful for sealing high pressure fuel passage. This material is also useful for satellite antennas, as the nitinol will change shape with a change with merely a shift of temperature.

The plight of this miraculous product, however, falls in that the nickel is still very reactive. Many people suffer from nickel allergies, and there is a high chance that the metal could even be carcinogenic. To prevent the chance of free radicals escaping from the surface of the metal, a self-assembled monolayer must be produced to encapsulate the reactive ions. To produce this, the nanopowder must be modified. The method proposed employs the use of acids to increase the phosphorous content of the metal alloy. Self-assembled monolayers are an assembly of organic molecules on the surface on the substance, often including head groups such as thiols, silanes, or phosphonates, as presented in the project. The head group binds to the substrate to suspend the molecule, and a protective layer is formed over the surface of the nitinol.⁵ Through this project, the goal is to modify the nanoparticles in a way that their vital properties are not lost, but the fallacies are improved.

PROJECT DESCRIPTION

Octadecylphosphonic acid, commonly used for surface coverage and corrosion prevention,⁷ will be used in this project as an organic modifier on the Nitinol surface. In terms of monolayers, the acid is popular for producing a lubricant atop the metal alloy, producing a flat and nonpolar surface.⁶ Octadecylphosphonic acid (Figure 1) contributes wetting, adhesion, and friction to the surface of the substance, assembling through hydrogen bonding and van der Waals forces. However, sometimes, the monolayer does not form an even, thorough covering, but rather, island-like bodies with gaps and disorder. Octadecylphosphonic acid could create a more structured monolayer on nitinol due to the phosphorus's high affinity to the titanium metal and tendency to form a metal-cation coordination bond.⁶ The incredible strength of this bond accounts for the protective characteristic of the self-assembled monolayer, completed via submersion in octadecylphosphonic acid, or a similar solution, such as the carboxylic acid to be employed concurrently and during the summer.

Figure 1. Octadecylphosphonic acid structure.



In Dr. Quinones's previous work, she has found that functionalized alkyl phosphonic acid molecules assembled these monolayers on the surface of the nanomaterial via the solidification of the vaporous acid.³ Phosphonic acids are the most useful due to the low acid dissociation constant, making carboxylic phosphonic acid more likely to react with the free nickel oxide radicals.

Experimental Approach: Acid Type, Concentrations of Acids, Treatment for Images and Spectroscopy

To modify the nanoparticles, an acid, carboxylicphosphonic acid is added to the nitinol powder in low concentrations. The concentration of carboxylic phosphonic acid, diluted with a solvent,

tetrahydrofuran, is used in concentrations ranging from 7.5 to 30 mM. Following the scans of the unrinsed modified nitinol, a rinsed sample of the concentration must be prepared using sonication and a vacuum centrifuge. This procedure helps to remove molecules physically attracted to the surface. Infrared spectroscopy is used in the project to monitor the extent to which the acid bonds to the surface of the nitinol. When placed in the infrared beam, the molecules of the material vibrates. Because structures with different chemical properties give off different identity vibrations, the information from the infrared spectrometer can be used to identify elemental chemical properties.⁸

Other than changing the concentration of the acid in order to achieve the optimal phosphorous content, the modification of the nanoparticles is fairly routine. One of the more daunting challenge lies in producing the optimal energy-dispersive X-ray spectroscopy scans and scanning electron microscopy images (Figure 2). Over the past year, Marshall University has collaborated with West Virginia University to produce excellent images of the nanoparticles. Additionally, energy dispersive x-ray spectroscopy and x-ray photoelectron spectroscopy has provided information about the presence of phosphorous in the modified samples.

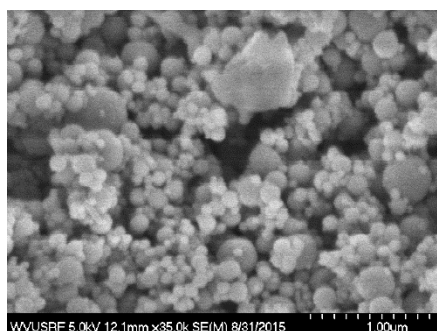


Figure 2. Scanning electron microscope image at 50,000x magnification of nitinol nanoparticles modified with carboxylic phosphonic acid after rinse with tetrahydrofuran.

Furthermore, powder X-ray diffraction can be used to identify the “fingerprint” of a chemical by the pattern diffracted by the powder when a beam of radiation is shown through.⁸ Powder X-ray diffraction is advantageous due to the simplicity, the speed of the process, and broad arrange of phase analysis. Ordinarily, preparing a rinsed sample requires several days to ensure that the solvent has completely evaporated before the nanoparticles can be evaluated by the infrared spectrometer. Also, this method is best for small and new materials.¹¹

Cyclic voltammetry is used to characterize the ability of the substance to participate in reduction-oxidation reactions at the surface. A control of the nitinol has been analyzed, and from there, different concentrations of the acids can be compared to the unmodified nanoparticles. Thus far, the nitinol has proven to be significantly less corrosive when modified, but further investigation and employment of electrical impedance spectroscopy will help to confirm this.

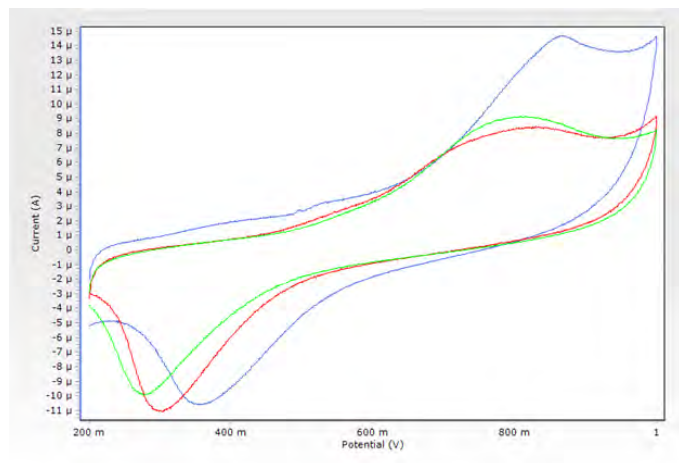
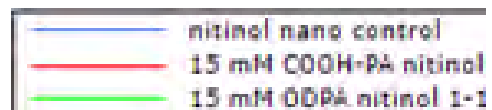


Figure 3: Cyclic Voltammetry data for unmodified particles, particles modified with 15 mM COOH-PA, and particles modified with 15 mM ODPa.



CONCLUSION

Phosphorous has appeared in energy dispersive X-ray and X-ray photoelectron spectroscopy, proving that 16-phosphonohexadecanoic acid and octadecylphosphonic acid is binding to the surface of the nanoparticles. There is a CH peak in the infrared spectroscopy, so there is evidence of the acid, even in low concentrations. The powder x-ray diffraction scan of the modified nanoparticles are consistent with the expected results of an austenite sample as given by the manufacturer. The cyclic voltammetry data suggests that the modification of the nanoparticles decreases redox reactions on the surface of the nitinol based on the decreasing area of the graph from unmodified to modified nanoparticles of moderate concentrations of either 16-phosphonohexadecanoic acid or octadecylphosphonic acid. Given that the nitinol is of expected composition, the head group of the self-assembled monolayer is present, the organic component of the acid is present, and the redox activity has decreased on the surface of the modified nitinol nanoparticles, the project is progressing significantly. In the future, it is planned to be done with electrochemical impedance spectroscopy to supplement the cyclic voltammetry results. Solid state nuclear magnetic resonance of the modified nanoparticles will also be analyzed. Additionally, there will be trials with other phosphonic acids to test efficiency in creating self-assembled monolayers.

ACKNOWLEDGEMENTS

- NASA West Virginia Space Grant Consortium
- Marshall University, Chemistry Department
- Marshall University, Geology Department
- Marshall University, Biological Imaging Center
- DOW-Marshall University STEM Partnership
- West Virginia University Shared Research Facilities

- Pennsylvania State University, Chemistry Department

REFERENCES

- (1) Rao C., T. P., and Kulkarni G. *Springer* **2007**, 1.
- (2) Morgan, W., DiCello, and Graham. *The International Conference on Shape Memory and Superelastic Technologies*. **2006**, 2.
- (3) Quiñones, R.; Gawalt, E. S. *Langmuir* **2007**, *23*, 10123.
- (4) Buehler, W. J.; Gilfrich, J. V.; Wiley, R. C. *Journal of Applied Physics* **1963**, *34*, 1475.
- (5) Quiñones, R.; Gawalt, E. S. *Langmuir* **2008**, *24*, 10858.
- (6) Nie H., W. M., and McIntyre N. *Surface Science Western*. **2006**, 1.
- (7) Nie H., M. D., Francis M., and McIntyre N. *Surface Science Western*. **2006**, 1.
- (8) *Materials Characterization and Chemical Analysis*; Wiley-VCH Inc., 1996.
- (9) I., J. *Stockholms University* **2012**, 33.
- (10) Raman, A.; Quiñones, R.; Barriger, L.; Eastman, R.; Parsi, A.; Gawalt, E. S. *Langmuir* **2010**, *26*, 1747.
- (11) Roy, S.; Quiñones, R.; Matzger, A. J. *Crystal Growth & Design* **2012**, *12*, 2122.

FIBRIN-BASED MICROENVIRONMENTS FOR RECRUITMENT OF ADULT NEURAL STEM CELLS

Lydia Hager
Biology
Marshall University
Huntington, WV 25755

ABSTRACT

For many neurodegenerative diseases, including Parkinson's, Alzheimer's, and Huntington's, as well as traumatic brain injury, neural stem cells have been proposed as a therapy. These therapies require the implantation of exogenous cells into damaged areas of the brain. However, these therapies pose serious problems, such as immune response, tumorigenicity, cell availability, functional effectiveness, and ethical concerns. Therefore, few therapies exist for patients of neurodegenerative diseases. We propose a novel method in which a cylindrical fibrin matrix steers endogenous neural stem cells from their niche in the subventricular zone to target areas of the striatum or cortex. Using various factors, including VEGF, NGF, GDNF, and BDNF, we are able to attract cells and influence their migration, proliferation, and differentiation. It is our belief that the maturation of neural progenitor cells is stimulated and controlled by growth factors, which are introduced sequentially to cells in order to control their development. To determine the effects of various growth factors, we conducted experiments *in vitro* in which cells were exposed to a single factor at a time. Immunocytochemistry was then performed to observe the presence of antibodies indicative of immature, migrating, and mature neurons. The results of these assays led to the inclusion VEGF, NGF, and GDNF in our fibrin cylinders that were implanted into rat brains.

INTRODUCTION

The long-term aim of our lab is to develop a therapy for Parkinson's disease (PD), which affects over seven million people around the world [1]. PD is caused by the apoptosis of dopaminergic neurons in the substantia nigra, leading to a deficit in the neurotransmitter, dopamine. A hallmark of PD is lack of motor control, as levels of dopamine in the brain decrease and activation of motor neurons in the striatum is hindered. This leads to muscle deterioration, and eventually, death, as movement of both voluntary and involuntary muscles require increasingly intense exertions.[2]

An ideal therapy for PD would replace the dead cells in the substantia nigra with healthy dopaminergic cells. Our lab has developed a novel therapy, in which endogenous neural stem cells are recruited to repopulate damaged areas of the brain. This is accomplished through implantation of a cylinder of biomaterial (fibrin), which provides cells with a scaffold to guide their migration. Neurotrophins are incorporated into the cylinders in order to stimulate proliferation, migration, and differentiation. Fibrin is a naturally-occurring extracellular matrix protein, making it biocompatible and biodegradable. In the adult rat brain, there are two natural reservoirs of neural progenitor cells (NPC's): the subventricular zone (SVZ) and the hippocampus. Our lab's focus is on SVZ-derived NPC's, which travel along the rostral migratory stream (RMS) to the olfactory bulb. The cylinder is implanted such that it intersects the RMS, thereby diverting SVZ-NPC's to target areas of the striatum or cortex.

Before implanting the cylinders, the correct growth factor must be determined. For this, we used multiple assays that tested the effects of various neurotrophins. The four growth factors focused on were VEGF, NGF, GDNF, and BDNF. Studies have suggested that NGF increases survival of neural stem cells, while VEGF signals migration and differentiation [3]. GDNF is believed increase expression of BDNF receptors. BDNF has been shown to influence speed and direction of cell migration, as well as increasing arborization, synaptic plasticity, and neuroprotection [4, 5]. We utilized three primary assays for determining cellular response to neurotrophins: the five-dome, the cylindome, and cylinder-in-cylinders (CinC's). The five-dome assay consists of a central fibrin dome containing SVZ-NPC's surrounded by four domes with different growth factors crosslinked to the fibrin. As proteases degrade the central dome, the cells are free to migrate to the outer domes, where they are exposed to a single neurotrophin at a time. The cylindome assay also includes a fibrin dome containing NPC's, but this time a fibrin cylinder containing growth factors is then juxtaposed. This simulates the conditions of our implants in the brain, as the cylinder intersects the RMS and draws cells along its length. Cylinder-in-cylinders are two concentric fibrin cylinders, with the inner being more fluid and containing SVZ-NPC's. This assay allows the cells to be exposed to two different paradigms as they degrade the inner cylinder and encounter the outer.

Once the factor(s) had been tested, they were incorporated into fibrin cylinders to be implanted into a cohort of 18 rats. The rats were sacrificed 14 weeks after the implantation and immunohistochemistry was performed on the brain slices in order to detect the presence of migrating, proliferating, or mature neurons.

METHODS

Cylindomes

We have developed methods to covalently incorporate aprotinin, neurotrophins and laminin into fibrin cylinders. We have demonstrated the ability to uniformly incorporate these into fibrin cylinders using a common amino-group directed crosslinker disuccinimidyl suberate (DSS). Due to the frequency with which lysines are found in peptides and proteins (e.g., factors, ECM, aprotinin, fibrinogen), it is very likely that high efficiency cross-linking is achieved using DSS and that the function of the crosslinked material will not be deleteriously affected (ref ref). Fibrinogen was dissolved in PBS at a final concentration of 64 μM . An 8 μl aliquot was placed on a square of Parafilm® to which was added aprotinin (30 μM final), laminin 1 (50 $\mu\text{g}/\text{ml}$ final), VEGF (10 $\mu\text{g}/\text{ml}$ final) and NGF (10 $\mu\text{g}/\text{ml}$ final). The volume of the sample was topped off to 18 μl with PBS. Disuccinimidyl suberate (DSS) was dissolved in dry DMSO and 1 μl (50 μM final) was added to the sample which was then mixed via trituration. The crosslinking reaction was allowed to proceed for ten minutes at ambient temperature in a humidified chamber. Thrombin (1 μl of 0.1 U/ μl) was added and the sample quickly mixed and drawn 7 mm into a quartz tube (0.7 mm inner dia., 3.5 cm in length). The dimensions of the final fibrin cylinder are 0.7 mm dia. x 6 mm following the polymerization and concomitant shrinkage of the fibrin. Each experimental condition entails preparing fibrin cylinders in quadruplicate, which are extruded from the quartz tube onto #1 glass disks in 24 well tissue culture plates. SVZ-NPCs are harvested and maintained according to standard methods, and aliquots are disaggregated with Accutase and resuspended in 20 μl of 22 μM fibrinogen (no aprotinin) and, following the addition of 0.5 U thrombin (as 0.5 μl aliquot), 3-4 μl of the neurospheres suspension is placed near (but not touching) the side of each replicate cylinder. Following 10 minutes of curing, the cylinder end is gently pushed against the

hardened dome of fibrin/cells (Figure 1). All of the cylinders have covalently incorporated aprotinin, which is omitted from the domes. This facilitates the rapid escape (degradation of the fibrin and migration) of the cells from the dome and allows them to interact with the cylinder and its components.

Five-dome Assay

The central dome is constructed as described in the cylindome protocol. The four outer domes are prepared by making four 20 μ l solutions of (26 μ M final), aprotinin (15 μ M final), and laminin (100 μ g/ml final). A different growth factor (VEGF, NGF, GDNF, or BDNF is added to each of the domes before crosslinking with DSS (500 μ M final) for ten minutes. After crosslinking, thrombin (0.1 U) is added to the mixture, which is then pipetted onto the glass disk adjacent to the central dome. The domes are incubated at room temperature for twenty minutes until polymerization is complete (Figure 2).

Cylinder-in-Cylinder for in vitro study

To make a CinC, a 0.20 I.D. x 0.33 O.D. (x 5 cm) quartz tube is inserted into a 0.70 mm I.D. x 0.87 mm O.D. (x 3 cm length) quartz tube, which is adhered to a piece of dental wax on the bottom of a petri dish. The outer cylinder is made first by preparing a 20 μ l solution of fibrinogen (26 μ M final), aprotinin (15 μ M final), laminin I (100 μ g/ml final), NGF (carrier-free, 10 μ g/ml final) and VEGF (carrier-free, 10 μ g/ml final). The solution is subject to chemical crosslinking for ten minutes using DSS (500 μ M final). One μ l of thrombin (0.1 U) is added, the solution mixed and then quickly added to the quartz tube assembly so that the solution fills the space between the inner and outer tubes. The samples are incubated at room temperature for 20 minutes to allow the fibrin to cure. The inner 0.20 I.D. x 0.33 O.D. quartz tube is then slowly withdrawn from the cured fibrin and discarded, leaving a 0.33 mm diameter “tunnel” down the length of the cured 0.70 mm diameter fibrin cylinder still in the 3 cm long 0.7 mm I.D. tube. This “tunnel” is then filled with a second solution, made as above with the following exceptions: fibrinogen is used at 6 μ M final (which increases the fluidity), aprotinin is omitted (which causes the inner cylinder to degrade faster than the outer), and Accutased SVZ cells are included. Thrombin is added and this solution is drawn into the sample so that it fills the tunnel in the outer cylinder. Refer to Figure 3 for a diagram of the CinC.

Cylinder-in-Cylinder for implantation

These CinC's are produced as above, except the inner cylinder lacks SVZ cells. The CinC is allowed to fully cure for at least one hour before surgical implantation.

Immunocytochemistry

Samples were processed via immunocytochemistry (ICC) using markers for neural cell phenotype and neurotrophin factor expression. In brief, samples are washed, fixed with paraformaldehyde, permeabilized with Triton X-100, treated with NH₄Cl to minimize background, blocked with BSA/goat serum, and probed with primary antibodies in acetylated BSA/goat serum. Antibodies (typically purchased from Abcam or EMB Millipore) are usually used at 1:200-1:500 dilution. Fluorescent Alexa Fluor-conjugated isotype specific secondary antibodies (Invitrogen Life Technologies) are used for detection and images are collected with our Zeiss AxioObserver. We have numerous filter cubes for this instrument, allowing the simultaneous observation of Alexa 350, Alexa 488, Alexa 568, and Alexa 680. We used the following antibodies to establish the neural phenotypes that arise in these cell culture experiments: DCX (marker for migrating

neuroblasts); NF160 (marker for mature neuron processes); beta-tubulin (marker for neurons, including immature); GFAP (astrocyte marker); MAP2 (mature neurons, including dendrites).

Implantation

The cylinders (6 mm long) were made as described for the cylindome (minus the dome). A short (ca. 0.5 mm) length of PVDF was inserted into the quartz tube containing the fibrin cylinder and served as a plunger head, and a stainless steel wire of 0.6mm diameter served as a plunger. Female Sprague-Dawley rats (200-250 gm) were anesthetized using isoflurane (5% induction, 2% maintenance) with an oxygen flow of 0.8 L/min. Animals were positioned into a Kopf stereotaxic frame that was outfitted with two manipulators, one on each arm of the Kopf “U” frame, and both were angled 17° to the right of midline. The fibrin cylinder-containing quartz tube was affixed to the right manipulator and the wire plunger was placed on the left manipulator. A small hole was drilled using a round dental bur at, relative to the bregma, 0.13 cm anterior and 0.30 cm lateral right of midline. The dura was pricked with a 25 gauge needle and the quartz tube driven 0.73 cm down the dorsoventral axis on an angle 17° off midline to the right. The wire plunger was lowered into the fibrin cylinder-containing tube until just touching the PVDF plunger head, which was on top of the fibrin cylinder. The plunger was held immobile with the left manipulator arm while the quartz tube was slowly raised (1/4 turn/45 seconds) via the right manipulator. This maneuver results in the fibrin cylinder being placed in the brain along a predetermined path as the quartz tube is pulled out of the brain with the plunger holding the cylinder in place. After complete extraction of the quartz tube and a five minute incubation period, the plunger was slowly removed, the skull hole plugged with bone wax, and the scalp closed with absorbable sutures. Animals were injected with dexamethasone (0.4 mg/kg s.c. in 0.9% sterile saline) once at the time of anesthesia induction and then each day for four days post-operatively to reduce glial scarring. For pain management, animals were injected with buprenorphine (0.15 mg/kg s.c.) immediately after surgery and then daily for two additional days.

Immunohistochemistry

After 8 weeks animals were sacrificed via bilateral pneumothoracotomy, fixed via transcardial perfusion with 0.9% NaCl with 2U/ml heparin followed by 4% PFA, and the brains were removed. Following overnight fixation in 4% PFA, brains were equilibrated in 30% sucrose until no longer buoyant and sectioned into 20 µm sections using our Leica cryostat. Brains were probed for DCX, a marker for migrating neuroblasts. Sections were mounted in Superfrost Plus slides (Fisher) using Fluoro-Gel II with DAPI (Electron Microscopy Sciences) as a mountant. Sections were observed on our Zeiss Axio Observer fluorescence microscope (Figure 6).

RESULTS

Cells incorporated into our Cylindomes quickly degraded the cell dome within 24 hours. This allowed the cells to migrate along the cylinder, simulating the environment of our cylinders in the rat brain.

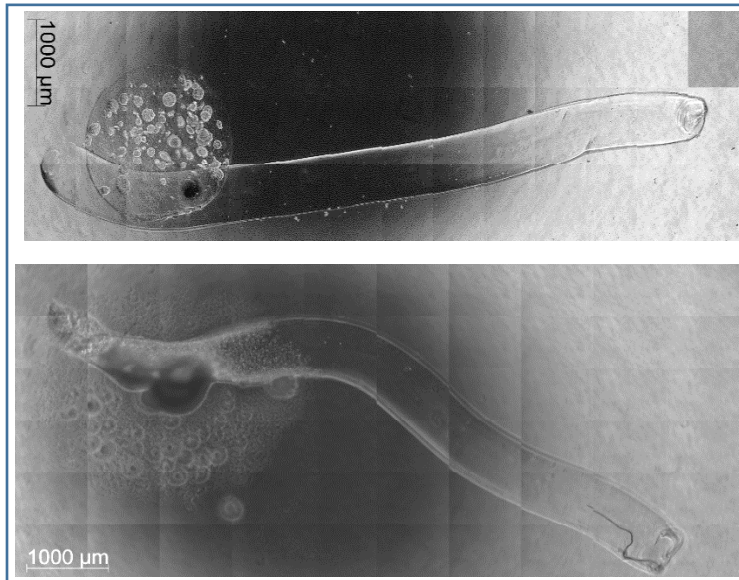
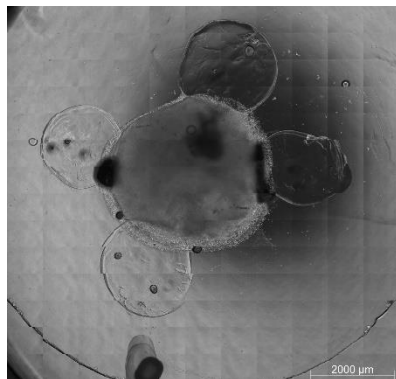


Figure 1

Top left is a photomicrograph of a cylindome with a SVZ-NPC containing fibrin dome adjacent to a fibrin cylinder containing factors. T=Day 0

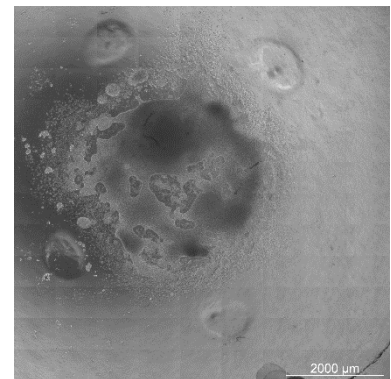
Bottom is photomicrograph of a similar cylindome, T=Day 2. The SVZ-NPCs have degraded the fibrin dome and have begun migrating along the cylinder.

The five-dome assay allowed cells to migrate to each of the outer factor domes, where they were exposed to a single growth factor. The cells were then assessed for migration progression and neurite length and arborization.



Left is five dome assay at day 0. The central dome has not yet degraded.

Right is five dome assay at day 3. The central dome has completely degraded, allowing cells to migrate to factor domes.



Cylinder-in-cylinders allow the observance of differentiation of the cells as they are exposed to the factors in the outer cylinder. Neurite length and branching is indicative of maturation. Immunocytochemistry tagging for neural markers (beta-tubulin) provided definitive measure of development.

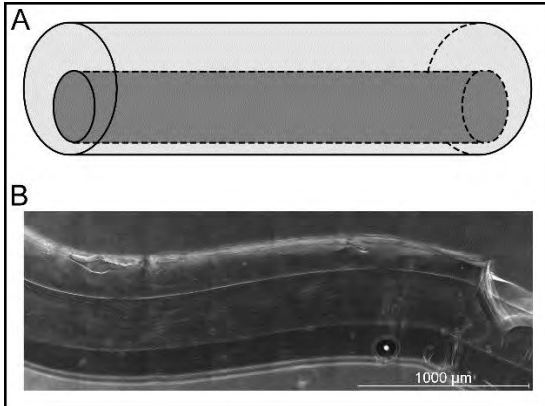


Figure 3

Top left is a diagram of a CinC. The outer and inner cylinders can be prepared containing different factors and/or cells.

Bottom left is photomicrograph of a CinC

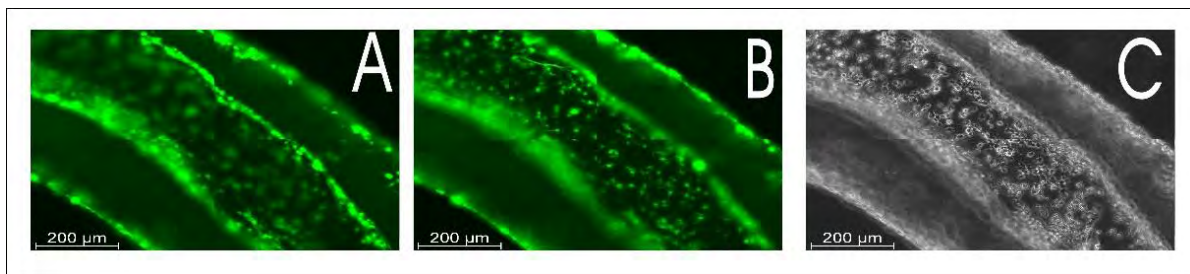
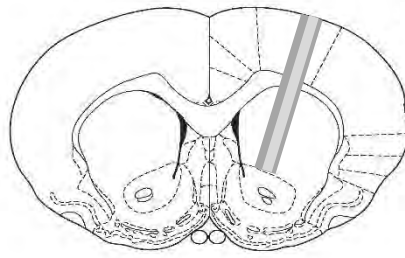


Figure 4

Panels A and B are ICC images, focused at a point midway through (A) and on top (B), showing beta-tubulin+ cells (green) are lining the sides of the lumen.

Panel C is the bright field image of Panel B.

Rats were sacrificed fourteen weeks post-implant and immunohistochemistry was performed to test for the presence of markers for migrating and mature neurons. DCX (red) is present in migrating neurons, MAP2 (green) is indicative of neuritogenesis, and NF-160 (magenta) shows mature neurons. DAPI (blue) integrates into the DNA, thereby tagging all cells present.



A.

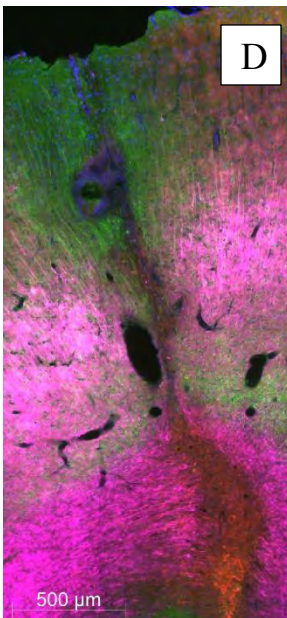
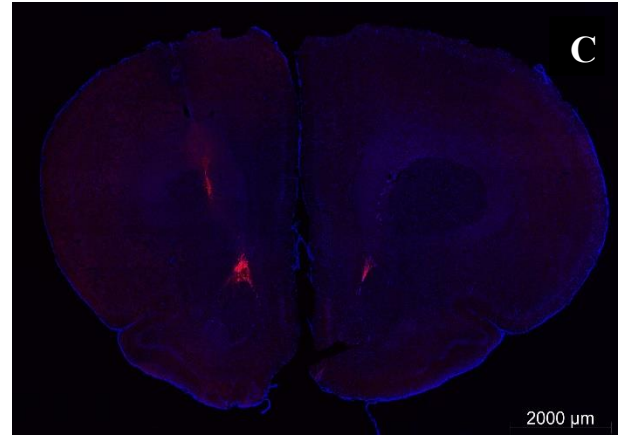
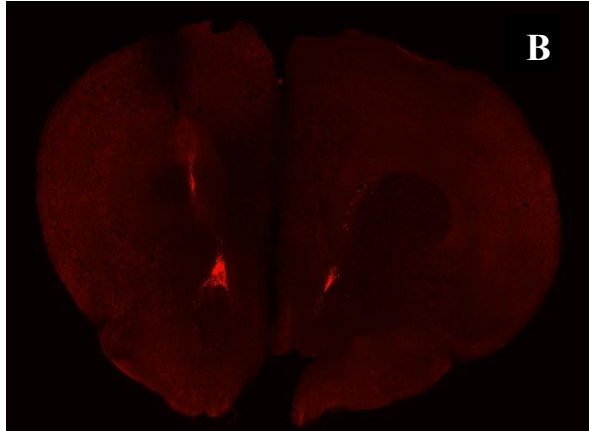
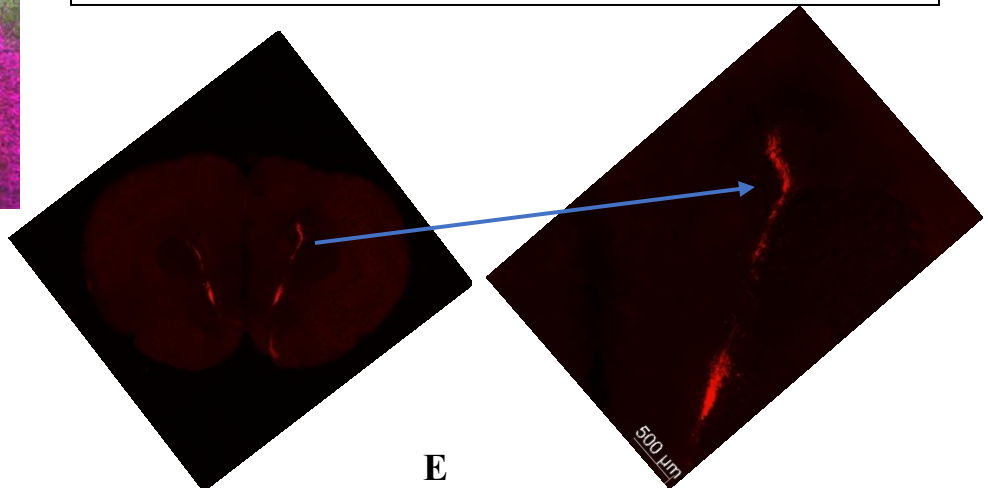


Figure 6

A. Diagram of the implantation of a cylinder such that it intersects the RMS and diverts SVZ cells to the striatum and cortex

B.-D. Immunocytochemistry of implanted brain slices (D. is enlarged image of the cortex region of the implant.)

E. Implantation of the cylinder lead to development of an “elbow” as cells are diverted along the new path.



FUTURE PLANS

For *in vitro* studies, the anticipated directions of our labs will include testing not only single factors, but combinations of growth factors, as well as combinations of adding various factors sequentially in order to discover the order in which neural stem cells are exposed to neurotrophins to instigate proliferation, migration, differentiation, and integration.

Our lab has proven the ability of our cylinders to redirect neural stem cell migration to repopulate damaged areas of the brain. Future experiments will include injections of the thymidine analog 5-ethynyl-2'-deoxyuridine (EdU) at regular intervals post-implant to measure the rate of neurogenesis and migration along the cylindrical matrix. Another anticipated step is to quantify the number of mature neurons that develop in the striatum and cortex. Thus far, our lab has simply tested for their presence, without counting how many migrate or measuring neurite length and counting branching points of neurites. We will also be performing implants of 6-hydroxydopamine Parkinson models in order to test for decreased Parkinsonian behavior post-implant.

DISCUSSION

The assays developed in our lab allow the signaling pathway for neural proliferation, migration, and differentiation to be dissected in order to discover the order of signals that a cell needs to be exposed to in order to mature. The five-dome assays were especially useful in testing the effects of individual growth factors on neural progenitor cells, as cells were exposed to neurotrophins at the same rate, under the same conditions. Under these conditions, the VEGF and NGF domes attracted more cells, while the BDNF dome degraded at the fastest rate. This is indicative of BDNF occupying one of the latest time frames of development because the increased number of proteases are most likely produced in order to degrade extracellular matrix in order to make room for maturing neurites.

Rats that were implanted with the engineered matrices, which contained VEGF and NGF, showed normal behavior as rapidly as 1 hour after surgery, eating treats and interacting with the enrichment placed in their cages. When sacrificed 14 weeks later, the cylinders had completely degraded, being replaced with subventricular zone neural progenitor cells (Figure 6D, blue DAPI staining). The IHC staining showed that our cylinders had, indeed, redirected the migration of SVZ cells along the matrix of the fibrin hydrogel (Figure 6E). This proves that cylindrical fibrin hydrogels are a potential therapy for neurodegenerative disorders.

CONCLUSION

As our lab has an interest in Parkinson's disease, this therapy holds clinical significance in the ability to direct repopulation of the substantia nigra, where dopaminergic cells have died. With the technology proposed by our lab, neural stem cells not only reach the striatum, but are conducted all the way to the outer cortex, making it applicable to traumatic brain injury. Implantation of cylinders themselves provide a model of traumatic brain injury as the quartz tube containing the hydrogels are driven through the brain to the RMS, yet analyzed brain slices show complete healing all the way out to the surface of the cortex. The conducted assays reveal the effects of growth factors incorporated in the cylinders will have on SVZ-NPC's, while implantations in live rats allow us to see the effects on living brains. Our fibrin hydrogels are completely biocompatible

and biodegradable, supporting the repopulation of damaged areas of the brain with healthy, endogenous cells.

ACKNOWLEDGEMENTS

This work was supported by an undergraduate fellowship from the WV NASA Space Grant Consortium. The project was performed in the lab of Dr. Elmer Price (Marshall University Department of Biology) under his advisement.

REFERENCES

- [1]www.parkinsonsinfo.org, 2012.
- [2]Göbel K1, Erb C, Neuro disorders and glaucoma - an overview. *Klin Monbl Augenheilkd.* 231(2): p. 130-5
- [3]Bozoyan, L., Khlghatyan, and Saghatelyan, A., Astrocytes control the development of the migration-promoting vasculature scaffold in the postnatal brain via VEGF signaling. *J Neurosci.* 32(5): p. 1687-704
- [4]Bagley, J, & Belluscio, L., Dynamic imaging reveals that BDNF can independently regulate motility and direction of RMS neuroblast migration. *Neurosci.* 169(3): p. 1449–1461
- [5] Rothman, S. M., K. J. Griffioen, et al. "Brain-derived neurotrophic factor as a regulator of systemic and brain energy metabolism and cardiovascular health." *Ann N Y Acad Sci* **1264**(1): 49-63.

DNA ORIGAMI PLATFORM FOR PROTEIN FLUORESCENCE ENHANCEMENT WITH GOLD NANOPARTICLES

Andrea Hensley
Chemistry
Marshall University
Huntington, WV 25755

ABSTRACT

Many modern diagnostics for protein analysis, including tests for various infections, rely on fluorescence. In order to create an easy to use and versatile biosensor, optical detection of single molecules of a fluorescent protein is ideal. To do this, a uniform DNA platform can be used to present the protein, so patterns in optical images are discernable. Any background signal must be removed in order to detect single molecules because optical microscopes have a resolution limit that makes multiple nearby proteins nearly impossible to distinguish. Based on the results of AFM, the ideal ratio of protein to DNA platform can be determined to optimize binding while reducing the number of unbound molecules observed on the mica substrate. We have found the ideal ratio of fluorescent protein to binding site on DNA origami platforms to be 25 to 1. Because our protein yields a weak signal, as expected, gold nanoparticles are proposed for enhancement and will be the focus of future studies.

INTRODUCTION

The purpose of this project is to precisely position single molecules of a model protein for optical detection using fluorescence. The project uses a cross shaped DNA origami as the platform for positioning the protein. Dendra2 is the protein used because it is photoactivatable; the signal it emits can be switched from one wavelength to another via a photoconversion event. Dendra2 is conjugated with the linker protein streptavidin and purified via gel electrophoresis. The concentration of the purified sample is determined using fluorescence, and then protein binding on origami is observed using atomic force microscopy (AFM). With the eventual goal of creating a biosensor utilizing optical detection of single molecules, future studies will explore the use of gold nanoparticles in enhancing the detection of the fluorescent protein.

BACKGROUND

The world of nanotechnology has been rapidly developing over the last several decades. The recent birth of nanotechnology as a science is largely accredited to Richard Feynman who is considered the father of nanotechnology. In 1959, Feynman gave a presentation titled “There’s Plenty of Room at the Bottom” at the California Institute of Technology (Caltech) where he proposed the manipulation and control of atoms (1). To illustrate the power and possibility of nanotechnology, Feynman gave the example of writing 24 volumes of the *Encyclopedia Britannica* on the head of a pin. Even at such a small scale, one period would be 32 atoms in diameter. At the time of his speech, technology to provide such precise control over individual atoms had not been developed. In order to manipulate atoms, one must first be able to see the atoms (1). Two great advances in nanotechnology have been the scanning tunneling microscope (STM) and the atomic force microscope (AFM).

Atomic force microscopy plays a crucial role in the development of the DNA origami platform for protein presentation. AFM imaging uses a small probe to tap along the surface of a sample and determines topography. The probe and the sample are moved relative to each other in a raster pattern (2). Quantitative measurements are made at discrete points which translate to pixels in the image. This measurement is the vertical displacement of the free end of the tip as it comes in contact with the sample (2). AFM imaging gives three dimensional depictions of the sample in question for complete topographical analysis. This allows the binding of small, discrete molecules on larger platforms to be observed and analyzed.

In 2006, Paul Rothemund of Caltech published a study, “Folding DNA to create nanoscale shapes and patterns,” in the journal *Nature* (3). Rothemund’s study demonstrated the ability of DNA to be folded into predefined patterns using staple strands to guide the folding process. Staple strands are short, single stranded segments of DNA that employ complementary Watson-Crick base pairing to link together hundreds of unique pairs of locations on a longer single stranded DNA segment called a scaffold (3). Like Rothemund, we form DNA origami using DNA from the M13mp18 virus, which has a circular, single strand sequence as its genome. Based on Rothemund’s demonstration that the DNA of M13mp18 can be folded into different patterns using staples, Liu designed a DNA origami construct in the shape of a cross (4). We use this cross shaped structure as the platform for our fluorescence enhancement project, so we can modify it as we learn more.

The protein Dendra2 used in this fluorescence project is photoactivatable. That is to say, it undergoes a chemical change in response to illumination. The photoconversion properties of Dendra2 protein are shown in Table 1 (5). In this case, the protein undergoes a permanent, irreversible photoconversion from a green to a red fluorescent form (5). Dendra2 is an advantageous protein to work with for several reasons. First, Dendra2 is a monomer and therefore switches in one step. The protein’s structure is shown in Figure 1 (6). Secondly, it has been modified by Manjira Kumar of the Norton group to provide two types of binding sites. A his-tag is used in protein purification, and an Avitag amino acid sequence can be modified to generate an appropriate binding site label, biotin. Thirdly, its photoconverted state is highly photostable. The stability of the photoconverted state is important because it enables the protein to be imaged for extended periods of time. Lastly, efficient maturation of Dendra2 occurs in the temperature range of 20°C and 37°C (5). This ensures that a large fraction of the harvested protein is fluorescent. The combination of properties listed above led to the selection of Dendra2 as the model protein molecule for these fluorescent enhancement studies.

Table 1: Fluorescent Properties of Dendra2

	Before Photoconversion	After Photoconversion
Fluorescence Color	Green	Red
Excitation Max	490nm	553nm
Emission Max	507nm	573nm

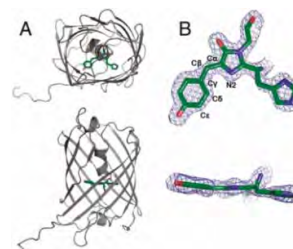


Figure 1: A) Dendra2 monomer structure with chromophore center. B) Chromophore structure from the center of Dendra2 (6).

Dendra2 has a long radiative lifetime and is not a brilliant fluorophore. A study performed at Braunschweig University of Technology in Germany obtained enhancement results in the fluorescence of a dye molecule of up to 117-fold (7). Acuna et. al. obtained these results by binding two 100-nm gold nanoparticles to two locations on a DNA “tower” shaped origami structure. Then, a dye molecule was placed between the two gold nanoparticles in a gap spanning 23-nm (7). The results of this study encourage the use of gold nanoparticles in fluorescence enhancement. However, we propose to use an entirely different, flat origami structure, cross origami, and optimize the nanoparticle diameter and separation in order to enhance the fluorescence of a model protein, Dendra2, instead of a dye molecule.

EXPERIMENTAL

In order to recognize single molecules of a fluorescent protein optically, a large scale, uniform pattern of platforms is necessary. Therefore, a one dimensional array of cross shaped DNA origami is used as the platform for protein presentation. The DNA scaffold, m13, is a bacteriophage with a genome that is composed of circular single stranded DNA and infects *E. coli*. The 6,407 nucleotide viral DNA can be replicated in the host *E. coli* (8). Knowing the sequence of the viral DNA allows it to be manipulated into adopting any structure. In this experiment, staple sequences of DNA are added to fold the M13 circular single-stranded DNA scaffold into the cross shape. With the goal of using the DNA origami as a platform for protein presentation, two staple strands on two of the arms of the cross are labeled with the molecule biotin. Biotin is used because it forms a very strong bond with streptavidin which can be used as a linker protein later (9). Thus, folding the scaffold occurs by adding core staples and biotinylated staples in a buffer solution, so that the final concentration of DNA origami is 10nM with a 4 fold excess of staples.

The buffer used throughout this project was 1x cross origami buffer (1xCOB). 1x COB is a mixture of 12.5mM Mg^{2+} and 1x TAE (Tris base, acetic acid, and EDTA) diluted in water. This buffer is ideal for DNA origami because the Mg^{2+} ions allow the negatively charged DNA strands to come into close proximity to one another in order to form hydrogen bonds. The TAE buffer stabilizes the pH. Once the scaffold and staples have been added, the mixture is placed in a Primus 96^{Plus} Thermal Cycler by MWG AG Biotech. A 13 hour annealing cycle ranging from 95°C to 8°C is used to denature any hydrogen bonds that may have formed at room temperature and form new hydrogen bonds between the scaffold and the staples. A schematic of the process for making zero dimensional (0D) cross origami permutation 1 (CO-01) from M13 ssDNA, biotinylated staples, and core staples is shown in Figure 2a. The newly formed DNA origami can be stored at 4°C before use. The final product can be seen in the AFM image shown in Figure 2b.

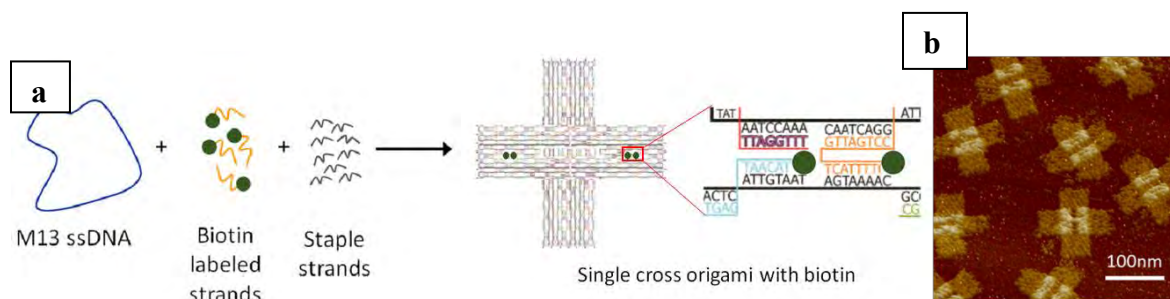


Figure 2: a – Depiction of the process by which 0D CO-01 is made using M13 scaffold DNA and staple strands (10). b – AFM image of the single DNA origami crosses on mica.

Now that a uniform DNA cross unit has been made, they can be connected in a one dimensional array for protein presentation. A one dimensional array of DNA cross origami is used because it is a uniform pattern of platforms upon which fluorescent protein can be presented. The uniform platform pattern can be recognized in fluorescence images, and thus, single molecule arrays of the fluorescent protein can be distinguished from randomly presented fluorophores. One dimensional (1D) cross origami is made by adding sticky ends to the ends of two of the arms of the single (0D) origami. These sticky ends are overhang sequences of DNA that join adjacent crosses through the left and right arms of the structure. This can be accomplished one of two ways. First, the sticky ends can be added to the original mixture of 0D components before annealing in a 1 to 5 ratio of scaffold to sticky ends. The sticky ends will find their places along the left and right arms of the crosses and bind as the cross folds as in Figure 3. Alternatively, the sticky ends can be added to already annealed 0D cross origami as in Figure 4. In this case, the sticky ends are added in fivefold excess to the 0D crosses and reannealed in the thermocycler from 45°C to 20°C overnight. A maximum temperature of 45°C is used prevent the crosses from denaturing. The final product is a one dimensional array of DNA crosses as shown in the AFM image in Figure 5.

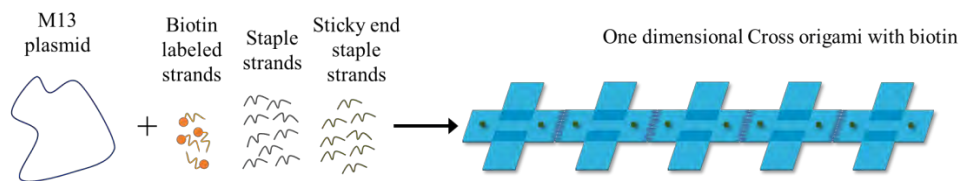


Figure 3: The image above depicts the process by which 1D cross origami is made by adding sticky ends before annealing (10)

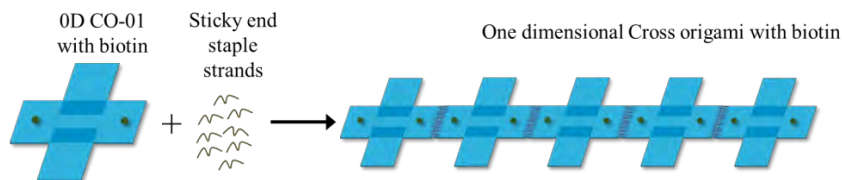


Figure 4: The image above depicts the process by which 1D cross origami is made by adding sticky ends to already formed 0D crosses and reannealing (10).

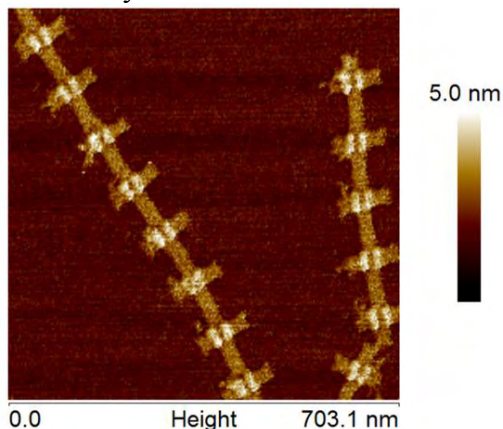


Figure 5: AFM image of 1D CO-01 on mica.

The next step in the experiment is to add a fluorescent protein to the DNA cross origami platform. The biotinylated Dendra2 is linked to the biotinylated staples in the DNA cross origami by a molecule of the protein streptavidin. Streptavidin has four binding sites, so it can easily bind to three biotin molecules; one on the Dendra2 and two on the staples (9). In order to ensure there is no free streptavidin in solution, biotinylated Dendra2 is conjugated with streptavidin before being introduced to the DNA structure. A ratio of three streptavidin proteins per Dendra2 molecule is used to optimize the amount of streptavidin proteins with only one Dendra2 bound to it.

Since the ultimate goal of this project and future projects is to optically distinguish between single molecules of a fluorescent protein, the Dendra2-streptavidin complex is purified to get a one to one ratio of Dendra2 to streptavidin. This is accomplished using a 6-inch 8% polyacrylamide preparative gel electrophoresis (PAGE) system. The ideal concentration of Dendra2 in order to not overload the gel is $2\mu\text{g}/20\mu\text{L}$. If the gel is overloaded with too high of a concentration, the bands used for purification become indistinguishable. To obtain the most one to one protein complexes, streptavidin is starved for Dendra2 with a ratio of 3 to 1. Equal volumes of $10\mu\text{M}$ streptavidin and $3.33\mu\text{M}$ Dendra2 are loaded with $2\mu\text{L}$ glycerine for a total volume of $42\mu\text{L}$ in each lane. The gel is run overnight using a NESLAB RTE 211 water circulator/chiller to keep the gel at a constant 4°C (11). This prevents the gel from becoming overheated which can cause the gel to curl and become brittle. A running buffer of 1xTris-glycine is used to maintain current across the gel. The negative cathode is connected at the top of the gel near the wells while the positive anode is connected to the bottom of the gel. This provides the necessary voltage across the gel to move the protein toward the anode. Because the gel runs overnight, a low voltage of 100V is applied to the gel to gradually move the protein complexes down the gel. Polyacrylamide gel has small pores that allow proteins to be separated approximately according to their charge to molecular weight ratio. If they have the same charge, the smallest and lightest proteins move the fastest while the largest and heaviest proteins move the slowest. Therefore, the Dendra2 protein should move the fastest, and among the complexes, the 1:1 Streptavidin:Dendra2 complex should run the fastest as depicted in the proposed key in Figure 6. Separation progress is monitored by fluorescence under UV illumination.

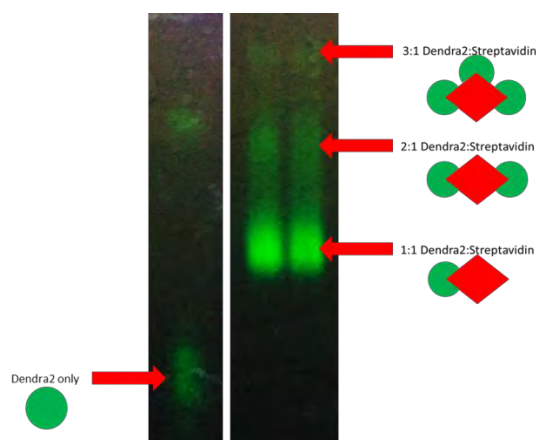


Figure 6: Image of PAGE gel used for purification of 3:1 Streptavidin:Dendra2; Dendra2 locations are apparent when the gel is illuminated with UV light.

Once the 1:1 protein complex has been separated from other complexes by gel electrophoresis, it needs to be extracted for use. David Neff and Tanner Bakhshi designed the extraction system

shown in Figure 7. First, the lanes are excised using a razor blade. In the case pictured above, two lanes were excised together. The gel lanes are then laid across a hydrophobic bridge between two wells of 1xTris-Glycine buffer. Both wells contain an electrode, either an anode or a cathode, and the gel is laid so that the protein will move toward the anode. Next, a small well is cut out below the bright 1:1 band in the gel. The idea is to run the protein into the well and extract it using a pipette. The well is filled with 50% sucrose in 1xCOB to slow down the protein complexes, so they will not run through the well and into the gel on the other side before it can be extracted.

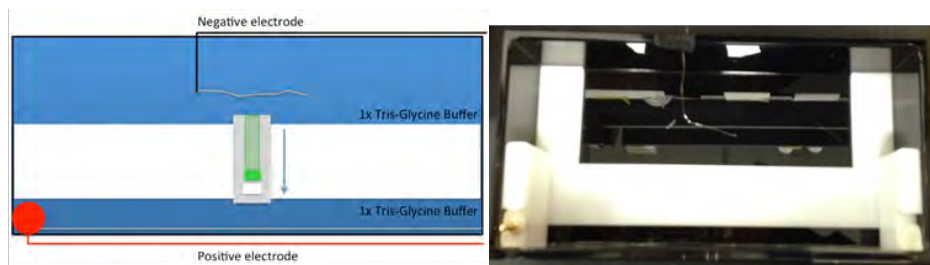


Figure 7: The left image shows a schematic of the extraction process where the protein complex is run into a well cut in the gel on the side toward the anode. The right image is the actual box containing the extraction apparatus (the gel is not shown here).

After the 1:1 streptavidin:Dendra2 complex has been purified and extracted from the well, the concentration was determined. Knowing the concentration of the sample will allow precise ratios of protein to DNA origami to be used to determine concentrations yielding optimal binding efficiency. The concentration of the extracted samples was determined using fluorescence microspectroscopy with a Leica TCS SP5 II confocal microscope. As reference solutions, Manjira Kumar’s purified Dendra2 was diluted to known concentrations. The emission spectra of known concentrations of Dendra2 were recorded over a range of 495nm to 670nm. Under identical conditions, the emission spectra of three unknown samples from the gel purification system were recorded. The results are shown in Figure 8.

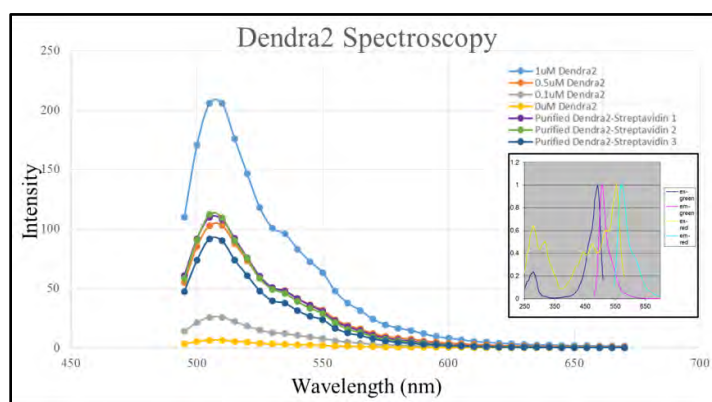


Figure 8: Micro-fluorescence spectroscopy of purified Dendra2-streptavidin complexes and Dendra2 protein of known concentrations. The inset depicts the excitation and emission spectra of Dendra2 as provided by Evrogen (4).

From the emission spectra, a calibration curve was constructed using the average intensity over a range of 510-550nm. The average intensity was then plotted against concentration resulting in the

calibration curve shown in Figure 9. The data was fitted to a linear trendline, $y=0.1142x+8.1807$. The trendline was used to calculate the concentrations of the unknown samples using the average intensity over 510nm to 550nm. The data is summarized in Table 2, and the plotted unknowns can be seen in Figure 9.

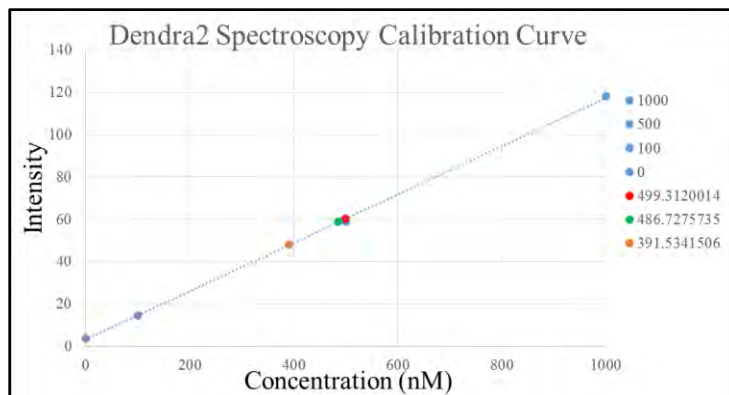


Figure 9: Calibration curve from the average intensities over 510-550nm of known concentrations of Dendra2 and unknown concentrations of Dendra2-Streptavidin.

Table 2: Summary of Determined Concentrations of Unknown Dendra2-Streptavidin complexes

Sample	Avg Intensity y (510-550nm)	Concentration nM $y=0.1142x+3.1807$
Purified Dendra2-Streptavidin 1	60.20213056	499.312
Purified Dendra2-Streptavidin 2	58.76498889	486.7276
Purified Dendra2-Streptavidin 3	47.8939	391.5342

Once the Dendra2-streptavidin complex is formed and purified, it can be reacted with the DNA origami, and the resultant product can be characterized using AFM. The protein complex binds to the DNA platform through the strong bond of streptavidin in the complex and biotin on the DNA staples. AFM imaging was used to demonstrate that the streptavidin-biotin system provides a successful mechanism for binding the fluorescent protein to the DNA origami platform, as shown in Figure 10.

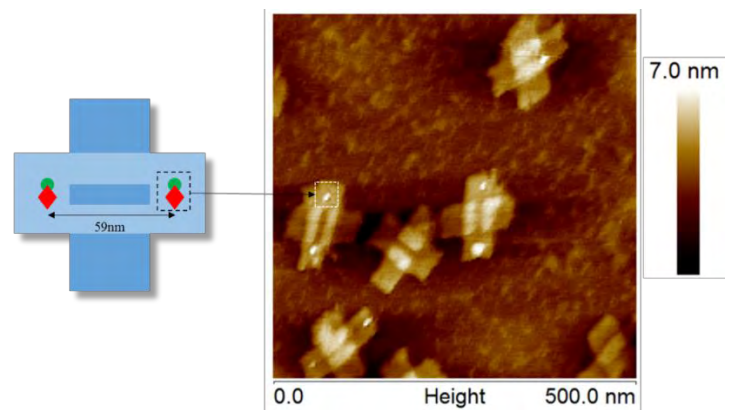


Figure 10: Left- Schematic of DNA cross origami (blue) with two biotinylated staples on each arm attached to streptavidin (red) conjugated with a biotinylated Dendra2 protein (green). Right- AFM image of single DNA crosses labeled with Dendra2-Streptavidin complex.

RESULTS

With the basic procedures for protein binding to DNA origami mastered, larger structures were constructed. These larger structures consist of chains of single DNA crosses. This provides a large, uniform platform on which to present protein. The linear structure of these chains will allow us to better distinguish single molecules of Dendra2 optically. For now, the goal has been to fully occupy every binding site with a protein complex. Different ratios of Dendra2 to DNA origami were tested with an optimum found to be 50:1 by concentration for unpurified 1D cross origami. At a ratio of twenty-five protein complexes per protein binding site, the DNA cross origami chains display nearly 100% coverage where each cross has at least one protein bound to it, as determined by AFM imaging (Figure 11).

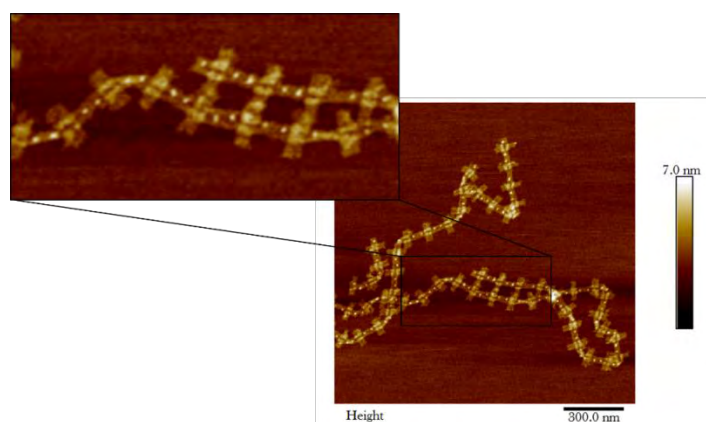


Figure 11: AFM image of unpurified DNA cross origami chain with nearly 100% site occupancy with Dendra2-streptavidin, obtained from solution with a 25:1 ratio of protein to binding site.

Analysis of images taken of three areas of the same origami sample on mica shows a nearly 100% coverage of protein complex on 1D DNA cross origami (Figure 12). Of approximately 171 crosses, 76% of them possess two protein complexes while 24% possess one protein complex. Future studies will be directed toward improving the efficiency of protein binding. Ideally a 1:1 ratio of protein complex per binding site will yield 100% coverage of DNA cross origami with two bound protein complexes. With good coverage, 1D DNA cross origami provides a uniform platform upon which to observe fluorescent proteins optically.

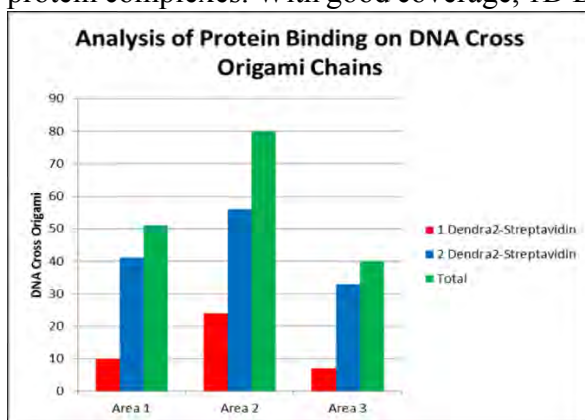


Figure 12: Statistical analysis of protein binding on 1D cross origami at a solution ratio of 25 proteins complexes per binding site.

Optical imaging is still being optimized for the study of individual molecules of Dendra2. In the meantime, Cy3, a fluorescent molecule, has been tested in the place of Dendra2. Cy3-streptavidin, with no unconjugated Cy3 molecules, was purchased from Life Technologies. However, each streptavidin may have more than one Cy3 molecule bound to it, so individual molecules cannot be

discerned optically. The Cy3-streptavidin conjugate was bound to 1D DNA cross origami in the same manner as the Dendra2-streptavidin complex. This time a ratio of ten fluorescent complexes to one binding site was used. The results were analyzed by atomic force and optical microscopy with resulting images shown in Figure 13.

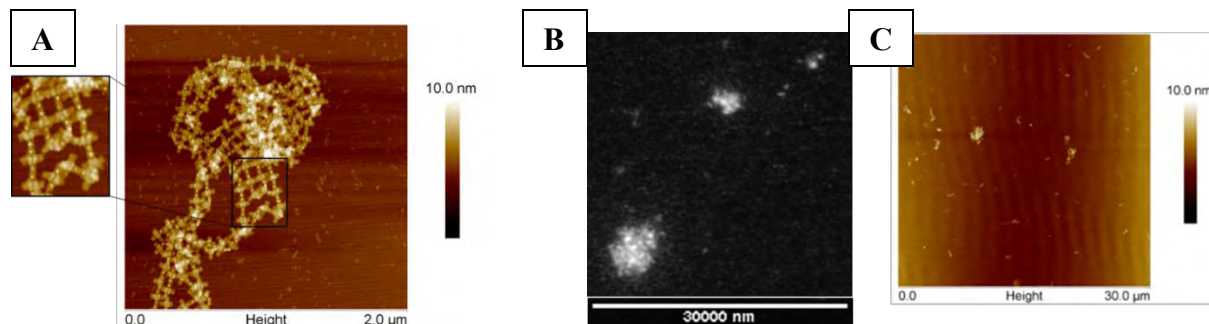


Figure 13: A – AFM image of Cy3-SA on 1D cross origami array. B – Optical image of Cy3-SA on 1D cross origami. C – AFM image of Cy3-SA on 1D cross origami (to scale with B).

The bright areas of the optical image correspond to roughly the same size and shape of a tangled mass of 1D cross origami with “frayed” edges observed by AFM imaging. Therefore, a fluorescent molecule can be observed optically when presented on our DNA origami platform.

FUTURE STUDIES

The next step is to enhance the protein’s fluorescent signal for improved single molecule detection. Future studies will focus on using gold nanoparticles to enhance the fluorescence of Dendra2 on DNA cross origami. The gold nanoparticles are coated with DNA of a specific sequence, so they will bind to the DNA origami crosses. Staple strands pointing out of the crosses hybridize with DNA on the gold nanoparticles to bind the particles to the constructs. Thacker et al describe the process of attaching gold nanoparticles to DNA origami in their paper, “DNA origami based assembly of gold nanoparticle dimers for surface-enhanced Raman scattering” (4). This procedure involves coating the gold nanoparticles in single stranded DNA by suspending them in a solution of thiolated DNA, followed by purification using gel electrophoresis. Finally, an excess of the gold nanoparticle solution is incubated with the origami to ensure attachment of the gold nanoparticles to the origami. Fluorescence and optical studies will be conducted to measure the amount of enhancement and to view individual molecules of fluorescent protein, both before and after photoconversion.

CONCLUSION

In conclusion, the fluorescent protein Dendra2 was successfully conjugated with streptavidin by biotin interactions. Through the linker protein streptavidin, the fluorescent protein was presented with nearly 100% efficiency on the one dimensional array of DNA cross origami. The next step is to enhance the fluorescence using the plasmonic properties of gold nanoparticles in order to optically detect individual molecules. Another fluorophore, Cy3, has been used to confirm that optical detection of fluorescent molecules on the DNA origami platform is possible in the Imaging Laboratory at Marshall. The NASA WVSGC has allowed me to gain real-life experience in the research field while learning invaluable skills and lessons. I have been able to present my research

and feel accomplished in my work. I am excited to continue a career in research over the upcoming year. This would not have been possible without funding from NASA WVSGC.

ACKNOWLEDGEMENTS

I would like to thank Dr. Michael Norton for inspiration and encouragement throughout this experience. Thanks to Dr. Masudur Rahman, David Neff, and Dr. Manjira Kumar for mentorship and guidance along the way and to Tanner Bakhshi for his excellent work leading up to this project. I would like to extend my gratitude to the Norton Nanolaboratories as a whole for an enjoyable experience. Funding for this project was provided by the NASA West Virginia Space Grant Consortium and NSF Cooperative Agreement No. OIA-1458952.

REFERENCES

1. Feynman, R. (1992). There's Plenty of Room at the Bottom. *Journal of Microelectromechanical Systems* 1(1), 60-66.
2. Bruker Nano Surfaces Division. (2011). *Introduction to Bruker's ScanAsyst and PeakForce Tapping AFM Technology*. Santa Barbara, California: Bruker Corporation.
3. Rothemund, P. (2006). Folding DNA to create nanoscale shapes and patterns. *Nature*, 440(16), 297-302.
4. Liu, W., Zhong, H., Wang, R., & Seeman, N. C. (2011). Crystalline two-dimensional DNA-origami arrays. *Angewandte Chemie International Edition in English*, 50(1), 264-267.
5. Evrogen. *Green-to-red Photoswitchable Fluorescent Protein Dendra2*. Moscow, Russia: Evrogen JSC.
6. Adam, V., Nienhaus, K., Bourgeois, D., & Nienhaus, G. U. (2009). Structural Basis of Enhanced Photoconversion Yield in Green Fluorescent Protein-like Protein Dendra2. *Biochemistry*, 48(22), 4905-4915.
7. Acuna, G. P., Moller, F. M., Holzmeister, P., Beater, S., Lalkens, B., & Tinnefeld, P. (2012). Fluorescence Enhancement at Docking Sites of DNA-Directed Self-Assembled Nanoantennas. *Science*, 338(6106), 506-510.
8. Huang, Y., Chiang, C., Lee, S. K., Gao, Y., Hu, E. L., de Yoreo, J., & Belcher, A. M. (2005). Programmable Assembly of Nanoarchitectures Using Genetically Engineered Viruses. *Nano Letters*, 5(7), 1429-1434.
9. Chivers, C. E., Koner, Apurba, L., Lowe, E. D., & Howarth, M. (2011). How the Biotin–Streptavidin Interaction Was Made Even Stronger: Investigation via Crystallography and a Chimaeric Tetramer. *Biochemical Journal*, 435, 55-63.
10. Wu, T. C., Rahman, M., & Norton, M. L., (2014). From Nonfinite to Finite 1D Arrays of Origami Tiles. *Accounts of Chemical Research*, 47, 1750-1758.

11. Thermo NESLAB. (2000). *RTE Series Refrigerated Bath/Circulators Digital Controller*. Newington, NH: Thermo NESLAB LLC.

ISOTOPIC CHARACTERIZATION OF LIPID CONTENT IN *CHLORELLA VULGARIS*

Aaron Holland
Biomedicine
Marshall University
Huntington, WV 25755

ABSTRACT

Due to the many limitations of fossil fuels, the scientific community is exploring a variety of alternative fuel sources. One of these alternatives is marine microalgae, which are advantageous because they produce fatty acids that may be used to generate biodiesel. In addition, they do not compete for land used for agriculture¹, and can potentially be grown under arduous conditions such as in waste water containing ammonia and phosphorus². While growing algal crops seems to be a promising alternative fuel for the near future, petroleum-based diesel is still cheaper to produce than algal biodiesel. To remedy this problem, serious advances need to occur to further optimize lipid production in algae.

Previous experiments performed by the Kolling lab have shown that nitrogen deprivation and glycerol addition to the liquid growth medium causes higher lipid accumulation in *Chlorella vulgaris* (a single-cell green alga). This could be due to the glycerol being taken into the cell and used as a precursor to biosynthesize triacylglycerols or it may be a result of an increase in stress (potentially osmotic pressure). To investigate the mechanism for the increase in lipid production, *C. vulgaris* was grown mixotrophically in (0.5% w/v) glycerol with C¹³-labeled glycerol while other cultures were grown in (0.5% w/v) ethylene glycol, a compound that is somewhat similar to glycerol, but would not impart a metabolic advantage (i.e., it would not serve as a precursor or carbon source).

Results from this experiment showed no significant difference in lipid production between the glycerol and ethylene glycol exposure, which suggests the lipid increase was due to stress on the cells. However, to verify these findings samples are currently being tested via GCMS for C¹³ presence in the acyl groups and glycerol of the triacylglycerols. Any C¹³ levels above the control in the acyl groups will show that the glycerol is being used as a carbon source. A higher C¹³ level in the glycerol—relative to the acyl group—will indicate that glycerol is being directly used in triacylglycerol biosynthesis. Outcomes of these experiments will be discussed in context of efficient biodiesel production in algae.

INTRODUCTION

As technology continues to advance, space travel and even colonization becomes a feasible venture for humanity. Recently, the private non-profit organization Mars One has put forth a conceptual plan to attempt to establish a permanent colony on Mars. The ambitious plan projects that four astronauts will be on Mars by 2023 to establish conditions for more settlers.

One challenge we are confronted with in the logistics of Mars terraformation is oxygen production. With the Martian atmosphere being 96% carbon dioxide¹, a popular solution to this is plant life. Unfortunately, for photosynthesis to produce oxygen it also needs water. Mars One planned to obtain drinkable and usable water by baking it from the soil, but a study conducted by MIT said that that was beyond the capabilities of existing technology².

Another challenge of terraformation will be fuel production. According to *Planets*, A journal of geographic research, methane hydrate could exist under the surface of Mars produced by microbes that performed methanogenesis at a time when the Martian surface paralleled that of Earth's. The caveat to this possible fuel source is that the methane hydrate would only be stable approximately 15 meters under the Martian surface³ and the existence of methane on Mars is refuted by Kevin Zahnle of the NASA Ames research center⁴.

A potential solution to both of these problems is the microorganism algae. Algae has the potential of being used as a fuel source by harvesting the energy rich lipids within the cell and would be useful in the terraformation given that it produces oxygen through photosynthesis. Algae would be more advantageous than other plants since it can be effectively grown in waste waters which contain toxic heavy metals⁵. This process would treat the waste water conserving reserves and provide additional fuel in the form of biodiesel.

There has been significant research into making algae more efficient for the use in biodiesel that involves optimizing triacylglycerol (TAG) concentration. Triacylglycerols are fat storage molecules derived from glycerol and three fatty acids. Fatty acids which are useful in biodiesel (palmitic acid and stearic acid) are commonly found in TAGs. If we can effectively produce an abundance of TAGs, it will make the algae a more viable resource in terms of fuel production.

Previous research has shown that nitrogen deprivation increases lipid content by halting protein synthesis. This forces the cell to sequester energy in the form of fatty acids. To further coax the cell into forming TAGs we introduced glycerol into the liquid medium at a concentration of 0.5% (w/v). Our hypothesis was that the glycerol would increase TAG production in two ways; 1. It will allow the cell to bypass glycolysis, pyruvate processing, and the citric acid cycle and take advantage of a glycerol transporter in the cell membrane. The extracellular glycerol would diffuse directly into the cell and glycerol-3-phosphate, the backbone of TAGs, is created by a glycerol kinase. And 2. It will allow TAGs to be preferentially formed over other biomolecules by increasing the glycerol concentration in the cell and shifting equilibria to favor formation of the TAGs.

Our data from this research supplied evidence that *Chlorella vulgaris* cells had increased lipid concentrations by approximately 6.3%/mL of dry mass in the nitrogen deplete with glycerol cultures compared to just the nitrogen deplete cultures. While this is a promising prospect we have yet to identify if the glycerol molecule was utilizing the glycerol transporter and providing the backbone for TAGs or if the glycerol molecule was simply stressing the cell which would lead to an increase in lipid content. To resolve this problem, we would like to repeat this experiment using glycerol with carbon 13 isotopes. Then, using the procedure listed below, we will isolate the lipids from the cell and use GCMS to examine if the carbon isotope is more abundant glycerol fraction of the TAG than in the fatty acids.

METHODS

The experimental procedure contains five main steps: cell cultivation, growth determinations, dry mass determinations, lipid extraction, and GCMS. For the cell cultivation; aseptic techniques will play a major role in the production of algae as well as growth conditions. All glassware will be autoclaved, then sterilized with UV to reduce the risk of contamination. Furthermore, all cultivation will be done in a laminar flow hood for the same reason. Using these techniques two cultures will be grown; both of which will lack typical nitrogen reserves necessary for standard cell growth and contain 0.5% (w/v) glycerol. The difference is that one culture will contain isotopic labelled glycerol. Both cultures will be put in an incubator with a temperature of 25°C on an orbital shaker plate with 24-h lighting.

Throughout the duration of cultivation two types of growth determinations will be taken periodically: relative cell number per volume and photosynthetic activity. To measure these values a UV spectrophotometer will be used measuring wavelengths 750nm, 649.1nm, and 665.1nm. The value at 750nm measures the relative cell number per volume (via turbidity) and will give a reliable value for cell growth. The values 649.1nm and 665.1nm measure the amount of chlorophyll *a*. The chlorophyll *a* will be removed from the sample using dimethylsulfoxide and will serve as a secondary growth determination and will give insight on the photoactivity of the cells as it directly correlates to the number of photoreaction centers present.

The next assay that will be done is the total dry mass which will be done periodically throughout the experiment just as the chlorophyll *a* and turbidity measurement. To obtain a value for the total dry mass, 1 mL of cells from each culture will be pipetted onto 1 micron microfiber filters. The filters will then be put into an oven and dried at 70°C for 24 hours. Once dry, the filters will be measured on an analytical balance.

Another pertinent part of the experiment will be the extraction of lipids from the algal cells. To start the process, the cells are lysed with methanol to release the lipids from the plasma membrane. Then methyl t-butyl ether (MTBE) will be used to partition the lipids. This will also separate the MTBE from the methanol because of MTBE's low density. The lipids and MTBE are removed from the tubes and placed in tared snap-cap tubes in a vacuum for drying. They are then measured using an analytical balance subtracting the final weight of the tube with cells vs. the initial weight of tube without cells.

The final part of the procedure is gas chromatography mass spectrometry which is especially important because of how closely related complex lipids are. GCMS uses a capillary column to separate molecules based on their chemical composition. It is in this portion of the experiment where we will exam the TAGs for the carbon isotope.

DATA

Figure 1

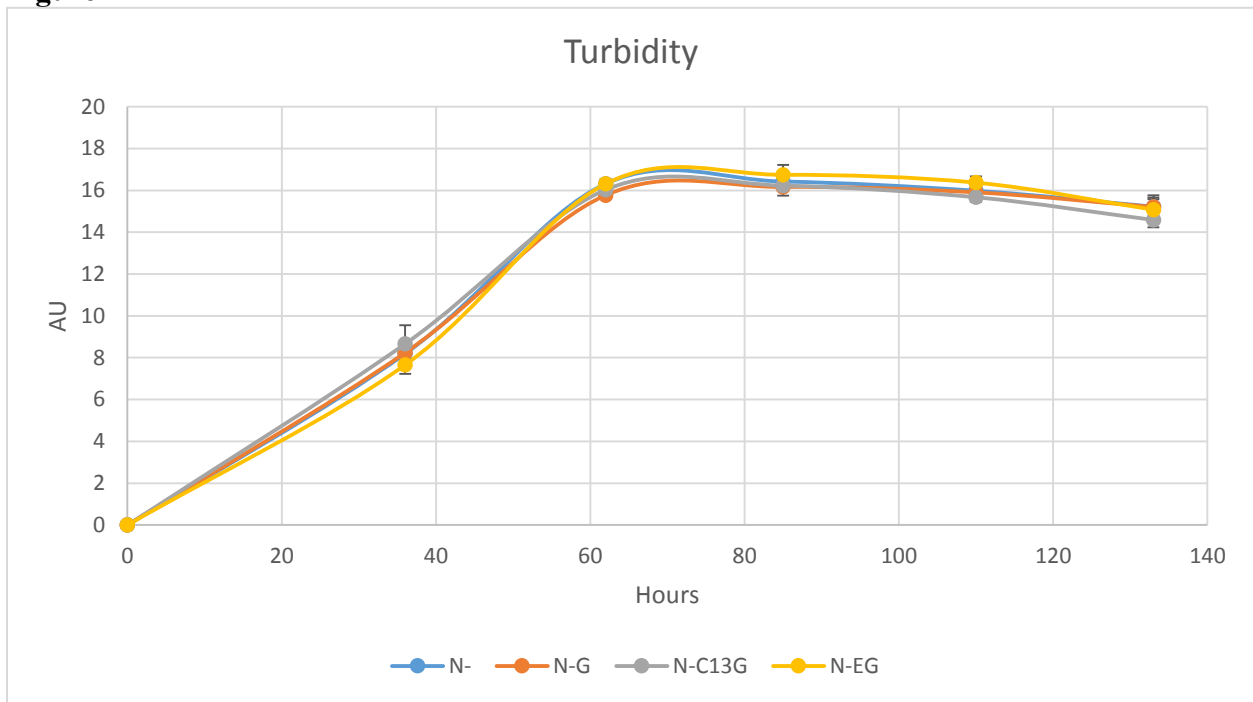


Figure 2

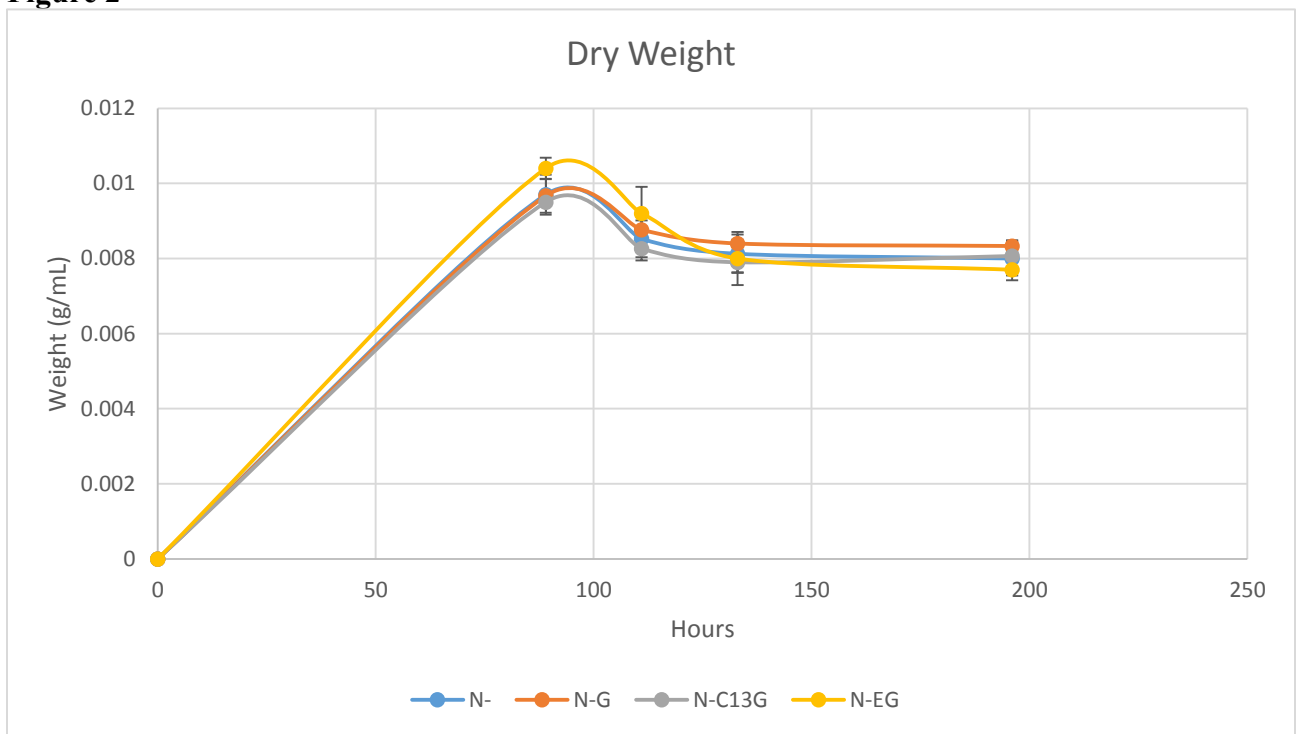
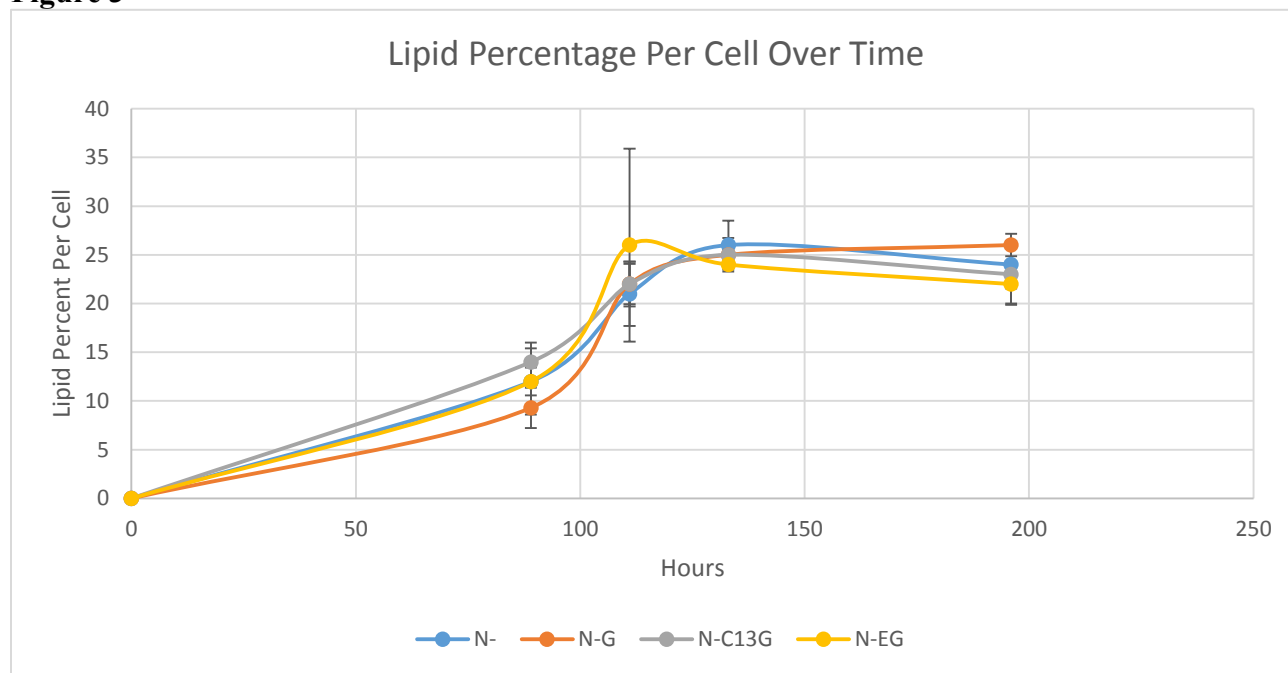


Figure 3



For each graph legend N- stands for nitrogen deprived, N-G stands for nitrogen deprived with glycerol, N-C13G stands for nitrogen deprived with carbon 13 glycerol and N-EG stands for nitrogen deprived with ethylene glycol.

CONCLUSIONS

Unfortunately, the results from the lipid extractions didn't support the data that was obtained in 2014. In the past experiment, the nitrogen deprived with glycerol cultures accumulated 6.3% more lipids than the nitrogen deplete cultures. In the final growth stages of this experiment each culture contained approximately 24% lipids per cell. Furthermore, there was not a significant difference in the biomass for the nitrogen deprived cultures compared to the nitrogen deprived with glycerol cultures. A difference in biomass between these two types of cultures are generally associated with higher lipid percentages. Though these results don't reflect previous data, it is still possible that the glycerol molecules incorporated into the media is still being utilized in triacylglycerols. Preparations are currently being made to analyze the glycerol with C13 samples using NMR to verify that hypothesis.

Furthermore, a new hypothesis is being tested to try and increase the amount glycerol transporters in the cell membrane. We are doing this by adding a minute concentration of glycerol (0.1% w/v) to the cell culture early in the growth phase. We hypothesize that the cells will respond to the chemical cue and increase the concentration of glycerol transporters in response to the signal. In exponential phase the glycerol concentration was increased to 0.5% (w/v) then to 1.0% (w/v) in stationary phase to maximize the amount of glycerol being utilized by the cell.

ACKNOWLEDGEMENTS

- NASA WV Space Grant Consortium

- Derrick Kolling
- Ethan Adkins
- Anthony Stephenson

REFERENCES

Chisti, Yusuf. "Biodiesel from microalgae." *Biotech. Adv.* 2007. 25: 294-306.

Velichkova K., Sirakov I., Stoyanova S. 2014, BIOMASS PRODUCTION AND WASTEWATER TREATMENT FROM AQUACULTURE WITH CHLORELLA VULGARIS UNDER DIFFERENT CARBON SOURCES. *Scientific Bulletin. Series F. Biotechnologies*, Vol. XVIII, ISSN 2285-1364, 83-90.

CITATIONS

1. Mahaffy Paul R. (2013) Abundance and Isotopic Composition of Gases in the Martian Atmosphere from the Curiosity Rover. *Science Magazine Vol. 341* no. 6143 pp. 263-266
2. Chu, J. (2014, October 14). Mars One (And done?). *MIT News*. Retrieved from <http://newsoffice.mit.edu/2014/technical-feasibility-mars-one-1014>
3. Pellenbarg, R. E., M. D. Max, and S. M. Clifford (2003), Methane and carbon dioxide hydrates on Mars: Potential origins, distribution, detection, and implications for future in situ resource utilization, *J. Geophys. Res.*, 108, 8042, doi:10.1029/2002JE001901, E4.
4. Zahnle K. and Freedman R. S. (2010) Is there methane on Mars? *Icarus* 212 (2), 493-503
5. Pitman, J. K. (2010) The potential of sustainable algal biofuel production using wastewater resources. *Bioresource Technology* 102(1), 17-25

INVESTIGATION OF ENZYMATIC MECHANISM AND CELLULAR EXPRESSION OF DPY-19L4

Alexis Kastigar
Anthropology, Biological Sciences, Latin
Marshall University
Huntington, West Virginia 25701

ABSTRACT

DPY-19 is aglycosyltransferase that mediates the C-mannosylation of tryptophan and mannose via the second carbon in the indole ring of tryptophan. Four homologs are present in humans, and each increasing homolog is more divergent from the canonical single homolog of DPY-19 first observed in *C. elegans*. DPY-19L4 was chosen for this research specifically for its increased divergence from the canonical homolog and due to the lack of prior isolation of this enzyme by biochemical means. Insertion and DPN digestion of a DNA insert for DPY-19L4 into a linearized, DPN-digested plasmid of pcDNA3.1 was used to tag the present of DPY-19L4 in a eukaryotic tissue panel. RNA digestion of mouse liver, mouse kidney, and rabbit aorta tissues has been achieved with significant yield to continue on to analyze gene expression of DPY-19L4. As such, it has been demonstrated the DPY-19L4 can be amplified using the techniques described in Benoit *et al.*, that ligation needs to take place to combine the DNA insert with the linearized plasmid, and that process can be utilized by the other three homologs of DPY-19 (L1, L2, L3, L4) (Benoit *et al.*, 2006, *Protein Expr. Purif.*)².

INTRODUCTION

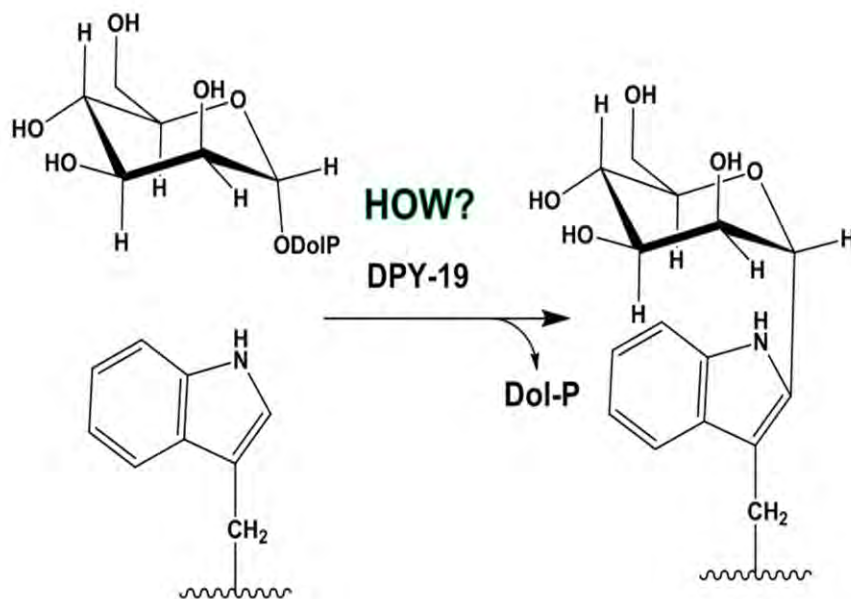


Figure 1: The C-mannosylation of tryptophan. Within DPY-19, a C-glycosyltransferase, attaches a mannose sugar to the second carbon of the indole ring of tryptophan residues resulting in a C-mannosylated tryptophan and dolichyl-phosphate.

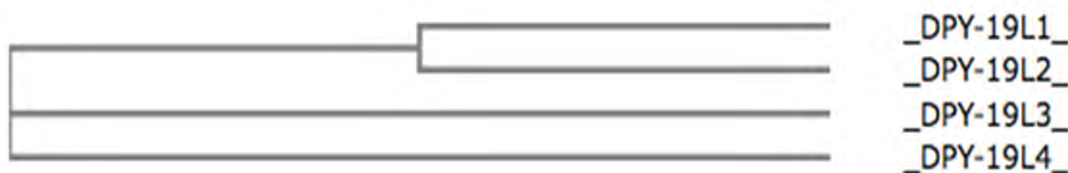


Figure 2: The cladogram depicting the comparative divergence of each human homolog of DPY-19 with percent identity compared to the single DPY-19 homolog in *C. elegans* as determined by the comparison of mRNA sequences as follows²: L1 - 51%; L2 – 41%; L3 – 36%; L4 - 33%.

Many proteins require a co- or post-translational carbohydrate molecule addition to properly achieve fundamental structural and functional roles. This process, known as glycosylation, is enzyme-directed and site-specific and usually achieved by an N- or O- glycosidic linkage. However, there exists a specific class of glycosyltransferases that forms glycosidic bonds with sugar moieties through a C-linked carbon-carbon bond. The mammalian enzyme DPY-19, attaches a mannose sugar to the second carbon of the indole ring of tryptophan residues in a tryptophan-x-tryptophan consensus sequence ('x' is any amino acid). DPY-19 was first identified in *Caenorhabditis elegans*, where a single homolog exists, but the human genome contains four such homologs (DPY-19L1, DPY-19L2, DPY-19L3, DPY-19L4) that are increasingly more divergent¹. This specific research focused upon DPY-19L4, which has not been isolated biochemically for studies of enzymatic activity.

A gene insert of DPY-19L4 was amplified, *DpnI* digested, and mixed with *DpnI*-digested, linearized pcDNA3.1 plasmid to be able to assay for the presence of DPY-19L4 in eukaryotic cell tissues as described by Benoit *et al.* (Benoit *et al.*, 2006, *Protein Expr. Purif.*)². InFusion enzymes mediated the mixture of the insert and plasmid and the cells were cultured on agar plates to produce a plasmid colony that can be used to tag spun down RNA samples from a eukaryotic tissue panel that contain DPY-19L4. Thus far, the amplification of the DPY-19L4 insert and linearization of pcDNA3.1 plasmid have been successful and tentative success has been achieved in regards to the mixing of the digested products, but clarification of control results is still needed. Likewise, a small panel consisting of tissue from mouse liver, mouse kidney, and rabbit aorta has yielded significant amounts of RNA to analyze for gene expression.

METHODS

DPY-19L4 was isolated by means of Pcr4-Topo plasmid mutation to remove the polyhistidine tags and amplified by means of PCR. After which, the plasmid was DPN digested with DPN1. The plasmid linearization of pcDNA3.1 was achieved by means of PCR and restriction digest, gel purification, and ligation was used for cloning (Benoit *et al.*, 2006, *Protein Expr. Purif.*). As such, the plasmid also underwent DPN digestion with DPN1 before being mixed with the amplified plasmid of DPY-19L4. Both the amplified insert and the linearized plasmid were mixed after DPN digestion with the Infusion cloning mixture shown below in Figure 3. To culture extra plasmid and insert, a pcDNA3.1-DPY-19L4 cell culture, and a pcDNA3.1 cell culture were plated on agar plates containing ampicillin. Before plating, the pcDNA3.1-DPY19-L4 cell culture underwent a ten-fold dilution and each dilution was plated to view comparatively. Liquid cell culturing was

performed on cultures from both cells where a sufficient, isolated colony was present. Miniprep was used to isolate the plasmid and insert, and both were eluted in elution buffer.

A eukaryotic tissue panel of mouse liver, mouse kidney, and rabbit aorta was acquired and the Qiagen RNeasy Mini Kit with DNase digestion protocols were utilized to extract RNA. Tissues were cleaned with PBS and tissue lysed in RLT Buffer by pipetting. Supernatant from the tissue lysing was mixed with 1 volume of ethanol, centrifuged, and underwent DNase digestion to digest remaining DNA. After which, a DNase incubation mix containing 10 μ L of DNase 1 to 70uL of Buffer RDD was added to the supernatant sample, incubated on the table top for 15 minutes, and spun down by centrifuge. The remaining samples were washed with Buffer RWI and measured for concentration.

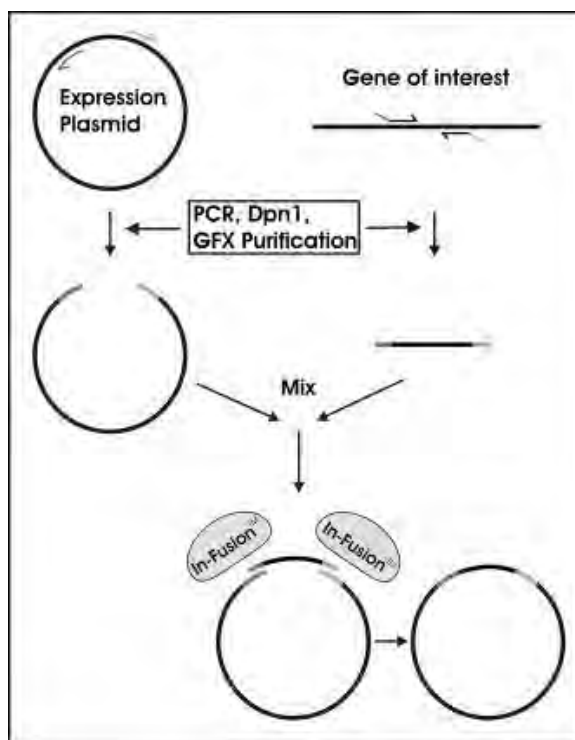


Figure 3: The schematic representation of the process demonstrated by by Benoit *et al.* (Benoit *et al.*, 2006, *Protein Expr. Purif.*)². The right side of the graph demonstrates the isolation of the gene of interest, in this case DPY-19L4, which is cut out of the chain, amplified via PCR, DPN digested with DPN1, and then mixed with plasmid within the InFusion cloning mixture. As such, the left side of the graph depicts the separation of the tails within the plasmid that are homologous to the gene insert. The plasmid undergoes linearization through PCR and is also DPN digested with DPN1 before being mixed with the insert.

RESULTS

Linearization of pcDNA3.1 has demonstrated successful results, however low levels of L4 present during DPY-19L4 amplification have become difficult for insertion. Very small amounts of DPY-19L4 were able to be amplified by PCR techniques. Both the pcDNA3.1 plasmid and the DPY-19L4 insert demonstrated, though, that the temperature range used in the annealing range did not

matter. A range from 65°C to 75 °C was used in the annealing step and both the linearized plasmid and the amplified DNA had steady bands present across an agarose gel (Figure 4). Both samples were able to undergo DPN digestion at this point, and DPN1 was utilized as the medium. The yield of the insert after DPN digestion was not incredibly successful, and further attempts were made to amplify more insert in the PCR step before digestion so the sample would not be destroyed in the process. However, a malfunction with the fridge in the lab caused a loss of DPY-19L4 and pCDNA3.1 template samples. As stated in the methods, a pCDNA3.1 culture was plated on agar plates containing ampicillin and underwent liquid cell culturing and mini-prep protocols to isolate and elute the plasmid. Re-culturing DPY-19L4 alone was not so easy, and even with a standard ten-fold dilution and plating on agar plates containing ampicillin, after overnight incubation the pCDNA3.1-DPY-19L4 cultures that were plated were overgrown.

At the same point, three eukaryotic tissue samples were obtained that included mouse liver, mouse kidney, and rabbit aorta. The Qiagen RNeasy mini kit was used to spin down the tissue samples and harvest RNA. All three tissue samples underwent the PCR process as described by the Qiagen RNeasy mini kit, including the protocols for DNase digestion. The final concentrations for the RNA samples are displayed in Table 1 below. All samples show a significant yield to be utilized in a TaqMan Gene Expression Assay.

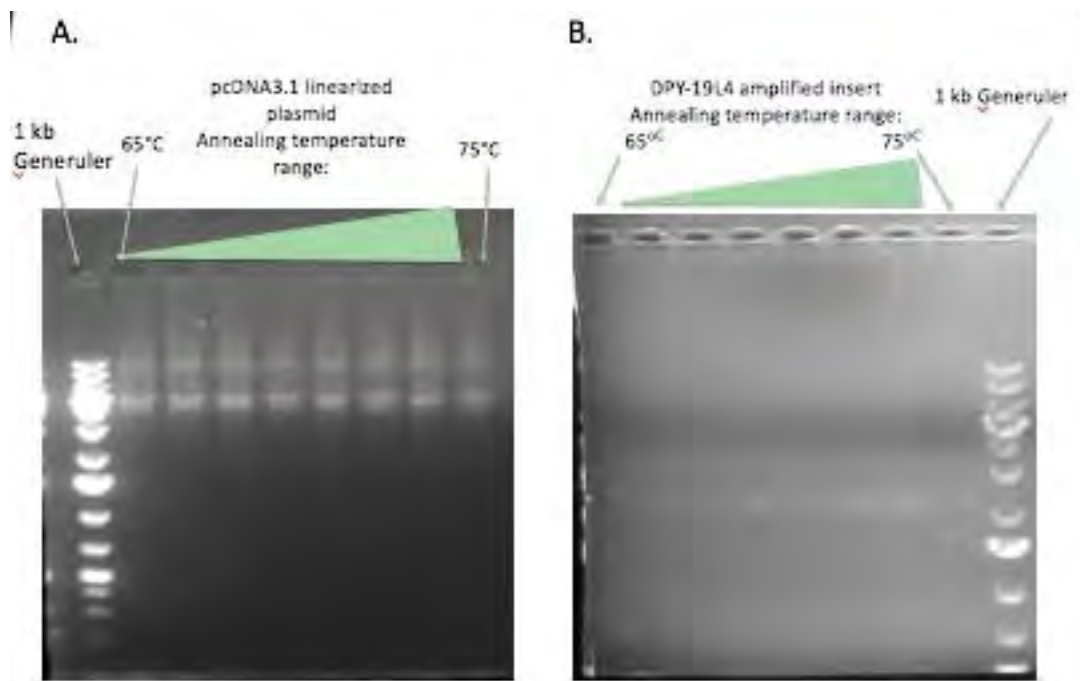


Figure 4: (A) Agarose gel of linearized pCDNA3.1 plasmid over the annealing temperature range of 65°C to 75 °C as compared to a 1kb Generuler. (B) Agarose gel of amplified DPY-19L4 insert over the annealing temperature range of 65°C to 75 °C as compared to a 1kb Generuler.

Species	Tissue	Concentration of RNA (ng/ μ L)
Mouse	Liver	28.3 ng/ μ L
Mouse	Kidney	28.8 ng/ μ L
Rabbit	Aorta	40.4 ng/ μ L

Table 1: The depiction of the eukaryotic tissue panel utilized for this research. The species and type of tissue is shown with the concentration of the RNA after using the Qiagen RNeasy mini kit to obtain a sample of RNA and digest down any remaining sample of DNA present in the supernatant. The concentrations above are all high enough to be used in a TaqMan Gene Expression Assay.

CONCLUSION

Major conclusions from this research are still limited. However, from the work performed above, it can be concluded that small amounts of DPY-19L4 insert are able to be amplified using PCR. Likewise, the pCDNA3.1 plasmid can be linearized using the same process and ligation must be used to combine the two together. This is significant, as the process is easy and cheap, and can be performed on the other three homologs of DPY-19 (L1, L2, L3) for further analysis. Also, it is apparent that significant amounts of RNA are able to be obtained through Qiagen RNeasy Mini Kit protocols, and that these concentrations of RNA are able to be used in further expression research.

FUTURE PLANS

Further plans for this research are soon to be underway. A TaqMan Gene Expression Assay primer has been bought for all four homologs of DPY-19 (L1, L2, L3, L4). Through reverse transcriptase and PCR, an assay will be performed on the RNA samples from the eukaryotic tissue panel above for all four homologs. Likewise, a greater sample of tissues will be obtained and added to the panel to further map the expression of DPY-19. Once gene expression within these tissues has been mapped sufficiently we will have a better idea on how to approach this research biochemically to isolate and observe the enzymatic activity within different parts of the body.

DISSEMINATION AND PROJECT WORTH

This project was disseminated through a poster presentation at the 2016 meeting of Experimental Biology which includes six separate societies including the American Society for Biochemistry and Molecular Biology. The meeting was held in San Diego, California from April 2 to April 6, abstract number 624.2: "Investigation of Enzymatic Mechanism and Cellular Expression of DPY-19L1 and DPY-19L4". Attending a conference as large as EB opened up routes that were incredibly beneficial to our research, as during the poster session, I presented alongside Dr. Haltiwanger from the University of Georgia who offered to send our lab a recipe for competent cells that would transfect DPY-19 inserts much more sufficiently than HEK293 cells.

As always, this project constantly teaches about the importance of lab safety and aligning to proper lab procedures. Working with something as small as an enzyme truly tests the ability of a scientist to perform the experiments free of contamination. Furthermore, my personal plans after obtaining my undergraduate degree include attending the University of York for a master's degree in bioarchaeology. The research that will be associated with my master's degree will still follow the field of proteomics, specifically analyzing proteins that have remained on or in Roman

archaeological artifacts not only to provide insight into ancient life through archaeology, but also to determine why those certain proteins managed to survive and remain intact into contemporary time. Therefore, the usage of PCR techniques, transfection, cell-culturing, and overall analysis will provide invaluable in my academic future.

ACKNOWLEDGMENTS

A large thanks goes out to the NASA West Virginia Space Consortium for funding in this project, Dr. John Rakus of Marshall University's Department of Chemistry for mentoring and advising this project, Dr. Elizabeth Murray of Marshall University's Department of Integrated Sciences and Technology for the assistance in development of an RT-PCR probe suitable for usage on DPY-19L4, and to Dr. Leslie Frost of Marshall University's Department of Chemistry for access to the tissues utilized in this research.

REFERENCES

- ¹Buettner, F.; Ashikov, A.; Tiemann, B.; Lehle, L.; Bakker, H.: C. elegans DPY-19 Is a C-Mannosyltransferase Glycosylating Thrombospondin Repeats. *Molecular Cell*. 50. 295-302.
- ²Benoit, R.M. et al. 2005. "An improved method for fast, robust, and seamless integration of DNA fragments into multiple plasmids." *Protein Expression and Purification* vol. 45, no. 1 66-71..

ANALYTICAL COMPARISON OF ELECTRODE MATERIAL FOR USE WITH PLASMA DIELECTRIC BARRIER DISCHARGE ACTUATORS WITH EXPERIMENTAL VALIDATION

Magdalena Krasny
Mechanical and Aerospace Engineering
West Virginia University
Morgantown, WV 26506

ABSTRACT

Plasma actuators have become increasingly popular among researchers as a potential solution to enhance aerodynamic flow control. Recently there has been a strong push for optimizing these actuators by lowering the overall cost and increasing their overall capabilities in enhancing flow control. While there are several types of plasma actuators, including glow discharge and resistive barrier plasma actuators, the dielectric barrier discharge (DBD) actuator has shown promise and received a substantial amount of attention as a potential tool for augmenting flow control. The DBD actuator is composed of three main components used in the generation of plasma, and in turn, flow control. The three elements are the electrical generating system, the dielectric material, constructing the actual barrier, and the electrodes. The electrode material plays an important role in the actuator's robustness and economic feasibility as well as the quality of plasma discharge generated.

Five electrode materials were selected to undergo experimentation based on conductivity, the work function of the material, the cost of the material, the thermal expansions coefficient, and the ease application in order to allow for robust flow control and commercial viability of developed actuator. The vast majority of any research done with DBD actuators has solely utilized a standard copper electrode. The four materials that underwent testing were compared to this standard. Titanium, Tungsten, Stainless Steel, and Graphite were selected based on their projected ability to produce a robust and high quality plasma. By finding an ideal electrode material, the DBD plasma actuator developed with this electrode will be a more robust product with greater mechanical strength over time with the ability to withstand higher temperatures. Finding an ideal electrode material will also aid in the improvement of the overall quality of the plasma discharge, and in turn improve the actuator as a tool for flow control.

BACKGROUND

The capability to manipulate flow over aircraft wings promises to yield a great number of benefits. A main focus within the flow manipulation has been concerning the boundary layer of the fluid. Controlling the boundary layer allows for increased lift performance and drag reduction, which could promise increased maneuverability and lower fuel consumption (Erfani et al., 2014). DBD actuators are a flow control technique that has shown a substantial amount of promise recently. The typical DBD system comprises of two electrodes separated by a thin dielectric layer. Popular materials for the dielectric layer are Kapton, glass, quartz, and ceramics (Vasile et al., 2015). The electrode below the dielectric is grounded and the exposed electrode is connected to a high voltage

supply. A typical voltage required is approximately 10 kV, and the AC frequency is in the kHz range (Erfani et al., 2014). When the DBD actuator is turned on, the purplish glow of the plasma is visible originating from the exposed electrode. The plasma produces a steady jet that flows away from the exposed electrode and across the grounded electrode. DBD actuators are incredibly lightweight and flexible. As there are no moving parts, the actuators are easy to repair and as they are electric, they can easily be turned on and off, or even programmed to turn on and off at regular intervals (Jahanmir et al., 2015). Currently, DBD actuators are being optimized in order to maximize the induced velocity by manipulating the electrode material and the geometry of the electrodes.

EXPERIMENT

Selection Process

Four materials were selected to undergo experimentation based on conductivity, the work function of the material, the cost of the material, the thermal expansions coefficient, and the ease of application in order to allow for robust flow control and commercial viability of dielectric barrier discharge actuators. Copper 110 was to be used as a comparable standard, as the vast majority of research done with DBD actuators has involved copper. The three other materials to undergo testing will be titanium, tungsten, and stainless steel.

Each material has been effectively utilized as an electrode material for a variety of other applications including vacuum filaments and for naphtha cracking. Titanium was selected due to its excellent corrosion resistance and strength to weight ratio. Tungsten has been used to produce extremely high quality plasmas, and exhibited a substantial amount of potential for use with DBD actuators. Austenitic stainless steel was selected as it is the most common type of steel and possesses a higher resistance to corrosion. (Jahanmir et al., 2015) Stainless steel is also one of the most common electrode types besides copper.

Actuator Assembly

Each actuator was assembled with a constant dielectric of glass. Two glass slides were implemented in the construction of the actuator. One slide provided a barrier between the table surface and the actuator, while the other acted as the dielectric material for the actuator. Each electrode material was purchased in the form of a 1/32" foil. Two 4" long electrodes were then cut from each individual material to act as the encapsulated and exposed electrodes. For each actuator the electrodes were adhered to the glass dielectric with an aqueous adhesive to avoid accelerating electrode oxidation and overall decay of the material. The configuration of the DBD actuator can be seen in Figure 1.

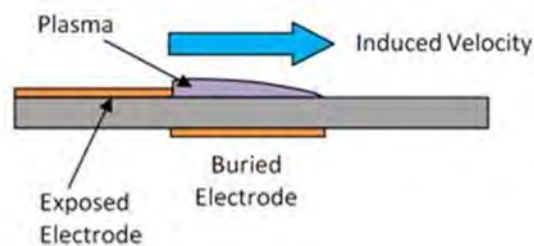


Figure 1. DBD Actuator Geometry (Erfani)

Testing

The actuator was connected as shown in Figure 2. The overall purpose of the circuit configuration was to provide a large voltage through the actuator without compromising the integrity of the equipment or the assembled actuator. The BK Precision 4054 signal generator supplied 2KHz sine wave to the Crown XTi 4002 Power Amplifier that increased the signal before it reached the transformer. A Corona Magnetics Step Up Transformer was then implemented to step up the

voltage and step down the current. The transformer had a winding ratio of 1:140, which allowed for the increase supplied AC signal. The actuator was then connected to the transformer and grounded. A constant 14 kV was supplied to the actuator, using the oscilloscope to view the signal.

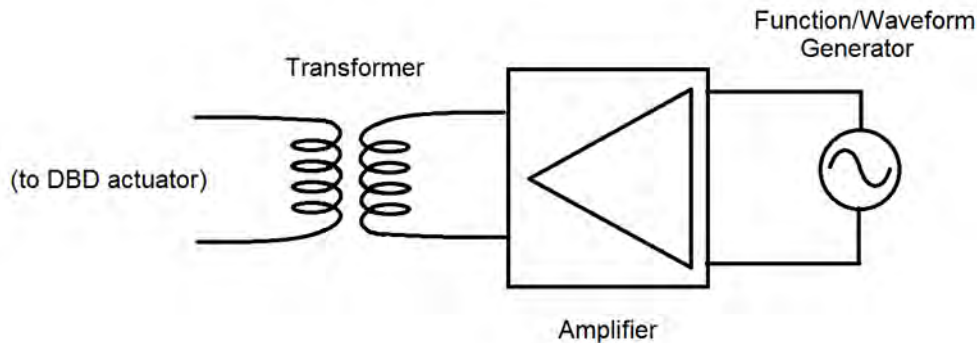


Figure 1. Circuit Schematic for DBD Actuator

The plasma generated by each individual electrode was then visually observed to determine the overall quality of the actuator. The plasma was then directly observed under a microscope with a Nikon D7100 digital single lens reflex (DSLR) camera. The light sensitivity of the camera was set to Nikon's proprietary Hi 0.3 setting, to give an ISO equivalence of 8000, in order to fully read the light emitting from the DBD actuator. The exposure time was also set accordingly with a shutter speed of 5 seconds.

RESULTS

Each image below depicts the plasma field that developed from each different actuator. The plasma flow begins at the bottom-most edge of the exposed electrode (the dark black line at the top of each image) and extends over top of the encapsulated electrode. For a plasma DBD actuator, the field needs to be as diffuse and consistent as possible. In contrast to diffuse plasma, filamentary plasma has distinct separated fingers of varying plasma quality flowing throughout the extent of the plasma region, causing inconsistencies throughout the plasma field. As the quality of the plasma directly affects its capabilities for airflow manipulation, actuators that create a more filamentary plasma are less than ideal.



Figure 36. Copper Plasma Field



Figure 37. Stainless Steel Plasma Field



Figure 38: Titanium Plasma Field

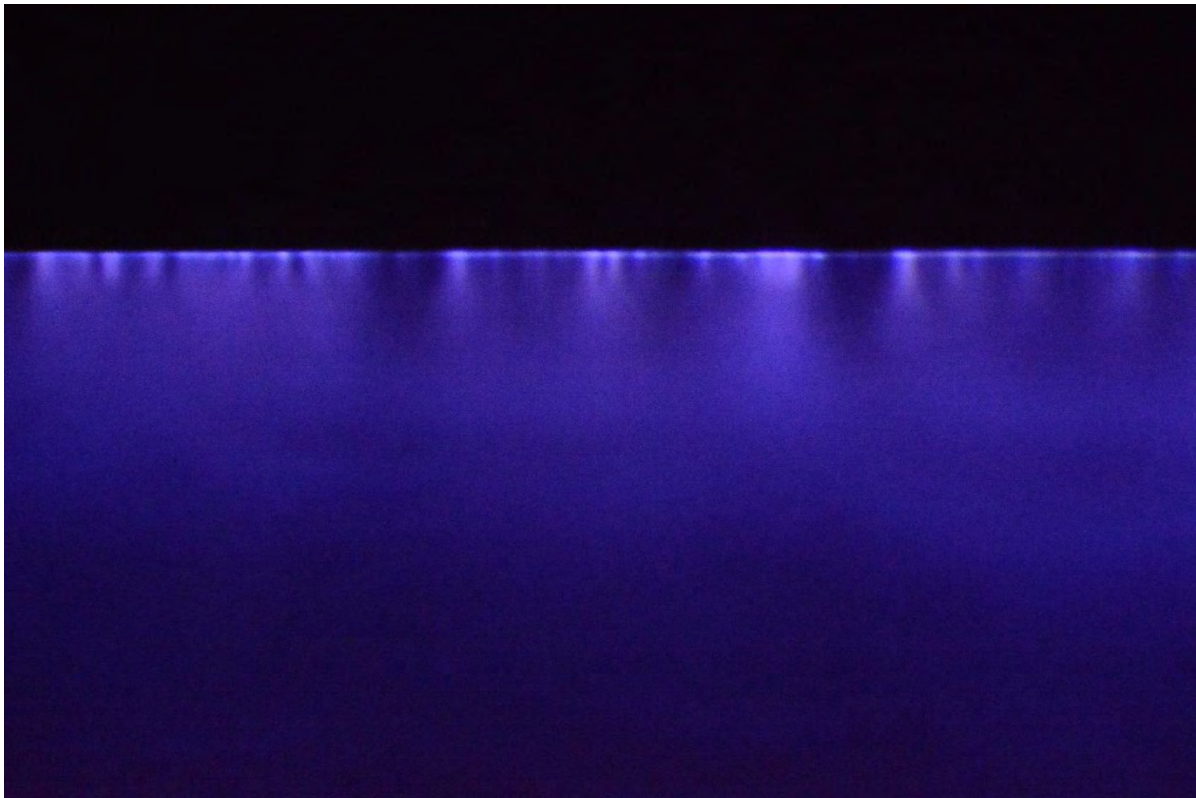


Figure 39: Tungsten Plasma Field

DISCUSSION

Each different electrode generated plasmas of varying quality. The plasmas were visibly different to the naked eye, and the different actuators produced a distinctly different sound when being tested. Copper, stainless steel, and tungsten maintained a relatively constant plasma field composition throughout the duration of testing. Titanium initially produced a diffuse plasma that began visibly decayed throughout the testing process.

The plasma developed by copper had visibly obvious filaments that extended throughout the field. Within the span of the photographed field waves developed horizontally throughout the plasma. Despite the filaments and waveforms, the intensity of the copper field is mostly consistent and even throughout. While not an ideal field, the copper actuator is definitely a viable option.

Stainless Steel was not as consistent as copper near the beginning of the plasma field, however as the field progress it became much more diffuse and homogenous throughout. Stainless Steel also produced the most robust plasma of all the actuators tested. It is visibly brighter and more intense than the other tested actuators. However the actuator developed a visible wave pattern on a section of the actuator. This could be contributed to a flaw in the material used in the construction of the actuator.

Titanium was incapable of maintaining an even plasma field for any duration of time. Initially, titanium seemed to produce the most robustly diffuse plasma field. Upon further investigation the plasma field became incredibly uneven with strong filaments cutting through the developing field. Due to the sporadic nature of the plasma from titanium, it is not a recommended material for applications where quality and consistency of the plasma field is considered.

Overall, the field produced by tungsten was much more even than any of the other actuators. While it was initially filamentary, the filaments did not extend throughout the plasma. The field produced by tungsten was comparable to copper, although slightly more robust, and the plasma field produced by Tungsten was more evenly distributed throughout the field area.

In terms of diffusivity, Tungsten and Stainless Steel produced the most evenly diffuse plasma.

Stainless Steel produced a substantially stronger plasma field than any other electrode material.

CONCLUSION

Electrode Material has a distinctive impact on the plasma quality generated by a Dielectric Barrier Discharge Actuator. Each electrode material generated a unique plasma field configuration visible in Figures 4-6. Based on the electrodes sampled, the DBD Actuator constructed with Stainless Steel generated a visibly stronger plasma when directly compared with the other actuators. Tungsten was comparable in diffusivity but lacked the overall robustness of the Stainless Steel. The use of Stainless Steel as an electrode also allows for a more cost effective construction as opposed to Tungsten.

Future research could implement the use of alloy electrode materials, such as Copper Tungsten. Copper Tungsten is a metal matrix composite that combines the properties of Copper and Tungsten, resulting in a heat resistant and highly conductive material, and could possibly produce

a quality and enduring plasma. Carbon steel also has shown promise when implemented as an electrode for use in a variety of applications. These different metals could further optimize the design of the DBD actuator and further its potential for use in aerodynamic flow control applications.

ACKNOWLEDGEMENTS

This research was made possible by the NASA West Virginia's Space Grant Consortium Undergraduate Fellow program.

I would like to express my appreciation to Dr. Patrick Browning and Joseph Dygert for their support and guidance throughout the duration of the fellowship.

REFERENCES

- Erfani, Rasool, Hossein Zare-Behtash, Craig Hale, and Konstantinos Kontis. "Development of DBD Plasma Actuators: The Double Encapsulated Electrode." *Development of DBD Plasma Actuators: The Double Encapsulated Electrode*. Science Direct, 30 Dec. 2014. Web. 6 July 2015.
- Jahanmiri, A., M.r. Rahimpour, M. Mohamadzadeh Shirazi, N. Hooshmand, and H. Taghvaei. "Naphtha Cracking through a Pulsed DBD Plasma Reactor: Effect of Applied Voltage, Pulse Repetition Frequency and Electrode Material." *Chemical Engineering Journal* (2012): 416-25. Elsevier. Web. 25 Feb. 2015.
- Joussot, R., A. Leroy, R. Weber, and D. Hong. "Plasma Morphology and Induced Airflow Characterization of a DBD Actuator." *Universite D'Orleans*, 25 Feb. 2013. Web. 6 July 2015.
- Vasile I Pavulescu, Monic Magureanu, Petr Lukes. *Plasma Chemistry and Catalysis in Gasses and Liquids*. Weinheim: Wiley-VHC, 2013. Web. 02 Mar. 2015.

TERRA RESPONSE – DETECTION OF UNDERGROUND ANOMALIES

Samantha Melroy
Mechanical Engineering
West Virginia University
Morgantown, WV 26506

ABSTRACT

Terra Response, LLC is an underground anomalies detector company with patent pending technology to detect metallic and nonmetallic objects up to 100 feet from earth's surface. It does so by using earth's naturally occurring electric field to find differentials that obscure, or interfere, with the ray. Many types of location systems are available, such as ground penetrating radar (GPR), but have many handicaps including the inability to use in wet soil and unable to detect some objects that interfere with the GPR technology. A lightweight, inexpensive detector of water, voids, PVC pipe, metal, and bone, just to name a few, is to be described for the duration of this paper. All the parts are lightweight, inexpensive, and are readily available. Descriptions of current technology and the billion dollar market will be discussed along with the prototype technology.

INTRODUCTION

Sensing the presence of subsurface objects and underground utilities can save time and costly explorative excavation. The danger of inadvertently cutting into high-energy electrical lines, high-pressure water pipes, or lines carrying explosive fuels can be greatly mitigated if remote sensing is able to locate these hazards prior to excavation. Terra Response offers a novel and patent pending technology to individuals in the energy sector who need a lightweight, portable, easy-to-use and reliable underground detection solution.

This technology passively interprets variations in the low-level radiation naturally emitted by the Earth in order to monitor, detect, and characterize subsurface objects. Using only a handheld, aboveground detection device, the depth, size, and composition of subterranean anomalies can be determined. This technology will revolutionize the energy sector by providing a simple and inexpensive method of identifying underground utilities, voids, and other buried materials, increasing the efficiency, scalability, and safety of new construction and utility maintenance.

Current subterranean inspection technologies are limited either in scope or convenience of use. Modern metal detectors, while portable and lightweight, are less sensitive to non-ferrous metals than ferrous ones, and are completely incapable of sensing non-metallic obstacles. Metal detectors are also unable to determine the composition, depth, or size of the objects they locate. More complex systems, such as ground-penetrating radar, are capable of sensing the size and depth of underground anomalies, but are expensive, heavy, and cumbersome. It can be very inconvenient to operate such systems over rough, undeveloped terrain and must be used by a trained person.

As stated in the proposal a model of the device will be made and field testing will be done to advance the state of the technology.

BACKGROUND

Currently, some more widely used methods of subsurface utility detection include excavation, ground penetrating radar, acoustic location, and conduction/induction techniques [1] [2]. As mentioned previously, each system offers unique advantages and disadvantages, but not one demonstrates the overall effectiveness that Terra Response has to offer, especially concerning plastics and passiveness. For example due to the spectrum analysis it can detect anomalies buried deeper than most hand held detection methods on the market today. The technology also allows for detection of a vast array of materials, specifically nonmetallic materials which makes Terra Response stand out amongst the competition. No one method has been accepted as a standard within the detection fields and methods are selected based on the demands of individual applications. Terra Response aims to become the standard for subsurface utility detection as the technology develops. Terra Response has the potential to be the standard underground detection company in the billion dollar market.

Ground penetrating radar (GPR) has emerged as the most effective method within the utility detection industry due to its ability to locate nonmetallic objects. GPR systems work by sending a tiny pulse of energy into a material via an antenna. An integrated computer tracks the strength and time of any reflected signal to map below the surface [3]. This is essential as companies use plastic, more frequently than metallic, piping for their underground needs based on its cost and non-corrosive properties [4]. GPR also offers the ability to detect voids and density differentials located underground, where backfill from previously excavated trenches, mines, wells, caves and tunnels may be located. However, GPR is incredibly costly; individual units can be priced up to \$100,000 and GPR technicians require extensive training in order to ensure consistent, high-quality results [4]. The high cost of the units, joined with that of technician training are reflected in the prices that GPR firms are able to charge for their services. Additionally, GPR units are generally unwieldy and difficult to use as a hand-held unit, and despite its ability to detect plastics and other non-metals, the method is limited to ideal ground conditions, and in non-ideal conditions, such as wet soil, the range of a GPR unit becomes severely limited and the technique becomes useless for many applications [5].

In addition to GPR, utility location firms also employ acoustic techniques. This method requires an artificial vibration that is physically introduced onto a pipe while highly sensitive microphones are employed to detect the acoustic waves generated as the vibration travels through the pipe. However, this technique is limited by the material of the pipe; acoustic vibrations travel notably more readily through metal than plastic, and acoustic location is restricted mainly to use with metal piping. Furthermore, acoustic location is limited by the condition that the pipe must be physically accessed at some point in order to induce the vibration; consequentially this becomes useless in the event of the pipe being inaccessible. The intensity of the vibration and sensitivity of the microphone must also be considered. High frequency vibrations do not propagate to the extent of low frequency vibrations, are more challenging to detect, and in addition they have highly sensitive microphones, consequently a higher cost associated with them. Finally, acoustic techniques are limited by the characteristics of the soil creating yet another disadvantage. Denser soils, such as clay, limit the propagation of the wave and limit the effectiveness of this type of detection along with it [5] [6].

Subsurface utility detection methods also include electronic induction, conduction, and passive techniques. Inductive and conductive methods are strictly limited to electronically conductive materials, such as metal, and even so, insulation can pose a problem to both techniques. The limitation of electric conductivity makes plastic detection impossible. Title 49 of the Federal Code of Regulation, Section 192-321, now requires that all plastic pipe installed underground be equipped with conductive “tracer” wire or alternate means to assist locating methods. This tracer wire results in \$7 million annually. Additionally, passive detection is limited to lines that normally carry a detectable electric current, including telecommunication and electric utility lines [6].

Induction transmits an electronic signal into the ground that induces a charge onto the utility that, in turn, transmits its own signal that can be detected by a receiver at the surface. A primary advantage of induction is its ability to remotely detect objects where the unit is not required to be in direct contact with the utility. However, this also implies that there can be some difficulty coupling the utility with the transmitted signal and also coupling the induced signal with the receiver. Induction techniques can sometimes be affected by interference. For examples power lines in the area can generate their own signal that may interfere with the induction readings. With induction, the transmission is not strictly directed into the ground and can be recognized by other metal materials in the area, such as fencing, which will produce their own signal which again will interfere with the readings. Also, the range of induction techniques is limited by the size of the utility; larger utilities can be detected at greater depths, while smaller utilities become less detectable as depth increases [7].

Terra Response Technology combines all of the good qualities of current detection techniques while eliminating the draw backs. The technology allows for the detection of non-active utility lines without the fear of interference that can be found with induction techniques. The technology also does not require any connection to what it is detecting required for some pipe and cable locators. It allows for the detection of non-metallic anomalies and a fraction of the price of GPR. Two of the largest and have the most market depth are MALA Geosciences and Geophysical Survey Systems, Inc. (GSSI). Both have portable systems with the MALA Easy Locator ranging from \$11,000 - \$18,000, and the GSSI ranging from \$13,000 - \$100,000, with an average per unit cost of \$25,000 [8].

The Terra Response technology uses Earths signal, modified by the weakening in the magnitude and other properties; this should be most pronounced in close proximity and directly above the subsurface object. Figure 1 illustrates this general idea, although possible diversion of the signal on the subsurface object may create more complicated effects than Figure 1. [9]

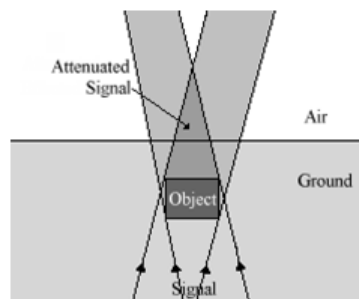


Figure 40: Object affecting directional signal [9]

The nature of the distortions will be characterized by the differences in material properties between the subsurface object and its surroundings. The most influential of these electromagnetic properties are conductivity, permittivity, and permeability. These are in turn affected by other properties, such as material porosity, size, shape, and moisture content. Figure 2 shows the electric field intensity in and around an object in a uniform field. Figure 3 displays the polarization charge density responsible for distortion of fields. [9]

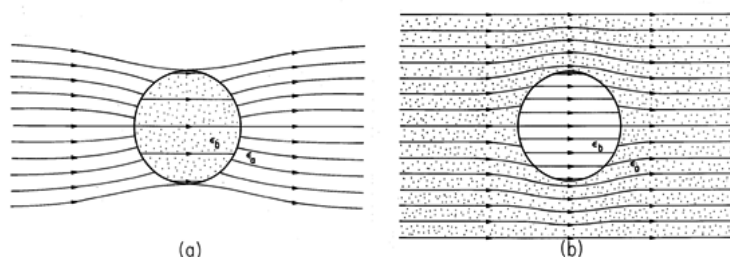


Figure 2: Electric field intensity for (a) $\epsilon_b > \epsilon_a$; and for (b) $\epsilon_b < \epsilon_a$. [9]

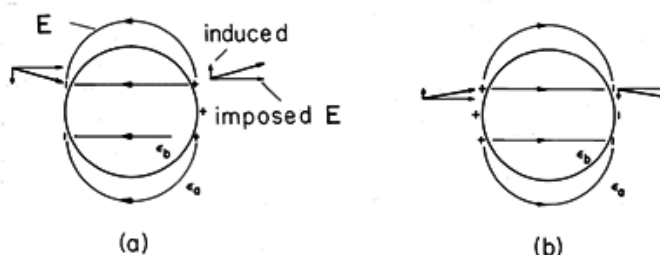


Figure 3: Surface polarization charge density responsible for distortion of fields. [9]

MARKET SUMMARY

The market for the detection of anomalies, or man-made artifacts, is large and diverse. For example, with counter-IED efforts through the military, the total yearly detection equipment and professional service expenditures are over \$6 billion. Similar dollar amounts, of the same order of magnitude, can be shown for metal and other man-made structures in applications comparable to gate- and threshold-metal and explosives detection, plus chemical detection. Additionally, a field of study has sprung out of these types of needs and efforts called Subsurface Utility Engineering, which specifically looks to find the buried utilities as a means to insure proper placement and protection and often more importantly to reduce financial and personnel risk to mitigate loss due to incurred liabilities and negligence.

While there are commercial systems that are directed at the resolution of specific buried objects such as metal detectors for metallic objects and ground penetrating radar for size, shape, and specific material properties, all of these commercially available systems are active in nature, in contrast to the passive and much less expensive system to own and operate is in the development by Terra Response, LLC. More importantly, the system under development is a universal system that looks for anomalies that can be differentiated from the surroundings. Therefore metal, plastics, tunnels, voids, etc. are all detectable with a passive system that can discern the materials' composition, size, and depth. These are attributes that no current system on the market can

accomplish, and not at a price that will allow the average workman to afford and have in his possession.

Based on the preliminary data obtained, where the market is considerably larger than the information supplied so far indicates, the detection of surface and sub-surface man-made objects of a variety of sizes and shapes, which are made from any variety of current man-made materials is a multi-billion dollar per year industry, both in system and professional service costs. This system is a total technical departure from the current detection systems that developed a sensor to detect a unique material property or feature of the target object. Terra Response, in contrast, has developed a sensor that passively uses the earth supplied electromagnetic signals to look for all differentiations from the surroundings and thus finds, evaluates and codifies each anomaly in the target area. Over sixty percent of underground utility damages in the United States occurs by contractors, most of which are phone lines [10].

Introduction

It is desirable to sense the location of subsurface objects from outside of the surface of the material in which it is encased (i.e. an object buried underground). Sensing the presence of subsurface objects can save time plus costly explorative excavation. Dangers related to digging up objects, such as explosive land mines, gas mains, or other utility lines, do not have to be contended with or can be reduced, if sensing from the surface locates the object prior to excavation. Plus, proper detection and identification can avoid possible damage through unguided excavation to the object being sought or adjacent unintended objects. Potential end users for such a system could include surveyors, contractors, excavation operators, on-site safety officers, general workers, archeologists, and soldiers.

Nondestructive testing and detection amounts to over \$600 million per year. Annual utility locating and detection market totals approximately \$1.6 billion per year. The military spends approximately \$6 billion per year on research and commercial device to detect anti-personnel mines and improvised roadside explosives.

Given these areas reflect spending only in the United States, the potential market for a device that could not only sense the presence, but determine the position, orientation, depth, and material composition of a subsurface anomaly, without physically disturbing the object or actively sending it electromagnetic energy, could be additional billions of dollars per year.

Current Available Systems

Current available systems for actively detecting underground objects include ground penetrating radar, and handheld metal detectors.

Ground penetrating radar (GPR)

There are approximately 10 commercial GPR manufacturers in the world. Two of the largest and have the most market depth are MALA Geosciences and Geophysical Survey Systems, Inc. (GSSI). Both have portable systems with the MALA Easy Locator ranging from \$11,000 - \$18,000, and the GSSI ranging from \$13,000 - \$100,000, with an average per unit cost of \$25,000 [11]. Currently, there are approximately 1,000 working systems among research, industry, commercial, and universities facilities in the United States. [11]

Handheld metal detectors

Handheld metal detectors, are perhaps the most affordable and readily available piece of equipment, "... are used in airports, government buildings, military operations, manufacturing facilities and other locations that require the detection of metal where it is not easily visible," according to the Metal Detector Manufacturing Industry in 2012. Ranging from \$150 to \$25,000 [12], these portable, handheld metal detectors produce a market size in the United States alone of approximately \$800 million. [13]. It has been estimated that, in 2011, upward of 47,000 of these handheld metal detectors were sold [14].

Potential Systems Applications

Although there is not a current, specific market for such a device, the subsurface anomalies detector could be successful in applications such as mineral prospecting, nondestructive testing, military/defense scenarios, treasure hunting, as well as locating underground structures and utilities.

Prospecting for minerals

In the detection range of the subsurface anomalies device, prospecting for minerals would be limited to rare stones and ores that are above the bedrock. Amateur prospecting, in recent years, has been booming due to unusually high market prices for silver and gold. It has been suggested that this yearly market is approximately \$500 million [12].

Nondestructive testing (NDT)

Nondestructive testing, as its namesake suggests, is very popular because the object to be tested does not have to be sacrificed, replaced, or in most cases moved or brought offline. For these reasons, test objects are often structural, delicate, or not easily replicable. One area of NDT uses ultrasonic systems, in which a suggested market valuation is \$615.5 million Error! Reference source not found.Invalid source specified.

Military and defense

Used for defense and general readiness, there are several areas in which the military currently, actively has a need for subsurface anomalies detection. Two of the most predominant areas include mine detection and improvised ordinance detection. Anti-personnel mine detection for the U.S. alone nets a market valuation of approximately \$443.7 million [15]. In addition, recent research and products for detection of improvised explosive devices (IEDs) suggest a U.S. military market alone of between \$298.6 million [15] to \$6 billion [16].

Locating underground structures and utilities

Perhaps the largest domestic market for subsurface anomalies detection is for locating underground structures, voids, or utilities. This market includes (1) pipes and conduits, power lines; (2) Sewage, water, and gas mains; (3) Street lighting and signal cables; and (4) Telecommunications, including phone, CATV, and CCTV feeds. Combined, the suggested valuation is approximately \$1.6 billion. [17]. This method may potentially be more beneficial due to the idea of a lightweight and portable system that is capable of detecting non-metallic anomalies. Since not all pipelines are metallic in nature and GPR can be bulky and costly, this new method of detecting anomalies can save time, money, resources, and energy.

RESEARCH RESULTS

Design

The Terra Response CAD model is shown in Figure 4a while the prototype is shown in Figure 4b. A prototype was built off of these specifications and used to print 3D models of various parts. The prototype is about the size and weight of a handheld metal detector. The structural system of this prototype is made of PVC pipe; this was used for cost and convenience reasons. The clamps (in yellow, blue and green at the base of the model) were made using a 3D printer. Additional 3D printed parts include the green box by the clamps and the red screen tilt. The antenna, not shown, would be placed in Clamp C. Clamp B connects Clamp C to the PVC Pipe while Clamp A connects the Electronic Container to the PVC Pipe.



Figure 4: CAD Model and Prototype

The data collected with this prototype has significant errors. These errors can include the signals from the PRT, AM radio and noise. The next section will discuss field testing and the tests that were completed using this prototype.

Field Testing

In the field testing stage of this research project specific guidelines were followed. A testing matrix was determined according to the different materials. As shown in Figure 5, the testing matrix was composed of a storm drain, asphalt, concrete and grass; an image of the test loop; this clearly indicates four different materials to be measured. Clearly this is the most efficient way to determine if the system works with the indicated fields.

The test completed was using a General Radio Co. Test Loop, as the antenna, with a data collection software, ProScope. This antenna was chosen because it is lightweight, inexpensive and has a large radius for data collection, while the ProScope was used because it is lightweight, small and will collect the needed data. The test was approximately 2.6 seconds long. This created 262,155 data points to plot. As shown in Figure 5, there is no difference between each of the materials tested. The test's data shown is saturated and possible reasons for the data include noise, radios, and the nearby PRT.

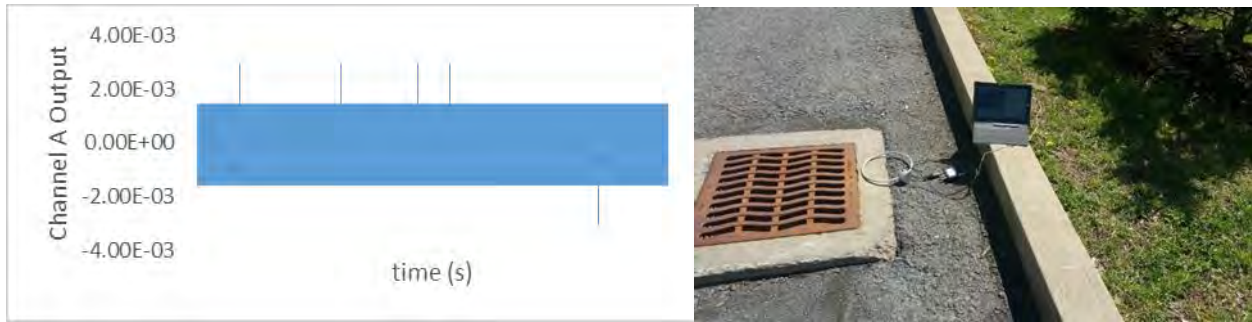


Figure 5: Data from test and testing matrix (storm drain>concrete>asphalt>concrete>grass)

Due to the data being saturated with the test, added is a graph of this technology in a larger form. This test was used using a heavy antenna but displays that this technology does in fact work. Figure 6 displays a test from HPI Proprietary with the same technology use. This test was used with heavy expensive equipment. The figure shown that the antenna went over Hains Point Metro Tunnel, Hains Point Overpass, Hains Point Underground Utilities, Hains Point Overpass and Hains Point Metro tunnel; a map is shown in Figure 6. From the figure, it is shown where those were passed in yellow. There is slight discrepancies due to other signals including radio signals but the accuracy displays that this technology has the capability to do amazing things.

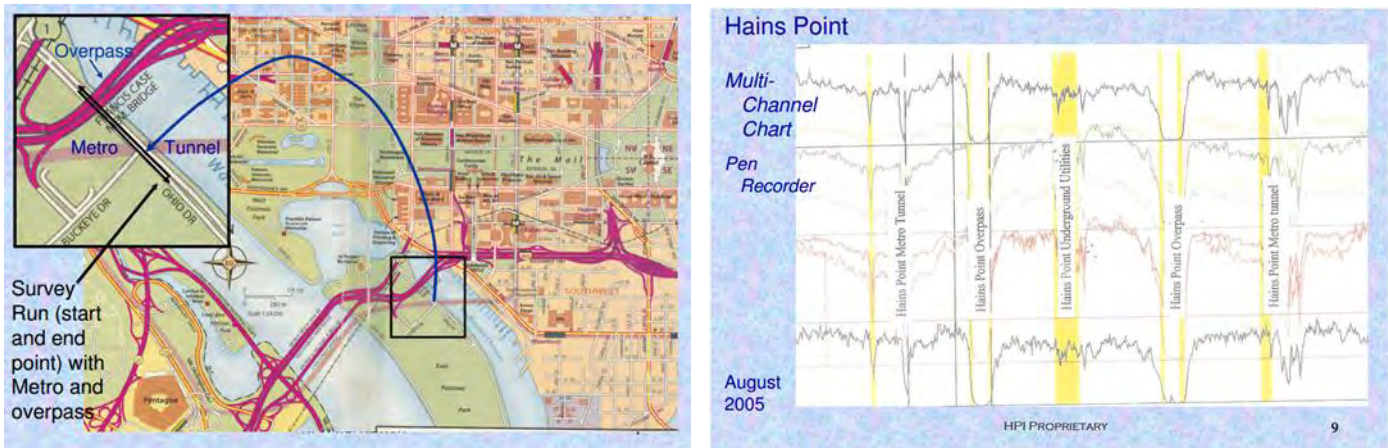


Figure 6: Helms Point Imaging Corporation test [18]

FUTURE ENDEVORS

Future opportunity with this technology includes more testing with higher grade equipment. With this higher grade equipment the cost of the testing will increase but by slowly eliminating things that are found to be unneeded the cost and weight of this technology will decrease. Future goals of this technology is to create a simple, easy to use detector that will clearly map out underground anomalies with the addition of sensors and various software.

ACKNOWLEDGMENTS

I would like to thank West Virginia Space Grant Consortium for the opportunity given and the doors that have opened. I would also like to thank Andrew Lowery and my research mentor, James E. Smith, a professor in mechanical and aerospace engineering at West Virginia University. I have had the opportunity to work with many professionals to be able to have those hands on experiences we all need to truly understand how the world works.

REFERENCES

- S. Bender, "Natural Gas Measurement, Underground Utilities and More Blog," 15 April 2013. [Online]. Available: <http://www.lincenergysystems.com>.
- H. Scholzel, "A Summary of Pipe Location Technologies Compiled on behalf of Tonga Water Board," SOPAC , 1999.
- "Ground Penetrating Radar Frequently Asked Questions," Geophysical Survey Systems, Inc., [Online]. Available: www.geophysical.com.
- "Plastic Pipe," American Gas Association, [Online]. Available: www.aga.org.
- J. Rodriguez, "Utility Locator: Pipe Locators," About Money, [Online]. Available: www.construction.about.com.
- "Avoiding Utility Relocations," U.S. Department of Transportation Federal Highway Administration, [Online]. Available: www.fhwa.dot.gov.
- "Making locating Easier and More Accurate - Introduction," Ridge Tool Company, [Online]. Available: www.seektech.com.
- "Ground Penetrating Radar (GPR) - Fact Sheet," in *Geophysical Survey Systems, Inc.*, 2002.
- J. Smith, F. Pertl, R. Nutter and A. Lowery, "Method and Apparatus for Passive Detection of Near-Surface Human-Scale Underground Anomalies Using Earth Field Measurements". United States of America Patent US 20140266211 A1, 18 September 2014.
- "Damage Incident Statistics and Trends," Vermont Utility Damage Prevention, [Online]. Available: <http://damageprevention.vermont.gov/>.
- "Ground Penetrating Radar (GPR) - Fact Sheet," Geophysical Survey Systems, Inc., March 2002.
- "The Booming Business of Metal Detectors," Wall Street Journal Online, July 2011.
- "Metal Detector Manufacturing in the US Industry Market Research Report," IBISWorld, November 2012.
- "Message Board Post," Investorshub, 16 June 2014. [Online]. Available: http://investorshub.advfn.com/boards/read_msg.aspx?message_id=85961084.

"Global Anti-tank, anti-personnel, IED DEtection Systems Market by Product (Vehicle Mounted, Hand Held, Robotics, Biosensors), Application (Defense, Homeland Security and Commercial), Region & Country - Global Trends & Forcasts to 2014 - 2020,," Markets and Markets, April 2014. [Online]. Available: marketsandmarkets.com.

"Terra Acoustics Inc. Overview," Terra Acoustics, Inc., February 2010.

"United States Infrastructure Corporation: Setting High Marks in Underground Utility Locating," US Builders Review, 2013.

Geophysical Surveys Oil & Gas Exploration, Helms Passive Imaging Corporation, 2007.

PRECISE ORBIT DETERMINATION ON STF-1 CUBESAT MISSION

Nicholas Ohi
Mechanical and Aerospace Engineering
West Virginia University
Morgantown, West Virginia 26506

ABSTRACT

The objective of this project is to create, integrate, and test the flight software for the Global Positioning System (GPS) capability for the first spacecraft mission built entirely in the state of West Virginia, the NASA CubeSat spacecraft called Simulation To Flight 1 (STF-1). This report documents the development and integration of the GPS Flight Software (FSW) for STF-1, which falls under the mission's Science Objective 1 for precise orbit determination.

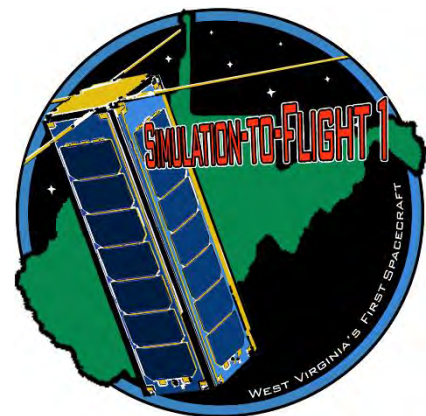
INTRODUCTION

This report documents the work I completed on the STF-1 GPS FSW during the 2015-16 school year. My project is focused on the development of the Global Positioning System (GPS) capability for STF-1, which falls under the mission's Science Objective 1 for precise orbit determination [Morris]. My work on the GPS FSW supports the effort of the overall GPS team towards the STF-1 Science Objective 1 and was conducted under the leadership and direction of Dr. Jason Gross, the STF-1 Principle Investigator for the GPS experiment. My work was supported by the West Virginia University Navigation Laboratory. The original hardware design for the STF-1 GPS experiment centered on the FOTON GPS receiver, but mid-way through the project, technical challenges led the GPS experiment team to decide to change to a NovAtel GPS receiver. To integrate with the STF 1 spacecraft, the GPS flight software has to be developed as a NASA Core Flight Executive (CFE) application. The GPS flight software has two major components: the Data Input Library (DIL) and the Telemetry Handler (TH).

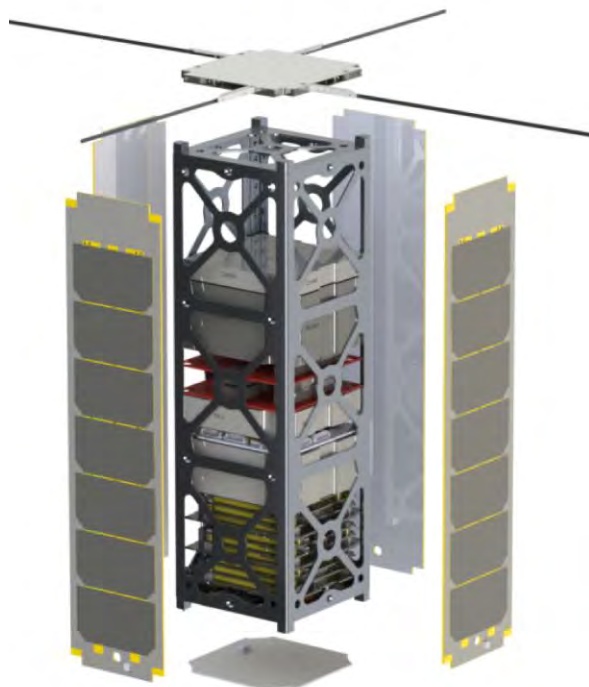
PROJECT

The Simulation-to-Flight 1 (STF-1) mission will be the first CubeSat from the state of West Virginia and has adopted the slogan "The Time is Now! West Virginia in Space". This project is a partnership between the NASA Independent Verification and Validation (IV&V) Program's Independent Test Capability (ITC) team and the West Virginia Space Grant Consortium and West Virginia University [Morris].

The NASA IV&V ITC team has developed a set of simulation technologies, called NASA Operational Simulator (NOS). The primary objective of the STF-1 mission is to demonstrate the utility of the NOS technologies across the CubeSat development cycle, from concept planning to mission operations. The STF-1 mission will demonstrate a highly portable simulation and test platform that allows seamless transition of mission development



artifacts to flight products. This environment will be highly portable and will decrease the development time of future CubeSat missions by lessening the dependency on hardware resources.



The secondary objective of this mission is to advance engineering and physical-science research currently being developed at West Virginia University. Specifically, the STF-1 mission has three science goals in the areas of navigation, magnetosphere-ionosphere coupling and space weather, and the performance and durability of III-V Nitride-based materials. As part of the science objective, the first goal of the STF-1 mission proposes to advance CubeSat navigation systems. This will be accomplished by demonstrating a new concept for inertial sensing that promises to enable a new class of inertial navigation performance by combining the output of many low-cost Microelectromechanical Systems (MEMS) Inertial Measurement Units (IMUs) to approximate the performance of a higher quality IMU. Additionally, the STF-1 mission will be equipped with a Global Navigation Satellite Systems (GNSS) space receiver that promises to significantly improve the Precise Orbit Determination (POD) on CubeSat

platforms. My project is to develop the flight software that enables the collection of GNSS data to support POD that will significantly enhance the value of other science data collected by this mission by providing an orbital position component to the observations from other instruments.

Advancing POD technologies will have benefits beyond the STF-1 mission. GPS POD on Low Earth Orbiting (LEO) spacecraft has achieved 1 cm level accuracy. However, the accuracy achieved on CubeSats has only been demonstrated to the 1-10 m level. Demonstrating improved accuracy of CubeSat POD on STF-1 will enable inexpensive, but impactful space-based scientific measurements on the CubeSat platform. In addition, the GNSS experiment will enable GNSS-based atmospheric sounding experiments on CubeSats. The GNSS receiver will be able to measure total electron content over a wider segment of atmosphere from space than from the ground. This will provide the opportunity to generate atmospheric temperature profiles with greater accuracy.

METHODS

I worked as part of a team with specific responsibility for the development and testing of the following software components:

- Low-level drivers in C for a space hardened GPS receiver.
- Command processing and telemetry generation capability integrated with the GPS drivers and designed to interface with the Goddard Space Flight Center (GSFC) developed spacecraft interrupt handler called Core Flight Executive (CFE).

This software is an essential component for accomplishing the STF-1 Mission Science Objective 1, where these flight software components provide the capability for collecting the data needed to accomplish the science objective. I used the following steps to accomplish the software development tasks: system and software needs analysis, software design and development, and testing.

System and Software Needs Analysis – The goal of this task was to obtain sufficient understanding of the system and existing software components, such that capabilities needed for the software to be developed can be identified. The high-level design for the STF-1 spacecraft had already been defined and was largely specified in the proposal submitted by the project team for this mission [Morris]. Throughout development, adjustments were made based on additional emerging information from developers of the hardware and other software components being integrated in this system.

Software Design and Development – The goal of this task was to establish an organized approach to the software under development. Software modules were identified and the software needs defined in the first step were allocated to each module. Interfaces with other system components were also addressed. The software source code was implemented and unit tested incrementally. Software documentation was automated by the use of Doxygen, to allow for easier maintenance for future WVU CubeSat missions.

Testing – The goal of this task was to verify that the software developed in the second step addresses the needs defined in the first step above. Once my algorithms were shown to be operating correctly, they were integrated with the other software capabilities of the system, such as the GSFC Core Flight Executive and the target operating system. A set of hardware integration tests are still planned to be conducted using GPS signal generators at NASA GSFC. The GPS signal generator will allow for an on-orbit environment scenario to be used to verify that the receiver and interface software function properly.

RESULTS

The results of the STF-1 GPS flight software project include the concept of operations, the subsystem architecture, software requirements, software design, and integration and test results. These results are presented below.

Concept of Operations

The concept of operations for the STF-1 Flight Software (FSW) is relatively straightforward. It must collect Global Navigation Satellite System (GNSS) data from an onboard GPS receiver. From the data collected from the receiver, the GPS FSW is to provide the computed navigation solution and GPS time to other software applications running on the STF-1 spacecraft. In addition, when commanded to run the full experiment, the GPS FSW is to relay the full GNSS data set to the telemetry handling application for downlink to ground and subsequent analysis. Figure 1 shows these aspects of the GPS FSW concept of operations.

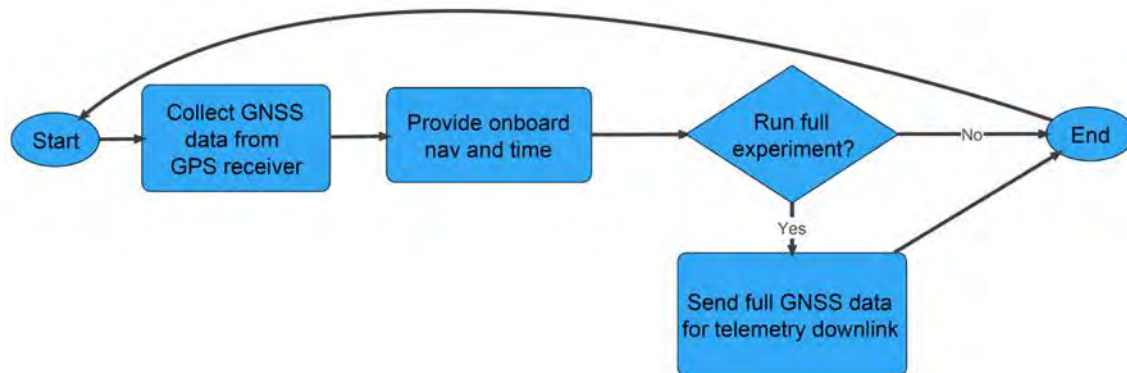


Figure 41: STF-1 GPS FSW Concept of Operations

Subsystem Architecture

The GPS subsystem architecture and flight software were originally developed targeting the FOTON GPS receiver, but after experiencing a number of integration challenges, the team decided to change to a receiver with a better known track record, the NovAtel receiver. On October 21, 2015, a successful integration test with the NovAtel receiver was performed with a Raspberry Pi computer simulating the flight computer. The GPS flight software functionality was verified as processing Position, Velocity, and Time (PVT) packets as well as the full set of GNSS observables directly from the NovAtel receiver. The flight computer communicates with the GPS receiver over an RS-232 serial port.



Figure 1: NovAtel GPS Receiver

Flight Software Requirements

Table 1 lists the GPS FSW requirements that have been defined to satisfy the concept of operations. It also includes requirements that were derived to satisfy robust operations given the GPS hardware design and the overall STF-1 FSW architecture.

Table 4: GPS FSW Requirements

Requirement #	Description
GPSFSW-001	The GPS flight software (FSW) shall gather GNSS science data from a NovAtel OEM615 receiver via UART protocol per the data format specified in OEM615 Firmware Reference Guide.pdf onboard STF-1.
GPSFSW-002	The GPS FSW shall output the GNSS science data for telemetry downlink as well as the GPS time and on-board navigation solution when commanded to perform “full science downlink” operations.
GPSFSW-003	The GPS FSW shall output only the GPS time and on-board navigation solution when commanded to perform “pvt only” operations.
GPSFSW-004	The GPS FSW shall produce no output when commanded to perform “no op” operations.
GPSFSW-005	The GPS FSW shall pre-allocate all internal memory at compile-time.
GPSFSW-006	The GPS FSW shall provide an interface for scaling the rate and quantity at which data is collected and outputted for optimization and efficiency.
GPSFSW-007	The GPS FSW shall respond to command inputs within TBD seconds.
GPSFSW-008	The GPS FSW shall output GNSS science data via CFE Bus Messages in a binary byte array data format specified in “STF-1 GPS Data Format.xlsx”.
GPSFSW-009	The GPS FSW shall output GPS time via CFE Bus Messages in a data format specified in “STF-1 GPS Data Format.xlsx”.
GPSFSW-010	The GPS FSW shall output the on-board position and velocity solutions via CFE Bus Messages in a data format specified in “STF-1 GPS Data Format.xlsx”.
GPSFSW-011	The GPS FSW shall detect a power-off condition for the NovAtel receiver and reinitialize data processing once NovAtel operation is restored.
GPSFSW-012	The GPS FSW shall provide an interface for commanding the NovAtel to use different data output configurations while on-orbit.
GPSFSW-013	The GPS FSW shall command two possible data output configurations to the NovAtel. One configuration is normal operations, which includes time, nav, and GNSS data, and the other configuration is debugging, which includes the same data with additional health and status data about the NovAtel.
GPSFSW-014	The GPS FSW shall perform a 32-bit CRC checksum validation on all data packets received from the NovAtel via serial communications.
GPSFSW-015	If the checksum is not valid, then the GPS FSW shall set the error flag for that segment of data in the telemetry to a value of 1 and the GPS FSW shall not publish any new position, velocity, or time data.
GPSFSW-016	The serial reading function in the GPS FSW shall not block the program from continuing if no data is available on the serial port.

Requirement #	Description
GPSFSW-017	The serial reading function in the GPS FSW shall attempt to retrieve the requested number of bytes for TBD number of iterations before exiting and returning that serial read has failed if not all bytes have been received.
GPSFSW-018	If a serial read has failed, the GPS FSW shall reject that data packet and move on to attempt to read the next data packet.

Flight Software Design

To integrate with the STF 1 spacecraft, the GPS flight software has to be developed as a NASA Core Flight Executive (CFE) application. The GPS flight software has two major components: the Data Input Library (DIL) and the Telemetry Handler (TH).

The role of the Data Input Library (DIL) is to acquire data from the GPS receiver over a serial port. The GPS flight software is designed to read data from the serial buffer and recognize the packets with the data of interest. In the non-science mode, the flight software identifies, parses, and packs time and navigation data for output where it can be used by other flight applications. When the GPS flight software is commanded to perform full science, it will process the full set of Global Navigation Satellite System (GNSS) data products into the output buffers where it can be included in the telemetry stream to the ground. Figure 3 shows the GPS Receiver data packet format and DIL logic flow.

0xAA	0x44	0x12	Remainder of header	Body	CRC
------	------	------	---------------------	------	-----

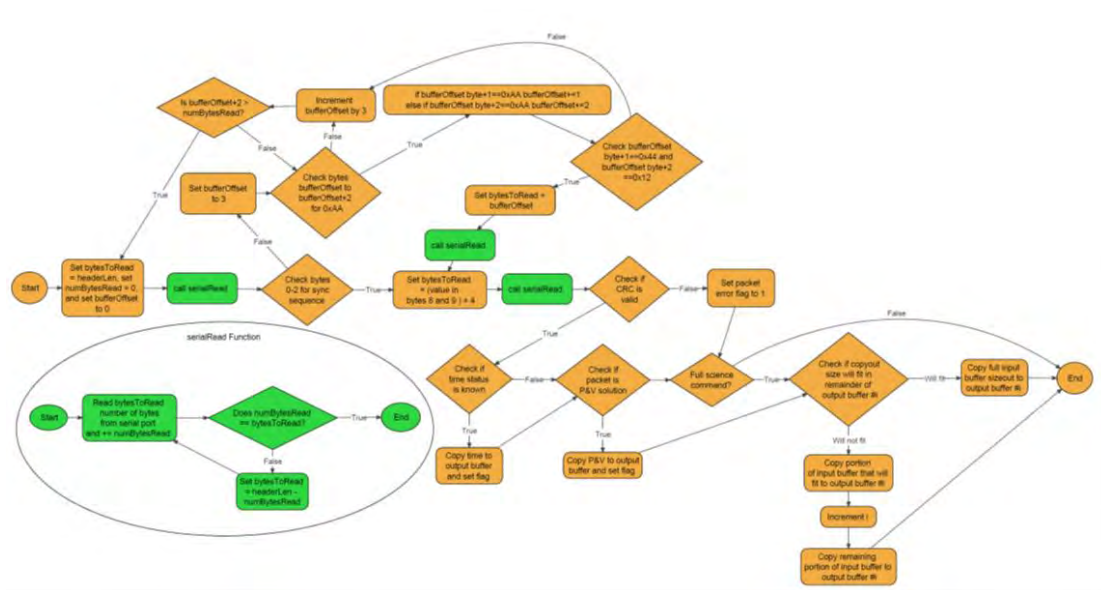


Figure 42: GPS Receiver Data Packet Format and Data Input Library Logic Flow

The Telemetry Handler (TH) is the other major component of the GPS flight software, and it serves as the interface to the CFE spacecraft system for sending telemetry data. The TH data publishing function is triggered when DIL data is ready for outputting. The DIL output buffers are shared between DIL and TH. When TH receives new time and navigation messages from DIL, it publishes that data to the CFE message bus. When operating in full science mode, DIL uses a pair of buffers.

When it fills one buffer it switches to the other, and TH is triggered to publish the science data to the CFE message bus.

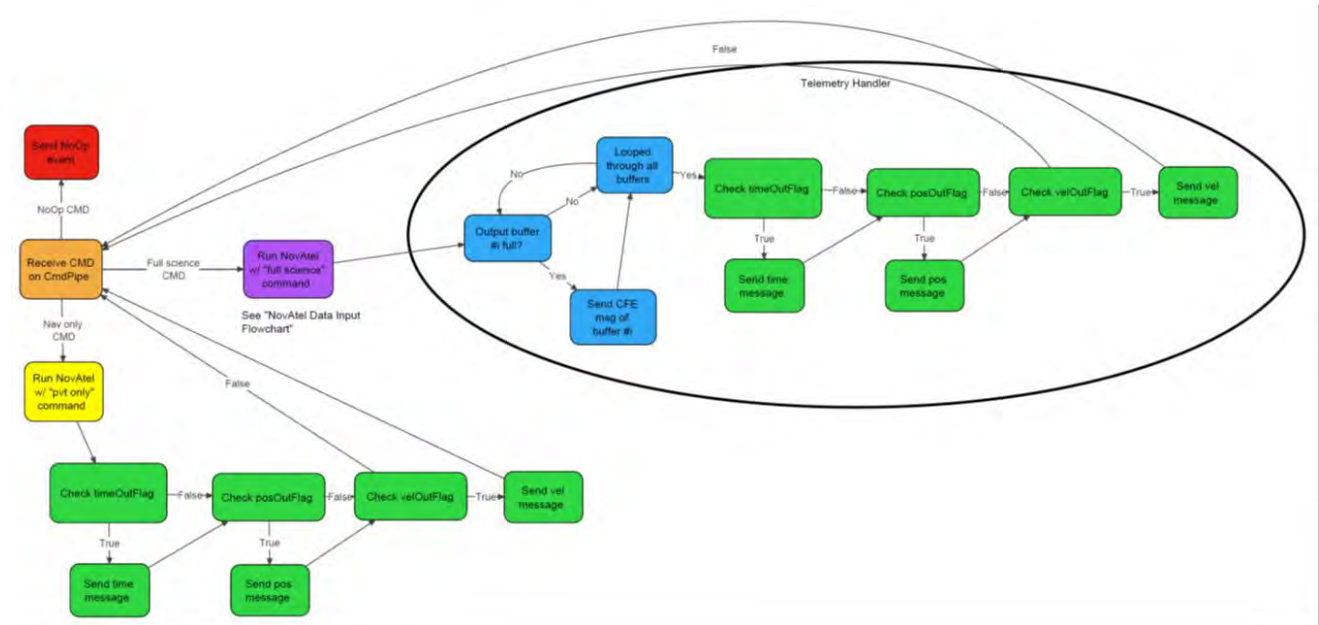


Figure 43: Telemetry Handler Logic Flow

Integration and Test Results

To enable a rapid initiation of this work, the initial software design and development was done on a readily available Linux desktop computer. The target processor will be running freeRTOS and the last major flight software development task is to convert the working software model to operate as a CFE application running under freeRTOS. The first step in this conversion was to change all system-dependent function calls over to the Operating System Abstraction Layer (OSAL) library versions, and this step is complete. This process was also useful for uncovering some latent software bugs, and thus has resulted in higher quality software with the latest fixes. One major challenge remains: serial communications for the target platform. During CFE/OSAL conversion, I discovered that there is no OSAL support for serial port communication. I had a working software version for Linux, but needed to re-host the lower-level serial communications functions for interacting with the GPS receiver for freeRTOS and the target Nanomind processor. To support continued development in the Linux platform, I used compiler directives to support easily switching the compilation process to build the code for Linux OS serial port communications or the FreeRTOS target platform.

The most recent tests successfully demonstrate that the GPS FSW reads data from the NovAtel receiver correctly and publish telemetry messages to the CFE. However, there are some reliability issues where the GPS application seems to crash after a short time, and no longer publishes telemetry. At the moment, it is not obvious what the nature of the crash is. Normally when a program crashes, it tells you what happened (e.g., segmentation fault, etc.). The observed behavior appears to mimic a segmentation fault in the GPS app, but since the CFE runs itself and the GPS application all as one executable, there is no error message displayed. Once the cause of the process

crashes is discovered and corrected, the GPS FSW will be ready for integration testing with the rest of the STF 1 system.

DISCUSSION

Since flight software development was started with the FOTON receiver, the change in receiver required some adjustment to the software design to accommodate a different data interface for the NovAtel unit. DIL was developed and tested as a standalone C library. DIL was originally designed for the FOTON GPS receiver, but with the change to the NovAtel GPS receiver, DIL was adapted to its data interface. On October 21, 2015, a successful integration test with the NovAtel receiver was performed with a Raspberry Pi computer simulating the flight computer. The DIL GPS flight software functionality was verified as processing Position, Velocity, and Time (PVT) packets, as well as the full set of GNSS observables directly from the NovAtel receiver.

An initial version of TH was also developed and tested in the Linux environment. To support integration with the CFE architecture, TH CFE bus message definitions for each data product have been created, and the necessary CFE application functions were integrated into TH logic. Targeted code reviews were used to identify where changes to logic may need to be made based on CFE standards and requirements. The STF-1 project engineers at NASA IV&V provided excellent support to get their virtual machine running to where I could test integration of the GPS FSW, and specifically the TH functions for telemetry and commanding that interface directly with the corresponding CFE capabilities.

The STF-1 mission project had supplied a microprocessor board that closely approximates the target processor; however, it was later discovered that there were certain incompatibilities that prevented a flight-like hardware-in-the-loop test. The virtual machine supplied by the STF-1 provides an adequate simulation of the target processor to support initial validation testing of the GPS FSW.

Writing software for a spacecraft platform has certain challenges. There will be few or no opportunities to debug software problems after launch. Therefore, it is imperative to design software to be very robust and fault tolerant. All of the possible error conditions need to be identified and handled properly. All memory used by the program must be allocated at compile-time. Very simple and basic C programming constructs must be used to create complex behavior. More advanced libraries could make certain things easier, but they must be lean enough to be able to be run on microprocessor boards. Most libraries written for general purpose applications are not robust and fault tolerant enough to meet the requirements of a spacecraft system. Because of the performance requirements and the fact that there was no support for serial communications in the CFE and OSAL platforms, low level buffer/data handling all had to be custom written for STF-1. This work is tedious, but ensures fully defined behavior and minimal possibilities of memory leaks or other errors that could impact software reliability or impact mission success.

On November 13, 2015, I gave a presentation on this project at the American Institute of Aeronautics and Astronautics (AIAA) Young Professional, Student, and Education (YPSE) Conference 2015 hosted at Johns Hopkins University's Applied Physics Laboratory in Columbia, Maryland. On February 25, 2016, I presented a poster on this project at the West Virginia Undergraduate Research Day at the West Virginia State Capitol in Charleston, West Virginia.

ACKNOWLEDGEMENTS

I would like to acknowledge the financial support for this work provided by the NASA WV Space Grant Consortium. I would also like to acknowledge the facilities and opportunities provided by the West Virginia University, Benjamin M. Statler College of Engineering and Mineral Resources, and I would like to especially acknowledge the time, help, advice, and support provided by my mentor, Dr. Jason Gross.

REFERENCES

Morris, Justin M, and Matthew Grubb. "Simulation-to-Flight (STF-1) Proposal." NASA IV&V and West Virginia University, November 25, 2014. Proposal.

REMOTE SENSING WATER BODY EXTRACTION AND DOWNSCALING

Marissa Poultney
Civil Engineering
West Virginia University
Morgantown, West Virginia 26506

ABSTRACT

The following paper briefly discusses various methods of water body extraction and downscaling from remotely sensed data. Many different satellites provide different data for places all around the world. The sensors on board these satellites are optical systems or imaging radars. There are many categories of extraction including object-based, supervised classification, unsupervised classification, etc. Many downscaling algorithms have been, are being, and will be developed based on current research in the field of remote sensing. The ultimate purpose of the findings in this research is to develop an algorithm to downscale data and extract water bodies for the purpose of tracking water-borne diseases across the world.

INTRODUCTION

Satellite images can be very useful in water body extraction. Remote sensing allows for data to be collected and accessed from miles away from a site. Using satellite data with varying resolutions, spectrums, and from different time periods, maps of land and water bodies can be made. Developing these maps requires algorithms to extract information. Many algorithms are already being employed for water body extraction, but there is a chance for many more to be discovered in the future. There is also room for improvement on current algorithms due to setbacks such as noise and low resolution. Although visual identification is the easiest way to identify features from remote sensing images, it is too lengthy and requires more automated methods of analysis. Remote sensing data can be limited by certain factors such as coverage, cost, and spatial resolution. Spatial resolution can be increased by downscaling algorithms that will be reviewed in the following paper. The following section summarizes some of the important indices and methodology used in water body extraction. The next section summarizes some algorithms employed to downscale water body data.

BACKGROUND

The following is a list of satellites that have been used in water body extraction in the past: Landsat 1,2,3,7 NOAA/TIRO, Nimbus-7, Landsat 4,5, SPOT 1,2,3,4,5, IRS 1A, 1B, 1C, 1D, IKONOS, Terra, Quick Bird, Worldview 1, GEOEYE 1, and ICESat (Nath & Deb, 2010).

The most widely used satellite because of its large time span of data availability is Landsat.

There are two kinds of sensors used on satellites, optical systems and imaging radars (Nath & Deb, 2010). The wavelengths used in optical sensors are near those of visible light. Unlike imaging radars, optical sensors record electromagnetic energy. This means that images created from these satellite sensors are a product of the reflection of electromagnetic waves off of earth's surface.

When wavelengths used in remote sensing are within visible light, water tends to show weak reflectance (2-5%) (Haibo et al., 2011). One of the downfalls of distinguishing water based on reflectance is its similarity to other objects such as building shadows (Chunxi et al., 2008). Synthetic Aperture Radar (SAR) is one imaging radar system used by scientists to create images that information can be extracted from (Chunxi et al., 2008). Of these sensors, optical are used more commonly in water body extraction.

Landsat TM/ETM+ is an optical satellite sensor that produces high resolution satellite images that are can be used for efficient water body extraction, but the data is not mostly available free of cost (Zhu et al., 2014).

Onboard NASA's Terra and Aqua satellites, is a sensor called MODIS (Moderate Resolution Imaging Spectroradiometer) (Zhu et al., 2014).

ICESat is home to the Geoscience Laser Altimeter System (GLAS). It was the world's first laser altimetry satellite when launched in 2003. ICESat's main mission was to collect data regarding elevation changes in ice caps, but has since been found to have accurate uses in many other change detection areas (Zhu et al., 2014).

WATER BODY EXTRACTION METHODS

Some of the many methods of water body extraction from remote sensing images include: supervised classification, unsupervised classification, and object-based image classification (Nath & Deb, 2010). These are broad categories that have many specific algorithms that have and will be developed within them.

Unsupervised Classification

Unsupervised classification is a type of extraction where the pixels of remotely sensed images are put into clusters based on their spectrum distribution (Haibo et al., 2011). In this classification, classes are formed for the similar clusters without having prior knowledge or case studies. The classes should be designed so that the reflectance within classes varies very little but reflectance between classes is highly varied (Haibo et al., 2011). One problem with unsupervised classification is the creation of too many or too few classes. This can cause the corresponding image to be distorted or inaccurate. In a study performed by Haibo et al., unsupervised classification was among the many methods assessed in extraction of water bodies, including the Miyun reservoir. In this study, unsupervised classification was quick and accurate for the classification purpose that was required of it.

Supervised Classification

Supervised classification is the opposite of unsupervised classification. The remotely sensed image is known. This allows easy identification of the different classes based on knowing which pixels are associated with which type of ground cover. Analysts can then have predetermined classes for pixels before classifying each pixel (Haibo et al., 2011). Haibo et al. also used supervised classification as one of the methods of analysis in the same area as unsupervised classification. In that study, supervised classification was complicated and required a great accuracy.

Supervised and unsupervised classification techniques are pixel-based classifications because both methods analyze remote sensing images pixel-by-pixel (Weih & Riggan, 2010).

Object-based Classification

Object-based extraction differs from pixel-based in that object-based classifies groups of pixels based on similarities instead of pixel-by-pixel classification (Chunxi et al., 2008). This method was utilized in a study done by Chunxi et al. because it was proven by Cao Bao et al. to have more precision in classification than pixel-based analysis.

NDWI

The Normalized Difference Water Index is an index used in water body extraction (Zhou et al., 2014). NDWI allows for water features to stand out while suppressing features such as vegetation and land (McFeeters, 1996). NDWI is calculated using the NIR radiation and visible green light as follows:

$$NDWI = \frac{Green - NIR}{Green + NIR}$$

(Zhou et al., 2014).

MNDWI

MNDWI is the Modified Normalized Difference Water Index proposed by Hanqiu Xu. The purpose of implementing a modified NDWI is to account for the error occurred when using NDWI for sites that have extensive land surrounding the water bodies that are trying to be extracted. The difference in calculations exists in the use of MIR versus NIR. The equation to calculate MNDWI is as follows:

$$MNDWI = \frac{Green - MIR}{Green + MIR}$$

(Xu, 2007). This method works similarly to NDWI but allows for water features to stand out even more as well as suppressing other features such as land and vegetation. In the study done by Haibo et al., both NDWI and MNDWI were used in analyzing the effectiveness of different water body extraction methods. The results were as follows: NDWI was good at extracting water bodies, but it still disordered some buildings and water with soil. MNDWI was found to have the highest precision of the water body extraction indices. Rokni et al. also uses NDWI and MNDWI in a study attempting to extract water features of Lake Urmia in Iran. This study attempted to detect surface water changes from years 2000 to 2013. While comparing these methods, plus a few more, the proposed method in this study was a combination of NDWI and principal component analysis. NDWI was found to have the highest overall accuracy in detecting surface water changes over the given years. Of the multiple NDWI-PC's used in this study, some had high accuracy while others were completely inefficient.

MNDWI analysis was used in a study done by Mishra & Prasad where shallow water occurred. The reasoning behind using NDWI over MNDWI in that study was to increase the precision of the results.

NDMI

The Normalized Difference Moisture Index (NDMI) calculates the levels of humidity for different aspects of earth's surface, such as soil, land, etc., on a normalized scale to help identify features

from remote sensing images (Herbei & Oncia, 2012). In regards to the spectral bands, NDMI is calculated as follows

$$NDMI = \frac{(near - infrared) - (mid - infrared)}{(near - infrared) + (mid - infrared)}$$

(Wilson & Sader, 2002).

This is another index Rokni et al. used in the study comparing different index methods for water body surface change over time, although it was disqualified part way through evaluation because of its ineffectiveness in that particular project.

NDVI

The Normalized Difference Vegetation Index (NDVI) is a normalized measure of green vegetation existent in an area. NDVI takes on values between -1 and 1, with 1 being a highly vegetated area (Herbei & Oncia, 2012). In regards to the spectral bands, NDVI is calculated as follows

$$NDVI = \frac{NIR - R}{NIR + R}$$

With R being visible red (Herbei & Oncia, 2012). Although this index is normally used for identifying land rather than water, in the study done by Rokni et al., it resulted in high accuracies when detecting the change in surface water.

NDVI was used in a study done by Lu et al., in combination with NDWI. The study area consisted of three different regions in China. The proposed algorithm subtracts NDWI from NDVI in an attempt to have a greater accuracy in distinguishing land from water. Slopes from DEM data were compared to the elevations of the water bodies to sort out shadows from water bodies when trying to extract the water bodies.

DOWNSCALING METHODS

Downscaling data is a process of retrieving low resolution data and converting it to higher resolution data that can be used for predictions and other scientific purposes (Atkinson, 2013). Without this process, water body data can be useless for any applied information because of its coarse spatial resolution. Downscaling to higher resolutions allows for more precision and accuracy when evaluating data. It is important to be able to distinguish between noise and actual downscaling results when employing different downscaling methods (Atkinson, 2013).

In a study done by Li et al., 30-m SRTM DEM data is combined with TERRA/MODIS 500-m water fraction data to produce 30-m water maps for use in exploring flood analysis through satellite data. This is a common method of downscaling remote sensing data. The area being studied was the Mississippi River flood of 2011. To retrieve water fractions from MODIS data, a dynamic nearest neighboring searching method is used. This method basically finds pixels that are solely land pixels and pixels that are mixed land and water pixels. Using these pixels, fractions of the water within the mixed pixels are found. This water fraction data has a resolution of 500 meters and must be downscaled to be able to retrieve the necessary information from it. This water fraction

method was proposed a year earlier by Li et al. in a paper that combines medium resolution MODIS data with low resolution Landsat TM data.

To downscale the 500 meter water fraction data the following steps are taken. The water fraction is equal to the integral of the increment of flooded water fraction with respect to the change in surface elevation. The boundaries are the minimum surface elevation that is the same between both SRTM and MODIS data and the maximum surface elevation in the SRTM. This analysis is done until the water fractions from the integrated method and MODIS are equal. If found to be equal, the cells are marked as water cells. If the water fraction is equal to 1.0, the cells are also assigned to be water cells. The final surface elevation is the max elevation used as the boundary in the integral used for analysis.

This method has errors because it only has an accuracy of 80%. The errors are as much as meters of elevation differences in neighboring cells where there should obviously only be differences of close to 0 meters. Finding the standard deviation and assuming that the errors are distributed randomly from -0.2 to 0.2, the uniformity process is employed to reduce the errors in the integration process.

When integrating the SRTM and MODIS data, water polygons of four neighboring water pixels of MODIS data are formed into groups. The average max water elevation for each cluster is found. If the water polygon is too large for each pixel to have the same average maximum height, a smaller set portion of the polygon is used to calculate average max height. If a polygon is too small, neighboring pixels with water fractions less than 1.0 are used to calculate the max height. A 30-m resolution cell is determined to be water if the elevation of the SRTM data is between the minimum and average maximum height of water elevation of the clusters. It is not water if the elevation in the SRTM data is above the average maximum water elevation height. By doing this, 30-m resolution water maps are created from the combined data.

After the model was created, it was tested on the Mississippi River study area. After using the method on the study area, the results give the same coverage as the 500-m resolution MODIS data but with 18 times the size, so that flooded and nonflooded areas are more clearly defined in the image. The results are then compared with Landsat/TM 30-m water maps. When comparing the two maps using statistics, the total number of water cells, the number of matching water cells, the number of undetected water cells in the integrated map, the number of unmatched water pixels, and the number of water pixels having cloud coverage are used. The two different maps used are one day apart which can account for some error. The matched rates were above 90%. Different land types resulted in different accuracies. Some small water bodies were misclassified as pure land pixels in the integrated method.

The integrated maps are also compared to Worldview-2 2-m resolution maps of Cairo, Illinois and station data such as river gauges for a more accurate evaluation of the proposed new method. The results shown are good because when compared to all of the other maps, the integrated method produced similar located and shaped water bodies. Water elevation levels were also quite similar to the gauge data.

Although this is a feasible method that can be used to create high resolution water maps from low-medium resolution data, there are still errors within each step that need to be worked out to increase the accuracy of the proposed method.

In a study done by Étienne Fluet-Chouinard and Bernhard Lehner, two different data sets were used in an attempt to downscale the data to create high resolution flood maps of African wetlands. The two datasets used are as follows: Global Lake and Wetland Database (GLWD) and Global Surface Water Extent Dataset (GSWED).

GSWED was created from multiple satellite sources having a coarse resolution. GLWD has inconsistencies and errors that the authors attempted to overcome through their study. GSWED data was downsampled to USGS HydroSHEDS data. A probabilistic method was used to downscale; various topographic variables were combined with validated inundation/wetland extent maps. The data was put through a decision tree learner to create inundation probability maps. The process underwent thresholding and validation to prove its accuracy.

The classification tree approach used in the study done by Fluet-Chouinard and Lehner was an expansion of a method proposed by Bwangoy et al. in 2010. This method involves making different datasets the same resolution then using the decision tree to quantify probabilities for each pixel as to whether it does or does not contain what the user is looking for. In this case, the probabilities represented the probability of a wetland being in that pixel area.

Trishchenko et al. proposed a method for deriving 250 m spatial resolution images for all 7 spectral bands of MODIS. Bands B1 and B2 already exist in 250 m resolution. Bands B3 and B7 are used in the new proposed method to create higher resolution bands for MODIS. NDVI was also employed in this method. Non-linear regression models were used to create 250 m resolution spectral bands B3-B7. Bands B1 and B2 and NDVI were used as predictors in the model.

Geostatistics is a form of statistics that involves spatial modeling. This methodology uses spatial variables to predict and create downsampled models.

Wang et al. proposed a recent study that uses a geostatistical method to downscale remotely sensed images. The general idea behind the study was to combine MODIS and Landsat ETM+ images. Bands 1 and 2 of MODIS have a 250 meter resolution while the Landsat's panchromatic band has a 15 meter resolution. Image fusion techniques are used to create images with finer spatial and spectral resolutions. This paper proposes a method to downscale the images to a fine image and then goes through a pansharpening process to make the resolution even finer.

Particularly in this study, the PAN image is sharpened even more through an ATPRK-based downscaling method. ATPRK stands for area-to-point regression kriging. This method is able to keep the same spectral properties of the coarse image so the coarse image could be restored without any distortion from the original. The PAN image is the covariate in the downscaling process. First, during the ATPK regression modeling stage, the PAN band is taken to the same resolution as the coarse band. A regression model is developed using coefficients found by least squares. The model is used to predict a specific location, but the regression model does not fully use all aspects of the coarse band. These residuals are taken care using ATPK downscaling.

ATPRK is then used to downscale the downscaled images to a resolution finer than any of the spatial resolutions that are input into the algorithm originally.

Another example of a study done that is similar to that of Wang et al., is one done by Atkinson et al. that also uses a downscaling cokriging approach that results in a “super-resolution” image. In other words, the result is an image finer than the resolutions of the input images. This is done by a method that predicts subpixel levels. That is how the smaller resolutions are created. The downscaling method used in this paper is called multivariate area-to-point prediction approach. One benefit to the approaches taken in this study and the one done by Wang et al., is the ability of the method to allow use of supplemental information such as station measurements and other ground observations. The process of downscaling cokriging involves supports. A support is the domain from which the variables information and/or measurement comes from. Cokriging uses statistics to find the weights of the two variables being considered in this study. Downscaling cokriging develops two covariance functions. Convolution is done by integration of the random and deterministic function. A process called regularization in geostatistics is used to produce the desired image.

This same regularization process is used in a study done by Zhang et al. that involves super-resolution reconstruction. This study, like the two previously discussed, involves input images of different resolutions being enhanced to one finer resolution. The main methodology behind this study is an adaptive weighted super-resolution. This method accounts for the images different angles and resolutions in the study.

Summary of Downscaling

Downscaling is the increase in spatial resolution of a remotely sensed image. In other words, the pixel size of the image is made smaller so details of the image become finer. According to Peter M. Atkinson’s “Downscaling in Remote Sensing,” there are two goals of downscaling an image: area-to-point prediction and super-resolution mapping.

Many downscaling methods have been proposed over the years. Some of these methods include ATPP, ATPK, maximum entropy, Bayesian approaches, generalized cross-validation, etc. All of the methods have pros and cons and still contain room for improvement.

CONCLUSION

The root of water body extraction algorithms being employed to remote sensing data are the indices previously discussed. Different extraction algorithms exist for many different kinds of satellite data, but new and/or expanded algorithms are being created every day. Future work will include development of a new or modified algorithm for automated water body extraction with high precision. Downscaling techniques are equally important as water body extraction algorithms because downscaled data is much more useful and practical to work with. Future work will include development of a downscaling algorithm to produce maps of water bodies with fine spatial resolutions.

ACKNOWLEDGEMENTS

I would like to acknowledge the grant given to me by the NASA WV Space Grant Consortium to fund the research for this project and for helping further my knowledge in the field of civil

engineering. I would also like to acknowledge my research advisor, Dr. Antarpreet Jutla, for helping and supporting my research for the past year.

This research fellowship has benefitted me in many ways over the past year. This year being my senior year of undergraduate college, I am trying to be fully prepared for my future and next step of life. I will be attending West Virginia University for graduate school beginning in the summer of 2016. The past year has prepared me for what to expect during graduate school. Working with other graduate students as a research team opened my eyes to all of the work that really goes in to research, writing a thesis, and publishing articles. I am now more comfortable with the tedious process of researching a topic and being able to write a literature review to help support any of my own findings. I have gained extensive knowledge about the field of remote sensing. This is a field that not many civil engineers are familiar with, so my knowledge will set me apart in my future career.

The financial support from my research fellowship helped support me during my senior year of college for groceries, rent, graduation expenses, books, etc.

REFERENCES

- Atkinson, P.M. (2013). Downscaling in remote sensing. *International Journal of Applied Earth Observation and Geoinformation*, 22, 106-114.
- Bwangoy, J.B, Hanson, M.C., Roy, D.P., De Grandi, G., & Justice, C.O. (2011). Wetland mapping in the Congo Basin using optical and radar remotely sensed data and derived topographical indices. *Remote Sensing of Environment*, 114, 73-86.
- Cao, B., Qin, Q., Ma, H., & Qiu, Y. (2006). Application of Feature Enhancement Techniques Combined with Object-Oriented Classification Approach. *Geoscience and Remote Sensing Symposium*, 4217-4220.
- Chunxi, X., Jixian, Z., Zheng, Z., & Jiao, W. (2008). Water Body Information Extraction from High Resolution Airborne SAR Image with Technique of Imaging in Different Directions and Object-Oriented. *The International Archives of the Photogrammetry, Remote Sensing and Spatial Information Sciences*, 37, 165-168.
- Gao, B. (1996). NDWI-A Normalized Difference Water Index for Remote Sensing of Vegetation Liquid Water From Space. *Remote Sensing of Environment*, 58, 257-266.
- Haibo, Y., Zongmin, W., Hongling, Z., & Yu, G. (2011). Water body Extraction Methods Study Based on RS and GIS. *Procedia Environmental Sciences*, 10, 2619-2624.
- Herbei, M., Dragomir, L., & Oncia, S. (2012). Using Satellite Images Landsat TM for Calculating Normalized Difference Indexes for the Landscape of Parang Mountains.
- Jia, S., Zhu, W., Lu, A., & Yan, T. (2011). A statistical spatial downscaling algorithm of TRMM precipitation based on NDVI and DEM in the Qaidam Basin in China. *Remote Sensing of Environment*, 115, 3069-3079.

- Li, M., Xu, L., & Tang, M. (2011). An Extraction method for Water Body of Remote Sensing Image Based on Oscillatory Network. *Journal of Multimedia*, 6, 252-260.
- Li, S., & Sun, D. (2013). Derivation of 30-m-resolution water maps from TERRA/MODIS and SRTM. *Remote Sensing of Environment*, 134, 417-430.
- Li, S., Sun, D., Yu, Y., & Csiszar, L. (2013). A New Short-Wave Infrared (SWIR) Method for Quantitative Water Fraction Derivation and Evaluation With EOS/MODIS and Landsat/TM Data. *Geoscience and Remote Sensing*, 51, 1852-1862.
- Lu, S., Wu, B., Yan, N., & Wang, H. (2011). Water body mapping method with HJ-1A/B satellite imagery. *International Journal of Applied Earth Observation and Geoinformation*, 13, 428-434.
- Mishra, K., & Prasad, P.M.C. (2014). Automatic Extraction of Water Bodies from Landsat Imagery Using Perceptron Model. *Journal of Computational Environmental Sciences*, 2015, 1-9.
- Myint, S.W., Gober, P., Brazel, A., Grossman-Clarke, S., & Weng, Q. (2010). Per-pixel vs. object-based classification of urban land cover extraction using high spatial resolution imagery. *Remote Sensing of Environment*, 115, 1145-1161.
- Nath, R.K., & Deb, S.K. (2010). Water-Body Area Extraction from High Resolution Satellite Images-An Introduction, Review, and Comparison. *International Journal of Image Processing*, 3, 353-372.
- Rokni, K., Ahmand, A., Selamat, A., & Hazini, S. (2014). Water Feature Extraction and Change Detection Using Multitemporal Landsat Imagery. *Remote Sensing*, 6, 4173-4189.
- Wang, H., Dai, S., & Huang, X.B. (2013). The Remote Sensing Monitoring Analysis Based on Object-Oriented Classification Method. *Communications in Computer and Information Science*, 363, 92-101.
- Weih Jr, R. C., & Riggan Jr, N. D. (2010). Object-based classification vs. pixel-based classification: comparative importance of multi-resolution imagery. *Proceedings of GEOBIA 2010: Geographic Object-Based Image Analysis*, 38, 6
- Wilson, E.H., & Sader, S.A. (2001). Detection of forest harvest type using multiple dates of Landsat TM imagery. *Remote Sensing of Environment*, 80, 385-396.
- Xu, H. (2006). Modification of normalized difference water index (NDWI) to enhance open water features in remotely sensed imagery. *International Journal of Remote Sensing*, 27, 3025-3033.
- Zhou, Y., Luo, J., Shen, Z., Hu, X., & Yang, H. (2014). Multiscale Water Body Extraction in Urban Environments From Satellite Images. *IEEE Journal of Selected Topics in Applied Earth Observations and Remote Sensing*, 7, 4301-4312.

Zhu, W., Jia, S., & Lv, A. (2014). Monitoring the Fluctuation of Lake Qinghai Using Multi-Source Remote Sensing Data. *Remote Sensing*, 6, 10457-10482.

POLYMORPHISM: CHANGING ACTIVE PHARMACEUTICALS BY SURFACE MODIFICATION

Noah Searls
Biological Science: Pharmacy Emphasis
Marshall University
Huntington, WV 25755

ABSTRACT

Polymorphism, the ability to for molecules to modify their physical structure, has recently triggered concerns in pharmaceuticals by changing drugs' crystalline lattices. Upon a molecule's adjustment in structure, the physical and chemical properties are influenced. Revision of the unit cell and lattice free energy determines the stability of a drug compound. Stability impacts solubility, which is a crucial factor in absorption, secretion, and site of activity for pharmaceuticals. Therefore, the drugs' pharmacokinetics and pharmacodynamics will vary upon physical modification, which has led to drug recalls. For this study, the effect of surface interaction with these pharmaceuticals was examined through surface modification methodology. The basis of the surface interaction consisted of self-assembling monolayers (SAMs) developed on a nickel metal stage. Organic acids (phosphonic and sulfonic) cooperated with the pharmaceutical compounds used upon application of the drugs. The drugs analyzed were cimetidine, tolfenamic acid, and flufenamic acid. All of these drugs were thermodynamically applied to the reformed surface to aide in recrystallization. It was hypothesized and confirmed after instrumentation analysis that the force assisting polymorph development was intermolecular bonds, especially hydrogen bonding, occurring between the SAMs and the pharmaceutical drugs. The study was successful by revealing two forms of each drug, including their commercial form and a metastable form. Physical structure was analyzed in a series of instrumentation, and the property of solubility was examined under ultraviolet-visible spectroscopy (UV-Vis). The results demonstrated the vital chemical stability variances between polymorphs. Ultimately, the research revealed how active pharmaceutical compounds can be influenced by surface interaction to change their physical structure, whether that could be result during manufacturing or transportation, leading to different pharmacokinetic and pharmacodynamics properties for each polymorph.

INTRODUCTION

Solid-state chemistry defines polymorphism as the capacity for molecules to develop multiple organizations of their crystalline lattice¹. The unit cell acts as the building block for solid crystal forms by influencing the overall organization of the lattice². The product of disoriented unit cells deviates the connection, intermolecular bonds, between unit cells (Figure 1).



Figure 1. The diagram of intermolecular change from neighboring unit cells illustrates the basis for the construction of polymorphic crystalline lattices.

The effects of polymorphism generate different physical and chemical properties, including solubility, bioavailability [in pharmaceuticals], kinetics, and phase transition temperatures³. Medicinal chemistry of the pharmaceutical compounds responds to the variation in properties between polymorphs by changing pharmacokinetics and pharmacodynamics affecting the reactivity and stability upon consumption of drugs⁴. The surface modification method presented a reformed surface for the drug to interact with using nickel as the stage and organic acids as the SAMs. The nickel was used mainly for its “friendliness”, or reactivity, by forming an overall uniform adsorbed layer⁵. The surface for the interface and what the pharmaceuticals were actually in contact with, were the organic acid SAMs. These SAMs provided communication between the drug compound and the surface through hydrogen-bonding and other van der Waals forces, as well as a corrosion inhibitor from the spontaneous formation of nickel oxide^{5,6}. They formed by their highly electronegative “head” groups being attracted to the positively charged nickel metal stage. Once the reformed surface was constructed, the drug compounds were applied through thermodynamic procedures needed for kinetic energy, enhancing interaction, and the nucleation process, leading to recrystallization. As the pharmaceuticals came into contact with the surface, intermolecular attraction occurred. Each organic acid (phosphonic and sulfonic acids) and drugs were chosen because they had the capacity to form strong intermolecular bonds, mainly hydrogen bonding. The active pharmaceuticals analyzed, [cimetidine, tolfenamic acid, and flufenamic acid] possess the ability to hydrogen bond with the surface⁷⁻⁹. This attribute was determined because the study hypothesized that hydrogen bonds would be the driving force to develop polymorphs. The product drug samples were analyzed for physical structure in a series of instrumentation; involving Infrared Spectroscopy (IR), IR Microscope, Powder X-ray Diffraction (PXRD), Raman Spectroscopy, and Solid State-Nuclear Magnetic Resonance (SS-NMR). All three pharmaceutical drugs analyzed developed one metastable form (Form B) in contrast to the commercial form (Form A). The polymorphs were also tested under the influence of humidity using a chamber with near constant humidity and solubility properties analyzed by UV-Vis^{10,11}. The research studies and summarizes the impact of surface interaction with common active pharmaceuticals by developing metastable forms as a result of surface modification.

BACKGROUND

Polymorphism has been explored and confirmed by changes in temperature and pressure, but surface interaction studies are limited. Past methods of reproducing polymorphs include: solvent-base screening, seeded melt crystallization, and solid-state transformation⁸. As polymorphism is expanding in research, pharmaceutical compounds currently on the market are facing examination for these metastable forms and possible causes. Polymorphism can adjust a drug’s bioavailability under modifications to pharmacokinetics and pharmacodynamics. Pharmacokinetics deals with the delivery of the drug compound by absorption, distribution, metabolism, and excretion⁴. Important qualities to pharmacokinetics are pKa, polarity, and solubility. Pharmacodynamics depicts the intensity of the response of the drug on the biologic receptor⁴. This interaction between drug and receptor relies on induced-fit and intermolecular bonds. According to the Food and Drug Administration (FDA), the most stable form of a drug that is least likely to convert is often used¹. Therefore, polymorphism with changes in bioavailability has led to several drug recalls, such as Ritonavir (1998), Avalide (2010), Rotigotine (2003)¹². For this study, the drugs used were cimetidine (CIM), tolfenamic acid (TFA), and flufenamic acid (FFA).

CIM ($C_{10}H_{16}N_6S$), also called Tagamet, classifies as an anti-histamine drug used for the treatment of ulcers and common heartburn symptoms by decreasing stomach acid production. The drug prevents retrograde flow of stomach acid, which would normally cause injury to one's esophagus⁷. Few publications are available listing the compound's known polymorphs, including three anhydrous forms and one monohydrate form⁷. CIM's physical structure allows several places for it to form its own hydrogen bonds, as well as participate with others (Figure 2).

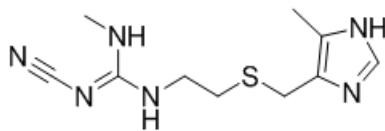


Figure 2. CIM's molecular structure shows possible hydrogen bonding because a hydrogen atom is bonded to a highly electronegative nitrogen atom. As a whole, the compound reveals a permanent dipole-dipole moment increasing its polarity.

TFA ($C_{14}H_{12}ClNO_2$), or Clotam, has five known polymorphs. It is a non-steroidal anti-inflammatory drug used for pain relief of migraine headaches⁸. TFA also shows dipole-dipole moments along with hydrogen bonding opportunities (Figure 3).

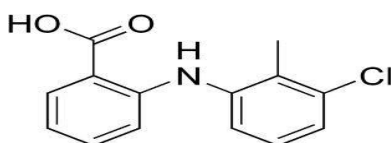


Figure 3. TFA's physical shape shows the electronegative carboxyl group and a nitrogen-hydrogen bond, both capable of forming strong intermolecular hydrogen bonding. The chlorine atom also adds to the polarity shift increasing the molecule's interaction.

Lastly, the third drug of choice is the current leading polymorphic compound with eight known forms⁹. FFA ($C_{14}H_{10}F_3NO_2$) is a non-steroidal anti-inflammatory drug commonly named Achless as it is clinically applied to relieve joint pain. FFA is a highly electronegative atom with a large polarity shift (Figure 4).

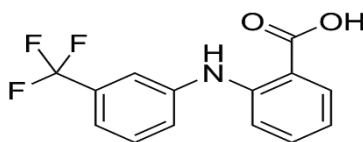


Figure 4. FFA's molecular structure encompasses a carboxyl group for hydrogen bonding and three fluorine atoms around a single carbon for high sensitivity and a deshielded electron density around the carbon atom.

All three pharmaceuticals compounds were capable of hydrogen bonding and are currently available for public consumption. Therefore, these drugs provided critical information needed for the advancement of the study. The research assists in the understanding of the pharmaceutical uproar of polymorphism, specifically by surface contact.

EXPERIMENT

The experimentation for the research contained several variables, which needed to be successful and reproducible. The variables included: the SAM organic acid, the solvent for drug solution, and

the thermodynamics of each drug's application. These attributes were test simply on a trial-and-error basis with between 50-70 for each successful combination.

Self-Assembling Monolayers and Surface Construction

The SAMs consisted of six different organic acids all possessing certain qualities required to construct a reformed surface and act as a protectant from the spontaneous nickel oxide formation⁵. The organic acids had a highly electronegative "head" group comprising a phosphate or sulfate group, which was attracted to the positive charge of the nickel metal stage. The nickel metal stage was used for its sensitivity to reaction, which shows why several biomaterials contain nickel metal, such as wires and switches⁵. The middle of the structures was a long hydrocarbon chain with eleven to eighteen carbon atoms. The tail group for each acid was different to observe affects of multiple surface interactions. The functional groups on the tail groups were alkyl, alkyne, hydroxyl, carboxyl, and phosphate. These functional groups were able to provide the interaction between the surface and the drug molecule via hydrogen bonding and/or other van der Waals forces⁶. The following organic acids were used to form the SAMs: octadecylphosphonic Acid (ODPA), 1-hexadecanesulfonic acid sodium salt (HD-SA) [synthesized to 1-hexadecanesulfonic acid], (12-phosphonododecyl) phosphonic acid (Di-PA), 16-phosphonohexadecanoic Acid (COOH-PA), 11-hydroxyundecylphosphonic acid (HU-PA), and 10-Undecynylphosphonic acid (U-PA). By mixing the organic acids with tetrahydrofuran at a 1.0mM concentration, 1 cm by 1 cm nickel tiles were submerged in the acid solution. The solutions were heated to tetrahydrofuran's boiling point for an increase in kinetic energy and allowed to evaporate to form a uniform SAM on the nickel tiles (Figure 5).

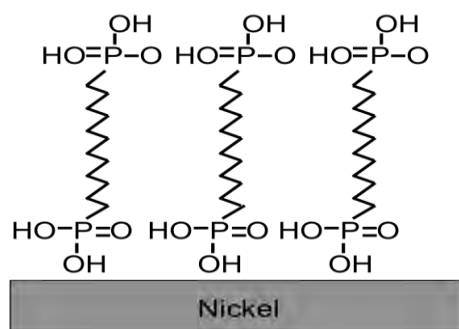


Figure 5. The picture serves to demonstrate the formation of the SAM by example of Di-PA being attracted to the nickel stage to construct the reformed surface.

One obstacle to overcome was hypothesized for possible "bending" of the middle hydrocarbon chain with the acids containing an electronegative tail because of competition with the head group. This was overcome by keeping a balanced concentration of acid solution on the tiles; too high of concentration would lead to a film rather than a monolayer, and too little concentration could lead to bending. To test the SAM formation, the nickel tiles were analyzed under IR. Therefore, once the surface was cultivated the drug was ready to be applied.

Drug Application to the Surface

The three drugs examined were placed on the reformed surface to evaluate surface interaction under certain conditions. First, the drugs were dissolved in a suitable solvent at a certain concentration. Control of the thermodynamics of the solutions allowed benefit to the build up of

kinetic energy for application and nucleation for the recrystallization process during solvent evaporation. The solutions were either heated to the solvents' boiling point or rapidly cooled by heating and then immediately placing in an environment of 0-5°C. Slow evaporation was desired in order to give time for the drug-surface interface interaction, which was achieved by covering the tested well plate with perforated aluminum foil. Also, humidity was assessed for influence on drugs by placing the system in a chamber kept at a near constant temperature and humidity level (~80%) The solvent evaporated over the course of three to five days, with eventually a solid crystalline structure left on the tile. The sample collected on the top of tiles were collected and analyzed for polymorphs.

Instrumental Analysis

The collected samples were investigated through a series of instrumentation and testing to observe possible physical structural differences and property changes. IR provided the first spectra for analysis of possible polymorphs by examining the vibrations between chemical bonds within the molecule¹³. These particular spectra gave respectable information on the hydrogen bonding within the molecule. Following IR, Raman Spectroscopy was used to provide a complementary spectrum for bond vibration¹³. At this point, the samples were sent to WVU Shared Research Facilities for PXRD. The PXRD gave a “fingerprint” for each crystalline structure¹⁴. For measurement of magnetic spin, nuclear magnetic resonance (NMR) testing was completed. Liquid NMR requires there the solid to be in a solvent, which could ruin the physical structure of a crystalline lattice; therefore, SS-NMR was performed. The SS-NMR permitted the sample to stay in its solid form by loading a rotor full of sample into the intended probe and spinning at a certain angle (54.7°) and frequency¹⁵. Confirmed polymorphs were observed under IR-microscope for up close images of each crystal form. Lastly, solubility properties for the two forms of CIM were assessed via UV-Vis¹³. During this test, 50 mg of each form was placed into 250 mL diethyl ether (C₄H₁₀O). Diethyl ether was used as the solvent because of its octanol-water partition coefficient of 0.89, which gives a good estimation of solubility and absorption into body cells¹⁶. The suspension was not aggravated and was measured for absorption at 218 nm wavelength for CIM highest point of absorption over the course of approximately four hours¹⁷.

RESULTS

The instrumentation displayed a reputable comparison between the commercial form (Form A) and the metastable forms developed through surface modification (Form B). The results from the IR spectra in percent reflection from 2100-3500 cm⁻¹ show the vibrations in the hydrogen bonding area (Figure 6).

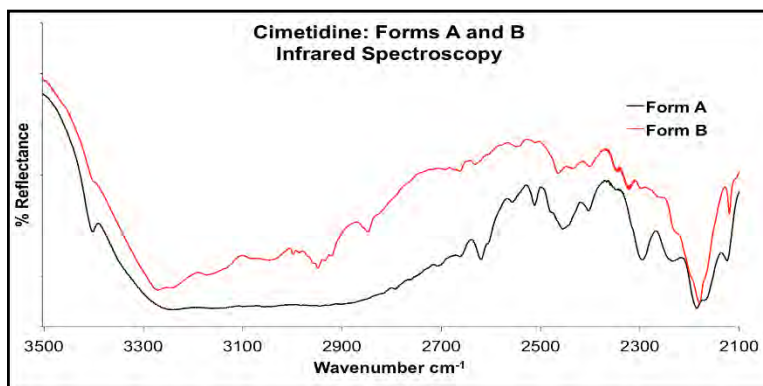


Figure 6. The IR spectrum of CIM from 2100-3500 cm^{-1} shows the distinction between Form A and Form B in vibration between chemical bonds within the molecule, specifically the hydrogen bonding areas.

Raman Spectroscopy expressed other vibrations in the lower portion wavenumbers of the spectra for vibration by means of intensity to complement the IR (Figure 7).

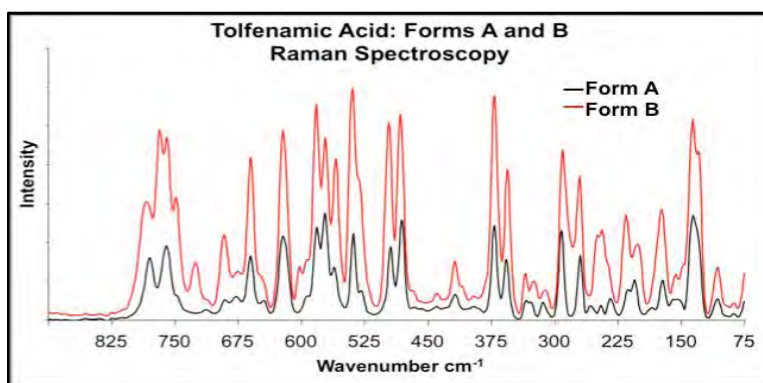


Figure 7. TFA’s spectrum under Raman Spectroscopy serves as an example of the different vibrational patterns between each polymorphic form.

After the vibrational spectra were gathered, PXRD helped reveal the actual differences in the overall crystalline lattices by illustrating the “finger print” of each form. PXRD was measured with the degrees of X-ray diffraction and intensity (Figure 8).

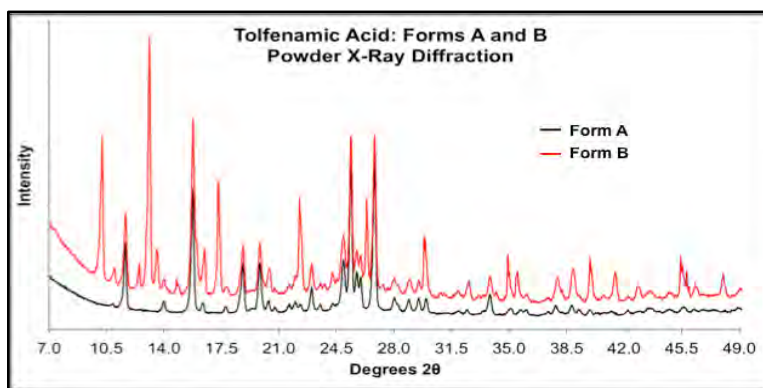


Figure 8. Form A and Form B of TFA are shown in the PXRD analysis to indicate the differences by the angle of X-ray diffraction from the solid crystals.

The last instrument for analysis of physical structure was SS-NMR. The testing gave a clearer “picture” of the influence of the surface interaction. Fluorine-19, proton-1, and carbon-12 probes were used to key on specific atoms (Figure 9).

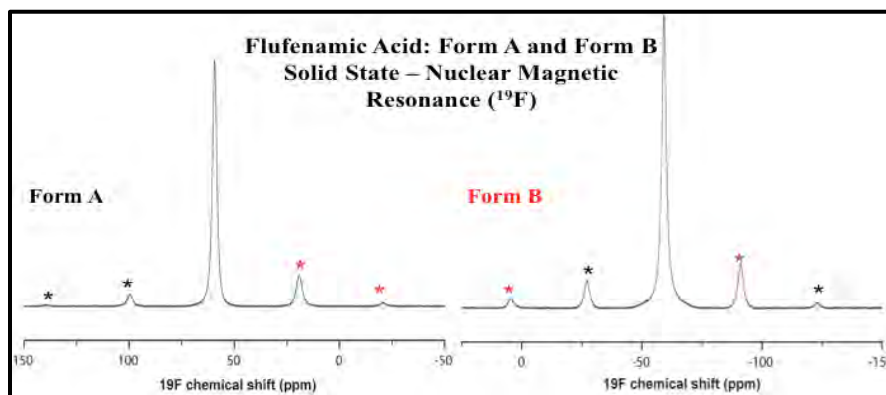


Figure 9. The graph displays the ¹⁹F-NMR of FFA polymorphs revealing the chemical shifts and the intensity of peaks, including side bands (noted by stars).

The trial-and-error method during testing shown several successful and reproducible combinations of SAMs, solvents for the drug solution, and the way these drugs could be applied to the modified surface (Table 1).

Table 1. The table shows the successful and reproducible combinations of the variables in surface modification as means to construct drug polymorphs.

Active Pharmaceutical Drug	Solvents	SAM Modification	Application Procedure
Cimetidine	Methanol Ethanol Acetonitrile	Di-PA COOH-PA ODPA HD-SA	Heat to solvents boiling points and rapid cooling
Tolfenamic Acid	Ethanol Acetone Ethyl Acetate Dimethyl Sulfoxide (DMSO)	Di-PA COOH-PA HU-PA	Heat to solvents boiling points and rapid cooling
Flufenamic Acid	Chloroform Ethanol Acetonitrile DMSO	Di-PA COOH-PA HU-PA ODPA HD-SA	Heat to solvents' boiling points and cooling (DMSO)

Apart from structure, the physical property of solubility of CIM forms were studied by means of absorption under ultraviolet light. The UV-Vis of absorption at 218 nm wavelength gives CIM's highest absorption point. This point acted as the basis for comparison of solubility in diethyl ether under no agitation for approximately four hours (Figure 10).

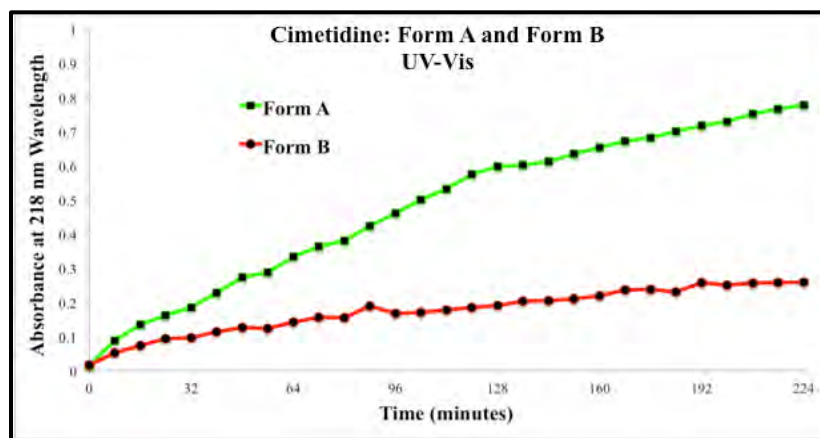


Figure 10. The solubility curves of both forms of CIM are shown by the absorption under UV-Vis at 218 nm wavelength over the course of approximately four hours.

Along with the confirmation of differences in the polymorphs from each pharmaceutical drug, imaging from IR-microscope was conducted for observational distinction (Figure 11).

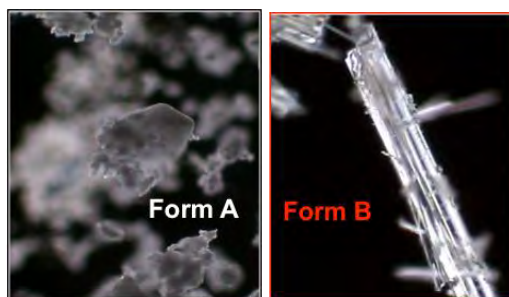


Figure 11. The left picture exhibits Form A of TFA, while the right shows Form B. These images were captured using the IR-Microscope.

With the amount of spectra and information about the physical structure and property for the forms of each drug, the results aid in the understanding of the research's impact on polymorphism.

DISCUSSION/CONCLUSION

All three drugs shown successful polymorph development by demonstrating different physical structures between forms, and being reproducible. The IR (Figure 6) and Raman spectroscopy (Figure 7) revealed different vibrational peaks amongst forms for each pharmaceutical compound, indicating two forms per drug. The IR mainly displayed variances in the hydrogen bonding area ($\sim 3100\text{ cm}^{-1}$), supporting the hypothesis of this particular interaction with the reformed surface. These distinctive vibrations signify a sort of “twisting”, or conformational changes, to the overall physical structures; ultimately, explaining that there were bonds either at different lengths between atoms or being influenced by a new neighboring polar bonds (hydrogen bonding)¹³. The crystal lattices measured under PXRD (Figure 8) validated the resultant unit cell connection. The demarcations in the angles of diffraction, rather than the intensity, confirms that the two samples had different repeating array of unit cells¹⁴. The SS-NMR spectrum (Figure 9) demonstrates a phenomenon known as chemical shift anisotropy¹⁸. The chemical shift of the peaks appears to be the same in both Form A and Form B; however, the side band symmetry illustrates the variation. By observation, Form A's right primary and secondary side bands are larger than that of the left

primary and secondary side bands respectively. Form B displays asymmetric side bands as the right primary band is larger than the left primary, and the left secondary side band is larger than the right secondary side band. The anisotropic shift denotes inconsistencies in magnitude based on the direction of measured¹⁸; therefore, the spectrum states that the two solid crystalline structures differ in their anisotropy, which is affected by their physical structure. IR, Raman Spectroscopy, PXRD, and SS-NMR allowed the research to provide evidence of polymorph formation for all three analyzed pharmaceuticals.

Further conclusions can be made about the research in terms of success. In Table 1, several combinations are found evident for effective trials in the polymorph progression. The study demonstrated that the SAMs with an electronegative tail group seemed to be more likely to produce different drug forms. This observation may be the effect of other SAMs did not possess the ability to hydrogen bond with the tail group. The few sufficient trials with these organic acids could have been the result of a film being produced rather than a monolayer, leaving the head group to form hydrogen bonds. With diversity in many successful solvents and drug applications, it can be determined that the underlying factor for the cause of multiple drug forms was the surface interaction through hydrogen bonding. It must also be noted that although humidity trials were pursued at 80% humidity, collected samples did not yield presentable data. These trials are inferred to have established hydrates, which make the first instrument in the series, IR, very “fuzzy” and unobservable.

The final analysis of physical property and observational differentiation consisted of testing the solubility of polymorphs (Figure 10) and imaging (Figure 11). The solubility of a drug directly corresponds to its stability². In the experiment, Form A and Form B of CIM were tested by UV-Vis in a solution with diethyl ether. The solubility curves display Form A being more soluble, and hence, less stable than Form B. The type of stability change can drastically altered a drug’s bioavailability upon consumption of this compound. Lastly, imaging was completed under IR-microscope for observational analysis. These images displayed how not only the crystal lattice modified, but the crystal habit changed as well². The pictures show the altered commercial bulk crystal shifting into acicular, or needle-like structures.

Consequently, the active pharmaceuticals analyzed in this study shown to be impacted by their interaction with a reformed surface. These findings can be applied to “real-world” events by understanding a drug’s surroundings during manufacturing, transportation, or storage. The influence a surface has upon a drug may permit the compound to alter its physical structure, which in turn, changes its properties. Concluding that, the surface modification method adds to the comprehension on the subject of polymorphism, which can affect active pharmaceutical compounds’ properties and lead to altered, or even harmful, bodily responses following human consumption.

RESEARCH EXPERIENCE

The research project has continued for nearly two years, and I have definitely benefitted from this experience. Support was brought from sponsors, collaborators, and my mentor. All three supporters played a vital role in carrying out this study. My supporters from NASA WV Space Grant Consortium, DOW Chemical, the Marshall University Research Corporation, and the Dean’s Office of the College of Science funded the project for materials, use of instrumentation,

travel, and presentation at professional conference. Without the funds, my research would have not consisted of any experimentation, or presentations. I am genuinely grateful that I was able to purchase the materials for the project, including pharmaceuticals, organic acids, nickel, use of instruments, etc. I was also very privileged to be able to present a poster at the 2015 and 2016 Undergraduate Research Day at the Capitol for West Virginia and the 2014 American Chemical Society (ACS) Central Regional Meeting in Pittsburgh, PA. I will continue presentations by giving an oral discussion at the 2016 ACS Central Regional Meeting in Covington, KY. I was given the opportunity to study and collaborate at Penn State University with Dr. Karl Mueller's lab for SS-NMR. I had several other collaborators along the way included below in the "Acknowledgements" section. My mentor, Dr. Rosalynn Quiñones, taught me the skills to work in a laboratory, to present research professionally, and the overall development for this project.

ACKNOWLEDGEMENTS

- NASA WVSGC Undergraduate Fellowship: Funding
- MU-DOW STEM Fellowship Program from the Dean's Office of the COS: Funding
- Marshall University Research Corporation: Funding Collaboration
- Dr. Rosalynn Quiñones, Assistant Analytical Professor: Mentor
- Marshall University Department of Chemistry: Laboratory and IR
- Dr. Laura Richards-Waugh, Forensic Chemistry: Raman Spectrometry
- Dr. Karl T. Mueller, Professor of Chemistry, and Jonathan W. Fagan, Ph.D. Candidate, at Pennsylvania State University: SS-NMR
- Dr. Weiqiang Ding at WVU Shared Research Facilities: PXRD

REFERENCES

1. *Food and Drug Administration (FDA)*. http://www.fda.gov/ohrms/dockets/ac/02/briefing/3900b1_04_polymorphism.htm (Accessed April **2016**).
2. Florence, A.T., Attwood, D. *Physicochemical Principles of Pharmacy (5th ed.)* **2011**. 8-24.
3. Zhou, J., Kye, Y.S., Harbison, G.S. *J Am Chem Soc.* **2004**. *126(27)*: 8392–8393.
4. Desai, A., Lee, M. *Gibaldi's Drug Delivery Systems in Pharmaceutical Care.* **2007**. 11-20.
5. Quiñon s, R., Raman, A., and Gawalt, E. *Thin Solid Films.* **2008**. *516*: 8774–8781.
6. *Encyclopedia Britannica*. <http://www.britannica.com/science/van-der-Waals-forces>. (Accessed April **2016**).

7. Jantratid, E. Prakongpan, S., et al. *Biowaiver Monographs for Immediate Release Solid Oral Dosage Forms: Cimetidine*. **2006**. doi: 10.1002/jps.20614.
8. Kampf J., Matzger A., Vilmali L. *J. Amer Chem Soc.* **2009**. *131*: 4554-4555.
9. Kampf J., Matzger A., Vilmali L. *J. Amer Chem Soc.* **2012**. *134*: 9872-9875.
10. Brittain, H., Grant, D., Myrdal, P. *Polymorphism in Pharmaceutical Solids (2nd ed.)*. **2009**. 436-453.
11. Ramberger, R., Burger, A. and Schulte, K. *Berichte der Bunsengesellschaft für physikalische Chemie*. **1980**. *84*: 1261–1264.
12. *Particle Analytical*. <http://particle.dk/examples-of-polymorphocrystals-transitions-in-real-life/>. (Accessed April **2016**).
13. Sibilial, J.P. *Materials Characterization and Chemical Analysis (2nd ed.)*. **1996**. 17-38.
14. *Particle Analytical*. <http://particle.dk/methods-analytical-laboratory/xrd-analysis/>. (Accessed April **2016**).
15. Geppi, M. Mollica, G. Borsacchi, S. Veracini, C. *Applied Spectroscopy Reviews*. **2008**. *43*: 202-302.
16. Sangster, J. *J. Phys. Chem. Ref. Data*. **1989**. *18*(3): 1145.
17. *US Pharmacopeia Monographs: Cimetidine Tablets*. http://www.pharmacopeia.cn/v29240/usp29nf24s0_m17700.html. (Accessed April **2016**).
18. Rangus, M. *NMR Spectroscopy in Solids: A Comparison to NMR spectroscopy in Liquids*. **2007**. 6-12.

THE THERMAL DECOMPOSITION OF 4-NITROSOOXY-2-BUTANONE

Eric Sias
Chemistry
Marshall University
Huntington, WV 25755

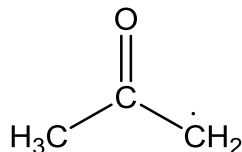
ABSTRACT

The thermal decomposition or pyrolysis of 4-nitrosooxy-2-butanone is believed to proceed via a decomposition pathway producing the acetyl radical. The acetyl radical is unique in that the radical has never been created or isolated in a controlled environment before using the techniques presented in this experiment. Therefore, no full vibrational spectra of the acetyl radical has been published under the conditions presented in this experiment to date. The acetyl radical occurs in combustion and atmospheric chemistry. The primary goal of this project is to create and isolate the acetyl radical and acquire vibrational data on the radical. To attempt to create the acetyl radical a precursor molecule is needed, in this case, 4-nitrosooxy-2-butanone. Thermal decomposition was performed on synthesized 4-nitrosooxy-2-butanone in an oxygen free environment via a pyrolyzer. The 4-nitrosooxy-2-butanone was mixed with argon in a ratio of 1:250 of 4-nitrosooxy-2-butanone to argon. The mixture was then sent through a resistively heated silicon carbide (SiC) nozzle at temperatures ranging from 500 K to 1000 K where thermal decomposition resulted. The decomposition products were sprayed onto a cesium iodide (CsI) window cooled to 15 K and frozen in an argon matrix on the CsI window. This technique known as matrix-isolation allowed for the decomposition products to be analyzed using Fourier transform infrared (FTIR) spectroscopy, collectively known as matrix-isolation Fourier transform infrared (MIFTIR) spectroscopy. The MIFTIR spectra gathered showed evidence of the presence of formaldehyde and ketene at the higher pyrolysis temperatures. The existence of formaldehyde as a decomposition product suggests that the 4-nitrosooxy-2-butanone decomposed via a pathway producing the acetyl radical. The presence of ketene suggests that the acetyl radical continued to decompose forming ketene. The MIFTIR spectra of pyrolysis at 500 K showed evidence of formaldehyde, no evidence of ketene, and weak evidence of peaks at 702 cm^{-1} , 1217 cm^{-1} , and 1563 cm^{-1} . These unidentified peaks were consistent with computational predictions on the vibrational frequencies of the acetyl radical at 738 cm^{-1} , 1245 cm^{-1} , and 1557 cm^{-1} .

INTRODUCTION

The acetyl radical has never been created or isolated in a controlled environment before, making this experiment particularly interesting. The acetyl radical (Figure 1) is thought to be an intermediate in certain atmospheric reactions that involve peroxides.¹ With this experiment's attempt to create, isolate, and analyze the acetyl radical, the conditions at which the radical can be formed and preserved may be realized. Gaining analytical data about the acetyl radical, in this case, vibrational data, will further add to the tabulation of frequencies at which radicals absorb in vibrational spectroscopy.

Figure 1. The structure of the acetyl radical.



The primary goal of this experimental investigation is to create and isolate the acetyl radical by performing pyrolysis and matrix-isolation on the nitrite precursor, 4-nitrosooxy-2-butanone. Radicals can be difficult to isolate because it is known that radicals are highly reactive and short lived. The reactivity and short life-time of radicals is due to an unpaired electron on radicals that will readily react with other species to produce a more stable paired electron. Therefore, it is not possible to synthesize the acetyl radical via standard wet chemistry methods. To attempt to produce the radical, a precursor molecule, in this case 4-nitrosooxy-2-butanone, underwent thermal decomposition. The 4-nitrosooxy-2-butanone precursor compound was not available on the market for purchase. Therefore, the 4-nitrosooxy-2-butanone precursor was synthesized from the starting compound 4-hydroxy-2-butanone, which was available for purchase from TCI America (Figure 2). The 4-nitrosooxy-2-butanone precursor was synthesized from 4-hydroxy-2-butanone with the addition of sodium nitrite and sulfuric acid. The precursor synthesis was modeled after the similar synthesis of *n*-butyl nitrite from Noyes *et.al*, which proved to be successful when performed by this lab.² Nuclear magnetic resonance (NMR) spectroscopy was used to confirm the identity and purity of the synthesized 4-nitrosooxy-2-butanone precursor.

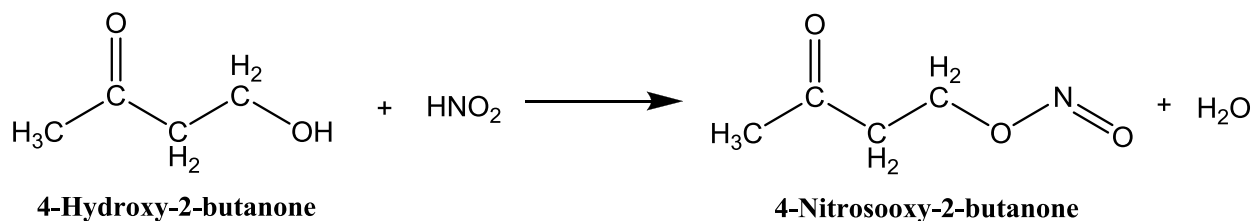


Figure 2. Reaction scheme for the synthesis of 4-nitrosooxy-2-butanone. Nitrous acid was produced *in situ* from the addition of sodium nitrite and sulfuric acid.

The thermal decomposition of 4-nitrosooxy-2-butanone was achieved by performing pyrolysis on 4-nitrosooxy-2-butanone. Pyrolysis is a technique where a compound is heated and allowed to thermally decompose in the absence of oxygen. The absence of oxygen prevents any combustion processes from occurring in the experiment. This method allows for a clean analysis of products formed by pyrolysis reactions and not combustion.³ This process takes place in what is known as a pyrolyzer (Figure 3), where the compound of interest is sent through a hyperthermal nozzle similar to a Chen nozzle.³⁻⁴ In this experiment, the hyperthermal nozzle is a resistively heated silicon carbide (SiC) tube where thermal decomposition results. The decomposition products leave the pyrolyzer in a super sonic jet of possible radicals. The products are then frozen on a cesium iodide (CsI) window in a process called matrix isolation and are ready for spectroscopic analysis. Matrix-isolation is a technique of freezing pyrolysis products in a extremely cooled matrix surrounded by an inert species for spectroscopic analysis. Following matrix-isolation, Fourier transform infrared (FTIR) spectroscopy can be performed on the products. This technique is known collectively as matrix-isolation Fourier transform infrared (MIFTIR) spectroscopy and is

used to identify radicals and various other products.^{4a} Matrix-isolation increases the probability of isolating radicals as the reduced temperature increases radical stability and the inert gas matrix helps to separate radicals from other species with which the radicals could react with and terminate. The method of MIFTIR spectroscopy provides a spectrum with sharp peaks and therefore products can be distinguished from one another.⁵ The techniques described in this experiment allow for short reaction times as well as the advantage of immediately capturing pyrolysis products for analysis as the products are instantaneous sprayed from the SiC tube to the CsI window. This along with short reaction times reduces the chance of any post-pyrolysis reactions taking place.

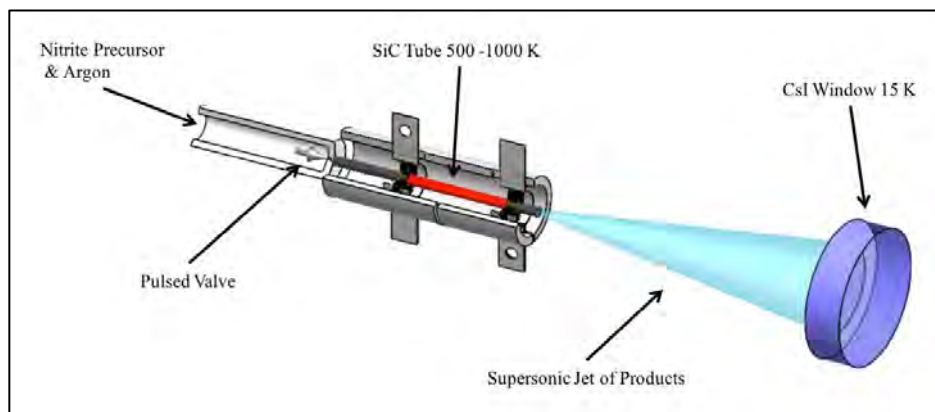


Figure 3. The pyrolysis and matrix isolation technique. The nitrite precursor is mixed with argon and sent through the pyrolyzer via a pulsed valve with subsequent deposition onto a CsI window.

EXPERIMENTAL METHODS

Synthesis of 4-Nitrosooxy-2-butanone

The procedures were performed in a properly ventilated hood, as the synthesis involved the evolution of toxic HONO gas. Into a 25 mL round bottom flask situated in an ice bath with a magnetic stir bar was placed 1.90 g of sodium nitrite and 2.20 mL of 4-hydroxy-2-butanone. Added to the flask were 8.00 mL of distilled water and 0.70 mL of sulfuric acid. The sulfuric acid was added drop-wise via a Pasteur pipette to reduce the evolution of toxic yellow HONO gas. After the addition of sulfuric acid, the solution was allowed to stir for 15-30 minutes. A sodium chloride/sodium bicarbonate solution (25.00 g sodium chloride, 2.00 g sodium bicarbonate, and 100 mL distilled water) in the amount of 0.25 mL was added to the flask to neutralize any unreacted sulfuric acid. Two layers formed in the flask. The top layer (4-nitrosooxy-2-butanone) appeared a greenish yellow color. The bottom layer was an aqueous layer that appeared clear and of semi-solid consistency likely due to the ice bath.

The 4-nitrosooxy-2-butanone was separated from the aqueous bottom layer by pipetting the bottom layer out first. The remaining 4-nitrosooxy-2-butanone was then decanted into a conical vial and any remaining aqueous bottom layer was pipetted out. The 4-nitrosooxy-2-butanone was dried with anhydrous sodium sulfate and placed in a storage vial. The headspace of the storage vial was filled with nitrogen. The storage vial was capped, sealed with Parafilm and placed in a freezer for storage. Following the synthesis of 4-nitrosooxy-2-butanone, the purity and identity of the sample was determined using proton and carbon-13 nuclear magnetic resonance (NMR) spectroscopy performed with a Bruker Ascend 400 with CDCl_3 as the solvent (Figure 4). The main contaminant

was determined to be the starting material, 4-hydroxy-2-butanone. Due to the short shelf-life of the synthesized 4-nitrosooxy-2-butanone, pyrolysis was performed only during a span of about 4 days following synthesis. The NMR spectra (Figure 4) show that the compound 4-nitrosooxy-2-butanone was suitable for pyrolysis for at least 3-4 days following synthesis.

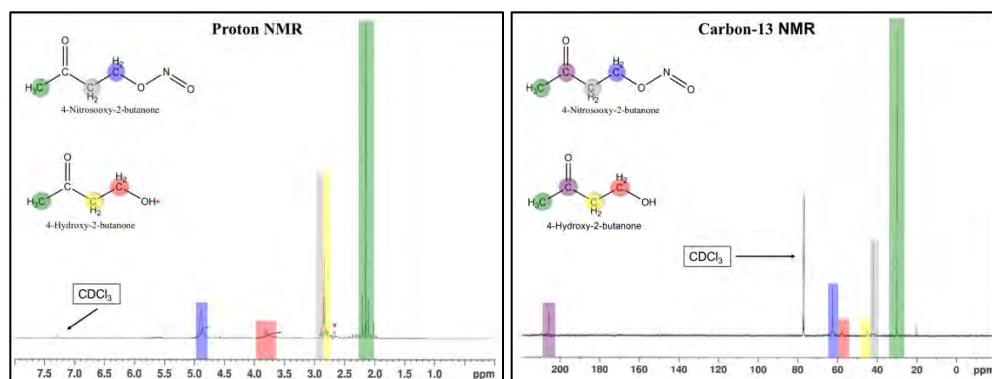


Figure 4. Proton and carbon-13 NMR performed on trial 5 of the synthesized of 4-nitrosooxy-2-butanone. The proton NMR spectrum was taken 4 days following synthesis, while the carbon-13 NMR was taken 3 days following synthesis.

Pyrolysis and Matrix-Isolation

The thermal decomposition of 4-nitrosooxy-2-butanone was achieved by performing pyrolysis on 4-nitrosooxy-2-butanone mixed with argon forming a gaseous mixture. Approximately 2.8 Torr of 4-nitrosooxy-2-butanone vapor was mixed with 700 Torr of argon giving a 1:250 mixture ratio of 4-nitrosooxy-2-butanone to argon. A General Valve Series 9 pulsed valve expanded the mixture at 40 Hz through a silicon carbide (SiC) nozzle that measured 1.5 in. x 1mm. The SiC nozzle was heated resistively to temperatures spanning 500 K to 1000 K. Trials were also performed with the SiC nozzle unheated for a control. A Love Controls Series 16A temperature controller fitted with a variac was employed to regulate the SiC nozzle's temperature.

The products formed in the hypothermal nozzle were sprayed and deposited onto a cooled cesium iodide (CsI) window. The CsI window was cooled to 15 K via a Sumitomo Heavy Industries Ltd. closed-cycle helium refrigerator. A Lake Shore 331 Temperature Controller was employed to help maintain the temperature. The CsI window was mounted inside a cryostat (Janis Research) which was maintained at a base pressure of approximately 1.0×10^{-6} Torr. A frozen matrix of pyrolysis products in argon was formed on the CsI window. The window was then cooled to 4 K and the pyrolysis products were analyzed using Fourier transform infrared (FTIR) spectroscopy performed by a Bruker Vertex 70 under a nitrogen purge. Each FTIR measurement acquired involved 120 scans at 0.5 cm^{-1} resolution.

Computational Chemistry

Because no vibrational data on the acetyl radical has been published under the conditions in this laboratory, there exists no spectra published to help assign the acetyl radical. Computational chemistry was used to predict the structure and vibrational frequencies of the acetyl radical. The computational predictions were performed on a Dell Optiplex 960 Intel® Core™ i7 CPV with a

32 bit operating system and Windows 7 Enterprise running the program *Gaussian 09*. The program *Gaussian 09* provided a computer generated optimization of the structure of the radical and produced predicted vibrational frequencies that gave some insight into where evidence of the radical would appear in the MIFTIR spectrum. The calculations performed by *Gaussian 09* were completed at two levels of theory, the first being HF/6-311++G(d,p) and the second being DFT B3LYP/6-311++G(d,p).

RESULTS AND DISCUSSION

Pyrolysis was performed on 4-nitrosooxy-2-butanone at 500 K, 600 K, 700 K, 800 K, and 1000 K. Additionally, unheated experiments were conducted on 4-nitrosooxy-2-butanone as a control for reference. Analysis of the MIFTIR spectra of the pyrolysis of 4-nitrosooxy-2-butanone showed evidence of the presence of formaldehyde and ketene as pyrolysis products (Figure 5). Evidence of formaldehyde was seen at 2865 cm^{-1} , 2799 cm^{-1} , 1742 cm^{-1} , 1498 cm^{-1} , and 1169 cm^{-1} in the heated spectra.⁶ The formaldehyde peak at 1742 cm^{-1} grew larger as the temperature at which pyrolysis was performed increased, indicating that the specific decomposition pathway was more common at higher temperatures. The presence of formaldehyde suggests that the 4-nitrosooxy-2-butanone sample thermally decomposed via a pathway producing formaldehyde, the acetyl radical, and the nitric oxide radical (Figure 6). The presence of ketene was also evident in the heated MIFTIR spectra. A ketene peak was seen at 2142 cm^{-1} in the heated MIFTIR spectra at 600 K and above.⁷ Similar to the formaldehyde peak at 1742 cm^{-1} , the ketene peak at 2142 cm^{-1} also grew larger as the pyrolysis temperature was increased.

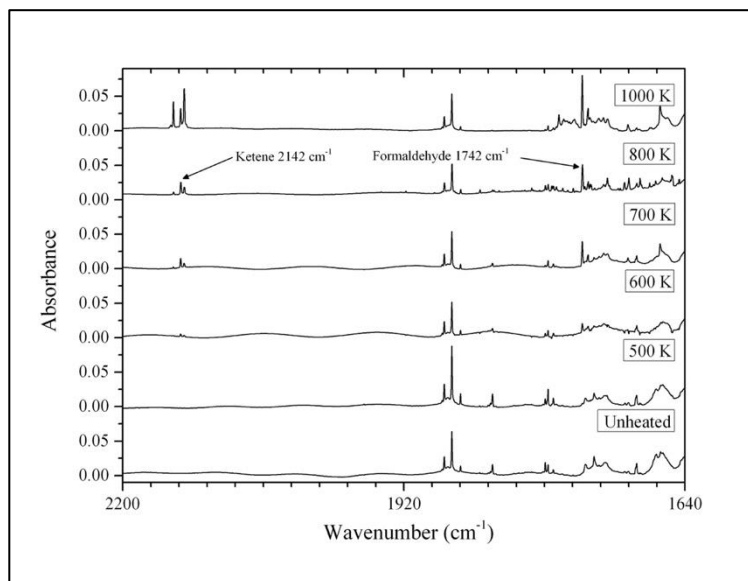


Figure 5. MIFTIR spectra of pyrolysis performed on 4-nitrosooxy-2-butanone showing a temperature study across a range of 500 K to 1000 K, as well as an unheated spectrum.

Ketene is a product not expected in the initial decomposition pathway of 4-nitrosooxy-2-butanone. Therefore, ketene is suspected to arise from a secondary decomposition pathway involving one of

the products of the primary decomposition pathway of 4-nitrosooxy-2-butanone. The primary decomposition pathway product that is believed to give rise to ketene is the acetyl radical. Radicals are highly reactive species and not likely to remain intact for very long under the conditions produced in pyrolysis experiments. The acetyl radical is believed to have decomposed in a secondary decomposition pathway forming ketene and the methyl radical (Figure 6). The presence of ketene decreases at the lower pyrolysis temperatures, suggesting that the secondary decomposition pathway is less active at lower temperatures. Accordingly, the MIFTIR spectra at the lower temperatures are more likely to show any evidence of the acetyl radical.

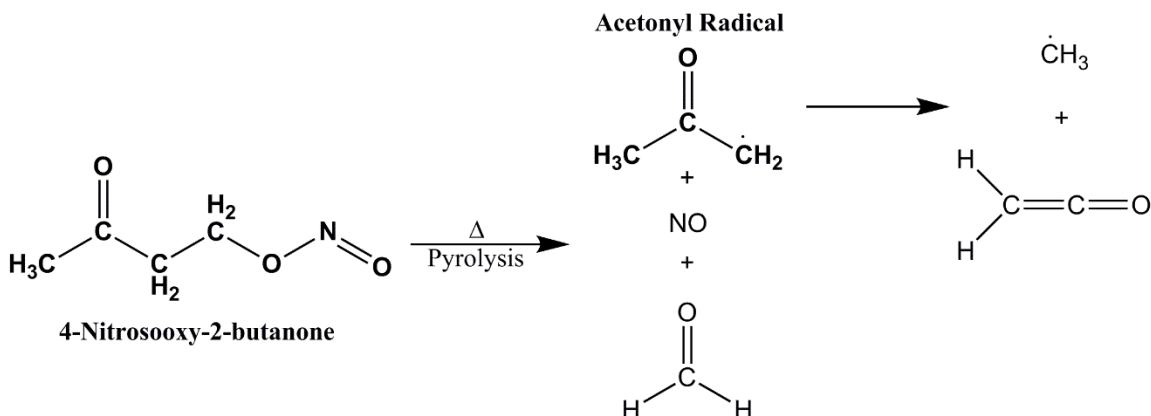


Figure 6. Proposed decomposition pathway of 4-nitrosooxy-2-butanone forming the acetyl radical, a nitric oxide radical, and formaldehyde. The acetyl radical is suspected to further decompose giving rise to a secondary decomposition pathway forming ketene and the methyl radical.

There were several weak unidentified peaks that appeared at pyrolysis at 500 K. The peaks were at 702 cm^{-1} (Figure 7), 1217 cm^{-1} (Figure 8), and 1563 cm^{-1} (Figure 9). These peaks are particularly interesting as it is more likely that the radical exists at lower temperatures. Computational chemistry was employed to predict the vibrational frequencies of the acetyl radical. The program, *Gaussian 09* optimized the structure of the acetyl radical and predicted vibrational frequencies at two levels of theory (Table 1). The two levels of theory used were: HF/6-311++G(d,p) and DFT B3LYP/6-311++G(d,p). Interestingly, the DFT B3LYP/6-311++G(d,p) calculations predicted several absorption frequencies of strong relative intensities at 738 cm^{-1} , 1245 cm^{-1} , and 1557 cm^{-1} that may correspond to the peaks observed in the MIFTIR spectra at 500 K.

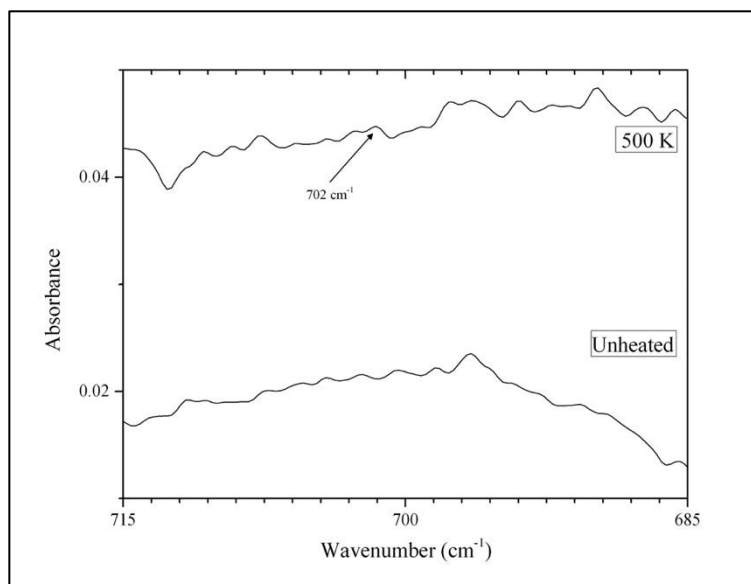


Figure 7. MIFTIR spectra of pyrolysis performed on 4-nitrosooxy-2-butanone at 500 K compared to an unheated trial. A peak at 702 cm⁻¹ is shown to be stronger at 500 K.

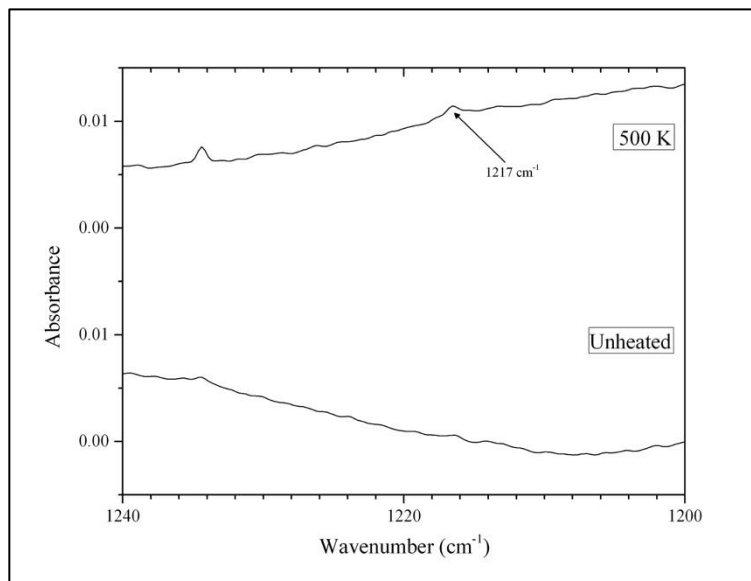


Figure 8. MIFTIR spectra of pyrolysis performed on 4-nitrosooxy-2-butanone at 500 K compared to an unheated trial. A peak at 1217 cm⁻¹ is shown to be stronger at 500 K.

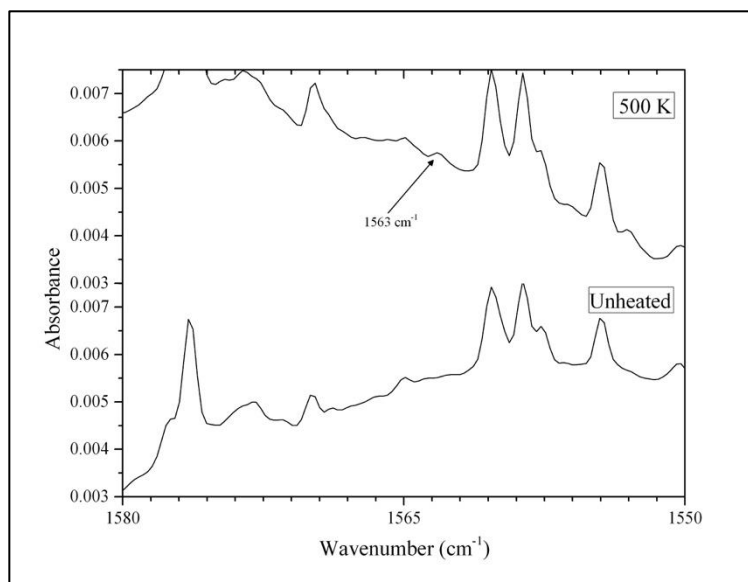


Figure 9. MIFTIR spectra of pyrolysis performed on 4-nitrosooxy-2-butanone at 500 K compared to an unheated trial. A peak at 1563 cm⁻¹ is present at 500 K.

Table 1. Scaled *Gaussian 09* computational chemistry predictions of the vibrational frequencies of the acetonyl radical performed at HF/6-311++G(d,p) and DFT B3LYP/6-311++G(d,p) modes of theory. The particular vibrations of interest are shown shaded in grey.

Scaled HF/ 6-311++G(d,p) (cm ⁻¹)	Relative Intensities	Scaled DFT B3LYP/ 6-311++G(d,p) (cm ⁻¹)	Relative Intensities
55.16	0.1007	34.83	0.0311
369.34	3.1207	349.61	0.1046
389.43	0.3682	381.72	2.5479
493.89	0.7456	498.78	1.4366
508.92	17.6116	517.89	12.9718
676.68	42.7734	738.05	33.0134
793.04	0.0712	803.84	2.9589
896.51	14.1857	910.89	5.0279
1009.96	2.2781	1006.86	5.0549
1031.17	2.3497	1046.73	5.2673
1210.94	57.1464	1245.33	56.9453
1377.67	9.8119	1367.78	30.4821
1393.59	4.9049	1431.29	33.9948
1441.23	11.4757	1449.01	14.5659
1444.74	9.2774	1452.13	10.5471
1455.85	41.0467	1557.22	87.1539
2867.77	10.7602	2902.11	4.1869
2917.24	21.9803	2955.28	10.7207

2963.17	10.7364	3006.54	0.7407
2973.52	7.4405	3008.30	9.0543
3076.97	4.0321	3117.55	3.1479

HF Scaling Factor⁸: 0.9044

DFT Scaling Factors⁹: if <2000 cm⁻¹, then 0.983, if >2000 cm⁻¹, then 0.958

FUTURE PLANS

The MIFTIR peaks at 702 cm⁻¹, 1217 cm⁻¹, and 1563 cm⁻¹ provide some valuable insight into whether the acetyl radical may or may not be forming. However, due to the weak intensity of the peaks, the formation and isolation of the acetyl radical is not definitive. Future studies that would benefit this investigation would be to perform pyrolysis on the 4-nitrosooxy-2-butanone compound at 500 K for a longer period of time. This would increase the total amount of pyrolysis products deposited on the CsI window and would likely increase the intensities of the observed peaks of interest. Also, performing pyrolysis at lower temperatures may also increase the likelihood of the acetyl radical forming. Lastly, more insight may be gained by using computational chemistry at a higher level of theory. Doing so may give more accurate predictions about the structure and vibrational frequencies of the acetyl radical.

OUTCOMES

Obtaining the NASA WVSGC Undergraduate Fellowship grant and becoming part of the program has been a very valuable experience for me. Through the fund, I have had the opportunity to conduct research on a project that has applications in atmospheric and combustion chemistry. Being part of the program has given me the financial support needed to conduct my research as well as present my findings at the American Chemical Society National Meeting & Exposition in Boston, MA. At the exposition I was able to present my research in the form of a poster. I was able to collaborate and network with other students and professionals that were passionate about science. Through the NASA WVSGC Undergraduate Fellowship program I have been able to obtain valuable laboratory and scientific research skills that I will be able to apply to my future scientific endeavors.

ACKNOWLEDGEMENTS

The research presented here was funded by the NASA WVSGC Undergraduate Fellowship Grant as well as the ACS Petroleum Research Fund. The project was led by Laura McCunn, PhD of Marshall University. John Hubbard, PhD, Ken O'Connor, PhD, and Robert Morgan, PhD of Marshall University are recognized for their valuable insight regarding the synthesis of 4-nitrosooxy-2-butanone. The author would also like to thank Barney Ellison, the Camille and Henry Dreyfus Foundation, Emily Wright, Brian Warner, and John Ellison for all assisting with the project.

REFERENCES

1. (a) Seinfeld, J. H.; Pandos, S. N., *Atmospheric Chemistry and Physics: From Air Pollution to Climate Change*. 2nd ed.; John Wiley and Sons, Inc.: Hoboken, N.J., 2006; (b) Alligood, B. W.; FitzPatrick, B. L.; Szpunar, D. E.; Butler, L. J., Chloroacetone photodissociation at

- 193 nm and the subsequent dynamics of the $\text{CH}_3\text{C}(\text{O})\text{CH}_2$ radical-an intermediate formed in the OH + allene reaction en route to CH_3 + ketene. *J. Chem. Phys.* **2011**, *134* (5), 054301.
2. Noyes, W. A.; Noller, C. R.; Wilcoxon, B. H., *n*-BUTYL NITRITE. *Org. Synth.* **1936**, *2*, 108-109.
 3. Kohn, D. W.; Clauberg, H.; Chen, P., Flash pyrolysis nozzle for generation of radicals in a supersonic jet expansion. *Rev. Sci. Instrum.* **1992**, *63* (8), 4003-5.
 4. (a) Zhang, X.; Friderichsen, A. V.; Nandi, S.; Ellison, G. B.; David, D. E.; McKinnon, J. T.; Lindeman, T. G.; Dayton, D. C.; Nimlos, M. R., Intense, hyperthermal source of organic radicals for matrix-isolation spectroscopy. *Rev. Sci. Instrum.* **2003**, *74* (6), 3077-3086; (b) Blush, J. A.; Clauberg, H.; Kohn, D. W.; Minsek, D. W.; Zhang, X.; Chen, P., Photoionization mass and photoelectron spectroscopy of radicals, carbenes, and biradicals. *Acc. Chem. Res.* **1992**, *25* (9), 385-92.
 5. Dunkin, I., *Matrix Isolation Techniques: A Practical Approach*. Oxford University Press: New York, 1998; p 256 pp.
 6. Khoshkhoo, H.; Nixon, E. R., Infrared and Raman spectra of formaldehyde in argon and nitrogen matrices. *Spectrochimica Acta Part A: Molecular Spectroscopy* **1973**, *29* (4), 603-612.
 7. Moore, C. B.; Pimentel, G. C., Infrared Spectrum and Vibrational Potential Function of Ketene and the Deuterated Ketenes. *J. Chem. Phys.* **1963**, *38* (12), 2816-2829.
 8. Özhamam, Z.; Yurdakul, M.; Yurdakul, Ş., HF and DFT studies and vibrational spectra of 1,2-bis(2-pyridyl)ethylene and its zinc (II) halide complexes. *Vib. Spectrosc.* **2007**, *43* (2), 335-343.
 9. Sundaraganesan, N.; Ilakiamani, S.; Saleem, H.; Wojciechowski, P. M.; Michalska, D., FT-Raman and FT-IR spectra, vibrational assignments and density functional studies of 5-bromo-2-nitropyridine. *Spectrochim. Acta, Part A* **2005**, *61* (13-14), 2995-3001.

PREPARATION AND STABILITY OF CIS-DICARBONYLBIS(DIORGANODITHIOCARBAMATO)IRON(II)

Brett Szeligo
Chemistry
Wheeling Jesuit University
Wheeling, West Virginia, 26003

ABSTRACT

The Chemistry Department at WJU has been collaborating with Dr. Aloysius Hepp at NASA Glenn Research Center for a number of years on the thermal decomposition of metal dithiocarbamate complexes to form metal sulfides. These metal sulfides have numerous applications including simulated lunar regolith, photovoltaics, and catalysis. In the case of Fe(III), the addition of the carbonyl ligands produces a stable iron(II) complex, allowing for the possible study of its thermal decomposition. For these dicarbonyl complexes, the postulated mode of decomposition was first a loss of carbon monoxide, followed by loss of dithiocarbamate ligands and fragments, resulting in the formation of iron sulfides.

Iron(II) dithiocarbamate complexes are known to be especially stable; however, recent PNMR of our sample of cis-dicarbonylbis(dibenzylidithiocarbamato)iron(II) revealed, in addition to the expected peaks for the iron(II) complex, a broad peak in the range of 24 ppm. This peak corresponds to the location of the CH₂ peak for the corresponding paramagnetic Fe(III) complex, thus calling into question the extent of decomposition over time of the numerous other cis-dicarbonyl-bis(dioorganodithiocarbamato)iron(II) complexes.

Currently, various cis-dicarbonylbis(dioorganodithiocarbamato)iron(II) complexes have been synthesized and their stability investigated using thermogravimetric analysis (TGA) and PNMR. At ambient temperature, traces of the corresponding paramagnetic tris(dioorganodithiocarbamato)iron(III) have been found for some derivatives, indicating possible room temperature decomposition of Fe(II) to Fe(III) or contamination during preparation. Parallel TGA studies have indicated a variety of paths for thermal decomposition, involving simultaneous or step-wise loss of carbon monoxide, leading to intermediates of varying thermal and kinetic stability. These observations will be discussed, along with the implications of the effect of the organic substituents.

INTRODUCTION

Since their first reported preparation in 1964 (1), the cis-dicarbonylbis(dioorganodithiocarbamato)iron(II) complexes have been the subject of continuing research. These early studies reported preparation (1-4), infrared spectra (1-4), ¹H NMR (2), Mössbauer spectra (3), and a crystal structure (5) of derivatives with various organic substituents. In 1988, Duffy and Appleton reported the multinuclear NMR of a series of these complexes and correlated the ¹³C signal of the CO ligands to the basicity of the lone pair of electrons on the N of the parent secondary amine (6). They found no correlation between the ¹⁵N signals and any other properties of the complexes.

In 2012, Jack, Hoops, Hepp, and Duffy reported (7) the thermogravimetric analysis (TGA) of eight of these dicarbonyl complexes. Based solely on the indirect evidence of mass loss as a function of temperature, thermal decomposition schemes for each of the complexes studied were proposed. The postulated usual mode of decomposition was first a loss of carbon monoxide, followed by loss of dithiocarbamate ligands and fragments, resulting in the formation of iron sulfides and/or iron.

The apparent mass loss assigned to the two carbon monoxide ligand loss sometimes occurred simultaneously and sometimes stepwise. A stepwise loss would suggest either the formation of a five-coordinate intermediate, $\text{Fe}(\text{CO})(\text{S}_2\text{CNRR}')_2$, or some sort of bridged complex, $[\text{Fe}(\text{CO})(\text{S}_2\text{CNRR}')_2]_2$, which might be stable kinetically in the solid state.

In 2012, Coffield, Duffy, Hoops, and Beck (8) reported the loss of CO ligands from cis-dicarbonylbis(methylphenyldithiocarbamato)iron(II) and cis-dicarbonylbis(dibenzylidithiocarbamato)iron(II). Loss of the mass equivalent of one CO produced compounds that were stable under nitrogen, and in the case of the methylphenyl derivative, stable in air. Empirically, these new compounds are monocarbonylbis(methylphenyldithiocarbamato)iron(II) complexes, and have not previously been reported in the literature. In 2012 and 2013 several students continued the investigation of these compounds. In particular, it was observed that changing the rate of heating for the thermogravimetric analysis may alter the mechanism of thermal decomposition.

This study is investigating the mechanism of CO ligand loss as well as other thermal decomposition processes using thermogravimetric analysis coupled with infrared spectroscopy of the gaseous decomposition products and decomposition residues. In particular, decomposition intermediates, energy changes associated with the decomposition, and the kinetics of the decomposition are being investigated. Results indicate a thermal decomposition that not only dependent on the rate of heating, but also possibly dependent on the flow rate of the purge gas. In addition, thermal loss of the second CO ligand appears to occur at a significantly higher temperature than the first CO suggesting an additional reaction between the second CO and the complex prior to thermal loss of that CO.

EXPANDED RESEARCH

Halfway through the fall semester, the TGA analysis of the dicarbonyl compounds was placed on hold due to a break in the equipment. After initial investigations this semester into potential sources of trace CO gas in the exit stream of the TGA, the electronics malfunctioned and the TGA no longer communicate with the computer. In the meantime, the research expanded to the use of NMR for the study of the compounds. Previous work by other student researchers investigated the exchange of ligands between different tris(diorganodithiocarbamato)iron(III) complexes. The fact that the iron (III) in the complexes is paramagnetic, it shifts the NMR signal for the closest protons. This shift is influenced by the nature of the other ligands, allowing the use of the NMR to determine whether ligand exchange has occurred and if the mix of ligands on the iron centers matches the statistically expected ratios. The appearance of Fe(III) signals in the NMR spectra of some of the previously prepared samples of the Fe(II) dicarbonyl complexes has raised concern about the long-term thermal stability of these samples and is being further investigated.

METHODS

Thermogravimetric analysis (TGA) will be performed using a TA Instruments SDT Q600 under a dynamic inert gas. Samples will be heated at rates ranging from 5 °C/min and 20 °C/min with gas flows from 25 to 100 mL/min. Infrared analysis of gaseous thermal decomposition products will be performed using a ThermoFisher Nicolet iS10 FTIR Spectrometer fitted with a Pike Technologies, Heated Gas Cell.

FTIR analysis of solid, thermal decomposition intermediates and products will be performed using a diamond attenuated total reflection (ATR) attachment. The ability of the ATR to non-destructively analyze small sample sizes (<5 mg) should be ideal for tracking the identity of the thermal decomposition residues at selected points during the TGA analysis.

The Nuclear Magnetic Resonance Spectrometer (NMR) will be performed using an Anasazi multinuclear conversion of a Varian EM-360 (60 MHz) NMR. Most proton spectra were collected using a spectral window of 7000Hz.

RESULTS

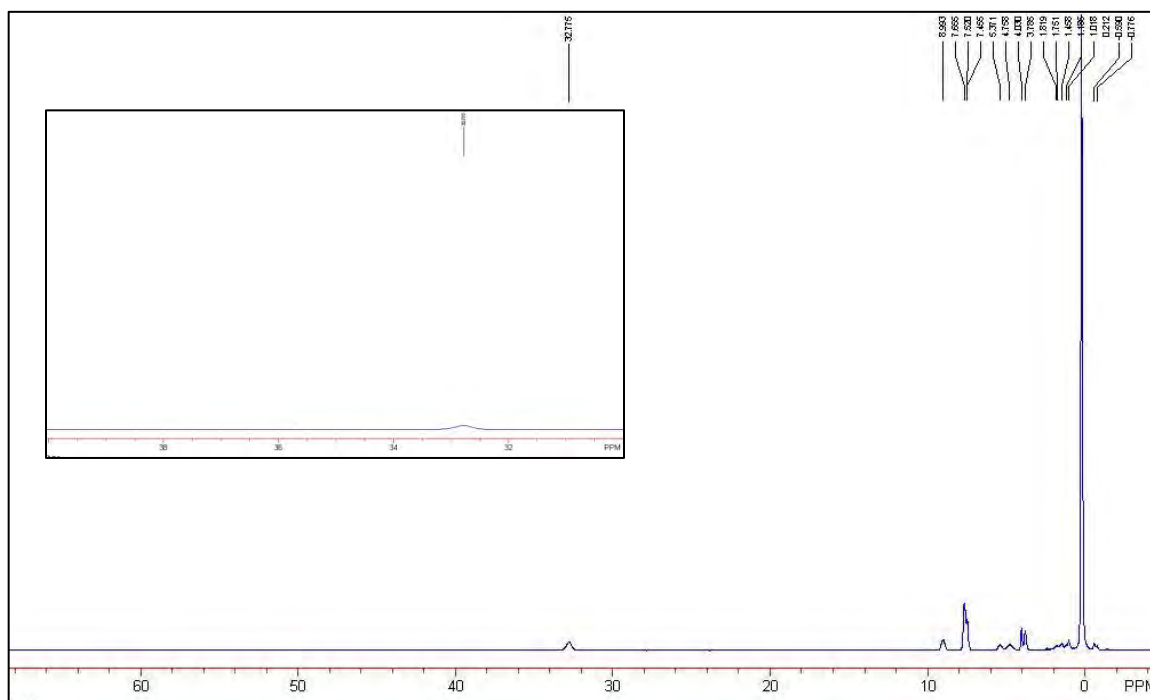


Figure 1: Sample 8574 Methylphenyl Derivative $\text{Fe}(\text{S}_2\text{CNCH}_3(\text{C}_6\text{H}_5))_2(\text{CO})_2$. TMS at 0.209 ppm, sharp peak at 31.996 ppm.

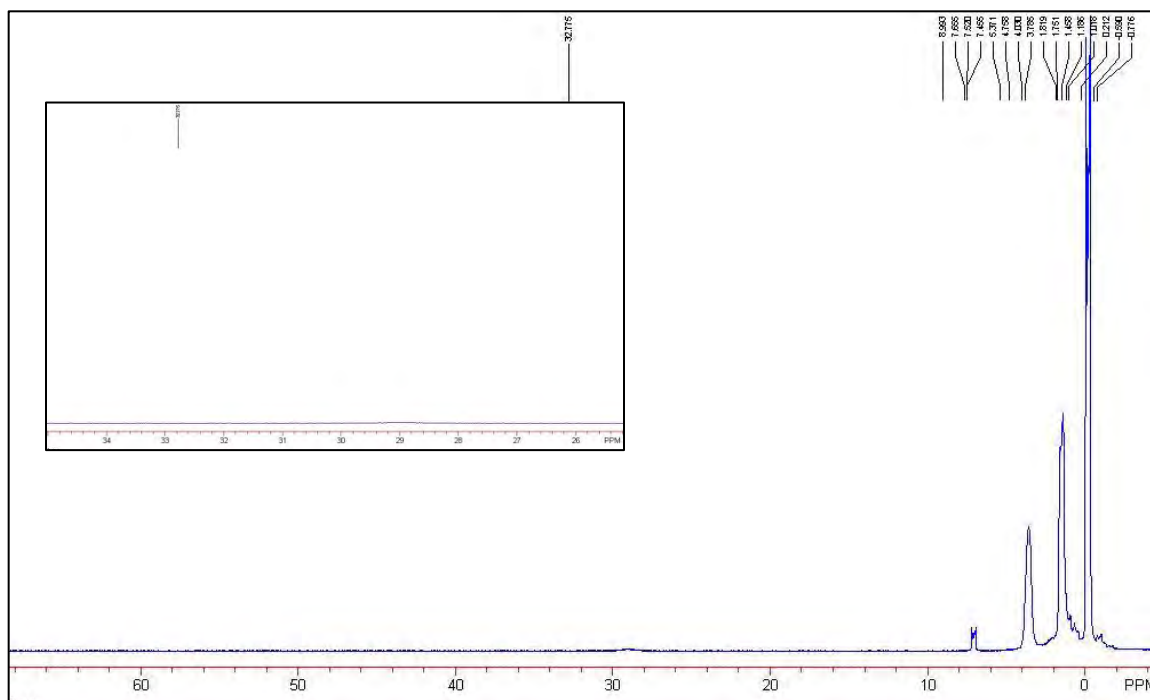


Figure 2: Sample 6174 Piperidine Derivative $\text{Fe}(\text{S}_2\text{CN}(\text{CH}_2)_5)_2(\text{CO})_2$. TMS 0.262, broad peak at 28.883 ppm.

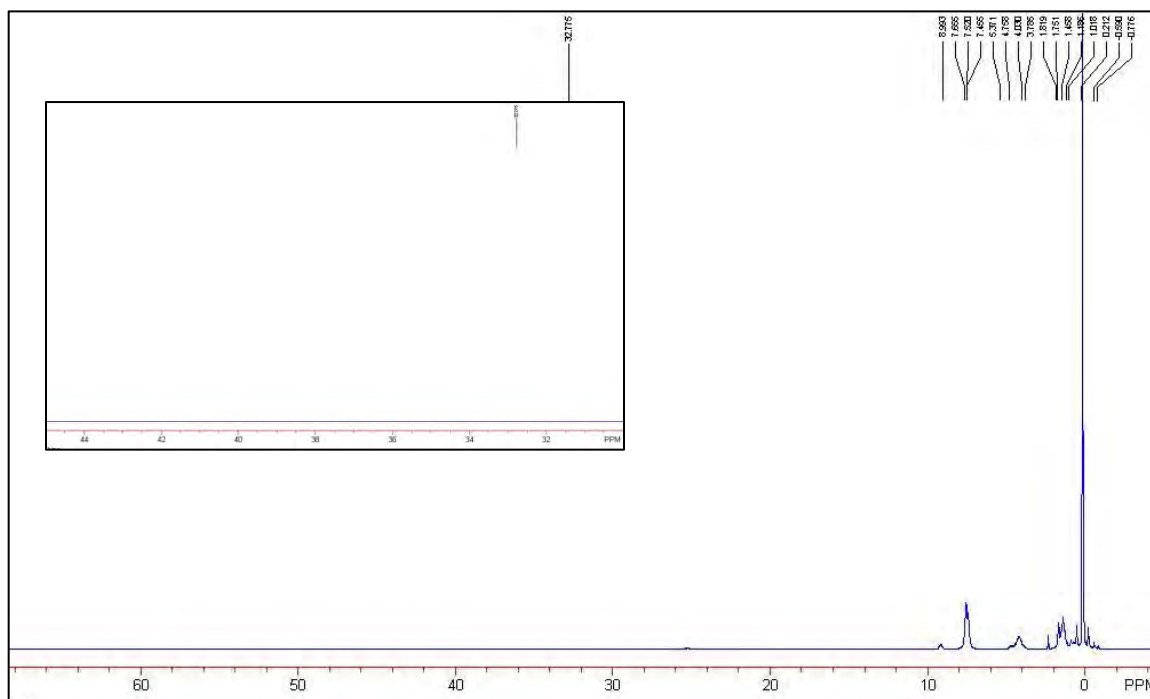


Figure 3: Sample 110909 Ethylphenyl Derivative $\text{Fe}(\text{S}_2\text{CN}(\text{C}_6\text{H}_5)(\text{C}_2\text{H}_5)_2(\text{CO})_2$. TMS 0.212 ppm, broad peak at 31.964 ppm.

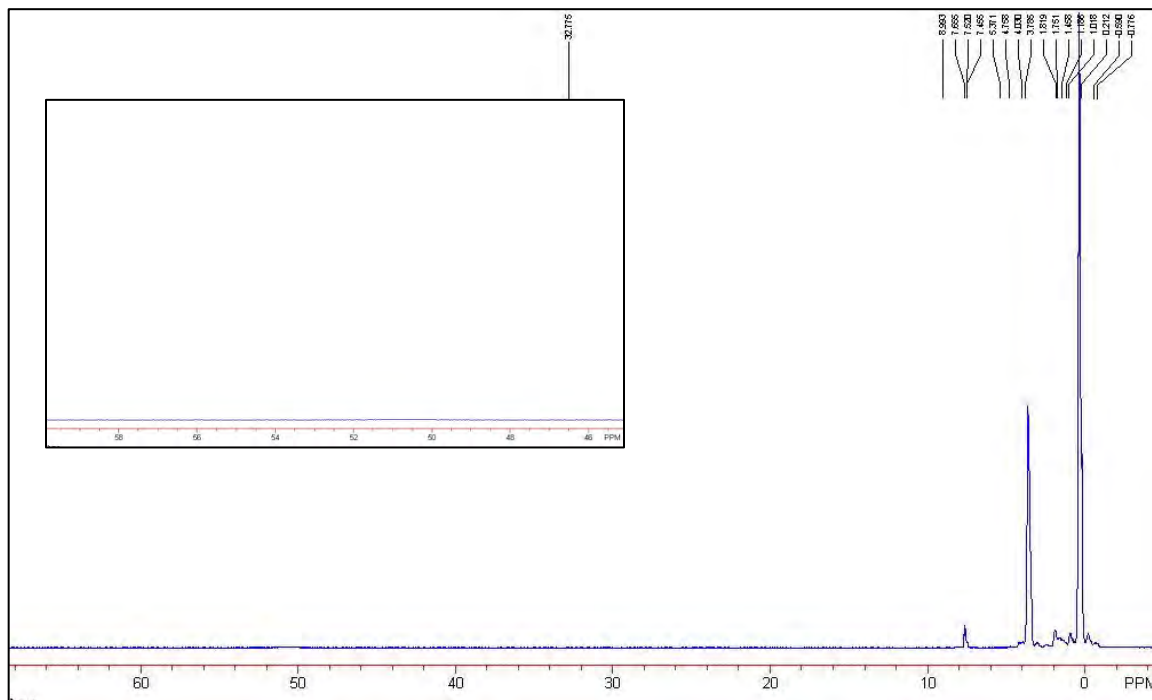


Figure 4: Sample 41174 Dimethyl Derivative $\text{Fe}(\text{S}_2\text{CN}(\text{CH}_3)_2)(\text{CO})_2$. TMS 0.377 ppm, broad peak at 50.134 ppm.

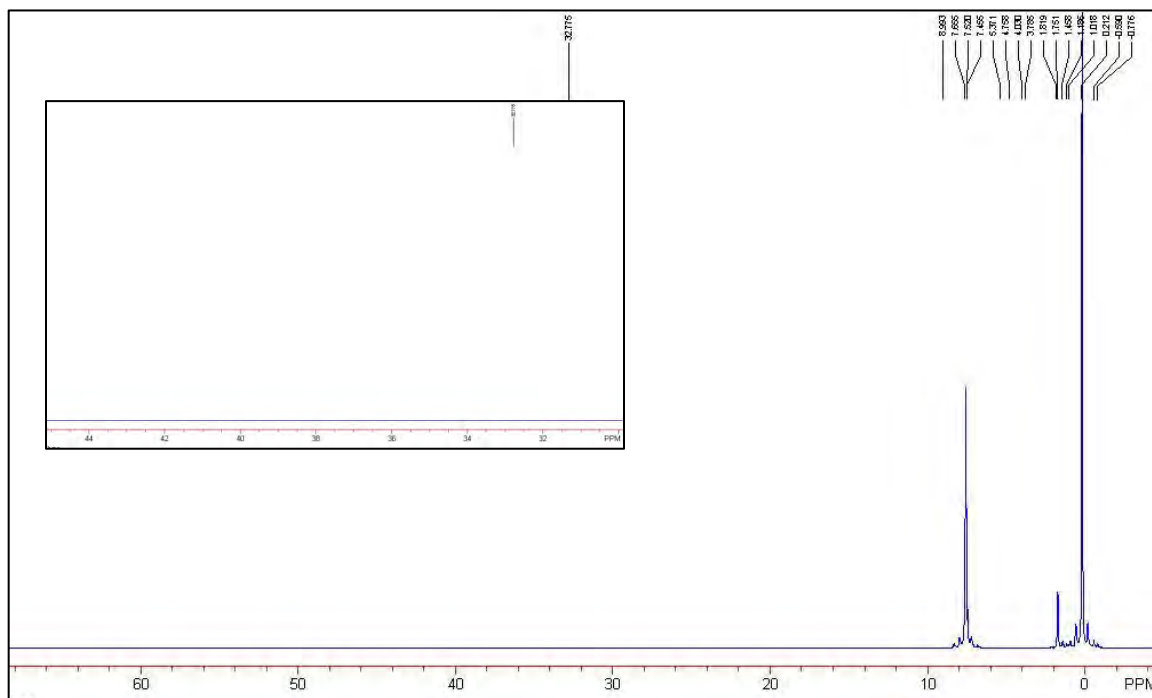


Figure 5: Sample 111009 Diphenyl Derivative $\text{Fe}(\text{S}_2\text{CN}(\text{C}_6\text{H}_5)_2)(\text{CO})_2$. TMS at 0.212 ppm

DISCUSSION

Sample 111009 the diphenyl derivative, have elemental analyses from 1974, 1986 and 2009. The % C was theoretically 56.01% but found 55.85 (1974); 55.25 (1986); and 54.92 (2009). The % H was theoretically 3.36 % but found 3.29 (1974); 3.34 (1986); and 3.35, 3.35, 3.38 (2009). The % N was theoretically 4.67 % found 4.56 (1974); 4.57 (1986); and 4.62, 4.67, 4.66 (2009). Since Fe and CO are empirically the same, they should produce similar results. A simple loss of CO would cause a higher % C and it was determined that the decomposition to Fe(III) was little to none.

The absence of an alpha proton, may not produce a shift and cause the appearance of a broad peak. Nevertheless, it was determined that the samples contained little decomposition of Fe(II) to Fe(III) and appear to be relatively stable at room temperature. Future work will investigate the thermal stability of dithiocarbamate iron(II) complexes using TGA and FTIR analysis. Various inert purge gasses, temperature increase, and variable scan rates with different amounts of gas flow to purge the system will be investigated.

PRESENTATIONS

This work was presented at the WJU Research and Scholarship Symposium and NASA Space Day 2016.

ACKNOWLEDGEMENTS

I would like to take this opportunity to thank the NASA West Virginia Space Grant Consortium for helping to support this research and for their continued support with the award of an Undergraduate Research Fellowship. I would also like to thank Dr. James Coffield, Dr. Norman Duffy, and Dr. Jason Fuller for their help and guidance. Without WVSGC funding and my mentors assistance and guidance, this research would not have been feasible by myself.

REFERENCES

- (1) F.A. Cotton and J.A. McCleverty, *Inorg. Chem.*, **1964**, 3, 1398-1402.
- (2) H. Buettner, and R.D. Feltham, *Inorg. Chem.*, **1972**, 11, 971-976.
- (3) J.B. Zimmerman, T.W. Starinshak, D.L. Uhrich, and N.V. Duffy, *Inorg. Chem.*, **1977**, 16, 3107-3111.
- (4) M.R. Houchin, *Inorg. Chim. Acta*, **1984**, 83, 103-110.
- (5) J.S. Ricci, Jr., C.A. Eggers, and I. Bernal, *Inorg. Chim. Acta*, **1972**, 6, 97-105.
- (6) N.V. Duffy and T.G. Appleton, *Inorg. Chim. Acta*, **1988**, 143, 273-277.
- (7) C.C. Jack, M.D. Hoops, A.F. Hepp and N.V. Duffy, *J. Undergrad. Chem. Res.* **2012**, 11, 11-14.

(8) J.E. Coffield, N.V. Duffy, M.D. Hoops and R.Z. Beck, *J. Undergrad. Chem. Res.* **2012**, 12, 7-10.

DISCRIMINATION OF INKJET PRINTER INKS USING RAMAN BY LASER INDUCED BREAKDOWN SPECTROSCOPY

Robyn Wiseman

Chemistry and Forensic and Investigative Science
West Virginia University
Morgantown, WV 26506

ABSTRACT

Inkjet printers are commonplace in today's society due to their widespread availability and affordable prices. They are capable of producing high quality prints, so it is not surprising that inkjet technology is often utilized in the illegal production of questioned documents such as banknotes, fraudulent contracts, and extortion letters. Currently, the majority of ink analyses are done by subjective visual spectral comparisons (i.e., filtered colored light, ultraviolet, infrared reflectance, and infrared luminescence) followed by an extraction of the colorant from the printing substrate for chromatographic analysis. However, this approach is time consuming and destructive to the evidence. Many types of ink are made of dyes and/or pigments, which due to their chemical nature, further complicates analysis. In this project the fast and non-destructive instrumental analysis methods of micro Raman Spectroscopy and Laser induced breakdown spectroscopy (LIBS) were tested on eight inkjet printer inks. Spectra of cyan, magenta, and yellow ink components were collected for the eight ink samples using the Raman technique. Five replicates of each of the three colored spots for all samples were obtained for a total of 120 spectra. Five replicates were taken of the black ink components of the eight samples using the LIBS method for a total of 40 spectra. While the Raman data allowed for differentiating inkjet inks from different sources, the LIBS method proved to be ineffective due to the strong paper signal that masked the emission lines attributed to the ink elemental profile. The use of all three colors from each sample produced spectra which discriminated all but two of the eight ink samples from each other.

INTRODUCTION

Inkjet printers are affordable and capable of producing high-quality prints. The combination of these factors explains the popularity of these printers in counterfeiting crimes such as the production of fraudulent banknotes and passports. The current methods of ink development often use visual comparison of spectral data from instruments such as the Visual Spectral Comparator (VSC) followed by Thin Layer Chromatography (TLC) for color analysis. This method becomes ineffective for inks that contain pigments, which are insoluble and cannot be extracted for TLC.¹ The increasing quality of counterfeit documents along with the complications in analyzing new ink formulations with traditional methods calls for the development of new standard methods for inkjet ink analysis. Additionally, perpetrators of counterfeit crimes often move throughout the country, but they maintain a characteristic printing profile. The development of a searchable database of inkjet printers will help increase the efficiency with which multiple counterfeit crimes can be attributed to the same suspect. Additionally, the collection of data for the database being completed with fast, non-destructive analytical methods will help shorten examination time and preserve evidence.

The goal of this project was to initiate the development of a searchable database of inkjet printer inks using Raman spectroscopy for cyan, magenta, and yellow inks and LIBS analysis to create elemental profiles for black ink samples. The combination of these two methods should allow the discrimination of a wider range of ink combinations and printers to be possible. The samples will be obtained from the collection of printers at the United States Secret Service Counterfeit Division. A Bruker Model Senterra Raman paired with a Bruker BX51M will be used for the color ink samples. Five spectra will be taken at different locations of each sample, and all of the data will be collected and stored in Opus Spectroscopy software version 6.0. A Foster & Freeman ECCO² will be used to collect the LIBS data. Five spectra will again be taken at different portions of the black ink samples.

INSTRUMENT BACKGROUND

Micro Raman Spectroscopy is one method that has been investigated for the analysis of inkjet inks. The method is fast and relatively nondestructive to evidence. Raman works by exciting molecules in a sample by exposure to a laser beam.² The molecules then undergo vibrations to return back to the ground state. In most cases, the molecules will release the same amount of energy they absorbed, and this is elastic Rayleigh scattering. If the molecule releases more or less energy than was absorbed, this is the Raman effect and creates characteristic spectra for the molecule.

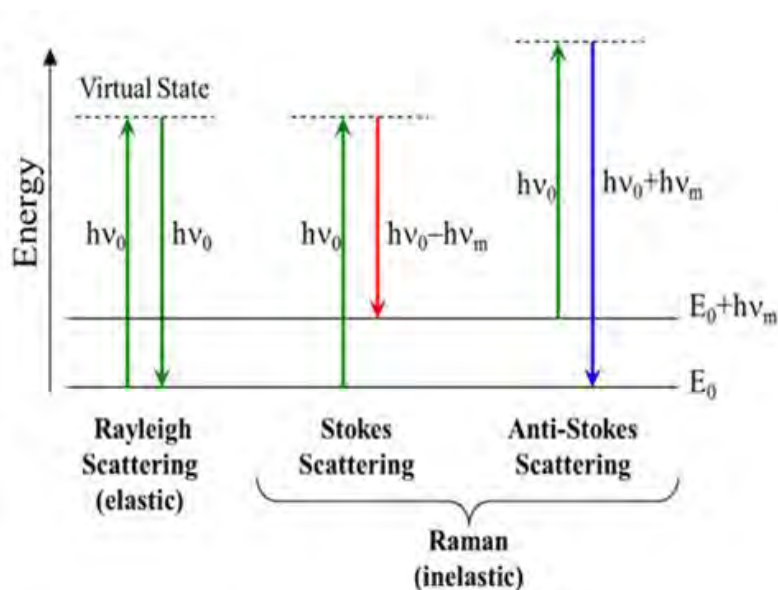


Figure 1.⁴ Image representing the energy transitions a molecule undergoes to produce a Raman Spectrum.

Micro Raman spectroscopy has the additional benefit of being attached to a light microscope, so individual, microscopic spots of ink in a sample can be analyzed individually. Preliminary testing done in the lab at West Virginia University (WVU) showed that Raman would potentially work to discriminate the three main colors of inkjet printer ink: cyan, magenta, and yellow. A second technique was desired to further discriminate black ink samples.

An additional analytical instrument being used for inkjet printer ink analysis is Laser Induced Breakdown Spectroscopy (LIBS). LIBS uses a laser pulse to form a plasma of elements on the surface of a sample.³ Each element will create a characteristic peak on a LIBS spectrum. A very

small portion of the sample is damaged by the laser pulse, and this technique allows the development of an elemental profile of different inkjet printer inks.

EXPERIMENTAL METHODS

Raman Spectroscopy



Figure 1. Picture of the Bruker model Senterra micro Raman Spectrometer used for data collection.

The printed ink samples were obtained from the Treasury Obligations Unit of the United States Secret Service. The color spots were then analyzed using The Bruker model Senterra Raman spectrometer coupled with the Olympus BX51M microscope. All data collection was done with the 785nm laser and 50x objective lens. 100% power, 20 second integration times, and 3 co-additions were used for collection of data for magenta and yellow samples. The power was reduced to 25% for cyan samples to avoid sample thermo-degradation. Five spectra were taken at different locations of each sample. The collected spectra were visually compared for peaks that could discriminate the individual inks of the same color.

LIBS



Figure 2.⁵ Image of the Foster & Freeman ECCO² used for data collection.

Small cuttings of the black inks were placed on a flat cylindrical sample holder in the Foster & Freeman ECCO². Five different portions of each black ink samples were hit once with the laser pulse. The collected LIBS spectra were then visually compared to each other and the blank paper spectrum.

RESULTS

The table below shows the results of attempted discrimination of eight different inkjet printer inks using Raman spectroscopy. Cyan, magenta and yellow inks were analyzed with Raman. The inks that are grouped into the same box on the table were unable to be differentiated by visual spectral comparison. The inks depicted in the same color are the different colors of a single ink sample. All three colors of every sample are not shown in the table because some samples did not produce clear spectra, likely because components in the ink mixture caused fluorescence which masked the Raman scattering signal in the spectrum.

Table 1. Discrimination of Inkjet Inks by Raman

Magenta	Cyan	Yellow
HP #88 124	HP 3052A 454	HP 449
HP 3052A 454	HP #88 126	HP 3052A 454
HP 564 451	HP #60 438	HP #60 438
HP #60 438	HP 564 448	HP 564 449
	Epson Stylus NX 625 445	HP #88 125
	Epson Stylus Photo R800 419	Epson Stylus NX 625 444
		Epson Stylus Photo R800 417

The spectra were able to be differentiated by visual comparison. Examples of two inks of the same color overlaid on the same chart for comparison are shown below. The last spectra is an example of how the black ink samples produced oversaturated spectra that included little useable data for discrimination purposes.

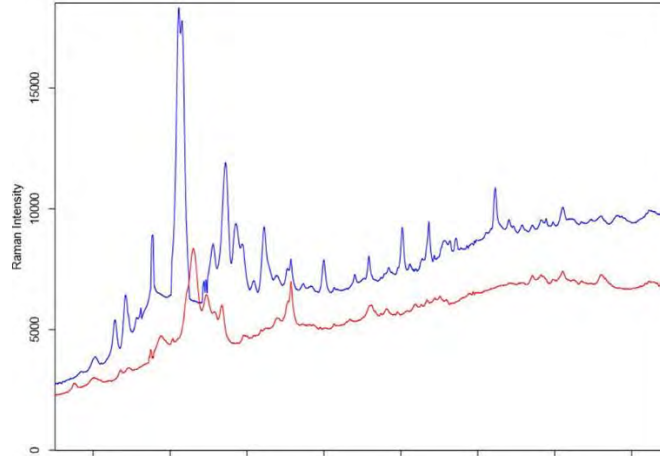


Figure 3. The blue line is magenta ink HP 451 and the red line is magenta ink HP 124.

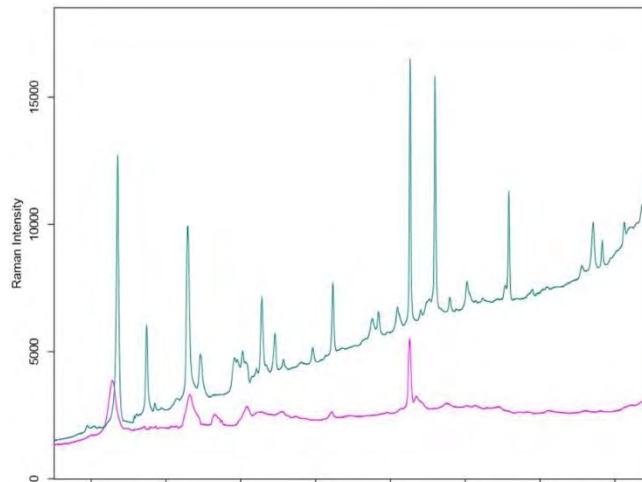


Figure 4. The teal line is cyan Epson 445 and the pink line is cyan HP 126.

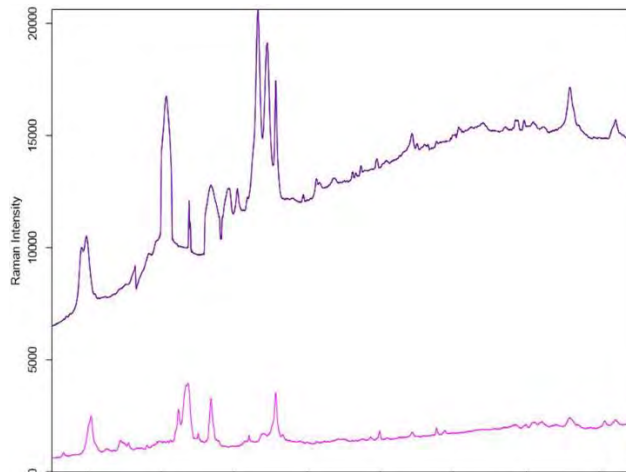


Figure 5. The purple line is yellow HP 454 and the pink is yellow Epson 417.

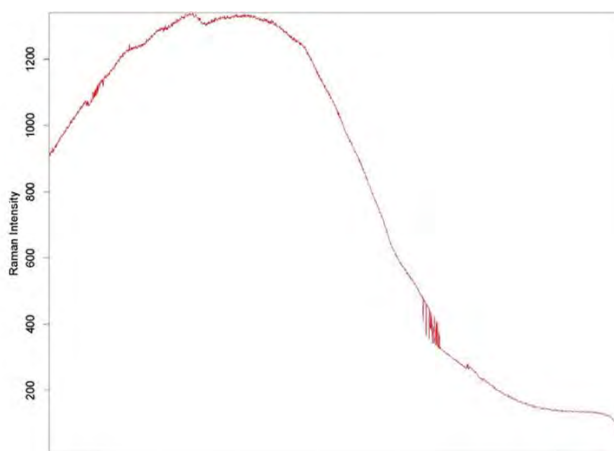


Figure 6. Spectra of black HP 408.

An example LIBS spectrum of black ink is shown below.

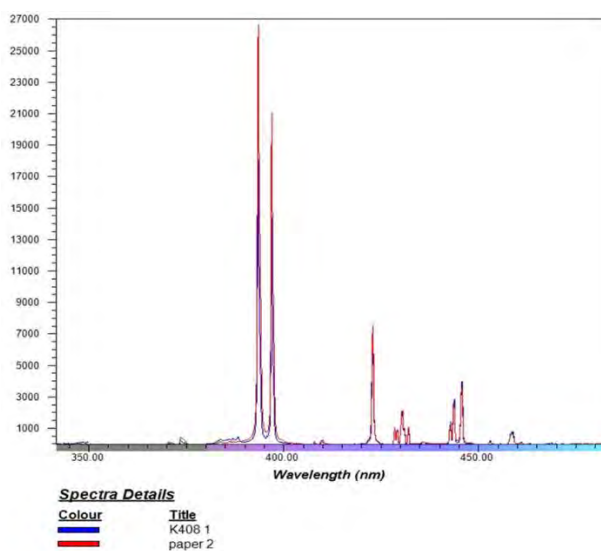


Figure 7. LIBS spectrum of HP black ink 408 superimposed with a control spectrum of paper.

DISCUSSION AND CONCLUSION

During the second half of this project, The USSS office was not able to provide new samples until after the first of the year in 2016. Progress was delayed because new samples had to be collected from inkjet printers around campus and at local print centers. Once the new samples were collected, the Raman began to malfunction. There were no other Raman spectrometers on campus that produced spectra and had a 785nm laser for analysis.

From the data that I was able to collect, it is evident that Raman spectroscopy offers a promising method for the discrimination of inkjet printers inks. The method is fast and nondestructive, so a large amount of data can be collected and the evidence samples can be preserved for further

analysis and use in criminal investigations. LIBS analysis was not successful at the discrimination of black inks, so a different spectroscopic method or a LIBS instrument with a weaker laser pulse need to be investigated in the future for discrimination of black inks.

Future directions of research include using different wavelengths of laser to compare the efficiency of discrimination. Laser printers are also capable of producing high-quality prints, so examination of the ability of Raman to differentiate inks from laser printers should also be investigated.

MOST SIGNIFICANT EXPERIENCES

The funding provided by the WVSGC for this project allowed me to devote more time to my research. I did not have to wait for departmental approval to spend money regarding the project, and the stipend provided to me ensured I did not have to work any additional jobs during the course of the semester.

Through completion of this research project, I have been given multiple opportunities to share my work with other people within and outside scientific fields. By presenting my research, I gain important skills that I can apply in my future career. The ability to effectively communicate the results of a research project to people in or outside of the field in which the work was done is one of the most important skills a researcher must have. I attended Undergraduate Research Day at the Capitol in Charleston, WV. This event allowed me to show legislators how important it is to continue supporting programs that fund undergraduate research projects. I was also able to interact with professors and students from other universities throughout the state. I was also selected to present my poster at the WVSGC S.P.A.C.E. day where I came in first place for the presentation of my poster.

I was trained on instruments such as the Raman Spectrometer and Laser Induced Breakdown Spectrometer which I otherwise would not have been trained to use. When I completed my summer internship at the National Institute of Standards and Technology during the summer of 2015 my supervisors immediately wanted to take advantage of my ability to run their new Raman. I have also learned how to budget my time by balancing my classwork with the time I needed to spend in the research lab.

ACKNOWLEDGEMENTS

This project would not have been possible without the generous contributions from the WV Space Grant Consortium. I would also like to thank The United States Secret Service Counterfeit Division for providing me with ink samples to test as well as my mentor Dr. Patrick Buzzini for guiding me through this project.

REFERENCES

- 1.) Papson, K., Stachura, S., Boralsky, L., & Allison, J. (2008). Identification of Colorants in Pigmented Pen Inks by Laser Desorption Mass Spectrometry. *Journal Of Forensic Sciences (Wiley-Blackwell)*, 53(1), 100-106.
- 2.) CRAIC Technologies. Science of micro Raman Spectroscopy. <https://www.microspectra.com/support/technical-support/raman-science/35-technical-support/126-science-of-micro-raman-spectroscopy> (accessed Apr 15, 2016).

- 3.) Applied Spectra. What is LIBS? <http://appliedspectra.com/technology/libs.html> (accessed Apr 15, 2016).
- 4.) Theory of Raman Scattering - B&W Tek. BW Tek, <http://bwtek.com/raman-theory-of-raman-scattering>
- 5.) ECCO®. (n.d.). Retrieved February 15, 2016, from <http://www.fosterfreeman.com/trace-evidence/ecco-col-180-laser-induced-breakdown-spectrometer.html>

III. NASA Graduate Research Fellowship Reports

EXERCISE IMPROVES SKELETAL MUSCLE FUNCTION IN THE ‘STRESS-LESS’ MOUSE

Deborah Amos

PhD Student, Biomedical Science Program

Marshall University

Huntington, WV 25755

ABSTRACT

Oxidative stress plays a key role in the metabolic syndrome, which includes obesity, Type II diabetes (T2D), and cardiovascular diseases (CVD). Oxygen-derived free radicals generated during mitochondrial electron transport chain alter the function of lipids and proteins thus impacting glucose and lipid metabolism. Within the skeletal muscle, oxidative damage affects fiber types, myonuclear number and location, and protein synthesis thus altering signaling pathways. Reactive oxygen species (ROS) also activate obesogenic pathways that effect body and fat mass as well as altered levels in adipokines. Therefore, increased oxidative stress will put a person at higher risk for developing metabolic disorders. Astronauts and space traveling rodents have higher levels of oxidative stress, once the atmospheric barrier is broken, as well as upon return from space. Oxidative stress also continues to increase as organisms remain for longer periods in space. Exercise by modulating the redox system increases ROS, which then signals antioxidant protection. Thus, exercise helps to lower fat mass, improves metabolic parameters, and improves skeletal muscle function. Therefore, I hypothesized that reducing oxidative stress would improve lean to fat body mass and improve skeletal muscle function. To study this hypothesis, two types of ‘stress-less’ mouse models ($n \geq 3$) (i) that expresses 4 fold higher antioxidant, catalase (**Cat-tg**) and (ii) that is a hybrid between Cat-tg and obese mice (Ob-Ob) called **Bob-Cat** were subjected to an exercise or sedentary regimen. Each group of mice was moderately exercised on a mouse treadmill for 8 weeks along with sedentary controls. Weekly Body weight and food intake was measured weekly. Fat and lean mass (ECHO-MRI), as well as metabolic parameters (CLAMS technology) were measured at baseline, 4, and 8 weeks. The effects of exercise on blood lipid profile, insulin, glucose, adipokines, and skeletal muscle function was determined. Statistics including the T-test and ANOVA followed by Post-hoc tests were used to compare exercise versus sedentary groups and the differences among genotypes. Statistical analysis of results revealed all mice lost weight compared to the C57 sedentary group and there was a decrease in percentage fat mass of exercised groups in comparison to their sedentary controls. There was also a trend for exercised mice to have a higher level of energy expenditure and greater food intake except in the Bob-Cat group. There was a significant increase of insulin in the Bob-Cat exercise group. Exercise also trended to increase HDL and glucose levels. Skeletal muscle was not significantly different in terms of muscle fiber type, grip strength test, nor did it reveal increases in damaged fibers (myonuclear location) between the groups of mice tested. My studies thus far showed that as expected, exercise evoked positive changes in fat mass. However, Cat-tg mice revealed overall different results than Bob-Cat, indicating a need for further investigation on catalase’s role in combination with exercise. To better define the role of increased antioxidant in combination with exercise on the obesogenic pathways in the ‘stress-less’ mouse, the adipose-brain axis will be investigated.

INTRODUCTION

Oxidative stress plays a key role in the metabolic syndrome, which includes obesity, Type II diabetes, and cardiovascular diseases [1]. Exercise has shown to both cause an increase in the production of ROS as well as increase the levels of antioxidants [2] [3] [4]. Exercise results in lower fat mass and improves skeletal muscle function [2]. Being a post-collegiate athlete, I desire to study the effects of exercise on oxidative stress levels, body composition, metabolism, and skeletal muscle function. To study my objectives, I bred and maintained two different “stress-less” mouse models: (i) Catalase Transgenic (Cat-tg) mice: that express 3-4 fold higher human catalase levels compared to its parent strain C57Bl6 mice (thus ‘stress-less’) and (ii) Bob-Cat mice: a hybrid between Cat-tg and Ob/Ob leptin deficient mice. C57BL6 mice were the control group. Sixteen week old Cat-tg ($n \geq 7$) and Bob-Cat mice ($n=8$) were assigned to a sedentary or exercise group. The exercise group ran 30 min., 5 days per week for 8 weeks at 15 m/min (moderate rate) on a mouse treadmill (Mice 3/6 Animal Treadmill, Columbus Instruments, Columbus, OH). The IACUC committee of Marshall University approved this study. Weekly food and body weights were measured. ECHO-MRI (magnetic resonance imaging) was performed at the beginning, 4 week, and 8 weeks time point to analyze fat and lean body mass percentages. CLAMS (Comprehensive Laboratory Animal Monitoring System) was performed at the end of the 8 weeks to measure Respiratory Exchange Rate (RER), Heat Production (Kcal/h), Food Intake (g/24h), and Locomoter Activity (X-Ambulatory Counts/day). Grip strength tests were performed at the end of the protocol where the groups were acclimated to the environment and tested. Scores for strength were calculated according to how much weight was held for 1-3 seconds. [5] At the end of 8 weeks, mice were fasted, anesthetized, and then blood was obtained by cardiac puncture. Blood was centrifuged 10 minutes to obtain plasma. 35 μ L of plasma was then used in an LDX Cholestech machine to obtain the lipid profile for each mouse. A glucometer was used to determine fasting blood glucose level. Tissues, with the exception of muscle, were collected, weighed, and flash frozen in liquid nitrogen then stored at -80°C . Gastrocnemius and Soleus (hind leg) muscles were removed, weighed (g), and measured (mm) using Calipers. Muscle was then frozen by subjecting it to isopentane, cooled by liquid nitrogen then immediately cut. The middle segment was used for cryostat sectioning after being frozen in O.C.T (Optimal Cutting Temperature) filled molds and frozen (-80°C). A Leica CM1900 Cryostat was used to slice muscle into 5-8 μm sections and then placed on warm slides and stored in -80°C until staining. The remaining muscle was frozen in -80°C . To analyze skeletal muscles for Type 1 (oxidative), Type 2 (glycolytic), and myonuclear number and location, slides were warmed from -80°C and Myosin ATPase Protocol (Kelly Lab-ATPase Histology Stain 2006) was followed to stain Gastrocnemius (Gas) right and left (R and L) and Soleus R and L for each muscle at pH 4.3 to determine the fiber type ratio. Hematoxylin and Eosin Staining (H&E) was used to determine the myonuclear number and location, (Peripheral and Central Myonuclei). Myosin ATPase stained slides were analyzed at 10X magnification, while H&E stained slides were analyzed at a magnification of 40X on a Nikon Eclipse Ti Inverted Microscope. Muscle parameters were analyzed with ImageJ software and saved as JPEG files. Milliplex Mouse Adipokine Magnetic Bead Panel was used to measure levels of IL-6, MCP-1, TNF- α , Leptin, Insulin, and Resistin using 10 μL of thawed plasma from each mouse according to manufacturer’s protocol in a Luminex 200 system. Results were calculated by T-tests and 2 way ANOVA with post-hoc tests and plotted using Excel and GraphPad Prism as mean \pm SEM or mean \pm SD as stated in the legend. $p < .05$ was considered statistically significant. All associated personnel had passed the CITI Certification Tests for Mouse and Rodent Handling. Animals were

treated in compliance with Marshall University Animal Committee (Institutional Animal Care and Use Committee) regulations.

BACKGROUND

Oxidative stress plays a key role in the metabolic syndrome including obesity, Type II diabetes and cardiovascular diseases [1]. It is implicated that oxygen-derived free radicals generated during mitochondrial electron transport chain alter the function of specific biological components [1]. With regard to skeletal muscle, damage affects fiber types [6], myonuclear location, and protein synthesis creating a change in myokine production [6]. Reactive oxygen species (ROS) also activate obesogenic pathways including glucose and lipid signaling [7] and persistent oxidative stress in heart and skeletal muscle has been repeatedly demonstrated to have causal roles in the etiology of heart disease and insulin resistance [8]. Therefore, increased oxidative stress increases risk for developing the metabolic syndrome [1]. In space, and upon return from aerospace conditions, studies have shown that there are increased levels of oxidative stress in rodents and humans [9]. This puts astronauts and “space rodents” at a higher risk for harming skeletal muscle and negatively impacting the organism’s metabolism. Exercise has shown to both cause an increase in the production of ROS as well as increase the levels of antioxidants [2] [3] [4]. Exercise results in lower fat mass and improves skeletal muscle function [2]. As a former college athlete, I am interested in looking at the impact of exercise on the level of oxidative stress and its impact on muscle function.

EXPERIMENT

I hypothesized that reducing oxidative stress would improve lean to fat body mass and skeletal muscle function. To study this, I bred and used two novel antioxidant mouse models. I anticipated that exercised mice would decrease oxidative stress within muscle tissue which thus preventing muscle damage and lower the risk of obesity-related complications. Indications of these effects were evaluated by body composition changes, metabolic parameters, measurement of adipokine levels, and skeletal muscle changes.

PROJECT

To test the proposed hypothesis, my **first aim** was to investigate the impact of exercise on the fat/lean body mass, ROS, and adipokine markers in novel mouse model. My **second aim** entailed analyzing the impacts of exercise on the skeletal muscle to see if there is any evidence of muscle damage comparing the exercise group to the sedentary group.

METHODS

Animal Models and Exercise

C57Bl6, Catalase Transgenic (Cat-tg), and “Bob-Cat” mice were housed in cages according to their respective groups. C57Bl6 mice (n≥6) were bought from Hilltop Laboratories and acclimated to mouse facilities at Marshall University. All groups were fed Normal Rodent Chow (Lab Diet 5001) ad libitum. Cat-tg mice (n=7), which were a gift from Arlan Richardson’s Laboratory [10] were bred and housed in Marshall University Animal Facility. “Bob-Cat” mice (n=8) from each group were housed in cages of 3 to 4 mice per group. “Bob-Cat” mice are a novel mouse model generated in our laboratory, by crossing Cat-tg mice with Ob-Ob (obese, leptin deficient, Jax Labs). All guidelines were followed according to IACUC rules and regulations in

accordance with approved study protocol. Each of the three mouse models were divided into exercise and sedentary groups. Sedentary mice remained in their respective cages in the same environment as the exercised mice. Exercised mice are subjected to a week long acclimation period to the treadmill (Columbus Instruments) prior to beginning the exercise protocol: 8 weeks of exercising, 5 days per week for 30 minutes at a rate of approximately 15 m/min. Animals were treated in compliance with Marshall University Animal Committee (Institutional Animal Care and Use Committee) regulations.

Body Weight and Food Consumption

Body mass (g) was measured weekly along with total food intake (g). Calculations were conducted to determine the average body weight per mouse group as well as food intake per mouse each week.

ECHO-Magnetic Resonance Imaging (ECHO-MRI)

Body fat and lean mass composition of the six groups of mice: C57Bl6, Cat-tg, Bob-Cat (sedentary and exercise) were determined using ECHO-MRI (Houston, TX). Total water content and free water content were also calculated. Mice were individually placed into the MRI machine. To determine body composition, mice were weighed and then five MRI readings were conducted per mouse. Calculations were made using Microsoft Excel for the median values of each parameter. Body weights were then used to calculate fat and lean percentage by the ECHO-MRI machine.

Comprehensive Laboratory Animal Monitoring System (CLAMS)

Metabolic parameters were measured indirectly by assessing O₂ consumption (VO₂) and CO₂ production, respiratory exchange rate (RER) as well as body movement. Mice are supplied with ground rodent chow (Lab Diet 5001) for three days as the analysis is conducted. Computations are made on the middle 48 hours the mice are subjected to the machine, which is approximately 0600 hour of the first day to 0600 hour of the third day. Heat production (energy expenditure), RER average, average food intake per day, as well as x-ambulatory locomotor activity (counts movement was made across the cage) per day were calculated.

Grip Strength Tests

At the end of the 8 week study period, mice are tested for grip strength. The apparatus for assessment consists of a ball of tangled fine gauge metal wire, a "scale collector" as attached to a metal wire clip. The scale collector is first attached to one chain length. The number of links ranges from one to five (additional weights may be added). Weights were therefore: approximately 25.7 (1 link), 34.97 (2 links), 44.24 (3 links), 53.51 (4 links), and 62.79 (5 links). Mice are held by the middle/base of the tail and lowered to allow it to grasp the first weight (25.7g) which is lying on the laboratory bench. It grasps the wire scale collector with its forepaws. A hold of three seconds is the criterion. If the mouse drops the weight in less than 3 sec the mouse is allowed to rest for about 10 sec and tested on the same weight once again. If it fails three times, that terminates the trial, and the mouse is assigned the maximum time/weight achieved. If it holds it for 3 sec then the next heaviest weight is utilized. A final total score is calculated as the product of the number of links in the heaviest chain held for the full 3 sec, multiplied by the time (sec) it is held. If the heaviest weight is dropped before 3 sec an appropriate intermediate value is calculated [5].

Tissue Collection

After 24h fasting, mice were removed from their cages, and animals were anesthetized using Isoflurane. Blood was obtained by cardiac puncture; red blood cells (RBCs) and plasma were separated by centrifugation for 10 min. Mice were perfused intracardially with cold phosphate buffered saline (PBS). Tissues including adipose, brain, etc. were removed, weighed, and flash frozen in liquid nitrogen. To preserve tissues, all were stored in -80°C.

Lipid Profile/Glucometer

Whole blood was used to measure fasting glucose levels by Precision Xtra Glucometer. 35 uL of plasma was placed on a cassette and read on a LDX Cholestech Machine to determine glucose, LDL, HDL, total cholesterol, and triglyceride levels. The remaining plasma was frozen at -80°C.

Cryostat Sectioning of Skeletal Muscle

Muscle tissue collection was conducted by removal of the gastrocnemius (Gas) and soleus (Sol) muscle of each leg. Muscle weight (g) and length (mm) is measured. Muscle is then frozen by subjecting it to a vial of cooled Isopentane and frozen slowly by lowering the cooled isopentane in liquid Nitrogen. Once fully frozen, muscle is sliced into three segments. The middle segment is used for cryostat sectioning where it is frozen in O.C.T (Optimal Cutting Temperature) medium and frozen (-80°C) until cryostat sectioning. Leica CM1900 Cryostat is used to slice muscle into 5-8 µm sections and then transferred to room temperature slides that are then placed in -80°C until staining.

Myosin ATPase Staining

Slides are warmed from -80°C and Myosin ATPase Protocol (Kelly Lab-ATPase Histology Stain 2006) was followed to stain Gastrocnemius (Gas) right and left (R and L) and Soleus R and L for each muscle. pH 4.3 was used to determine the fiber type ratio of Type 1 (Oxidative) to Type 2 (Glycolytic) fibers within each mouse group.

Hematoxylin and Eosin Staining (H&E)

H&E staining was used to determine the myonuclear location within the collected muscles of each mouse. (Peripheral and Central Myonuclei)

Microscope Analysis

Myosin ATPase stained slides were analyzed at 10X magnification, while H&E stained slides were analyzed at a magnification of 40X on a Nikon Eclipse Ti Inverted Microscope. Parameters were evaluated using ImageJ Software and saved as JPEG files.

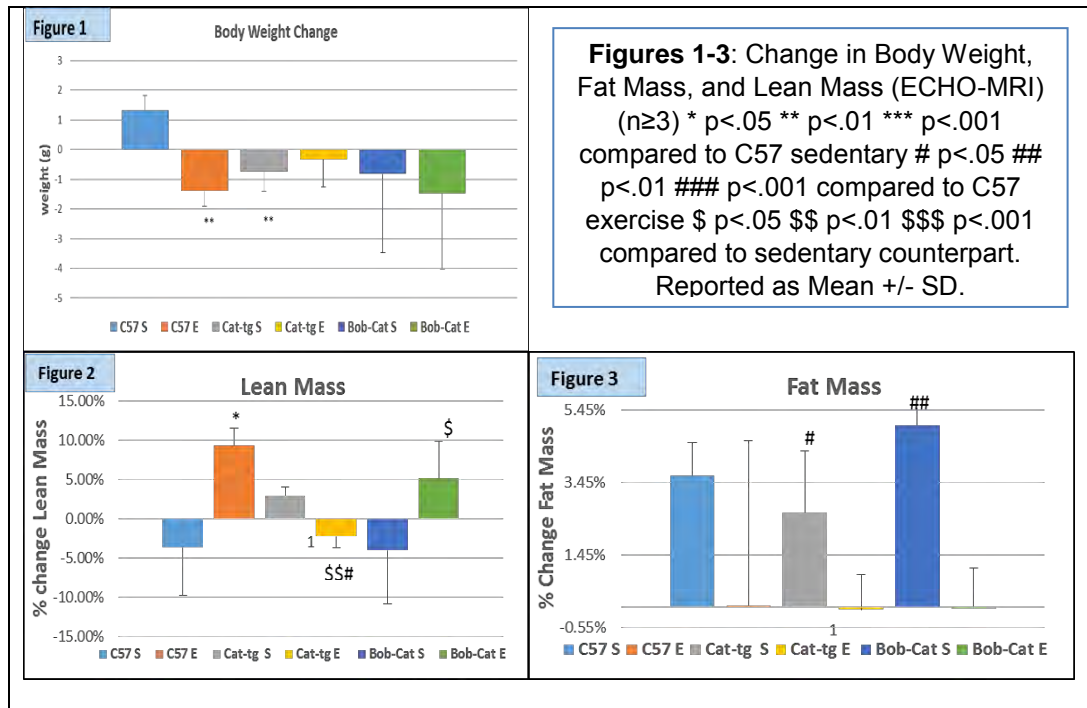
Statistical Analysis

Results are expressed as mean +/- SEM or mean +/- SD as stated in the legend. The difference in each group was evaluated by T-Test and/or a 2-factor ANOVA when applicable with GraphPad Prism. Statistical significance was accepted at $p < 0.05$.

RESULTS

Body Weight, Fat Mass (ECHO MRI), and Lean Mass (ECHO MRI)

C57 sedentary mice gained while all other groups showed a trend towards a lower body weight. (Fig. 1) Exercise groups trended to have a lower % fat mass compared to their sedentary counterparts. However, exercised Cat-tg and Bob-Cat mice significantly lost fat mass throughout the study in comparison to their sedentary controls. (Fig. 2) Lean mass was gained in all exercise groups except Cat-tg exercised mice. Groups that overexpressed antioxidant did not increase lean mass percentage to the degree of C57 exercise mice. (Fig. 3)



Comprehensive Laboratory Animal Monitoring System (CLAMS)

All exercised mice showed an increase in RER (Respiratory Exchange Rate) in comparison to sedentary controls. Cat-tg mice showed an increase in RER in comparison to C57 exercised mice while Bob-Cat mice showed a decrease. Bob-Cat mice trended to show the highest energy expenditure. However, exercise affected energy expenditure of Cat-tg and Bob-Cat mice differently. Food intake was increased in all exercised mice, except Bob-Cat, compared to their sedentary counterpart. (Table 1)

Table 1	RER	Energy Expenditure	Food Intake	XAMB (Activity)
Group	VCO ₂ /VO ₂	Kcal/h	g/24h	counts/24h
C57 Sed	0.93 +/- .015	0.40 +/- .02	4.40 +/- .24	25310 +/- 12277
C57 Exercise	0.95 +/- .01 *	0.42 +/- .02	4.89 +/- .25 *	14585 +/- 5132
Cat-tg Sed	0.94 +/- .01	0.40 +/- .03	3.72 +/- .26 *	22003 +/- 9384
Cat-tg Exercise	0.98 +/- .02 ###	0.44 +/- .04	6.36 +/- 1.72 \$	12056 +/- 4470
Bob-Cat Sed	0.88 +/- .03 *	0.49 +/- .02 ***	4.36 +/- .90	24755 +/- 16406
Bob-Cat Exercise	0.92 +/- .02 \$#	0.44 +/- .03 \$	4.33 +/- 1.49	24749 +/- 5640 #

* p<.05 *** p<.001 sig. difference compared to C57 sed. , # p<.05 ## p<.01 sig. difference compared to C57 Exercise, \$ p<.05 \$\$ p<.01 sig. difference compared to sedentary counterpart

Lipid Profile, Glucose, and Adipokine Array

Glucose was averaged between glucometer and LDX cholestech machine readings and HDL measurement was taken from LDX cholestech machine. There was an overall trend for exercised mice to have both higher levels of HDL and Glucose. Insulin, leptin, and resistin were measured using an adipokine array. A trend for Cat-tg Exercise mice to have lower levels of insulin, higher levels of leptin, was noted with the opposite effect in Bob-Cat mice. (Table 2)

Table 2	HDL (mg/dl)	Glucose (mg/dl)	Insulin (pg/ml)	Leptin (pg/ml)	Resistin (pg/ml)
C57 Sed	61.8 +/- 22.4	188.4 +/- 21	287.1 +/- 211.6	29.60 +/- 13.8	19.53 +/- 2.4
C57 Exercise	54.3 +/- 11.1	222.5 +/- 39.9	150.2 +/- 88.8	84.2 +/- 18.8	36.4 +/- 5.7
Cat-tg Sed	58 +/- 8.2	180 +/- 20.8	67.20 +/- 20.9	14.93 +/- 5.3	11.67 +/- 3.0
Cat-tg Exercise	53 +/- 15.3	193.6 +/- 70.6	17.52 +/- 6.2\$\$\$	113 +/- 46.8**	24.72 +/- 5.9
Bob-Cat Sed	61.8 +/- 9.3	208.5 +/- 54.5	47.83 +/- 16.2	43.51 +/- 6.5	25.13 +/- 7.4
Bob-Cat Exercise	59.3 +/- 9.4	225.8 +/- 45.6	146 +/- 41.0***\$\$	27.50 +/- 5.5	43.9 +/- 7.6

(n≥3) * p<.05 ** p<.01 *** p<.001 compared to C57 sedentary # p<.05 ## p<.01 ### p<.001 compared to C57 exercise \$ p<.05 \$\$ p<.01 \$\$\$ p<.001 compared to sedentary control.

Skeletal Muscle Analysis

Post cryosection of Gas and Sol right and left (R and L) muscles, slides were stained for detection of Myosin ATPase (Fig. 5 and Images 1 and 2) or myonuclear number and location (H&E staining) (Fig. 6-7 and Images 3-4). Grip Strength Test was also performed for each group of mice (Fig.7). No significant differences were noted between the groups. This is indicative that moderate exercise does not cause significant changes in muscle integrity or strength between the groups of mice. It also provides evidence that increased antioxidant does not cause deleterious effects to skeletal muscle by changes in the redox state.

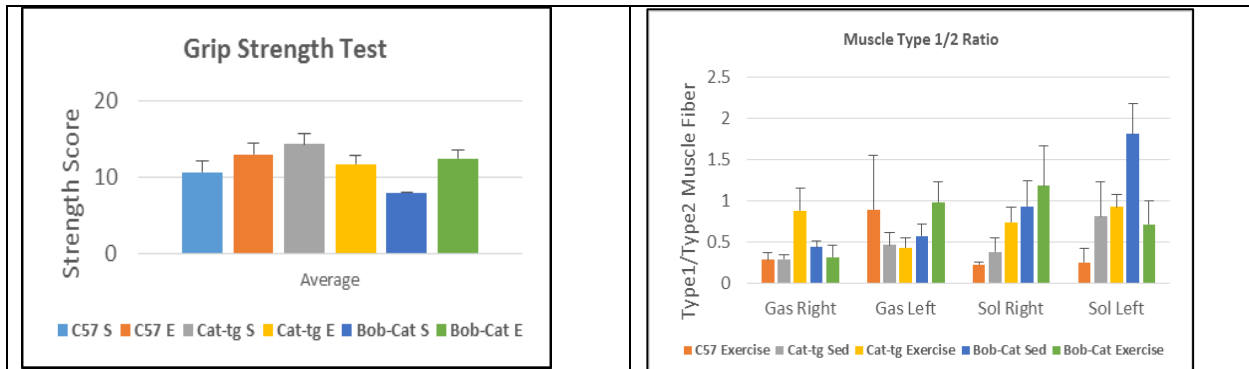


Figure 4

Figure 5

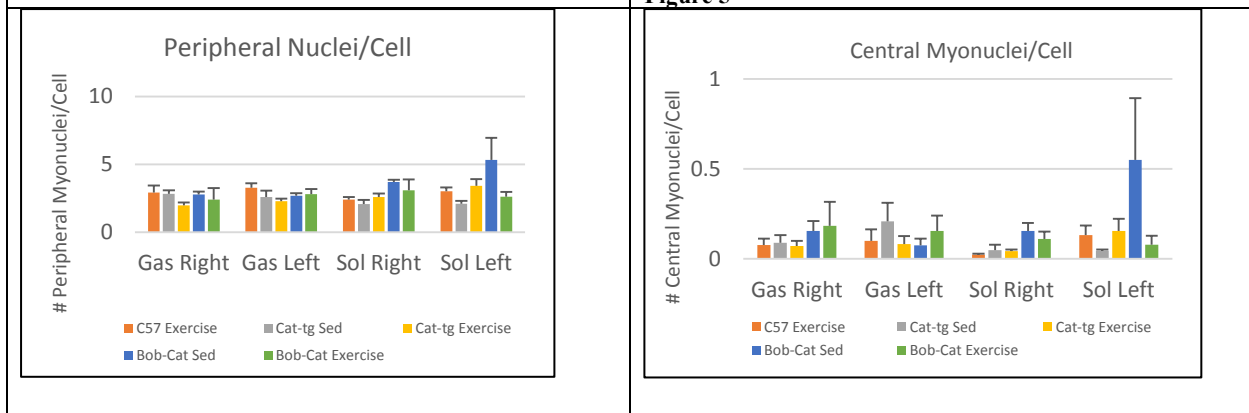
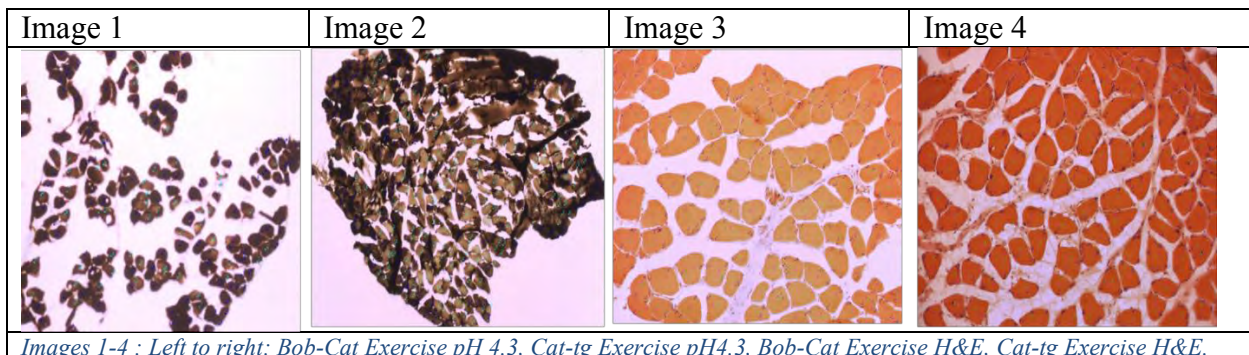


Figure 6

Figure 7

Figures 4-7: Grip Strength, Muscle Fiber Type, and Myonuclei. All values reported as mean +/- SEM (n>3)



DISCUSSION

Moderate exercise and overexpression of catalase (antioxidant) has resulted in a decrease of body weights along with decreased fat mass % in all groups of mice compared to the C57 sedentary control mouse. However, Bob-Cat and Cat-tg lean mass changes were affected differently when comparing exercise and sedentary groups. In addition to different lean mass changes, metabolic parameters with regard to energy expenditure and food intake were also differentially affected along with plasma analysis of insulin and leptin levels which play key roles in appetite and energy regulation mandating further investigation. However, the combined beneficial effects of moderate exercise and antioxidant excess on skeletal muscle fiber type, myonuclear number or location, and grip strength of each group was inconclusive with minimum numbers of mice in each group. On

the other hand, it seems evident that increase in antioxidant has not negatively affected the muscle fibers of any genotype.

OUTCOMES

Based on our results, it is evident that the effects of exercise and overexpression of antioxidant has an additive influence on metabolic parameters. The “stress-less” mice are a good model to study the beneficial impact of lowering oxidative stress in obese individuals, athletes, space traveling rodents, and astronauts.

FUTURE PLANS

Since we observed differences in the effects of exercise and catalase overexpression between mouse models, analysis of signaling mechanisms involved in redox regulation and the adipose-brain axis will be studied in the future. This includes, but is not limited to the leptin regulation of appetite genes as well as key neurons in the hypothalamic region of the brain.

ACKNOWLEDGEMENTS

I acknowledge the generous support by WV-NASA Space Grant Consortium. I would also like to acknowledge Dr. Jung Han Kim for training and use of ECHO-MRI and CLAMS machinery, as well as lab members, and most of all, my research mentor, Dr. Nalini Santanam for her continual advice and support throughout the past year.

VALUABLE ASPECTS

Not only did the WV-NASA Grant provide me funds to continue my education at Marshall University, it also allowed me to develop further as a young researcher. I was able to enhance my knowledge on techniques I had previously learned, as well as learn new methods to analyze and calculate experimental results. It also enabled me to present five poster presentations, for two of which I received an award (ASBMB travel award to present at Experimental Biology meeting in San Diego, April 2016 and 1st Place in the poster competition at NASA S.P.A.C.E. Day, April 2016). I am also grateful for the experience I have had teaching and training undergraduates and graduate students rotating through our laboratory about techniques and protocols related to my project. I am truly thankful for the experience and hope to continue to be funded by NASA for my future research work.

PUBLICATIONS AND PRESENTATIONS

- Poster Presentation: Marshall University Biomedical Science (BMS) program, Research Retreat August 2015
- Poster Presentation: Appalachian Regional Cell Conference (ARCC) Fall 2015
- Publication : Walters, J. W., Amos, D. L., Ray K. L., Santanam, N. (2016). "Mitochondrial redox status as a target for cardiovascular disease." *Curr Opin Pharmacol* 27: 50-55.
- Poster Presentation: Joan C. Edwards School of Medicine Research Day March 2016

- Oral Presentation: Marshall University BMS program, State of the Art Review: “Exercise and It’s Myriad of Benefits: A Mechanistic Update”
- Poster Presentation: Experimental Biology (EB) National Conference, San Diego, April 2016 (ASBMB Travel Award Recipient)
- Poster Presentation: NASA S.P.A.C.E. Day April 16, 2016 (1st Place Poster Competition)

REFERENCES

1. Luque-Contreras, D., et al., *Oxidative stress and metabolic syndrome: cause or consequence of Alzheimer's disease?* Oxid Med Cell Longev, 2014. **2014**: p. 497802.
2. Golbidi, S., A. Mesdaghinia, and I. Laher, *Exercise in the metabolic syndrome.* Oxid Med Cell Longev, 2012. **2012**: p. 349710.
3. Shern-Brewer, R., et al., *Exercise and cardiovascular disease: a new perspective.* Arterioscler Thromb Vasc Biol, 1998. **18**(7): p. 1181-7.
4. Meilhac, O., et al., *Role of arterial wall antioxidant defense in beneficial effects of exercise on atherosclerosis in mice.* Arterioscler Thromb Vasc Biol, 2001. **21**(10): p. 1681-8.
5. Deacon, R.M., *Measuring the strength of mice.* J Vis Exp, 2013(76).
6. Li, F., et al., *Protective effect of myokine IL-15 against H2O2-mediated oxidative stress in skeletal muscle cells.* Mol Biol Rep, 2014. **41**(11): p. 7715-22.
7. Ballal, K., et al., *Obesogenic high fat western diet induces oxidative stress and apoptosis in rat heart.* Mol Cell Biochem, 2010. **344**(1-2): p. 221-30.
8. Alleman, R.J., et al., *The "Goldilocks Zone" from a redox perspective-Adaptive vs. deleterious responses to oxidative stress in striated muscle.* Front Physiol, 2014. **5**: p. 358.
9. Stein, T.P., *Space flight and oxidative stress.* Nutrition, 2002. **18**(10): p. 867-71.
10. Chen, X., et al., *Catalase transgenic mice: characterization and sensitivity to oxidative stress.* Arch Biochem Biophys, 2004. **422**(2): p. 197-210.

EFFECTS OF LOW-LEVEL SILVER NANOPARTICLE EXPOSURE ON ADULT NEURAL STEM CELL DIFFERENTIATION

Robert Cooper
Master of Science, Biological Sciences
Marshall University
Huntington, WV 25755

ABSTRACT

Silver nanoparticles (AgNP) are an emerging environmental contaminant with unique chemical and physical properties. They are utilized in products like medical dressings and toys for their antimicrobial action. Though AgNP's bioaccumulative nature and high-level toxicity are established, low-level effects from chronic exposure to AgNP-containing products and environmental AgNP remain unclear. This study uses adult neural stem cells, a model for neural cell function and neurodevelopment, to assess changes in cell differentiation and behavior following low-level AgNP exposure. *In vitro*, low-level AgNP produced dose- and time-dependent formation of co-localized f-actin inclusions and β -catenin puncta. Neurite extension and arborization were also reduced, indicating that AgNP disrupt cytoskeleton dynamics, possibly via β -catenin disruption. *In vivo*, AgNP treatment caused accumulation and persistence of Ag in brains at levels comparable to *in vitro* studies without overt toxicity. Together, this indicates that low-level AgNP exposure from consumer products may impair normal brain function and neurodevelopment.

INTRODUCTION

Adult neural stem cells (NSC) are multipotent stem cells present in several niches in the adult brain, namely the subgranular zone of the hippocampus and the subventricular zone (SVZ) of the lateral ventricles (Aimone et al., 2014; Altman and Das, 1965; Gage, 2000). In the SVZ, NSC proliferate and maintain a persistent population of stem cells, giving rise to rapidly-dividing progenitors that begin differentiation and migrate down the rostral migratory stream (RMS) towards the olfactory bulb (OB) bulb (Doetsch et al., 1997; Luskin, 1993; Luskin and Boone, 1994). Once there, they complete differentiation into glia or neurons and integrate into existing circuits, primarily as GABAergic interneurons (Gerard et al., 1994; Scheffler et al., 2005). This process of NSC proliferation, migration, and differentiation is collectively known as adult neurogenesis, and is important in basic processes such as learning, memory, and endogenous repair (Snyder et al., 2001; van Praag et al., 1999; Zhang et al., 2007; Zheng et al., 2013). However, NSC can be isolated from the SVZ and maintained in culture as organized spheres of progenitor cells called neurospheres (Doetsch et al., 2002; Reynolds and Weiss, 1992; Wachs et al., 2003). Cells in these neurospheres can be induced to differentiate *in vitro* by withdrawal of growth factors and provision of an extracellular matrix. Differentiating NSC in culture follow the same cellular mechanism observed in neurodevelopment and adult neurogenesis *in vivo* (Ge et al., 2008). Further, SVZ-derived NSC (SVZ-NSC) give rise to functional neurons and glia *in vitro*. Altogether, this makes them a powerful and accessible system to investigate changes to neurodevelopment, adult neurogenesis and repair, and brain cell function in general.

Silver nanoparticles (AgNP) are an emerging environmental contaminant defined as silver structures with at least one dimension between 1-100nm (Kruszewski et al., 2011). Due to their small size, AgNP have incredibly high surface area to volume ratios, giving them unique chemical and physical properties. One of these is incredibly potent antimicrobial effects (Baker et al., 2005; Panacek et al., 2006; Samuel and Guggenbichler, 2004; Sondi and Salopek-Sondi, 2004). This has led to AgNP's unregulated use in many consumer products like food packaging, toys, and washing machines (Cushen et al., 2013; Quadros et al., 2013; von Goetz et al., 2013). Indeed, AgNP are even used in the water filtration system aboard the MIIR space station (Silvestry-Rodriguez et al., 2007). However, AgNP shed from these products, resulting in direct consumer exposure through ingestion and inhalation (Benn et al., 2010; Benn and Westerhoff, 2008; Quadros et al., 2013; Yang and Westerhoff, 2014). They bypass bodily defenses like the blood-air barrier in the lungs (Ji et al., 2007; Oberdorster et al., 2004), the lumen in the gut (Boudreau et al., 2016; Gaillet and Rouanet, 2015; Kovvuru et al., 2015; Xu et al., 2015). Once in the body, they bypass internal defenses like the blood-brain barrier (Lee et al., 2013; Sosedova et al., 2015; Tang et al., 2008; Tang et al., 2010) and accumulate in tissues, especially the brain, and persist over time (Lankveld et al., 2010; Lee et al., 2013; Wen et al., 2016). AgNP have been shown to be toxic to eukaryotic cells in high concentrations, capable of breaking down the cytoskeleton, causing oxidative stress, and inducing apoptosis and necrosis (Bartlomiejczyk et al., 2013; Kruszewski et al., 2011). However, significantly less is known about their effects at lower concentrations that do not induce cell death, especially in target organs like the brain.

Previous work with SH-SY5Y neuroblastoma cells found that low-level AgNP increased neural differentiation through activation of the Akt and ERK signaling pathways (Dayem et al., 2014), suggesting that low-level AgNP could increase neurogenesis. Conversely, work with SVZ-NSC from our lab has found that low-level AgNP exposure results in the formation of f-actin inclusions *in vitro* (Cooper and Spitzer, 2015) that are visually similar to those seen following application of f-actin stabilizing (Lazaro-Dieguez et al., 2008) or depolymerizing toxins (Muller et al., 2013). Further, low-level AgNP were found to disrupt the cytoskeleton-dependent processes of neurite extension, dynamics, and arborization, all of which are vital for neural differentiation (Cooper and Spitzer, 2015). Altogether, this led to the conclusion that low-level AgNP disrupt cytoskeleton dynamics and therefore neurogenesis *in vitro* (Cooper and Spitzer, 2015). However, no specific cellular mechanism was identified.

This project aimed to determine the molecular mechanism of previously-observed deficits in cytoskeleton dynamics and cytoskeleton-mediated processes. Dayem et al. previously identified ERK and Akt signaling as potential targets by AgNP (Dayem et al., 2014), pathways both known to promote NSC proliferation, survival, and differentiation (Conti et al., 2001; Huang et al., 2014; Jin et al., 2005; Liu et al., 2014). However, Wnt/ β -catenin signaling also plays a large role in control of NSC proliferation and differentiation (Marinero et al., 2012; Varela-Nallar and Inestrosa, 2013; Wisniewska, 2013), and has been shown to affect neurite dynamics and arborization (Lee et al., 2014; Pino et al., 2011; Yu and Malenka, 2003). This pathway is therefore another potential target for disruption by AgNP.

Further, this project aimed to investigate whether or not previous *in vitro* effects are recapitulated *in vivo*. Previously, studies of AgNP exposure in rodents produced mixed results. One study showed no changes to neurogenesis (Liu et al., 2013) after 7 days. However, another showed that the neurogenesis-associated processes plasticity and spatial cognition were reduced following 14

day's AgNP exposure (Liu et al., 2012) but did not directly investigate changes to neurogenesis. Therefore, this study investigated AgNP's effects on adult neurogenesis by assessing changes to NSC number and fate in the entire SVZ-RMS-OB system in rats following 28 days' exposure to AgNP.

Finally, this project aimed to determine if there are any changes to membrane properties in cells derived from SVZ-NSC exposed to low-level AgNP. NSC are normally hyperpolarized before differentiation (Scheffler et al., 2005; Stewart et al., 1999). However, during differentiation, they undergo a complex series of changes that make them more excitable and allow them to fire action potentials (Belluzzi et al., 2003; Carleton et al., 2003; Scheffler et al., 2005; Stewart et al., 1999; Wang et al., 2003). This process is necessary for NSC to complete differentiation into mature neuronal phenotypes (Scheffler et al., 2005). However, AgNP have previously been shown to inhibit voltage-gated sodium channels (Busse et al., 2013; Liu et al., 2009) and voltage-gated potassium channels (Liu et al., 2011) in mature cells. Therefore, this work investigated whether or not the development of these same currents were disrupted in differentiating NSC. Altogether, this work aimed to investigate the effects of low-level AgNP exposure on NSC behavior and differentiation *in vivo* and *in vitro*, disruption of which could lead to deficits in adult neurogenesis and basic processes like learning and memory.

METHODS

Cell Culture

SVZ neural stem cells were isolated from female young adult (3-6 months old) Sprague-Dawley rats (Hilltop Lab Animals, Scottsdale, PA) according to established protocols (Muraoka et al., 2008; Reynolds and Weiss, 1992; Wachs et al., 2003). Rats were deeply anesthetized with inhaled isoflurane (Kent Scientific Corp., Torrington, Connecticut) and decapitated. The brain was removed and placed in cold phosphate-buffered saline 1 (PBS1, in mM: NaH₂PO₄, 2.69 (Sigma, St. Louis, Missouri, United States); Na₂HPO₄, 11.9 (AMRESCO, Solon, Ohio); NaCl, 137 (Fisher, Fair Lawn, New Jersey); KCl, 27 (AMRESCO); pH 7.4) containing 1% penicillin-streptomycin (P/S; Life Technologies, Grand Island, New York) before the subventricular zone was isolated. The tissue was chopped in PBS1 plus 4.5g/L glucose (Sigma) with a scalpel blade, then enzymatically digested in fresh PDD (0.01% papain (Fisher); 0.01% DNase I (Sigma); 0.1% Dispase II (Sigma); 12.4mM MgSO₄ (Sigma)) for 40 minutes with trituration every 10 min. After digestion, cells were collected by centrifugation, washed three times with DMEM/F12 (Life) and suspended in Neurosphere medium (DMEM/F12 + Glutamate, non-essential amino acids (NEAA), P/S, B27, 20ng/ml EGF, 5ng/ml bFGF, (all from Life) and 1.25U/ml Heparin sodium (Sigma)). Fungizone antimycotic (Life) was included in the medium for the first week of culture. Fresh medium was added every 2-3 days and neurospheres formed within two weeks of culture in non-TC flasks at 37°C, 5% CO₂. Cells in neurospheres were dissociated with accutase (Life) before reaching a diameter greater than 500µm (every 7-14 days), with passaged cells giving rise to new neurospheres.

In vitro differentiation of SVZ-NSCs and Exposure to AgNP

Undifferentiated neurospheres (passage 4-18) were collected by centrifugation and plated on poly-L-lysine (0.01%) and laminin (10µg/mL) coated coverslips or wells in 24-well plates in differentiation medium (Neurobasal (Life), 2% B27 (Life), 1% NEAA, 1% Glutamax (Life), and 1% P/S) lacking EGF and bFGF. After being allowed to attach and differentiate for 2-3 days,

medium was replaced with fresh medium containing 1.0 μ g/mL AgNP stabilized in 2mM citrate (Sigma). Filter-sterilized 2mM sodium citrate was used as a vehicle control. For time-response experiments, media was replaced with fresh and stock AgNP solution was added to individual wells at the appropriate time (24hr, 6hr, 2hr, 1hr).

Immunocytochemistry

Cells were washed with PBS1, fixed on coverslips with 4% paraformaldehyde for 15min, washed with phosphate buffered saline 2 (PBS2; 100mM sodium phosphate, 150mM NaCl, pH 7.4) and then permeabilized with 0.3% Triton-X/PBS2 for 10 minutes. Preparations were blocked with 5% bovine serum albumin (BSA, Fisher) and 10% normal goat serum (NGS, Life) for one hour before being incubated overnight with primary antibodies specific to cell fate marker proteins. Primary antibody used was rab- α - β -catenin (Santa Cruz, Dallas, Texas, United States), with goat- α -rabbit Alexa 488 (Life) as secondary. Phalloidin Alexa 568 (Life) was used to stain the f-actin cytoskeleton, and DAPI (Sigma) was used as a nuclear counterstain. Coverslips were washed with D.I. H₂O before being mounted on slides using Prolong Gold (Life). Slides were allowed to cure at room temperature overnight and stored at 4°C. Images were acquired using epifluorescent microscopy.

Western Blot

Immunoblot analysis was run on whole protein homogenates from cells exposed to 1.0 μ g/mL AgNP for 24hr. Briefly, cells were collected using Laemmli solution (2% SDS, 6M Urea, 625mM Tris, 160mM DTT, 160mM DTE), heated to 70°C for 15min and triturated to homogenize, cooled, and homogenates stored at -20°C. 10 μ L protein was mixed with 5 μ L fresh loading buffer (58% glycerol, 0.36M Tris, 6% Tris, 6% β -mercaptoethanol, 0.01% bromophenol blue) and loaded into 10% poly-acrylamide gels. Gels were run in running buffer (40mM Trizma Base, 200mM Glycine, 0.1% SDS) at 85V for 90min. Gels were washed in transfer buffer (25mM Tris, 192mM Glycine, pH 8.3) and proteins were transferred to PVDF (Biorad) at 85V for 1hr at 4°C. Membrane was washed in TTBS (20mM Tris, 0.5M NaCl, 0.1% Tween 20, pH 7.5) then blocked for 2hr (4% skim milk in TTBS). After washing again with TTBS, membrane was incubated overnight with primary antibody in TTBS with 5% bovine serum albumin (BSA). Primary antibodies used were rab- α -pAkt (1:2000; Cell Signaling Technologies (CST), Danvers, Massachusetts), rab- α -pMAPK (1:2000; CST), or rab- α - β -catenin (1:5000; Santa Cruz). Membranes were washed in TTBS and incubated with goat- α -rabbit conjugated with HRP (1:1000; CST) as secondary antibody in TTBS with 5%BSA for 1hr. After secondary incubation, membranes were washed and imaged in a darkroom using film (GE Healthcare Life Sciences, Pittsburgh, Pennsylvania) and WesternBright ECL solutions (Advansta, Menlo Park, California). After imaging, membranes were stripped using stripping buffer (Fisher) before blocking again and incubating with either a second primary or HRP-conjugated α -pan-actin (1:5000; CST) for loading control. Membranes were stripped two times at most. Photographs were scanned for quantification.

In vivo AgNP exposure and BrdU treatment

Young adult Sprague-Dawley rats were purchased from Hilltop and cared for under Marshall University IACUC protocol 598. Animals were maintained in environmentally-controlled cages on a 12-hour day/night cycle with access to standard chow and water *ad libitum*. After being allowed to acclimate, animals were trained daily for 7d to take 10% sucrose (Fisher) solution orally from a syringe when presented (Atcha et al., 2010) at 1:00pm plus or minus 2hr. Following training, control animals (n=16, 8 male, 8 female) were maintained on daily feedings of 10%

sucrose. Experimental animals (n=16, 8 male, 8 female) were given 100mg/kg 40nm uncoated AgNP (NanoAmor, Houston, Texas) suspended in 10% sucrose. Dosing volume was 2mL/kg. Each group of animals consisted of equal numbers of males and females, with equal numbers of each treated with AgNP or sucrose vehicle for 28d. Sucrose solutions and AgNP suspensions were prepared fresh daily as 20% sucrose and 100mg/mL AgNP in diH₂O. AgNP suspensions were made by fifteen minutes of sonication and cooled to room temperature on ice. Solutions for feeding were made as a 1-to-1 mixture of 100mg/mL AgNP and 20% sucrose for AgNP-treated animals or as 20% sucrose with diH₂O for control animals.

To label the entire subventricular zone-rostral migratory stream-olfactory bulb (SVZ-RMS-OB) system, animals were given intraperitoneal injections of BrdU at 14, 7, 2, and 1d before collection. Injections were administered following brief anesthesia with isoflurane (Kent Scientific) to reduce animal stress. Tissue from half of each group was collected following 28d of treatment. Other animals in each group were allowed 28d recovery, with no AgNP or sucrose treatment. Animal weight and behavior were monitored daily during treatment.

Tissue collection and sectioning

Animals were deeply anesthetized with inhaled isoflurane and subjected to bilateral pneumothorax. Cardiac perfusion was performed first with 150mL PBS1 to ensure exsanguination followed by perfusion with 500mL of fresh 4% paraformaldehyde (PFA) in PBS1. Upon completion, heads were removed and brains collected. As AgNP are known to accumulate in cerebellum at levels similar to neurogenic niches (Wen et al., 2016), cerebella were removed using a razor blade and placed in tared tubes for silver content analysis, and brains were placed in 4% PFA postfix for one day. After postfix, brains were moved to 30% sucrose with 0.01% sodium azide (Sigma) in PBS2 and stored at 4°C. Fixed tissue was embedded in Tissue Tek OCT Compound (Sakura Finetek, Torrance, California), sectioned at 30µm using a Leica CM3050 S cryostat (Leica), and stored as free-floating sections in cryoprotectant (30% Glycerol (AMRESCO), 30% Ethylene Glycol (AMRESCO), 40% PBS2) at -20°C.

Immunohistochemistry

Sections were placed in four 5min washes with PBS2, then immersed in 1% NaBH₄ (Sigma) in PBS2 for 20 minutes to reduce background autofluorescence (Spitzer et al., 2011). After washing six times with PBS2 and once with diH₂O, sections were immersed in 2N HCl for 30min at 48°C and neutralized in 0.1M Borate (pH 8.5; Fisher) for 12 minutes, followed by washing once with diH₂O, then three times with PBS2. Sections were blocked in 10% normal goat serum (NGS; Life) in PBS2 + 0.3% Triton-X (PBTx) for 1hr, followed by PBS2 washes. Sections were placed in tubes with primary antibody at 1:500 in 1% NGS in PBTx overnight. Primary antibodies used were mouse- α -BrdU (Abcam) and rabbit- α - β -tubulinIII (Abcam), rabbit- α -nestin (Abcam), rabbit- α -DCX (Millipore), or rabbit- α -NeuN (Abcam). Sections were washed four times, then placed in tubes with secondary antibody at 1:500 in 1% NGS and PBTx overnight. Secondary antibodies were goat- α -rabbit-Alexa 488 (Life) and goat- α -mouse Alexa 568 (Life). After washing with PBS2, sections were immersed in CuSO₄ solution (1mM CuSO₄ (Sigma), 50mM Ammonium Acetate (Fisher)) for 1hr, washed again with diH₂O and PBS2, and then counterstained with DAPI in PBS2 for 1hr. Sections were floated onto Fisherbrand Superfrost Plus slides (Fisher) and sealed in Prolong Gold and allowed to cure overnight. Sections were imaged using an epifluorescent microscope (Leica).

Silver content analysis

Silver content of cerebella was analyzed by Dr. John W. Olesik in the Trace Element Research Laboratory at Ohio State University School of Earth Sciences by inductively coupled plasma mass spectrometry.

Patch clamp electrophysiology

Cells were cultured and plated as described. For experiments, cells were constantly perfused with warm sterile bath solution (130mM NaCl (Fisher); 3mM KCl (BioExpress); 4mM MgCl₂ (Sigma); 1mM CaCl₂ (Avantor; Center Valley, Pennsylvania, United States); 2.5mM EGTA (Sigma); 10mM HEPES (Fisher); 5mM Glucose (BioExpress); pH 7.4) and maintained at approximately 35°C. Whole-cell recordings were taken using an Axopatch 200B (Molecular Devices; Sunnyvale, California, United States) with CV 203BU headstage (Molecular Devices), with the program CLAMPEX 10.3 (Molecular Devices) delivering command potentials. Electrodes were 2-3 MΩ and pulled from thin-wall capillary glass (A-M Systems; Sequim, Washington, United States) using a P-97 Flaming/Brown micropipette puller (Sutter Instruments; Novato, California, United States). In-electrode solution consisted of 140mM KCl, 2mM MgCl₂, 1mM CaCl₂, 2.5mM EGTA, 1mM HEPES, and 3mM ATP at pH 7.4 with a final 287mOsm. A step protocol was applied that held cells between -80 and +60mV for 100ms following 50ms prepulse at -80mV. Tail currents were analyzed with 50ms voltage steps between -100mV and -50mV following a 75ms prepulse at +20mV. Both protocols utilized a holding potential of -80mV. Inactivation/activation dynamics were analyzed using a step protocol that held cells between -100 and +60mV for 100ms from a holding potential of -40mV.

Data Analysis

ImageJ was used to count cells in immunocytochemistry and quantify bands in Western blot. Data in bar graphs are presented as mean ± standard deviation of at least three independent experiments as detailed. Graphs were generated and statistical significance was determined using Prism (Graphpad, San Diego, CA). Following one-way ANOVA tests, Tukey's multiple comparisons test was used to determine significance between groups. Additionally, the more conservative Sidak's multiple comparisons test confirmed significance levels. Following two-way ANOVA tests, Sidak's multiple comparisons test was used to determine significance between groups.

RESULTS

Intracellular β-catenin distribution and levels are altered by AgNP.

When SVZ-NSC were immunolabeled for β-catenin, control cells contained very uniform distribution of β-catenin (Fig1A). However, in cells exposed to 1μg/mL AgNP for up to 24hr, β-catenin label changed to a more punctate distribution (Fig1B). These β-catenin puncta appeared in significantly more cells over time (Fig1C). At the same time, cells exposed to 1μg/mL AgNP contained increased levels of intracellular β-catenin. As β-catenin levels and distribution are hallmarks of β-catenin signaling, these results suggest a change to β-catenin signaling following AgNP exposure.

β -catenin puncta and f-actin inclusions co-localize.

Cells immunolabeled for β -catenin were subsequently stained for f-actin. When exposed to AgNP, as expected, both β -catenin puncta (Fig2A) and f-actin inclusions (Fig2B, described previously in

Cooper and Spitzer, 2015) form. When the two are overlaid (Fig2C), β -catenin puncta and f-actin inclusions tend to co-localize. Indeed, following AgNP exposure, the proportion of cells with co-localized β -catenin puncta and f-actin inclusions increases significantly in a time-dependent manner (Fig2D) while the proportion of cells with only β -catenin puncta or f-actin inclusions does not change. The proportion of cells with both β -catenin puncta and f-actin inclusions but no co-localization was less than 1% across all experiments (data not shown).

AgNP do not alter rat growth and accumulate in brain tissue.

When animals were exposed to AgNP for 28 days, no change in animal weight was observed during treatment or after 28 days of recovery compared to animals in control conditions (Fig3A). However, analysis of cerebella revealed that AgNP treatment significantly increased Ag content of brain tissue both immediately after treatment and after 28 days of recovery. Further, Ag levels in brain tissue were not reduced following recovery (Fig3B).

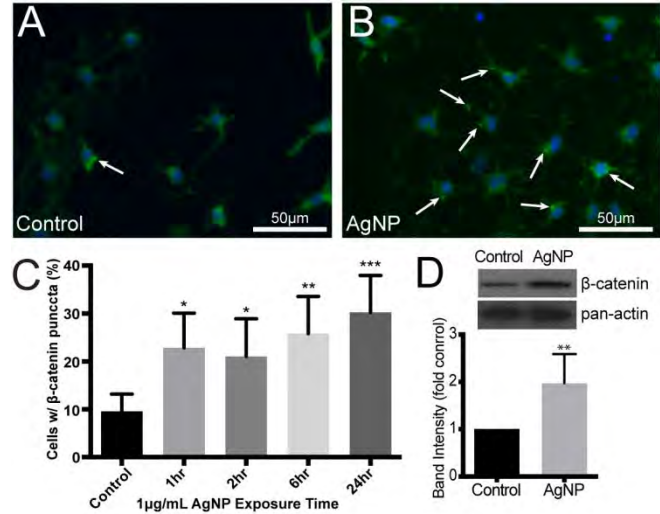


Fig1: Low-level AgNP alters β -catenin levels and localization. Few β -catenin puncta (arrows) form in control (A) cells, but many cells contain puncta in AgNP-treated NSC (B). Puncta appear significantly more often with longer AgNP exposure (C; $p < 0.01$ ANOVA $n = 6$; * $p < 0.05$, ** $p < 0.01$, *** $p < 0.001$ compared to control, Tukey). After 24hr AgNP exposure, NSC contain significantly more β -catenin (D; $p < 0.01$ two-tailed t-test $n = 3$)

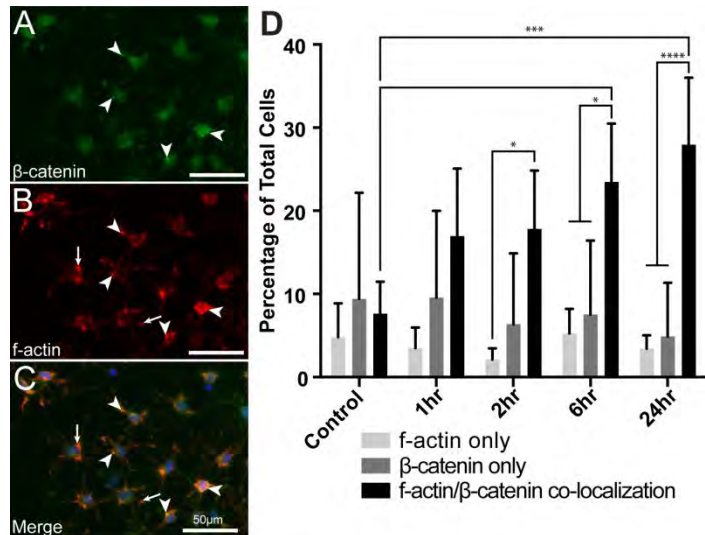


Fig2: β -catenin (A) puncta and f-actin (B) inclusions (arrows) co-localize (arrowheads) when overlaid (C). The proportion of cells with co-localized inclusions and puncta increased significantly over time, while the proportion of cells with only inclusions or only puncta remained the same (D; $p < 0.05$ Two-way ANOVA $n = 6$; * $p < 0.05$ *** $p < 0.001$ *** $p < 0.0001$, Sidak)

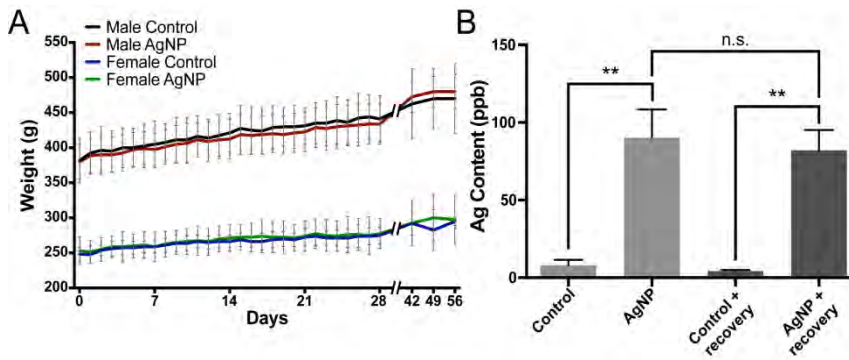


Fig3: The growth of AgNP-treated animals and control animals was not significantly different (A; $p=0.9995$ Two-way ANOVA $n=4$). However, AgNP-treated animals' brains contained significantly greater Ag loads than control animals, even after 28 days' recovery. Ag content did not decrease significantly during recovery (B; $p<0.01$ ANOVA $n=3$; $**p<0.01$, Tukey)

BrdU label in SVZ-RMS-OB system is incomplete.

Cells in the SVZ-RMS-OB system were immunolabeled for BrdU and markers of differentiation (Fig4A). However, while there were BrdU-positive cells in the SVZ (Fig4B,E) and OB (Fig4D,G), there were gaps in the RMS (Fig4C,F). Further, the number of BrdU-positive cells was too low for the analysis originally envisioned.

These results show that

BrdU successfully labels NSC in the SVZ and that NSC successfully migrate to the OB through the RMS, but an alternate BrdU regimen is required to label the entire system.

NSC exhibit typical K^+ currents.

Control cells' membrane currents were measured in response to different voltage steps to assess the development of voltage-activated currents (Fig5). We found evidence suggesting that cells contained developed fast-activating, fast-inactivating A-type K^+ currents (Fig5,arrow) and slow-activating, slow-inactivating K^+ currents (Fig5,arrowhead), both of which are hallmarks of typical NSC differentiation (Scheffler et al., 2005). However, due to time constraints and technical failures, no data could be gathered from cells exposed to AgNP.

DISCUSSION

The data show that low-level AgNP exposure ($1\mu\text{g}/\text{mL}$) alters β -catenin levels and localization in SVZ-NSC (Fig1). As canonical β -catenin signaling takes place through an increase in intracellular levels of β -catenin and translocation of β -catenin into the nucleus (Molenaar et al., 1996; Munemitsu et al., 1995), these results indicate that β -catenin signaling is being altered by AgNP exposure. However, β -catenin activation promotes neurite extension and arborization (Lee et al., 2014; Pino et al., 2011; Yu and Malenka, 2003), both processes that are reduced by AgNP exposure. Therefore, though intracellular β -catenin levels are increasing, typically a sign of Wnt/ β -catenin signaling activation (Munemitsu et al., 1995), some other mechanism is in play. Further, the f-actin inclusions we previously found to form following low-level AgNP exposure contain β -catenin (Fig2). β -catenin may be sequestered within these inclusions, resulting in a reduction of β -catenin signaling despite increased protein levels.

Normally, β -catenin interacts with cadherin in adherens junctions, acting as a bridge to the actin cytoskeleton (Wheelock and Knudsen, 1991). However, if the affinity of cadherin for β -catenin is increased, it will sequester β -catenin at the membrane, effectively halting β -catenin signaling even when associated pathways are activated (Chigita et al., 2012). A similar process may be occurring

here. β -catenin also interacts with the actin-bundling protein fascin (Tao et al., 1996; Vignjevic et al., 2007) which is necessary for SVZ-NSC migration (Sonego et al., 2013). It may therefore also be possible that β -catenin is the mediator of initial f-actin inclusion formation, and that the agglomeration of fascin and β -catenin within the inclusions is inhibiting both their activity. Further experiments would be required to determine this definitively. However, these results still show that low-level AgNP exposure is interfering with β -catenin signaling, which further suggests that low-level AgNP are capable of disrupting signaling necessary for proper NSC proliferation and differentiation (Adachi et al., 2007; Kuwabara et al., 2009; Lee et al., 2014; Lie et al., 2005; Marinaro et al., 2012; Yu and Malenka, 2003).

Originally, this project's goal was to analyze NSC behavior and fate in the SVZ-RMS-OB system *in vivo* and using patch clamp electrophysiology *in vitro*. We found that AgNP at 100mg/kg/day do not significantly alter rat growth (Fig3), a standard measure of overt toxicity. We have also shown that AgNP traverse the lumen of the gut and blood-brain barrier, accumulating and persisting in the brains of animals for up to a month after treatment (Fig3) as expected (Buzulukov Iu et al., 2014; Ji et al., 2007; Kim et al., 2008; Lee et al., 2013; Wen et al., 2016). Further, the treatment regimen used resulted in brain Ag levels roughly a single order of magnitude away from the concentrations used *in vitro*, indicating that they are comparable. Therefore, given the longer exposure time *in vivo* than *in vitro* experiments, we would expect to see similar effects.

However, inconsistent BrdU label in the SVZ-RMS-OB system and fewer than expected labeled cells resulted in an

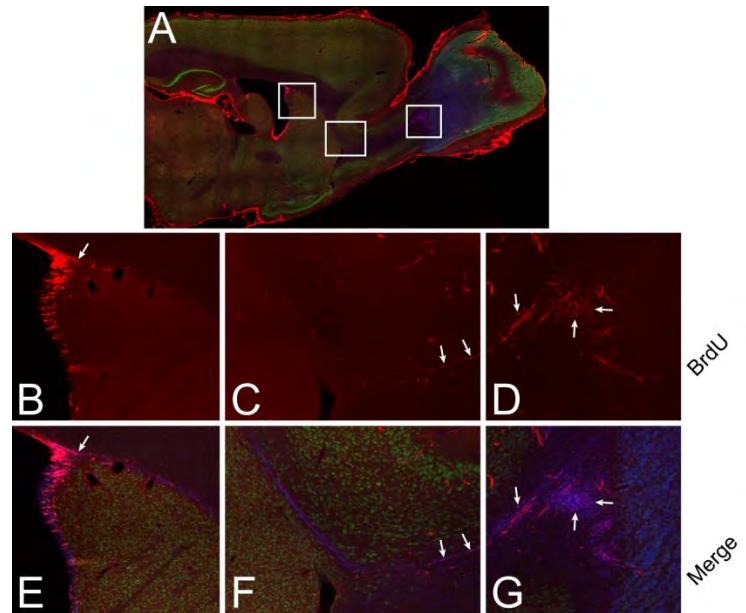


Fig4: Brain immunolabeled for BrdU (red) and NeuN (green)(A). Some BrdU positive cells (arrows) were seen in the SVZ (B,E), RMS (C,F), and OB (D,G), but there were significant gaps in the RMS. Further, not enough cells were present to perform the desired analysis comparing AgNP-exposed brains to control.

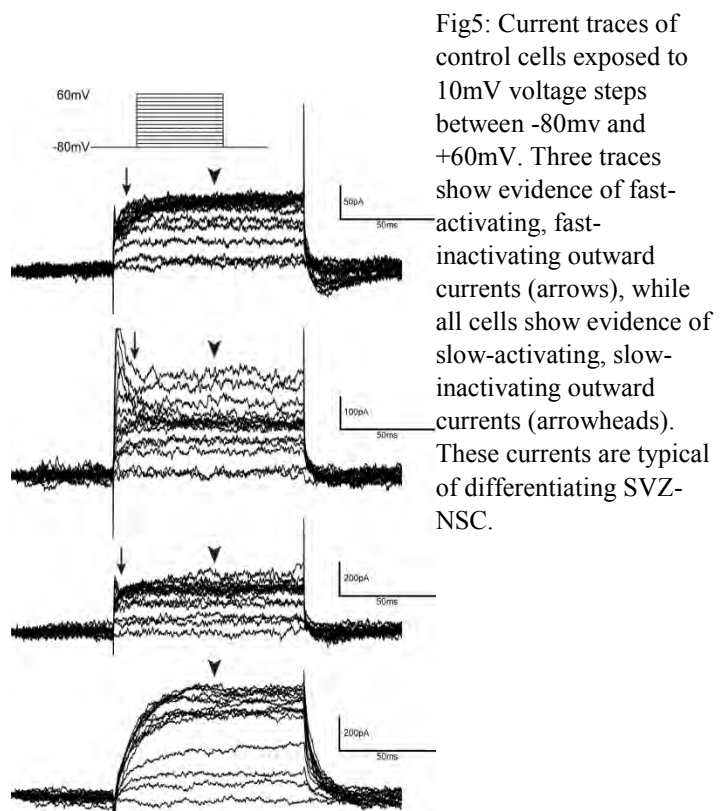


Fig5: Current traces of control cells exposed to 10mV voltage steps between -80mV and +60mV. Three traces show evidence of fast-activating, fast-inactivating outward currents (arrows), while all cells show evidence of slow-activating, slow-inactivating outward currents (arrowheads). These currents are typical of differentiating SVZ-NSC.

inability to perform the analysis that was originally proposed (Fig4). BrdU injection time points (14, 7, 2, and 1 days pre-collection) were chosen based on literature stating that it takes approximately 4-15 days for SVZ-NSC to traverse the RMS and integrate in the OB (Lois and Alvarez-Buylla, 1994). However, the actual travel and maturation time of SVZ-NSC within the SVZ-RMS-OB system appears to be highly variable (Parent et al., 2002; Perez-Asensio et al., 2013; Petreanu and Alvarez-Buylla, 2002), ranging from 2-29 days. Therefore, future experiments will take this into consideration, with more frequent BrdU administration to ensure labeling of sufficient numbers of cells and the entire SVZ-RMS-OB system.

Finally, the proposed experiment to compare electrophysiology of control NSC and NSC exposed to AgNP showed that SVZ-NSC in our lab do develop the expected outward currents (Fig5), likely K^+ currents, typical of differentiated SVZ-NSC (Scheffler et al., 2005). However, time constraints prevented collection of data concerning AgNP-exposed SVZ-NSC. As electrophysiological development of SVZ-NSC is vital to their differentiation and ability to form functional neurons (Scheffler et al., 2005), further experiments should be conducted to determine what effect AgNP might have. Given that AgNP have previously been shown to decrease currents from voltage-gated Na^+ (Busse et al., 2013; Liu et al., 2009) and K^+ (Liu et al., 2011) channels, it is expected that future studies will show that AgNP interfere in the electrophysiological development of SVZ-NSC.

CONCLUSIONS

Overall, these data provide evidence that AgNP are capable of disrupting SVZ-NSC differentiation and intracellular signaling. β -catenin signaling, which is known to be vital for both NSC proliferation and differentiation, was altered following 24hr AgNP exposure. Also, treatment with AgNP *in vivo* led to comparable levels of Ag in the brains of test animals without any overt toxic effects, and these levels persisted in brains even after 28d of recovery. This indicates that, even after cessation of AgNP treatment, adverse effects may still be observed. Future experiments are needed, therefore, to confirm that AgNP-mediated deficits in SVZ-NSC behavior and signaling *in vitro* are recapitulated *in vivo*. Similarly, more electrophysiology experiments are needed to show whether or not AgNP interfere in the development of active membrane properties necessary for SVZ-NSC differentiation.

PROGRAM BENEFITS

Funding from the NASA West Virginia Space Grant Consortium ensured that more time could be devoted to the proposed project. Further, this grant funded travel to the annual meeting for the Society for Neuroscience, an international conference attended by over 30,000 neuroscientists from around the world, increasing dissemination of this work.

ACKNOWLEDGMENTS

Robert Cooper was supported by the NASA WV Space Grant Consortium. This work was supported by NSF Cooperative Agreement Award number EPS-1003907. The author would like to thank his mentor, Dr. Nadja Spitzer, for excellent advice and guidance. The author would also like to thank Maya N. Menking for help with immunocytochemistry experiments, and all the other members of the Spitzer lab for their constant support.

REFERENCES

- Adachi K, Mirzadeh Z, Sakaguchi M, Yamashita T, Nikolcheva T, Gotoh Y, et al. Beta-catenin signaling promotes proliferation of progenitor cells in the adult mouse subventricular zone. *Stem cells*. 2007;25:2827-36.
- Aimone JB, Li Y, Lee SW, Clemenson GD, Deng W, Gage FH. Regulation and Function of Adult Neurogenesis: From Genes to Cognition. *Physiological reviews*. 2014;94:991-1026.
- Altman J, Das GD. Autoradiographic and histological evidence of postnatal hippocampal neurogenesis in rats. *The Journal of comparative neurology*. 1965;124:319-35.
- Atcha Z, Rourke C, Neo AH, Goh CW, Lim JS, Aw CC, et al. Alternative method of oral dosing for rats. *Journal of the American Association for Laboratory Animal Science : JAALAS*. 2010;49:335-43.
- Baker C, Pradhan A, Pakstis L, Pochan DJ, Shah SI. Synthesis and antibacterial properties of silver nanoparticles. *Journal of nanoscience and nanotechnology*. 2005;5:244-9.
- Bartłomiejczyk T, Lankoff A, Kruszewski M, Szumiel I. Silver nanoparticles -- allies or adversaries? *Annals of agricultural and environmental medicine : AAEM*. 2013;20:48-54.
- Belluzzi O, Benedusi M, Ackman J, LoTurco JJ. Electrophysiological differentiation of new neurons in the olfactory bulb. *The Journal of neuroscience : the official journal of the Society for Neuroscience*. 2003;23:10411-8.
- Benn T, Cavanagh B, Hristovski K, Posner JD, Westerhoff P. The release of nanosilver from consumer products used in the home. *J Environ Qual*. 2010;39:1875-82.
- Benn TM, Westerhoff P. Nanoparticle silver released into water from commercially available sock fabrics. *Environmental science & technology*. 2008;42:4133-9.
- Boudreau MD, Imam MS, Paredes AM, Bryant MS, Cunningham CK, Felton RP, et al. Differential Effects of Silver Nanoparticles and Silver Ions on Tissue Accumulation, Distribution, and Toxicity in the Sprague Dawley Rat Following Daily Oral Gavage Administration for 13-Weeks. *Toxicological sciences : an official journal of the Society of Toxicology*. 2016.
- Busse M, Stevens D, Kraegeloh A, Cavelius C, Vukelic M, Arzt E, et al. Estimating the modulatory effects of nanoparticles on neuronal circuits using computational upscaling. *International journal of nanomedicine*. 2013;8:3559-72.
- Buzulukov Iu P, Arianova EA, Demin VF, Safenkova IV, Gmoshinskii IV, Tutel'ian VA. [Bioaccumulation of silver and gold nanoparticles in organs and tissues of rats by neutron activation analysis]. *Izv Akad Nauk Ser Biol*. 2014:286-95.
- Carleton A, Petreanu LT, Lansford R, Alvarez-Buylla A, Lledo PM. Becoming a new neuron in the adult olfactory bulb. *Nature neuroscience*. 2003;6:507-18.

- Chigita S, Sugiura T, Abe M, Kobayashi Y, Shimoda M, Onoda M, et al. CD82 inhibits canonical Wnt signalling by controlling the cellular distribution of beta-catenin in carcinoma cells. *Int J Oncol.* 2012;41:2021-8.
- Conti L, Sipione S, Magrassi L, Bonfanti L, Rigamonti D, Pettirossi V, et al. Shc signaling in differentiating neural progenitor cells. *Nature neuroscience.* 2001;4:579-86.
- Cooper RJ, Spitzer N. Silver nanoparticles at sublethal concentrations disrupt cytoskeleton and neurite dynamics in cultured adult neural stem cells. *Neurotoxicology.* 2015;48:231-8.
- Cushen M, Kerry J, Morris M, Cruz-Romero M, Cummins E. Migration and exposure assessment of silver from a PVC nanocomposite. *Food chemistry.* 2013;139:389-97.
- Dayem AA, Kim B, Gurunathan S, Choi HY, Yang G, Saha SK, et al. Biologically synthesized silver nanoparticles induce neuronal differentiation of SH-SY5Y cells via modulation of reactive oxygen species, phosphatases, and kinase signaling pathways. *Biotechnology journal.* 2014;9:934-43.
- Doetsch F, Garcia-Verdugo JM, Alvarez-Buylla A. Cellular composition and three-dimensional organization of the subventricular germinal zone in the adult mammalian brain. *The Journal of neuroscience : the official journal of the Society for Neuroscience.* 1997;17:5046-61.
- Doetsch F, Petreanu L, Caille I, Garcia-Verdugo JM, Alvarez-Buylla A. EGF converts transit-amplifying neurogenic precursors in the adult brain into multipotent stem cells. *Neuron.* 2002;36:1021-34.
- Gage FH. Mammalian neural stem cells. *Science.* 2000;287:1433-8.
- Gaillet S, Rouanet JM. Silver nanoparticles: Their potential toxic effects after oral exposure and underlying mechanisms - A review. *Food and chemical toxicology : an international journal published for the British Industrial Biological Research Association.* 2015;77C:58-63.
- Ge S, Sailor KA, Ming GL, Song H. Synaptic integration and plasticity of new neurons in the adult hippocampus. *The Journal of physiology.* 2008;586:3759-65.
- Gerard C, Langlois X, Gingrich J, Doucet E, Verge D, Kia HK, et al. Production and characterization of polyclonal antibodies recognizing the intracytoplasmic third loop of the 5-hydroxytryptamine1A receptor. *Neuroscience.* 1994;62:721-39.
- Huang JH, Cai WJ, Zhang XM, Shen ZY. Icariin promotes self-renewal of neural stem cells: an involvement of extracellular regulated kinase signaling pathway. *Chinese journal of integrative medicine.* 2014;20:107-15.
- Ji JH, Jung JH, Kim SS, Yoon JU, Park JD, Choi BS, et al. Twenty-eight-day inhalation toxicity study of silver nanoparticles in Sprague-Dawley rats. *Inhalation toxicology.* 2007;19:857-71.

- Jin L, Hu X, Feng L. NT3 inhibits FGF2-induced neural progenitor cell proliferation via the PI3K/GSK3 pathway. *Journal of neurochemistry*. 2005;93:1251-61.
- Kim YS, Kim JS, Cho HS, Rha DS, Kim JM, Park JD, et al. Twenty-eight-day oral toxicity, genotoxicity, and gender-related tissue distribution of silver nanoparticles in Sprague-Dawley rats. *Inhalation toxicology*. 2008;20:575-83.
- Kovvuru P, Mancilla PE, Shirode AB, Murray TM, Begley TJ, Reliene R. Oral ingestion of silver nanoparticles induces genomic instability and DNA damage in multiple tissues. *Nanotoxicology*. 2015;9:162-71.
- Kruszewski M, Brzoska K, Brunborg G, Asare N, Dobrzyńska M, Dušinská M, et al. Toxicity of Silver Nanomaterials in Higher Eukaryotes. In: James CF, editor. *Advances in Molecular Toxicology*: Elsevier; 2011. p. 179-218.
- Kuwabara T, Hsieh J, Muotri A, Yeo G, Warashina M, Lie DC, et al. Wnt-mediated activation of NeuroD1 and retro-elements during adult neurogenesis. *Nature neuroscience*. 2009;12:1097-105.
- Lankveld DP, Oomen AG, Krystek P, Neigh A, Troost-de Jong A, Noorlander CW, et al. The kinetics of the tissue distribution of silver nanoparticles of different sizes. *Biomaterials*. 2010;31:8350-61.
- Lazaro-Dieguez F, Aguado C, Mato E, Sanchez-Ruiz Y, Esteban I, Alberch J, et al. Dynamics of an F-actin aggresome generated by the actin-stabilizing toxin jasplakinolide. *Journal of cell science*. 2008;121:1415-25.
- Lee JH, Kim YS, Song KS, Ryu HR, Sung JH, Park JD, et al. Biopersistence of silver nanoparticles in tissues from Sprague-Dawley rats. *Particle and fibre toxicology*. 2013;10:36.
- Lee SH, Ko HM, Kwon KJ, Lee J, Han SH, Han DW, et al. tPA regulates neurite outgrowth by phosphorylation of LRP5/6 in neural progenitor cells. *Molecular neurobiology*. 2014;49:199-215.
- Lie DC, Colamarino SA, Song HJ, Desire L, Mira H, Consiglio A, et al. Wnt signalling regulates adult hippocampal neurogenesis. *Nature*. 2005;437:1370-5.
- Liu F, Xuan A, Chen Y, Zhang J, Xu L, Yan Q, et al. Combined effect of nerve growth factor and brain-derived neurotrophic factor on neuronal differentiation of neural stem cells and the potential molecular mechanisms. *Molecular medicine reports*. 2014;10:1739-45.
- Liu P, Huang Z, Gu N. Exposure to silver nanoparticles does not affect cognitive outcome or hippocampal neurogenesis in adult mice. *Ecotoxicology and environmental safety*. 2013;87:124-30.
- Liu Y, Guan W, Ren G, Yang Z. The possible mechanism of silver nanoparticle impact on hippocampal synaptic plasticity and spatial cognition in rats. *Toxicology letters*. 2012;209:227-31.

- Liu Z, Ren G, Zhang T, Yang Z. Action potential changes associated with the inhibitory effects on voltage-gated sodium current of hippocampal CA1 neurons by silver nanoparticles. *Toxicology*. 2009;264:179-84.
- Liu Z, Ren G, Zhang T, Yang Z. The inhibitory effects of nano-Ag on voltage-gated potassium currents of hippocampal CA1 neurons. *Environ Toxicol*. 2011;26:552-8.
- Lois C, Alvarez-Buylla A. Long-distance neuronal migration in the adult mammalian brain. *Science*. 1994;264:1145-8.
- Luskin MB. Restricted proliferation and migration of postnatally generated neurons derived from the forebrain subventricular zone. *Neuron*. 1993;11:173-89.
- Luskin MB, Boone MS. Rate and pattern of migration of lineally-related olfactory bulb interneurons generated postnatally in the subventricular zone of the rat. *Chem Senses*. 1994;19:695-714.
- Marinero C, Pannese M, Weinandy F, Sessa A, Bergamaschi A, Taketo MM, et al. Wnt signaling has opposing roles in the developing and the adult brain that are modulated by Hipk1. *Cerebral cortex*. 2012;22:2415-27.
- Molenaar M, van de Wetering M, Oosterwegel M, Peterson-Maduro J, Godsave S, Korinek V, et al. XTcf-3 transcription factor mediates beta-catenin-induced axis formation in *Xenopus* embryos. *Cell*. 1996;86:391-9.
- Muller P, Langenbach A, Kaminski A, Rychly J. Modulating the actin cytoskeleton affects mechanically induced signal transduction and differentiation in mesenchymal stem cells. *PLoS one*. 2013;8:e71283.
- Munemitsu S, Albert I, Souza B, Rubinfeld B, Polakis P. Regulation of intracellular beta-catenin levels by the adenomatous polyposis coli (APC) tumor-suppressor protein. *Proceedings of the National Academy of Sciences of the United States of America*. 1995;92:3046-50.
- Muraoka K, Shingo T, Yasuhara T, Kameda M, Yuen WJ, Uozumi T, et al. Comparison of the therapeutic potential of adult and embryonic neural precursor cells in a rat model of Parkinson disease. *Journal of neurosurgery*. 2008;108:149-59.
- Oberdorster G, Sharp Z, Atudorei V, Elder A, Gelein R, Kreyling W, et al. Translocation of inhaled ultrafine particles to the brain. *Inhalation toxicology*. 2004;16:437-45.
- Panacek A, Kvitek L, Prucek R, Kolar M, Vecerova R, Pizurova N, et al. Silver colloid nanoparticles: synthesis, characterization, and their antibacterial activity. *J Phys Chem B*. 2006;110:16248-53.
- Parent JM, Valentin VV, Lowenstein DH. Prolonged seizures increase proliferating neuroblasts in the adult rat subventricular zone-olfactory bulb pathway. *The Journal of neuroscience : the official journal of the Society for Neuroscience*. 2002;22:3174-88.

- Perez-Asensio FJ, Perpina U, Planas AM, Pozas E. Interleukin-10 regulates progenitor differentiation and modulates neurogenesis in adult brain. *Journal of cell science*. 2013;126:4208-19.
- Petreanu L, Alvarez-Buylla A. Maturation and death of adult-born olfactory bulb granule neurons: role of olfaction. *The Journal of neuroscience : the official journal of the Society for Neuroscience*. 2002;22:6106-13.
- Pino D, Choe Y, Pleasure SJ. Wnt5a controls neurite development in olfactory bulb interneurons. *ASN neuro*. 2011;3:e00059.
- Quadros ME, Pierson R, Tolve NS, Willis R, Rogers K, Thomas TA, et al. Release of Silver from Nanotechnology-Based Consumer Products for Children. *Environmental science & technology*. 2013;47:8894-901.
- Reynolds BA, Weiss S. Generation of neurons and astrocytes from isolated cells of the adult mammalian central nervous system. *Science*. 1992;255:1707-10.
- Samuel U, Guggenbichler JP. Prevention of catheter-related infections: the potential of a new nano-silver impregnated catheter. *Int J Antimicrob Agents*. 2004;23 Suppl 1:S75-8.
- Scheffler B, Walton NM, Lin DD, Goetz AK, Enikolopov G, Roper SN, et al. Phenotypic and functional characterization of adult brain neurogenesis. *Proceedings of the National Academy of Sciences of the United States of America*. 2005;102:9353-8.
- Silvestry-Rodriguez N, Sicairos-Ruelas EE, Gerba CP, Bright KR. Silver as a disinfectant. *Reviews of environmental contamination and toxicology*. 2007;191:23-45.
- Snyder JS, Kee N, Wojtowicz JM. Effects of adult neurogenesis on synaptic plasticity in the rat dentate gyrus. *Journal of neurophysiology*. 2001;85:2423-31.
- Sondi I, Salopek-Sondi B. Silver nanoparticles as antimicrobial agent: a case study on E. coli as a model for Gram-negative bacteria. *Journal of colloid and interface science*. 2004;275:177-82.
- Sonego M, Gajendra S, Parsons M, Ma Y, Hobbs C, Zentar MP, et al. Fascin regulates the migration of subventricular zone-derived neuroblasts in the postnatal brain. *The Journal of neuroscience : the official journal of the Society for Neuroscience*. 2013;33:12171-85.
- Sosedova LM, Novikov MA, Titov EA, Rukavishnikov VS. [Evaluation of biologic effects caused by nano-silver influence on brain tissue of experimental animals]. *Med Tr Prom Ekol*. 2015:26-30.
- Spitzer N, Sammons GS, Price EM. Autofluorescent cells in rat brain can be convincing impostors in green fluorescent reporter studies. *Journal of neuroscience methods*. 2011;197:48-55.

- Stewart RR, Zigova T, Luskin MB. Potassium currents in precursor cells isolated from the anterior subventricular zone of the neonatal rat forebrain. *Journal of neurophysiology*. 1999;81:95-102.
- Tang J, Xiong L, Wang J, Liu L, Li J, Wan Z, et al. Influence of silver nanoparticles on neurons and blood-brain barrier via subcutaneous injection in rats. *Applied Surface Science*. 2008;255:502-4.
- Tang J, Xiong L, Zhou G, Wang S, Wang J, Liu L, et al. Silver nanoparticles crossing through and distribution in the blood-brain barrier in vitro. *Journal of nanoscience and nanotechnology*. 2010;10:6313-7.
- Tao YS, Edwards RA, Tubb B, Wang S, Bryan J, McCrea PD. beta-Catenin associates with the actin-bundling protein fascin in a noncadherin complex. *The Journal of cell biology*. 1996;134:1271-81.
- van Praag H, Christie BR, Sejnowski TJ, Gage FH. Running enhances neurogenesis, learning, and long-term potentiation in mice. *Proceedings of the National Academy of Sciences of the United States of America*. 1999;96:13427-31.
- Varela-Nallar L, Inestrosa NC. Wnt signaling in the regulation of adult hippocampal neurogenesis. *Frontiers in cellular neuroscience*. 2013;7:100.
- Vignjevic D, Schoumacher M, Gavert N, Janssen KP, Jih G, Lae M, et al. Fascin, a novel target of beta-catenin-TCF signaling, is expressed at the invasive front of human colon cancer. *Cancer research*. 2007;67:6844-53.
- von Goetz N, Fabricius L, Glaus R, Weitbrecht V, Gunther D, Hungerbuhler K. Migration of silver from commercial plastic food containers and implications for consumer exposure assessment. *Food additives & contaminants Part A, Chemistry, analysis, control, exposure & risk assessment*. 2013;30:612-20.
- Wachs FP, Couillard-Despres S, Engelhardt M, Wilhelm D, Ploetz S, Vroemen M, et al. High efficacy of clonal growth and expansion of adult neural stem cells. *Laboratory investigation; a journal of technical methods and pathology*. 2003;83:949-62.
- Wang DD, Krueger DD, Bordey A. Biophysical properties and ionic signature of neuronal progenitors of the postnatal subventricular zone in situ. *Journal of neurophysiology*. 2003;90:2291-302.
- Wen R, Yang X, Hu L, Sun C, Zhou Q, Jiang G. Brain-targeted distribution and high retention of silver by chronic intranasal instillation of silver nanoparticles and ions in Sprague-Dawley rats. *Journal of applied toxicology : JAT*. 2016;36:445-53.
- Wheelock MJ, Knudsen KA. Cadherins and associated proteins. *In Vivo*. 1991;5:505-13.
- Wisniewska MB. Physiological role of beta-catenin/TCF signaling in neurons of the adult brain. *Neurochem Res*. 2013;38:1144-55.

- Xu L, Shao A, Zhao Y, Wang Z, Zhang C, Sun Y, et al. Neurotoxicity of Silver Nanoparticles in Rat Brain After Intra-gastric Exposure. *Journal of nanoscience and nanotechnology*. 2015;15:4215-23.
- Yang Y, Westerhoff P. Presence in, and release of, nanomaterials from consumer products. *Adv Exp Med Biol*. 2014;811:1-17.
- Yu X, Malenka RC. Beta-catenin is critical for dendritic morphogenesis. *Nature neuroscience*. 2003;6:1169-77.
- Zhang RL, LeTourneau Y, Gregg SR, Wang Y, Toh Y, Robin AM, et al. Neuroblast division during migration toward the ischemic striatum: a study of dynamic migratory and proliferative characteristics of neuroblasts from the subventricular zone. *The Journal of neuroscience : the official journal of the Society for Neuroscience*. 2007;27:3157-62.
- Zheng W, ZhuGe Q, Zhong M, Chen G, Shao B, Wang H, et al. Neurogenesis in adult human brain after traumatic brain injury. *J Neurotrauma*. 2013;30:1872-80.

MODELING AND SIMULATION OF A DIRECT-WRITE MANUFACTURING PROCESS

John Cordonier
Chemical Engineering
West Virginia University
Morgantown, West Virginia 26505

ABSTRACT

Additive manufacturing (AM) is of great interest to NASA since designer materials can be developed for aeronautical applications based on the performance criteria. However, the impact of operating conditions on microstructure evolution and its impact on the properties of the final product are poorly understood. A model that can satisfactorily estimate the material properties based on the operating conditions can be very useful for controlling the operating conditions so that materials of desired properties can be manufactured. In this project, direct writing of an ink composed of a conductive material dispersed in a polymer medium is used to create conductive substrates for use in flexible electronic devices.

To develop an efficient controls system, the parameters that affect the printed fluid must first be understood. The pattern morphology and properties created by the direct writing method mainly depend on three main factors: the properties of the ink, the parameters used in the operation of the direct-writing machine, and the ink-substrate interaction. Simulation and analysis of these components, and comparison with experimental data are being carried out to gain better understanding of structure-property relationships and for designing a control system that can manipulate the degrees of freedom to obtain the desired conductive and mechanical properties.

BACKGROUND

NASA's interest in AM, especially in the area of modeling and simulation of AM is clearly reflected by a thorough literature review titled "Additive Manufacturing Modeling and Simulation" published by the Langley Research Center in April of 2014 [1]. The literature review shows lack of papers in the area of modeling and simulation of AM. In particular, there are only 12 papers cited on modeling of molten pool physics. Most of the cited papers are for typical arc welding process of alloys. Even though electric arc welding is a fusion-based process, the preferred energy insertion for most AM processes is through laser beam, or electron beam, or plasma beam for precise control and flexibility. The thermal distribution is very different for these energy sources due to keyhole energy physics, vaporization losses, and energy loss to vapor clouds. It can be noted that the microstructure evolution during AM not only impacts the properties, but also the residual stress that adversely impacts the mechanical integrity of the manufactured parts. Numerical models are very useful tools for evaluating the effect of operating parameters such as total power and power intensity distribution of the energy source, translation path, travel speed, and material feed rate on the properties of final products. Such models can be used for optimizing operating conditions without running thousands of experiments. In addition, the operating parameters can be manipulated during manufacturing to control the functionality of each layer during manufacturing [2].

Similarly, there has been a thorough lack of investigation into the numerical modeling of fluid track-deposition, and especially the breakup of the fluid, through the direct-write manufacturing process. Ubal et al. cite only nine articles on the subject in their own investigation of the direct write process [3]. Additionally, Ubal et al. state that the breakup of liquid during deposition, specifically around the nozzle, has received little attention. Ubal et al. have taken the opportunity to analyze the steady state solution space in terms of the flow rate of the fluid and the nozzle-substrate standoff distance for a vertically pointing nozzle and a nozzle tilting at a slight angle. All other parameters in their work are held constant. Their work serves as a basis for the research pursued in this paper.

INTRODUCTION

The additive manufacturing process known as direct writing involves the extrusion of a liquid polymer into a desired geometry. Direct-write technologies allow the polymeric material to be printed freely in three dimensions. By using an ink composed of a conductive material, direct writing can be used to create conductive substrates or wiring for use in flexible electronic devices. However, there is a lack of literature on the control and optimization of nozzle-based robotic deposition (NBRD) of polymers for the creation of multi-functional substrates. The work presented in this paper aims to decrease that gap of knowledge.

The pattern morphology and properties created by the direct writing method can be classified into three main categories: the properties of the ink, the parameters used in the operation of the direct writing machine, and the ink-substrate interaction [4]. These categories are further broken down in Table 1.

Table 5. Pattern Morphology and Properties

Ink Properties	Viscosity
	Surface tension
Direct Writing Parameters	Tip size
	Air pressure
	Writing speed
	Dispensing height
Ink-Substrate Interactions	Adhesion
	Contact profile

COMSOL Multiphysics® software is used in the analysis and comparison of these parameters [5]. COMSOL® allows the user to construct a unique geometry, in this case the inner dimensions of a nozzle provided by Nordson EFD™, and apply appropriate boundary conditions to attain the resultant solution. As stated earlier, the focus of this project is the analysis of the properties summarized in Table 1 to determine which parameters affect the characteristics of the printed track the most. Additionally, a parallel simulation is being conducted in MATLAB to verify the results attained in COMSOL®. This simulation uses the same operating parameters with the exception that the fluid is treated simply as a Newtonian fluid rather than a non-Newtonian fluid.

METHODOLOGY

The work in this project consists primarily of data gathered by simulations in COMSOL® and MATLAB. The meshing used in MATLAB is created using a rectangular grid system whereas the meshing in COMSOL® is completed automatically with a free-form triangular scheme. Future work will involve the comparison of these simulations to physical experiments. Following that, a controls system will be developed so that the user of the NBRD technology will be able to print conductive inks with the characteristics that they desire.

Simulation in MATLAB - Initial

Similarly to COMSOL®, the parallel simulation in MATLAB makes use of the equations of motion and continuity to solve for the velocity and pressure profiles in the given geometry. Part of the initial COMSOL® simulation is validated for flow in the axial direction through a pipe. The fluid flow is assumed to be uniform in the z-direction, such that velocities in the r- and θ -directions are zero. Simplification of the equation of continuity is given by:

$$\rho \frac{dv_z}{dz} = 0 \quad (1)$$

Applying Equation 1 results in the following simplification of the z-component of the Navier-Stokes equation for incompressible fluids in cylindrical coordinates:

$$\frac{dv_z}{dt} = -\frac{1}{\rho} \frac{dP}{dz} + \frac{\mu}{\rho} \frac{d^2 v_z}{dr^2} \quad (2)$$

where ρ is the density, μ is the viscosity, and P is the pressure. Since the solution for fluid flow through a pipe is well-documented, comparison of this solution with a solution obtained in COMSOL® is a simple way to validate the simulation software.

Simulation in MATLAB - Advanced

Since the complexity of the simulation to be solved is not limited to unidirectional flow, the complexity of the simulation in MATLAB must also increase. This is accomplished by assuming there is a sudden contraction in diameter of the flow channel. Thus, this requires solving the Navier-Stokes equation in the r- and z- directions, with gravity, velocity in the θ direction, and changes in the θ direction assumed to be zero. The fluid used in this simulation is assumed to be a Newtonian fluid with constant density and viscosity. The resulting equation in the z direction is given by:

$$\frac{dv_z}{dt} = -\frac{1}{\rho} \frac{dP}{dz} - v_r \frac{dv_z}{dr} - v_z \frac{dv_z}{dz} + \frac{\mu}{\rho} \left[\frac{d^2 v_z}{dr^2} + \frac{1}{r} \frac{dv_z}{dr} + \frac{d^2 v_z}{dz^2} \right] \quad (3)$$

Similarly, the resulting equation in the r direction is given by:

$$\frac{dv_r}{dt} = -\frac{1}{\rho} \frac{dP}{dr} - v_r \frac{dv_r}{dr} - v_z \frac{dv_r}{dz} + \frac{\mu}{\rho} \left[\frac{d^2 v_r}{dr^2} + \frac{1}{r} \frac{dv_r}{dr} - \frac{1}{r^2} v_r + \frac{d^2 v_r}{dz^2} \right] \quad (4)$$

where ρ is the density, μ is the viscosity, and P is the pressure. Equations 3 and 4 are solved simultaneously with the equation of continuity to solve the velocity and pressure profiles in the

geometry. At the time of this writing, this advanced simulation in MATLAB is still in progress, with plans to increase the complexity of the geometry and resultant mesh to more closely resemble the geometry used by Nordson EFD.

Simulation in COMSOL®

The inner dimensions of the nozzle used in this work were taken from the CAD files that Nordson EFD™ use for manufacturing. The geometry is split in half axially for use in an axisymmetric simulation. In the CFD module provided by COMSOL®, the simulation has been completed for two main cases, both in single-phase flow – one for comparison with MATLAB and one for simulation of flow through the nozzle. In each case, both the continuity equation and the equation of motion are coupled to solve for the velocity and pressure profiles in the geometry. In this simulation software, the boundary conditions and fluid properties chosen by the user are automatically applied to obtain the resultant solution for each geometry.

The geometry of the nozzle is shown in Figure 1. The geometry of the nozzle is kept constant throughout the different simulations except for a change in the diameter of the tip of the nozzle, which begins a distance 9.1 mm from the bottom of the geometry. This area is highlighted in blue in Figure 1. All other variables, including inlet and outlet pressure, fluid viscosity and density, and boundary conditions are kept constant. Solutions from these simulations are used to extract information on both the radial velocity profiles and the axial pressure profiles.

In addition to the study of flow through the nozzle, an attempt is being made to recreate the physical model employed by Ubal et al. to model the printed track of ink. This model fails to account for factors such as the wetting of the tip. However, it is considered by the author of this paper to be a good place to start. This process has proven to be more complicated than originally thought and is still being investigated through COMSOL®.

RESULTS

The results obtained from the various simulations can be broken down into several main categories. First, there is the initial comparison between the velocity profiles attained in COMSOL® and MATLAB. Secondly, there are the velocity and pressure profiles determined by COMSOL® for the nozzle geometry shown in Figure 1. Thirdly, there are the velocity and pressure profiles determined by MATLAB for the “advanced” validation simulation. However, due to time constraints and problems with the in-house MATLAB solver, this has not been completed yet.

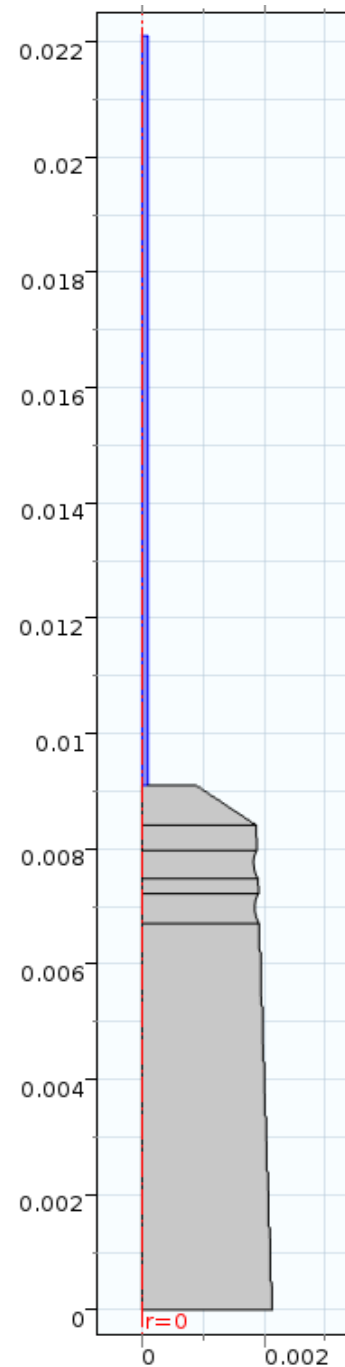


Figure 44. Geometry of the nozzle used in the pressure and velocity profile studies.

Initial Comparison

The initial simulation completed in MATLAB was performed for a simple nozzle geometry. The inlet and outlet boundary conditions used are 20 psi and 14.7 psi, respectively. The dimensions of the nozzle are 5 mm wide by 10 mm long. The fluid density ρ is 998 kg/m^3 and the viscosity is $30 \text{ Pa} \cdot \text{s}$. The radial velocity is shown in Figure 2.

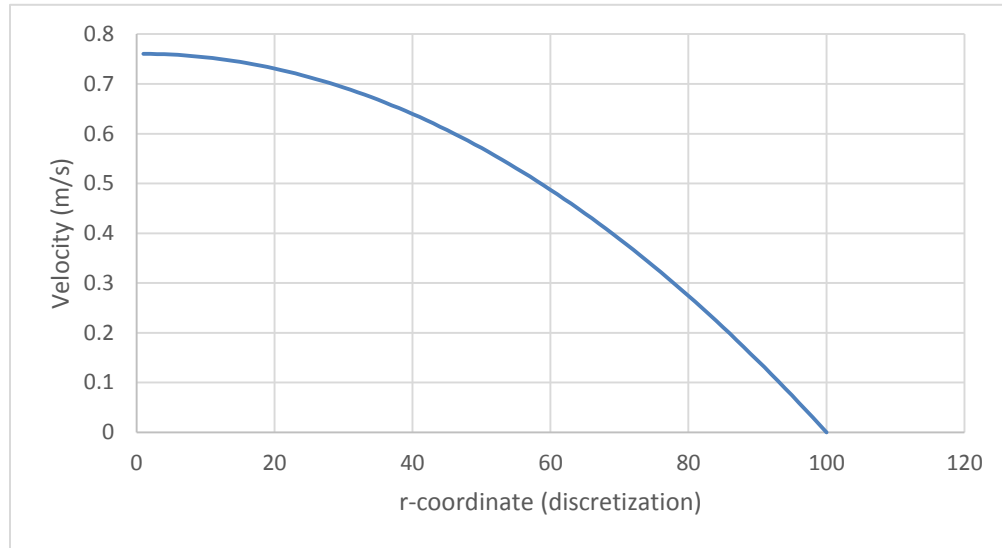


Figure 45. Velocity profile through the nozzle. Results from MATLAB.

The parallel simulation in COMSOL® is shown in Figure 3. This simulation uses the same boundary conditions as the initial simulation in MATLAB, including the Newtonian behavior of the fluid.

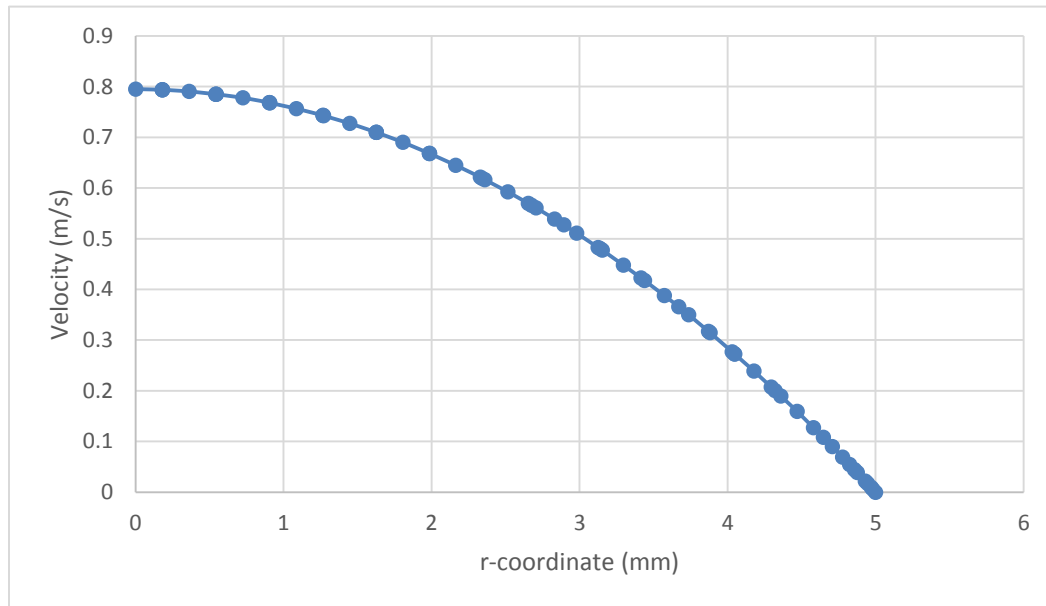


Figure 46. Velocity profile through the nozzle. Results from COMSOL®.

Velocity and Pressure Profiles

Figures 4 and 5 show the velocity profiles for axial positions at 9.1 mm and 15 mm, respectively. The contraction from the main body of the nozzle to the tip occurs at 9.1 mm. Unlike the “initial comparison” data, the viscosity of the fluid used in these profiles is modeled as a power-law fluid.

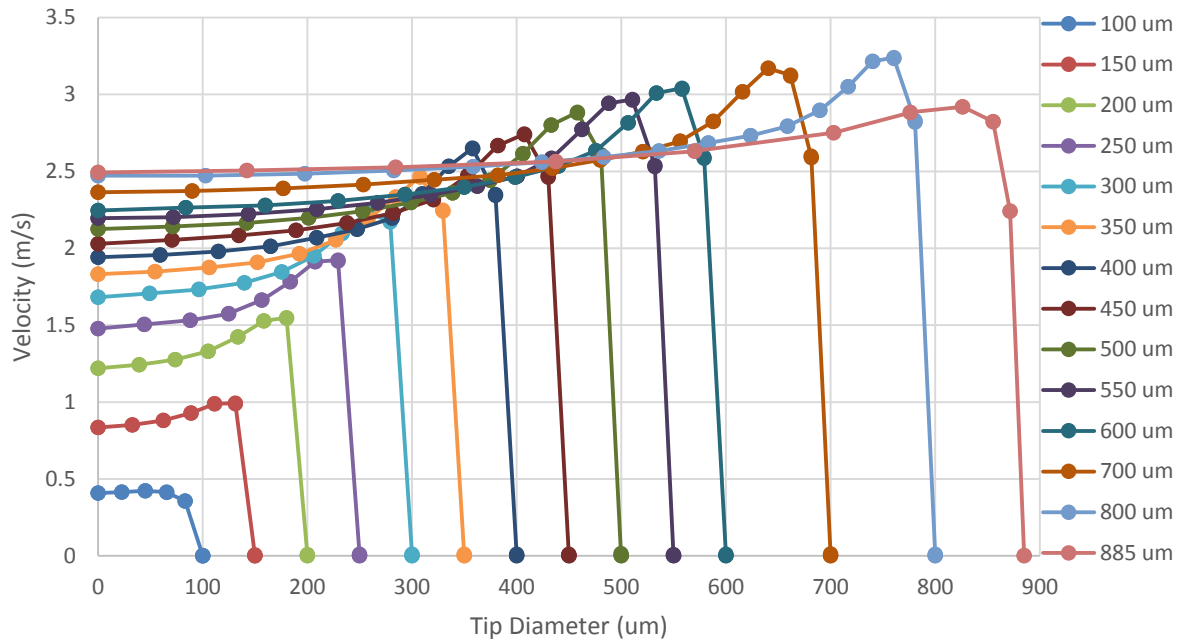


Figure 47. Velocity profile in the radial direction at axial position 9.1 mm.

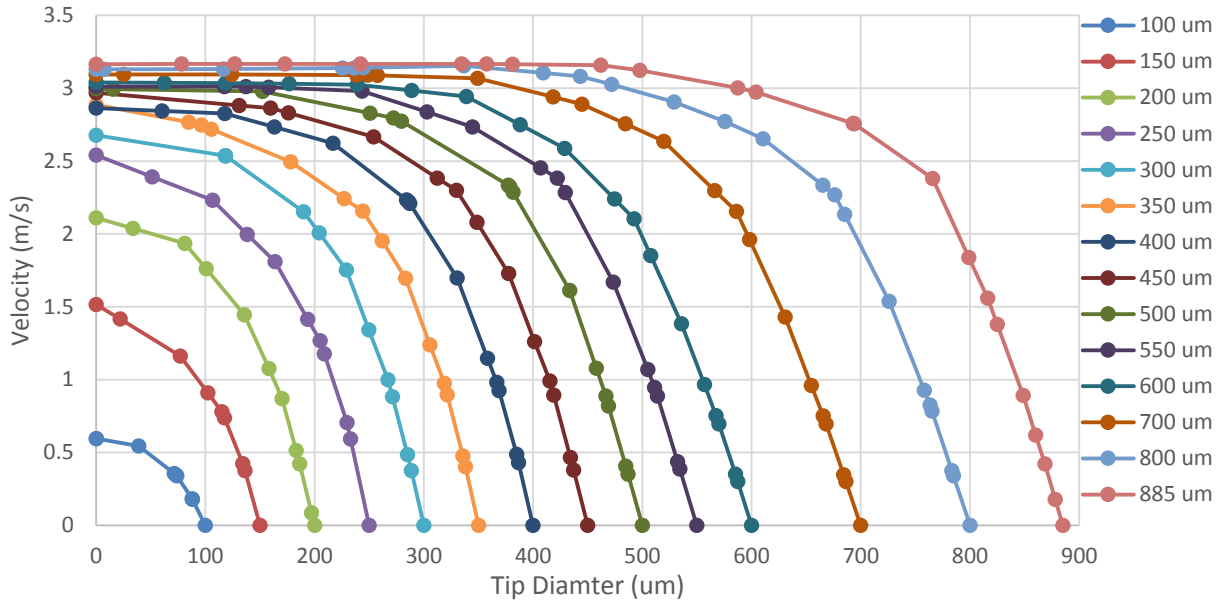


Figure 48. Velocity profile in the radial direction at axial position 15 mm.

Figures 6 and 7 show the pressure profiles that correspond to the same axial positions as Figures 4 and 5, respectively. Note that for Figure 6, the drop in pressure near the wall corresponds with the increase in velocity shown in Figure 4.

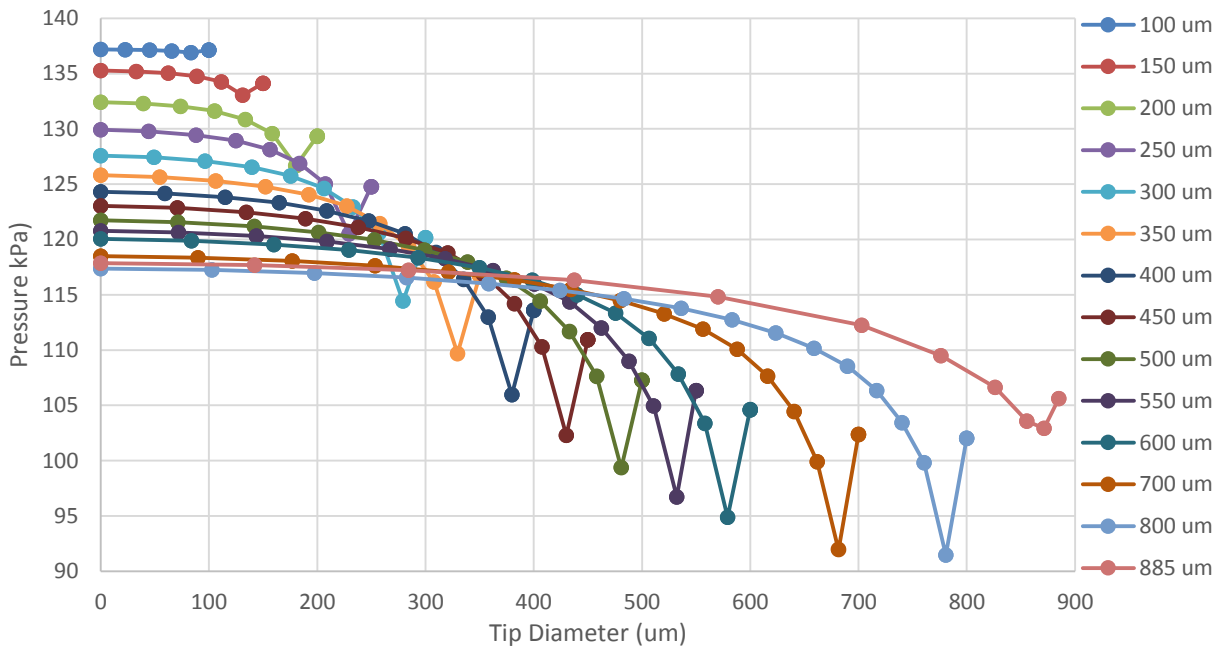


Figure 49. Pressure profile in the radial direction at axial position 9.1 mm

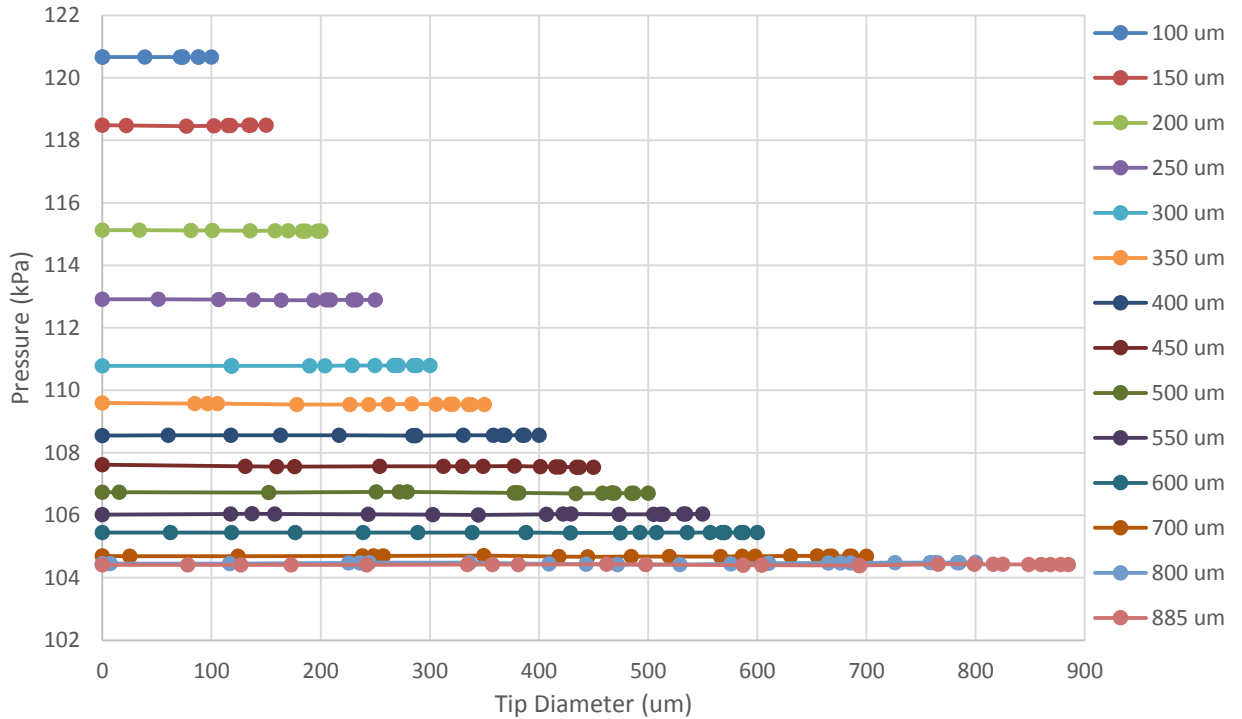


Figure 50. Pressure profile in the radial direction at axial position 15 mm.

DISCUSSION

Initial Comparison

As shown in Figures 2 and 3, there is very good agreement between the two simulations. The Hagen-Poiseuille equation for flow through a pipe is given by:

$$v = \frac{1}{4\mu} \frac{\Delta P}{\Delta z} (R^2 - r^2) \quad (5)$$

For the given boundary conditions, the value of the maximum velocity v_{max} is expected to be 0.762 m/s at the centerline of the pipe. This value is approached in both simulations. However, in the COMSOL® simulation, the value of the maximum velocity actually exceeds this value. It is thought that COMSOL® may be automatically accounting for end effects of the pipe flow. Such effects are not reflected in the MATLAB simulation.

Velocity and Pressure Profiles

The data shown in Figures 4 and 6 suggest that the fluid may be undergoing a phenomenon known as vena contracta. Fluids that flow through a sudden contraction in diameter, such as through a nozzle, will exhibit behavior in which the diameter of the stream of fluid is smallest immediately following the contraction in the geometry and then widens and approaches a parabolic profile downstream of the nozzle. This has the effect of increasing the velocity of the fluid near the contraction.

An important aspect to note is the drop in velocity near the wall when the tip diameter is increased to the maximum of 885 μm . At this point, the 90° edge present in the other tip diameter cases disappears and the fluid profile becomes somewhat smoother. This may lend credence to the possibility that vena contracta is being observed in the cases with smaller tip diameters. Additionally, the pressure profiles shown in Figures 6 and 7 indicate the behavior expected when vena contracta is occurring. The pressure profile drops rapidly at the contraction and then flattens out further downstream. However, the tip of the nozzle is long enough that the vena contracta phenomenon will have little to no effect on the parabolic velocity profile at the outlet of the nozzle.

Viscosity Assumption

For the data gathered through the various COMSOL® simulations, the viscosity of the fluid was modeled as a non-Newtonian power-law fluid. However, it may not be necessary to consider the non-Newtonian behavior of the fluid in the numerical model of the nozzle/substrate system. According to Ubal et al., the shear-thinning effect of a non-Newtonian fluid is unnoticeable at normal operating conditions of the direct-writing system [3]. A decrease in the velocity of the substrate by two orders of magnitude is needed to see any substantial shear-thinning of the fluid on the printed track. Figure 8 shows a comparison of fluids with three different viscosities, ranging in behavior from Newtonian ($K=0$) to the non-Newtonian ink ($K=0.084$) used by Ubal et al.

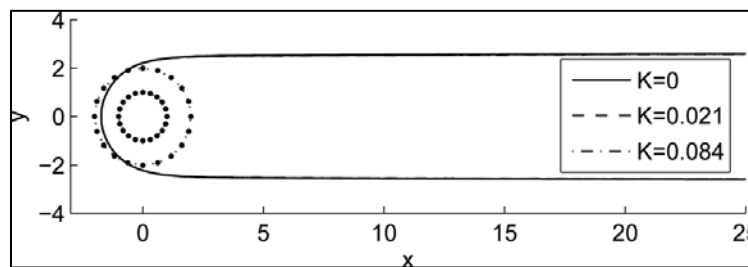


Figure 51. Resultant fluid track for different ink viscosities [3].

Figure 8 shows that there is no noticeable difference in the resultant track shape. Therefore, the non-Newtonian nature of the fluid can be ignored and the viscosity can be considered constant. This assumption will have to be justified for a fluid with properties similar to the in-house conductive ink.

CONCLUSION

The intent of this research is to investigate the pattern morphology and properties of a track of fluid printed through the direct-write process. This is being accomplished by simulating the deposition process using COMSOL Multiphysics® software. Through this research, the accuracy of the COMSOL® software was validated to an extent. Additionally, the flow of fluid through the nozzle experiences a phenomenon known as vena contracta. However, because the length of the tip of the nozzle is great enough, this may have no impact on the velocity profile at the outlet of the nozzle.

Ongoing and future aspects of this work include the completion of the “advanced” simulations in MATLAB to further validate the accuracy of COMSOL®. Also, work will continue to duplicate the model developed by Ubal et al. for the in-house ink. This model will incorporate the entirety of the nozzle with a pressure inlet, not just an imposed velocity profile at the outlet. This will be

followed by physical experiments to validate the model. Finally, the information gathered from this simulations and experiments will be used to develop a controls system for the NBRD technology.

ACKNOWLEDGEMENTS

Funding for this research was provided by the NASA West Virginia Space Grant Consortium. Special thanks is given to Dr. Debansu Bhattacharyya for his expertise, patience, and steadfast assistance with this project. Additional thanks is due to the COMSOL® technical support team, for putting up with my incessant questions.

REFERENCES

- [1] W. Seufzer, *Additive Manufacturing Modeling and Simulation*, NASA Langley Research Center, Virginia: NASA/TM-2014-218245, 2014.
- [2] L. Murr, S. Gaytan, D. Ramirez, E. Martinez, J. Hernandez, K. Amato, P. Shindo, F. Medina and R. Wicker, "Metal Fabrication by Additive Manufacturing Using Laser and Electron Beam Melting technologies," *Journal of Materials Science & Technologies*, vol. 28, no. 1, pp. 1-14, 2012.
- [3] S. Ubal, B. Xu, B. Derby and P. Grassia, "Continuous Deposition of a Liquid Thread onto a Moving Substrate. Numerical Analysis and Comparison With Experiments," *Journal of Fluids Engineering*, vol. 134, no. 2, 2012.
- [4] M. Torres Arango, *Electro-mechanical Characterization of Directly Written Ag patterns On Plastics*, ICMCTF, 2015.
- [5] COMSOL Multiphysics, Stockholm: COMSOL AB.
- [6] S. Ubal, B. Xu, B. Derby and P. Grassia, "Continuous Deposition of a Liquid Thread onto a Moving Substrate. Numerical Analysis and Comparison With Experiments," *Journal of Fluids Engineering*, vol. 134, 2012.

COMPARATIVE ANALYSIS OF UNINHIBITED AND CONSTRAINED AVIAN WING AERODYNAMICS

Jordan Cox
MS, Aerospace Engineering
West Virginia University
Morgantown, West Virginia 26506

ABSTRACT

The flight of birds has intrigued and motivated man for many years. Bird flight served as the primary inspiration of flying machines developed by Leonardo Da Vinci, Otto Lilienthal, and even the Wright brothers. Avian flight has once again drawn the attention of the scientific community as unmanned aerial vehicles (UAV) are not only becoming more popular, but smaller. Birds are once again influencing the designs of aircraft. Small UAVs operating within flight conditions and low Reynolds numbers common to birds are not yet capable of the high levels of control and agility that birds display with ease. Many researchers believe the potential to improve small UAV performance can be obtained by applying features common to birds such as feathers and flapping flight to small UAVs. Although the effects of feathers on a wing have received some attention, the effects of localized transient feather motion and surface geometry on the flight performance of a wing have been largely overlooked. In this research, the effects of freely moving feathers on a preserved red tailed hawk wing were studied.

A series of experiments were conducted to measure the aerodynamic forces on a hawk wing with varying levels of feather movement permitted. Angle of attack and air speed were varied within the natural flight envelope of the hawk. Subsequent identical tests were performed with the feather motion constrained through the use of externally-applied surface treatments. Additional tests involved the study of an absolutely fixed geometry mold-and-cast wing model of the original bird wing. Final tests were also performed after applying surface coatings to the cast wing. High speed videos taken during tests revealed the extent of the feather movement between wing models. Images of the microscopic surface structure of each wing model were analyzed to establish variations in surface geometry between models. Recorded aerodynamic forces were then compared to the known feather motion and surface geometry to correlate the performance to these two features.

The results of this study revealed that the performance of the bird wing was directly affected by feather motion. It was also found that the motion of covert and secondary covert feathers had the greatest influence on the performance. Increased coefficients of lift and drag were found when higher frequencies of these feathers were observed. Noticeable reductions in the coefficient of drag were found to be associated with micron level variations in the depth of surface features on the wing.

INTRODUCTION

As the world changes, so do the requirements of technology. In the beginning, avian served as the prime inspiration for human flight. The influence of the natural design of birds can be seen in the flight pursuits of Leonardo da Vincie, Otto Lilinthal, and even the Wright brothers. However, as

the requirements of aircraft changed throughout the 20th century, avian flight principals became less relevant for larger, faster, and higher flying aircraft.

Today the focus of the world of aviation is changing. Although still significant, much attention is being siphoned from manned aircraft and applied to unmanned aircraft. A key category of unmanned aerial vehicles (UAV) is micro air vehicles or MAVs. Small UAVs intended for low speed applications are considered to be MAVs [1].

Many MAVs are required to operate under flight conditions and Reynolds numbers similar those experienced by birds. As a result, new and inspiring methods to increase the performance and efficiency of MAVs maybe found in avian flight. This research focuses on the effects of freely moving feathers, just one characteristic of bird flight that may hold the key.

“The genius of man may make various inventions, encompassing with various instruments one and the same end; but it will never discover a more beautiful, a more economical, or a more direct one than nature’s, since in her inventions nothing is wanting and nothing is superfluous.”

-Leonardo Da Vinci [2]

BACKGROUND

Avian feathers have different shapes, colors, and specialized structures that can vary from species to species. The major variations between the feathers of different species depend on the natural adaptations the species has developed. However, the basic structure of feathers remains the same.

Feathers are primarily made up of the protein keratin. They are also considered to be dead and not a living organ, like the epidermis, or skin, of an animal [3]. Therefore, the feathers of a bird do not repair themselves and must be replaced at various intervals in a process called molting [4].

The primary shaft of the feather is known as the rachis. Extending from the rachis are the inner and outer vanes. Vanes are composed of individual rows of parallel barbs. Each of these barbs is then covered with microscopic fibers called barbules. An example of these structures can be seen in Figure 52.

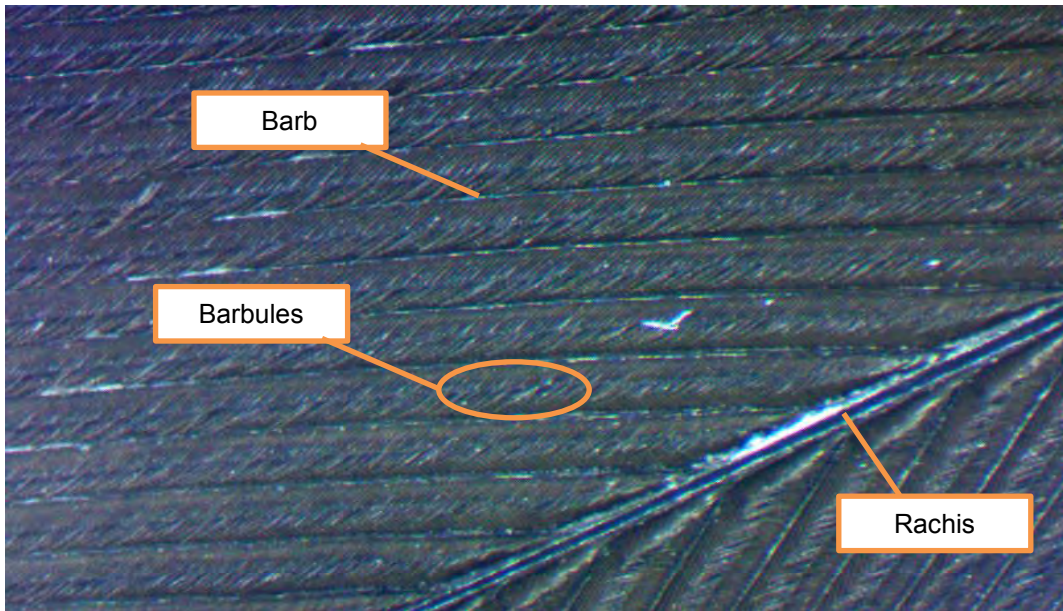


Figure 52: The Major Feather Structures

Most flying birds have four major feather groups that impact flight: the coverts, primaries, secondaries, and alula as seen in Figure 53. Primary feathers are located at the tip of the wing. These feathers are sometimes thought of as the fingers. Secondary feathers are located along the trailing edge of the wing between the primaries and the scapulars attached to the bird's body. Covert and secondary covert feathers make up the center portion of the wing between the leading edge and the secondaries. These feathers are believed to act independent of a bird's nervous system. In other words, covert feathers are believed to be passively controlled during flight. This is attributed to the randomness of their recorded movement during flight scenarios in which they become active. Alula feathers are located in a small section of feathers between the coverts and the primaries at the leading edge of the wing. These feathers are the beginning of the hand wing and are often thought of as the thumb. Alula are actively controlled by the bird [5, 6, 7].

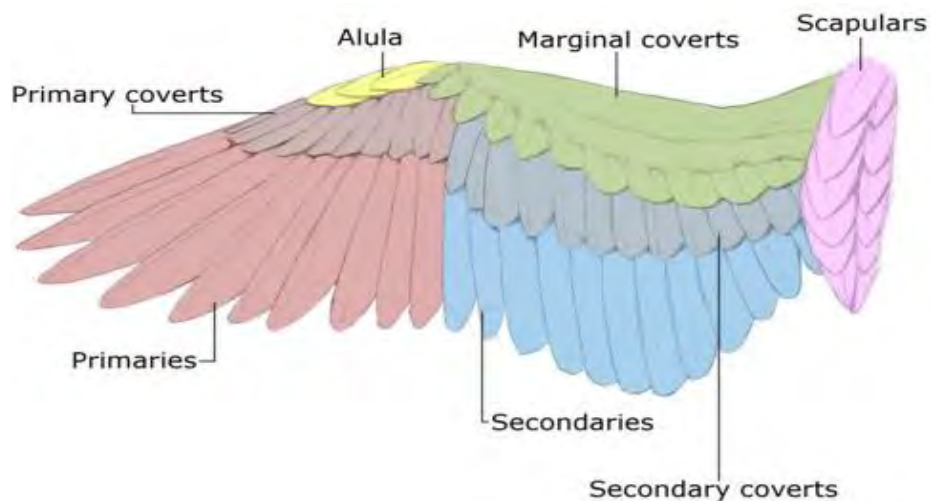


Figure 53: The Major Feather Groups of a Bird [8]

High speed imagery of a Steppe Eagle has shown that the active extension of the alulae also affects the marginal coverts located at the leading edge of the arm wing. After alulae have been extended, covert feathers begin to extend. The coverts extend first nearest the alulae and cascades along the leading edge to the scapular feathers near the body of the bird. Together they work as a leading edge flap. This process repeatedly occurred during the final moments as the trained eagle used in the test performed a landing maneuver. However, only high speed video of this phenomenon was taken. Therefore, the researchers could only hypothesize actual effects of this process [5].

Through observations of birds in flight, it has been noticed that covert feathers are most active when the bird is gliding with its wings at high angles of attack. This observation has led many experts to believe these feathers act as a high-lift device or stabilizer during these situations. A similar hypothesis suggests these feathers act as a type of passive flap that works to keep air flow over the upper surface of the wing attached at increased angles of attack. As a result, similar systems have been investigated for use on MAVs. However, a measure of this effect on a bird's wing has not yet been found [1, 5].

Although it has been shown that the shape, size, location, and make up of a feather affect the wing's overall performance, a deficiency in our knowledge still exists. We know how each feather group effects flight. However, the question "what effect does the free movement of these feathers have on the wing?" continues to go unanswered.

METHOD

A series of tests were conducted to collect the aerodynamic force data exhibited by five variations of the same wing. These variations were used to isolate and study the effects of fluid structure interaction in the form of feather motion and the influence of surface geometry on the performance of the wing. The aerodynamic force data was collected using the test set up shown in Figure 54. The West Virginia University closed-loop wind tunnel was used to facilitate the environment needed for testing. During testing, the angle of attack (α) of the wing was varied. This was repeated at multiple different wind speeds for each wing. The wind speeds selected for testing were chosen to be within the natural flight speeds of an adult Red Tailed Hawk. High speed videos were recorded of the wings during testing. Using these videos the changes in the frequency and amplitude of the four feather groups was found.

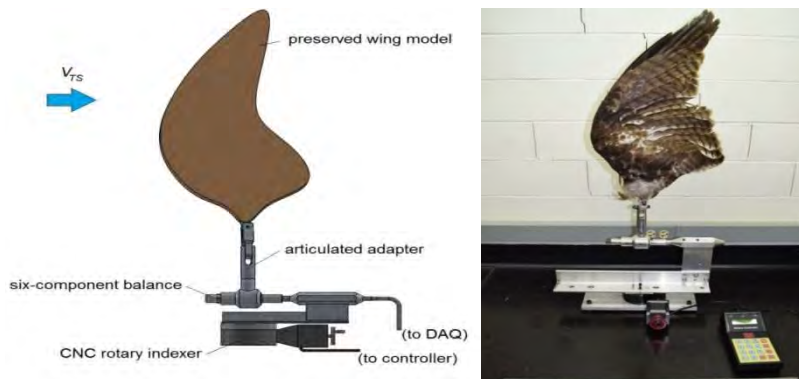


Figure 54: A Schematic Representation of the Experimental Test Setup (left) and the Actual Setup Used for Testing (right)

Creating the Preserved Wing Model

In order to isolate the effects of freely moving feathers, a method was developed to create variations of the same wing with different levels of permitted feather frequency for testing. A harvested Red Tailed Hawk wing was chosen to be the foundation of this research. This wing was harvested from the cadaver of a young adult red-tailed hawk (*Buteo jamaicensis*) carcass. The cadaver was donated by a local rehabilitation center for wounded wildlife, the Avian Conservation Center of Appalachia [9]. No animals were harmed or euthanized for the purpose of this research.

As with any deceased animal, the extremity was limp and could not hold a suitable shape for testing on its own. Another problem present was the decay of the wing. The more time the wing spent out of the freezer, the more the wing would decay. It was known that if this decay was allowed to continue, potentially harmful bacteria would begin to grow on the wing. The condition of the wing would also deteriorate over time.

To overcome these issues a natural method was developed to dry and preserve the wings. The method that was developed uses disodium tetraborate as a desiccant to absorb moisture from the wing without damaging the feathers. The disodium tetraborate also killed any parasites that were on or in the wing. This process also stiffened the wing in a desirable outstretched shape for testing, similar to if the bird were gliding.

Surface Applications to Reduce Feather Motion

After the wing was preserved and aerodynamic force data was collected, Aqua Net hair spray was applied to the wing to reduce feather motion. Hair spray was chosen as the first surface application for several reasons. One reason was that the hair spray would restrict, but not inhibit feather motion. Another reason hair spray was chosen, was the belief that it would not seriously alter the surface geometry of the wing.

Once the required aerodynamic force data had been collected from the hair sprayed wing model, the wing was ready for the next application to reduce feather motion, Minwax Fast Drying Polyurethane. However, before polyurethane was applied to the wing, molds were taken of the wing. It was believed that the polyurethane coating would severely alter the surface geometry of the wing. Therefore, molds of the wing were taken at this point.

The wing was remounted in the test setup and aligned in the same orientation as the previous two wings. Alignment of the wing was checked using photographic documentation of the original set up. Aerodynamic force data was then collected from the polyurethane wing model in the same manner as the previous models.

Isolating the Effects of Feather Motion

Although very little feather motion was observed on W3, aerodynamic force data from a wing with no moving feathers was still required for comparison. It was determined; the best way to accomplish this was to reproduce a copy of the wing that still maintained the same macroscopic or overall shape and microscopic surface geometry. The final solution was to create a silicon rubber mold and polyurethane cast of the wing but, this had never been done.

The cast wing shown in Figure 55 was created using a two part mold method developed specifically for this research. AeroMarine AM 125 silicon mold was used to create a two part mold of the hair sprayed wing. AeroMarine polyurethane casting resin was then used to form the cast wing.



Figure 55: The Final Cast Wing Model Prepared for Testing

Surface Application to Isolate the Effect of Surface Geometry on the Wing

After the required aerodynamic force data had been collected from the cast wing model, the wing was coated with Performix Plasti Dip Multi-Purpose Rubber Coating. Applying Plasti Dip to the surface of the wing reduced the surface geometry of the cast wing by filling in the gaps between the barbs and barbules on the model's surface. Feather movement was not possible on the cast wing. Therefore, the resulting Plasti Dip wing model allowed the effects of the surface geometry to be isolated from the effects of feather movement.

RESULTS

Effects of Feather Motion on the Performance of the Wing

Applying hair spray to the preserved wing drastically decreased the amplitude of the feathers. However, the frequency of the covert and secondary covert feathers was increased at positive angles of attack. The application of polyurethane to the hair sprayed wing further reduced the amplitude of the feathers and inhibited the motion of the covert and secondary covert feathers.

When the performance of the hair sprayed wing (W2) was compared to the performance of its cast (W4), the hair sprayed wing showed higher coefficient of lift (C_L) values at the same angles of attack where increased covert and secondary covert motion were observed. The same results were found when the hair sprayed wing was compared to either the preserved (W1) or polyurethane coated (W3) wings. At angles of attack where W2 had the highest covert and secondary covert feather frequencies, the wing had favorable C_L values. This pattern was also found when W1 was compared to the W3. These results can be seen in Figure 56.

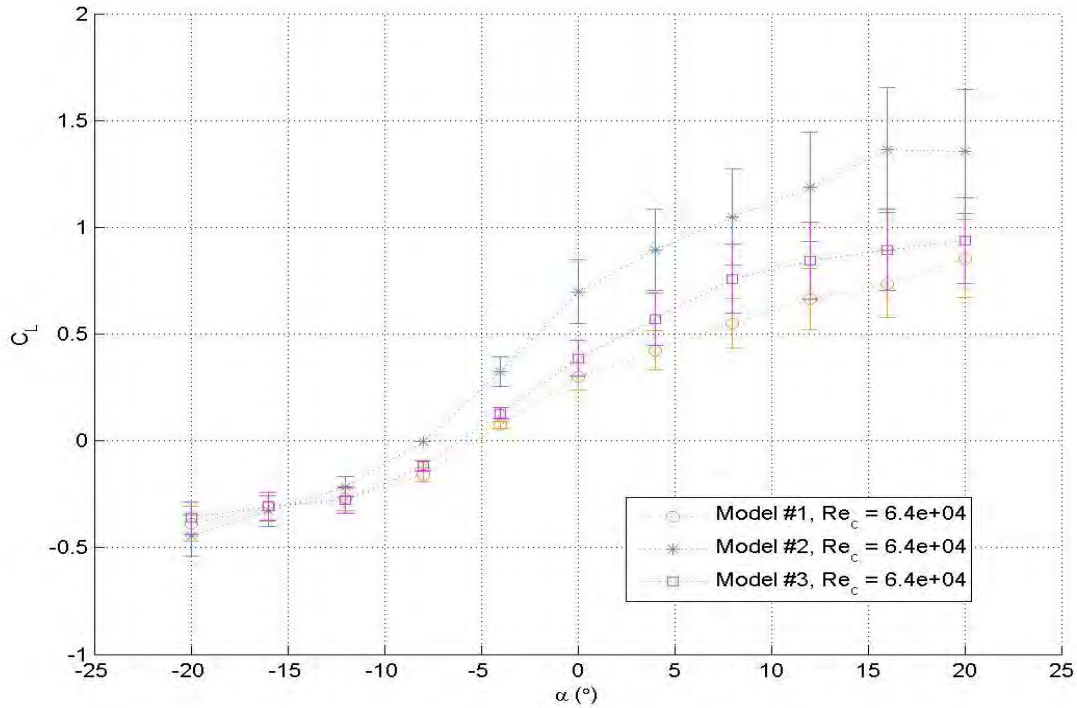


Figure 56: Performance Differences Related to Feather Motion

Performance Impacts of Feather Surface Geometry

Figure 57 provides an example of the change in the feature of the surface of a feather caused by applying Plasti Dip. The depth of the surface features was reduced. As a result, the finer features such as individual barbules were no longer distinguishable.

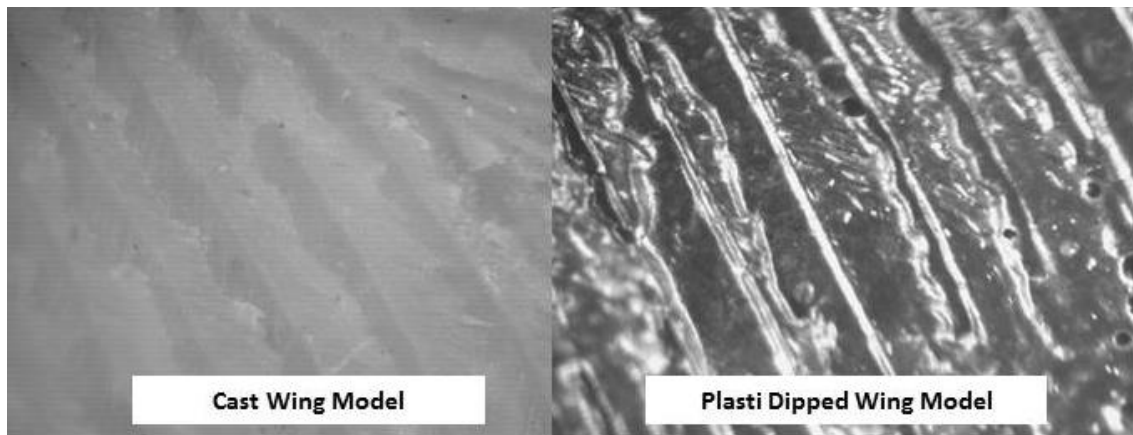


Figure 57: Effects of Plasti Dip on the Surface of a Cast Feather

Little change in the coefficient of lift values was noticed when the W4 and the Plasti Dipped wing (W5) were compared. Yet, the coefficient of drag (C_D) was reduced outside of the uncertainty between -10° and -5° α . This change is shown in Figure 58. Applying polyurethane to the surface of the wing caused W3 drastically decreased the depth of the surface geometry.

However, these same changes in performance were not found. When the performance of W3 and W5 was compared, almost no differences in performance could be found outside of the uncertainty.

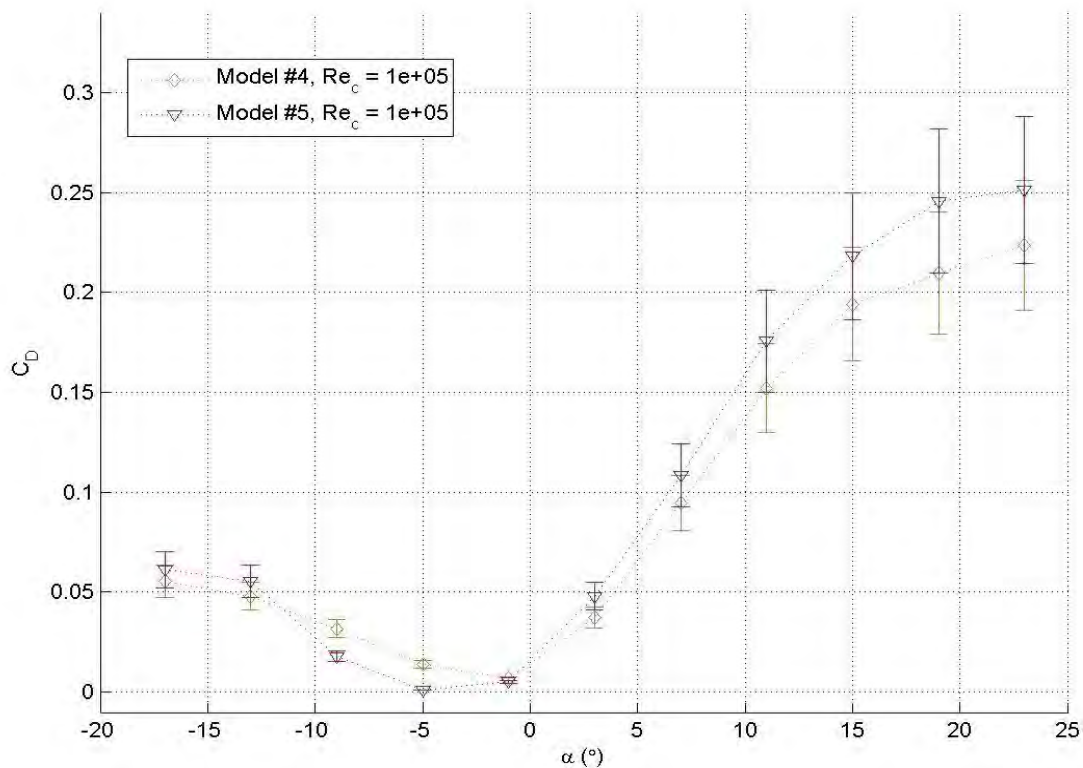


Figure 58: Differences in the C_D Values of the Cast and Plasti Dipped Wings

CONCLUSION

Effects of Feather Motion on the Performance of a Bird's Wing

Through a comparative analysis of aerodynamic force data taken from four variations of the same red tailed hawk wing with different levels of feather motion permitted, it was found that fluid structure interaction in the form of covert and secondary covert feather frequencies effects there performance of a bird's wing. Increased covert and secondary covert frequencies occurred under the same conditions as increased C_L values. Decreases in the amplitude of the covert and secondary covert feathers also occurred under the same conditions. This supports that increasing the frequency and decreasing the amplitude of covert and secondary covert feathers can increase the performance of a bird's wing. No relationship between the motion of the primary or secondary feathers and the performance of the wing was found.

Influences of the Microscopic Surface Geometry on the Performance of a Bird's Wing

The aerodynamic force data of a two wings with an identical macroscopic shape was compared. The resulting aerodynamic force data of the wing with the microscopic surface geometry filled in was found to have lower C_D values and in turn favorable performance. As a result, it was found that removing the fine features such as the barbules decreased the C_D and increased the performance of the wing.

RECOMMENDATIONS

Applying synthetic structures similar to feathers to the wing surface of small UAV operating at low Reynolds numbers could improve the performance of that UAV. Increasing the frequency of the feathers located in the same area of the UAV's wing as covert and secondary covert feathers could further increase the performance of the UAV. This could be done by adjusting the material, thickness, and geometry of the feathers to increase their frequency.

Replication the surface geometry of feathers on the synthetic feathers of a UAV could also improve the performance of the UAV by reducing the UAV's C_D . However, replicating the fine surface features of a feather is not believed to have a positive effect on the performance of a wing. Therefore, tooling and machining cost can be reduced by allowing lower tolerances.

ACKNOWLEDGEMENTS

I would like to express my gratitude to the West Virginia Space Grant Consortium for all of their help and for the opportunities they have made possible for me during both my graduate and undergraduate careers. My time in SPACE at West Virginia University Institute of Technology helped me to realize the career in STEM that I wanted. Their support throughout my graduate studies helped me find a way to make my career goals a reality. Without the support of the West Virginia Space Grant I would not have been able to achieve my goal of obtaining a master's degree in aerospace engineering.

Finally, I would like to thank Dr. Patrick Browning for his help and guidance throughout my graduate studies. He was constantly willing put extra time into my project to make sure I was off on the right track. Dr. Browning spent many late nights away from his family to help me during testing or data collection over the past two years. As a result, I would like to thank him, not only for his dedication to developing my project, but also his dedication to developing me.

REFERENCES

- [1] J. Wang and J. Schluter, "Low Reynolds Number Application of Feather Inspired Passive High Lift Device on Finite Wing," *AIAA*, 2013.
- [2] L. De Vinci and E. MacCurdy, *Leonardo Da Vinci's Note-Books*, New York: Empire State Book, 1923.
- [3] J. J. Videler, *Avian Flight*, Oxford: Oxford UP, 2005.
- [4] D. Blood, V. P. Studdert and C. C. Saunders, *Comprehensive Veterinary Dictionary*, Edinbrugh: Elsevier Saunders, 2007.
- [5] A. C. Carruthers, G. K. Taylor, S. M. Walker and A. L. Thomas, "Use and Function of a Leading Edge Flap on the Wings of Eagles," *AIAA*, 2007.
- [6] E. F. Blick, "The Aerodynamics of Birds," *AIAA Student Journal*, 1976.

- [7] J. J. Videler, E. J. Stamhuis and G. Povel, "Leading-Edge Vortex Lifts Swift," *Science*, pp. 1960-1962, 2004.
- [8] D. White, "Parrot Anatomy," Parrot Fun Zone, [Online]. Available: <http://parrotfunzone.com/learn-about-parrots/parrot-anatomy/external-anatomy>. [Accessed 21 February 2016].
- [9] "Red-Tailed Hawk," National Geographic, [Online]. Available: <http://animals.nationalgeographic.com/animals/birds/red-tailed-hawk/>. [Accessed 28 February 2016].
- [10] T. Prindle, "Preserving Bird Wings, Tails, or Talons".

AMBUSH SITE SELECTION IN EASTERN DIAMONDBACK RATTLESNAKES (*CROTALUS ADAMANTEUS*)

Berlyna Heres
Master of Science in Biological Sciences
Marshall University
Huntington, WV 25755

ABSTRACT

I examined ambush site selection in Eastern Diamondback Rattlesnakes (*Crotalus adamanteus*, EDB). The EDB is an imperiled, ambush predator endemic to southeastern pine savannas and woodlands. Eastern diamondbacks prey on small mammals that feed on hard and soft mast (e.g., nuts and fruits). In this study, I hypothesized that due to a bottom-up trophic effect, intra-seasonal shifts in masting vegetation would cause intra-season shifts in ambush site selection in EDBs. I quantified EDB foraging site selection using radio telemetry data and vegetation analysis within a naturalized study site. When EDBs were encountered in ambush posture, I quantified vegetation structure at the ‘selected’ location and at two random locations. I measured understory, overstory structure and masting characteristics within each vegetation plot. Over the study period (June-August), I quantified vegetation structure at 35 ambush sites and paired random locations, totaling 105 plots. I used conditional logistic regression to model ambush site selection. I developed five *a priori* models to examine ambush site selection, including soft mast presence, hard mast presence, and canopy cover as predictors. Top models supported my hypothesis, indicating that EDB foraging sites were associated with soft mast producing vegetation during times when soft mast was present. Hard mast presence was also an important predictor of EDB ambush sites. The results of this study indicate that EDB foraging site selection reflects mast availability, which is an example of a bottom up trophic effect. Mast presence should be considered in efforts to manage EDB populations and their prey.

INTRODUCTION

Eastern diamondback rattlesnakes (*Crotalus adamanteus*; EDBs) are ambush foragers that prey on small mammals, many of which are granivores [1]. The EDB, which is associated with pine savannas and woodlands in the southeastern Coastal Plain [2], is in review for federal protection under the Endangered Species Act [3]. Population declines have been linked to habitat loss, fragmentation, and wanton killing [2].

Eastern diamondback rattlesnakes exhibit high site fidelity, [4], and follow predictable behaviorally-based patterns that can aid land managers and conservationist in restoration of the species [5] [6]. Changes in behavior are categorized into three “seasons”: foraging (March-August), reproduction (August-November), and hibernation (November-March) [5]. The season which restores and maintains body condition for EDBs is the foraging season, a time when snakes are actively searching for prey and acquiring energy for reproduction in the fall and hibernation in the winter.

Eastern diamondback rattlesnakes prey on small mammals, such as the white footed mouse (*Peromyscus leucopus*), cotton rat, (*Sigmodon hispidus*), and fox squirrel (*Sciurus niger*). These

prey items are granivores, i.e., they feed on mast such as acorn and pine nuts. The EDB foraging season is concurrent with the production of both soft and hard masting vegetation. Mast is the seed, nuts or complete fruit produced by trees and smaller plants [7]. Masting vegetation produces fruit or nuts during short time periods, exhibiting seasonal productivity. Within the southeastern Coastal Plain, blueberry (*Vaccinium spp.*) and blackberry (*Rubus spp.*) ripen late May to mid-July [7]. Hickory and walnut species (*Carya spp.* & *Juglan spp.*) produce nuts (i.e., hard mast) from late July through to the fall [7]. Oaks produce acorns later in the summer toward August [7].

Mast-producing plants in the southeastern Coastal Plain (e.g., oak species, hickory species and soft mast producers such as blackberries) provide food resources to granivores, and thus indirectly affect EDB food availability. Mast is a key nutrient source for granivores [8], and the productivity of masting plants has been linked to population dynamics and habitat selection of the organisms that feed on mast [9].

While seasonal EDB movement patterns have been examined, intra-seasonal movement patterns in relation to ambush-site selection remains unstudied, [6] [5]. In this study, I quantified EDB foraging site selection using radio telemetry data and vegetation analysis within a naturalized study site. I expected that masting vegetation would be an important component of foraging site selection, given that the majority of EDB prey items are granivores. I hypothesized that as a result of a bottom-up trophic effect, intra-seasonal shifts in masting vegetation would cause intra-season shifts in ambush site selection in EDBs.

METHODS

I conducted this study on a privately-owned property in Colleton County, SC. This site was part of the Ashepoo, Combahee, and South Edisto (ACE) Basin Conservation program and was managed for bobwhite quail (*Colinus virginianus*) with prescribed fire and timber harvests [10]. It consisted of 4,600 hectare of mixed pine and hardwood as well as lowland hardwood stands. This site contained high integrity stands of longleaf pine (*Pinus palustris*) interspersed with turkey oak (*Qercus laevis*) and pignut hickory (*Carya galbra*), an open canopy understory of bracken fern (*Pteridium aquilinum*), as well as, various species of fire tolerant grasses and forbs.

I captured and surgically implanted transmitters into five eastern diamondback rattlesnakes, (*Crotalus adamanteus*, EDBs) (SI-2, 11-13 g, Holohil Systems, Carp, Ontario) using procedures outlined by Waldron et al. [4]. One additional EDB was underweight so a temporary transmitter was attached to the rattle, to minimize stress [11]. I radiotelemeterically monitored EDBs, (Female=4, Male=2), three times weekly over the foraging season (May-August, 2015) using a Telonics TR-4 radio receiver and a Yagi antenna (Telonics, Inc., Mesa, AZ). Snakes were visually identified and their locations were recorded using a GPS device with 5-m spatial accuracy, (Trimble Juno, Sunnyvale, CA, USA). All snakes were mature adults throughout the study, as shown by both size and previous copulation observations [6](Brad O’Hanlon, unpublished data).

I collected vegetation density and composition data at all EDB ambush sites recorded between 1 June and 16 August, 2015 in a modified methodology described by Reinert, Cundall and Bushar [12]. I assumed that a location was a foraging or “ambush site” if I observed EDBs in ambush posture. I used a modified James and Shugart [13] vegetation plot (plot) to quantify vegetation and masting characteristics of foraging sites. I recorded canopy vegetation and groundcover vegetation at each plot. I divided canopy into two groups, conifers (e.g., pines), and hardwoods,

(e.g., hardwoods such as oaks, and hickories, and some miscellaneous species such as palmettos). Both canopy and groundcover were categorized by the presence or absence of mast.

I estimated groundcover density by laying two perpendicular transects, creating a circular plot with a radius of 11.28 meters. I sampled vegetation along a random azimuth and along that azimuth's cardinal directions totaling 34 points. I quantified groundcover density by the number of plants present at each point along the 34 point transect. Within the two categories, masting and non-masting groundcover, I further divided vegetation according to Table 1. Examples of common masting groundcover include *Vaccinium*, *Rubus*, and legumes. I defined soft mast understory species (Percent Understory) as any shrub-sized plant that exceeded breast height (1.35 meters) but whose trunk did not exceed 8 cm diameter at breast height (DBH).

Table 1. Parameters used to examine ambush site selection of EDBs in relation to masting vegetation.

Category	Parameter	Definition
Canopy	Percent Canopy Cover (PCC)	Canopy cover density at 5 points on each plot expressed as a percentage.
	Hard Mast Basal Area (HMBA)	Basal Area (BA, $1 \text{ m}^2 / \text{ha}$) of hardwood trees with the capacity of masting e.g., <i>Carya</i> spp.
Understory	Soft Mast Groundcover (SMG)	All woody plants along transect, e.g., <i>Rubus</i> as a percentage
	Percent Understory (PU)	All shrubs along transect, e.g., <i>Myrica cerifera</i> as a percentage

I measured DBH and identified all tree species that exceeded 8 cm DBH within the circumference created by the two transects. I estimated canopy cover using an ocular tube at the center of transects as well as at the midway point of the transect in all four directions, totaling 5 points, which were then averaged as a percentage.

I performed three vegetation analysis plots for each ambush site. One plot was located at the ambush site (i.e., where the snake was observed in ambush posture). The second plot was located 40 m (within daily movement) away from the ambush site along a random azimuth. The third plot was located 300 m (outside of daily movement) from the ambush site along a random azimuth.

Statistical analysis was performed using SAS (SAS Institute). Comparison at two separate scales, 40m and 300m, lacked the necessary power to reveal any trends, therefore, the random plots were combined and compared to the primary ambush plots. I ran correlation analysis (PROC CORR), to examine collinearity and excluded correlated parameters ($r \geq 0.70$). I used conditional logistic regression in PROC GLIMMIX to compare used versus random ambush locations. I accounted for the lack of independence among observations of the same snake by treating individual snakes as a random effect during analysis. I used Akaike's Information Criterion corrected for small sample size (AIC_c), retaining models with $\Delta AIC_c \leq 2.00$ for inference [14]. I used weighted-average parameter estimates based on AIC_c weights with unconditional standard error. I used model-

specific (β) beta estimates to examine covariate effects. I assessed goodness-of-fit by examining Pearson's Chi-Squared on the global candidate model.

I examined EDB ambush site selection using five candidate models that included predictors of hard and soft mast, specifically, hardwood trees (i.e., Hard Mast Basal Area) that produce hard mast and understory vegetation, (i.e., the Soft Mast Groundcover and Percent Understory parameters), which often produce soft mast (Table 2). I analyzed the candidate models within two time frames, the soft mast time frame and the hard mast time frame. The soft mast time frame encompassed the date soft mast (e.g., blackberries & blueberries) were recorded in a vegetation plot, between 4 June 2015 and 16 July 2015. The hard mast time frame encompassed the date hard mast (e.g., oak acorns, and hickory nuts) was present, recorded between 10 July 2015 and 12 August 2015. Vegetation analysis was organized by soft or hard mast, then by presence or absence of mast, totaling four analyses. This approach allowed me to examine intra-seasonal ambush site selection.

Table 2. Candidate models used to examine EDB ambush site selection at two temporal scales of hard and soft mast availability. (Percent Canopy Cover (PCC), Hard Mast Basal Area (HMBA), Soft Mast Groundcover (SMG), Percent Understory (PU))

Model Name	Model Parameters
Global	(SMG + PU+HMBA + PCC)
Soft Mast Groundcover	(SMG)
Total Soft Mast Understory	(SMG+ PU)
Hard Mast Basal Area	(HMBA)
Canopy& Hard Mast	(PCC + HMBA)

RESULTS

Over the study period (May-August), I quantified vegetation structure at 35 ambush sites and at paired random locations, totaling 105 vegetation plots. Within the Soft Mast Absent analysis, two models were used for inference (Table 3). The top model included the Soft Mast Groundcover Model as the sole predictor of ambush site selection. The Soft Mast Groundcover parameter accounted for 46% of model weights, but I failed to detect a significant association between Soft Mast Groundcover and ambush site selection ($\beta = -1.8599 \pm 2.0975$, $p = 0.3821$). The second-ranking model included Hard Mast Basal Area as a predictor of EDB ambush site selection. The Hard Mast Basal Area Model accounted for 30% of model weights, but I failed to detect a significant association between ambush site selection and Hard Mast Basal Area. The fit statistic of the global model indicated good model fit, Pearsons $\chi^2/df = 0.98$.

Within the Soft Mast Present analysis (Table 3), two models were used for inference. The top ranking model (Total Soft Mast Understory; Table 3) included Soft Mast Groundcover and Percent Understory as predictors. The Total Soft Mast Understory model accounted for 50% of model weights. Both Soft Mast Groundcover and Percent Understory were positively associated with ambush site selection when soft mast was present (Soft Mast Groundcover, $\beta = 8.343 \pm 2.682$, $p < 0.0028$; Percent Understory, $\beta = 6.670 \pm 3.090$, $p < 0.0348$, Table 4). The Global Model was also supported and accounted for 35% of model weights. The global model indicated that ambush sites

were positively associated with Soft Mast Groundcover and Percent Understory parameters (Soft Mast Groundcover, $\beta = 8.681 \pm 2.763$, $p < 0.0026$; Percent Understory, $\beta = 7.1004 \pm 3.2042$, $p < 0.0305$). I failed to detect significant effects of in the remaining global model parameters: Hard Mast Basal Area ($\beta = -0.0901 \pm 0.0568$, $p < 0.1182$) and Percent Canopy Cover ($\beta = 1.7722 \pm 1.0951$, $p < 0.1109$). The fit statistic of the global model indicated good model fit, Pearsons χ^2/df : 0.90.

Within the Hard Mast Absent analysis (Table 3), two models were used for inference, the Soft Mast Groundcover Model, which included only the Soft Mast Groundcover predictor, and the Total Soft Mast Understory model, which included both the Soft Mast Groundcover and Percent Understory predictors. Soft Mast Groundcover model accounted for 60% of model weights. There was a significant and positive association between ambush site selection and Soft Mast Groundcover ($\beta = 8.2661 \pm 2.769$, $p < 0.0045$). The Total Soft Mast Understory model made up 33% of model weights and indicated significant positive association between ambush site selection and Soft Mast Groundcover ($\beta = 8.219 \pm 2.795$, $p < 0.0051$). The Total Soft Mast Understory model failed to detect a significant effect of Percent Understory on EDB ambush site selection ($\beta = 3.517 \pm 3.338$, $p < 0.2975$). The fit statistic of the global model indicated good model fit, Pearsons χ^2/df : 0.96.

Within the Hard Mast Present analysis (Table 3), four out of five models were used for inference; Hard Mast Basal Area, Soft Mast Groundcover, Canopy & Hard Mast, and Total Soft Mast Understory accounting for 33%, 31% 17%, and 17% of model weights, respectively. I failed to detect significant associations between my predictors and ambush site selection in either inferable models: Hard Mast Basal Area ($\beta = -0.038 \pm 0.065$, $p < 0.5656$), Soft Mast Groundcover ($\beta = -0.852 \pm 1.831$, $p < 0.6441$), Canopy & Hard Mast, composed of predictors Hard Mast Basal Area and Percent Canopy Cover, respectively, ($\beta = -0.067 \pm 0.074$, $p < 0.3663$; $\beta = 0.950 \pm 0.967$, $p < 0.3308$) and Total Soft Mast Understory, composed of Soft Mast Groundcover and Percent Understory predictors, respectively, ($\beta = -0.062 \pm 1.847$, $p < 0.7369$; $\beta = 2.382 \pm 2.389$, $p < 0.3242$). The fit statistic of the global model indicated good model fit, Pearsons χ^2/df : 0.99.

Table 6. Logistic regression models, ranked according to statistical support, examining EDB ambush site selection when soft or hard mast is absent or present. Models ranked using AIC_c model selection. (Percent Canopy Cover (PCC), Hard Mast Basal Area (HMBA), Soft Mast Groundcover (SMG), Percent Understory (PU))

Rank	Model Name	Model Parameters	k ^a	AIC _c ^b	ΔAIC _c	w _i ^c
SOFT MAST ABSENT						
1	Soft Mast Groundcover	SMG	2	49.33	0	0.46
2	Hard Mast Basal Area	HMBA	2	50.19	0.86	0.30
SOFT MAST PRESENT						
1	Total Soft Mast Understory	SMG+ PU	3	75.68	0	0.51
2	Global	SMG+PU+HMBA+PCC	5	76.4	0.72	0.35

HARD MAST ABSENT						
1	Soft Mast Groundcover	SMG	2	60.32	0	0.60
2	Total Soft Mast Understory	SMG+ PU	3	61.53	1.21	0.33
HARD MAST PRESENT						
1	Hard Mast Basal Area	HMBA	2	68.81	0	0.33
2	Soft Mast Groundcover	SMG	2	68.95	0.14	0.31
3	Canopy & Hard Mast	HMBA +PCC	3	70.09	1.28	0.17
4	Total Soft Mast Understory	SMG+ PCC	3	70.17	1.36	0.17

^a number of estimated parameters

^b Akaike Information criterion for small samples

^c Akaike weight

DISCUSSION

The results supported my hypothesis that intra-seasonal shifts in masting vegetation influence intra-seasonal EDB ambush site selection and demonstrate a bottom up trophic effect. I detected a strong preference for Soft Mast Groundcover and Percent Understory for ambush sites. Both Soft Mast Groundcover and Percent Understory parameters had a positive association with ambush sites when soft masting fruits were present (Figure 3). Groundcover and understory plants observed during the study included blueberries (*Vaccinium* spp.), blackberries (*Rubus* spp.), American beautyberry (*Callicarpa americana*), waxmyrtle (*Myrica cerifera*), (*Rhus* spp.), muscadine grape (*Vitis rotundifolia*), yellow jessamine (*Gelsemium sempervirens*), and pawpaw (*Asimina* spp). During the study period, blueberries, blackberries, and muscadine grapes produced soft mast, which were likely a source of food for EDB prey. Models including Soft Mast Groundcover vegetation and Percent Understory parameters performed well in both the Soft Mast Present and Hard Mast Absent data sets, (i.e., both represent times when hard mast was absent).

When hard mast was present and soft mast was absent, I expected to see a higher model weight within the Hard Mast Basal Area, and the Canopy & Hard Mast models, as they contained the Hard Mast Basal Area parameter, a parameter that emphasizes hard masting vegetation. During the hard mast present/ soft mast absent time period (mid-July to mid-August), acorns and hickory nuts were matured and available to small mammals. Hard Mast Basal Area was an important predictor of ambush sites in both the hard mast present and soft mast absent datasets, accounting for 30% and 33% of model weights respectively. However, I failed to detect a significant association between Hard Mast Basal Area and ambush site selection.

My failure to detect significant associations within the Hard Mast Present and Soft Mast Absent datasets might be explained by the timing in which hard mast became available to granivores. At my field site, hickories and walnuts produced nuts in mid-July and oak species produced acorns in early August. By August, some of the telemetered snakes exhibited reproductive behavior, e.g., courting, copulation (personal observation; unreferenced). Because foraging behavior became limited (due to reproduction) when oaks began masting, I was unable to make inferences about the importance of masting hardwoods proximity in ambush site selection.

Another possible explanation for my failure to detect significant associations between hard mast and ambush site selection could be temperature. Average temperatures over the study period were 32 ± 1 ° C but could reach up to 38 ° C (personal observation; unreferenced) [15]. The use of shade likely factored into ambush site selection due to rattlesnakes thermoregulatory requirements. Thermoregulation has been shown to effect habitat selection in multiple rattlesnake studies [16] [17].

My study is an example of a bottom-up trophic effect, starting with the primary producer (masting vegetation) and ending with the predator (EDB) [18]. My study examines only one season, but over multiple seasons larger changes in resources can occur. For example, an influx of mast, or masting pulse, causes an increase in rodent densities which in turn causes an increase in rodent predator densities, as seen in studies with Accipiters and mice [19]. Fifty-five mammal species and 67 bird species have been reported to respond to masting events. No studies have linked snake densities to mast pulses, despite the importance of mast to snake prey [20]. Long-term research is required to describe the importance of oak masting pulses on snake ambush site selection. I suspect that long-term studies will reveal a bottom-up effect on populations of small mammals at the site, and should therefore, affect the population and possibly the body condition of rattlesnakes in the years that follow [21].

Previous research examining snake foraging site selection by chemical secretions of prey species and conspecifics is important to the selection process [22]. I do not suggest that EDBs select ambush sites in response to vegetation mast; however, my results indicate that vegetation composition is important for ambush site selection, in part, because prey should be influenced by mast. Eastern diamondbacks are likely using chemical cues, and thermoregulatory and camouflage needs, to select ambush sites.

CONCLUSIONS

Rattlesnakes are an oft maligned species. Linking snake behavior to the management of pest species, such as rats and the parasites that reside on them, can improve rattlesnake image, which will aid conservation efforts. Previous research has examined the number of ticks that are removed from the population through the timber rattlesnakes consumption of rats [23]. Other research has examined booms in granivore populations after masting pulses [8] [24]. Further research into the effects of masting pulses could improve the public's relationship with venomous snakes. Using vegetation analysis to quantify microhabitat selection provides an informative look at foraging habitat within a 'use-availability' framework. Eastern diamondback rattlesnake ambush site selection can provide valuable information about habitat needs during the foraging season. Analysis of vegetation composition and masting species can aid our understanding of predator and prey relations and improve land management practices.

EXPERIENCE

Over the last two years, I have gained an incredible amount of knowledge and experience working toward a Master's of Science degree at Marshall University. I have learned to think critically, like a scientist. I have also learned highly valuable field techniques, which will help me continue to do research and aid in conservation efforts. I was fortunate to have the NASA WV Space Grant Consortium to provide financial support that made my research possible and saved me from student loan debt. Working with my advisors, being surrounded by hard working intelligent

people, spending months in the field problem solving and learning my trade have given me everything I could hope to achieve from the graduate school experience. I am confident that I will use what I've gained to continue my career and do my part to expand human knowledge and conserve the planet.

ACKNOWLEDGEMENTS

I would like to thank Marshall University Biology Department and the NASA WV Space Grant Consortium as well as my mentor, Dr. Jayme Waldron, and my committee, Dr. Shane Welch, Dr. Anne Axel, and Dr. Thomas Pauley. I would like to thank Lew and Helen Crouch for their generosity and experience. I would also like to thank those that helped me with my project, Donna Boucher, Theresa Houze, and Jonathan Cooley. Finally, I'd like to thank my fellow Marshall Herpetology lab members for all of their support.

REFERENCES

- 1 Means D. Diamonds in the rough. *North Florida Journal*. 1994;2:1-28.
- 2 Martin W, Means D. Distribution and habitat relationships of the eastern diamondback rattlesnake (*Crotalus adamanteus*). *Herpetological Natural History*. 2000;7(1):9-34.
- 3 Department of the Interior: Fish and Wildlife Service. Endangered and threatened wildlife and plants; 90-day findings on a petition to list the eastern diamondback rattlesnake as threatened. *Federal Register*. 2012;77(91):27403-27411.
- 4 Waldron J, Welch S, Bennett S. Vegetation structure and the habitat specificity of a declining North American reptile: a remnant of former landscapes. *Biological Conservation*. 2008;141:2477-2482.
- 5 Waldron J, Lanham J, Bennett S. Using behaviorally-based seasons to investigate canebrake rattlesnake (*Crotalus horridus*) movement patterns and habitat selection. *Herpetologica*. 2006;62(4):389-398.
- 6 Waldron J, Welch S, Bennett S, Kalinowsky W, Mousseau T. Life history constraints contribute to the vulnerability of a declining North American rattlesnake. *Biological Conservation*. 2013;159:530-538.
- 7 Greenberg C, Levey D. Long-term monitoring of fleshy fruit and hard mast production and seasonal bird distribution at the Savannah River Site, South Carolina. *USDA Forest Service*; 2009.
- 8 Ostfeld R, Jones C, Wolff J. Of mice and mast: ecological connections in eastern deciduous forests. *Bioscience*. 1996;46(5):323-330.
- 9 Stephens R, Anderson E. Habitat associations and assemblages of small mammals in natural plant communities of Wisconsin. *Journal of Mammalogy*. 2014;95(2):404-420.

- 10 Fill J, Waldron J, Welch S, Gibbons J, Bennett S, Mousseau T. Using multiscale spatial models to assess potential surrogate habitat for an imperiled reptile. *PLOS One*. 2015;10(4).
- 11 Martin M, Waldron J, Welch S, Holloway J, Mousseau. Non-invasive technique for external transmitter attachment on rattlesnakes [Poster]. 2014.
- 12 Reinert H, Cundall D, Bushar L. Foraging behavior of the timber rattlesnake, *Crotalus horridus*. *Copeia*. 1984;1984(4):976-981.
- 13 James F, Shugart H. A quantitative method of habitat description. *Audubon Field Notes*. 1970;24(6).
- 14 Burnham K, Anderson D. Model selection and multimodel inference: a practical information-theoretic approach. Springer Science & Business Media; 2002.
- 15 NOAA. National Weather Service Forecast Office. [Internet]. 2015.
- 16 Moore J, Gillingham J. Spatial ecology and multi-scale habitat selection by a threatened rattlesnake: the eastern massasauga (*Sistrurus catenatus catenatus*). *Copeia*. 2006;4:742-751.
- 17 Brown W, Pyle D, Greene K, Friedlaender J. Movements and temperature relationships of timber rattlesnakes (*Crotalus horridus*) in northeastern New York. *Journal of Herpetology*. 1982;16(2):151-161.
- 18 Burghardt K, Schmitz O. Trophic ecology: bottom-up and top-down interactions across aquatic and terrestrial systems. Cambridge: Cambridge University Press; 2015.
- 19 Schmidt K, Ostfeld R. Songbird populations in fluctuating environments: predator responses to pulsed resources. *Ecology*. 2003;84(2):406-415.
- 20 Bogdziewicz M, Zwolak R, Crone E. How do vertebrates respond to mast seeding? *Oikos*. 2016;125:300-307.
- 21 Ostfeld R, Holt R. Are predators good for your health? Evaluating evidence for top-down regulation of zoonotic disease reservoirs. *Frontiers in Ecology and the Environment*. 2004;2(1):13-20.
- 22 Roth E, May P, Farrell T. Pigmy rattlesnakes use frog-derived chemical cues to select foraging sites. *Copeia*. 1999;3:772-774.
- 23 Kabay E. Timber rattlesnakes may reduce incidence of Lyme disease in the northeastern United States. Poster session. Minneapolis 2013.

24 Wolff J. Population fluctuations of mast-eating rodents are correlated with production of acorns. *Journal of Mammalogy*. 1996;77(3):850-856.

FYN-DEPENDENT PHOSPHORYLATION OF MITOCHONDRIAL ELONGATION FACTOR TU MAY LEAD TO METABOLIC SYNDROME BY MITOCHONDRIAL DYSFUNCTION

Caroline Hunter
Ph.D. Student, Biomedical Sciences
Marshall University
Huntington, WV 25755

ABSTRACT

Fyn kinase, a member of the non-receptor Src family tyrosine kinases, has been shown to play a significant role in a number of metabolic diseases. It has also been identified as a key regulator in mitochondrial fatty acid metabolism. In our preliminary studies, we demonstrated that Fyn kinase was associated with mitochondrial translation components including mitochondrial elongation factor Tu (mtEF-Tu) in bovine liver and found to be responsible for its Tyr phosphorylation *in vitro*. To investigate the role of Fyn kinase on mitochondrial translation and energy metabolism, two human liver cancer cell lines, Hep3B and HepG2, were grown at varying nutritional conditions. Interestingly, we observed a significantly reduced expression of Fyn kinase associated with decreased expression of oxidative phosphorylation (OXPHOS) complexes I, III, and IV in Hep3B cell lines. On the other hand, higher levels of Fyn kinase in HepG2 cells resulted in increased expression of OXPHOS complexes and complex IV enzymatic activity accompanied with increased mtEF-Tu and mtEF-Ts protein levels. In this study, we also investigated the roles of natural antioxidants kaempferol and resveratrol in the regulation of cell proliferation and mitochondrial energy metabolism at high and low glucose levels, mimicking high and low caloric intake, respectively. Increased mitochondrial activity and reduced cell proliferation were observed in both HepG2 and Hep3B cell lines in the presence of resveratrol and kaempferol. The results from our study demonstrate how Fyn kinase regulates mitochondrial energy metabolism in a translation-dependent manner and how this can be an important step in the remodeling of energy metabolism in metabolic dysfunctions that can lead to metabolic diseases such as cancer, obesity, and type 2 diabetes.

INTRODUCTION

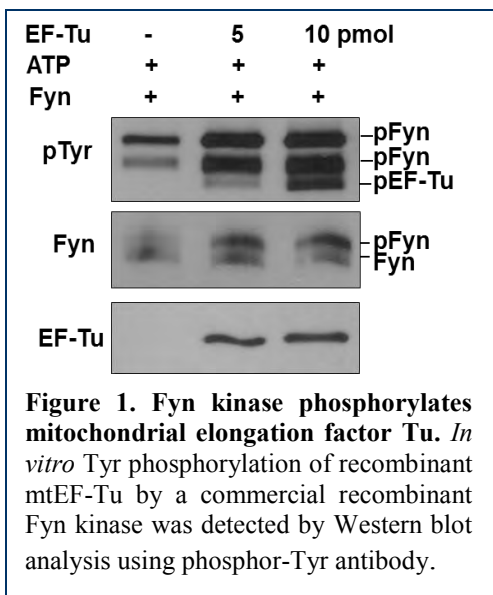
Mitochondria are one of the most complex, multifunctional organelles in the cell and play a central role in the regulation of cellular energy metabolism and apoptosis. Each of the metabolic pathways present in the mitochondria, such as fatty acid oxidation, tricarboxylic acid cycle, and the urea cycle all contribute to oxidative phosphorylation and energy production by providing key substrates for oxidative phosphorylation (OXPHOS) complexes. The high energy substrates NADH and FADH₂ produced during these catabolic pathways are shuttled to OXPHOS complexes and used to produce ATP.

In addition to housing the major metabolic pathways and OXPHOS complexes, mitochondria also contain their own circular genome and transcription and translation machineries. Mitochondrial translation machinery is responsible for the synthesis of 13 essential subunits of OXPHOS

complexes. Our laboratory has been involved in identification and studying post-translational modifications, such as phosphorylation and acetylation, of mitochondrial translation components [1-7]. Identification of specific phosphorylated Ser/Thr and Tyr residues in mitochondrial ribosomal proteins (MRPs) and mitochondrial elongation factor Tu (mtEF-Tu) by mass spectrometry (MS)-based proteomics allowed us to investigate their functional roles in the regulation of mitochondrial translation and OXPHOS [1, 8, 9]. In unpublished studies from our laboratory, we also identified the association of Fyn kinase with mitochondrial translation components including MRPs, mtEF-Tu, and mtEF-Ts and as a kinase responsible for the Tyr phosphorylation of mtEF-Tu. Mitochondrial mtEF-Tu is responsible for recruiting the aminoacyl-tRNA to the ribosome during the elongation cycle of protein synthesis [10]. Mitochondrial elongation factor Ts (mtEF-Ts) is a guanine nucleotide exchange factor that forms a complex with mtEF-Tu and releases it from the ribosome after GTP hydrolysis [11].

Fyn kinase, a non-receptor Src family tyrosine kinase, has been identified in the mitochondria and shown to play a significant role in many different cellular processes, including immune response, proliferation, and a major role in metabolism and insulin signaling, as well as a significant role in metabolic syndrome [12, 13]. Fyn kinase has been shown to be activated by oxidative stress, inhibits AMP-activated protein kinase (AMPK) and reduces fatty acid oxidation in the mitochondria [14-17]. LKB1 is tyrosine phosphorylated at Tyr residues 261 and 365 by Fyn kinase [18]. The phosphorylation at these residues inactivates LKB1 and prevents its exportation into the cytoplasm where it cannot phosphorylate AMPK and therefore inhibits the activity of AMPK [19]. In the absence of Fyn kinase, AMPK is activated by phosphorylation of LKB1 which leads to the activation of downstream pathways, such as fatty acid oxidation and mitochondrial biogenesis [12, 20, 21]. Along with the regulation of AMPK, Fyn kinase has also been shown to phosphorylate OXPHOS complex subunits at Tyr residues and stimulate OXPHOS [22, 23]. The AMPK pathway can act on the mitochondria by stimulating de novo mitochondrial biogenesis and/or triggering the destruction of dysfunctional mitochondria [24].

During AMPK activation, many substrates from fatty acid oxidation are being fed into the electron transport chain and producing ATP. Interestingly, as a byproduct of OXPHOS, reactive oxygen species (ROS) are produced through leakage from between complexes III and IV of the respiratory chain in the mitochondria [25]. An uncontrolled production of ROS can contribute to cell damage, mitochondrial dysfunction, or mitochondrial DNA damage which can lead to mutations in the mtDNA [26]. Therefore an overstimulation of OXPHOS by Fyn kinase can result in a high production of ROS and can lead to mitochondrial dysfunction. Mitochondrial dysfunction is often found associated with many metabolic disorders, including obesity, type 2 diabetes and cancer [27]. Intracellular ROS levels are found to be elevated in different metabolic disorders, including cancer. High ROS are a result of oxidative stress to the cells and can lead to cell damage and dysfunction and the progression of many diseases, including heart disease, cancer, type 2 diabetes, Parkinson's disease and Alzheimer's disease. An increase in the caloric intake also contributes to an overstimulation of OXPHOS and increase in ROS [28, 29]. In space, radiation is one of the major risk factors and continuous low levels of galactic cosmic radiation, made of high energy, high charged (HZE) particles, can cause a prolonged induction in oxidative stress [30-32]. The prolonged induction can lead to mitochondrial dysfunction and the development of a number of metabolic disorders.



Due to the potential increase in the exposure to radiation and long-term oxidative stress in space, we proposed to try to identify a regimen of antioxidants that will reduce oxidative stress and increase mitochondrial activity through Fyn kinase regulation of metabolic pathways and mitochondrial translation. Human hepatocellular carcinoma cell lines, HepG2 and Hep3B, were used as models for our treatments with antioxidants. Intracellular ROS levels are elevated in cancer cells. Hep3B and HepG2 cells were grown in the presence of high and low glucose concentrations and the changes in Fyn kinase, mitochondrial translation, and OXPHOS were observed by Western blot analyses. Cells were also treated with natural antioxidants, kaempferol and resveratrol, and changes in energy metabolism were observed by

measuring mitochondrial dehydrogenase activity with MTS assays, observing changes in mitochondrially-encoded OXPHOS complexes IV subunit COII by Western blot analyses, and determining the amount of reactive oxygen species produced during these treatments. The objective of the study was to determine how changes in Fyn kinase regulate mitochondrial translation by phosphorylation of mtEF-Tu and the role this plays in energy metabolism in the mitochondria and how mitochondrial dysfunction and the development of metabolic disorders can be prevented through the use of natural antioxidants and to uncover the role of Fyn kinase during antioxidant treatments.

PRELIMINARY STUDIES

Our laboratory has previously shown mitochondrial translation components are phosphorylated at Tyr and Ser/Thr residues which regulate mitochondrial protein synthesis [9]. While trying to identify kinases responsible for the phosphorylation of mitochondrial translation components, Fyn kinase and mtEF-Tu were identified in a kinase-enriched strong cation exchange (SCX) fraction of liver mitochondrial lysate by tandem mass spectrometry (Miller et. al. unpublished studies). We have shown the association of Fyn kinase with mtEF-Tu and other mitochondrial translation components and fatty acid oxidation enzymes (data not shown). Fyn kinase was identified with mtEF-Tu and was shown to be responsible for the phosphorylation of both endogenous and recombinant mtEF-Tu (data not shown). *In vitro* phosphorylation assays were performed with recombinant mtEF-Tu and commercially available recombinant Fyn kinase to confirm tyrosine phosphorylation of mtEF-Tu (Figure 1). These results demonstrate mtEF-Tu is phosphorylated at Tyr residues and is possibly one of the more prominent Fyn kinase substrates regulating mitochondrial translation. We also showed in the presence of Fyn kinase in HEK293 cells, Tyr phosphorylation of mtEF-Tu and expression of mitochondrially-encoded OXPHOS subunit of complex IV, COII, was increased, while the nuclear encoded subunits remained unchanged at steady-state levels (data not shown). Due to our preliminary studies, we propose that the stimulation of Fyn-dependent mitochondrial translation may increase mitochondrial dysfunction and the development of metabolic syndrome through the increased ROS generation, specifically in high caloric intake. Natural antioxidants, resveratrol and kaempferol, can alleviate the complications associated with Fyn-dependent activation of mtEF-Tu and ROS generation.

METHODS

Cell Culture and Viability

Human hepatocellular carcinoma cell lines, Hep3B and HepG2, were purchased from the American Type Culture Collection (ATCC). Cells were grown in Dulbecco's Modified Eagles Media (DMEM) (Corning) containing 4.5 g/L and 1g/L glucose supplemented with 10% fetal bovine serum (FBS) (Rocky Mount Biomedical) and 100ug/mL streptomycin and 100 U/mL penicillin (Corning). Cells were cultured in a humidified atmosphere at 37°C in the presence of 5% CO₂.

For antioxidant treatments, cells were seeded in a 60mm culture dish at 25x10⁴ cells in DMEM containing 0.2% fetal bovine serum and incubated for 16 hours. Cell culture media was replaced with fresh DMEM containing 10% fetal bovine serum and the antioxidants, resveratrol and kaempferol. Resveratrol (Calbiochem) 20-40 μM in DMSO and kaempferol (Calbiochem) 25-50 μM in DMSO were added to the cells and cultures were incubated for 48 h. Cells cultured in the presence of DMSO were used as controls. At 48 h, viable cells were calculated using Trypan blue exclusion test and collected for cell viability (MTS) assays, reactive oxygen species assays, and western blot analyses.

Transfections of Hep3B cells were performed by the addition of pRK5 plasmid carrying Fyn kinase in the presence of Mirus transfection reagent at 2:1 ratio in Opti-MEM reduced serum media. Transfected cells were then incubated for 48 h and were collected and used for western blot analyses.

Western Blot Analyses

Cells were harvested by collecting Hep3B and HepG2 treated cells. Whole-cell lysates were prepared by lysing harvested cells in lysis buffer containing 50 mM Tris-HCl (pH7.6), 150 mM NaCl, 1 mM EDTA, 1 mM EGTA, 1% NP40, 0.1% SDS, 1 mM PMSF, and proteinase and phosphatase inhibitor cocktails. The protein fraction was then collected by centrifugation at 13,000 rpm at 4°C. BCA assay (Pierce Inc.) was used to determine the protein concentration of the supernatant, with various amounts of bovine serum albumin (BSA) as standards. Protein samples were separated on a 10% SDS-PAGE and transferred to a nitrocellulose membrane (Bio-Rad). After blocking, the membranes were incubated in primary and the corresponding secondary antibodies. The protein immunoreactivity was detected by Amersham ECL Western Blotting Detection Kit (GE Healthcare).

MTS Assays

Hep3B and HepG2 cells were treated with antioxidants, resveratrol and kaempferol, for 48 h. Cells were then reseeded in triplicates (10x10³ cells/well) into 96-well plates and were incubated in DMEM media containing 10% FBS in the absence of the antioxidants for 4 h at 37°C with 5% CO₂. After the incubation, mitochondrial dehydrogenase activity was used as an index of cell viability and was measured using CellTiter96 Aqueous One Solution Cell Proliferation Assay (MTS) (Promega). The reaction mixture containing a tetrazolium compound was added to the cells and incubated for 2 h, per the manufacturer's instructions. The activity was measured by reading the absorbance at 490 nm.

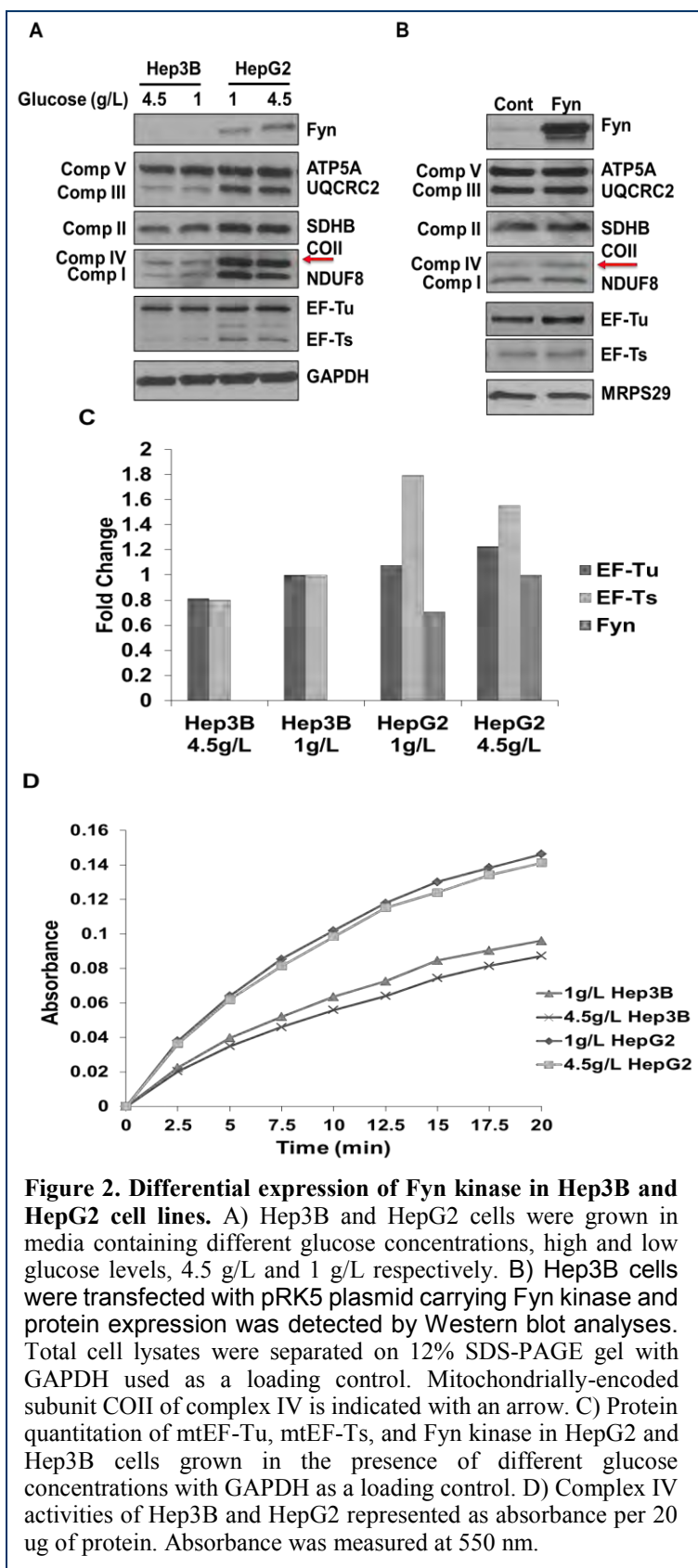
Reactive Oxygen Species (ROS) Assays

Similarly to MTS assays, Hep3B and HepG2 cells were grown in the presence of natural antioxidants, resveratrol and kaempferol, for 48 h. After the incubation with these antioxidants, 5×10^4 cells/well from each treatment were resuspended in Krebs-Ringer phosphate (KRPG) buffer (145mM NaCl, 5.7 mM sodium phosphate, 4.86 mM KCl, 0.54 mM CaCl₂, 1.22 mM MgSO₄, 5.5 mM glucose, pH 7.35) and seeded in triplicates in 96-well plate. Amplex Red reagent (Molecular Probes) was added to each of the cell suspensions and used to measure the amount of H₂O₂ released from treated Hep3B and HepG2 cells, with various amounts of H₂O₂ as standards. Cells were incubated in the dark for 4 h and the fluorescence was measured at an excitation of 545 nm and emission at 590 nm and an absorbance at 560 nm every 30 min, per the manufacturer's instructions.

RESULTS

Fyn kinase increases mitochondrial translation and activity in HepG2 cells.

Fyn kinase has been shown to play a role in the majority of cellular functions and processes throughout the cell cycle and has also been shown to play an important role in many pathways regulating energy metabolism. Our previous studies have identified the association of Fyn kinase with mitochondrial translation machinery and Fyn-dependent phosphorylation of mtEF-Tu. Hep3B and HepG2 cell lines were grown in the presence of different glucose concentrations, 4.5 g/L and 1 g/L to determine the role of Fyn-dependent phosphorylation of mtEF-Tu in the regulation of mitochondrial translation, OXPHOS and energy metabolism at different nutritional conditions. HepG2 cells expressed a high level of Fyn kinase, which was accompanied by an increase in nuclear and mitochondrially-encoded OXPHOS complexes I, III, and IV compared to Hep3B cells which have a significantly lower level of OXPHOS complexes I, III and IV and almost no expression of Fyn kinase in both 1 g/L and 4.5 g/L glucose. Mitochondrial translation is stimulated



in the presence of Fyn kinase in HepG2 cells. Accompanied by an increase in the expression of complex IV in HepG2 cells is an increase in complex IV enzymatic activity. In the presence of high and low glucose, Hep3B cells have approximately a 50% reduction in complex IV activity, which can be attributed to the absence of Fyn kinase and reduced mtEF-Tu phosphorylation by Fyn, resulting in reduced mitochondrial translation and complex IV expression and activity (Figure 2D). Since Hep3B cells have an absence of Fyn kinase and reduced mitochondrial translation and complex IV expression and activity, Fyn kinase was overexpressed in Hep3B cells. With the addition of plasmid containing Fyn kinase in Hep3B cells, mitochondrial translation was stimulated, as demonstrated by the increase in mitochondrially-encoded complex IV subunit, COII (Figure 2B). The increase in mitochondrial translation and the expression of COII subunit can be attributed to the increase in Fyn kinase and the stimulation of translation by Tyr phosphorylation of mtEF-Tu. The expression levels of Fyn and mtEF-Tu are correlated in both HepG2 and Hep3B cell lines and are associated with an increase in mitochondrial translation. Our initial hypothesis predicted Fyn-dependent stimulation of mtEF-Tu will increase mitochondrial translation and the expression of mitochondrially-encoded subunit of complex IV, COII. Fyn kinase may be regulating translation through the phosphorylation of mtEF-Tu; however, the expression levels of mtEF-Tu and mtEF-Ts were also increased in HepG2 cells by approximately 20% and 60%, respectively (Figure 2C). An increase in mtEF-Tu and mtEF-Ts is also observed when Fyn kinase was overexpressed in Hep3B cell lines

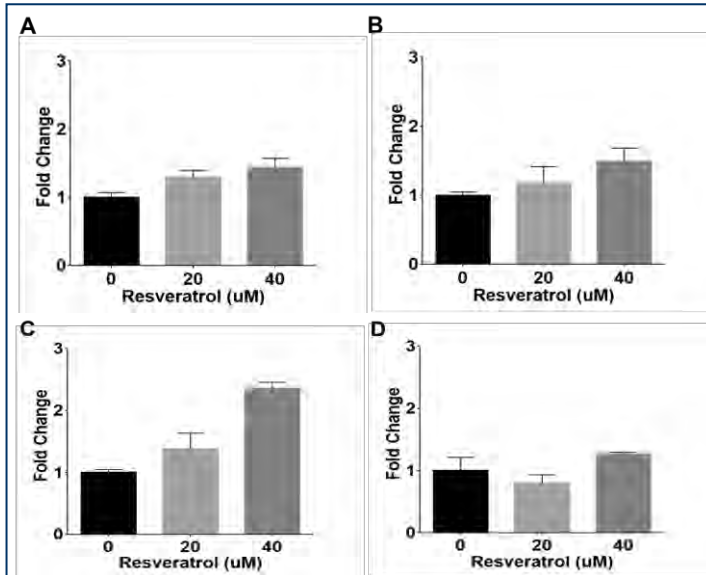


Figure 3. Resveratrol increases mitochondrial activity in Hep3B and HepG2 cells. A and B) HepG2 and Hep3B (C and D) cells were treated with resveratrol for 48 h under different media conditions, 4.5 g/L glucose (A and C) and 1 g/L glucose (B and D). Mitochondrial activity was measured with cell viability (MTS assay) by measuring the absorbance at 490 nm. Mean \pm SD of at least three experiments are shown. One-way ANOVA was used on treated samples for MTS assays to calculate p-value ($p < 0.05$).

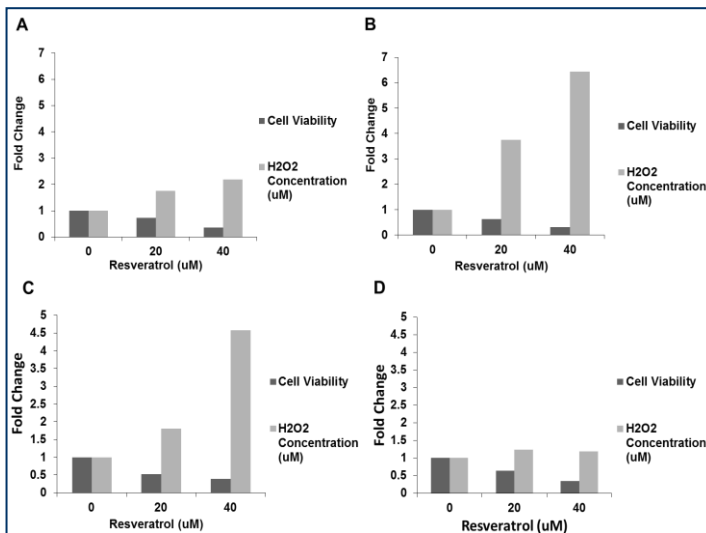


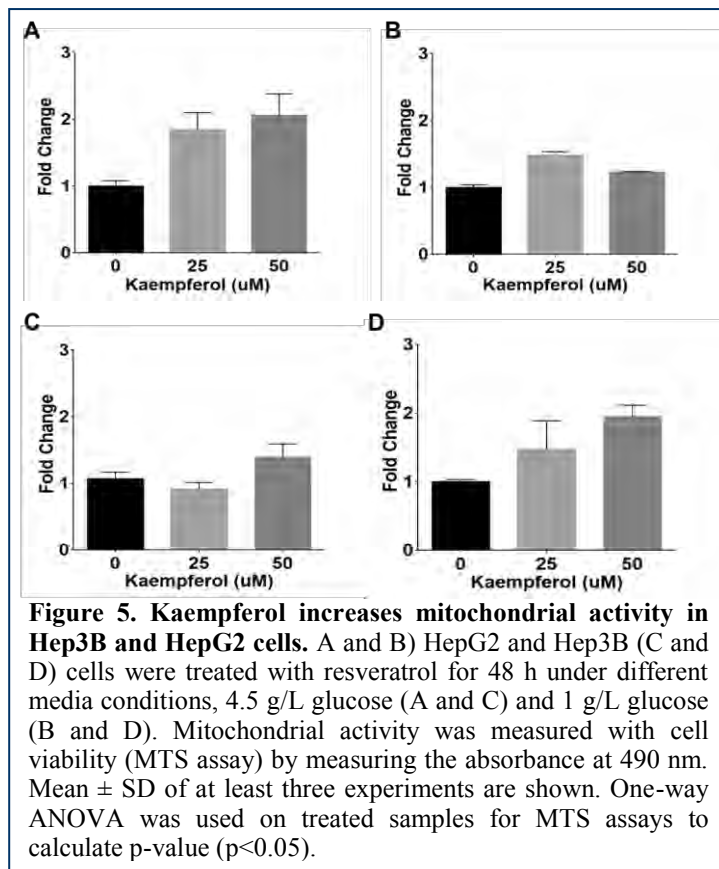
Figure 4. Cell proliferation decreases as ROS production increases in HepG2 and Hep3B cells in the presence of resveratrol. HepG2 cells (A and B) and Hep3B (C and D) cells were grown in the presence of 4.5 g/L (A and C) and 1 g/L (B and D) glucose containing DMEM. Cell viability was measured at the time of collection after 48 h treatment with antioxidants using Trypan blue exclusion test. ROS levels were measured using Amplex Red reagent to detect varying amounts of H₂O₂ produced in treated cells. Absorbance was read at 590 nm.

(Figure 2B). The increase in mitochondrial translation, shown by an increase in complex IV, COII subunit, is possibly due to a higher expression of mtEF-Tu and mtEF-Ts. The translation deficiency observed in Hep3B cells, demonstrated by decreased complex IV activity and COII expression, was a contribution to not only the absence of Fyn kinase but also the decreased expression levels of mtEF-Tu and mtEF-Ts. It is possible that Fyn kinase stimulates mitochondrial translation elongation by regulating phosphorylation of mtEF-Tu and/or mtEF-Ts. However, due to the changes in mtEF-Tu and mtEF-Ts expression levels in the presence and absence of Fyn kinase in HepG2 and Hep3B cells, respectively, we will test the Fyn-dependent phosphorylation of mtEF-Tu and/or mtEF-Ts in our future studies using an in vitro model system.

Antioxidant treatments of Hep3B and HepG2 increase mitochondrial activity

Mitochondrial dysfunction has been shown to be present in a number of metabolic disorders, including cancer. One of the contributing factors to mitochondrial dysfunction is the dysregulation of oxidative phosphorylation by the stimulation or inhibition of mitochondrial translation. In the presence of Fyn kinase, mitochondrial translation is increased, leading to an increase in the expression of COII. The overstimulation of OXPHOS by Fyn kinase can lead to a high development of intracellular ROS. Resveratrol has been shown to be an effective natural antioxidant that improves mitochondrial function by increasing MnSOD activity and causing resistance to mitochondrial dysfunction in the cells [33-35]. Along with resveratrol, kaempferol, also a natural antioxidant and Src kinase

inhibitor, has also been shown to increase mitochondrial complex II activity [36]. Each of these antioxidants has also been shown to activate AMPK and increase fatty acid oxidation and mitochondrial biogenesis. We predicted, based on these studies, that resveratrol and kaempferol will increase mitochondrial activity by regulating the expression of Fyn kinase on mitochondrial translation and mitochondrial energy metabolism. Hep3B and HepG2 cells were treated with resveratrol and kaempferol in the presence of high and low glucose for 48 h. Cells that were treated with resveratrol and kaempferol show an increase in cell viability and dehydrogenase activity, which were measured using MTS assay and were correlated to changes in mitochondrial activity. Resveratrol and kaempferol stimulated mitochondrial energy metabolism in Hep3B and HepG2 cells.



Upon measurement of the absorbance change in treated samples compared to the control, the MTS assay was significantly increased by approximately 50% in both Hep3B and HepG2 in the presence of high and low glucose and resveratrol and kaempferol (Figures 3 and 5). Resveratrol and kaempferol treatments in both Hep3B and HepG2 cells stimulate mitochondrial energy metabolism and mitochondrial activity. To determine the effects of resveratrol and kaempferol on Fyn kinase and mitochondrial translation, further experimentation needs to be performed. The expression levels of Fyn kinase and OXPHOS will be observed using Western blot analyses to determine if these antioxidants alter the activity of Fyn kinase, mtEF-Tu and/or mitochondrial translation.

Resveratrol and kaempferol decrease cell proliferation and increase ROS generation.

Resveratrol and kaempferol antioxidants reduce overall stress in cells by increasing the level of intracellular reactive oxygen species therefore activating ROS-dependent apoptosis and prohibiting the progression of metabolic disorders [37]. In the presence of resveratrol and kaempferol, in both high and low glucose, Hep3B and HepG2 cells have a significantly reduced cell proliferation rate (Figures 4 and 6). Cells treated with the highest concentration of resveratrol have almost a 70% reduction in the proliferation rate, while cells treated with kaempferol have almost a 60% reduction. The reduction in cell proliferation can be attributed to the high amount of reactive oxygen species produced during the treatments with resveratrol and kaempferol. Taken together, the results of treatments with resveratrol and kaempferol demonstrate a significant decrease in cell proliferation and an increase in mitochondrial activity and ROS generation.

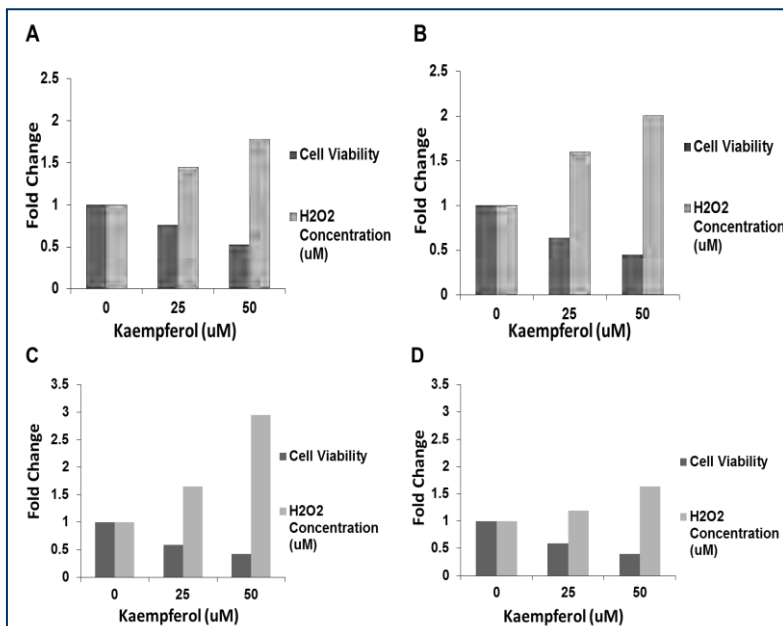


Figure 6. Cell proliferation decreases as ROS production increases in HepG2 and Hep3B cells in the presence of kaempferol. HepG2 cells (A and B) and Hep3B (C and D) cells were grown in the presence of 4.5 g/L (A and C) and 1 g/L (B and D) glucose containing DMEM. Cell viability was measured at the time of collection after 48 h treatment with antioxidants using Trypan blue exclusion test. ROS levels were measured using Amplex Red reagent to detect varying amounts of H₂O₂ produced in treated cells. Absorbance was read at 590 nm.

Resveratrol and kaempferol act to regulate mitochondrial energy metabolism by increasing the mitochondrial activity, decreasing cell proliferation, and increasing intracellular levels of ROS to induce ROS-dependent autophagy and apoptotic pathways. All of these results are in agreement with the natural antioxidants stimulating mitochondrial energy metabolism, resulting in cells overcoming metabolic dysfunction.

DISCUSSION

The findings of this study have provided evidence for the regulation of mitochondrial translation by Fyn kinase. Since mitochondrial translation is responsible for the production of

13 key subunits of OXPHOS complexes, alterations in mitochondrial translation can cause significant changes in mitochondrial energy metabolism. The reduction of nuclear and mitochondrially-encoded subunits of OXPHOS complexes I, III, and IV found in the absence of Fyn kinase demonstrate Fyn plays a role in the regulation of mitochondrial metabolism and activity and regulates mitochondrial translation (Figure 1). The presence of Fyn kinase in HepG2 cells and the overexpression of Fyn kinase in Hep3B cells increasing mitochondrial COII demonstrate Fyn kinase-dependent regulation of mitochondrial translation. In both cell lines, high levels of Fyn kinase are associated with increased expression of mtEF-Tu and mtEF-Ts, which contribute to the stimulation of mitochondrial translation and the increase in the expression and activity of OXPHOS complexes IV and I. In the presence of natural antioxidants, resveratrol and kaempferol, reduced cell proliferation and increased intracellular ROS levels were found, as well as an increase in mitochondrial activity. These results demonstrate the ability for resveratrol and kaempferol to regulate mitochondrial energy metabolism and overcome metabolic dysfunction (Figures 3-6).

Our results demonstrate in the presence of Fyn kinase, mitochondrial translation is increased, shown by increases in nuclear and mitochondrially-encoded OXPHOS complexes I, III, and IV. mtEF-Tu and mtEF-Ts levels were also found to be elevated in the presence of Fyn kinase, contributing to the stimulation of mitochondrial translation. We were unable to use Hep3B and HepG2 cells as a model for Fyn-dependent phosphorylation of mtEF-Tu and stimulation of mitochondrial translation and will develop an *in vitro* modeling system for future studies. Fyn kinase has also been shown to play a role in a number of metabolic pathways with the major

regulation in energy metabolism through the inhibition of AMPK pathway. In the presence of Fyn kinase, LKB1 is tyrosine phosphorylated, preventing the activation of AMPK and therefore inhibiting fatty acid oxidation [14, 18]. Our results from this study demonstrate changes in mitochondrial energy metabolism in HepG2 and Hep3B cells with natural antioxidants, resveratrol and kaempferol. However, we were unable to demonstrate the Fyn-dependent regulation of these treatments. Further studies will be performed to look at the change in Fyn kinase in the presence of resveratrol and kaempferol and how this contributes to changes in mitochondrial translation.

Resveratrol is a polyphenol commonly found in the skin of grapes and has been shown to have protective effects against cardiovascular disease, age-related deterioration, and cancer [38]. Resveratrol has many different uses including antifungal, anti-inflammatory, and anticancer effects, inhibits the growth of cancer cells through cell-cycle arrest and the induction of apoptosis [39-41]. It has been shown through the inhibition of PDE enzymes and several inhibitory steps to activate AMPK and increase mitochondrial activity [42, 43]. The activation of AMPK via resveratrol has been shown to improve mitochondrial function and protection against metabolic disease [35]. Activation of AMPK pathways leads to an increase in fatty acid oxidation and mitochondrial biogenesis and an inhibition in fatty acid synthesis and lipid synthesis in resveratrol treated cells [44, 45]. Resveratrol treatments have shown to increase protective effects in HepG2 cells through the activation of AMPK [45]. Our data is in agreement with previous studies demonstrating resveratrol treatments decrease cell proliferation and increase mitochondrial activity. The increase we observed in mitochondrial activity and reduction in cell proliferation from resveratrol treatments in HepG2 and Hep3B cells can possibly be attributed to a differential regulation of Fyn kinase expression and stimulation of fatty acid oxidation. During the treatment of HepG2 cells with resveratrol, Fyn kinase expression levels are likely to reduce which will cause an increase in the activity of AMPK, fatty acid oxidation and mitochondrial biogenesis and energy metabolism, shown by MTS assays. The results from this study with resveratrol treatment are in agreement with a reduction in cell proliferation and increase in mitochondrial activity and therefore energy metabolism; however, we were unable to show changes in Fyn kinase during these treatments at this time. Further studies need to be performed to confirm changes in Fyn kinase in resveratrol treatments.

Along with changes in energy metabolism in the presence of resveratrol, the level of intracellular reactive oxygen species increases. Resveratrol acts to induce cell death, apoptosis, in several different types of cancer by significantly increasing the intracellular ROS levels and therefore inducing autophagy and apoptosis [37]. Our ROS generation data is in agreement with resveratrol treatments of cancer cell lines. In the presence of resveratrol, cancer cells significantly increase the level of intracellular ROS to activate ROS-dependent apoptotic pathways. Our data collected from treatments of HepG2 and Hep3B cells are in agreement with previous studies. Associated with an increase in ROS and activation of ROS-dependent apoptotic pathways is a decrease in cell proliferation.

Kaempferol is a phytoestrogen molecule, belonging to the flavonoid family, and is a natural antioxidant commonly found in many different fruits and vegetables. Our laboratory has previously shown treatment with kaempferol, which is also an antidiabetic and Src kinase inhibitor, increases mitochondrial complex II activity [36, 46, 47]. Along with resveratrol, kaempferol has also been shown to activate AMPK and inhibit AKT and mTOR. The activation of AMPK contributes to the cells treated with kaempferol to become arrested in the G2/M phase of the cell

cycle and induction of autophagy which contribute to reduce cell proliferation [48]. The activation of AMPK by kaempferol demonstrates that the expression of Fyn kinase needs to be reduced in the cells. Kaempferol not only activates AMPK and fatty acid oxidation, which would ultimately activate OXPHOS and mitochondrial energy metabolism, but kaempferol has also been identified as a Src kinase inhibitor [46, 47]. c-Src and Fyn kinase, two mitochondrial non-receptor Src family tyrosine kinases, have been shown to have very similar structure and sequence [49]. Due to the similarity of the two structures, Fyn kinase could also be inhibited by kaempferol, which would decrease Fyn expression, activate AMPK and increase fatty acid oxidation and contribute to the increase in mitochondrial energy metabolism. Our data collected from kaempferol treatments of Hep3B and HepG2 cells are in agreement with studies showing how mitochondrial energy metabolism is increased in the presence of kaempferol. Similarly to resveratrol treatments, further studies need to be performed to observe any changes in Fyn kinase during kaempferol treatments that can contribute to changes in mitochondrial metabolism or mitochondrial translation.

Resveratrol and kaempferol treatments both activate AMPK, via slightly different pathways, and contribute to the activation of fatty acid oxidation and increase in mitochondrial activity, as we have confirmed in our results. Our results also confirm increases in mitochondrial energy metabolism shown in previous studies in the presence of resveratrol and kaempferol. It is possible the AMPK pathway in Hep3B cells can be more easily activated by resveratrol and kaempferol due to the significant reduction in Fyn kinase expression. In Hep3B and HepG2 cells, the presence of resveratrol and kaempferol activate AMPK and fatty acid oxidation and contribute to a higher mitochondrial activity with lower cell proliferation.

CONCLUSIONS

The data we have collected and presented has demonstrated that Fyn kinase is important player in the role of mitochondrial translation and energy metabolism. In the presence of Fyn kinase, we have shown increases in mtEF-Tu and mtEF-Ts which translates to a stimulation in mitochondrial translation, demonstrated by an increase in nuclear and mitochondrially-encoded subunits of OXPHOS complexes I, III, and IV and an increase in complex IV enzymatic activity. We have also demonstrated by treating cancer cells with natural antioxidants, resveratrol and kaempferol, cell proliferation was significantly reduced while mitochondrial activity was significantly increased. The treatment with antioxidants works to return the cancerous cells to a more normal metabolic state by altering mitochondrial energy metabolism and improving metabolic dysfunction. Future studies will include observing the effects of resveratrol and kaempferol on mitochondrial translation and oxidative phosphorylation, and confirming the role of Fyn-dependent phosphorylation of mtEF-Tu in mitochondrial translation.

PRESENTATION AND PUBLICATION OF FINDINGS

This work has been presented at Marshall University School of Medicine Health Sciences Research Day and WV NASA S.P.A.C.E. Day this spring and will also be presented at the United Mitochondrial Disease Foundation Mitochondrial Medicine Conference in June 2016. We are also anticipating the submission of a publication from the work presented in this report.

ACKNOWLEDGEMENTS

The graduate fellowship award given to be my WV Space Grant Consortium NASA is one of the main reasons this research was performed. By providing funding for the 2015-2016 year, I was able to complete work in my area of research that has contributed to my knowledge in uncovering how mitochondrial activity is altered in disease states and how this can possibly be prevented. Along with providing funding for my stipend, it made more funding available for our lab to be able to purchase what was needed for this project. Without the assistance from WVSGC NASA, it would have been more difficult to perform at the level I was able to, which I am grateful for. I would also like to acknowledge Marshall University School of Medicine for providing the other half of my stipend, as well as my research mentor, Dr. Emine Koc, who has provided me with tools that have made me a better student and scientist, whom without her guidance, I would not be where I am today.

REFERENCES

1. Miller, J.L., et al., *Phosphorylated proteins of the mammalian mitochondrial ribosome: implications in protein synthesis*. J Proteome Res, 2009. **8**(10): p. 4789-98.
2. Yang, Y., et al., *NAD⁺-dependent deacetylase SIRT3 regulates mitochondrial protein synthesis by deacetylation of the ribosomal protein MRPL10*. J Biol Chem, 2010. **285**(10): p. 7417-29.
3. Koc, E.C., Haque, M.E., and Spremulli, L.L. , *Current views of the structure of the mammalian mitochondrial ribosome*. Israel Journal of Chemistry, 2010. **50**(1): p. 45-59.
4. Koc, E.C., et al., *A proteomics approach to the identification of mammalian mitochondrial small subunit ribosomal proteins*. J Biol Chem, 2000. **275**: p. 32585-32591.
5. Koc, E.C., et al., *The small subunit of the mammalian mitochondrial ribosome: Identification of the full complement of ribosomal proteins present*. J Biol Chem, 2001. **276**: p. 19363-19374.
6. Koc, E.C., et al., *Identification and characterization of CHCHD1, AURKAIP1, and CRIF1 as new members of the mammalian mitochondrial ribosome*. Front Physiol, 2013. **4**: p. 183.
7. Koc, E.C., et al., *A new face on apoptosis: Death-associated protein 3 and PDCD9 are mitochondrial ribosomal proteins*. FEBS Lett, 2001. **492**: p. 166-170.
8. He, H., et al., *Phosphorylation of mitochondrial elongation factor Tu in ischemic myocardium: basis for chloramphenicol-mediated cardioprotection*. Circ Res, 2001. **89**(5): p. 461-7.
9. Miller, J.L., H. Koc, and E.C. Koc, *Identification of phosphorylation sites in mammalian mitochondrial ribosomal protein DAP3*. Protein Sci, 2008. **17**(2): p. 251-60.
10. Hunter, S.E. and L.L. Spremulli, *Mutagenesis of glutamine 290 in Escherichia coli and mitochondrial elongation factor Tu affects interactions with mitochondrial aminoacyl-tRNAs and GTPase activity*. Biochemistry, 2004. **43**(22): p. 6917-27.

11. Jeppesen, M.G., et al., *Crystal structure of the bovine mitochondrial elongation factor Tu.Ts complex*. J Biol Chem, 2005. **280**(6): p. 5071-81.
12. Koo, J.H., et al., *Fyn inhibition by cycloalkane-fused 1,2-dithiole-3-thiones enhances antioxidant capacity and protects mitochondria from oxidative injury*. Mol Pharmacol, 2012. **82**(1): p. 27-36.
13. Saito, Y.D., et al., *Fyn: a novel molecular target in cancer*. Cancer, 2010. **116**(7): p. 1629-37.
14. Bastie, C.C., et al., *Integrative metabolic regulation of peripheral tissue fatty acid oxidation by the SRC kinase family member Fyn*. Cell Metab, 2007. **5**(5): p. 371-81.
15. Lee, T.W., et al., *Fyn deficiency promotes a preferential increase in subcutaneous adipose tissue mass and decreased visceral adipose tissue inflammation*. Diabetes, 2013. **62**(5): p. 1537-46.
16. Yamada, E. and C.C. Bastie, *Disruption of Fyn SH3 domain interaction with a proline-rich motif in liver kinase B1 results in activation of AMP-activated protein kinase*. PLoS One, 2014. **9**(2): p. e89604.
17. Yang, H.B., et al., *cAMP-dependent protein kinase activated Fyn in spinal dorsal horn to regulate NMDA receptor function during inflammatory pain*. J Neurochem, 2011. **116**(1): p. 93-104.
18. Yoder, S.M., et al., *YES, a Src Family Kinase, Is a Proximal Glucose-specific Activator of Cell Division Cycle Control Protein 42 (Cdc42) in Pancreatic Islet beta Cells*. J Biol Chem, 2014. **289**(16): p. 11476-87.
19. Yamada, E., et al., *Fyn-dependent regulation of energy expenditure and body weight is mediated by tyrosine phosphorylation of LKB1*. Cell Metab, 2010. **11**(2): p. 113-24.
20. Steinberg, G.R. and B.E. Kemp, *AMPK in Health and Disease*. Physiol Rev, 2009. **89**(3): p. 1025-78.
21. Jorgensen, S.B., et al., *Effects of alpha-AMPK knockout on exercise-induced gene activation in mouse skeletal muscle*. FASEB J, 2005. **19**(9): p. 1146-8.
22. Kowalczyk, J.E. and B. Zablocka, *[Protein kinases in mitochondria]*. Postepy Biochem, 2008. **54**(2): p. 209-16.
23. Ogura, M., et al., *Mitochondrial c-Src regulates cell survival through phosphorylation of respiratory chain components*. Biochem J, 2012. **447**(2): p. 281-9.
24. Austin, S. and J. St-Pierre, *PGC1alpha and mitochondrial metabolism--emerging concepts and relevance in ageing and neurodegenerative disorders*. J Cell Sci, 2012. **125**(Pt 21): p. 4963-71.

25. Rolo, A.P. and C.M. Palmeira, *Diabetes and mitochondrial function: role of hyperglycemia and oxidative stress*. Toxicol Appl Pharmacol, 2006. **212**(2): p. 167-78.
26. Rocha, M., et al., *Perspectives and potential applications of mitochondria-targeted antioxidants in cardiometabolic diseases and type 2 diabetes*. Med Res Rev, 2014. **34**(1): p. 160-89.
27. Vernochet, C. and C.R. Kahn, *Mitochondria, obesity and aging*. Aging (Albany NY), 2012. **4**(12): p. 859-60.
28. Johannsen, D.L. and E. Ravussin, *The role of mitochondria in health and disease*. Curr Opin Pharmacol, 2009. **9**(6): p. 780-6.
29. Yu, L., et al., *Dietary fat, fatty acid saturation and mitochondrial bioenergetics*. J Bioenerg Biomembr, 2014. **46**(1): p. 33-44.
30. Cherry, J.D., et al., *Galactic cosmic radiation leads to cognitive impairment and increased abeta plaque accumulation in a mouse model of Alzheimer's disease*. PLoS One, 2012. **7**(12): p. e53275.
31. Datta, K., et al., *Exposure to heavy ion radiation induces persistent oxidative stress in mouse intestine*. PLoS One, 2012. **7**(8): p. e42224.
32. Schoenfeld, M.P., et al., *A hypothesis on biological protection from space radiation through the use of new therapeutic gases as medical counter measures*. Med Gas Res, 2012. **2**: p. 8.
33. Baur, J.A., et al., *Resveratrol improves health and survival of mice on a high-calorie diet*. Nature, 2006. **444**(7117): p. 337-42.
34. Haohao, Z., et al., *Resveratrol improves high-fat diet induced insulin resistance by rebalancing subsarcolemmal mitochondrial oxidation and antioxidantion*. J Physiol Biochem, 2015. **71**(1): p. 121-31.
35. Lagouge, M., et al., *Resveratrol improves mitochondrial function and protects against metabolic disease by activating SIRT1 and PGC-1alpha*. Cell, 2006. **127**(6): p. 1109-22.
36. Cimen, H., et al., *Regulation of succinate dehydrogenase activity by SIRT3 in mammalian mitochondria*. Biochemistry, 2010. **49**(2): p. 304-11.
37. Miki, H., et al., *Resveratrol induces apoptosis via ROS-triggered autophagy in human colon cancer cells*. Int J Oncol, 2012. **40**(4): p. 1020-8.
38. Baur, J.A., *Resveratrol, sirtuins, and the promise of a DR mimetic*. Mech Ageing Dev, 2010. **131**(4): p. 261-9.
39. Jang, M., et al., *Cancer chemopreventive activity of resveratrol, a natural product derived from grapes*. Science, 1997. **275**(5297): p. 218-20.

40. Liao, P.C., et al., *Resveratrol arrests cell cycle and induces apoptosis in human hepatocellular carcinoma Huh-7 cells*. J Med Food, 2010. **13**(6): p. 1415-23.
41. Nakagawa, H., et al., *Resveratrol inhibits human breast cancer cell growth and may mitigate the effect of linoleic acid, a potent breast cancer cell stimulator*. J Cancer Res Clin Oncol, 2001. **127**(4): p. 258-64.
42. Park, S.J., et al., *Resveratrol ameliorates aging-related metabolic phenotypes by inhibiting cAMP phosphodiesterases*. Cell, 2012. **148**(3): p. 421-33.
43. Um, H.J., et al., *Differential effects of resveratrol and novel resveratrol derivative, HS-1793, on endoplasmic reticulum stress-mediated apoptosis and Akt inactivation*. Int J Oncol, 2010. **36**(4): p. 1007-13.
44. Gnoni, G.V. and G. Paglialonga, *Resveratrol inhibits fatty acid and triacylglycerol synthesis in rat hepatocytes*. Eur J Clin Invest, 2009. **39**(3): p. 211-8.
45. Tang, L.Y., et al., *Resveratrol ameliorates lipid accumulation in HepG2 cells, associated with down-regulation of lipin1 expression*. Can J Physiol Pharmacol, 2015: p. 1-5.
46. Chen, A.Y. and Y.C. Chen, *A review of the dietary flavonoid, kaempferol on human health and cancer chemoprevention*. Food Chem, 2013. **138**(4): p. 2099-107.
47. Lee, K.M., et al., *Kaempferol inhibits UVB-induced COX-2 expression by suppressing Src kinase activity*. Biochem Pharmacol, 2010. **80**(12): p. 2042-9.
48. Huang, W.W., et al., *Kaempferol induces autophagy through AMPK and AKT signaling molecules and causes G2/M arrest via downregulation of CDK1/cyclin B in SK-HEP-1 human hepatic cancer cells*. Int J Oncol, 2013. **42**(6): p. 2069-77.
49. Superti-Furga, G., *Regulation of the Src protein tyrosine kinase*. FEBS Lett, 1995. **369**(1): p. 62-6.

TENOFOVIR INDUCED NEPHROTOXICITY: A MECHANISTIC STUDY

Rachel Murphy
Ph.D. Candidate, Biomedical Sciences
Marshall University
Huntington, WV 25755

ABSTRACT

Tenofovir disproxil fumarate (Viread) is a drug that is FDA approved to treat HIV and chronic Hepatitis B. It is effective in both novel and treatment experienced patients, and only requires once a day dosing. It is administered orally as tenofovir disproxil fumarate deesterified in the intestine to the active drug tenofovir. However, renal impairment is associated with its use; tenofovir can induce decreased glomerular filtration rate (GFR), renal failure, and Fanconi Syndrome. The exact mechanism of toxicity currently remains unknown, largely due to limited experimental models. Our laboratory has established that clinically relevant concentrations of tenofovir are toxic within 24h. The purpose of this specific study was to investigate the mechanism of cytotoxicity in an immortalized human proximal tubule cell line (HK-2). Tenofovir is the active form of Viread and was used for all studies. HK-2 cells were grown to confluency for 48h and then exposed to 0-1.15uM tenofovir for 24, 48, or 72h. The vehicle used for all studies was phosphate buffered saline (PBS). Tenofovir induces a loss of cell viability compared to the control within 24h as shown by an MTT assay. 72h exposure to tenofovir drastically reduces cellular ATP levels. Oxidative stress was assessed using OxyBlot and western blot probing for 4-HNE, and showed an increase in protein carbonylation and 4-HNE adduct formation at 48-72h exposure to 0.19-1.15uM tenofovir. Caspase 3 and 9 cleavage was induced by tenofovir compared to the vehicle, measured by western blot. These studies suggest that mitochondrial stress and apoptosis occur in HK-2 cells treated with tenofovir. Knowledge of subcellular events associated with tenofovir nephrotoxicity can be used to develop clinical methods to mitigate toxicity.

INTRODUCTION

Tenofovir disproxil fumarate is a nucleotide reverse transcriptase inhibitor that is approved in the United States to treat Human Immunodeficiency virus (HIV) and chronic Hepatitis B. It is considered a first line agent essential for the treatment of HIV by the World Health Organization (WHO Model list, 2015). The purpose of this study was to investigate the mechanism of tenofovir induced cytotoxicity in an immortalized human epithelial cell line (HK-2). The overall purpose can be divided into two specific aims: evaluation of oxidative stress in HK-2 cells following tenofovir exposure, and investigation into apoptosis induction in HK-2 cells following tenofovir exposure.

Evaluation of oxidative stress was done via OxyBlot and 4-hydroxy-2-nonenol (4-HNE) adduct formation. OxyBlot is a method kit established by Millipore that evaluates protein carbonylation as a result of exposure to reactive oxygen and nitrogen species (ROS, RNS). 4-HNE adduct formation on proteins is a common result of exposure to ROS, and thus can also be used to evaluate oxidative stress. Investigation of apoptosis was done using assessment of mitochondrial damage and activation of appropriate caspases. When mitochondria are damaged, it can be reasonably

assumed that production of energy becomes impaired. This hypothesis was evaluated using an ADP/ATP Ratio Assay Kit from Biovision. Apoptosis can be induced via many different pathways, and there are markers that denote each. Apoptosis induction was evaluated using western blotting with appropriate antibodies from Santa Cruz for caspase 3 and caspase 9, two proteins that are activated when apoptosis is induced via mitochondrial damage. All blots were exposed on a Chemi-Doc (BioRad) and appropriate densitometry was performed using Image Lab software (BioRad).

In order to perform these tests, cells were first exposed to various concentrations of tenofovir for varying time periods. HK-2 cells were plated the concentration 750,000 cells/mL and allowed to grow to confluency for 48h. Cells were then exposed to 0, 0.06, 0.12, 0.19, 0.58, or 1.15uM tenofovir dissolved in phosphate buffered saline (PBS) as a vehicle. Cells were exposed to these treatments for 24, 48, or 72h. At the end of the treatment period, cells were collecting using Trypsin (Gibco Life Technologies) and lysed with Cell Lysis Buffer (Santa Cruz). At this point total protein content was assessed and the appropriate experiments were run as stated above.

All experiments were analyzed using SigmaStat software. A one-way ANOVA was run on each experiment, followed by a Holm Sidak or Tukey post hoc test as appropriate. Statistical significance was set to a threshold of $\alpha < 0.05$ and all data is presented as mean \pm SEM (standard error of the mean). Additional detail regarding procedures and experiments can be found in the “Methods” section below.

This study showed that exposure to tenofovir reduces cell viability within 24h and drastically reduces ATP levels at 72h. OxyBlot and 4-HNE analysis showed an increase in protein carbonylation and 4-HNE adduct formation at 48-72h exposure to 0.19-1.15uM tenofovir. Caspase 3 and 9 cleavage was induced by tenofovir compared to the vehicle, measured by western blot. These results suggest that mitochondrial stress and apoptosis occur in HK-2 cells treated with tenofovir. Additional research based on this data can lead to a method to clinically mitigate or prevent tenofovir induced nephrotoxicity.

BACKGROUND AND SIGNIFICANCE

Tenofovir disproxil fumarate (TDF) is an antiretroviral drug that is FDA-approved to treat Human Immunodeficiency Virus (HIV) and chronic Hepatitis B. It is the only antiretroviral currently on the market that is a *nucleotide analogue* reverse transcriptase inhibitor. This means that tenofovir is an ATP analogue (Fig. 1). It is one of the first line drugs used to treat HIV as it is efficacious in both new and treatment-experienced patients; this is particularly beneficial for patients who may have become resistant to other medication options (Dore *et al*, 2004; Miller *et al*, 2007). Tenofovir also provides once a day dosing with relatively low day to day side effects compared to other antiretrovirals (Barditch-Crovo *et al*, 2001). Tenofovir has low oral bioavailability due to its highly polar structure (see Figure 1) and is therefore administered as the oral prodrug tenofovir disproxil fumarate (Van Gelder *et al*, 2000).

The main adverse effect associated with the use of tenofovir is renal damage. Tenofovir can reduce glomerular filtration rate (GFR) and increased serum creatinine, or more severely, can cause renal failure and Fanconi Syndrome (Hall *et al*, 2011, Del Palacio *et al*, 2012). Fanconi Syndrome is defined by damage to the proximal tubule cells of the kidney resulting in excess excretion of glucose, protein, urea, and phosphate. This excessive loss of nutrients and key molecules is due

to loss of normal proximal tubular reabsorption. Tenofovir is normally taken up into the proximal tubules by organic anion transporter 1 and 3 (OAT1, OAT3) (Kohler *et al*, 2011; Uwai *et al*, 2007) and is secreted into the tubular lumen by multidrug resistance protein 2 and 4 (MRP2, MRP4) (Kohler *et al*, 2011; Izzedine *et al*, 2006).

Figure 1

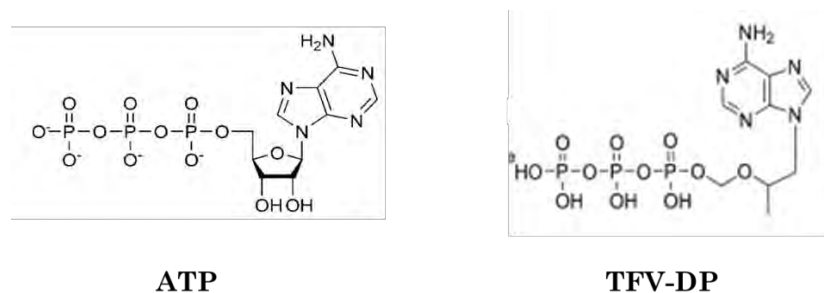


Fig. 1: Molecular structure of nucleotide adenosine triphosphate (ATP) and nucleotide analogue tenofovir diphosphate (TFV-DP)

The mechanism of tenofovir nephrotoxicity is not currently known. Mechanistic studies have been hampered up to this point, largely due to limited experimental models. Current published studies have used *in vivo* rodent treatment for 3 to 8 weeks (Ramamoorthy *et al*, 2014, Lebrecht *et al*, 2009) or primary renal cells exposed for up to 22 days (Vidal *et al*, 2006). The long duration of these experiments is not ideal and can hamper mechanistic studies. Additionally, daily oral gavage of rats for extended periods can cause significant stress, leading to other study problems. Cell lines can circumvent these issues and eliminate extrarenal factors and hemodynamics. For these reasons, we used a human renal proximal tubule cell line (HK-2 cells) to study the mechanism of tenofovir associated cytotoxicity. This cell line specifically allowed investigation of the subcellular events that occur following tenofovir exposure. Not only can these studies close the severe information gap regarding the mechanism of tenofovir nephrotoxicity, they can also lead to a clinical intervention to mitigate or prevent it.

METHODS

HK-2 Cell Model

Normal human epithelial renal cells (HK-2 cell) were used in all studies. HK-2 cells are an immortalized noncancerous human cell line that maintains activity and biochemical properties similar to *in vivo* proximal tubule cells (Gunnness *et al*, 2010, Paolicchi *et al*, 2003). Use of this cell line allowed for a comprehensive mechanistic study that eliminated species differences and extrarenal interactions, hemodynamic or inflammatory factors that would be found in an *in vivo* system. Additionally, this cell line retains OAT1 and OAT3 transporters (Kohler *et al*, 2011; Uwai *et al*, 2007). HK-2 cells were purchased from the American Type Culture Collection (ATCC); they were cultured according to ATCC guidelines in a keratinocyte-free medium with 50ug/mL bovine pituitary extract (BPE) and 5ng/mL recombinant epithelial growth factor (EGF) from Invitrogen (Carlsbad, CA).

Tenofovir Treatment

HK-2 cells were plated into six-well tissue culture plates at a concentration of 750,000 cells/mL (Corning, Sigma Aldrich) and allowed to grow for 48h in a warm humidified incubator with constant settings of 37°C and 5% CO₂. Cells were then treated with 0, 1.5, 3, 5, 15, or 30 μM tenofovir (Cayman Chemicals) for a final concentration of 0, 0.06, 0.12, 0.19, 0.58, or 1.15 μM tenofovir respectively. Cells were treated for 24, 48, or 72h in all experiments. The vehicle was phosphate buffered saline and was used for all studies (Invitrogen).

The peak tenofovir plasma concentration of tenofovir is 3 μM and the steady state concentration is 1.2 μM (Barditch-Crovo *et al.*, 2001). Therefore, the concentrations of tenofovir used in all studies were clinically relevant. Tenofovir concentrations in the kidney may be higher than plasma levels due to active transport in the proximal tubules. All treatments had an n=3 group and were repeated 3 times for a total n=9/group. Following the treatment period, cells were trypsinized (Invitrogen) and collected via centrifugation (1000rcf/10min at 4°C). Samples were then analyzed using western blot, and mitochondrial function assays (see below).

Cell Viability

Parallel cell viability assays were performed for every experiment to ensure treatment success. Cells were plated into 48-well tissue culture plates (Cyto One, USA Scientific) and allowed to grow for 48h in a warm humidified incubator with constant settings of 37°C and 5% CO₂. Cells were then treated with 0, 1.5, 3, 5, 15, or 30 μM tenofovir (Cayman Chemicals) for a final concentration of 0, 0.06, 0.12, 0.19, 0.58, or 1.15 μM tenofovir respectively. Cells were treated for 24, 48, or 72h in all experiments. The vehicle was phosphate buffered saline and was used for all studies (Invitrogen). All treatments had an n=3 group and were repeated 3 times for a total n=9/group. After treatment, cell viability was assessed using the MTT Assay. The MTT assay relies on the conversion of tetrazolium dye 3-(4, 5-dimethylthiazol-2-yl)-2,5-diphenyltetrazolium bromide (MTT) to formazan by NAD(P)H-dependent oxidoreductases (Humhrey *et al.*, 2005). 50 μL of MTT at a concentration of 5 mg/mL was added to cells; cells were then incubated for four hours. At the end of the incubation period, 100 μL of DMSO was added to dissolve the formazan granules and plates were read at 570nm.

ADP/ATP Ratio Assay

Cell lysates were assessed for ATP and ADP levels using a kit from Biovision. 100 μL of lysate was added to an opaque 96-well plate (Corning, Sigma Aldrich) and appropriate reaction mixture was added per the kit protocol. This assay relies on the conversion of d-Luciferin by firefly luciferase to oxyluciferin, releasing light that can be measured at 560nm. ATP and ADP concentration was assessed using a concentration curve of known standards.

OxyBlot and Western Blot

Cell lysates were run on a 12.5 or 15% polyacrylamide gel at concentrations of 25-40 μg protein/well at 55V for 18h. Gels were then transferred to a nitrocellulose membrane at 99V for 90min. Memcode staining (Thermo Scientific) was done to ensure transfer success and consistent loading concentration. OxyBlot primary antibodies bind to carbonylated proteins, a process that occurs when there is excessive ROS in the cell. Appropriate antibodies for OxyBlot and 4-HNE (Millipore, CellBio Labs) were diluted in 1% BSA in PBST and appropriate antibodies for caspase 3 and caspase 9 were diluted in 5% dry milk in TBST. Appropriate secondaries were used and all blots were analyzed using enhanced chemiluminescence from

Amersham™ ECL™ Western Blotting Detection Kit (GE Healthcare, Buckinghamshire, UK) on a Chemi-Doc (BioRad). Densitometry was performed for each blot and is presented as intensity as a percent of control.

Statistical Analysis

All experiments were analyzed using SigmaStat software. A one-way ANOVA was run on each experiment, followed by a Holm Sidak or Tukey post hoc test as appropriate. Statistical significance was set to a threshold of $\alpha < 0.05$ and all data is presented as mean \pm SEM (standard error of the mean).

RESULTS

Cell viability following tenofovir exposure

To determine cell viability, absorbance values were normalized to control with control groups set to 100%. Cell viability is expressed as percent of control as mean \pm SEM with $N > 6$. Cell viability was reduced at 0.06, 0.12, 0.19, 0.58, and 1.15 μ M tenofovir at 48 and 72h exposure, and was reduced at 0.12, 0.19, 0.58, and 1.15 μ M tenofovir at 24h exposure (Fig. 2). Based on this data, all treatment concentrations were used for the remainder of the experiments.

Figure 2

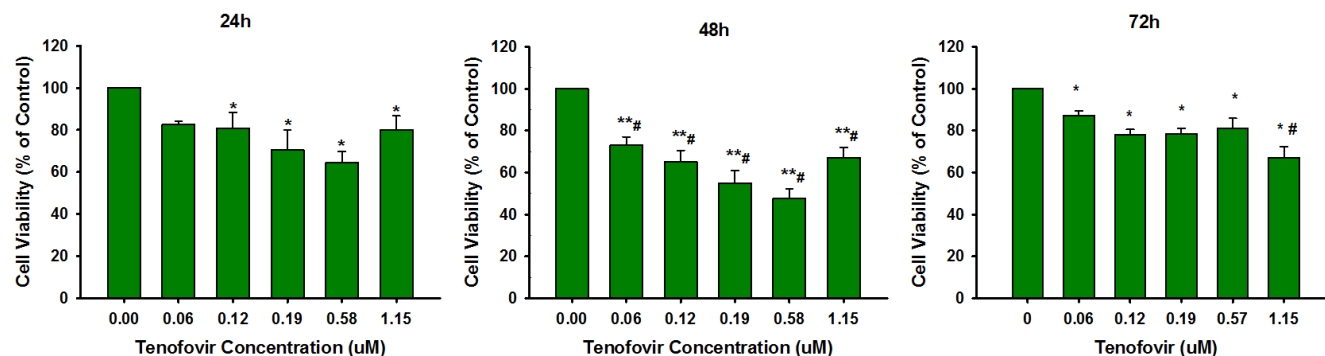
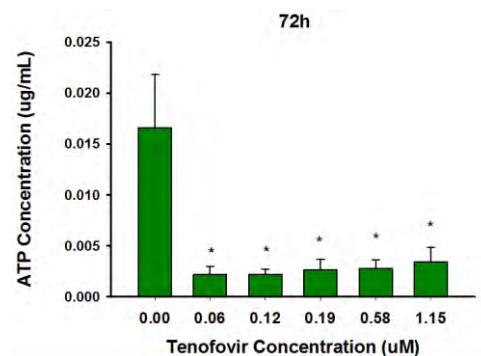


Fig. 2 Tenofovir is toxic to HK-2 cells. Cell viability following tenofovir exposure as measured by the MTT assay. All treatments are statistically significant (* $p < 0.05$, ** $p < 0.001$) relative to control and certain treatments are different between groups (#)

ATP concentration following tenofovir exposure

An ATP/ADP ratio assay (Biovision) was run to assess ATP concentration within cells following tenofovir treatment. ATP concentration is expressed in μ g/mL as mean \pm SEM with $N > 6$. ATP concentration was reduced at 0.06, 0.12, 0.19, 0.58, and 1.15 μ M tenofovir at 72h exposure (Fig. 3).

Figure 3



Oxidative stress following tenofovir exposure

To evaluate oxidative stress after tenofovir exposure, OxyBlot analysis (Millipore) and 4-HNE adduct formation (CellBio Labs) were performed. Protein carbonylation was increased at 0.19, 0.58, and 1.15uM tenofovir at 72h exposure and at 1.15uM tenofovir after 48h exposure (Fig. 4). 4-HNE adduct formation was increased at 0.58 and 1.15uM tenofovir after 72h exposure, but was not increased at 48h exposure (Fig. 4). Densitometry is presented as Intensity Percent of control as mean \pm SEM with $N > 6$.

Fig. 3 ATP concentration is reduced following tenofovir exposure. ATP concentrations following 72h tenofovir exposure. All treatments are significant ($*p < 0.05$) relative to control.

Figure 4

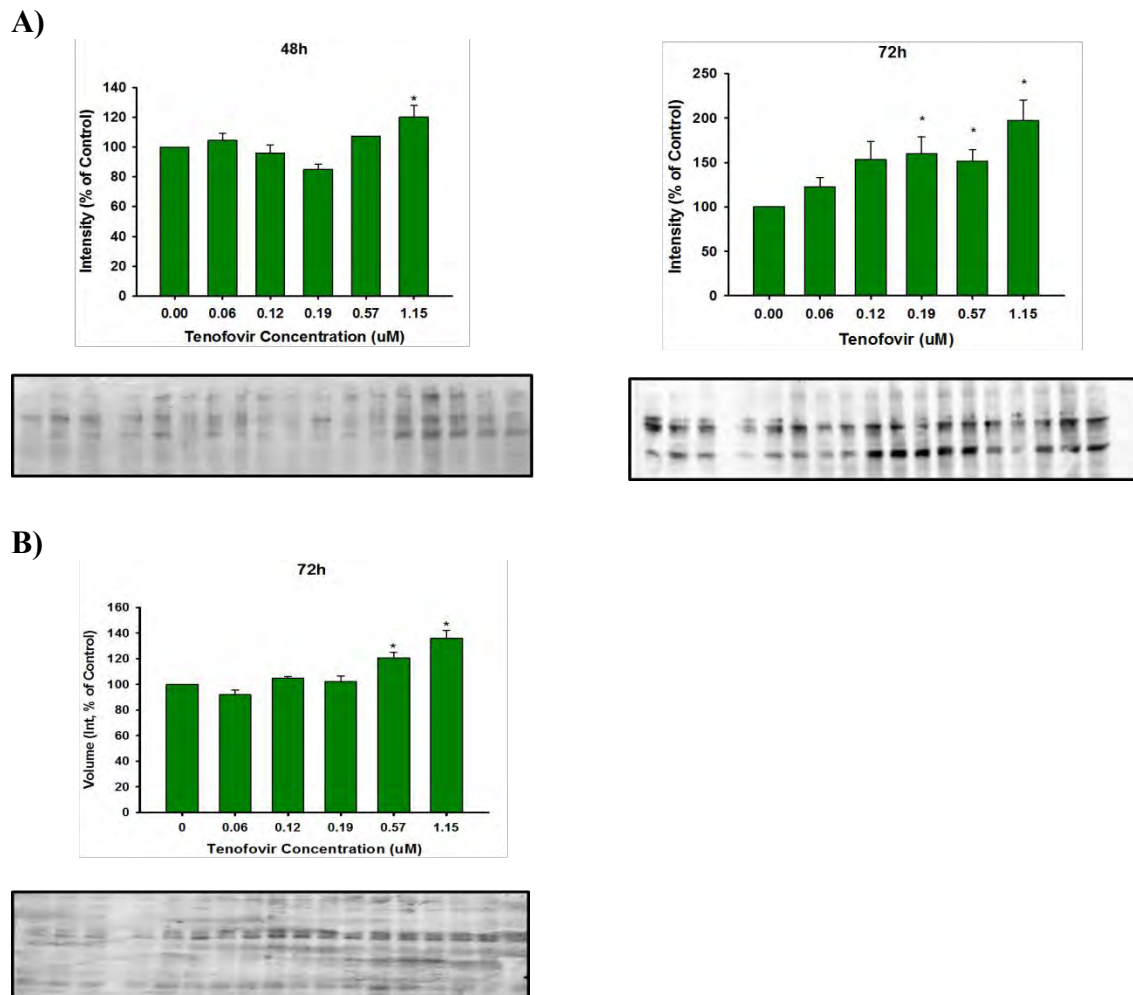


Fig. 4 Protein carbonylation and 4-HNE adduct formation are increased following tenofovir exposure. A) Protein carbonylation following 24-48h tenofovir. Blots are $n=3$ in concentrations 0, 0.06, 0.12, 0.19, 0.57, 1.15uM tenofovir from left to right. Protein carbonylation is increased ($*p < 0.05$) at 1.15uM TFV at 48h and at 0.19, 0.57, and 1.15uM TFV at 72h. B) 4-HNE adduct formation following 72h tenofovir exposure. The blot is $n=3$ in concentrations 0, 0.06, 0.12, 0.19, 0.57, 1.15uM tenofovir from left to right. 4-HNE adduct formation was increased ($*p < 0.05$) at 0.57 and 1.15uM tenofovir at 72h exposure.

Caspase 3 and 9 cleavage following tenofovir exposure

To determine by which mechanism apoptosis was induced, western blot with appropriate antibodies for caspase 3 and caspase 9 were performed on cell lysates. There was an increase in caspase 3 and caspase 9 cleavage for 0.06, 0.12, 0.19, 0.58, and 1.15 μ M tenofovir at 72h exposure (Fig. 5). Densitometry is presented as intensity percent of control with mean \pm SEM.

Figure 5

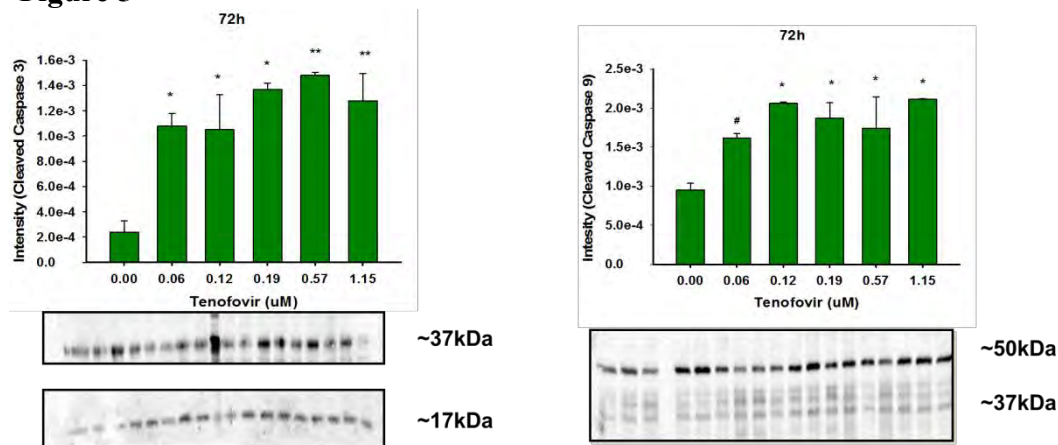


Fig. 5 Tenofovir increases caspase 3 and 9 activity in HK-2 cells. Blots are n=3 in concentrations 0, 0.06, 0.12, 0.19, 0.57, 1.15 μ M tenofovir from left to right. Caspase 3 expression is increased ($*p<0.05$) relative to control for all concentrations and 0.57 and 1.15 μ M tenofovir are increased ($**p<0.001$) relative to control. Caspase 9 expression is increased relative to control ($*p<0.05$) for 0.12, 0.19, 0.57, 1.15 μ M tenofovir and 0.06 μ M tenofovir increases caspase 9 expression ($\#p=0.05$) relative to control.

DISCUSSION

The results shown above give great insight to the mechanism of toxicity of tenofovir. We have shown that tenofovir is toxic to HK-2 cells at *clinically relevant concentrations* within 24-72h. Additionally, tenofovir increases oxidative stress within 48h and 4-HNE adduct formation within 72h. ATP levels are also drastically reduced following 72h tenofovir exposure. Lastly, tenofovir increases the expression of cleaved caspase 3 and 9 within 72h relative to control.

All of these data begin to give a clearer picture of the mechanism of cytotoxicity of tenofovir. We now know that tenofovir induces cell death via mitochondrially-induced apoptosis in HK-2 cells. Oxidative stress and a reduction in cellular energy also occur. We have generated a proposed mechanism of this toxicity based on this data (Fig. 6) and aim to generate more detail in the coming year.

Many questions still remained unanswered. While we now know the overall endpoint of tenofovir toxicity, cell death via apoptosis induced from the mitochondria, the exact mechanism still remains elusive. More experiments need to be done to determine what event occurs at what time point. There are two main hypotheses that can be extrapolated from the current data: tenofovir either directly induces reactive oxygen and nitrogen species that then damage the mitochondria and cause apoptosis, or, tenofovir directly damages the mitochondria, leading to oxidative stress and

apoptosis. Based on the current data showing reduction in cellular ATP concentration and increased oxidative stress, the latter hypothesis is more likely. Additional studies at 24 and 48h need to be run to determine what is occurring at what time point in this mechanism.

CONCLUSION

This project has been successful and looking more in depth into the mechanism of tenofovir induced cytotoxicity in HK-2 cells. Knowing that tenofovir induces oxidative stress, a reduction in cellular energy, and initiates apoptosis from the mitochondria gives a solid start to more detailed experiments. The generous funding I have received through the NASA West Virginia Space Grant Consortium has already allowed me to generate the data presented in this report, which has won at national and regional poster presentation competitions. I am submitting my first manuscript for publication with this data in the next two weeks. The financial support I have received has allowed me to focus solely on my training as a researcher, a gift that I have found invaluable.

This data and project that were made possible through this grant has also led me to the postdoctoral fellowship that I will be starting in May of 2017 at the University of Colorado Anschutz Medical Campus in Aurora, CO. This opportunity would not have been made possible if I hadn't had the funding to pursue this project. I have been fortunate to be awarded a NASA Graduate Research Fellowship through the NASA West Virginia Space Grant Consortium for an additional year. With this funding I plan to look more closely at different time points and intracellular compartments to more closely determine the mechanism of tenofovir induced toxicity. I also want to look at potentially mitigating or preventing this toxicity through protection studies; exploring compounds that have antioxidant and mitochondrial biogenetic activity may prove beneficial clinically in the long term.

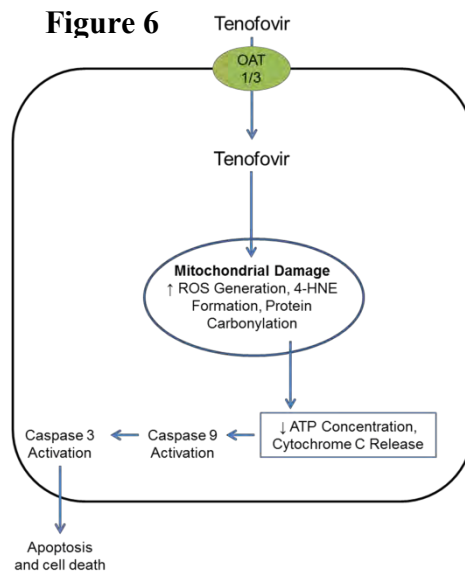


Fig. 6 Proposed mechanism of tenofovir toxicity. It is proposed that tenofovir enters the cell and mitochondria, and then induces oxidative stress, 4-HNE formation, and protein carbonylation, leading to a reduction in cellular ATP, the release of cytochrome c, and initiation of apoptosis.

ACKNOWLEDGEMENTS

I would like to extend my sincerest thanks to the NASA West Virginia Space Grant Consortium for funding this work and allowing me to pursue my training as a researcher. I would also like to thank my mentor, Dr. Monica Valentovic for her guidance and mentorship. I would not have gotten as far as I have without her help at every step of the way. I would also like to thank my colleagues Brooke Petrosavits and Reagan Stafford for their assistance in the lab on this project.

REFERENCES

- Barditch-Crovo P, Deeks SG, Collier A, Safrin S, Coakley DF, Miller M, Kearney BP, Coleman RL, Lamy PD, Kahn JO, McGowan I, Lietman PS. Phase i/ii trial of the pharmacokinetics, safety, and antiretroviral activity of tenofovir disoproxil fumarate in human immunodeficiency virus-infected adults.
- Del Palacio M, Romero S, Casado JL. Proximal tubular renal dysfunction or damage in HIV-infected patients. *AIDS Rev.* 2012. 14(3):179-87.
- Dore Gregory J, Cheng Andrew K (2004). "Efficacy of Tenofovir Disoproxil Fumarate in Antiretroviral Therapy–Naive and –Experienced Patients Coinfected with HIV-1 and Hepatitis B Virus." *Journal Of Infectious Diseases* 189: 1185–1192.
- Gunness P1, Aleksa K, Kosuge K, Ito S, Koren G. Comparison of the novel HK-2 human renal proximal tubular cell line with the standard LLC-PK1 cell line in studying drug-induced nephrotoxicity. *Can J Physiol Pharmacol.* 2010 Apr;88(4):448-55.
- Hall AM, Hendry BM, Nitsch D, Connolly JO. Tenofovir-associated kidney toxicity in HIV-infected patients: a review of the evidence. *Am J Kidney Dis.* 2011. 57(5):773-80.
- Izzedine H, Launay-Vacher V, Deray G. Antiviral drug-induced nephrotoxicity. *Am J Kidney Dis.* 2005 45(5):804-17.
- Kohler JJ, Hosseini SH, Green E, Abuin A, Ludaway T, Russ R, Santoianni R, Lewis W. Tenofovir renal proximal tubular toxicity is regulated by OAT1 and MRP4 transporters. *Lab Invest.* 2011 91(6):852-8.
- Lebrecht D, Venhoff AC, Kirschner J, Wiech T, Venhoff N, Walker UA. Mitochondrial tubulopathy in tenofovir disoproxil fumarate-treated rats. *J Acquir Immune Defic Syndr.* 2009 Jul 1;51(3):258-63.

- Paolicchi A, Sotiropoulou M, Perego P, Daubeuf S, Visvikis A, Lorenzini E, Franzini M, Romiti N, Chieli E, Leone R, Apostoli P, Colangelo D, Zunino F, Pompella A. gamma-Glutamyl transpeptidase catalyses the extracellular detoxification of cisplatin in a human cell line derived from the proximal convoluted tubule of the kidney. *Eur J Cancer*. 2003 May;39(7):996-1003.
- Ramamoorthy H, Abraham P, Isaac B. Mitochondrial dysfunction and electron transport chain complex defect in a rat model of tenofovir disoproxil fumarate nephrotoxicity. *J Biochem Mol Toxicol*. 2014. 28(6):246-55.
- Uwai Y, Ida H, Tsuji Y, Katsura T, Inui K. Renal transport of adefovir, cidofovir, and tenofovir by SLC22A family members (hOAT1, hOAT3, and hOCT2). *Pharm Res*. 2007 24(4):811-5.
- Van Gelder J, Shafiee M, De Clercq E, Penninckx F, Van den Mooter G, Kinget R, Augustijns P. Species-dependent and site-specific intestinal metabolism of ester prodrugs. *Int J Pharm*. 2000, 205:93-100.

COLLABORATIVE NAVIGATION BETWEEN A GROUND VEHICLE AND AN UNMANNED AERIAL VEHICLE IN GNSS-CHALLENGED ENVIRONMENTS

Victor Sivaneri
Ph.D. Aerospace Engineering
West Virginia University
Morgantown, WV 26508

ABSTRACT

Collaborative navigation uses many sensors to aid in navigating when Global Navigation Satellite System (GNSS) is degraded or not available. These sensors include Inertial Measurement Units (IMU), inter-nodal ranging, lasers, cameras, magnetometers, and various other aides. Many collaborative navigation techniques focus on the use of Vehicle Ad-Hoc Networks (VANETs) where multi-sensor fusion is used on individual nodes and the collaboration between nodes is opportunistic in nature. On the contrary, there has been less of an emphasis on the control or design for the location of the cooperative navigation nodes. As such, this paper considers the problem of collaborative navigation between a UAV in GNSS-challenged environments with a ground vehicle and focuses on the design of the optimal motion of the ground vehicle to best assist the UAV's navigation uncertainty. To conduct this study, a simulation environment is used to characterize the performance of the cooperative navigation between a UAV and a ground vehicle. The study is conducted to see the positioning accuracy during common GNSS-challenged scenarios such as: a vehicle in an urban environment, flying against a building, and flying under a bridge.

INTRODUCTION

Collaborative navigation is a research area that has been increasingly active over the past decade, especially in support of military operations and Intelligent Transportation Systems (ITS) (i.e. urban canyons). This is due to the fact that these environments are considered GNSS-challenged. In military situations, the Unmanned Aerial Vehicle (UAV) or ground vehicle, may go from situations where GNSS is readily available to completely denied (e.g. being jammed or traversing inside a cave). The major downside of GNSS is it requires an open sky and does not work in tunnels, underground, or in urban canyons (Kealy et al. 2015). In military operations, sub-meter level accuracy and high update rates (>10 Hz) are needed and this is not possible with standalone GNSS (Zador et al. 2000). In urban canyons, multipath and GNSS outages can cause positioning errors as large as a few hundred meters (Ko 2015). It has been shown that differential GNSS can compensate for the errors in the pseudorange measurements for Line of Sight (LOS) situations, but cannot for multipath and signal outages in urban canyons (Ko 2015). According to Titterton and Weston (2005), a number of techniques have been introduced to combat the issues in urban canyons, such as Inertial Navigation Systems (INS) and odometers; but it is well known that these sensors diverge rapidly over time and will not be able to handle long GNSS outages and multipath, which occurs in urban canyons. These scenarios are a few of the better-known cases when cooperative navigation would be beneficial. Other cases include, UAVs for bridge inspection or structural health monitoring (Guo 2011), UAVs for surveillance in urban environments (Alam 2013), or UAVs transitioning from indoor-to-outdoor or vice versa (Serrano 2014). It has been

well documented, that Dilution of Precision (DOP) is essential in determining the accuracy of a positioning system. The GDOP provides a relationship between the geometry and accuracy of the position estimate. The more favorable the geometry, the lower the DOP and the better position accuracy (Misra and Enge 2006).

TECHNICAL APPROACH

In this study, we will consider a cooperative navigation between a ground vehicle and a UAV and use a simulation environment to characterize the approach and evaluate various system design trades and sensitivities. For sensing, we will assume the use of Ultra Wide-Band (UWB) radio is used to provide very accurate, cm-level, range measurements between the two vehicles. In addition, each vehicle assumes the use of GNSS and INS. The objective of our cooperative approach will be to reduce the Dilution of Precision (DOP) of the GNSS-challenge UAV's navigation state through the motion of the ground vehicle.

Simulation Environment

The raw GNSS data used in the simulation was generated using a commercially available SatNav-3.04 Toolbox (GPSofT 2003), which is a GNSS constellation simulation toolbox. A Precise Point Positioning (PPP) observation model was used to be able to achieve centimeter-level positioning. The PPP approach uses dual-frequency undifferenced GNSS observables. For meter-level errors, it was possible to use just the pseudorange measurements, and use Differential GPS to reduce the pseudorange errors from a few meters to a meter. In order to achieve centimeter-level positioning with measurements from one receiver, carrier phase measurements are needed, and a method for incorporating GNSS error sources, such as ionospheric delay, troposphere delay, and receiver and clock bias. The benefit of PPP is the need for only one receiver and no limitation on the length of the baseline.

To mitigate the ionospheric delay, the dispersive nature of the ionosphere is used, and a linear combination of the GPS L_1 and L_2 , Galileo E_1 and E_{5b} , and GLONASS G_1 and G_2 frequencies is used to produce ionospheric-free (IF) pseudorange and carrier phase measurements for a dual-frequency receiver. The IF combination for GPS pseudorange and carrier-phase are shown in Eq. 1 and 2 (Watson et. al 2015).

$$\rho_{IF}^j = \rho_{L1}^j \left[\frac{f_1^2}{f_1^2 - f_2^2} \right] - \rho_{L2}^j \left[\frac{f_2^2}{f_1^2 - f_2^2} \right] = 2.546\rho_{L1}^j - 1.546\rho_{L2}^j \quad (1)$$

$$\phi_{IF}^j = \phi_{L1}^j \left[\frac{f_1^2}{f_1^2 - f_2^2} \right] - \phi_{L2}^j \left[\frac{f_2^2}{f_1^2 - f_2^2} \right] = 2.546\phi_{L1}^j - 1.546\phi_{L2}^j \quad (2)$$

In the above equations, the f_1 and f_2 are the L_1 and L_2 , E_1 and E_{5b} , and G_1 and G_2 frequencies, ρ_1 and ρ_2 are the pseudorange measurements of the respective frequencies, ϕ_1 and ϕ_2 are the carrier-phase measurements on the respective frequencies. The subscript j is used to designate the measurement between the platform and satellite j .

Using the IF combination, the pseudorange and carrier-phase measurements are modeled and shown in Eq. 6 and 7, respectively.

$$\rho_{IF}^j = R^j + c\delta t_u + T_z m(el^j) + \epsilon_\rho^j \quad (3)$$

$$\phi_{IF}^j = R^j + c\delta t_u + T_z m(el^j) + \lambda_{IF} N_{IF}^j + \epsilon_\phi^j \quad (4)$$

Where δt_u is the receiver's clock bias, T_z is the tropospheric delay in the zenith direction, $m(el^j)$ is the user to satellite elevation angle dependent mapping function, λ_{IF} is the wavelength corresponding to the IF combination, and N_{IF} is phase ambiguity. The geometric range between the platform and the satellite is denoted as R^j , and given as,

$$R^j = \sqrt{(x^j - x_u)^2 + (y^j - y_u)^2 + (z^j - z_u)^2} \quad (5)$$

where the subscript u represents the platforms position, and the superscript j represents the satellite, both in the same cartesian reference frame. In Equations 3 and 4 the remaining unmodelled error sources are indicated with ϵ . The tropospheric delay T_z is made up of a wet and dry component. The dry delay makes up the majority of the total zenith path tropospheric delay and can be well modeled. However, the wet delay is approximately 10% the dry delay and is typically estimated. Within this simulation, the Hoppfield model is used to model the dry component of the troposphere and estimated parameters are used to compensate for the residual error of the dry delay model and wet delay (Watson et. al. 2015). The mapping function used for this study was selected from Misra and Enge 2006 and is given in Eq. 6.

$$m(el^j) = \frac{1.001}{\sqrt{0.002001 + \sin(el^j)^2}} \quad (6)$$

Rover Position

In this context, an urban canyon scenario will be simulated with a UAV and ground vehicle. The UAV will be at a constant height and up against a building. The UAV and ground vehicle will start at arbitrary positions, and the UAV will capture the signals from all available GNSS satellites as well as a ranging signal from ground vehicle. The ground vehicle will then use knowledge of the GNSS satellites tracked by the UAV such that an optimal path of the ground vehicle can be determined.

The UAV and ground vehicle will start at arbitrary positions. Then the UAV will capture the signals from all available GNSS satellites and calculate its' position and send it to the ground vehicle. The ground vehicle will capture this information and calculate the range between the UAV and itself. From there the ground vehicle will determine what location it should move to, in order to reduce the DOP. This will be accomplished by the ground vehicle calculating the DOP, between the rover and ground vehicle, of all possible movements that can be made. A perimeter around the buildings is set up, to block the ground vehicle from coming too close to the buildings. These steps will be repeated until the UAV reaches its final destination or completes the mission.

Dilution of Precision

The accuracy of GNSS positioning is based on the geometry of the observable satellites, which is known as the DOP. The goal will be to reduce the DOP between the UAV and ground vehicle. This section will go through the derivation of the DOP. Beginning with the Weighted Linear Least Squares solution,

$$\Delta x = (G^T G)^{-1} G^T \Delta \rho \quad (7)$$

Where G is the Geometry Matrix and ρ is the pseudorange measurement. The Geometry Matrix is constructed by creating a unit vector, of the distance between the satellites and the quadcopter position. The UWB measurement is used as an additional satellite measurement, and is added to the end of the satellite measurement.

And we will denote H , as the Observation Matrix.

$$H = (G^T G)^{-1} = \begin{bmatrix} H_{11} & & & \\ & H_{22} & & \\ & & H_{33} & \\ & & & H_{44} \end{bmatrix} \quad (8)$$

From the Observation Matrix, H , the individual error estimates for the 3 position components and the clock bias can be calculated. The geometrical impacts on the 3D positioning error can be characterized using the DOP.

$$DOP = \sqrt{H_{11} + H_{22} + H_{33}} \quad (9)$$

RESULTS

The preliminary results show the rover path and the reduction of the DOP for GPS and GNSS. The rover starting location is arbitrary, and the number of points around the rover is changed. For Figure 1, the rover is starting (100,100) meters away from the quadcopter, and has 30 points to calculate the DOP around the rover at each time step. Whereas Figure 2, has 10 points to calculate the DOP around the rover at each time step. Figure 1 and 2 are based on GNSS configuration. The circle around the buildings is the perimeter, for which the rover cannot cross. The rover in both cases move in the same direction, but do not take the same path. Figure 3 and Figure 4, show the DOP of the 30 points and 10 points, respectively. The red line shows the DOP without a rover, and the blue line shows the DOP with a rover. It shows that having a rover makes the DOP improve greatly. There is a very slight difference between the DOP with the rover, when changing the number of points around the rover.

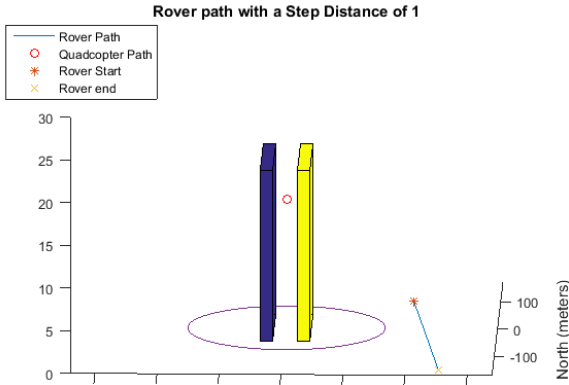


Figure 1: Rover Position using GNSS with a step distance of 1 and 30 points around rover

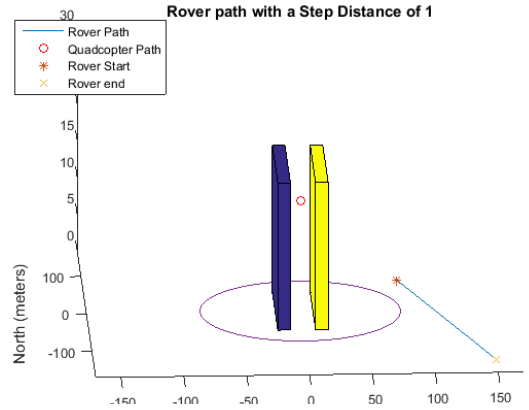


Figure 2: Rover Position using GNSS with a step distance of 1 and 10 points around rover

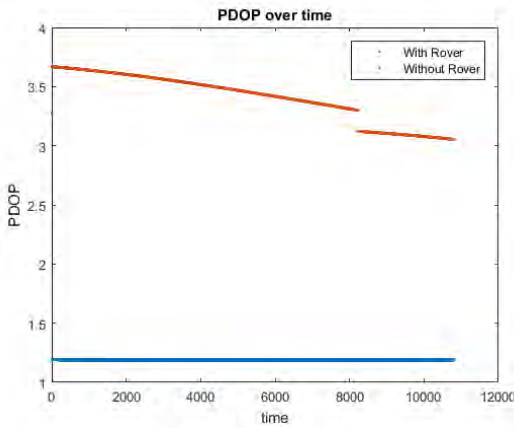


Figure 3: DOP using GNSS with a step distance of 1 and 30 points around rover

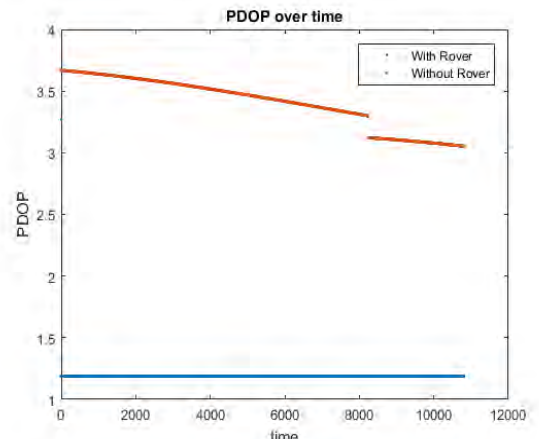


Figure 4: DOP using GNSS with a step distance of 1 and 10 points around rover

For Figure 5, the rover is starting (100,100) meters away from the quadcopter, and has 30 points to calculate the DOP around the rover at each time step. Whereas Figure 6, has 10 points to calculate the DOP around the rover at each time step. Figure 5 and 6 are based on GPS only configuration. The rover in both cases move in the same direction, but do not take the same path. Figure 7 and Figure 8, show the DOP of the 30 points and 10 points, respectively. The red line shows the DOP without a rover, and the blue line shows the DOP with a rover. It shows that having a rover makes the DOP improve greatly. There is a very slight difference between the DOP with the rover, when changing the number of points around the rover, which you can see a jump at the end of Figure 7.

Figures 5-8 have the same configuration as Figures 1-4, except Figures 5-8 use only GPS satellites, whereas Figures 1-4 use GPS, Galileo, and GLONASS satellites. The rover position, between the two configurations, move in opposite directions. For the GNSS setup the rover moves toward the quadcopter whereas for the GPS setup the rover moves away the quadcopter. And with the DOP,

the results are as expected, with the GNSS having a lower DOP than the GPS, due to the GNSS having more satellites in view, which improves the geometry matrix.

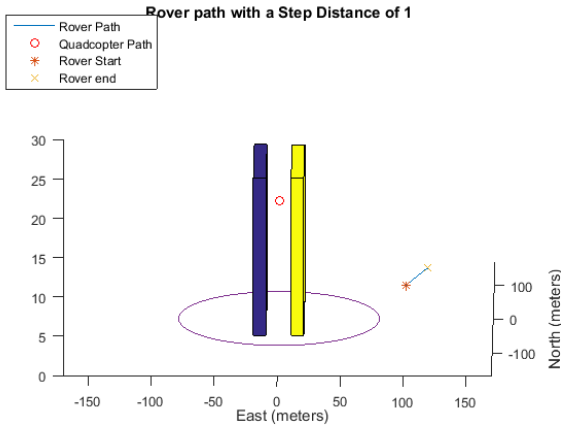


Figure 5: Rover Position using GPS with a step distance of 1 and 30 points around rover

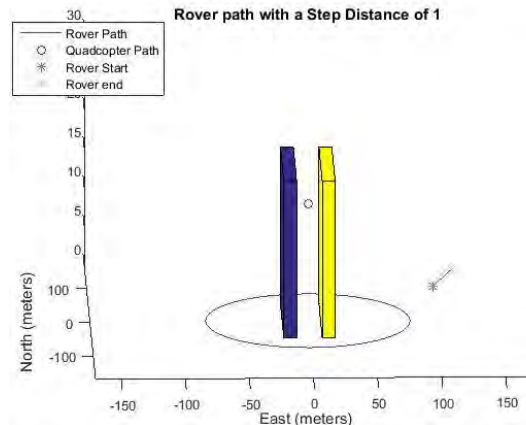


Figure 6: Rover Position using GPS with a step distance of 1 and 10 points around rover

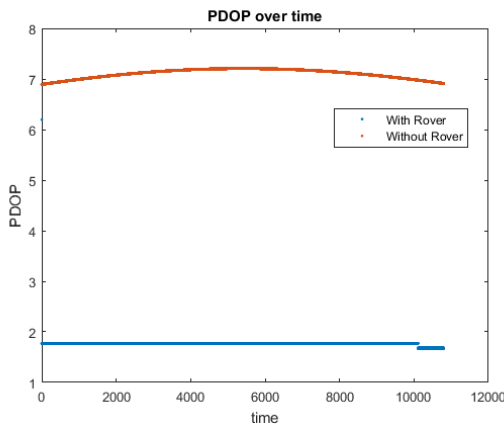


Figure 7: DOP using GPS with a step distance of 1 points, 30, around rover

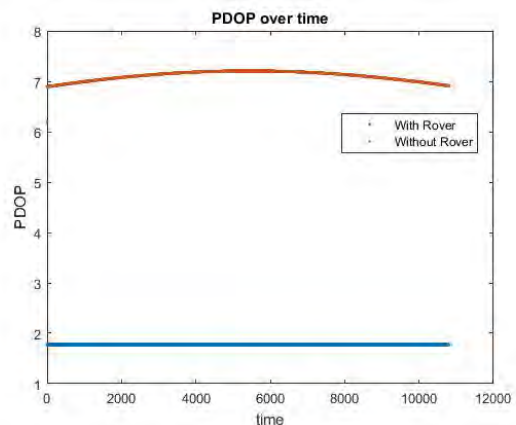


Figure 8: DOP using GPS with a step distance of 1 and 10 points around rover

For Figure 9, the rover is starting (100,100) meters away from the quadcopter, using GNSS configuration, and has 30 points to calculate the DOP around the rover at each time step. Whereas Figure 10, is using GPS configuration to calculate the DOP at each time step. The rover in both cases start in the same direction, away from the quadcopter, but eventually turn around and go toward the quadcopter, but do not take the same path. Both paths hit the perimeter and stay there for the rest of the duration. Figure 11 and Figure 12, show the DOP of the GNSS and the GPS

configuration, respectively. The red line shows the DOP without a rover, and the blue line shows the DOP with a rover. It shows that having a rover makes the DOP improve greatly. The DOP for GNSS with the rover and without the rover are lower than the DOP for GPS.

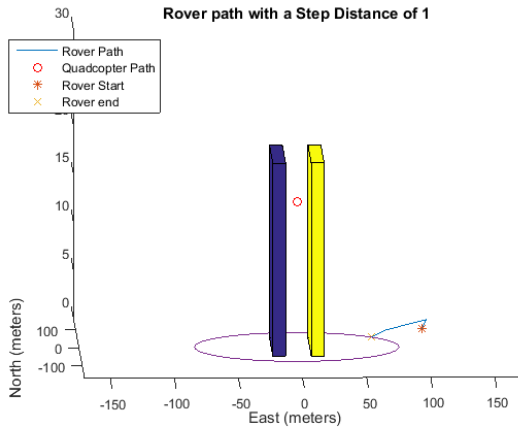


Figure 9: Rover Position using GNSS with a step distance of 1 and 30 points around rover

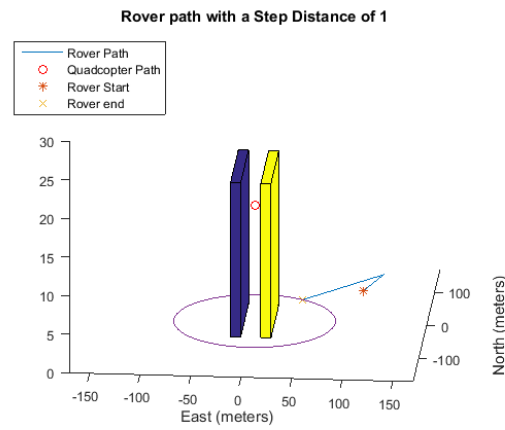


Figure 10: Rover Position using GPS with a step distance of 1 and 30 points around rover

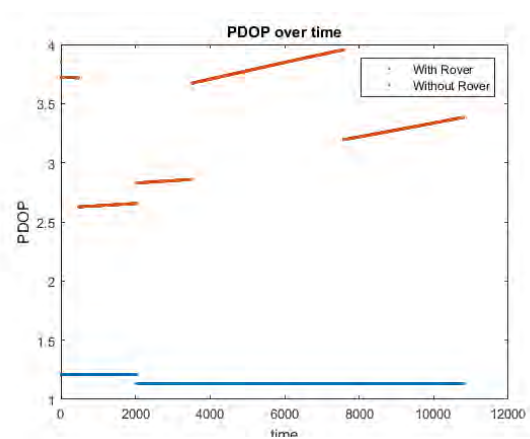


Figure 11: DOP using GNSS with a step distance of 1 and 30 points around rover

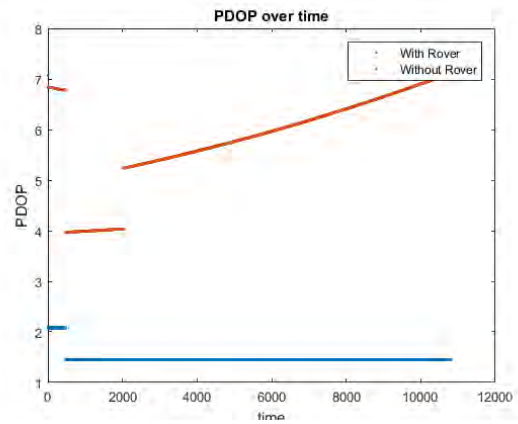


Figure 12: DOP using GPS with a step distance of 1 and 30 points around rover

CONCLUSION AND FUTURE WORK

This study will provide a way to control the path of a cooperative vehicle, or node, to assist a UAV in common GNSS-challenged environments. The preliminary results show that the dilution of precision can be used to navigate the rover to better position itself. The GNSS and GPS configurations showed different results, which shows the effect of having more satellites in the field of view. This is significant, as in urban canyons, satellites will be blocked due to buildings. So using the rover as another “satellite” significantly reduces the dilution of precision. The findings of this simulation study will be used to carry out this study experimentally. Future work will consist

of implementing an Extended Kalman Filter, to determine the errors in positioning. Further, future work will consist of instrumenting a UAV and a rover with GNSS/INS and UWB and perform flight tests. The experimental work will follow the same path as the simulation, starting with the rover driving in a predetermined path and then working up to having the rover autonomously maneuver to enhance the UAV navigation accuracy. Having a single UAV and a single ground vehicle, or node, will significantly help in situation where it will be difficult to carry more equipment or there is space restriction.

ACKNOWLEDGEMENTS

I would like to thank NASA WV Space Grant Consortium for the Graduate Fellowship as well as my advisor Dr. Jason Gross.

REFERENCES

- Alam, N., Kealy, A., & Dempster, A. (2013). Cooperative Inertial Navigation for GNSS-Challenged Vehicular Environment. *IEEE Transactions on Intelligent Transportation Systems*, 1370-1379.
- GPSofT. (2003). *Satellite Navigation TOOLBOX 3.0 User's Guide*. Athens: NavtechGPS.
- Guo, Y. (2011). Research of Structural Health Monitoring based on Mode Analysis for UAV Wings. *Prognostics and System Health Management Conference* (pp. 1-4). Shenzhen: IEEE.
- Kealy, A., Retscher, G., Toth, C., & Hasnur-Rabiain, A. (2015). Collaborative Navigation as a Solution for PNT Applications in GNSS Challenged Environments- Report on Field Trials of a Joint FIG/ IAG Working Group. *Journal of Applied Geodesy*, 244-263.
- Ko, H., Kim, B., & Kong, S.-H. (2015). GNSS Multipath-Resistant Cooperative Navigation in Urban Vehicular Networks. *IEEE Transactions on Vehicular Technology*, 5450-5463.
- Misra, P., & Enge, P. (2006). *Global Positioning System*. Lincoln: Ganga-Jamuna Press.
- Olsson, F., Rantakokko, J., & Nygard, J. (2014). Cooperative Localization Using a Foot-Mounted Inertial Navigation System and Ultrawideband Ranging. *International Conference on Indoor Positioning and Indoor Navigation* (pp. 122-131). Busan, Korea: IEEE.
- Serrano, D., Uijt de Haag, M., Dill, E., Vildardaga, S., & Duan, P. (2014). Seamless Indoor-Outdoor Navigation for Unmanned Multi-Sensor Aerial Platforms. *EuroCOW* (pp. 115-122). Castelldefels, Spain: International Archives of the Photogrammetry, Remote Sensing, and Spatial Information sciences.
- Titterton, D., & Weston, J. (2004). *Strapdown Inertial Navigation Technology*. London, UK: Institute Engineering Technology.
- Watson, R., Sivaneri, V., & Gross, J. (2015). Performance Characterization of Tightly-Coupled GNSS Precise Point Positioning Inertial Navigation within a Simulation Environment. *AIAA*, 1-17.

Zador, P., Krawchuk, S., & Voas, R. (2000). *Automotive Collision Avoidance System (ACAS) Program*. U.S.A: National Highway Traffic Safety Administration.

RESEARCH AND DEVELOPMENT OF A MULTI COMPONENT BALANCE SYSTEM FOR WIND TUNNEL APPLICATIONS

Vincent Spada
MS, Aerospace Engineering
West Virginia University
Morgantown, WV 26505

ABSTRACT

The wind tunnel has proven to be a very powerful tool in the area of aerodynamic research. In order to collect aerodynamic data using wind tunnel testing techniques, a strain gage type balance is often used. This type of device uses strain gages, also often referred to as load cells, to measure aerodynamic forces and moments. However, before a system such as this can be used, it must be very carefully calibrated. Historically, this has proven to be a very tedious task, due to the measurement of many forces and moments using many strain gages simultaneously. Therefore, a proper design and calibration of a “calibration bench” is essential. Many times, the set up and calibration process is more difficult than the actual testing.

This calibration bench was carefully designed and constructed using aluminum t-slots that encompasses the wind tunnel balance with a system of pulleys that connect to the top and both sides of the balance. Attaching known loads to the other end of the pulleys; Lift, drag and pitching moments can be applied to the balance and large amounts of data is then collected using a data acquisition system (DAQ). After the completion of the calibration process, the balance was mounted underneath the test section of WVU’s subsonic closed loop wind tunnel. A 3d finite wing with a leading edge sweep and dihedral of ten degrees was then placed inside the test section and was fixed to the balance using a constructed strut. The forces acting on the model were then calculated using the obtained calibration data at different angles of attack. This experiment was then converted into a learning tool for senior level students in the experimental aerodynamics lab. Students learned the fundamental concepts of the operations of wind tunnel balances by performing their own calibration and testing experiments. The exposure of a wind tunnel balance, data acquisition systems and calibration techniques provided the seniors’ hands on experience which directly enhanced the curriculum in the mechanical and aerospace engineering department.

INTRODUCTION

Wind tunnel balances can measure the basic longitudinal and lateral forces along a model along with their moments. It is a fundamental instrument for any aerospace engineer who works in the field of experimental aerodynamics. It is also essential for graduates of aerospace programs to have the knowledge of how these balances are calibrated and operated. It is of these reasons of what drove this research expenditure of developing a three component wind tunnel balance as a lab in the senior level experimental aerodynamics class along with making it available to any future researcher within the university to use for his/her own applications. In order to meet these objectives the balance itself must be researched. This research entails the construction of a precise calibration rig along with the experimental test on a 3d finite wing. A data acquisition system and proper load cells to measure these forces must also be purchased and setup.

APPARATUS

Wind Tunnel Balance

This particular model is a three component external balance. This means it can measure lift, drag and pitching moment and is mounted outside of the test section. Additionally, it can interchange into two components, measuring just lift and drag.

The wind tunnel balance is compatible with numerous types of compression-tension load cells. The load cells being used for this experiment are 25 lb., full bridge omega strain gauges as seen in Figure 2a. These load cells have a full Wheatstone bridge configuration which can measure compression and tension loading. The Wheatstone bridge is the key for measuring forces and moments. When a force is applied to the load cell, it will encounter a slight compression or tension, depending on the direction of the force. This will apply a strain to the variable resistor and change the resistance, which in effect will change the bridge voltage. This bridge voltage is measured, recorded and used to find the corresponding forces and moments using the calibration/coefficient matrix (LaCour 2015).

Calibration Bench

The calibration bench was constructed out of aluminum t-slots and balsa wood. Figure 1 below represents the constructed calibration bench.



a.) Overview of calibration bench



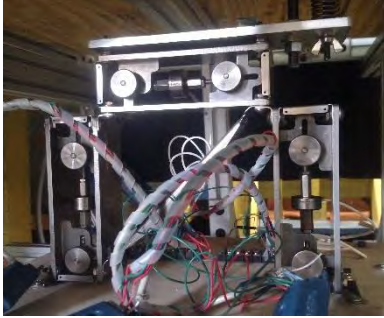
b.) Zoomed in view on calibration point

Figure 1: Calibration bench setup in test section

Three independent pulley systems were constructed and mounted onto the t-slots. The t-slots span over the top of the balance to allow a pulley to be placed directly above it. Two additional pulley systems were placed to the sides of the balance. String was fastened to the balance with known loads attached to the opposite ends. These loads were applied by the student to create an artificial lift, drag and pitching moment on the balance. The pulleys allowed these forces and moments to be directed downwards. The design of the pulley system allowed for free movement along the t-slots to allow the student to adjust the measurement between the forces.

Mounting Strut

The mounting strut was constructed using two threaded rods, an aluminum base plate, a spring and a wing nut. Figure 2 represents this design.



a.) Wind tunnel balance with attached strut



b.) Finite wing attached to balance in test section

Figure 2: Setup of finite wing with wind tunnel balance inside subsonic tunnel

The two threaded rods were attached to the baseplate (mounted to the top of the wind tunnel balance) and to the bottom of the model. The threaded rod towards the aft had a joint ball linkage between the rod and the fuselage. This allowed the aircraft's angle of attack to vary by ± 15 degrees. Underneath the baseplate and attached to the rear rod was the wingnut and above the baseplate was the spring. The spring provided a constant compression while the wingnut allowed the operator to change the angle of attack. When the wing nut was turned, the rod would slowly drop through the base plate, pulling the rear of the model downwards and effectively changing the angle of attack. The other threaded rod would be permanently mounted to the plate to increase stability. One rotation of the wingnut was equivalent to one degree angle of attack.

Data Acquisition System

The instrumentation used for this experiment consisted of a data acquisition system; Purchased from National Instruments. This system allowed for the simultaneous collection of high resolution voltages signals from the load cells. The specific 9237 model, 24 bit resolution module allowed for a variance in internal or external excitation voltage ranging from 3 to 10 volts. A four compartment chassis was also purchased to allow for additional modules to be added later. Figure 3 below represents the data acquisition system.



Figure 3: Data acquisition system purchased from National Instruments

The DAQ system was configured using a visual programming language created by National Instruments called LabVIEW. This program allows the user to set up a program pertaining to the user's specific needs. For this experiment, a program was created to collect all the voltage readings and store them into an excel worksheet.

METHOD

In order to validate the wind tunnel balance system, wind tunnel tests are geared towards airfoil and wing aerodynamics. More importantly, wind tunnel test must be conducted in which the experimental values can be reliably predicted. This can be done using previous experimental and empirical data corrected to reflect this application.

For strain gage balance calibrations, it is desirable to test an airfoil or a wing. NASA has published a great deal of experimental wind tunnel data on many airfoils. Therefore, an airfoil test would be ideal, however, a "pure" airfoil test is very demanding to set up and carry out. Often, instead of a two dimensional airfoil test, a three dimensional test is done using a finite wing. This is what was accomplished in this research effort.

After the construction of the calibration rig, it was mounted inside the test section of the wind tunnel. It is essentially to calibrate about the point where the quarter-cord will be located on the model when the wing is mounted. Earlier efforts attempted to calibrate outside of the tunnel around an arbitrary point in which the forces and moments measured about this arbitrary point by the balance can simply be translated using static equations. Theoretically this will work, however, experimentally it was proven ineffective. The second iteration of the calibration process moved the bench to inside the tunnel and the calibration point would be the quarter-cord. This can be seen in Figure 1b above. The calibration process itself consisted of applying known loads to the baskets which are the artificial lift, drag and pitching moments and recording the bridge voltages associated with them. After the completion of this tedious but very important task, the calibration rig was replaced with the actual finite wing. The wing was then tested at different angles of attack ranging from negative eight to positive ten degrees at different velocities ranging from 75ft/s to 150ft/s. This was made possible by the design of the strut, explained in the earlier section, which allowed for this change in angle of attack.

THEORY/BACKGROUND

In the field of experimental aerodynamics, aerospace engineers use wind tunnels to accurately predict how objects react when exposed to airflow using scaled models; arguably, the most important reactions being measured is the lift, drag and pitching moment. One of the instruments used that can accurately calculate these forces is the wind tunnel balance. There are a variety of force balances engineers can use, depending on their specific applications and they all have their advantages and disadvantages. The three most commonly used balances are the internal, external and rotary balance. The internal balance is placed inside the wind tunnel model which results in no drag interference from the flow. It also comes pre-calibrated from the manufacture. This is a major advantage due to the complex nature of calibrating; Calibration of the load cells are a nontrivial process that is extremely crucial for obtaining accurate results. However, this is also seem as a disadvantage for this balance because it will have to be returned to the manufacture for recalibration. This process can be time-consuming and expensive.

The external balance lies outside the model and the test section and is connected to the model using a strut or a sting. This allows the user easy access to the components of the balance which allows the engineer to perform his/her calibration and interchange for different load cells if needed. The downside for this balance comes from the mechanical strut/sting holding the balance. The balance will pick up the applied forces on the model along with the aerodynamic forces acting of the strut/sting. These interferences will have to be accurately measured and accounted for (González 2015).

DATA REDUCTION

Experimental Data Reduction

The lift, drag and pitching moment can be calculated by using the matrix representation of Equation 1 below.

$$\begin{pmatrix} \frac{\partial V_A}{\partial L} & \frac{\partial V_A}{\partial D} & \frac{\partial V_A}{\partial M} \\ \frac{\partial V_B}{\partial L} & \frac{\partial V_B}{\partial D} & \frac{\partial V_B}{\partial M} \\ \frac{\partial V_C}{\partial L} & \frac{\partial V_C}{\partial D} & \frac{\partial V_C}{\partial M} \end{pmatrix} \begin{pmatrix} L \\ D \\ M \end{pmatrix} \equiv \begin{pmatrix} V_A \\ V_B \\ V_C \end{pmatrix} \quad (1)$$

Each element inside the coefficient matrix represents the slope obtained during the calibration process. The voltages obtained during the experiment are represented by V_A , V_B and V_C on the right hand side of the equation. Multiplying this voltage array by the inverse of the coefficient matrix will result in the lift, drag and pitching moment about the calibration point. These values were then converted to pounds from grams. The coefficients for lift, drag and pitching moment were then calculated. The coefficient for lift is represented by Equation 2 below.

$$C_L = \frac{L}{q S} \quad (2)$$

The q value represents the dynamic pressure and the S is the reference area of the wing. Calculation of drag is then calculated using Equation 3.

$$C_D = \frac{D}{q S} \quad (3)$$

The drag is contributed to two main factors, the induced drag and the zero lift drag. The induced drag, C_{Di} , is contributed by the lifting forces, represented by Equation 4, and the zero lift drag, C_{D0} , is contributed only from the body. The zero lift drag can be calculated using Equation 5 (Corke 2003).

$$C_{Di} = \frac{C_L^2}{\pi AR e} \quad (4)$$

$$C_{D0} = C_D - C_{Di} \quad (5)$$

The moment coefficient can then be calculated using Equation 6 below.

$$C_M = \frac{M}{q S \bar{c}} \quad (6)$$

Theoretical Data Reduction

To predict the correct values for C_L and C_D , flat plate boundary theory can be applied along with various accepted corrections to calculate the actual finite wing values that should be expected in the tests. For the coefficient of lift, the lift curve slope must be calculated using the Equation 7 below (Napolitano 2012).

$$C_{L\alpha} = \frac{0.1097 AR}{2 + \sqrt{4 + (\beta AR)^2}} \quad (7)$$

The coefficient of lift values will then be calculated to eventually allow for a lift curve slope to be constructed.

It is difficult to calculate C_{Lmax} and the values obtained in Abbott and Doenhoff at much higher Re , rendering them unusable in this application. Therefore the objective is to merely calculate the lift curve prior to the stall and estimate the C_{Lmax} based on NASA's empirical results and standard corrections for finite wings.

The equation for the coefficient of lift can be calculated using Equation 8 below. The angle of attack at zero lift value is obtained from the *Theory of Wing Sections* (Abbott and Doenhoff 1949).

$$C_L = C_{L\alpha} (\alpha - \alpha_{0L} + i) \quad (8)$$

For determining C_{D0} , the coefficient of friction, C_f , is calculated based on flat plate boundary layer theory while assuming turbulent flow using Equation 9 below. As it can be seen, C_f is highly Reynolds number dependent as well as dependent on wing sweep and compressibility.

$$C_f = \frac{0.455}{(\log_{10} Re)^{2.58}} \quad (9)$$

This equation is then adjusted for a finite 3d wing. A finite wing has a lower and upper surface and the coefficients are always based on the planform or reference area. Adjustments are made for the actual surface and also for interference and pressure drag. Thomas Corke indicates a value f of

1.5 and Q of 1 for this finite wing. The calculation is represented by Equation 10 below (Corke 2003).

$$C_{D0} = (2.03)(1.5) \frac{0.455}{(\log_{10} Re)^{2.58}} \quad (10)$$

Finally the C_{Di} can be calculated using Munk's classic induced drag theory along with Oswald's efficiency factor in Equation 4. Equation 5 is then rearranged to calculate the total theoretical drag coefficient.

The moment coefficient is then calculated using Equation 11, where the coefficient of the pitching moment at zero lift, C_{M0} , and pitching moment curve slope, $C_{M\alpha}$, are obtained from Abbot and Doenhoff (Abbot and Doenhoff. 1949).

$$C_M = C_{M\alpha} \alpha + C_{M0} \quad (11)$$

RESULTS AND DISCUSSION

The voltage responses from applying known loads were extracted from LabVIEW to generate the coefficient matrix. The coefficient matrix is a 3x3 matrix, representing each force and moment, in which the elements represents a change in voltage over a change in load, which is the definition of a slope. The voltage responses as a function of load were plotted and the slopes of the lines were calculated. Figure 4 below represents three voltage responses from the three load cells for when lifting forces were applied.

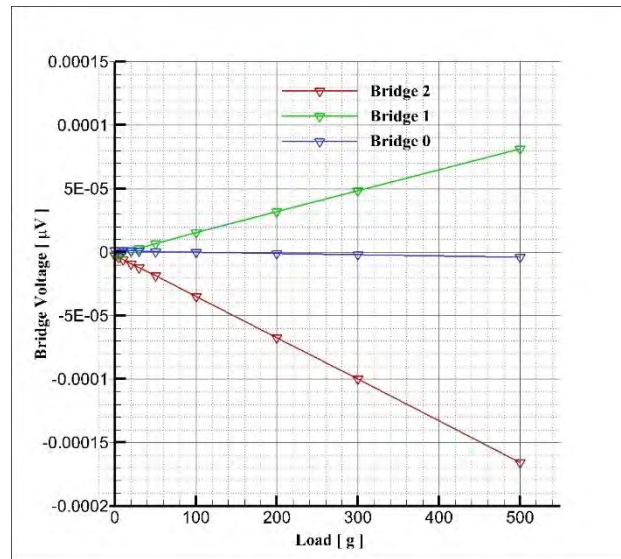
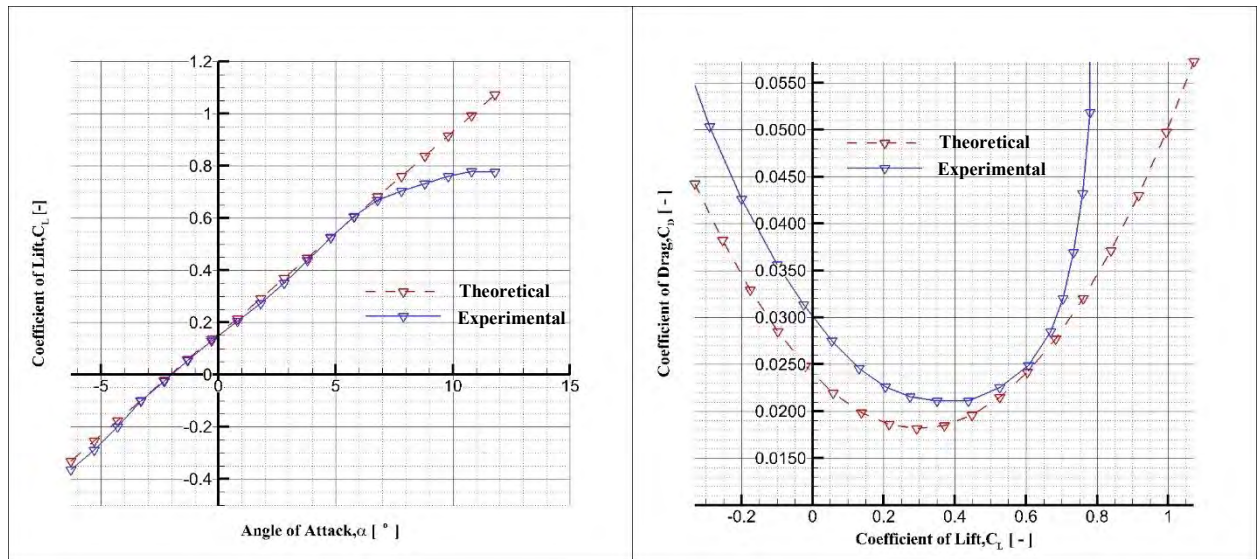


Figure 4: Voltage responses from applied lifting loads

As it can be seen the relationship between load and voltages are linear which was expected. By examining the responses, it can be seen how the balance reacts to pure lifting forces. Bridge 0 represents the middle vertical component of the balance while bridges 2 and 1 are the horizontal components. As pure lift is applied only the horizontal components are reacting. When pure drag force is applied it would be the opposite, in which only a reaction of bridge 0 would be seen. The slopes from the other two graphs representing pure pitching moment and drag were also calculated and used to complete the coefficient matrix.

The measured results of lift and drag forces were very favorable to the theoretical values. Figure 5a, seen below, shows the measured lift curve slope along with the theoretical values. The two curves are nearly identical expect at higher angles of attack. The finite wing starts to stall at around 10 degrees, when corrected for the incidence, and reaches its C_{Lmax} at around 13 degrees. The theoretical lift curve will not show this due to the reasons explained in the theoretical data reduction section.



a.) C_L as a function of α

b.) C_D as a function of C_L

Figure 5: Coefficient of lift and drag results for ΔP of 2.0 inH₂O

Figure 5b represents the relationship between drag and lift, which also represents the overall efficiency of the wing. It can be seen here that the measured drag is slightly higher which can be contributed to the drag interference from the strut. The results recorded at the different velocities are consistent with the results in Figure 5.

The results from the measured moments are at this time inconclusive. The pitching moment trend appears to be accurate, however, its magnitude between the experimental and theoretical values are slightly large. The experimental results also show a clockwise moment about the quarter-cord at low angles of attack and then counter-clockwise at around three degrees. This is consistent throughout all the data which suggest the flow angularity in the test section is not perfectly horizontal and is slightly angled at some negative degree. Even a small amount would significantly affect any measured pitching moment. Improvements will have to be made in order to correct for this possible source of error.

FUTURE PLANS

Research with the balance will continue to improve the imperfections in the current design. The current strut holding the wing will be modified to eliminate all the degrees of freedom except the longitudinal rotation around the aerodynamic center. The most notable being the yawing which is caused by the ball linkage joint that links the strut to the belly of the wing. The mechanical system for changing the angle of attack will also be redesigned. At higher free stream velocities (+100 ft/s) and at high angles of attack (+10°), there is a high pitching moment which pushes the aft rod downward which forbids the operator to accurately change the angle of attack. When redesigning the strut, additional attention will be given to reducing any interference drag caused by the strut to further increase accuracy

Flow angularity will also be measured using a five hole probe to determine the direction of the flow through the test section. A shunt calibration will also be conducted to cancel out any additional noise within the wire connections.

The wing will be reattached to the fuselage and the aircraft model will be tested in the same fashion. Control surface experiments will then be conducted by deflecting the elevators on the model.

CONCLUSIONS

For the final results for the lift and drag forces, the experimental values are within a reasonable range to the theoretical. However the pitching moment results were not as favorable possibly due to several reasons. The first, already mentioned in the results section, is from the flow angularity in the test section. Another contribution can come from the calibration phase. The calibration of wind tunnel balances are an extremely delicate and most often tedious process. The applied forces and moments must be perfectly lined up with the balance. A small deflection of even a degree can significantly alter the measured data. Steps were taken to properly eliminate this source of error, however it's very possible that the error can be contributed to the slight imperfections brought on by human error when setting up the rig. The pitching moment was calibrated around the quarter-cord of the wing which was measured. It is very possible that the coordinates for the quarter-cord could have been slightly off which would also explain the shift in the pitching moment data. It is also desirable to measure the pitching about the aerodynamic center when conducting these experiments which is located just aft of the quarter-cord for a 6 series airfoil. Future iterations of this experiment will correct these sources of error to further improve the pitching moment data.

Other notable causes of error from the drag results, already mentioned in the results and discussion section, is brought on by the drag interference on the strut. The exposure of the strut will pick up extra drag which often can match the drag of the model itself. Even though the experimental drag was within reason to the theoretical values, further steps can be taken to minimize these errors. The aluminum extruded strut, attached to the floor, was designed to eliminate as much interference drag as possible, however further improvements will be made to eliminate this drag altogether.

Other possible sources of error can stem from the process of data collection itself. Noise can always be a contributor of this. Electrical resistance in the wires leading from the DAQ to the load cells could affect the bridge voltages that are read. A shunt calibration can be conducted to eliminate this small resistance. These revisions will be made in time for the experimental aerodynamics lab in the fall of 2016.

In addition to successfully adding this lab to the experimental aerodynamics curriculum, a continuity binder was successfully created to help guide student/professors through the process of setting up the balance, calibration and DAQ system for their own research applications.

ACKNOWLEDGEMENTS

I would like to acknowledge the NASA WV Space Grant Consortium for rewarding us the grant for this project. I would also like to thank the Mechanical and Aerospace Engineering Department at West Virginia University for supplying the funds for the wind tunnel balance, data acquisition system and the three 25 pound load cells. I also greatly appreciate my advisor, Dr. Peter Gall along

with Dr. Patrick Browning for their unlimited support and input during the entire duration of this project.

REFERENCES

Abbott, Ira H. A., and Albert Edward Von Doenhoff. *Theory of Wing Sections; including a Summary of Airfoil Data*. New York: McGraw-Hill, 1949. Print.

"Acquiring an Analog Signal: Bandwidth, Nyquist Sampling Theorem, and Aliasing." *National Instruments*. N.p., n.d. Web. 18 Nov. 2015. <<http://www.ni.com/white-paper/2709/en/#toc2>>.

Corke, Thomas C. *Design of Aircraft*. Upper Saddle River, NJ: Prentice Hall, 2003. Print.

González, Miguel, José Ezquerro, Victoria Lapuerta, Ana Laverón, and Jacobo Rodríguez. "Components of a Wind Tunnel Balance: Design and Calibration." *Intech*. N.p., n.d. Web. Nov. 2015. <<http://www.intechopen.com/books/wind-tunnels-and-experimental-fluid-dynamics-research/components-of-a-wind-tunnel-balance-design-and-calibration>>.

LaCour, Joe. "KineOptics Wind Tunnel Balance." *KineOptics Wind Tunnel Balance*. N.p, n d Web. 6 June 2015. <<https://www.kineoptics.com/WTB.html>>.

"Measuring Strain with Strain Gages." *Measuring Strain with Strain Gages*. N.p., 2015. Web. 18 Sept. 2015. <<http://www.ni.com/white-paper/3642/en/>>.

Napolitano, Marcello R. *Aircraft Dynamics: From Modeling to Simulation*. Hoboken, NJ: J. Wiley, 2012. Print.

"Sensitivity." *HBM Test and Measurement: Transducers, Load Cells, DAQ*. N.p., n.d. Web. Jan.-Feb. 2015. <<http://www.hbm.com/en/3638/sensitivity/>>.

ARYL HYDROCARBON RECEPTOR REGULATION OF L-TYPE AMINO ACID TRANSPORTER 1 (LAT1) IN BREAST CANCER CELLS

Justin Tomblin
Ph.D. Candidate, Biomedical Sciences
Marshall University
Huntington, WV 25755

ABSTRACT

The aryl hydrocarbon receptor (AHR) is a ligand-activated transcription factor that is responsive to both endogenous and exogenous ligands, such as the classic AHR agonist, 2,3,7,8-tetrachlorodibenzo-p-dioxin (TCDD). L-Type Amino Acid Transporter 1 (LAT1) is a leucine transporter that is overexpressed in various tumor types, including breast tumors. The regulation of LAT1 by AHR in MCF-7 and MDA-MB-231 breast cancer cells (BCCs) was investigated after TCDD RNA sequencing (RNA-Seq) experiments revealed it to be a putative TCDD/AHR gene target. Ingenuity pathway analysis (IPA) software revealed that TCDD-regulated genes (termed TRGs in this report) were associated with molecular transport in BCCs. A prior chromatin immunoprecipitation sequencing (ChIP-Seq) study also revealed LAT1 to be a primary AHR/TCDD target. Short interfering RNA (siRNA)-directed knockdown of AHR confirmed that TCDD-stimulated increases in LAT1 mRNA and protein required AHR expression. TCDD-stimulated increases in LAT1 mRNA were also inhibited by the AHR antagonist CH-223191. Upregulation of LAT1 by TCDD coincided with increases in leucine uptake by MCF-7 cells in response to TCDD. Chromatin immunoprecipitation-quantitative PCR (ChIP-qPCR) assays revealed increases in AHR, AHR nuclear translocator (ARNT) and p300 binding and histone H3 acetylation at an AHR binding site in the LAT1 gene in response to TCDD. In MCF-7 and MDA-MB-231 cells, endogenous levels of LAT1 mRNA and protein were reduced in response to knockdown of AHR expression. Knockdown experiments demonstrated that proliferation of MCF-7 and MDA-MB-231 cells is dependent on both LAT1 and AHR. Collectively, these findings confirm BCCs are dependent on leucine uptake and has helped establish a mechanism for exogenous and endogenous regulation of LAT1 by AHR.

INTRODUCTION

Polycyclic aromatic hydrocarbons (PAHs) are environmental toxicants that are formed as byproducts of industry and municipal waste incineration [1, 2]. PAHs exert their effects through AHR activation [3], and given constitutively active AHR or aberrant high levels of AHR is common in tumors such as breast and prostate tumors [4-6], AHR is now accepted to be a potent tumor promoter. High levels of PAHs are also present in space and carry the infrared emission features that dominate the spectra of most galactic and extragalactic sources [7, 8]. Exposure to PAHs in space could therefore increase cancer risk in astronauts, especially those on long and/or repeated space missions. 2,3,7,8-Tetrachlorodibenzo-p-dioxin (TCDD) exhibits the highest affinity for AHR compared with other PAHs [9]. In the absence of ligand, AHR is associated with chaperone proteins including heat shock protein 90 (HSP90) [10, 11], hepatitis B virus X-associated protein 2 (XAP2) [12-14], and p23 [15] in the cytoplasm. Upon binding to TCDD, AHR

translocates from the cytoplasm into the nucleus and binds AHR nuclear translocator (ARNT) forming an active transcriptional complex [3, 16, 17]. TCDD-induced AHR/ARNT dimers bind specifically to AHR response elements (AHR-REs) that cluster near the promoter regions of TCDD/AHR target genes to drive increases in gene expression [16]. Two such TCDD/AHR target genes are CYP1A1 and CYP1B1, which are important enzymes involved in phase I xenobiotic metabolism [16]. The induction of CYP1A1 and CYP1B1 transcription by TCDD also requires several transcriptional coactivators including steroid receptor coactivator 2 (SRC1), steroid receptor coactivator 2 (SRC2), p300 and BRG-1 [18-20].

We performed TCDD-RNA-Sequencing (RNA-Seq) analysis and identified 137 TCDD-regulated genes (TRGs) in MCF-7 breast cancer cells (BCCs). One target gene that particularly peaked our interest among them was solute carrier family 7 (amino acid transporter light chain, L system) member 5 SLC7A5, which encodes the protein L-Type Amino Acid Transporter 1 (LAT1). LAT1 facilitates the uptake of large neutral amino acids including leucine, arginine, phenylalanine, and tryptophan [21-23]. LAT1 is overexpressed in a variety of tumor types, including breast, colorectal, and prostate, compared with surrounding normal tissue [24]. Upregulation of LAT1 is postulated to promote cancer growth by facilitating the uptake of leucine by tumor cells. Increases in intracellular leucine increases the activation of mTOR signaling, specifically mTORC1 [25, 26]. Increases in the activity of mTORC1 promotes the phosphorylation and activation of mTORC1 downstream targets such as ribosomal S6 kinase (p70S6K), eukaryotic initiation factor (eIF), and 4E binding proteins (4E-BPs) which promote protein synthesis and cell survival [25]. Hyperactivation of mTOR and its downstream constituents is associated with many tumor types, including melanoma, late-stage head and neck cancers, and ductal cell breast cancers [26, 27]. Importantly, prior reports have demonstrated that breast tumors that express high levels of LAT1 were more resistant to tamoxifen treatment than breast tumors that expressed low levels of LAT1 [28, 29]. Thus, uncovering how LAT1 is regulated in BCCs is highly relevant.

The objective of this report was to investigate exogenous regulation of LAT1 by TCDD activated AHR and endogenous regulation of LAT1 by AHR. Exogenous regulation of LAT1 by TCDD/AHR was investigated in MCF-7 cells. Endogenous regulation of LAT1 by AHR was investigated in MCF-7 and MDA-MB-231 cells as these BCC lines have been shown to exhibit endogenous AHR activity [30-34]. Based on our findings, we report a new role for AHR as an exogenous and endogenous regulator of LAT1 expression in BCCs and show that AHR binds to LAT1 AHR-REs as part of a transcriptional activator complex. Our findings suggest exposure to PAHs in space could make astronauts susceptible to developing various cancers like breast and prostate. Activation of AHR would drive increases in LAT1 expression which would in turn drive cancer cell growth and tumor survival by increasing the import of amino acids, like leucine.

METHODS

Materials

Dulbecco's Modified Eagle Medium/High glucose (DMEM) with l-glutamine and sodium pyruvate, phenol red-free DMEM, phosphate buffered saline (PBS), fetal bovine serum (FBS), penicillin, streptomycin, and dimethyl sulfoxide (DMSO) were purchased from Thermo Fisher Scientific (Pittsburgh, PA). Sodium dodecyl sulfate (SDS), 30% acrylamide/bis solution, ammonium persulfate, Tween-20, 2-mercaptoethanol and polyvinylidene difluoride (PVDF) membranes were obtained from BIO-RAD (Hercules, CA). Non-targeting short interfering RNA

(siRNA) (cat # D-001810-01-20), ON-TARGET plus human siRNAs against AHR (cat # J-004990-08-0010, and cat # J-004990-06-0010) and LAT1 (cat # J-004953-09-0010) were purchased from GE Dharmacon (Lafayette, CO). 2,3,7,8-Tetrachlorodibenzo-p-dioxin (TCDD) was obtained from Cambridge Isotopes Laboratory (Andover, MA). The AHR antagonist CH-223191 was purchased from Sigma–Aldrich (St. Louis, MO). MCF-7 and MDA-MB-231 BCCs were purchased from ATCC (Manassas, VA) and maintained in DMEM, 10% FBS, with penicillin (100 IU/mL) and streptomycin (100 IU/mL).

TCDD RNA-Seq

250,000 MCF-7 cells were seeded in 35 mm plates in DMEM supplemented with 10% FBS for 24 h, followed by overnight serum-starvation in phenol red-free DMEM, and then treated with vehicle (DMSO) or 10 nM TCDD for 6 h. RNA-Seq analysis was based on 4 biological replicates in each experimental group. Total RNA purification kits (Qiagen, Valencia, CA) were used to extract total RNA. RNA sample quality was assessed using Bioanalyzer RNA Nano chips (Agilent); all RNA samples had an RNA Integrity Number greater than or equal to 8. RNA-Seq libraries were prepared from 1 µg of total RNA using a TruSeq RNA Prep Kit (Illumina Inc., San Diego, CA). RNA-Seq was performed using an Illumina HiSeq1000 in a 2 × 100 base paired end design yielding a minimum of 50 million reads per sample. Differentially expressed genes were identified at a False Discovery Rate (FDR) of 5% as detailed in our prior report [33]. Raw reads and processed data (unnormalized and normalized read counts by gene) were deposited in the Gene Expression Omnibus (GEO) at the National Center for Biotechnology Information and are accessible via accession number GSE76608.

Ingenuity pathway analysis (IPA)

TCDD-regulated genes (TRGs) were expressed as a ratio of TCDD/DMSO and loaded into IPA software (Ingenuity Systems, Redwood City, CA). Of the 137 TRGs identified by RNA-Seq, 116 were mapped to known functions and pathways by IPA. The Core Analysis tool and the Fisher Exact Test in IPA were used to identify statistically significant associations between TRGs and cellular and molecular pathways. We configured the core analysis to report Benjamini–Hochberg corrected p-values.

Reverse transcription and real-time polymerase chain reaction (RT-qPCR)

RT-qPCR assays were carried out as described in our prior reports [33, 34]. In brief, total RNA was extracted using RNA purification columns (Qiagen) and 100–300 ng of extracted RNA was reverse transcribed to cDNA using High Capacity Reverse Transcription kits (Thermo Fisher Scientific). Real-time qPCR reactions were performed in triplicate using SYBR Green Master Mix according to the manufacturer’s instructions (Thermo Fisher Scientific). Relative changes in gene expression were calculated using the $2^{-\Delta\Delta CT}$ formula as described by Livak and Schmittgen [35]. Glyceraldehyde-3-phosphate (GAPDH) mRNA levels served as the internal control. The sequences of the qPCR primers used to amplify GAPDH and AHR mRNA have been published [34]. LAT1 mRNA qPCR primers were: forward, 5'-ccgaggagaaggaagagggc-3'; reverse, 5'-gaagatgcccagagccgataa-3'. The Student–Newman–Keuls (SNK) post hoc test was used to determine statistically significant differences among groups following one-way analysis of variance (ANOVA).

Short interfering RNA (siRNA) assays and Western blotting

The siRNA knockdowns were performed as detailed in our prior reports [33, 34]. Briefly, 200,000 cells (MCF-7 or MDA-MB-231) in 1 mL of DMEM supplemented with 10% FBS were mixed directly with 100 nM of siRNA that was non-targeting, AHR-targeting or LAT1-targeting and 3 μ L of Lipofectamine RNAiMAX transfection reagent (Thermo Fisher Scientific) and immediately plated in 35 mm tissue culture plates for 48 h. MCF-7 cells were then treated with vehicle (DMSO) or 10 nM TCDD for 16 h. Treatments were removed and cells were rinsed once with PBS. For Western blotting, total protein was extracted by scraping cells in 2 \times Laemmli Sample Buffer containing β -mercaptoethanol (BME). Laemmli sample buffer and BME were purchased from BIO-RAD. Standard Western blotting techniques were used to analyze \sim 10 μ g of protein per sample (please refer to our prior reports for technical details [33, 34]). Western blot analysis of GAPDH was used to confirm equal protein loading. Blots were probed with anti-GAPDH antibody (diluted 1:10,000), anti-AHR antibody (diluted 1:5,000) or anti-LAT1 antibody (diluted 1:2,000) overnight at 4 $^{\circ}$ C, followed by incubation with anti-HRP secondary antibody (1:5000) for 1 h at room temperature. The blots were then rinsed with PBS + 0.1% tween 20, and then developed with enhanced chemiluminescent substrate Millipore Corp., (Billerica, MA). The anti-GAPDH antibody was purchased from Millipore (Cat #MAB374). The anti-AHR antibody was obtained from Santa Cruz Biotechnology (Santa Cruz, CA, Cat #H-211) and the anti-LAT1 antibody was purchased from Cell Signaling Technology (Danvers, MA, Cat #5347). Densitometry was calculated with ImageJ PC-based software (National Institute of Health). The Student–Newman–Keuls (SNK) post hoc test was used to determine statistically significant differences among groups following one-way analysis of variance (ANOVA).

Chromatin immunoprecipitation followed by qPCR (ChIP-qPCR)

The ChIP-qPCR assays were carried out as described in our previous report [34]. In brief, nonspecific IgG, and antibodies that were specific for AHR, ARNT or p300 were obtained from Santa Cruz Biotechnology. The antibodies against acetylated lysine 9 or lysine 14 in histone H3 were purchased from Cell Signaling Technology. The magnetic protein A beads and proteinase K were purchased from Life Technologies (Carlsbad, CA). A recent TCDD-ChIP-Seq report identified an AHR binding site within a 900 bp region in LAT1 corresponding to coordinates 87,840,300–87,841,199 (human genome version 19 (Hg19)) [36]. This AHR binding site was investigated in this report by ChIP-qPCR with primers that span coordinates 87,840,403–87,840,544, which were: [forward 5'-GCACGTACCTGTAGGGGTTG-3' and reverse 5'-ATGCTCTCTCCCGGTGATT-3']. The ChIP-qPCR primers used to amplify the AHR binding sites in the CYP1B1 gene have been published [37]. ChIP-qPCR data were expressed as % input in which signals obtained from the ChIP are divided by signals obtained from an input sample. Statistical differences among groups were determined by the SNK post hoc test following one-way analysis of variance (ANOVA)

Leucine uptake experiments

Leucine uptake experiments were performed in MCF-7 cells grown to confluence on 24 well plates. The cells were first washed twice with Na-free buffer (130 mM TMACl, 4.7 mM KCl, 1 mM MgSO₄, 1.25 mM CaCl₂, 20 mM HEPES; pH 7.4) and incubated with the same for 10 min at room temperature. The uptake was then initiated by incubating the cells for 30 s with Na-HEPES buffer (130 mM NaCl, 4.7 mM KCl, 1 mM MgSO₄, 1.25 mM CaCl₂, 20 mM HEPES; pH 7.4) with 10 μ Ci of 3H-l-Leucine (PerkinElmer; Waltham, MA) and 10 μ M l-Leucine (Sigma–Aldrich). The reaction was stopped with ice cold Na-HEPES buffer after which the cells were washed twice

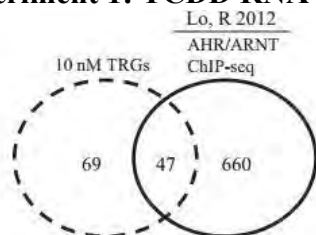
with the same ice-cold buffer. The cells were then lysed in 500 µl of 1 N NaOH followed by incubation for 20 min at 70° C. The lysed contents of each well was collected in a 7 ml scintillation tube and mixed with 5 ml Ecoscint A (National Diagnostics; Atlanta, GA). Leucine uptake experiments were conducted using chemicals obtained from Sigma–Aldrich. The vials were kept in the dark for 48 h and the radioactivity was determined in a Beckman 6500 scintillation counter.

MCF-7 and MDA-MB-231 proliferation experiments

20,000 MDA-MB-231 or 10,000 MCF-7 cells in 1 mL of DMEM + 10% FBS were mixed directly with siRNA's (100 nM) that were non-targeting, AHR-targeting or LAT1-targeting and 3 µL of RNAiMax Transfection Reagent. The cells were then plated into 96 well plates at a density of 2000 MDA-MB-231 or 1000 MCF-7 cells per well. After 3 days, cell proliferation was assayed with the Aqueous One Solution Cell Proliferation Assay (Promega, Madison, WI) in accordance with the manufacturer's protocol.

RESULTS

Experiment 1: TCDD RNA-Seq



47 TRGs genes that overlap with reported TCDD-AHR/ARNT ChIP set.

GENE ID	*fold change	GENE ID	*fold change	GENE ID	*fold change
CYP1A1	424.40	NEDD9	2.15	PYGL	1.57
CYP1B1	8.29	TMEM45B	2.03	AGPAT9	1.56
DRD1	6.08	NFE2L2	1.86	ATP9A	1.56
ALDH1A3	6.06	PPARG	1.85	SLC16A7	1.50
PITPNM2	3.77	NBPF10	1.80	SLC27A2	1.50
LMCD1	3.75	CABLES1	1.75	LRIG3	1.49
BMF	3.13	SYT12	1.79	FOSL2	1.49
GLDN	2.62	DNMBP	1.74	ELF4	1.48
ST3GAL1	2.61	SLC16A14	1.73	TMEM120B	1.47
FAM105A	2.49	STC2	1.70	ADAP1	1.43
RUNX2	2.38	TMTC2	1.68	DDIT4	1.41
SLC7A5 (LAT1)	2.33	HES1	1.64	GDF15	1.41
TNFRSF11B	2.32	AHRR	1.61	TUFT1	1.38
TTC39B	2.29	PRPS1	1.60	PSPC1	1.37
MB21D2	2.20	DLL1	1.59	C6orf132	0.70
PLEKHF1	2.18	LRP5	1.58		

*RNA-seq fold change expression values from TCDD-treated MCF7 cells compared to vehicle expressed as a ratio of TCDD/vehicle

Fig. 1. Genes common between TCDD RNA-Seq data and TCDD-ChIP-Seq data. Analysis of reported MCF-7 TCDD-ChIP-Seq data revealed that 47 of the 116 TCDD-RNA-Seq genes were TCDD-AHR/ARNT bound genes. The specific 47 TCDD-regulated genes and their associated fold changes are shown in the table.

RNA-Seq revealed TCDD induction of 137 genes in MCF-7 BCCs at a FDR of less than 5%, with all fold changes greater than or equal to 1.3 compared with DMSO vehicle treatment. Of these 137 TCDD-regulated genes (TRGs), 116 were mapped to known cellular functions by IPA. Comparison of TRGs with a published TCDD/AHR-ChIP-Seq dataset [36] revealed that 47 genes were shared between the two gene sets (Fig. 1). This included known TCDD target genes such as CYP1A1 [38], CYP1B1 [38] and ALDH3A1 [39] (Fig. 1). Bioinformatic analysis revealed that the 47 TCDD target genes were significantly associated with metabolic pathways including: lipid metabolism, carbohydrate metabolism, nucleic acid metabolism, vitamin and mineral metabolism and energy production (Table 1). The 47 TCDD target genes were also associated with cancer processes including: cell death and survival, cell cycle, cellular growth

and proliferation, and molecular transport (Table 1).

Experiments 2 & 3: TCDD/AHR regulation of LAT1 and leucine uptake

Our TCDD-RNA-Seq dataset revealed that LAT1 (also known as SLC7A5) was induced 2.33-fold by TCDD (Table 1), while TCDD-ChIP-Seq evidence suggested that AHR could directly bind to intron 2 of the LAT1 gene [36]. We decided to further investigate exogenous regulation of LAT1 by TCDD, considering that prior reports indicate that upregulation of LAT1 could be important for breast cancer progression [40-42]. To investigate whether TCDD increases LAT1 expression

Category	B-H p-value	Target molecules in dataset
Lipid metabolism	8.55E-03-3.52E-02	14
Small molecule biochemistry	8.55E-03-4.11E-02	26
Cell death and survival	8.55E-03-4.11E-02	30
Gene expression	8.55E-03-3.2E-02	12
Cell cycle	8.55E-03-3.91E-02	16
Cellular development	8.55E-03-3.54E-02	37
Cellular growth and proliferation	8.55E-03-3.93E-02	42
Carbohydrate metabolism	8.55E-03-3.2E-02	9
Drug metabolism	8.55E-03-3.71E-02	10
Energy production	8.55E-03-3.27E-02	8
Molecular transport	8.55E-03-3.71E-02	15
Vitamin and mineral metabolism	9.07E-03-3.2E-02	8
Nucleic acid metabolism	9.68E-03-3.2E-02	4

* p-Values are calculated by Fishers exact test and corrected for multiple testing by the Benjamini-Hochberger p-values (B-H) method (B-H p-value). Column 2 shows the range of B-H corrected p-values for the biofunctions in a given category. Target molecules in dataset are the number of RNA-Seq TRGs in a given biofunction.

Table 1. IPA cellular and molecular functions associated with the 47 TRGs that overlap with reported TCDD-AHR/ARNT ChIP-seq.

through AHR, MCF-7 cells were transfected with short interfering RNA against AHR (AHRi). Control MCF-7 cells were transfected with non-targeting siRNA (cRNAi). siRNA-treated cells were then exposed to either vehicle or TCDD (10 nM) for 6 h. Reductions in AHR mRNA were confirmed in MCF-7 cells transfected with AHRi compared with those transfected with cRNAi (Fig. 2A). As expected, TCDD-stimulated increases (3-fold) in LAT1 mRNA compared with vehicle in MCF-7 cells transfected with cRNAi (Fig. 2B). In contrast, AHRi significantly reduced the stimulatory effect of TCDD on LAT1 expression ($P < 0.01$; Fig. 2B). These results indicate that LAT1 regulation by TCDD is mediated by AHR.

To investigate whether TCDD increases LAT1 expression by binding to AHR, MCF-7 cells were treated with CH-221391, which is an AHR antagonist that specifically inhibits the binding of TCDD to AHR [43]. TCDD induction of CYP1A1 transcription is a commonly used readout of TCDD-induced AHR activity that requires TCDD to bind AHR. To verify that CH-221391 is an AHR antagonist in MCF-7 cells, its ability to suppress induction of CYP1A1 by TCDD was measured by RT-qPCR. The findings revealed that TCDD-induced increases in CYP1A1 were indeed reduced by CH-221391, indicating that it is an effective AHR antagonist in MCF-7 cells (Fig. 2C). As expected, TCDD-stimulated increases (~3-fold) in LAT1 mRNA in control MCF-7 cells not treated with CH-221391 (Fig. 2D). In contrast, CH-221391 significantly ($P < 0.01$) suppressed the stimulatory effect of TCDD on LAT1 expression (Fig. 2D). These results indicate that regulation of LAT1 by TCDD requires TCDD to bind AHR.

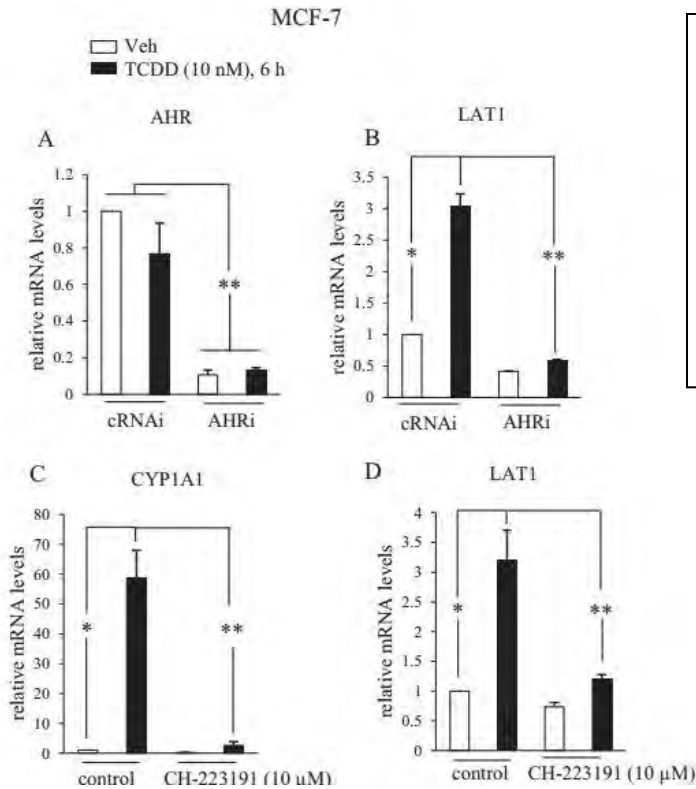


Fig. 2. AHR mediates TCDD-stimulated increases in LAT1 mRNA. (A and B) MCF-7 cells were transfected with siRNAs that were either non-targeting (cRNAi) or AHR targeting (AHRi) and then treated with DMSO vehicle (Veh) or TCDD (10 nM) for 6 h. (C and D) MCF-7 cells were treated vehicle or TCDD (10 nM) in the absence (controls) or presence of CH-223191 (10 μM) for 6 h. (A–D) AHR, LAT1, CYP1A1 or GAPDH mRNA were quantified by qRT-PCR from total RNA. GAPDH mRNA levels were used to normalize samples. *P < 0.05; **P > 0.01. Data shown are the mean ± S.E. of three independent experiments.

Western blot experiments were conducted to confirm that TCDD induction of LAT1 mRNA leads to increases in LAT1 protein. Exposure to TCDD stimulated robust increases (~10-fold) in LAT1 protein in MCF-7 cells transfected with cRNAi (Fig. 3A and B). Induction of LAT1 protein by TCDD was completely suppressed in MCF-7 cells transfected with AHRi (Fig. 3A and B). As expected, AHR protein levels in MCF-7 cells transfected with AHRi were lower than those transfected with cRNAi (Fig. 3A and C). Leucine uptake experiments were performed to investigate if the induction of LAT1 protein by TCDD coincided with increases in leucine uptake by MCF-7 cells. Significant increases in leucine uptake by cells was observed in response to TCDD exposure compared with vehicle-treated cells (Fig. 4). Taken together, these results indicate that the induction of LAT1 protein by TCDD leads to a functional increase in leucine uptake by MCF-7 cells.

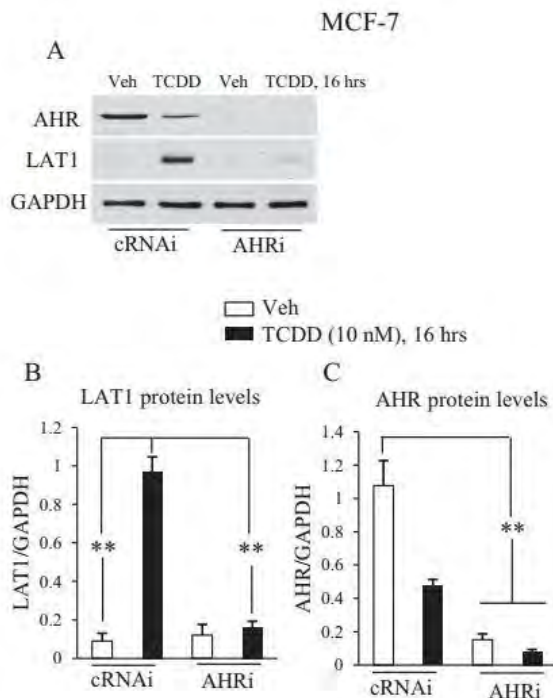


Fig. 3. AHR mediates TCDD-stimulated increases in LAT1 protein. (A–C) MCF-7 cells were transfected with siRNAs that were either non-targeting (cRNAi) or AHR targeting (AHRi) and then treated with vehicle (Veh) or TCDD (10 nM) for 16 h. Total cellular protein was then isolated and subjected to Western blot analysis. The blot was then probed with the indicated antibodies. Relative levels of AHR or LAT1 protein were expressed as a ratio to GAPDH loading control. *P < 0.05; **P > 0.01. Data shown are the mean ± S.E. of three independent experiments.

Experiment 4: AHR/p300/ARNT transcriptional regulation of the LAT1 gene

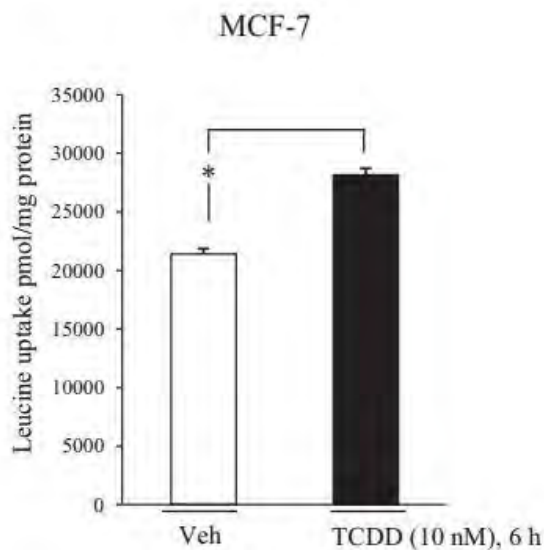


Fig. 4. TCDD increases leucine uptake. MCF-7 cells were treated with vehicle or 10 nM TCDD for 6 h, followed by analysis of leucine uptake as detailed in the material and methods. * $P < 0.05$. Data shown are the mean \pm S.E. of three independent experiments.

A prior report by Lo and Matthews (2012) identified an AHR binding site in intron 2 of the LAT1 gene by TCDD-ChIP-seq analysis in MCF-7 cells [36]. In order to characterize the mechanism of LAT1 induction, we measured AHR recruitment to the AHR response elements (AHR-REs) in LAT1 intron 2 by ChIP-qPCR analysis. The results showed a significant ($P < 0.05$) 4-fold increase in AHR binding to the intron 2 site in response to TCDD compared with vehicle (Fig. 5A). In accordance with its known mechanism of action, TCDD-increased (by 37-fold) AHR binding to AHR-REs that are located upstream from the CYP1B1 transcription start site (Fig. 5D).

By binding to AHR, the ARNT transcription factor promotes AHR recruitment to AHR-REs in TCDD target genes [16, 17]. We assessed ARNT binding to the LAT1 intron 2 and CYP1B1 using ChIP-qPCR analysis and the findings revealed its recruitment to AHR-

REs in the LAT1 and CYP1B1 genes was increased by 12- and 55-fold, respectively in response to TCDD (Fig. 5B and E). Prior reports indicate that AHR/ARNT heterodimers recruit the p300 transcription complex to TCDD target genes [19]. The AHR-REs in LAT1 and CYP1B1 genes exhibited 3-fold and 10-fold increases, respectively, in p300 binding in response to TCDD compared with vehicle (Fig. 5B and E).

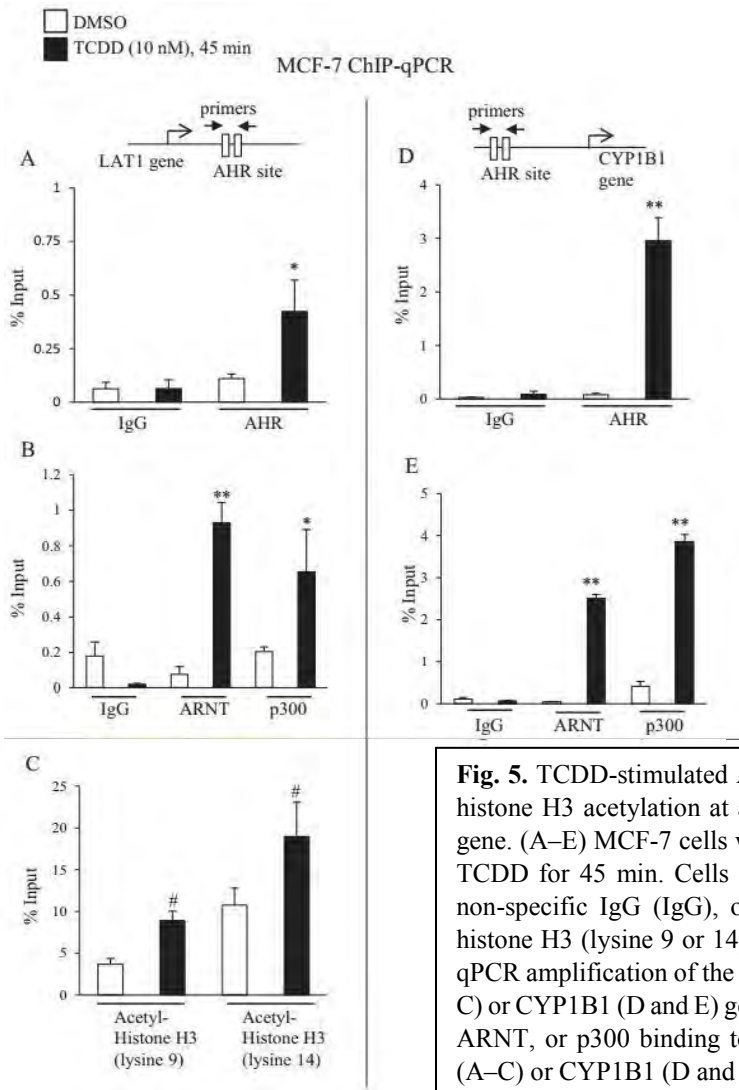


Fig. 5. TCDD-stimulated AHR/ARNT/p300 recruitment and histone H3 acetylation at an AHR binding site in the LAT1 gene. (A–E) MCF-7 cells were treated with DMSO or 10 nM TCDD for 45 min. Cells were then subjected to ChIP with non-specific IgG (IgG), or AHR, ARNT, p300, acetylated histone H3 (lysine 9 or 14) targeting antibodies, followed by qPCR amplification of the AHR binding site in the LAT1 (A–C) or CYP1B1 (D and E) genes. Significant increases in AHR, ARNT, or p300 binding to AHR binding sites in the LAT1 (A–C) or CYP1B1 (D and E) gene by TCDD are indicated by * $P < 0.05$, or ** $P < 0.01$. (C) Significant increases in the acetylation of lysine 9 or 14 in histone H3 at the AHR binding site in the LAT1 gene by TCDD are indicated by # $P < 0.05$. Data shown are the mean \pm S.E. of three independent experiments.

The p300 complex has inherent histone acetylase activity and is known to increase in histone H3 acetylation at lysine 9 and lysine 14, both of which are markers of active transcription [44]. Consistent with its physical recruitment to the LAT1 AHR-RE, we observed increases in the acetylation of histone H3 at lysine 9 and lysine 14 (by 2.4 and 1.8-fold, respectively) at the AHR-RE in response to TCDD (Fig. 5C). Collectively, these data indicate that exogenous regulation of LAT1 by TCDD is mediated via the AHR binding and recruitment of p300 to the AHR-RE in the LAT1 gene.

Experiment 5: Regulation of LAT1 by AHR promotes breast cancer cell proliferation

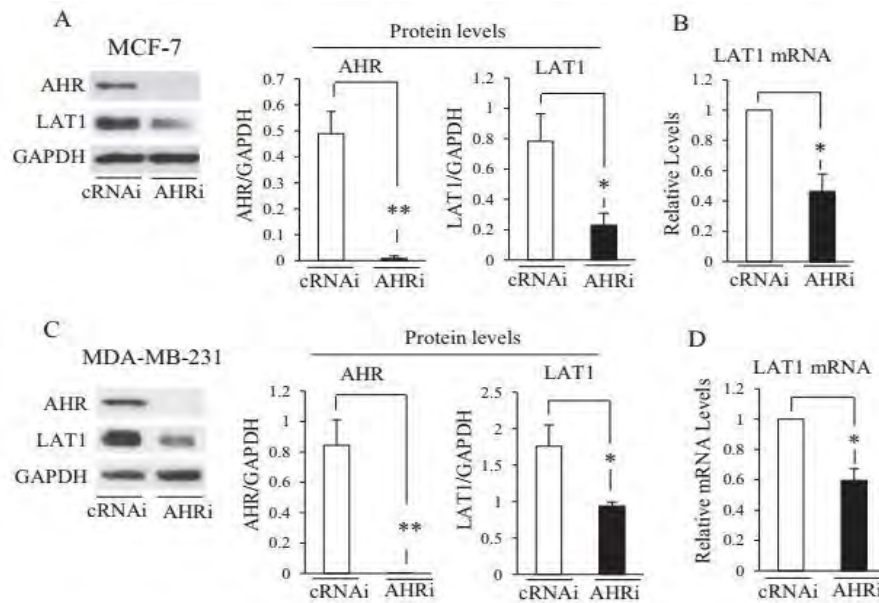


Fig. 6. Endogenous regulation of LAT1 by AHR in MCF-7 and MDA-MB-231 cells. (A–D), MCF-7 (A and B) or MDA-MB-231 (C and D) cells were transfected with control (cRNAi) or AHR (AHRi) siRNA for 72 or 48 h, respectively. (A and C) Total cellular protein was then isolated and subjected to Western blot analysis. Blots were then probed with the indicated antibodies. Relative levels of AHR or LAT1 protein was expressed as a ratio of AHR/GAPDH or LAT1/GAPDH, respectively. * $P < 0.05$; ** $P > 0.01$. (B and D) RT-qPCR analyses of LAT1 mRNA levels in MCF-7 (B) or MDA-MB-231 (D) cells transfected with cRNAi or AHRi. GAPDH mRNA levels were used to normalize samples. * $P < 0.05$. (A–D) Data shown are the mean \pm S.E. of three independent experiments.

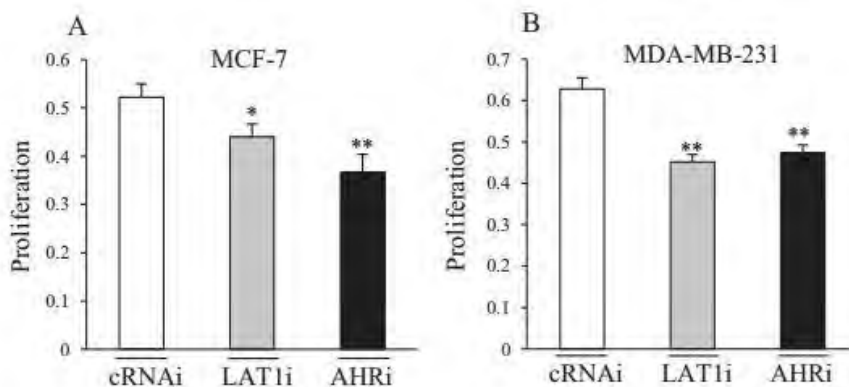


Fig. 7. AHR and LAT1 promote MCF-7 and MDA-MB-231 proliferation. (A and B), MCF-7 (A) or MDA-MB-231 (B) cells were transfected with cRNAi, LAT1i or AHRi for 3 days, followed by analysis of proliferation (please see methods for details). Significant decreases in proliferation by LAT1i or AHRi are indicated by * $P < 0.05$, or ** $P < 0.01$. Data shown are the mean \pm S.E. of nine replicates.

Endogenous regulation of LAT1 by AHR was investigated in MCF-7 and MDA-MB-231 cells because these BCC lines have been reported to exhibit endogenous AHR activity [30-34]. Western blot analysis revealed basal AHR and LAT1 protein expression in MCF-7 (Fig. 6A) and MDA-MB-231 (Fig. 6C) cells transfected with cRNAi. Transfection with AHRi reduced AHR protein in MCF-7 (Fig. 6A) and MDA-MB-231 cells (Fig. 6C) to levels that were not detected by standard Western blot analysis. Reducing AHR protein expression with AHRi also suppressed the levels of LAT1 protein in MCF-7 (by ~70%) (Fig. 6A) and MDA-MB-231 (by ~60%) (Fig. 6C) and the levels of LAT1 mRNA in MCF-7 (by ~50%) (Fig. 6B) or MDA-MB-231 (by ~40%) (Fig. 6D) compared with controls. These data indicate that endogenous AHR activity regulates LAT1 expression in MCF-7 and MDA-MB-231 cells.

Since LAT1 is known to promote cancer cell

proliferation by stimulating the amino acid uptake [24], we sought to determine if AHR expression and its regulation of LAT1 in MCF-7 and MDA-MB-231 are important for proliferation. To this end, MCF-7 and MDA-MB-231 cells were transfected with cRNAi, AHRi or LAT1-targeting siRNA (LAT1i). After 3 days, significant reductions in proliferation was observed in MCF-7 (Fig. 7A) and MDA-MB-231 (Fig. 7B) cells expressing LAT1i or AHRi compared with those transfected with cRNAi. These findings suggest that AHR regulation of LAT1 and LAT1 expression are important for the proliferation of MCF-7 and MDA-MB-231 cells.

DISCUSSION

The findings of this report provide new insight into exogenous and endogenous regulation of LAT1 by AHR. Reducing AHR with AHRi suppressed exogenous regulation of LAT1 by TCDD in MCF-7 cells (Fig. 2 and Fig. 3) and endogenous regulation of LAT1 in MCF-7 and MDA-MB-231 cells (Fig. 6). These findings indicate that AHR regulates LAT1 expression. ChIP-qPCR results indicate that exogenous regulation of LAT1 by TCDD is mediated via the AHR binding site in the LAT1 gene (Fig. 5). Indeed, the binding of AHR/ARNT/p300 and the acetylation of histone H3 at the AHR site in the LAT1 gene was increased by TCDD (Fig. 5). Consistent with reports showing that AHR promotes MCF-7 and MDA-MB-231 cancer processes [30, 34], our proliferation assays indicate that reducing AHR suppressed their proliferation (Fig. 7).

Prior reports have provided important insights into amino acid uptake by other transporters in MCF-7 and MDA-MB-231 cells. Karunakaran et al. demonstrated that SLC6A14 (also known as ATBo,+) is a Na⁺ dependent, estrogen-induced transporter that mediates the uptake of all essential amino acids, including leucine, in MCF-7 cells [45]. The SLC6A14 inhibitor α -methyl-dl-tryptophan stimulated apoptosis of MCF-7, but not MDA-MB-231 cells, which was attributed to selective expression of SLC6A14 in MCF-7, but not MDA-MB-231 cells [45]. Shennan et al. established that MCF-7, but not MDA-MB-231 cells express LAT2, which is an isoform of LAT1 that also mediates leucine uptake [46]. Our observation that MCF-7 cells exhibit high basal leucine uptake activity in the absence of TCDD can be explained by the transporter activity of SLC6A14 and LAT2 as well as basal LAT1 activity (Fig. 4). Since TCDD induction of SLC6A14 and LAT2 mRNA was not observed in our RNA-Seq data, we conclude that the increase in leucine uptake in the presence of TCDD in MCF-7 cells is mediated via increased expression of LAT1.

CYP1A1 and CYP1B1 harbor upstream AHR-REs within 1 kb of their transcription start sites [37, 47, 48]. Reported TCDD-ChIP-seq data indicated that the LAT1 gene lacks promoter AHR-REs [36], but its expression is regulated by an AHR binding site located in intron 2 (Fig. 5), which is 29 kb from the LAT1 promoter. Although long distance regulation of gene promoters by AHR-REs is relatively novel for TCDD, it is not uncommon for gene promoters to be regulated by distal enhancers [49].

AHR stimulation of transcription may rely on endogenous ligands. D'Amato et al. demonstrated that MDA-MB-231 cells synthesize kynurenine, which is a tryptophan metabolite and a known endogenous AHR ligand [30]. Production of kynurenine by MDA-MB-231 cells is mediated by tryptophan 2,3-dioxygenase (TDO2), which is the first and rate-limiting enzyme in the kynurenine synthesis pathway [30]. Thus, the observed AHR activity that is required for LAT1 expression in MDA-MB-231 cells could be attributed to kynurenine interacting with AHR. However, endogenous AHR activity could also reflect its interaction with the other tryptophan metabolites

that also function as AHR agonists such as kynurenic acid or xanthurenic acid [50]. Regulation of LAT1 by unliganded AHR is also a possibility, considering that AHR can be regulated by cyclic AMP [51, 52].

Previous reports have provided important evidence that breast cancer progression may require LAT1. For instance, LAT1 expression is upregulated in human breast tumors compared with normal breast tissue [40]. Shennan et al. demonstrated that 2-aminobicyclo-(2,2,1)-heptane-2-carboxylic acid (BCH), which inhibits L type transporters, suppressed the proliferation of MCF-7, MDA-MB-231 and ZR-75-1 BCCs [41]. Our findings now establish that specifically knocking down the expression of LAT1 with siRNA inhibits proliferation of MCF-7 and MDA-MB-231 cells (Fig. 7). In summary, our findings illustrate a new way AHR can drive tumor growth, by regulating the expression of the LAT1 transporter in tumor cells. Given the high levels of PAHs which activate AHR signaling are present in space [7, 8], exposure to PAHs in space could increase LAT1 expression in tissues and result in an increased risk for cancer development in astronauts, especially those on long and/or repeated space missions.

PRESENTATION AND PUBLICATION OF FINDINGS

This work was published in March 2016 in the journal, *Biochemical Pharmacology*. This work was also presented at Marshall University School of Medicine Health Sciences Research Day and at University of Kentucky Center for Clinical and Translational Science Spring Conference.

ROLE OF NASA IN THIS RESEARCH

The graduate fellowship award given to me by NASA is the sole reason this research was able to be done. Our laboratory is very small and has extremely limited funding. Without the assistance of NASA, I would have been forced to graduate early with limited experience. Now, with an extra first author publication, I am better suited for applying to jobs in the midst of this increasingly competitive research field. Without, NASA's assistance, my job search would likely be fruitless. For that I am forever thankful.

REFERENCES

1. Sorg, O., *AhR signalling and dioxin toxicity*. *Toxicol Lett*, 2014. **230**(2): p. 225-33.
2. Poland, A. and J.C. Knutson, *2,3,7,8-tetrachlorodibenzo-p-dioxin and related halogenated aromatic hydrocarbons: examination of the mechanism of toxicity*. *Annu Rev Pharmacol Toxicol*, 1982. **22**: p. 517-54.
3. Denison, M.S., et al., *Exactly the same but different: promiscuity and diversity in the molecular mechanisms of action of the aryl hydrocarbon (dioxin) receptor*. *Toxicol Sci*, 2011. **124**(1): p. 1-22.
4. Safe, S., S.O. Lee, and U.H. Jin, *Role of the aryl hydrocarbon receptor in carcinogenesis and potential as a drug target*. *Toxicol Sci*, 2013. **135**(1): p. 1-16.
5. Schlezinger, J.J., et al., *A role for the aryl hydrocarbon receptor in mammary gland tumorigenesis*. *Biol Chem*, 2006. **387**(9): p. 1175-87.

6. Shin, S.R., et al., *7,12-dimethylbenz(a)anthracene treatment of a c-rel mouse mammary tumor cell line induces epithelial to mesenchymal transition via activation of nuclear factor-kappaB*. *Cancer Res*, 2006. **66**(5): p. 2570-5.
7. Allamandola, L.J., S.A. Sandford, and B. Wopenka, *Interstellar polycyclic aromatic hydrocarbons and carbon in interplanetary dust particles and meteorites*. *Science*, 1987. **237**(4810): p. 56-9.
8. Allamandola, L.J., A.G. Tielens, and J.R. Barker, *Interstellar polycyclic aromatic hydrocarbons: the infrared emission bands, the excitation/emission mechanism, and the astrophysical implications*. *Astrophys J Suppl Ser*, 1989. **71**: p. 733-75.
9. Van den Berg, M., et al., *The 2005 World Health Organization reevaluation of human and Mammalian toxic equivalency factors for dioxins and dioxin-like compounds*. *Toxicol Sci*, 2006. **93**(2): p. 223-41.
10. Perdew, G.H., *Association of the Ah receptor with the 90-kDa heat shock protein*. *J Biol Chem*, 1988. **263**(27): p. 13802-5.
11. Kazlauskas, A., et al., *The hsp90 chaperone complex regulates intracellular localization of the dioxin receptor*. *Mol Cell Biol*, 2001. **21**(7): p. 2594-607.
12. Carver, L.A. and C.A. Bradfield, *Ligand-dependent interaction of the aryl hydrocarbon receptor with a novel immunophilin homolog in vivo*. *J Biol Chem*, 1997. **272**(17): p. 11452-6.
13. Meyer, B.K. and G.H. Perdew, *Characterization of the AhR-hsp90-XAP2 core complex and the role of the immunophilin-related protein XAP2 in AhR stabilization*. *Biochemistry*, 1999. **38**(28): p. 8907-17.
14. Meyer, B.K., et al., *Hepatitis B virus X-associated protein 2 is a subunit of the unliganded aryl hydrocarbon receptor core complex and exhibits transcriptional enhancer activity*. *Mol Cell Biol*, 1998. **18**(2): p. 978-88.
15. Kazlauskas, A., L. Poellinger, and I. Pongratz, *Evidence that the co-chaperone p23 regulates ligand responsiveness of the dioxin (Aryl hydrocarbon) receptor*. *J Biol Chem*, 1999. **274**(19): p. 13519-24.
16. Beischlag, T.V., et al., *The aryl hydrocarbon receptor complex and the control of gene expression*. *Crit Rev Eukaryot Gene Expr*, 2008. **18**(3): p. 207-50.
17. Reyes, H., S. Reisz-Porszasz, and O. Hankinson, *Identification of the Ah receptor nuclear translocator protein (Arnt) as a component of the DNA binding form of the Ah receptor*. *Science*, 1992. **256**(5060): p. 1193-5.
18. Beischlag, T.V., et al., *Recruitment of the NCoA/SRC-1/p160 family of transcriptional coactivators by the aryl hydrocarbon receptor/aryl hydrocarbon receptor nuclear translocator complex*. *Mol Cell Biol*, 2002. **22**(12): p. 4319-33.

19. Taylor, R.T., et al., *Roles of coactivator proteins in dioxin induction of CYP1A1 and CYP1B1 in human breast cancer cells*. Toxicol Sci, 2009. **107**(1): p. 1-8.
20. Wang, S. and O. Hankinson, *Functional involvement of the Brahma/SWI2-related gene 1 protein in cytochrome P4501A1 transcription mediated by the aryl hydrocarbon receptor complex*. J Biol Chem, 2002. **277**(14): p. 11821-7.
21. Kanai, Y., et al., *Expression cloning and characterization of a transporter for large neutral amino acids activated by the heavy chain of 4F2 antigen (CD98)*. J Biol Chem, 1998. **273**(37): p. 23629-32.
22. Segawa, H., et al., *Identification and functional characterization of a Na⁺-independent neutral amino acid transporter with broad substrate selectivity*. J Biol Chem, 1999. **274**(28): p. 19745-51.
23. Yanagida, O., et al., *Human L-type amino acid transporter 1 (LAT1): characterization of function and expression in tumor cell lines*. Biochim Biophys Acta, 2001. **1514**(2): p. 291-302.
24. Wang, Q. and J. Holst, *L-type amino acid transport and cancer: targeting the mTORC1 pathway to inhibit neoplasia*. Am J Cancer Res, 2015. **5**(4): p. 1281-94.
25. Laplante, M. and D.M. Sabatini, *mTOR signaling at a glance*. J Cell Sci, 2009. **122**(Pt 20): p. 3589-94.
26. Laplante, M. and D.M. Sabatini, *mTOR signaling in growth control and disease*. Cell, 2012. **149**(2): p. 274-93.
27. Populo, H., J.M. Lopes, and P. Soares, *The mTOR signalling pathway in human cancer*. Int J Mol Sci, 2012. **13**(2): p. 1886-918.
28. Bartlett, J.M., et al., *Mammostrat as an immunohistochemical multigene assay for prediction of early relapse risk in the tamoxifen versus exemestane adjuvant multicenter trial pathology study*. J Clin Oncol, 2012. **30**(36): p. 4477-84.
29. Bartlett, J.M., et al., *Mammostrat as a tool to stratify breast cancer patients at risk of recurrence during endocrine therapy*. Breast Cancer Res, 2010. **12**(4): p. R47.
30. D'Amato, N.C., et al., *A TDO2-AhR signaling axis facilitates anoikis resistance and metastasis in triple-negative breast cancer*. Cancer Res, 2015. **75**(21): p. 4651-64.
31. Goode, G., S. Pratap, and S.E. Eltom, *Depletion of the aryl hydrocarbon receptor in MDA-MB-231 human breast cancer cells altered the expression of genes in key regulatory pathways of cancer*. PLoS One, 2014. **9**(6): p. e100103.
32. Goode, G.D., et al., *Knockdown of aberrantly upregulated aryl hydrocarbon receptor reduces tumor growth and metastasis of MDA-MB-231 human breast cancer cell line*. Int J Cancer, 2013. **133**(12): p. 2769-80.

33. Salisbury, T.B., et al., *Endogenous aryl hydrocarbon receptor promotes basal and inducible expression of tumor necrosis factor target genes in MCF-7 cancer cells*. *Biochem Pharmacol*, 2014. **91**(3): p. 390-9.
34. Tomblin, J.K. and T.B. Salisbury, *Insulin like growth factor 2 regulation of aryl hydrocarbon receptor in MCF-7 breast cancer cells*. *Biochem Biophys Res Commun*, 2014. **443**(3): p. 1092-6.
35. Livak, K.J. and T.D. Schmittgen, *Analysis of relative gene expression data using real-time quantitative PCR and the 2(-Delta Delta C(T)) Method*. *Methods*, 2001. **25**(4): p. 402-8.
36. Lo, R. and J. Matthews, *High-resolution genome-wide mapping of AHR and ARNT binding sites by ChIP-Seq*. *Toxicol Sci*, 2012. **130**(2): p. 349-61.
37. Matthews, J., et al., *Aryl hydrocarbon receptor-mediated transcription: ligand-dependent recruitment of estrogen receptor alpha to 2,3,7,8-tetrachlorodibenzo-p-dioxin-responsive promoters*. *Mol Cell Biol*, 2005. **25**(13): p. 5317-28.
38. Spink, D.C., et al., *Differential expression of CYP1A1 and CYP1B1 in human breast epithelial cells and breast tumor cells*. *Carcinogenesis*, 1998. **19**(2): p. 291-8.
39. Vasiliou, V., et al., *Mouse cytosolic class 3 aldehyde dehydrogenase (Aldh3a1): gene structure and regulation of constitutive and dioxin-inducible expression*. *Pharmacogenetics*, 1999. **9**(5): p. 569-80.
40. Liang, Z., et al., *Potential Biomarker of L-type Amino Acid Transporter 1 in Breast Cancer Progression*. *Nucl Med Mol Imaging*, 2011. **45**(2): p. 93-102.
41. Shennan, D.B. and J. Thomson, *Inhibition of system L (LAT1/CD98hc) reduces the growth of cultured human breast cancer cells*. *Oncol Rep*, 2008. **20**(4): p. 885-9.
42. Shennan, D.B., et al., *L-leucine transport in human breast cancer cells (MCF-7 and MDA-MB-231): kinetics, regulation by estrogen and molecular identity of the transporter*. *Biochim Biophys Acta*, 2004. **1664**(2): p. 206-16.
43. Kim, S.H., et al., *Novel compound 2-methyl-2H-pyrazole-3-carboxylic acid (2-methyl-4-*o*-tolylazo-phenyl)-amide (CH-223191) prevents 2,3,7,8-TCDD-induced toxicity by antagonizing the aryl hydrocarbon receptor*. *Mol Pharmacol*, 2006. **69**(6): p. 1871-8.
44. Grant, P.A., *A tale of histone modifications*. *Genome Biol*, 2001. **2**(4): p. REVIEWS0003.
45. Karunakaran, S., et al., *SLC6A14 (ATB0,+) protein, a highly concentrative and broad specific amino acid transporter, is a novel and effective drug target for treatment of estrogen receptor-positive breast cancer*. *J Biol Chem*, 2011. **286**(36): p. 31830-8.
46. Shennan, D.B. and C.A. Boyd, *The functional and molecular entities underlying amino acid and peptide transport by the mammary gland under different physiological and pathological conditions*. *J Mammary Gland Biol Neoplasia*, 2014. **19**(1): p. 19-33.

47. Kress, S., J. Reichert, and M. Schwarz, *Functional analysis of the human cytochrome P4501A1 (CYP1A1) gene enhancer*. Eur J Biochem, 1998. **258**(2): p. 803-12.
48. Tsuchiya, Y., M. Nakajima, and T. Yokoi, *Critical enhancer region to which AhR/ARNT and Sp1 bind in the human CYP1B1 gene*. J Biochem, 2003. **133**(5): p. 583-92.
49. Jin, F., et al., *A high-resolution map of the three-dimensional chromatin interactome in human cells*. Nature, 2013. **503**(7475): p. 290-4.
50. DiNatale, B.C., et al., *Kynurenic acid is a potent endogenous aryl hydrocarbon receptor ligand that synergistically induces interleukin-6 in the presence of inflammatory signaling*. Toxicol Sci, 2010. **115**(1): p. 89-97.
51. Oesch-Bartlomowicz, B., et al., *Aryl hydrocarbon receptor activation by cAMP vs. dioxin: divergent signaling pathways*. Proc Natl Acad Sci U S A, 2005. **102**(26): p. 9218-23.
52. Oesch-Bartlomowicz, B. and F. Oesch, *Role of cAMP in mediating AHR signaling*. Biochem Pharmacol, 2009. **77**(4): p. 627-41.